



Bridge Pier Flow Interaction and Its Effect on the Process of Scouring

By

Chij Kumar Shrestha

A thesis submitted in fulfilment
of the requirement for the degree of
Doctor of Philosophy

Faculty of Engineering and Information Technology
University of Technology Sydney (UTS)

September 2015

CERTIFICATE OF ORIGINAL AUTHORSHIP

I certify that the work in this thesis has not previously been submitted for a degree nor has it been submitted as part of requirements for a degree except as fully acknowledged within the text.

I also certify that the thesis has been written by me. Any help that I have received in my research work and the preparation of the thesis itself has been acknowledged. In addition, I certify that all information sources and literature used are indicated in the thesis.

Chij Kumar Shrestha

Sydney, September 2015

ABSTRACT

Previous investigations indicate that scour around bridge piers is a contributor in the failure of waterway bridges. Hence, it is essential to determine the accurate scour depth around the bridge piers. For this purpose, deep understanding of flow structures around bridge piers is very important. A number of studies on flow structures and local scour around bridge piers have been conducted in the past. Most of the studies, carried out to develop a design criterion, were based on a single column. However, in practice, bridge piers can comprise multiple columns that together support the bridge superstructure. Typically, the columns are aligned in the flow direction. The design criteria developed for a single column ignore the most important group effects for multiple columns cases such as sheltering, reinforcement and interference effects. These group effects can significantly be influenced by the variation of spacing between two columns. This is evident by the fact that insufficient investigations and development have been reported for the flow structure and maximum scour depth around bridge piers comprising multiple columns. It is therefore necessary to investigate the effects of multiple columns and spacing between them on the flow structure and local scour around bridge piers and develop a practical method to predict the maximum scour depth.

The main objectives of this research work are to analyse the effect of spacing between two in-line circular columns on the flow structure and to develop a reliable method for prediction of the maximum local scour depth around bridge piers. To meet the objectives this research, detailed experimental studies on three dimensional flow structures and local scour around two-column bridge piers were carried out. A series of laboratory experiments were conducted for no column, a single column and two in-line columns cases with different spacing. Two in-line columns were installed at the centre of the flume along the longitudinal axis. Three dimensional flow velocities in three different horizontal planes were measured at different grid points within the flow using a micro acoustic doppler velocimeter (ADV). The velocity was captured at a frequency of 50Hz. Additionally, in vertical planes, particle image velocimetry (PIV) technique was employed to measure the two dimensional instantaneous velocity components. All experiments on flow structures were conducted under no scouring and clear water flow

conditions. Similarly, an array of experimental tests were conducted under different flow conditions for studying the temporal development of scour depth and the maximum local scour depth around a single column and two-column bridge piers.

The measured instantaneous three dimensional velocity components were analysed and the results for flow field and turbulence characteristics were presented in graphical forms using vector plots, streamline plots, contour plots and profile plots. The results indicated that the flow structures around two- columns bridge piers is more complex than that of a single column case. Furthermore, the spacing between two columns significantly affects the flow structures, particularly in the wake of the columns. It was observed that for the spacing-column diameter ratio (L/D) < 3 , the vortex shedding occurred only behind the downstream column. Hence, the flow pattern was more or less similar to that of the single column case. However, the turbulence characteristics such as turbulence intensity, turbulent kinetic energy and Reynolds shear stresses were notably different from those of a single column case. When the spacing was in the range of $2 \leq L/D \leq 3$, stronger turbulence structures were noticed behind the upstream column. Further increase in the spacing between two columns resulted in a decrease in the strength of turbulence characteristics.

The experimental results on temporal development of local scour depth reveal that approximately 90% of the maximum scour depth around the upstream column was achieved within the first 10 hours of the experiments. However, for the downstream column, 90% of the scour depth was achieved within 20 hours. Similarly, the results from the experiments on local scour indicated that the maximum scour depth occurred at the upstream column, when the spacing between two columns was $2.5D$. The maximum value of local scour depth for the two-column case was observed about 18% higher than the value obtained for the single column case. The reasons for maximum scour depth at the spacing of $2.5D$ were identified as the reinforcing effect of downstream column, the strong horseshoe vortex at upstream column, strong turbulence characteristics at the wake of upstream column, and the highest probability of occurrence of sweep events at upstream side of upstream column. Furthermore, a semi empirical equation was developed to predict the maximum scour depth as a function of the spacing between two

columns. The findings of this study can be used to facilitate the position of columns when scouring is a design concern.

ACKNOWLEDGMENT

This thesis could not be completed without the assistance, understanding and counselling of several people throughout the research work. I would like to express my sincere gratitude to my supervisors, Associate Professor Hadi Khabbaz and Professor Alireza Keshavarzi for their support and guidance during my PhD study. Apart from the academic supervision, inspiring suggestions for work-family life balance and future career development from my supervisors were the important factors for successful completion of my thesis.

I would like to express my sincere thanks to Dr. Behzad Fatahi for coordinating my Doctoral Assessment and for his valuable suggestions. I cannot forget external and internal assessors Dr. Farzad Meysami and Dr. Hamid Valipour, respectively for evaluating my Doctoral Assessment report and providing constructive recommendations. My sincere thanks also go to Professor Bruce W. Melville and Associate Professor James Ball for their great contributions and suggestions as co-authors for the publication of conference and Journal papers. Furthermore, I would like to thank Mr. Rami Haddad and Mr. David Hooper for their valuable support for smooth conduction of the experimental tests in the Hydraulics Laboratory. I would also like to thank my close friends Dr. Aslan Hokmabadi and Dr. Md. Mahbube Subhani for sharing their time and friendship to make a life more fun and easy.

I am greatly indebted to my parents, my brother Manoj and my sister Shanti for their love, support and encouragement. Without their many years of encouragement and support, I may never have reached where I am today. They always refuel me with courage and inspiration to overcome any hardship encountered in my life. Most importantly, I am extremely indebted to my wife Chandra Laxmi Shrestha for her great love, kind patience and invaluable support. Thank you very much for your sacrifice in shouldering far more than your fair share of parenting and for being a vital source of encouragement when I feel lack of faith and energy.

Finally, I would be remiss if I did not acknowledge my son Charchit and daughter Chaarvi for their understanding, love and affection throughout my PhD research.

LIST OF PUBLICATIONS BASED ON THIS RESEARCH

Peer-reviewed Conference Papers

1. SHRESTHA, C. K., KESHAVARZI, A., KHABBAZ, H. & BALL, J. 2012. Experimental Study of the Flow Structure Interactions between Bridge Piers 34th Hydrology and Water Resources Symposium (HWRS 2012), Sydney, Australia.
2. SHRESTHA, C. K., KESHAVARZI, A. & KHABBAZ, H. 2013. Flow Structure at Downstream Side of Two Sequential Bridge Piers. *In: Shoji Fukuoka, Hajime Nakagawa, Tetsuya Sumi & Hao Zhang, eds. International Symposium on River Sedimentation (ISRS 2013), Kyoto, Japan. CRC Press/Balkema, 199.*
3. SHRESTHA, C. K., KESHAVARZI, A. & KHABBAZ, H. 2013. Experimental Study of Bridge -Pier Interaction and its Effect on Bed Scour 6th International Perspective on Water Resources and the Environment (IPWE 2013), Izmir, Turkey.

CONTENTS

CERTIFICATE OF ORIGINAL AUTHORSHIP	i
ABSTRACT	ii
ACKNOWLEDGMENT	v
LIST OF PUBLICATIONS BASED ON THIS RESEARCH	vi
CONTENTS.....	vii
LIST OF NOTATIONS	xxiii
1. INTRODUCTION.....	2
1.1 Background	2
1.2 Research Objectives	5
1.3 Scope and Limitation of Research	6
1.4 Research Significance and Innovation	6
1.5 Research Methodology.....	7
1.6 Synopsis of Thesis	8
2. LITERATURE REVIEW.....	11
2.1 Introduction.....	11
2.2 Scour at Bridge Crossings.....	11
<i>2.2.1 General Scour.....</i>	<i>12</i>
<i>2.2.2 Localised Scour</i>	<i>13</i>
2.3 Sediment Transport and Local Scour around Bridge Piers	13
<i>2.3.1 Basics of Sediment Transport.....</i>	<i>13</i>
<i>2.3.2 Local Scour around Bridge Piers.....</i>	<i>24</i>

2.3.3 Mechanism of Local Scour	26
2.3.4 Parameters for Analysis of Pier Scour	29
2.3.5 Factors Affecting the Local Scour at Bridge Site	31
2.3.6 Equilibrium Scour Depth.....	43
2.3.7 Temporal Variation of Scour Depth.....	44
2.3.8 Estimation of Equilibrium Scour Depth	47
2.4 Open Channel Flow and Flow around Bridge Piers	58
2.4.1 Hydraulics of Open Channel Flow.....	58
2.4.2 Basic Equations for Flow in Open Channels	60
2.4.3 Boundary Layer in Open Channel Flow	63
2.4.4 Turbulence in Open Channel Flow	65
2.4.5 Flow around Bridge Piers	66
2.5 Summary and Identification of the Gap in Literature	78
3. EXPERIMENTAL SETUP AND METHODOLOGY	82
3.1 Introduction.....	82
3.2 Experimental Setup and Design.....	82
3.2.1 Flume and its Components	82
3.2.2 Electromagnetic Flow Meter.....	84
3.2.3 Vernier Point Gauge.....	84
3.2.4 Model Columns of Bridge Piers	85
3.2.5 Bed Materials	86

3.2.6	<i>Flow Conditions</i>	87
3.3	Velocity Measurement	89
3.3.1	<i>Acoustic Doppler Velocimetry (ADV)</i>	89
3.3.2	<i>Particle Image Velocimetry (PIV)</i>	91
3.4	Experimental Procedure and Data Acquisition	94
3.4.1	<i>Procedure for Fixed Bed Experiments in Flume 1</i>	94
3.4.2	<i>Procedure for Mobile Bed Experiments in Flume 1</i>	97
3.4.3	<i>Procedure for Fixed Bed Experiments in Flume 2</i>	97
3.5	Summary	99
4.	RESULTS AND DISCUSSION ON FLOW STRUCTURE	102
4.1	Introduction	102
4.2	Previous Investigations on Flow around Bridge Piers	102
4.3	Flow around the Bridge Piers in Horizontal Plane	106
4.3.1	<i>Flow Pattern</i>	107
4.3.2	<i>Three Dimensional Velocity Component</i>	110
4.3.3	<i>Turbulence Intensity</i>	124
4.3.4	<i>Turbulent Kinetic Energy</i>	132
4.3.5	<i>Reynolds Shear Stresses</i>	135
4.4	Flow around the Bridge Piers in Vertical Plane	138
4.4.1	<i>Flow Pattern</i>	140
4.4.2	<i>Time Average Velocity Components</i>	145

4.4.3	<i>Turbulence Intensity Components</i>	156
4.4.4	<i>Turbulent Kinetic Energy</i>	166
4.4.5	<i>Reynolds Shear Stresses</i>	171
4.5	Bursting Phenomenon and Quadrant Analysis	175
4.5.1	<i>Introduction</i>	175
4.5.2	<i>Review on Quadrant Analysis</i>	176
4.5.3	<i>Results of Quadrant Analysis</i>	181
4.6	Summary	191
5.	RESULTS AND DISCUSSION ON LOCAL SCOUR	196
5.1	Introduction	196
5.2	Previous Investigations on Scour around Bridge Piers	196
5.3	Temporal Development of Scour Depth	199
5.4	Equilibrium Scour Depth for Two-Column Case	202
5.5	Comparison of Observed and Predicted Maximum Scour Depths	209
5.6	Scour Profile along Centerline of the Bridge Piers	211
5.7	Width of the Scour Hole	213
5.8	Summary	215
6.	CONCLUSION AND RECOMMENDATIONS	219
6.1	Introduction	219
6.2	Conclusions	219
6.3	Recommendations of Future Research	225
	REFERENCES	227
	APPENDIX-A: PLOTS FOR VELOCITY COMPONENTS	243

A.1 Plots of Velocity Components in Horizontal Plane	243
A.2 Plots of Velocity Components for Vertical Plane	274
A.3 Table of Results on Velocity Components.....	297
APPENDIX-B: PLOTS FOR TURBULENCE INTENSITIES.....	303
B.1 Plots of Turbulence Intensity in Horizontal Plane	303
B.2 Plots of Turbulence Intensity in Vertical Plane.....	324
B.3 Table of Results on Turbulence Intensity Components	340
APPENDIX-C: PLOTS FOR TURBULENT KINETIC ENERGY.....	346
C.1 Plots of Turbulent Kinetic Energy in Horizontal Plane.....	346
C.2 Plots of Turbulent Kinetic Energy in Vertical Plane.....	355
C.3 Table of Results on Turbulent Kinetic Energy.....	363
APPENDIX-D: PLOTS FOR REYNOLDS STRESSES.....	364
D.1 Profile Plots of Reynolds Stresses in Horizontal Plane.....	364
D.2 Plots of Reynolds Stresses in Vertical Plane.....	368
D.3 Table of Results on Reynolds Shear Stresses	376
APPENDIX-E PLOTS FOR QUADRANT ANALYSIS	378
E.1 Probability of Occurrence of the Events at Upstream and Downstream sides	378
E.2 Profile Plots for Stress Fraction Contribution of the Events for the Production of Reynolds Stress.....	388

LIST OF FIGURES

Figure 1.1 Bridge piers experiencing the flood events (USGS (2014)	4
Figure 1.2 a) Scour around bridge piers on the Logan river, Australia; (Queensland Government (2013) ; and b) Scour around bridge piers on the Tinau river, Nepal, (KC (2014)	4
Figure 1.3 A bridge over the Gaula river in India washed away by flood in July 2008, (Bhatia (2013)	5
Figure 2.1 Types of scour at a bridge, (after Melville and Coleman, 2000).....	11
Figure 2.2 Classification of scour (after Melville and Coleman, 2000).....	12
Figure 2.3 Local scour at bridge piers; (Vasquez, 2006).....	13
Figure 2.4 Threshold condition for the sediment entrainment.....	15
Figure 2.5 Shields diagram for incipient motion of sediment (after Simons and Senturk, 1992)	17
Figure 2.6 Shear velocity chart for quartz sediment in water at 20° C; (after Melville and Coleman, 2000)	18
Figure 2.7 Definition sketch of suspended load transport; (after Van Rijn, 1993).....	22
Figure 2.8 Shape factor for different suspension numbers; (after Van Rijn, 1993).....	23
Figure 2.9 Local scour around bridge piers as a function of time; (after Richardson and Davis, 2001)	25
Figure 2.10 Flow field around bridge piers, (Ettema et al., 2011).....	27
Figure 2.11 Influence of flow shallowness on local scour depth, (after Melville and Coleman, 2000).....	33
Figure 2.12 Effect of sediment coarseness on local scour; (after Melville and Coleman, 2000)	34
Figure 2.13 Effect of sediment non-uniformity on local scour at bridge piers under clear water condition; (after Melville and Coleman, 2000).....	35

Figure 2.14 Variation of local scour depth with sediment non-uniformity, (after Melville and Coleman, 2000)	36
Figure 2.15 Basic pier shapes; (after Ettema et al., 2011)	37
Figure 2.16 Variation of local scour depth with pier alignment; (after Melville and Coleman, 2000)	38
Figure 2.17 Variation of local scour depth with flow intensity, V/V_c , (after Melville and Coleman, 2000)	39
Figure 2.18 Effect of flow intensity on local scour depth in uniform sediment (after Melville and Coleman, 2000)	40
Figure 2.19 Effect of flow intensity on local scour depth in non-uniform sediment (after Melville and Coleman, 2000)	41
Figure 2.20 Variation of scour depth with Froude number; (after Ettema et al., 2006) .	42
Figure 2.21 Time development of scour depth under clear water and live bed conditions; (after Ettema et al., 2011)	43
Figure 2.22 Temporal development of scour depth; (after Melville and Chiew, 1999) .	46
Figure 2.23 Notations for continuity equations; (after Chaudhry, 2007)	61
Figure 2.24 Notations for momentum equations and application; (after Chaudhry, 2007)	61
Figure 2.25 Notations for energy equations	63
Figure 2.26 Development of boundary layer in open channel (Simons, 1992)	64
Figure 2.27 Definition sketch of flow regions; (after Sumer and Fredsoe, 1997)	69
Figure 2.28 Flow regimes around smooth circular cylinder in steady current, (Sumer and Fredsoe, 1997)	72
Figure 2. 29 Definition sketch of flow interference region for two cylinders arrangements; (after Sumner, 2010)	73
Figure 2.30 Classification of flow regimes for two tandem cylinders; (after Sumner, 2010)	73

Figure 2.31 Schematics of vortex shedding a) Prior to shedding of Vortex A, Vortex B is being drawn across the wake, b) Prior to shedding of Vortex B, Vortex C is being drawn across the wake (Sumer and Fredsoe, 1997).....	77
Figure 2.32 Strouhal number as a function of Reynolds number; (Sumer and Fredsoe, 1997)	78
Figure 3.1 Schematic diagram of Flume 1	83
Figure 3.2 Schematic diagram of Flume 2	83
Figure 3.3 Electromagnetic flow meter (courtesy of Siemens).....	84
Figure 3.4 Vernier point gauge to measure the scour depth	85
Figure 3.5 Model columns showing the spacing between them	85
Figure 3.6 Grain size distribution curve of the sand used.....	87
Figure 3.7 Velocity measurement a) Acoustic Doppler Velocimeter (ADV) (SonTek (2012), and b) measuring velocity in laboratory	90
Figure 3.8 ADV probe and signal processor in splash proof housing (SonTek (2012)..	91
Figure 3.9 Schematic illustration of PIV system, (ILA-GmbH (2004).....	92
Figure 3.10 Digital charged coupled device (CCD) camera,(PCO-TECH (2008)	93
Figure 3.11 Laser source and the controlling system: a) laser head with mirrored arm (ILA-GmbH), and b) ICE450 power supply system (Quantel (2006)	94
Figure 3.12 Measurement grid in horizontal plane (top view)	96
Figure 3.13 Different axes of PIV measurements (top view)	98
Figure 4.1 Definition sketch of the bridge piers arrangement	106
Figure 4.2 Schematic diagram of different axis of data analysis in horizontal planes..	107
Figure 4.3 Flow pattern around a single column in horizontal plane at $Z/h = 0.09$ a) Vector plot, and b) Streamline plot.....	108

Figure 4.4 Flow pattern around two columns with $L/D = 3$ in horizontal plane at $Z/h = 0.09$ a) Vector plot, and b) Streamline plot.....	109
Figure 4.5 Contour plots of streamwise velocity component for the single column case in different horizontal planes a) at $Z/h = 0.09$, b) at $Z/h = 0.26$ and c). at $Z/h = 0.54$..	111
Figure 4.6 Profile plots of streamwise velocity component for the single column case in different horizontal planes along three different longitudinal axes a) at $Z/h = 0.09$, b) at $Z/h = 0.26$ and c). at $Z/h = 0.54$	112
Figure 4.7 Contour plots of streamwise velocity component for two columns case with $L/D = 3$ in different horizontal planes a) at $Z/h = 0.09$, b) at $Z/h = 0.26$ and c). at $Z/h = 0.54$	113
Figure 4.8 Profile plots of the streamwise velocity component for two-column case with $L/D = 3$ in different horizontal planes along three different longitudinal axes a) at $Z/h = 0.09$, b) at $Z/h = 0.26$ and c). at $Z/h = 0.54$	114
Figure 4.9 Contour plots of transverse velocity component for the single column case in different horizontal planes a) at $Z/h = 0.09$, b) at $Z/h = 0.26$ and c). at $Z/h = 0.54$	115
Figure 4.10 Profile plots of transverse velocity component for the single column case in different horizontal planes along three different longitudinal axes a) at $Z/h = 0.09$, b) at $Z/h = 0.26$ and c). at $Z/h = 0.54$	116
Figure 4.11 Contour plots of transverse velocity component for the two-column case with $L/D = 3$ in different horizontal planes a) at $Z/h = 0.09$, b) at $Z/h = 0.26$ and c). at $Z/h = 0.54$	117
Figure 4.12 Profile plots of transverse velocity component for the two-column case with $L/D = 3$ in different horizontal planes along three different longitudinal axes a) at $Z/h = 0.09$, b) at $Z/h = 0.26$ and c). at $Z/h = 0.54$	118
Figure 4.13 Contour plots of vertical velocity component for the single column case in different horizontal planes a) at $Z/h = 0.09$, b) at $Z/h = 0.26$ and c). at $Z/h = 0.54$	120
Figure 4.14 Profile plots of vertical velocity component for the single column case in different horizontal planes along three different longitudinal axes a) at $Z/h = 0.09$, b) at $Z/h = 0.26$ and c). at $Z/h = 0.54$	121

Figure 4.15 Contour plots of vertical velocity component for the two-column case with $L/D = 3$ in different horizontal planes a) at $Z/h = 0.09$, b) at $Z/h = 0.26$ and c). at $Z/h = 0.54$	122
Figure 4.16 Profile plots of vertical velocity component for the two-column case with $L/D = 3$ in different horizontal planes along three different longitudinal axes a) at $Z/h = 0.09$, b) at $Z/h = 0.26$ and c). at $Z/h = 0.54$	123
Figure 4.17 Contour plots of streamwise turbulence component for the single column case in different horizontal planes a) at $Z/h = 0.09$, b) at $Z/h = 0.26$ and c). at $Z/h = 0.54$	124
Figure 4.18 Profile plots of streamwise turbulence intensity component for the single column case in different horizontal planes along three different longitudinal axes a) at $Z/h = 0.09$, b) at $Z/h = 0.26$ and c). at $Z/h = 0.54$	125
Figure 4.19 Contour plots of streamwise turbulence intensity component for the two-column case with $L/D = 3$ in different horizontal planes a) at $Z/h = 0.09$, b) at $Z/h = 0.26$ and c). at $Z/h = 0.54$	126
Figure 4.20 Profile plots of streamwise turbulence intensity component for the two-column case with $L/D = 3$ in different horizontal planes along three different longitudinal axes a) at $Z/h = 0.09$, b) at $Z/h = 0.26$ and c). at $Z/h = 0.54$	127
Figure 4.21 Contour plots of transverse turbulence intensity component for the single column case in different horizontal planes a) at $Z/h = 0.09$, b) at $Z/h = 0.26$ and c). at $Z/h = 0.54$	128
Figure 4.22 Contour plots of transverse turbulence intensity component for the two-column case with $L/D = 3$ in different horizontal planes a) at $Z/h = 0.09$, b) at $Z/h = 0.26$ and c). at $Z/h = 0.54$	129
Figure 4.23 Contour plots of vertical turbulence intensity component for the single column case in different horizontal planes a) at $Z/h = 0.09$, b) at $Z/h = 0.26$ and c). at $Z/h = 0.54$	130

Figure 4.24 Contour plots of vertical turbulence intensity component for the two-column case with $L/D = 3$ in different horizontal planes a) at $Z/h = 0.09$, b) at $Z/h = 0.26$ and c). at $Z/h = 0.54$	131
Figure 4.25 Contour plots of turbulent kinetic energy for the single column case in different horizontal planes a) at $Z/h = 0.09$, b) at $Z/h = 0.26$ and c). at $Z/h = 0.54$	134
Figure 4.26 Contour plots of turbulent kinetic energy for the two-column case with $L/D = 3$ in different horizontal planes a) at $Z/h = 0.09$, b) at $Z/h = 0.26$ and c). at $Z/h = 0.54$	135
Figure 4.27 Profile plots of Reynold shear stresses for the single column case in different horizontal planes along axis of symmetry a) in u-v plane, b) in u-w plane, and c) in v-w plane.....	136
Figure 4.28 Profile plots of Reynolds shear stresses for two-column case with $L/D = 3$ in different horizontal planes along axis of symmetry a) in u-v plane, b) in u-w plane, and c) in v-w plane	137
Figure 4.29 Schematic diagram of different axis of data analysis at upstream and downstream side of the columns in vertical planes (US, B and DS stand for upstream side, between and downstream side of the columns, respectively).....	139
Figure 4.30 Vector plots for single column a) vertical plane at $Y/D = 0$, and b) vertical plane at $Y/D = 1.25$	142
Figure 4.31 Vector plots for two columns cases with $L/D = 3$ a) vertical plane at $Y/D = 0$, and b) vertical plane at $Y/D = 1.25$	143
Figure 4.32 Streamline plots for single column a) vertical plane at $Y/D = 0$, and b) vertical plane at $Y/D = 1.25$	144
Figure 4.33 Streamline plots for two columns cases with $L/D = 3$ a) vertical plane at $Y/D = 0$, and b) vertical plane at $Y/D = 1.25$	145
Figure 4.34 Contour plots of streamwise velocity component for the single column case in different vertical planes a) at $Y/D = 0$, and b) at $Y/D = 1.25$	146
Figure 4.35 Profile plots of streamwise velocity component for the single column case in vertical plane at axis of symmetry a) upstream side; b) downstream side.....	147

Figure 4.36 Contour plots of streamwise velocity component for the case of two in-line columns with $L/D = 3$ in different vertical planes a) at $Y/D = 0$, and b) at $Y/D = 1.25$	149
Figure 4.37 Profile plots of streamwise velocity component for two columns case with $L/D = 3$ in vertical plane at axis of symmetry a) upstream side; b) downstream side ..	150
Figure 4.38 Profile plots of velocity components between two columns with $L/D = 3$ in vertical plane at axis of symmetry a) streamwise component, b) vertical component ..	150
Figure 4.39 Contour plots of vertical velocity component for single column case in different vertical planes a) at $Y/D = 0$, and b) at $Y/D = 1.25$	152
Figure 4.40 Profile plots of vertical velocity component for single column case in vertical plane at axis of symmetry a) upstream side; b) downstream side.....	153
Figure 4.41 Contour plots of vertical velocity component for the two-column case with $L/D = 3$ in different vertical planes a) at $Y/D = 0$, and b) at $Y/D = 1.25$	154
Figure 4.42 Profile plots of vertical velocity component for the two-column case with $L/D = 3$ in vertical plane at axis of symmetry a) upstream side; b) downstream side ..	155
Figure 4.43 Profile plots of velocity components between two columns with $L/D = 3$ in vertical plane at axis of symmetry a) streamwise component, b) vertical component ..	156
Figure 4.44 Contour plots of streamwise turbulence intensity component for the single column case in different vertical planes a) at $Y/D = 0$, and b) at $Y/D = 1.25$	157
Figure 4.45 Profile plots of streamwise turbulence intensity component for the single column case in vertical plane at axis of symmetry a) upstream side; b) downstream side	158
Figure 4.46 Contour plots of streamwise turbulence intensity component for two columns case with $L/D = 3$ in different vertical planes a) at $Y/D = 0$, and b) at $Y/D = 1.25$	159
Figure 4.47 Profile plots of streamwise turbulence intensity component for two-column case with $L/D = 3$ in vertical plane at axis of symmetry a) upstream side, b) downstream side, and c) between two columns.....	161

Figure 4.48 Contour plots of vertical turbulence intensity component for the single column case in different vertical planes a) at $Y/D = 0$, and b) at $Y/D = 1.25$	162
Figure 4.49 Profile plots of vertical turbulence intensity component for the single column case in vertical plane at axis of symmetry a) upstream side; b) downstream side	163
Figure 4.50 Contour plots of vertical turbulence intensity component for two columns case with $L/D = 3$ in different vertical planes a) at $Y/D = 0$, and b) at $Y/D = 1.25$	164
Figure 4.51 Profile plots of vertical turbulence intensity component for the case of two in-line columns with $L/D = 3$ in vertical plane at axis of symmetry a) upstream side, b) downstream side, and c) between two columns	165
Figure 4.52 Contour plots of turbulent kinetic energy for the single column case in different vertical planes a) at $Y/D = 0$, and b) at $Y/D = 1.25$	167
Figure 4.53 Profile plots of turbulent kinetic energy for the single column case in vertical plane at axis of symmetry a) upstream side; b) downstream side.....	168
Figure 4.54 Contour plots of turbulent kinetic energy for the two-column case with $L/D = 3$ in different vertical planes a) at $Y/D = 0$, and b) at $Y/D = 1.25$	169
Figure 4.55 Profile plots of turbulent kinetic energy for the case of two in-line columns with $L/D = 3$ in vertical plane at axis of symmetry a) upstream side, b) downstream side, and c) between two columns.....	170
Figure 4.56 Contour plots of Reynolds shear stress for the single column case in different vertical planes a) at $Y/D = 0$, and b) at $Y/D = 1.25$	171
Figure 4.57 Profile plots of Reynolds shear stress for the single column case in vertical plane at axis of symmetry a) upstream side; b) downstream side.....	172
Figure 4.58 Contour plots of Reynolds shear stress for the case of two in-line columns with $L/D = 3$ in different vertical planes a) at $Y/D = 0$, and b) at $Y/D = 1.25$	173
Figure 4.59 Profile plots of Reynolds shear stress for the two-column case with $L/D = 3$ in vertical plane at axis of symmetry a) upstream side, b) downstream side, and c) between two columns.....	174

Figure 4.60 Definition sketch of four quadrant zones in u-w plane.....	177
Figure 4.61 Profile plots of probability of occurrence of different quadrants at upstream side (US1) for single column case	183
Figure 4.62 Profile plots of probability of occurrence of different quadrants at downstream side (DS1) for single column case.....	183
Figure 4.63 Profile plots of probability of occurrence of different quadrants at upstream side (US1) of Column 1 for the twocolumn case with $L/D = 3$	185
Figure 4.64 Profile plots of probability of occurrence of different quadrants at downstream side (DS1) of Column 2 for two columns case with $L/D = 3$	186
Figure 4.65 Profile plots of probability of occurrence of different quadrants between two columns (at B1) with $L/D = 3$	186
Figure 4.66 Profile plots for contribution of stress fraction of different quadrants for the production of Reynolds stress at upstream side of single column	188
Figure 4.67 Profile plots for contribution of stress fraction of different quadrants for the production of Reynolds stress at downstream side of single column	188
Figure 4.68 Profile plots for contribution of stress fraction of different quadrants for the production of Reynolds stress at upstream side of Column 1 for two columns case with $L/D = 3$	190
Figure 4.69 Profile plots for contribution of stress fraction of different quadrants for the production of Reynolds stress at downstream side of Column 2 for two columns case with $L/D = 3$	190
Figure 4.70 Profile plots for contribution of stress fraction of different quadrants for the production of Reynolds stress between two columns with $L/D = 3$	191
Figure 5.1 Temporal development of scour depth at Column 1 for a single column and two columns with $L/D = 1, 2 \& 3$; Time, $t = 72-75$ hours and $V/V_c = 0.74$	200
Figure 5.2 Temporal development of scour depth at Column 2 for a single column and two columns with $L/D = 2 \& 3$; Time, $t = 72-75$ hours and $V/V_c = 0.74$	201

Figure 5.3 Scour depths at upstream column (Column 1) for different spacing between two columns	203
Figure 5.4 Scour depths at downstream column (Column 2) for different spacing between two columns	204
Figure 5.5 Comparison of predicted and observed scour depths for two-column bridge piers	210
Figure 5.6 Length scale of scour profile (Ahmed (1995)).....	211
Figure 5.7 Scour profile for different column spacing.....	212
Figure 5.8 Variation of width of the scour hole for different spacing between two columns	214
Figure 5.9 Predicted and observed to width of the scour hole	215

LIST OF TABLES

Table 2.1 Classification of local scour processes at bridge piers (after Melville and Coleman, 2000).....	32
Table 2.2 Shape factors for different nosed shape piers; (after Richardson and Davis, 2001)	37
Table 2.3 List of previous equations for scour depth (after Ettema et al. 2011).....	48
Table 2.4 Different correction factors of Equation 2.38 (after Melville and Coleman, 2000)	52
Table 2.5 Shape factor ($K_{sh}K_a$) for multiple columns aligned in a row (after Melville and Coleman, 2000).....	54
Table 2.6 Correction factor K1 for pier nose shape (after Richardson and Davis, 2001)	55
Table 2.7 Correction factor K2 for angle of attack (after Richardson and Davis, 2001)	55
Table 2.8 Correction factor K3 for bed condition (after Richardson and Davis, 2001) .	56
Table 3.1 Specification of bed material	86
Table 3.2 Flow conditions for experimental tests	88
Table 5.1 Time for equilibrium scour depth and time factor K_t	202
Table 5.2 Test results for different piers arrangements.....	205
Table 5.3 Model constants	207

LIST OF NOTATIONS

a	=	Edge of the bed layer at $z=a$
C'	=	Chezy coefficient related to sediment grain
$C1$	=	Column at upstream side (Column 1)
$C2$	=	Column at downstream side (Column 2)
C_c	=	Coefficient of curvature
C_d	=	Drag coefficient
C_u	=	Coefficient of uniformity
c	=	Sediment concentration
D	=	Diameter of a pier
D_p	=	Projected width of a pier
d	=	Size of the sediment particle
d^*	=	Dimensionless particle parameter
d_1	=	Equilibrium depth for single column bridge pier
d_{50}	=	Mean grain size of the sediment
d_s	=	Depth of scour at any time
d_{se1}	=	Equilibrium depth of scour at Column 1
d_{se2}	=	Equilibrium depth of scour at Column 2
F	=	Dimensionless shape factor of sediment

F_c	=	Coulomb force of resistance
F_d	=	Drag force
F_g	=	Submerged weight of a particle
Fr	=	Froude number
f	=	Frequency of vortex shedding
G	=	Parameter describing the effects of lateral distribution of flow in the approach channel and the cross sectional shape of the approach channel
g	=	Acceleration due to gravity
H	=	Hole size (threshold level for bursting process)
h	=	Depth of flow
I_e	=	Sorting function for ejection event
I_s	=	Sorting function for sweep event
K_{Gmn}	=	Correction factor proposed by Ataie-Ashtiani and Beheshti (2006)
K_I	=	Flow intensity parameter
K_{s1}	=	Column-spacing factor for Column 1
K_{s2}	=	Column-spacing factor for Column 2
K_{sh}	=	Shape parameter of a pier
K_t	=	Time factor for equilibrium scour depth
K_w	=	Adjustment factor for wide pier

K_α	=	Angle of flow attack parameter of a pier
k_s	=	roughness height
L	=	Centre to centre distance between two columns
L'	=	Length of the pier / Distance between two-column measured outer to outer face of the columns.
m	=	Number of piles in line with flow as in Ataie-Ashtiani and Beheshti (2006)
n	=	Number of piles normal to the flow as in Ataie-Ashtiani and Beheshti (2006)
n_e, n_k	=	Dimensionless number to find the roughness height
P_i	=	Probability of occurrence of the events, where $i = 1, 2, 3$ and 4
Q_i	=	Quadrant zones, where, $i = 1, 2, 3$ and 4
q	=	The rate of local scour in volume per unit time
q_1	=	The rate at which sediment is transported out from the scour hole in volume per unit time
q_2	=	The rate at which sediment is supplied to the scour hole in volume per unit time
q_b	=	Rate of bed load transport
q_b^*	=	Dimensionless Einstein number to quantify bed load transport
q_s	=	Rate of suspended load transport
R	=	Radius of the vortex
Re	=	Reynolds number
Rel	=	Reynolds number with respect to length of boundary layer

S	=	Bed slope
S_i	=	Stress fraction, where $i = 1, 2, 3$ and 4
St	=	Strouhal number
s	=	Specific gravity of the water
s'	=	Submerged specific gravity of sediment particle
s_s	=	Specific gravity of the sediment
T	=	Dimensionless transport stage parameter
TI_u	=	Turbulence intensity component in stream-wise direction (x-direction)
TI_v	=	Turbulence intensity component in transverse direction (y-direction)
TI_w	=	Turbulence intensity component in vertical direction (z-direction)
TKE	=	Turbulence kinetic energy
t_e	=	Time to develop equilibrium scour depth
u	=	Velocity component in stream-wise direction (x-direction)
u_*	=	Bed shear velocity
u_c	=	Critical shear velocity
u'	=	Fluctuating component of velocity in stream-wise direction (x-direction)
V	=	Mean approach flow velocity
\bar{V}	=	Depth averaged velocity of fluid

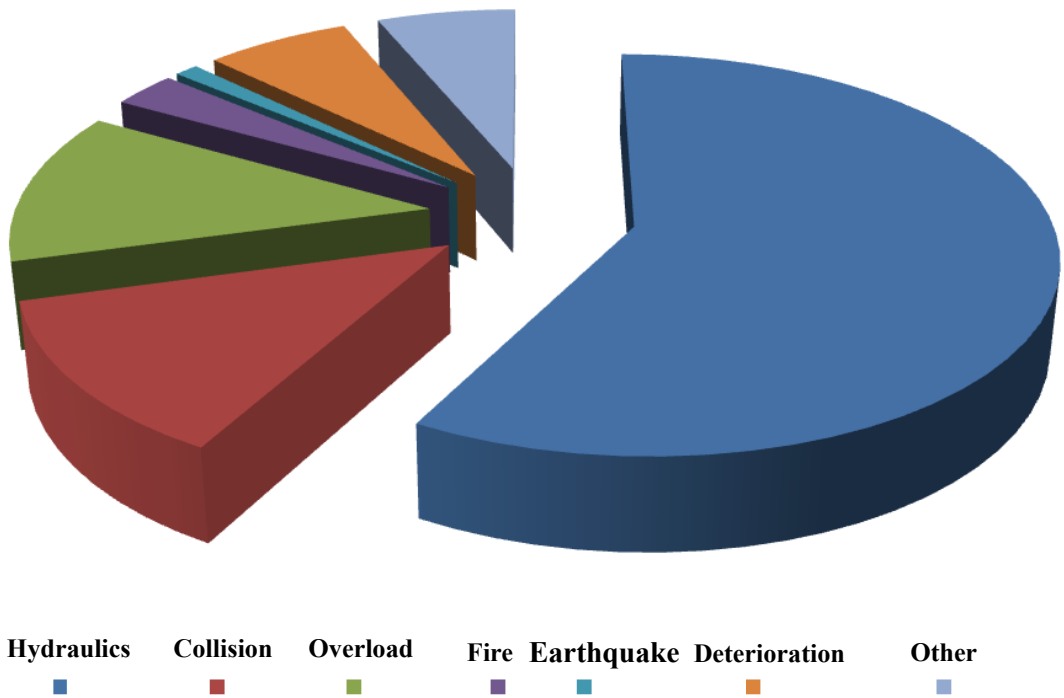
V_a	=	Critical mean flow velocity for armour peak
V_c	=	Critical mean flow velocity for sediment entrainment
V_{lp}	=	Live bed peak velocity of flow
V_θ	=	Tangential vortex velocity = $\omega_\theta R$
v	=	Velocity component in transverse direction (y-direction)
v'	=	Fluctuating component of velocity in transverse direction (y-direction)
W	=	Width of the flume
w	=	Velocity component in vertical direction (z-direction)
w'	=	Fluctuating component of velocity in vertical direction (z-direction)
w_s	=	Top width of the scour hole
x	=	Distance measured in stream-wise direction
y	=	Distance measured in transverse direction
Z, Z'	=	Sediment number
z	=	Distance measured in vertical direction
Γ	=	Vortex strength
δ	=	Thickness of boundary layer
μ_c	=	Coulomb friction coefficient
ν	=	Kinematic viscosity of fluid
ρ	=	Density of fluid

ρ_s	=	Density of sediment material
σ_g	=	Geometric standard deviation of the sediment
τ	=	Bed shear stress
τ_*	=	Dimensionless critical shear stress parameter (Shields parameter)
τ_c	=	Critical shear stress
τ_{uv}	=	Reynolds shear stress component in uv direction
τ_{uw}	=	Reynolds shear stress component in uw direction
τ_{vw}	=	Reynolds shear stress component in vw direction
ψ	=	Correction factor for stratification
ω_0	=	Angular velocity of revolution

CHAPTER 1

INTRODUCTION

Distribution of Bridge Failure Types



1.1 Background

1.2 Research Objectives

1.3 Scope and Limitation

1.4 Research Significance and Innovation

1.5 Research Methodology

1.6 Synopsis of Thesis

1. INTRODUCTION

1.1 Background

In the field of hydraulic engineering, the topic of river flow and the associated problems, such as sediment transport, deformation of the riverbed, scouring and flooding are considered as one of the major issues in the development of a country. Out of these issues, deformation of the riverbed at the bridge site is a key area of interest to hydraulic engineers and designers. According to Melville (1975), factors leading to the changes in bed elevation at a bridge site are mainly classified in three different categories. Firstly progressive aggradation and degradation of bed associated with a change in river regime; secondly, temporary scour associated with changes in river stages, or with shifting of the deep water channel; and thirdly, presence of hydraulic structure like bridge which obstruct the flow resulting in the constriction of flow and hence scouring around bridge piers or abutments.

In Australia, flood event has been reported as one of the main reasons of bridge failure. According to the information provided on Wikipedia-contributors (2015), Fremantle Railroad Bridge was collapsed in 1926 due to high flood event. In 2007, Gosford Culvert was washed away due to flood events and five people were killed. The heavy flood event in 2008 caused the Somerton Bridge was collapse. According to the recent study by Pritchard (2013), Majority of Queensland area was declared as a natural disaster zone because of the damaged caused by flooding. It was estimated that about 3 billion of the damages were resulted from the flood events of 2011. Out of this amount, 5% of the cost reflected to the bridge damage due to scour and piles undermine. Furthermore, it was reported that, the post disaster recovery was adversely affected due to bridge damage.

In the history of bridge failure, scour around the bridge pier has been identified as the main cause of failure. An analysis of 143 bridge failure incidents in different countries during the period from 1961 to 1975 was carried out by Smith (1976). It was found that about 70 bridges failed during floods of which about 45% could be attributed to the scour around bridge piers. According to Melville (1992), out of 108 bridge failures observed in New Zealand, between the period of 1960 and 1984, 29 were reported as failure due to abutment scour. Furthermore Melville and Coleman (2000) reported that in New Zealand,

at least one serious bridge failure each year can be attributed to the scour of the bridge foundation.

As reported by many researchers for example Jones et al. (1995); Mueller (1997); Lagasse and Richardson (2001); and Ameson et al. (2012); bridge scour is of significant concern in the United States causing approximately 60 percent of all the U.S.A highway bridge failures. Furthermore it was reported that in 1993 alone, more than 2500 bridges were destroyed or severely damaged due to scour caused by severe flooding, which reflects around \$178 million of the total repair costs. Additionally, in 1994, over 1000 bridges were reported closed in Georgia during flood, and the damage cost was estimated to be around \$130 million. There is a substantial amount of direct cost associated with repair and replacement of river bridges damaged by flood. However, the indirect cost to local businesses and industries due to disruption in commercial activities was estimated at more than five times the direct repair cost. The high profile catastrophic collapse of the Schoharie Creek Bridge in New York in 1987 in which 10 people died was caused by the cumulative effect of pier scouring. It was reported by Mueller (1997) that in 1989, according to Wardhana and Hadipriono (2003), more than 500 bridge failures in the United States between 1989 and 2000 were studied and it was reported that the average age of the failed bridges was 52.5 years (ranges from 1 year to 157 years).

According to an article reported by Novey (2013), the Colorado Department of Transportation, CDOT estimated a minimum of 30 state highway bridges were destroyed and 20 were seriously damaged by flood in the year 2013. Another article reported by KC (2014), due to the degradation of the bed material, one of the main highway bridges over the Tinau River in Nepal became deeper around the bridge pier by 1.5 m resulting in exposure of the foundation of the bridge pier. Because of this, a very high risk of bridge failure was reported. From the above review, it is justified to say that bridge scour is one of the main bridge safety problems all over the world. The pictures presented in Figures 1.1 to 1.3 give clear illustration of scour problem around bridge piers and its consequences as bridge failure.



Figure 1.1 Bridge piers experiencing the flood events (USGS (2014))



Figure 1.2 a) Scour around bridge piers on the Logan river, Australia; (Queensland Government (2013) ; and b) Scour around bridge piers on the Tinau river, Nepal, (KC (2014))



Figure 1.3 A bridge over the Gaula river in India washed away by flood in July 2008, (Bhatia (2013))

1.2 Research Objectives

The main objective of this study is to carry out an experimental investigation on three dimensional flow structure and scour around the bridge piers comprising two circular cylindrical columns in tandem arrangement. The effects of spacing between two columns on flow structure and local scour around bridge pier are proposed to be study in depth. In order to achieve this goal, the following specific objectives are proposed:

- a) Deep understanding of the flow structure concept and the scour mechanism for local scour around bridge piers such as horseshoe vortex, vortex shedding, vortex strength, vortex shedding frequency and shear velocity
- b) Detailed study of interaction of turbulence (coherent structures, bursting phenomenon, Reynolds shear stresses, turbulence intensity, turbulent kinetic energy, flow field, etc.) and the bridge piers.
- c) Assessing and analysing the suggested equations to predict the local scour depth around bridge piers and to determine the important factors affecting the local scour around a bridge pier
- d) Conducting detailed experimental studies on the flow structure and local scour around bridge piers using a single column and two column bridge piers with different column spacing arrangement
- e) Determination and evaluation of temporal variation of the local scour depth around bridge piers with a single and two columns based on the experimental data

- f) Comparison of single-column and twin-column bridge piers effects on the flow structure and local scour around the piers based on the results obtained from the experimental studies. Analysing the experimental results to obtain deep knowledge on the influence of the bridge piers interaction on the flow structure and scour around the bridge piers
- g) Suggesting a design method to predict the scour depth around bridge piers with two columns in tandem arrangements
- h) Comparing the results of experimental studies with the well-known scour depth prediction equations as well as a number of common definitions of equilibrium scour depth available from past studies

1.3 Scope and Limitation of Research

Due to the complex nature of flow around bridge piers and various uncertainties on different parameters affecting the scour depth, laboratory based experimental study is the widely adopted method for achieving precise and reliable results. Hence the present study is aimed to carry out an experimental investigation. However, there are some limitations on experimental setup and the parameters given as under:

- a) Cohesion-less and uniformly graded sand as bed material was used for all the experiments.
- b) It was considered that there is occurrence of local scour around bridge piers under the clear water flow condition.
- c) Only a cylindrical pier model with a circular cross-section was used
- d) The bridge piers comprising maximum number of two circular cylindrical columns were adopted throughout the research work.
- e) The columns of a bridge pier were installed in a tandem arrangement i.e. angle of flow attack is zero.

1.4 Research Significance and Innovation

Numerous studies have been carried out since the late 1950s on the flow structure and scour around bridge piers. However, problems in understanding the complicated flow and scouring mechanism remain challenging. Although numerous scour depth prediction

equations have been suggested by many investigators, almost all of them are developed based on a single pier arrangement. In contrast to vast amount of investigations carried out for the flow around a single pier, there are limited studies on flow around a group of piers. The flow around piers comprising a multiple in-line columns is not well investigated. However, in practice, bridge piers often comprise a number of circular columns aligned in the flow direction that together support the loading of the structure. Thus, a detailed study on flow around bridge piers with two in-line columns is studied experimentally in this research.

The present study aims to provide a notable contribution to the body of knowledge through the following innovations:

- a) Studying the three dimensional flow structure around the bridge piers with single and two columns using physical-hydraulic models in the laboratory
- b) Investigation of the interaction of bridge piers on the flow structure and scouring process around the bridge piers using two-column bridge piers model aligned in a line with different spacing between them
- c) Suggesting a design relationship to predict the local scour depth around bridge piers with two columns in tandem arrangements
- d) Employing advanced measurement techniques to capture accurate results

1.5 Research Methodology

The present study is primarily based on the laboratory experiments consisting of measuring instantaneous three dimensional velocity components, experimental investigation of temporal variation of scour depth around single and two columned bridge piers and analysis of equilibrium scour depth under various flow conditions and columns arrangements. The following conditions and parameters have been established for all the experimental work:

- a) Steady state approach flow with clear water scour condition was applied.
- b) The model bridge piers comprising single and two cylindrical columns with circular cross-sections were used in all experiments. For the two-column case, they were installed in tandem arrangements with different spacing between them.

All the experiments related to flow structures were carried out under flatbed condition establishing the rough bed surface using sand as the bed material. Instantaneous three dimensional velocity components were measured using Acoustic Doppler Velocimetry (ADV). The ADV measurements were carried out in different horizontal planes. Additionally the experiments on flow around bridge piers in different vertical planes were carried out using Particle Image Velocimetry (PIV) method. In the PIV method, a series of instantaneous images were captured and analysed to get the two dimensional velocity components. To measure the scour depth and the final bed profile, a vernier depth gauge with the least count of 0.1 mm was used.

The measured data were analysed and the results were presented in graphical form using profile and contour plots. Furthermore, the results were compared with the results from the previous investigations.

1.6 Synopsis of Thesis

This thesis contains altogether seven chapters. A brief outline of each chapter is as follows:

In Chapter 1, general background of bridge scour and associated problems are presented. Additionally, this chapter presents the objectives of the study, limitation, research significance and innovation, and methodology.

Chapter 2 is mainly focused on the compilation of existing knowledge in the field of bridge scour and identification of the scientific gap that needs to be fulfilled to achieve the objectives of this research. A synthetic review on the scour at bridge crossing is presented which is followed by local scour around bridge piers, mechanism of local scour and analysis of pier scour. Moreover, review on flow regime around bridge piers, temporal development of scour depth and various methods of prediction of local scour depth are presented in this chapter. In addition to this, theoretical development of open channel flow and sediment transport are presented. This chapter consists of governing equations of flow in open channel and theory of turbulence structures in open channel flow. It also summaries the basic concept of sediment transport providing the various relations related to various forms of sediment transport.

Chapter 3 gives a detailed description of facilities and equipment used for the experimental tests. In addition, design of the physical model, advance measurement techniques employed in the experiments and experimental procedures for this study are described in this chapter.

Chapter 4 and 5 provide the results obtained from the laboratory experiments on flow structures and scour around bridge piers. The various test results from single column and two column experiments are analyzed and compared in order to work out the effect of spacing between two columns on flow structures and scour around bridge piers.

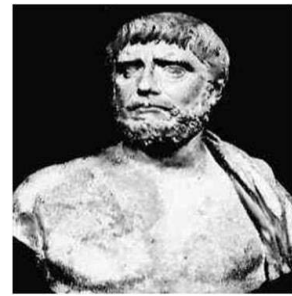
Finally, conclusions from this study and recommendations for future research are provided in Chapter 6, followed by References and Appendices containing the detailed figures of experimental results.

CHAPTER 2

LITERATURE REVIEW

624 – 546 BC

The Greek Thales, often described as the world's first scientist, declared water a substance rather than a mystic gift from the gods, thus paving the way for future research into water, and probably much irritating the local priesthood at the same time.



(<http://www.tiefenbach-waterhydraulics.com/waterhydraulics/historyofwaterhydraulics.html>)

2.1 Introduction

2.2 Scour at Bridge Crossings

2.3 Sediment Transport and Local Scour around Bridge Piers

2.4 Open Channel Flow and Flow around Bridge Piers

2.5 Summary and Identification of the Gap in Literature

2. LITERATURE REVIEW

2.1 Introduction

In the past decades, a number of studies have been carried out in the field of scour around bridge piers. Based on the previous investigations available in literature, this chapter summarises the basic concepts of scour around bridge piers. This explanation is followed by a description of different types of scour, factors that contribute in the process of scouring and description of the flow field around the pier. A comprehensive review on some previous studies on scour around bridge piers is also presented in this chapter.

2.2 Scour at Bridge Crossings

Scour is a phenomenon of sediment removal from around a hydraulic structure due to interaction between flow and the hydraulic structure such as bridge piers placed in flowing water. Breusers et al. (1977) defined scour as a consequence of the erosive action of flowing water, which removes and erodes materials from the bed and banks of streams and also from the vicinity of bridge piers and abutments. According to Melville and Coleman (2000) scour is defined as lowering the riverbed by water erosion such that there is a tendency to expose the foundations of a bridge. In this definition, it is assumed that the level of the riverbed prior to the commencement of the scour is the natural bed level and the amount of reduction below the natural bed level is termed as the scour depth.

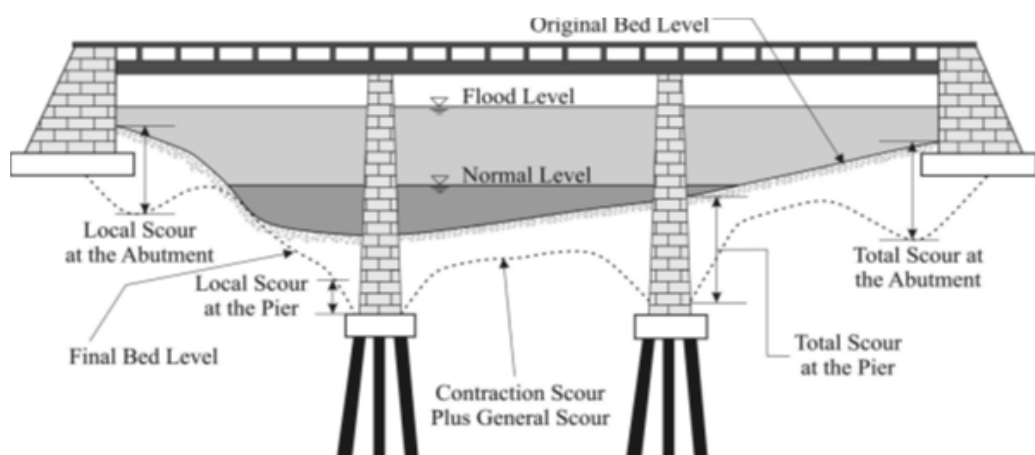


Figure 2.1 Types of scour at a bridge, (after Melville and Coleman, 2000)

Cheremisinoff et al. (1987) stated that scour can either be caused by normal flows or flood events. During a flood event, the rate of scouring is more than that in a normal flow condition because of the higher flow velocity. The different components of scour are clearly shown in Figure 2.1. Richardson and Davis (2001) explained that the total scour at a highway crossing is comprised of three components namely long term aggradation and degradation, general scour and local scour. Furthermore, Melville and Coleman (2000) suggested that various types of scour that can occur at a bridge crossing are typically referred to: general scour, contraction scour and local scour. A summarised form of scour types is shown in Figure 2.2.

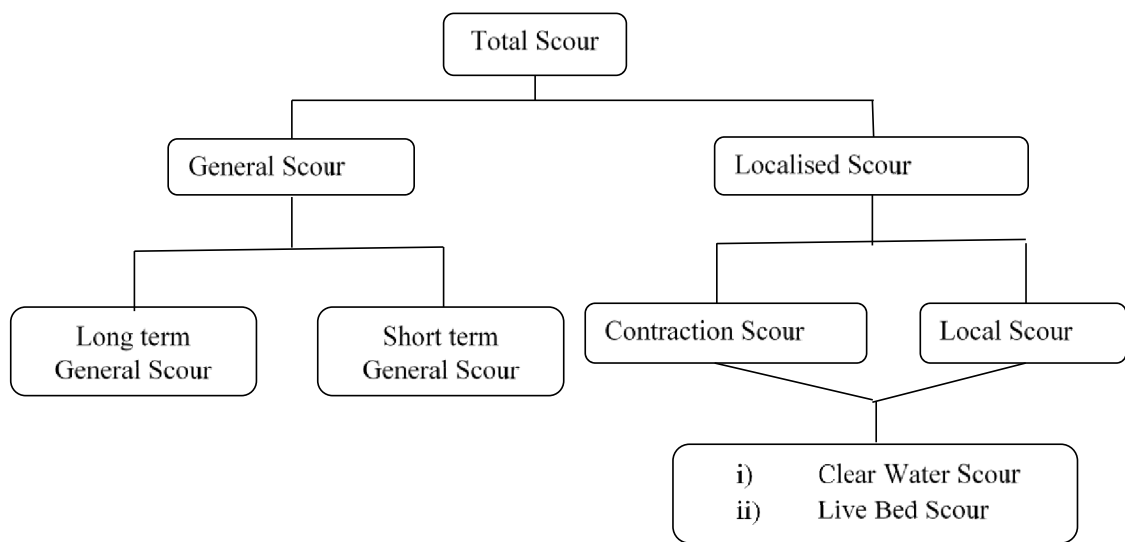


Figure 2.2 Classification of scour (after Melville and Coleman, 2000)

2.2.1 General Scour

According to Melville and Coleman (2000), general scour deals with the changes in river bed due to natural or human induced causes. Because of the general scour, overall longitudinal profile of the river channel is lowered. It occurs through a change in the flow regime in the river system resulting in general degradation of the bed level. General scour occurs irrespective of the existence of the bridge; and it can occur as either long-term scour or short-term scour. Short-term scour is because of a single flood or several closely spaced floods. On the other hand, long-term scour has a considerably extensive time scale (i.e. several years longer), and it includes progressive degradation and lateral bank erosion.

2.2.2 Localised Scour

As suggested by Melville and Coleman (2000), localised scour is a collective term of contraction scour and local scour, and they are directly attributable to the existence of the bridge. When the river flow approaches the bridge, it usually converges causing a constriction of flow. Because of this contraction, the flow accelerates to the narrowest section (vena contracta). The flow then decelerates and the live river expands beyond the vena contracta to defuse gradually into the full downstream width of the channel. The accelerated flow induces scour across the contracted section. This scour is referred to as contraction scour. On the other hand, when the flow approaches hydraulic structures such as bridge piers, abutments, spurs and embankments, there is a formation of interference between structures and the flow. This also causes acceleration of the flow around the structures resulting in removal of material from around piers, abutments, spurs and embankments. This scour is termed local scour, which is clearly illustrated in the photograph shown in Figure 2.3.



Figure 2.3 Local scour at bridge piers; (Vasquz, 2006)

2.3 Sediment Transport and Local Scour around Bridge Piers

2.3.1 Basics of Sediment Transport

The fragmental material formed by the physical and chemical disintegration of rocks is known as sediment. The size of the sediment varies from the large boulder to colloidal

size of fragments with a variety of shapes. Once the sediment particles are detached from their original source, they may either be transported by gravity, wind or water. Usually the sediments can be transported in three different modes of particle motion namely: rolling or sliding particle motion; saltation or hopping particle motion; and suspended particle motion.

When the value of shear velocity at the bed just exceeds the critical value, the bed material will start rolling or sliding in continuous contact with the bed. Further increasing the value of bed shear velocity, the particle will be moving along the bed by more or less regular jumps, which are called sediment transport by saltation. The transport of sediment particles by rolling and saltation is called bed load transport. As the bed shear velocity exceeds the fall velocity of the particles, there is lifting of sediment particles; as a result the particles may go into suspension. The transport of sediment particles in this way is called suspended load transport.

2.3.1.1 Threshold of Sediment Motion

Melville (1975) presented the definition of threshold of motion or critical condition as given in Sedimentation Manual published in 1966. It states that “when the hydrodynamic force acting on a grain of sediment has reached a value that, if increased even slightly will put the grain into motion, critical or threshold conditions are said to have been reached.” According to Chaudhry (2007), the drag force exerted on sediment particles on the riverbed is the main factor for initiating the sediment motion. For the initiation of sediment motion the applied drag force must exceed a threshold value. The resistance to motion is due to cohesion in the case of clay-rich sediment and from the Coulomb friction in the case of non-cohesive sediment. As shown in Figure 2.4, a simplified case of sediment motion, for a small bed slope, such that $S \ll 1$, consider that the roughness height, $k_s = n_k d_{50}$, where n_k is a dimensionless number and d_{50} is the mean size of the sediment particles. Consider an exposed particle protrudes up from the mean bed level by an amount $n_e d_{50}$, where n_e is again a dimensionless number. If the flow is turbulent, then the drag force, F_d and the submerged weight of the particle, F_g , is given by

$$F_d = \frac{1}{2} \pi \left(\frac{d_{50}}{2} \right)^2 \rho C_d V^2 \quad 2.1$$

$$F_g = \frac{4}{3} \pi \left(\frac{d_{50}}{2} \right)^2 \rho s' g \quad 2.2$$

where ρ is the fluid density, $s' = (s_s - s)$, is the submerged specific gravity of sediment particle, g is the acceleration due to gravity and V is the fluid velocity at the level of particle, C_d is the drag coefficient. The Coulomb resistive force F_c is given by

$$F_c = \mu_c F_g \quad 2.3$$

where, μ_c is the Coulomb friction coefficient. At threshold condition of sediment motion, Equations 2.1 and 2.3 give

$$\frac{V^2}{s' g d_{50}} = \frac{4 \mu_c}{3 C_d} \quad 2.4$$

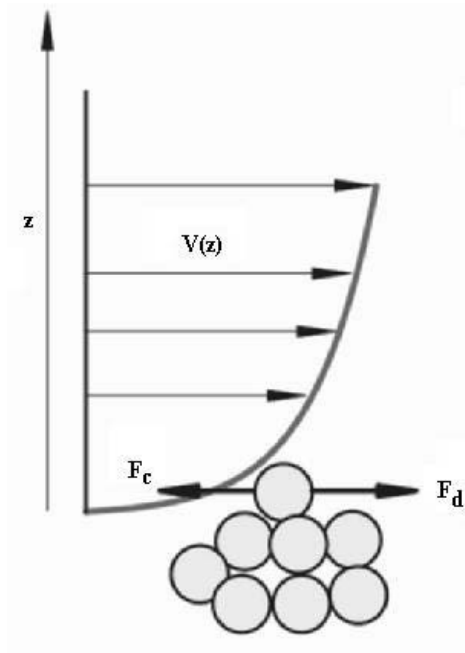


Figure 2.4 Threshold condition for the sediment entrainment

The expression for the velocity distribution over a rough boundary surface is given by:

$$\frac{V}{V_c} = 5.75 \log \frac{n_e}{n_k} + 8.5 \quad 2.5$$

Substituting the value of V from Equation 2.5 to Equation 2.4, gives

$$\frac{V_c^2}{s'gd_{50}} = \tau = \frac{4\mu_c}{3C_d} \left(\frac{1}{\left(5.75 \log \frac{n_e}{n_k} + 8.5\right)^2} \right) \quad 2.6$$

In Equation 2.6 the term τ is known as the bed shear stress. In order to entrain the sediment particle, the non-dimensional bed shear stress must exceed τ .

Melville and Coleman (2000) described that the Shields diagram can be used to evaluate threshold flow conditions for the motion of a given sediment. The Shields diagram indicates that the condition of the movement of bed material can be identified by using dimensionless critical shear stress under observed temperature, specific gravity and mean size of sediment material which is known as Shield's parameter and is expressed as:

$$\tau_* = \frac{\tau}{(s_s - s)gd_{50}} \quad 2.7$$

where,

τ_* = dimensionless critical shear stress parameter (Shields parameter)

τ = bed shear stress

s_s = specific gravity of sediment material

s = specific gravity of water

g = acceleration due to gravity

d_{50} = mean grain size of sediment

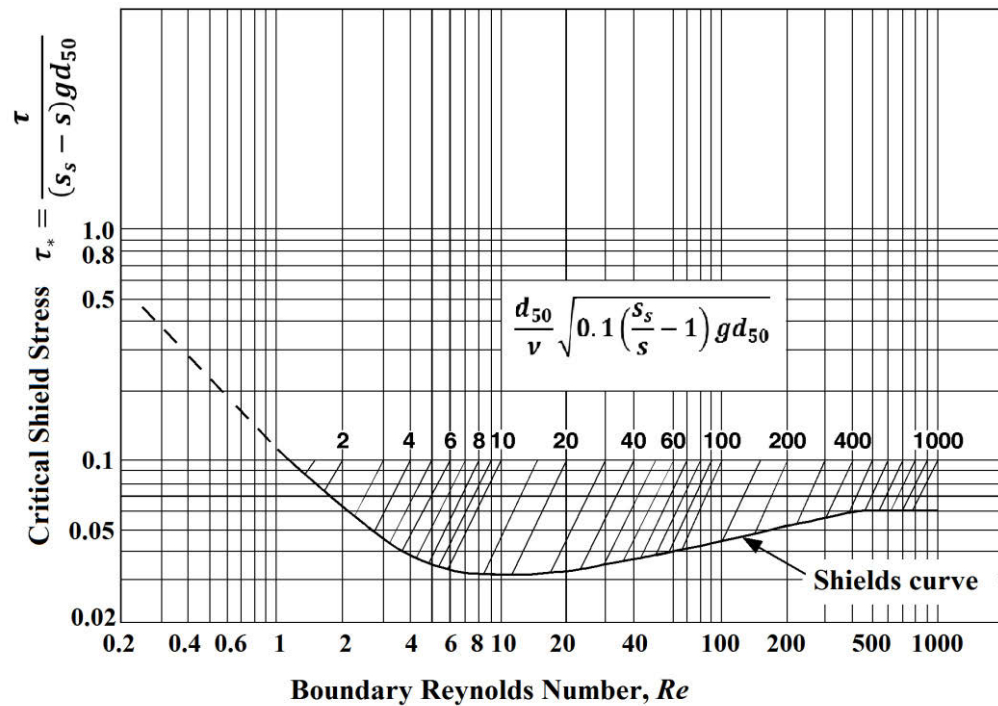


Figure 2.5 Shields diagram for incipient motion of sediment (after Simons and Senturk, 1992)

However Chang (1988), has indicated that the Shields diagram has the critical shear stress as an implicit variable that cannot be deduced directly; a parameter $\frac{d_{50}}{\nu} \sqrt{0.1 \left(\frac{s_s}{s} - 1 \right) g d_{50}}$ is proposed in ASCE Sedimentation Manual (1975). These parameters are represented by a family of lines in the Shields diagram as shown in Figure 2.5. The boundary Reynolds number, Re as shown in Shields diagram is also known as particle Reynolds number which is mathematically expressed as $Re = u_* d_{50} / \nu$ where, u_* is shear velocity of bed material of size d_{50} . The dimensionless critical shear stress can be read directly from the intersection of the lines representing that parameter and the Shields curve. Hence the critical shear stress τ_c can be calculated using the following relation:

$$\tau_c = \tau_* (s_s - s) d_{50} \quad 2.8$$

The value of critical shear stress can be used to calculate the critical shear velocity of the Inflow using the following relation:

$$\tau_c = \rho u_{*c}^2 \quad 2.9$$

where,

u_{*c} = critical shear velocity

ρ = density of water

According to Melville and Coleman (2000), critical shear velocity, u_{*c} for quartz material in water at 20° C, as shown in Figure 2.6 can be alternatively calculated using the following equations which is only based on the mean grain size of the sediment material:

For $0.1 \text{ mm} < d_{50} < 1 \text{ mm}$,

$$u_{*c} = 0.0115 + 0.0125 d_{50}^{1.4} \quad 2.10$$

For $1 \text{ mm} < d_{50} < 100 \text{ mm}$,

$$u_{*c} = 0.0305 d_{50}^{0.5} - 0.0065 d_{50}^{-1} \quad 2.11$$

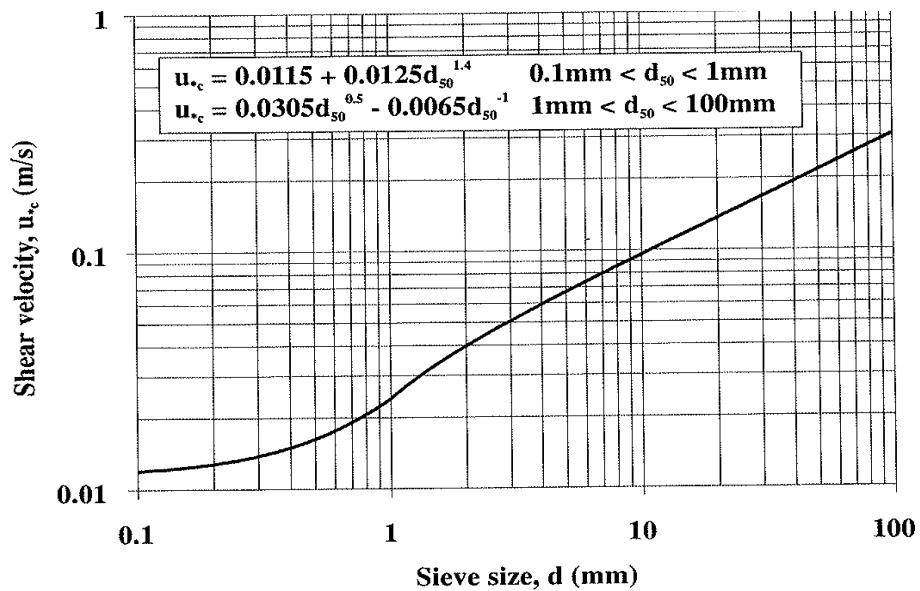


Figure 2.6 Shear velocity chart for quartz sediment in water at 20° C; (after Melville and Coleman, 2000)

If critical mean velocity of flow, V_c , is preferred to describe threshold motion of the sediment, it can be determined using the following relation given by Melville and Coleman (2000):

$$\frac{V_c}{u_{*c}} = 5.75 \log \left[5.53 \frac{h}{d_{50}} \right] \quad 2.12$$

where,

V_c = critical mean velocity of flow

h = depth of flow

Melville and Coleman (2000), further reported that the critical mean velocity of flow can be alternatively calculated using an empirical relation given by Neil (1968):

$$V_c = 1.41[(s_s - 1)gd_{50}]^{0.5} \left(\frac{h}{d_{50}} \right)^{\frac{1}{6}} \quad 2.13$$

2.3.1.2 Bed Load Transport

According to Van Rijn (1984a) bed load transport is defined as the transport of sediment particles by rolling and saltating along the bed surface. Another definition by Einstein (1950) states that it is the movement of the particles by rolling, sliding, and, sometimes by jumping in the bed layer which has the thickness of 2 grain diameters immediately above the bed. Van Rijn (1984a) has given a method to calculate the bed load transport rate which is given as

$$\frac{q_b}{[(s - 1)g]^{0.5} d_{50}^{1.5}} = 0.053 \frac{T^{2.1}}{d_*^{0.3}} \quad 2.14$$

where q_b is the bed load transport rate (in m^2/s), s is the specific gravity of sediment, d_* is the particle parameter and T is the transport stage parameter. The particle parameter, d_* , and the transport stage parameter, T , are given by the following equations:

$$d_* = d_{50} \left[\frac{(s-1)g}{\nu^2} \right]^{1/3} \quad 2.15$$

$$T = \frac{u_*^2 - u_c^2}{u_c^2} \quad 2.16$$

in which, g is the acceleration due to gravity, ν is the kinematic viscosity, u_* is the bed shear velocity related to sediment and u_c is the Shields critical bed shear velocity. If V is the mean flow velocity and C' is Chezy-coefficient related to grains then the bed shear velocity related to sediment, u_* is given by

$$u_* = \frac{g^{0.5}}{C'} V \quad 2.17$$

As reported by Chaudhry (2007), bed load transport can be quantified using an empirical relation of non-dimensional Einstein number, q_b^* , which is given by

$$q_b^* = \frac{q_b}{d\sqrt{\rho s' g d}} \quad 2.18$$

Some popular bed load transport relations based on Shields stresses for well graded sediments are reported by Chaudhry (2007) which are given as under:

1. Meyer-Peter and Muller relation

$$q_b^* = 8(\tau^* - \tau_c^*)^{3/2}; \tau_c^* = 0.047 \quad 2.19$$

2. Wong and Parker – correction of Meyer-Peter and Muller relation

$$q_b^* = 4.93(\tau^* - \tau_c^*)^{8/5}; \tau_c^* = 0.047 \quad 2.20$$

3. Einstein equation

$$1 - \frac{1}{\sqrt{\pi}} \int_{-(0.143/\tau^*)-2}^{+(0.143/\tau^*)-2} \exp(-t^2) dt = \frac{43.5q_b^*}{1 + 43.5q_b^*} \quad 2.21$$

4. Parker equation- fit to Einstein equation

$$q_b^* = 11.2\tau^{3/2} \left(1 - \frac{\tau_c^*}{\tau^*}\right)^{9/2}; \tau_c^* = 0.03 \quad 2.22$$

5. Ashida and Michiue relation

$$q_b^* = 17(\tau^* - \tau_c^*)(\tau^{*1/2} - \tau_c^{*1/2}); \tau_c^* = 0.05 \quad 2.23$$

6. Engelund and Fredsoe relation

$$q_b^* = 18.74(\tau^* - \tau_c^*)(\tau^{*1/2} - 0.7\tau_c^{*1/2}); \tau_c^* = 0.05 \quad 2.24$$

2.3.1.3 Suspended Load Transport

Bagnold (1966) defined the suspended load transport as the process in which the excess weight of the particles is supported by upward impulses of turbulent eddies. He further gave the condition of initiation of suspension, which states that when the value of bed shear velocity exceeds the particle fall velocity, suspension will occur. According to Van Rijn (1984b), suspension will start at considerably smaller bed-shear velocities. When the bed shear velocity is greater than the fall velocity of the particles, they can be lifted up to a level at which the upward turbulent force is higher than the submerged weight of sediment particle. This keeps the particles in suspension mode. He further reported that the behaviour of suspended sediment particles can be described in terms of sediment concentration. The suspended sediment concentration decreases with the distance from the bed, the rate of which depends on the ratio of the fall velocity and the bed shear velocity.

According to Van Rijn (1993) the rate of suspended load transport can be calculated by integrating the product of velocity and sediment concentration from the edge of the bed layer ($z=a$) to the water surface ($z=h$) as shown in Figure 2.7.

$$q_s = \int_a^h Vc \, dz \quad 2.25$$

or

$$q_s = c_a \bar{V} h \frac{1}{h} \int_a^h \frac{V}{\bar{V}} \frac{c}{c_a} \, dz = c_a \bar{V} h F \quad 2.26$$

with

$$F = \int_a^h \frac{V}{\bar{V}} \frac{c}{c_a} \, d(z/h) \quad 2.27$$

where q_s is the suspended load transport rate, V is the fluid velocity at height z above bed, c is the sediment concentration at height z from bed, \bar{V} is the depth averaged fluid velocity, c_a is the sediment concentration at height $z=a$ above bed, h is the depth of flow, and F is the dimensionless shape factor (as in Van Rijn, 1984).

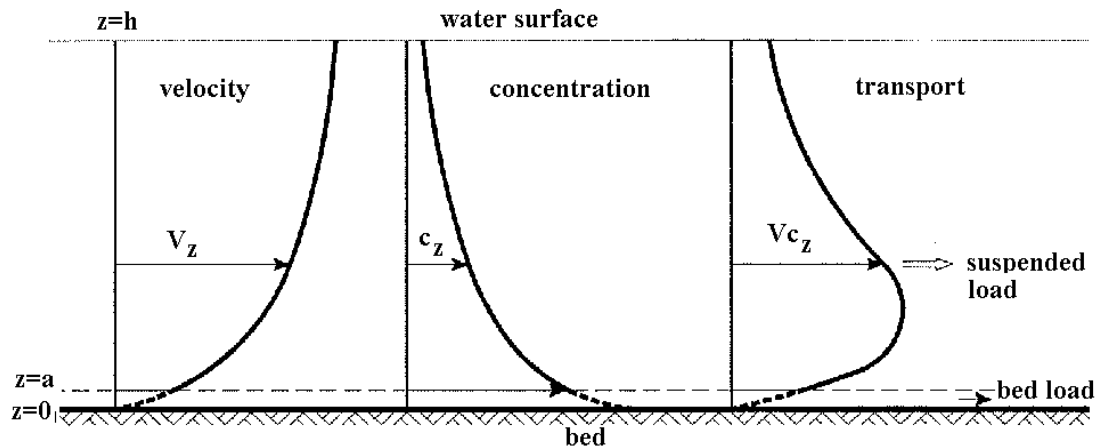


Figure 2.7 Definition sketch of suspended load transport; (after Van Rijn, 1993)

The parameters used in Equation 2.27 can be determined using the following relations:

Sediment concentration at height ($z=a$) is given by

$$c_a = 0.15 \frac{d_{50} T^{1.5}}{a d_*^{0.3}} \quad 2.28$$

In Equation 2.28, the values of the dimensionless parameter, d_* , and dimensionless transport stage parameter, T , can be computed using Equations 2.15 and 2.16, respectively.

Dimensionless shape factor, F , for $0.3 \leq Z' \leq 3$ and $0.01 \leq a/h \leq 0.1$ is given by:

$$F = \frac{(a/h)^{Z'} - (a/h)^{1.2}}{(1 - a/h)^{Z'}(1.2 - Z')} \quad 2.29$$

where $Z' = Z + \psi$ is the suspension number with correction factor for stratification ψ . The shape factor, F , for $a/h = 0.01, 0.05$ and 0.1 can be determined using Figure 2.8.

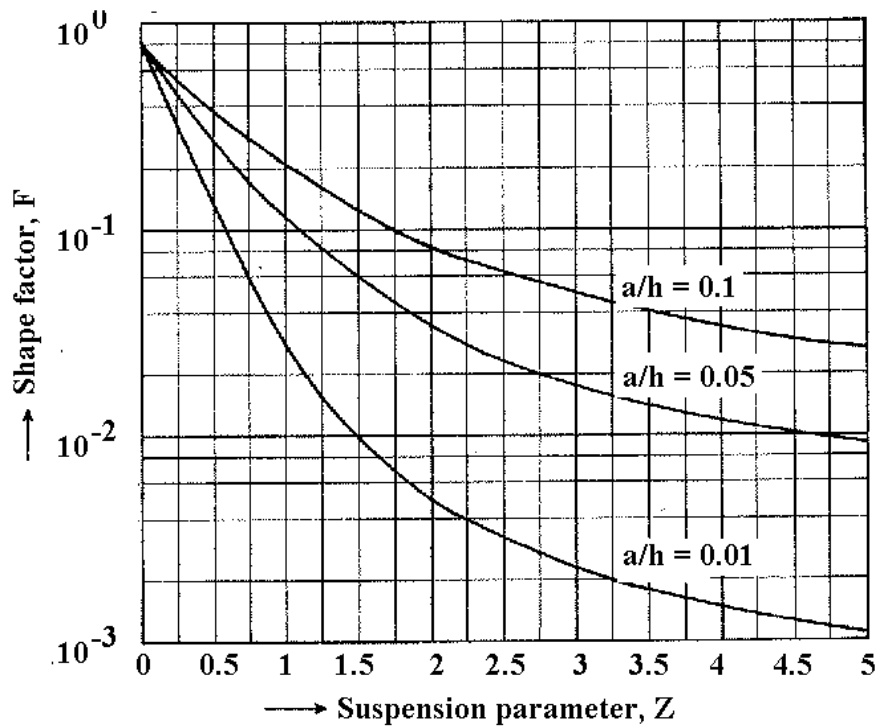


Figure 2.8 Shape factor for different suspension numbers; (after Van Rijn, 1993)

2.3.2 Local Scour around Bridge Piers

Melville (1975) suggested that the local scour can be classified according to the amount of bed material supplied into the scour area and the capacity of transport out of the scour area. The rate of scour hole in volume per unit time is expressed as the difference between the amount of sediment supplied in and transported out of the scour hole, which is expressed in the following equation:

$$q = q_1 - q_2 \quad 2.30$$

where,

q = the rate of local scour in volume per unit time

q_1 = the rate at which sediment is transported out from the scour hole in volume per unit time

q_2 = the rate at which sediment is supplied to the scour hole in volume per unit time

This leads to an identification of two types of local scour:

Clear Water Scour

Clear water scour occurs when there is no movement of bed material in the flow upstream of the crossing. This condition of scour is just because of the obstructions (piers, abutments) in the flow that accelerate the flow and create vortices around the obstructions cause bed material around them to move. In Equation 2.30, the rate of sediment supply to the scour hole is equal to zero ($q_2 = 0$) for clear water scour condition. In this case, the depth of scour hole continues to grow until the equilibrium scour depth is reached

Live-bed Scour

Live bed scour occurs when there is transport of bed material from upstream reach into the crossing. In live bed local scour, the scour hole is continuously supplied with the sediment transported from upstream reach. In this case the rates of sediment transport to and from the scour hole are greater than zero (i.e. $q_1, q_2 > 0$). Equilibrium scour depth is reached when the rate of sediment supply to the scour hole is equal to the rate of sediment transported out of the scour hole (i.e. $q_1 = q_2$).

Figure 2.9 shows the two types of scour and the equilibrium scour depth, in which the depth of the scour is presented as a function of time. It is clear from the figure that the equilibrium scour depth for clear water scour is approached asymptotically while for the live bed scour, there are non-periodic oscillations about equilibrium scour depth. Additionally it can be seen that the equilibrium scour depth for clear water scour is about 10% greater than that for live bed scour. According to the citation made by Melville (1975), the time development of local scouring is governed by an exponential law.

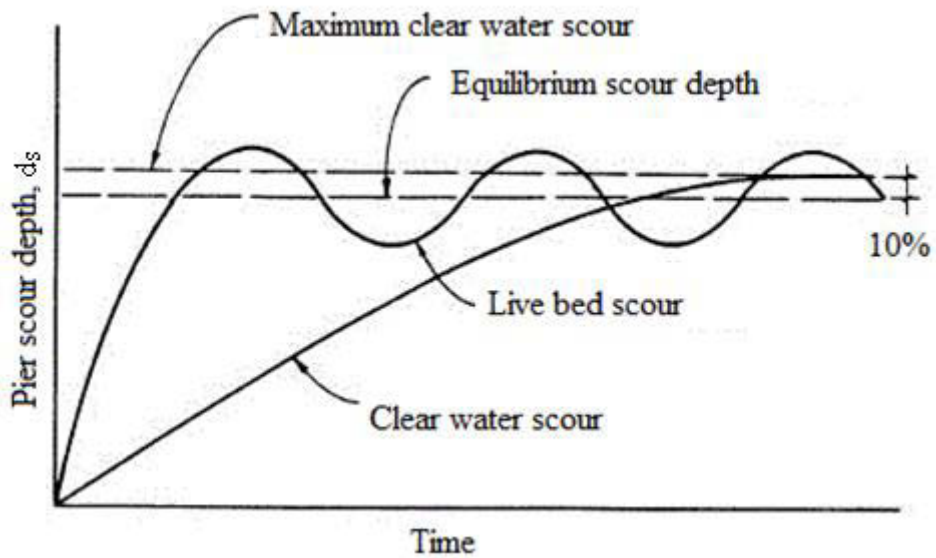


Figure 2.9 Local scour around bridge piers as a function of time; (after Richardson and Davis, 2001)

Carsten (1966) defined a sediment number, based on sediment size and the mean velocity of flow at which local scour begins. According to his definition, the sediment number is given by Equation 2.31.

$$Z = \frac{V}{\sqrt{(s_s - 1)gd}} \quad 2.31$$

where,

Z = sediment number

V = mean velocity of the undisturbed flow

s_s = the specific gravity of the sediment

g = acceleration due to gravity

d = mean grain diameter of the sediment

Furthermore Carsten (1966) defined two types of sediment numbers at which local scour begins and continuous sediment transport occurs, which are denoted by N_{sc1} and N_{sc2} , respectively. Additionally, he stated that “for irrotational flow, the velocity at the sides of the pier is twice the approach velocity. Therefore, a reasonable approximation is that $Z_{sc1} = Z_{sc2}/2$ ”. For the localized scour, the sediment number ranges from 1.12 to 2.24, corresponding to N_{sc1} and N_{sc2} , respectively.

2.3.3 Mechanism of Local Scour

Many researchers (Melville (1975); Ettema (1980); Qadar (1981); Chiew (1984); Davoren (1985); Hamill (1999); Melville and Coleman (2000); Richardson and Davis (2001); Sheppard (2004); (2005) in the past have believed that the basic mechanism of local scour is a system of vortices developed around bridge piers. Figure 2.10 shows the different components of flow field contributing to the scour around bridge piers.

Melville (1975) reported that the system of vortices (horseshoe vortex and wake vortex) developed around the bridge pier is the primary cause of the scour around the bridge pier. The horseshoe vortex increases the velocities near the bed, which results in an increase in sediment transport capacity of the flow. The wake vortex system keeps the sediment suspended condition and also acts as a ‘vacuum cleaner’ and the bed material is carried to downstream side by the eddies shaded from the pier.

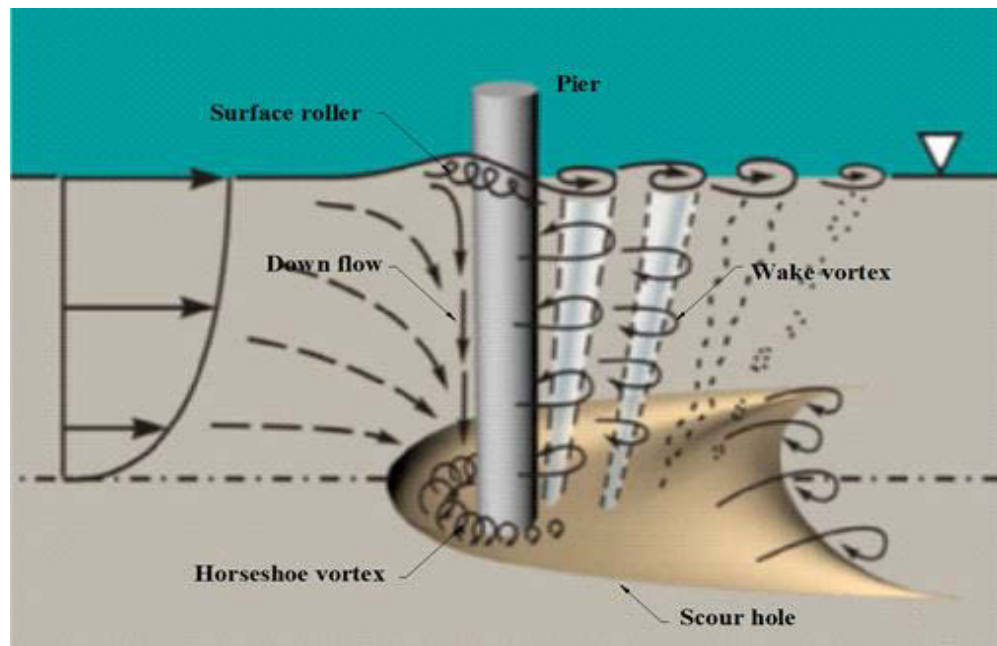


Figure 2.10 Flow field around bridge piers, (Ettema et al., 2011)

According to Qadar (1981), flow in front of a pier separated from the bed and rolls up to form a scouring vortex, which is identified as the basic mechanism of the local scour depth. He further concluded that the maximum depth of scour is a function of strength of the vortex, developing ahead of the pier. Chiew (1984) also suggested the same concept as Melville (1975). Additionally he has reported that the system of vortices can be separated into different components:

1. Down flow in front of the pier
2. Horseshoe vortex
3. Wake vortex and
4. Trailing vortex (in the case of submerged pier)

In order to understand the scour mechanism around a bridge pier, it is necessary to understand the flow field around piers. According to Ettema (1980), a flow field is a class of junction flow, which is characterised by the interaction of three dimensional turbulence structures. As reported by Melville and Coleman (2000), the principal features of the flow field at a bridge pier are down-flow at upstream side of the pier, the horseshoe vortex at the base of the pier, the surface roller at upstream side of the pier and wake vortices

downstream of the pier. Ettema et al. (2011) suggested three categories of pier flow field, depending on the width of the pier (D) and the depth of flow (h).

1. Narrow piers ($h/D > 1.4$)
2. Transitional piers ($0.2 < h/D < 1.4$)
3. Wide piers ($h/D < 0.2$)

The main features of flow field at narrow piers can easily be comprehended when considering a single column pier, installed in a relatively deep, wide channel as shown in Figure 2.10. In this type of pier, the scour is deepest at the pier face. Ettema et al. (2011) reported that the flow field at narrow piers consists of an interacting and unsteady set of flow features including, flow impact against the pier face producing down-flow and up-flow with rollers; flow converging, contracting then diverging; the generation, transport and dissipation of a large scale turbulence structure at the base of the pier foundation junction; detaching shear layer at each pier flank; and, wake vortices convected through the pier's wake. For the transition piers, there exists almost the same flow field as for narrow piers. However, the flow field (specially the down-flow) begins to alter in response to the reduction of the depth of flow or increase in the size of the pier. For wide piers, as the flow approaches the pier, it turns and flows laterally along the pier face before contracting and passing around the side of the pier. The weak down-flow is developed, causing less scouring at the centre of the pier in the upstream side. The wide pier increases flow blockage, which modifies the lateral distribution of approach flow over a longer distance upstream of a pier.

As flow approaches a pier, it decelerates and impinges against the pier's centreline. The flow comes to rest and the stagnation pressure on the upstream face of the pier attains a maximum near the level where the flow impinges. Hence, there is generation of a downward pressure gradient along the pier's leading face that causes the down-flow with a fully turbulent shear flow. In addition to this, the flow contracts as it pass around the sides of the pier with increase in flow velocity and bed shear stress. Hence, in most cases, the scour begins at the side of a pier and the high velocity washes the excavated bed materials to the downstream side. Melville (1975) concluded from his experiments that there was a strong vertical down-flow developed ahead of the cylinder as the scour hole

enlarged. He further noticed that the strength of the horseshoe vortex increased rapidly and the velocity near the bottom of the hole decreased as the scour hole was enlarged. Further increase in the scour hole results in the decrease in the vortex strength and reaches a constant value at the equilibrium stage. There is also an up-flow at the level of impinge, which interacts with the free water surface forming a surface roller and hence there is a rise in the water surface at the upstream side of the pier. The rise in the water surface depends on the approach velocity and the shape of the pier.

It was reported in the (2005) that the wake vortex system is also an important mechanism of scour around bridge piers. Wake vortices are developed due to flow separation on the bridge pier. Strong wake vortices may develop a large scour hole downstream from the piers. The vertical component of the flow at the wake put the bed material in suspension although there is a very weak streamwise and transverse component of velocity.

According to Sheppard (2004), the scour mechanism at the bridge pier also depends on the ratio of pier width to the sediment grain size, D/d_{50} . This mechanism results from the pressure gradient field generated by the presence of a structure such as a bridge pier in the flow. The pressure gradients impose pressure force on the sediment grains that can be much greater than the drag force due to the flow around the grains. The force due to this pressure gradient decreased with increase in the value of D/d_{50} .

2.3.4 Parameters for Analysis of Pier Scour

The local scour depth around bridge piers depends on various parameters, which are basically categorized in four different groups comprising the flow parameter, the bed sediment parameter, the pier geometry parameter and time. According to Melville and Coleman (2000), local scour can be defined as a function of the above mentioned parameters, which can be written as:

$$d_s = f(\rho, \nu, V, h, G, g, d_{50}, \sigma_g, \rho_s, V_c, D, K_{sh}, K_\alpha, t) \quad 2.32$$

where,

ρ = density of fluid

ν = kinematic viscosity of fluid

V = mean approach flow velocity

h = depth of flow

G = parameter describing the effects of lateral distribution of flow in the approach channel and the cross sectional shape of the approach channel

g = acceleration due to gravity

d_{50} = mean grain size of the sediment

σ_g = geometric standard deviation of the sediment

ρ_s = density of sediment material

V_c = critical mean flow velocity for sediment entrainment

D = diameter of a pier

K_{sh} = shape parameter of a pier

K_α = alignment parameter of the piers

t = time

As a result of dimensional analysis of the problem of local scour around bridge piers Equation 2.32 can be rewritten as follows:

$$\frac{d_s}{D} = f\left(\frac{V}{V_c}, \frac{h}{D}, \frac{D}{d_{50}}, \sigma_g, K_{sh}, K_\alpha, G, \frac{Vt}{D}, \frac{V}{\sqrt{gD}}, \frac{Vd}{\nu}\right) \quad 2.33$$

According to Ettema et al. (2011), the framework of sets of parameters in Equation 2.33 can be classified as primary and secondary parameters. The primary parameters were directly related to the structure and geometric scales of the pier flow field, which determine the major part of the maximum scour depth. For example h/D defines the

geometric scale of the pier flow field in a vertical plane parallel and perpendicular to the streamwise and the transverse direction, respectively; D/d_{50} is related to the length scale of pier width and mean grain size of bed material; K_{sh} and K_α indicate the pier shape and angle of flow attack parameters. On the other hand, the magnitudes of secondary parameters are prescribed by the primary parameters described above. $\frac{V}{V_c}$, $\frac{V}{\sqrt{gD}}$, $\frac{Vd}{\nu}$, and $\frac{Vt}{D}$ are the secondary parameters in which, V_c is prescribed by d_{50} , Euler number $\frac{V}{\sqrt{gD}}$ is related to the inertial force due to vortices. The term $\frac{Vd}{\nu}$ is the pier Reynolds number, which accounts for the vortex shedding behind the pier. The parameter $\frac{Vt}{D}$ characterizes the temporal development of scour associated with flow field and the foundation material. Detailed description of these parameters and their effects on the scour around bridge piers are presented in Section 2.3.5.

2.3.5 Factors Affecting the Local Scour at Bridge Site

Extensive investigations have been carried out for studying the factors affecting the local scour depth around bridge piers by many researchers, such as Laursen and Toch (1953); Ettema (1980); Raudkivi and Ettema (1983); Chiew (1984); Melville and Sutherland (1988); Yanmaz and Altinbilek (1991); Melville and Coleman (2000); and Ettema et al. (2011). According to Ettema et al. (2011), most of the studies have aimed to describe the influences of different parameters on the scour around bridge piers, although still there are significant gaps in overall understanding of the scour mechanism and the scour depth prediction. This may be due to the difficulties in conducting laboratory flume experiments on large geometric scales or insufficiency of reliable field data. Melville and Coleman (2000) provided comprehensive publications explaining the factors affecting the scour at bridge piers. They used laboratory data to assess the influence of each parameter as presented in Equation 2.33.

2.3.5.1 Effect of Flow Shallowness, h/D

According to Raudkivi (1998), the scour depth is independent of the depth of flow when it is greater than three times the pier diameter. He further reported that decrease in flow depth results in increase in the surface roller (bow wave) which interacts with the down-

flow and reduces its strength. Hence, no exact dependence of flow depth has been concluded.

The parameter flow shallowness, h/D represents the effect of depth of flow in relation to the width of the pier. Based on the D/h ratio Melville and Coleman (2000) classified scour processes in three different categories as shown in Table 2.1. The inequalities imply that the suggested relationships to evaluate the scour depth were derived from the plots of laboratory data, as shown in Figure 2.11. The same laboratory data were used to define the functional relationship, $d_s = f(D, h)$, describing the effect of flow shallowness on the local scour depth. For narrow pier or deep flow i.e. the large flow depth compared to the width of the pier, the scour depth is directly proportional to the width of the pier and is independent of the flow depth. Conversely, for the shallow flow or wide pier case, the depth of scour is directly proportional to the depth of flow and independent of the pier width. For intermediate depth of flow, the scour depth depends on both the depth of flow and the width of pier. These trends are clearly presented in Figure 2.11 in which the solid lines are the envelopes to the data applied to a wide pier, an intermediate pier and a narrow pier from left to right. The dashed lines represent the different values of V/V_c . These lines show that the scour depth is reduced considerably with the reduction in velocity of flow.

Table 2.1 Classification of local scour processes at bridge piers (after Melville and Coleman, 2000)

Pier Class	D/h	Local Scour Dependence
Narrow	$D/h < 0.7$	$d_s \propto D$
Intermediate width	$0.7 < D/h < 5$	$d_s \propto (Dh)^{0.5}$
Wide	$D/h > 5$	$d_s \propto h$

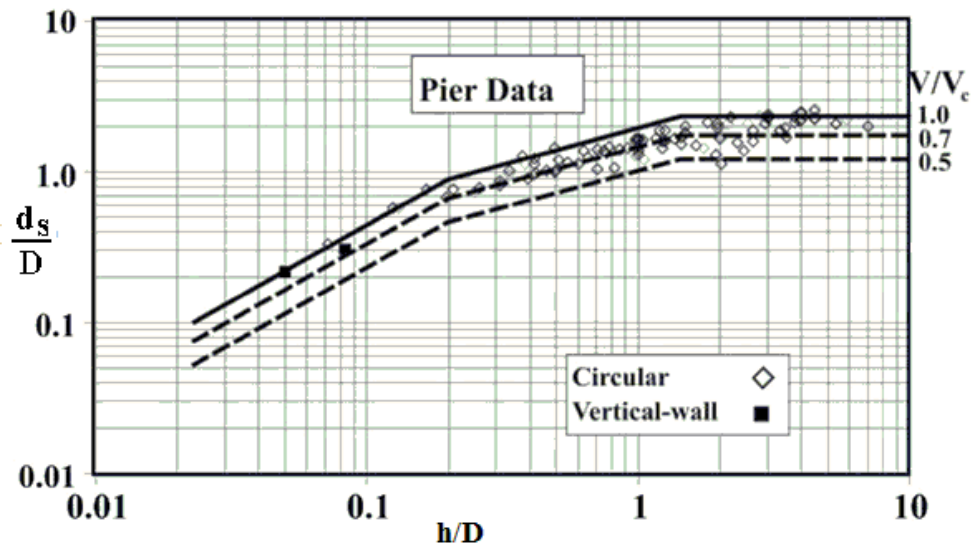


Figure 2.11 Influence of flow shallowness on local scour depth, (after Melville and Coleman, 2000)

2.3.5.2 Effect of Sediment Coarseness, D/d_{50}

The parameter D/d_{50} represents the relative coarseness of the flow boundary. According to Melville and Coleman (2000), for uniform sediments, local scour depths are unaffected by coarseness. However, the larger sediment size affects the local scour depth. If the value of sediment coarseness ratio, D/d_{50} is less than 50, local scour depth is influenced by sediment size. The relation between the sediment coarseness ratio and the local scour depth is clearly shown in Figure 2.12.

Ettema et al. (2011) reported that for uniform sediment, local scour depths are affected by sediment coarseness when the sediment is either relatively large or small. The smaller the value of sediment coarseness ratio, the larger the particle size. Hence, the scouring is reduced as the rough and porous bed dissipates some of the energy of the down-flow. It is suggested that when the value of sediment coarseness ratio, D/d_{50} , is less than 8, sediment particles are very large relative to the size of pier. In this case, the scouring is mainly due to erosion at the sides of the pier. Hence, there is a reduction in the scour depth.

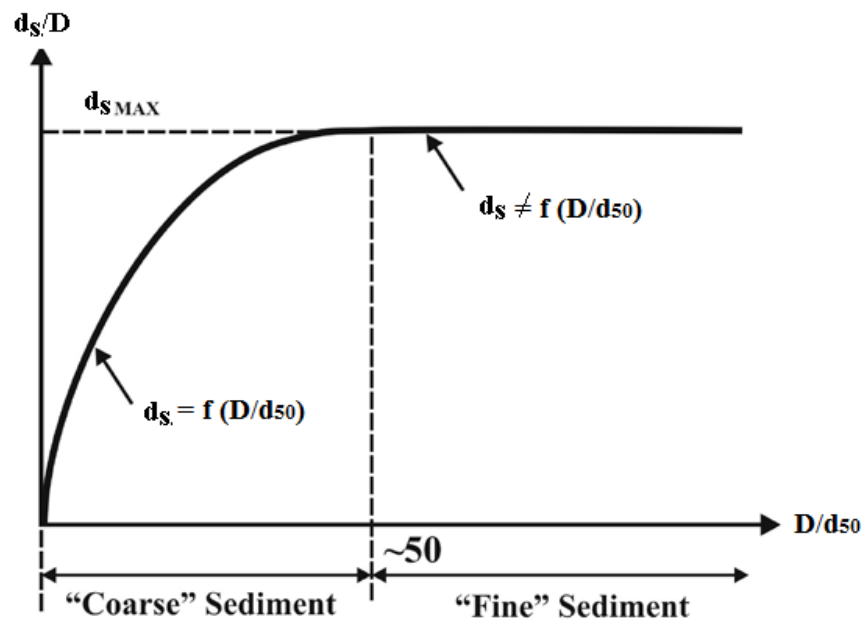


Figure 2.12 Effect of sediment coarseness on local scour; (after Melville and Coleman, 2000)

Breusers and Raudkivi (1991) reported that when the mean grain size of sediment, $d_{50} < 0.7$ mm, there was formation of ripples on the bed and for the sediment size of $d_{50} > 0.7$ mm ripples did not develop. Flatbed cannot be maintained for $d_{50} < 0.7$ mm under the clear water flow condition due to the development of ripples with a small amount of sediment transport taking place. This will replenish some of the sand scoured at the piers. Hence, local scour under the clear water flow condition cannot be maintained for ripple-forming sediment.

2.3.5.3 Effect of Sediment Non-uniformity, σ_g

The sediment non-uniformity is characterised using geometric standard deviation, σ_g , of the sediment particles. Sarlak and Tigrek (2011) expressed geometric standard deviation as $\sigma_g = (d_{84}/d_{16})^{0.5}$. As reported by Ettema et al. (2011) research since 1990 regarding the effect of sediment non-uniformity on local scour depth has not significantly updated the investigations from early laboratory studies by several investigators, such as Ettema (1976); Ettema (1980); Chiew (1984); and Baker (1986). Figure 2.13 shows the data on sediment non-uniformity and the corresponding scour depth under clear water condition from the previous studies.

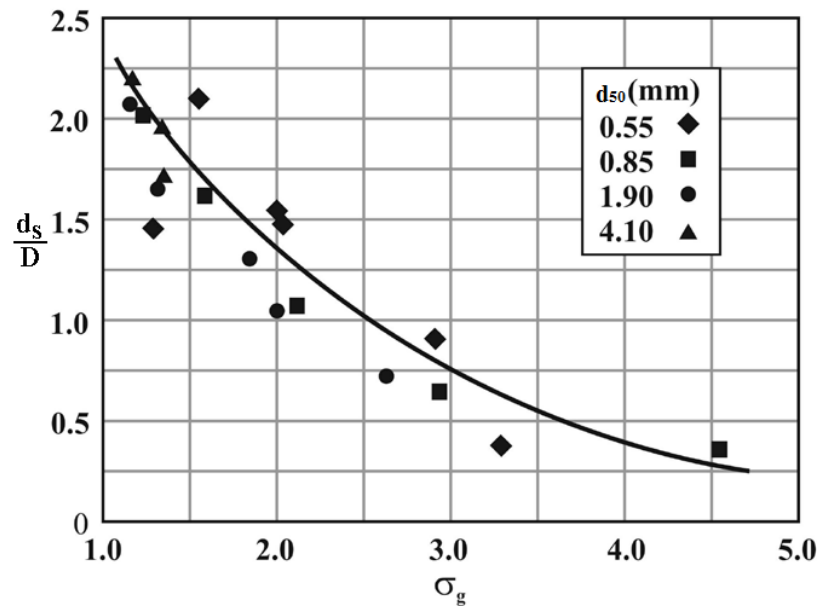


Figure 2.13 *Effect of sediment non-uniformity on local scour at bridge piers under clear water condition; (after Melville and Coleman, 2000)*

Melville and Coleman (2000) reported that a number of experimental studies were also carried out for the non-uniform sediment under live bed conditions by Ettema (1976) and Chiew (1984). The experiment was conducted at the threshold motion condition for the sediment used. From these studies, it can be concluded that the rate of scouring and the equilibrium scour depth decreases as the value of σ_g increases. Furthermore, it was reported that for a non-uniform sediment material, around the threshold condition, $V/V_c \approx 1$, armouring occurs at the base of the scour hole, leading to a considerable reduction of local scour depth. The effect of non-uniformity is minor for the higher values of V/V_c when the flow is capable of entraining most of the sediment particles. At intermediate values of V/V_c , the effect of sediment non-uniformity reduces with increasing flow velocity between these two limits because of which the grains are transported by the flow. This trend is clearly shown in Figure 2.14, which summarises the data schematically in a broader context for the effect of flow intensity, V/V_c , on the local scour depth.

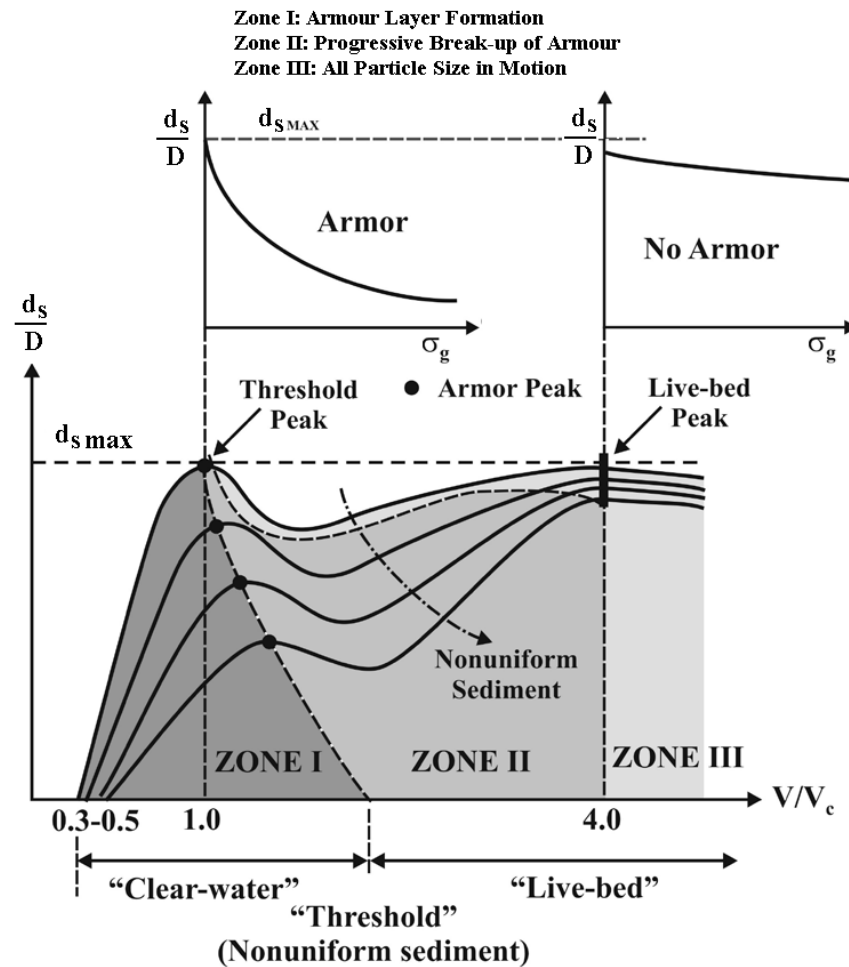


Figure 2.14 Variation of local scour depth with sediment non-uniformity, (after Melville and Coleman, 2000)

2.3.5.4 Effect of Pier Shape

Bridge piers are constructed in various basic shapes as illustrated in Figure 2.15. Most researchers believe that the depth of local scour depends on the obstruction inside the flow. As reported by Melville and Coleman (2000) the shape effects of bridge piers are usually given as a multiplying factors that accounts for the difference in local scour between a particular shape of pier and a simple circular cylindrical pier. These shape factors have been proposed by several investigators, such as Laursen and Toch (1956); Chabert and Engeldinger (1956); Melville and Coleman (2000); Richardson and Davis (2001); Sheppard and Miller (2006); and Ettema et al. (2011).

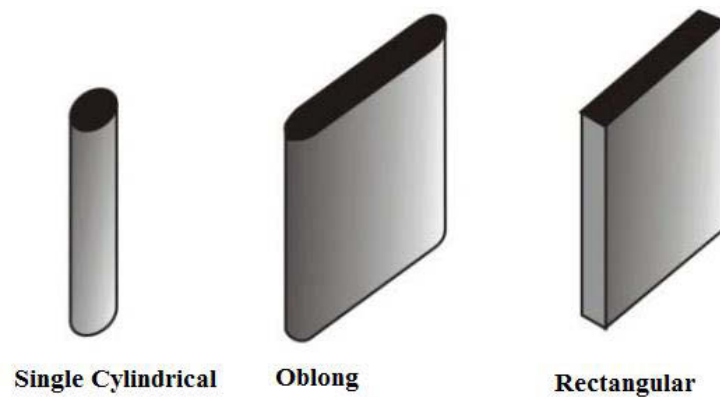


Figure 2.15 Basic pier shapes; (after Ettema et al., 2011)

Table 2.2 gives the value of shape factors for cylindrical piers as reported by Richardson and Davis (2001). They further suggested that these factors should be applicable to a pier only when it is aligned with the flow.

Table 2.2 Shape factors for different nosed shape piers; (after Richardson and Davis, 2001)

S.N	Pier Shape	Shape Factor, K_{sh}
1	Circular	1.0
2	Round Nosed	1.0
3	Square Nosed	1.1
4	Sharp Nosed	0.9

2.3.5.5 Effect of Pier Alignment, α

The pier alignment is also referred to as the angle of flow attack, representing the angle between the longitudinal axis of the bridge pier and the flow direction. According to Melville and Coleman (2000), the depth of local scour for all shapes of pier, except circular, is strongly affected by the angle of flow attack, α . This effect is shown in Figure 2.16 in which it is clear that increase in the angle results in increase in the scour depth. The multiplying factor, K_α , as shown in Figure 2.16 is recommended to be used in most of the existing pier scour equations. The projected width of pier is increased with increment of angle of flow attack; hence, the scour depth is also increased. Melville and

Coleman (2000) further reported that if the angle of flow attack is zero, there is no effect of length of the pier on the scour depth, whereas if the angle of flow attack deviates from zero i.e. the pier is skewed to the flow, the pier will experience a substantial effect. It was supported by an example that for a rectangular pier of aspect ratio eight, the scour depth is nearly tripled at an angle of flow attack of 30° when compared to the same pier with a zero angle of flow attack.

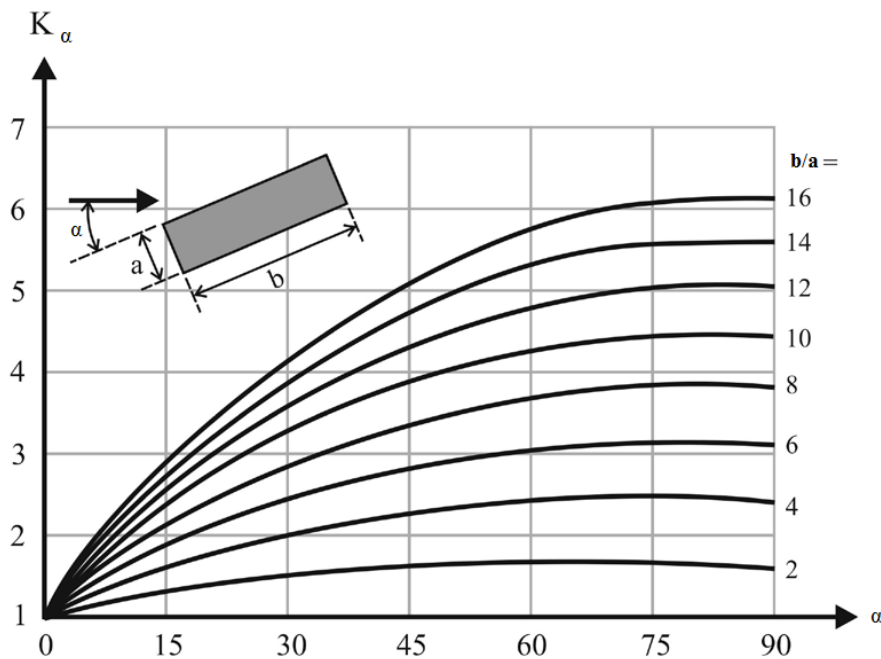


Figure 2.16 Variation of local scour depth with pier alignment; (after Melville and Coleman, 2000)

According to Breusers and Raudkivi (1991) the scour depth is a function of the projected width of pier, where the projected width is the width of the pier normal to the flow. They further suggested that the effect of angle of flow attack could practically be ignored for its value up to 5° to 10° . Ettema et al. (2011) reported that due to the influence of some parameters such as h/D and D/d_{50} , as discussed in the previous sections, the scour depth may not increase with an increase in the projected width. The effect of h/D and D/d_{50} on scour depth may vary with the angle of flow attack, affecting the projected width of the pier obstructing the flow. Although the effects of angle of flow attack, flow depth and mean grain size of the sediment are connected, recent studies on the prediction of scour depth have accepted them as mutually independent parameters.

2.3.5.6 Effect of Flow Intensity, V/V_c

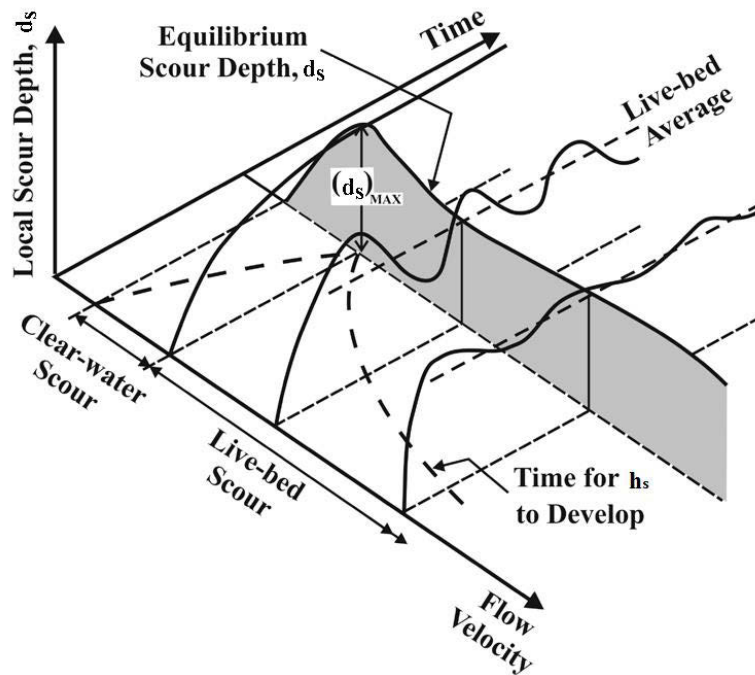


Figure 2.17 Variation of local scour depth with flow intensity, V/V_c , (after Melville and Coleman, 2000)

Melville and Coleman (2000) defined the flow intensity as the ratio of the free stream flow velocity, V , to the critical flow velocity of the sediment, V_c . Based on the flow intensity, the local scour at piers can be classified as local scour under the clear water condition and local scour under the live bed condition. Clear water scour occurs for the velocities up to the threshold condition, i.e. $V/V_c \approx 1$. In this condition, there is no supply of sediment to the scour hole; movement of the sediment materials occurs only around the obstruction like bridge piers. However, in the live bed scour condition, sediment is continuously supplied to the scour hole from upstream side. In live bed scour condition, the ratio V/V_c is greater than 1. The variation of scour depth at piers with flow intensity is schematically presented in Figure 2.17.

Figure 2.18 shows that the local scour depth in uniform sediment under the clear water flow condition increases almost linearly with velocity to the threshold peak (maximum) value at the threshold condition, $V/V_c \approx 1$. As the threshold velocity is greater than one, the local scour depth for uniform sediment first decreases and then increases again to a second peak with relatively small change in scour depth. However, the scour depths do

not exceed the threshold peak value and this second peak is called the live bed peak. According to Ettema et al. (2011), these trends of variation of scour depths have been observed by several investigators in their studies conducted over fifty years ago. It was concluded from the previous studies that the live bed scour depth is weakly dependent on the flow velocity.

Melville and Coleman (2000) presented the plots of laboratory data from several previous investigations for the schematic summarization of the effect of flow intensity on local scour depth under clear water and live bed scour conditions, as shown in Figures 2.18 and 2.19, respectively. In the figures, the data were presented for local scour depth in terms of the flow intensity parameter, K_l that is defined, for each set of data, as the ratio of scour depth for a particular flow intensity and the maximum scour depth for the whole data set. It is clear from the figures that for both uniform and non-uniform sediments under clear water conditions, the effects of the flow intensity factor are account for the local scour depth. However, for both the sediment types under live bed conditions, the flow intensity is insignificant for the variation of local scour depth.

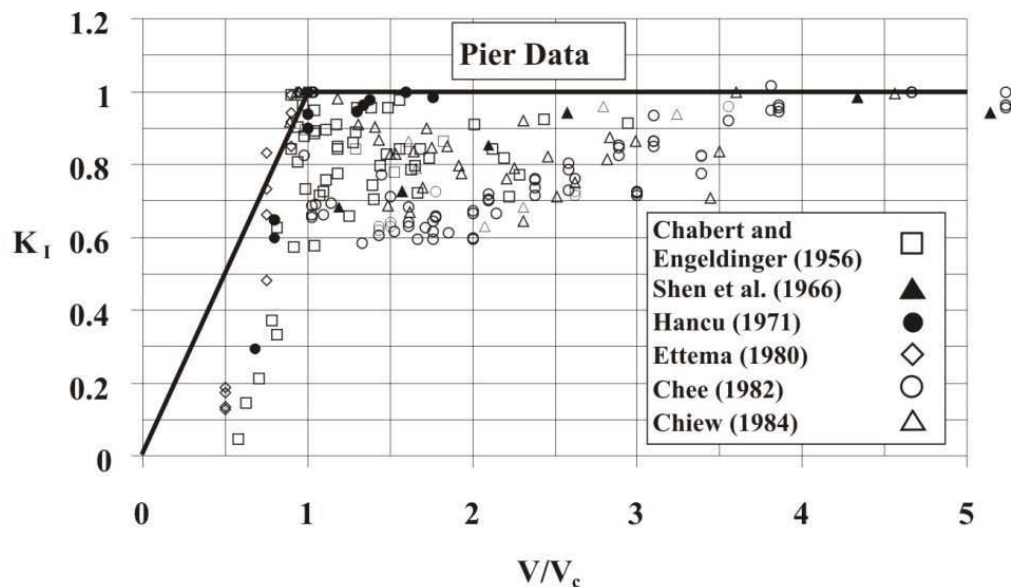


Figure 2.18 Effect of flow intensity on local scour depth in uniform sediment (after Melville and Coleman, 2000)

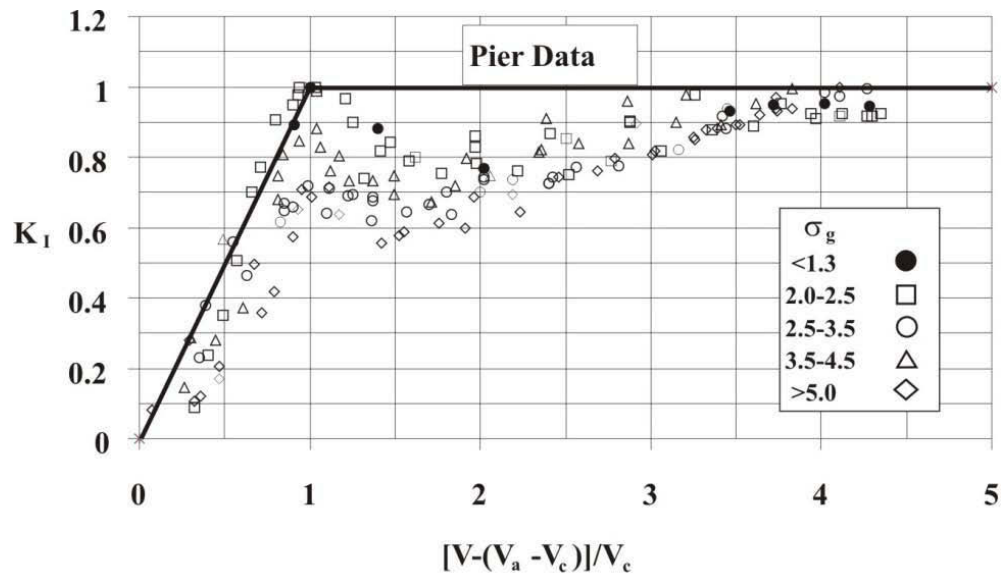


Figure 2.19 Effect of flow intensity on local scour depth in non-uniform sediment (after Melville and Coleman, 2000)

2.3.5.7 Effect of Froude Number, Fr and Reynolds Number, Re

According to Ettema et al. (1998) and Ettema et al. (2006), Froude number ($Fr = V/(gD)^{0.5}$) and Reynolds number ($Re = \rho VD/\mu$) are the turbulence structure parameters based on which the energy associated with turbulence structure and frequency of vortex shedding were characterised. Ettema et al. (1998) suggested that scour depth at pier does not scale linearly with pier width unless there is complete similitude of pier, flow and sediment particles. This non-linearity results in a deeper scour hole relative to a pier scour depth in a laboratory flume. They suggested that the Reynolds number in terms of viscosity is insignificant on pier scour depth. However, Reynolds number influences the frequency of shedding. They further showed that the Froude number could describe the energy gradient for flow around piers. The narrower the pier size, the larger the Froude number, and hence the lesser the scour depth. Another study by Ettema et al. (2006) defined the correction factor that could be used to account for the Froude number effect in laboratory scale tests. Figure 2.20 shows the variation of scour depth with Froude number.

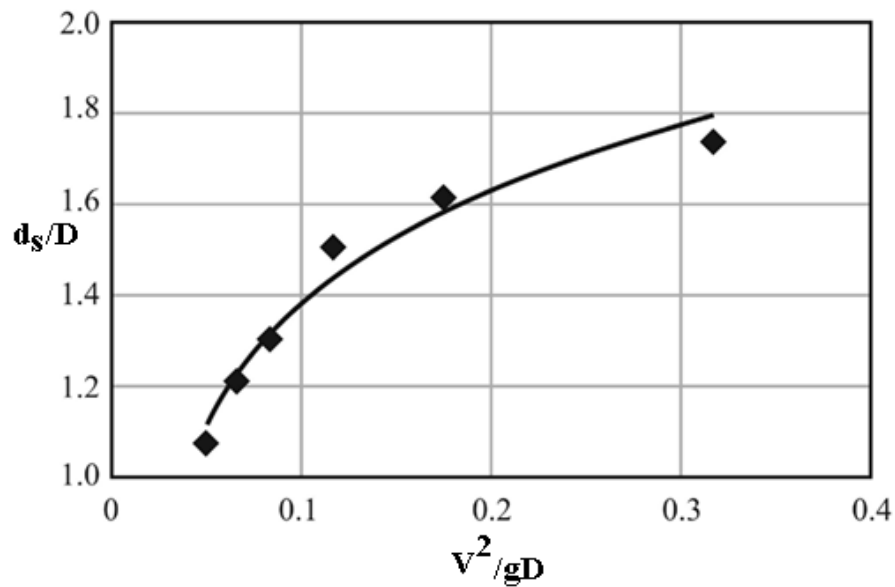


Figure 2.20 Variation of scour depth with Froude number; (after Ettema et al., 2006)

2.3.5.8 Effect of Time

Temporal variation of local scour depth has been extensively studied in the past by a number of investigators, such as Chabert and Engeldinger (1956); Hannah (1978); Ettema (1980); Melville and Chiew (1999); Oliveto and Hager (2002); Oliveto and Hager (2005); and Kothiyari et al. (2007). The most common conclusion from the previous studies is that the process of scouring is asymptotic. Ettema et al. (2011) reported that the local scour rate and equilibrium scour depth under clear water and live bed conditions are different. The conceptual illustration of time development trend of scour depth is presented in Figure 2.21. This figure shows that for clear water scour conditions, asymptotic development of scour depth occur towards the equilibrium condition. While, under live bed conditions, the equilibrium scour depth is reached more quickly and thereafter the scour depth oscillates due to the passage of bed materials past the piers. Hence, in most of the cases for the scour under live bed conditions, the time development of scour depth is not of major significance. The details on temporal development on scour depth are clearly explained in Section 2.3.7.

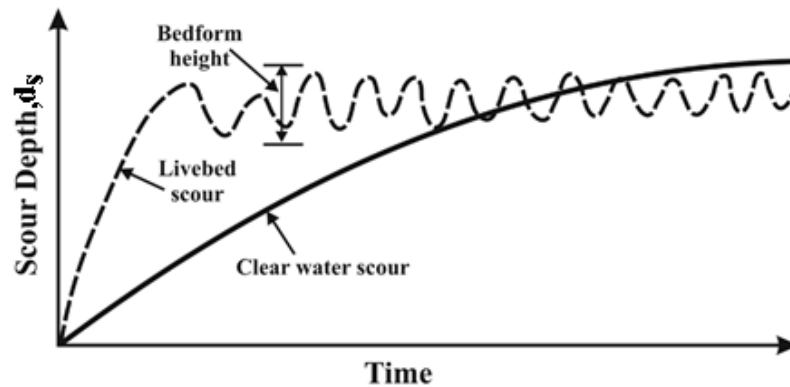


Figure 2.21 Time development of scour depth under clear water and live bed conditions; (after Ettema et al., 2011)

2.3.6 Equilibrium Scour Depth

Since the early stages of research on scouring, it has become clear that the equilibrium scour depth is the condition at which there is no further movement of bed material from the scour hole. Chabert and Engeldinger (1956), suggested that equilibrium scour occurs when the scour depth does not change appreciably with time. According to Ettema (1980), there are three phases of scour process in which the last phase is an equilibrium phase, where the scour depth does not increase anymore. However, Coleman et al. (2003), suggested that an equilibrium scour hole may continue to deepen at a relatively slow rate. Researchers have different opinions regarding the time to reach the equilibrium scour depth. For example, researchers such as Melville and Chiew (1999), Coleman et al. (2003), defined time to equilibrium as the time at which the rate of scour reduces to 5% of the pier diameter or abutment length in a 24 hour period. Ettema (1980), defined the time to equilibrium scour as the time at which no more than 1 mm of incremental scour can be realized within a timeframe of four hours. Furthermore, Melville and Coleman (2000), suggested that for small scale laboratory experiments of clear water scour depth development at bridge foundations, the time to achieve the equilibrium conditions should be several days. It is reported that the data obtained after lesser time, say 10 to 12 hours, can exhibit scour depths less than 50% of the equilibrium depth.

2.3.7 Temporal Variation of Scour Depth

As suggested by Breusers et al. (1977); and Melville and Chiew (1999), the local scour depth under the clear water condition reaches to equilibrium state asymptotically with time and hence time to develop equilibrium scour depth may be infinite. However, in the live bed scour condition, the scour depth reaches the equilibrium condition much more quickly and it oscillates in response to the translation of bed features. Figure 2.22 shows the basic concept of temporal variation of scour depth under the clear water and live bed conditions. Due to the complexity of the scour process, prediction of the maximum scour depth within a given time frame is very difficult. Hence, different investigators have considered several methods to work out the relationship of temporal variation of the scour depth. For the safe and economic design of bridge piers, it is very important to know the variation of the scour depth with time. Attempts to describe temporal variation of the scour depth around bridge piers have been made by several investigators, such as Chabert and Engeldinger (1956); Hannah (1978); Ettema (1980); Yanmaz and Altinbilek (1991); Kothyari et al. (1992); Nazariha (1996); Melville and Chiew (1999); Melville and Coleman (2000); Oliveto and Hager (2002); Mia and Nago (2003); and Kothyari et al. (2007).

Chabert and Engeldinger (1956) were the very first investigators who conducted complete sets of experimental studies to introduce the effect of time and velocity on the clear water and live bed scour at bridge piers. They conducted about 300 experimental tests using different channels, piers sizes and piers shapes over time ranging from a few hours to days. In addition to this, they conducted some experiments to study the protective measures of local scour. Hannah (1978) conducted an array of experimental tests including a single pile and two piles for the study of temporal variation of scour depth. The experiments were conducted for a seven hour duration. From that study no general relationships comprising the temporal variation was established.

It was reported by Ettema (1980) that the time to reach the equilibrium scour depth around a bridge pier was about 14 days. He classified the three different phases of the development of scour hole namely: the initial phase, the erosion phase and the equilibrium phase. In the initial phase, the scour hole was developed in a rapid rate of

scouring. In the erosion phase, the development of scour hole was due to the size and strength of the horseshoe vortex. Finally the equilibrium phase was associated with the equilibrium scour depth for a given size of the piers, sediment and the flow condition. Yanmaz and Altinbilek (1991) conducted a series of experimental tests for the determination of time-dependent shapes of scour holes around bridge piers. The experiments were run for different test durations such as 5 min, 20 min, 60 min, and 150 min. They developed a semi empirical differential equation based on the sediment continuity equation to determine the scour depth as a function of time.

Kothyari et al. (1992) conducted some experiments on temporal variation of scour depth around a circular bridge pier placed in uniform, non-uniform and stratified beds under steady and unsteady clear water flows. From this study, a procedure to compute the temporal variation of scour depth under the above mentioned conditions was developed which was based on the fact that the primary vortex in front of the pier is the primary agent causing the scour. Nazariha (1996) conducted long duration experimental tests to study the temporal variation of scour depth. The experiments were carried out for 90 hours long duration. From his experiment it was reported that the most sediment removal occurs during the first half hour, after this the rate of scouring was slowed down. Furthermore he concluded that about 83% of total scouring occurs within the first two hours.

Melville and Chiew (1999) carried out a set of experimental tests for the temporal development of clear water local scour at cylindrical bridge piers in uniform sand beds. The authors stated that the asymptotic nature of development of scour depth with time shows that it may take infinite time to reach equilibrium scour depth which creates a difficult situation to define a certain time to stop the experiment. In order to overcome such difficulty, they introduced a new definition of time to equilibrium scour depth as: “ t_e is defined as the time at which the scour hole develops to a depth at which the rate of increase of scour hole does not exceed 5% of the pier diameter in the succeeding 24 hours period” where t_e is the time to develop the equilibrium scour depth. The experimental data plotted in Figure 2.22, show that the scour depths at the same stage of development are reduced at lower values of V/V_c . The Authors also expressed the results, shown in Figure 2.22, in a mathematical form given in Equation 2.34.

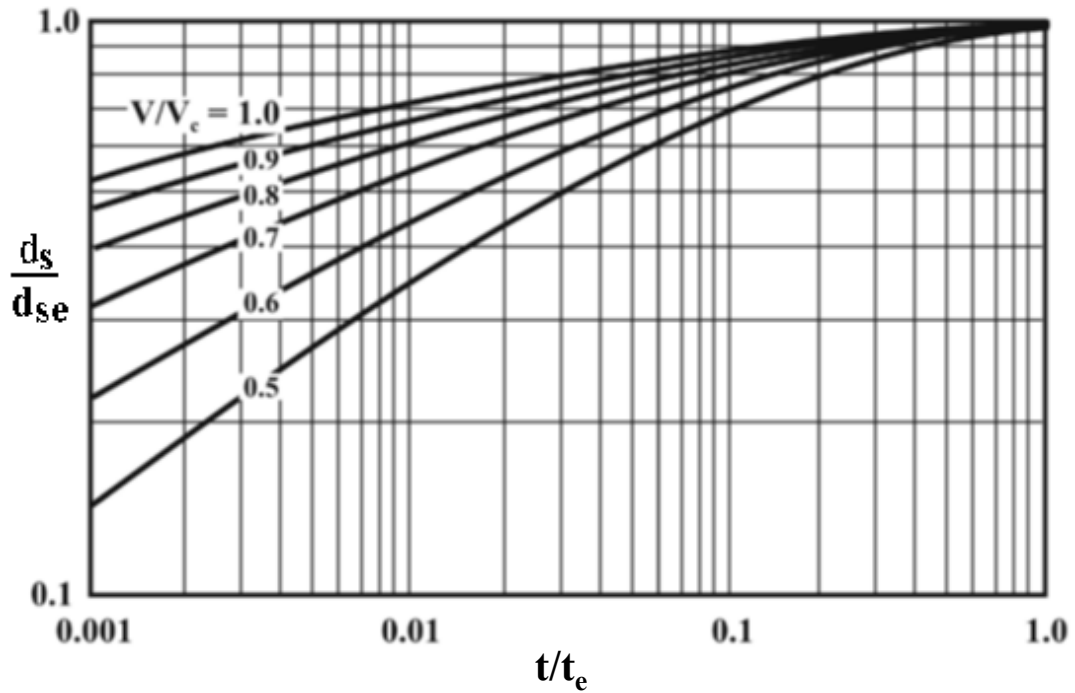


Figure 2.22 Temporal development of scour depth; (after Melville and Chiew, 1999)

$$\frac{d_s}{d_{se}} = \exp \left\{ -0.03 \left| \frac{V_c}{V} \ln \left(\frac{t}{t_e} \right) \right|^{1.6} \right\} \quad 2.34$$

where expression for t_e is given as:

$$t_e \text{ days} = 48.26 \frac{D}{V} \left(\frac{V}{V_c} - 0.4 \right) \quad \text{for} \quad \frac{y}{D} > 6, \quad \frac{V}{V_c} > 0.4 \quad 2.35$$

$$t_e \text{ days} = 30.89 \frac{D}{V} \left(\frac{V}{V_c} - 0.4 \right) \left(\frac{h}{D} \right)^{0.25} \quad \text{for} \quad \frac{y}{D} < 6, \quad \frac{V}{V_c} > 0.4 \quad 2.36$$

where,

D = diameter of the pier

V = average approach velocity

V_c = critical velocity of flow

h = flow depth

Oliveto and Hager (2002) conducted an experimental investigation on temporal evolution of clear water pier and abutment scour. In this study, six different sediments were tested. They derived an equation for temporal evolution of scour depth using similarity arguments and the analogy to the flow resistance. The proposed equation depends on three different parameters namely: the reference length of pier or abutment, the sediment Froude number and the relative time.

All of the above investigations on temporal variation of scour depth have a common outcome, stating that the local scour depth increases with time asymptotically and finally reaches the equilibrium value. However, nobody defined the exact time to reach the equilibrium scour depth. Although there are various equations developed to estimate the time to develop equilibrium scour depth, mathematical expressions given by Melville and Chiew (1999), given in Equations 2.34 to 2.36, have been observed to be very practical and simple, which can predict a reasonably precise outcome. Hence, for the present research, these equations are adopted for further analysis and calculation of temporal development scour depth around bridge piers.

2.3.8 Estimation of Equilibrium Scour Depth

In the past research history, numerous equations have been developed by several investigators for prediction of the local scour depth around bridge piers. A list of well-known equations reported by Ettema et al. (2011) are tabulated in Table 2.3.

Table 2.3 List of previous equations for scour depth (after Ettema et al. 2011)

Reference	Equation	Standard format
Inglis (1949)	$\frac{d_s + h}{D} = 2.32 \left[\frac{Q^{2/3}}{D} \right]^{0.78}$	$\frac{d_s}{D} = 2.32 \left[\frac{Q^{2/3}}{D} \right]^{0.78} - \frac{h}{D}$
	Q = average discharge intensity upstream of the bridge	
Ahmad (1951)	$d_s + h = K_s Q_2^{2/3}$	$\frac{d_s}{D} = K_s \frac{Q_s^{2/3}}{D} - \frac{h}{D}$
	Q_s = local discharge intensity in contracted channel	
Laursen (1958)	$\frac{D}{h} = 5.5 \frac{d_s}{h} \left[\left\{ \frac{d_s}{11.5y} + 1 \right\}^{1.7} - 1 \right]$	$\frac{d_s}{D} = 1.11 \left(\frac{h}{D} \right)^{0.5}$
	Applies to live bed scour	
Chitale (1962)	$\frac{d_s}{h} = 6.6 Fr - 0.51 - 5.49 Fr^2$	$\frac{d_s}{D} = [6.6 Fr - 0.51 - 5.49 Fr^2] \left(\frac{h}{D} \right)$
	Applies to live bed scour	
Larras (1963)	$d_s = 1.05 K_s K_\alpha D^{0.75}$	$\frac{d_s}{D} = 1.05 K_s K_\alpha D^{-0.25}$
Neil (1964)	$d_s = 1.5 D^{0.7} h^{0.3}$	$\frac{d_s}{D} = 1.5 \left(\frac{h}{D} \right)^{0.3}$
	The factor 1.5 applies for circular piers	
Breusers (1965)	$d_s = 1.4 D$	$\frac{d_s}{D} = 1.4$
	Derived from data for tidal flows	

Shen et al. (1969)	$d_s = 0.000223 \left(\frac{V_a}{\nu}\right)^{0.619}$	$\frac{d_s}{D} = 2.34 \left(\frac{h}{D}\right)^{0.381} Fr^{0.619} h^{-0.06}$
	Standard format equation is given for kinematic viscosity of water, $\nu = 1 \times 10^{-6} \text{ m}^2/\text{s}$	
Coleman (1971)	$\frac{V}{\sqrt{2gd_s}} = 0.6 \left(\frac{V}{D}\right)^{0.9}$	$\frac{d_s}{D} = 0.54 \left(\frac{h}{D}\right)^{0.19} Fr^{1.19} h^{0.41}$
Hancu (1971)	$\frac{d_s}{D} = 2.42 \left(\frac{2V}{V_c} - 1\right) \left(\frac{V_c^2}{gD}\right)^{1/3}$	$\frac{d_s}{D} = 2.42 \left(\frac{h}{D}\right)^{1/3} Fr^{2/3}$
	$\frac{2V}{V_c} - 1 = 1$ for live bed scour. Standard format equation is given for threshold condition	
Neill (1973)	$d_s = K_s D$	$\frac{d_s}{D} = K_s$
	$K_s = 1.5$ for round nosed and circular piers; $K_s = 2$ for rectangular piers	
Breusers et al. (1977)	$\frac{d_s}{D} = f\left(\frac{V}{V_c}\right) \left[2.0 \tanh\left(\frac{h}{D}\right)\right] K_s K_\alpha$	$\frac{d_s}{D} = \left[2.0 \tanh\left(\frac{h}{D}\right)\right] K_s K_\alpha$

	$f\left(\frac{v}{v_c}\right) = 0; \text{ for } \frac{v}{v_c} \leq 0.5$ $= 2\frac{v}{v_c} - 1; \text{ for } 0.5 < \frac{v}{v_c} < 1$ $= 1; \text{ for } \frac{v}{v_c} > 1$ <p>Standard equation is given at the threshold condition</p>	
Jain and Fischer (1980)	$\frac{d_s}{D} = 1.86 \left(\frac{h}{D}\right)^{0.5} (Fr - Fr_c)^{0.25}$	$\frac{d_s}{D} = 1.86 \left(\frac{h}{D}\right)^{0.5}$
	$Fr = \frac{V}{\sqrt{gh}}$ $Fr_c = \frac{V_c}{\sqrt{gh}}$ <p>Standard format equation is given at the threshold condition</p>	
Jain (1981)	$\frac{d_s}{D} = 1.84 \left(\frac{h}{D}\right)^{0.3} (Fr_c)^{0.25}$	$\frac{d_s}{D} = 1.84 \left(\frac{h}{D}\right)^{0.3}$
	<p>Standard format equation is given at the threshold condition</p>	
Chitale (1988)	$d_s = 2.5 D$	$\frac{d_s}{D} = 2.5$
Melville and Sutherland (1988)	$\frac{d_s}{D} = K_I K_h K_d K_s K_\alpha$	$\frac{d_s}{D} = 2.4 K_h K_d K_s K_\alpha$
	<p>For an aligned pier, $d_s \text{ max} = 2.4 K_s K_d$. Standard format equation is given at threshold condition</p>	

Froehlich (1988)	$\frac{d_s}{D} = 0.32 K_s Fr^{0.2} \left(\frac{D_p}{D}\right)^{0.62} \left(\frac{h}{D}\right)^{0.46} \left(\frac{D}{d_{50}}\right)^{0.08} + 1$	$\frac{d_s}{D} = 0.32 K_s Fr^{0.2} \left(\frac{D_p}{D}\right)^{0.62} \left(\frac{h}{D}\right)^{0.46} \left(\frac{D}{d_{50}}\right)^{0.08} + 1$
	$D_p = \text{projected width of pier}; Fr = \frac{v}{\sqrt{gh}}$	
Breusers and Raudkivi (1991)	$\frac{d_s}{D} = 2.3 K_h K_s K_d K_\sigma K_\alpha$	$\frac{d_s}{D} = 2.3 K_h K_s K_d K_\sigma K_\alpha$
	For an aligned pier $d_{\max} = 2.3 K_s K_d K_\sigma D$	
Richardson and Davis (1995)	$d_s = 2.0 K_1 K_2 K_3 K_w h^{0.35} D^{0.65} F_r^{0.43}$	$\frac{d_s}{D} = 2.0 K_1 K_2 K_3 K_w \left(\frac{h}{D}\right)^{0.35} F_r^{0.43}$
Ansari and Qadar (1994)	$d_s = 0.86 D_p^3 \quad \text{for } D_p < 2.2 \text{ m}$ $d_s = 3.6 D_p^{0.4} \quad \text{for } D_p >$	$\frac{d_s}{D_p} = 0.86 D_p^2 \quad \text{for } D_p < 2.2 \text{ m}$ $d_s = 3.6 D_p^{-0.6} \quad \text{for } D_p >$
Wilson (1995)	$\frac{d}{D^*} = 0.9 \left(\frac{h}{D^*}\right)^{0.4}$	$\frac{d_s}{D^*} = 0.9 \left(\frac{h}{D^*}\right)^{0.4}$ <p style="text-align: center;">$D^* = \text{effective width of pier}$</p>

2.3.8.1 Laursen and Toch Method

Laursen and Toch (1956) developed a series of design curves based on their prototype model studies. According to the citation made on Melville and Sutherland (1988), the curves were later presented in the form of a mathematical formula by Neill (1964). The equation is expressed as:

$$d_1 = 1.35 D^{0.7} h^{0.3} \quad 2.37$$

2.3.8.2 Melville and Coleman Method

Melville and Coleman (2000), presented a modified form of scour depth prediction equation, initially proposed by Melville (1997), inserting a time factor suggested by Melville and Chiew (1999). The equation consists of various multiplying factors for the effects of the various parameters influencing the scour depth. Equation 2.38 represents this modified equation for the scour depth prediction. This equation is applicable to predict the equilibrium local scour depth only.

$$d_1 = K_{hD} K_I K_d K_\alpha K_{sh} K_G K_t \quad 2.38$$

where,

K_{hD} = depth size factor

K_I = Flow intensity factor

K_d = Sediment size factor

K_α = Pier alignment factor

K_{sh} = Pier shape factor

K_G = Channel geometry factor

K_t = Time factor

The above factors are presented in Table 2.4.

Table 2.4 Different correction factors of Equation 2.38 (after Melville and Coleman, 2000)

Flow depth-pier size factor, K_{hD}		
$K_{hD} = 2.4D$	$\frac{D}{h} < 0.7$	2.39a
$K_{hD} = 2\sqrt{hD}$	$0.7 < \frac{D}{h} < 5$	2.39b

$K_{hD} = 4.5h$	$\frac{D}{h} > 5$	2.39c
Flow intensity factor, K_I		
$K_I = \frac{V - (V_a - V_c)}{V_c}$	$\frac{V - (V_a - V_c)}{V_c} < 1$	2.40a
$K_I = 1$	$\frac{V - (V_a - V_c)}{V_c} \geq 1$	2.40b
Sediment size factor, K_d		
$K_d = 0.57 \log \left(2.24 \frac{D}{d_{50}} \right)$	$\frac{D}{d_{50}} \leq 25$	2.41a
$K_d = 1$	$\frac{D}{d_{50}} > 25$	2.41b
Pier alignment factor, K_α		
$K_\alpha = \left(\frac{D_p}{D} \right)^{0.65}$	$\frac{D_p}{D} = 1,$ <i>for $\alpha = 0$</i>	2.42
Pier shape factor, K_{sh} for uniform pier	K_{sh}	
Circular	1.0	
Round Nosed	1.0	
Square Nosed	1.1	
Sharp Nosed	0.9	
Time factor, K_t as per Equations 2.34, 2.35 and 2.36		

Additionally, Melville and Coleman (2000) presented the pile group shape factor for a pier comprising a row of cylindrical columns in terms of flow angle, diameter of the column, spacing between two columns. These shape factors are based on the data provided by Hannah (1978) and is represented by $K_{sh}K_{\alpha}$, as summarised in Table 2.5.

Table 2.5 Shape factor ($K_{sh}K_{\alpha}$) for multiple columns aligned in a row (after Melville and Coleman, 2000)

S.N.	L/D	$K_{sh}K_{\alpha}$		
		$\alpha < 5^{\circ}$	$\alpha = 5^{\circ}$ to 45°	$\alpha = 90^{\circ}$
1	2	1.12	1.4	1.2
2	4	1.12	1.2	1.1
3	6	1.07	1.16	1.08
4	8	1.04	1.12	1.02
5	10	1.00	1.00	1.00

In order to predict the maximum scour depth around the group of piles, Ataie-Ashtiani and Beheshti (2006) have proposed a multiplying factor (K_{Gmn}) obtained by using their own data and others pre-existing scour data. The value of K_{Gmn} can be computed from Equation 2.43 as follows:

$$K_{Gmn} = 1.118 \frac{m^{0.0895}}{[(n)^{0.8949} (G/D)^{0.1195}]} \quad 2.43$$

Where, m = number of piles in line with the flow; n = numbers of piles normal to the flow and G = spacing between two columns measured inner-to-inner face (clear spacing between two columns).

2.3.8.3 HEC-18 Equation

Another famous equation, proposed by Richardson and Davis (2001) to estimate local scour depth, is the HEC-18 equation. The equation is also widely known as the Colorado State University Equation (CSU Equation), which is expressed as:

$$d_s = 2.0K_1K_2K_3K_w h^{0.35} D^{0.65} Fr^{0.43} \quad 2.44$$

where,

K_1 = adjustment factor for pier shape

K_2 = adjustment factor for angle of attack

K_3 = adjustment factor for bed condition

K_w = adjustment factor for wide pier

Fr = Froude number = $\frac{V}{\sqrt{gh}}$

In the above equation, the values of K_1 , K_2 and K_3 for various conditions are presented in Tables 2.6, 2.7 and 2.8, respectively as follows:

Table 2.6 Correction factor K_1 for pier nose shape (after Richardson and Davis, 2001)

S.N	Shape of Pier Nose	K_1
1	Square nose	1.1
2	Round nose	1.0
3	Circular cylinder	1.0
4	Group of cylinders	1.0
5	Sharp nose	0.9

Table 2.7 Correction factor K_2 for angle of attack (after Richardson and Davis, 2001)

S.N	Angle	$L'/D = 4$	$L'/D = 8$	$L'/D = 12$
1	0	1.0	1.0	1.0
2	15	1.5	2.0	2.5
3	30	2.0	2.75	3.5
4	45	2.3	3.3	4.3
5	90	2.5	3.9	5.0

Where, Angle = skew angle of flow; L' = length of pier

Table 2.8 Correction factor K_3 for bed condition (after Richardson and Davis, 2001)

S.N	Bed Condition	Dune height, ft	K_3
1	Clear water scour	N/A	1.1
2	Plane bed and Anti-dune flow	N/A	1.1
3	Small Dunes	$10 < H \leq 2$	1.1
4	Medium Dunes	$30 > H \geq 10$	1.2 to 1.1
5	Large Dunes	$H \geq 30$	1.3

The factor K_w can be computed from the following equation:

$$K_w = 2.58 \left(\frac{h}{D} \right)^{0.34} Fr^{0.65} \quad \text{for } \frac{V}{V_c} < 1.0 \quad 2.45$$

$$K_w = 1.0 \left(\frac{h}{D} \right)^{0.13} Fr^{0.25} \quad \text{for } \frac{V}{V_c} > 1.0 \quad 2.46$$

Furthermore, Richardson and Davis (2001) reported on the scour depth around multiple columns skewed to the flow. They stated that the scour depth depends on the spacing between the columns. Based on the statement by Raudkivi (1998) for the effect of alignment, Richardson and Davis (2001) stated that if the multiple columns are spaced 5 diameters or greater apart and debris is not a problem, the limit scour depth will be approximately 1.2 times the maximum local scour of a single column.

Ataie-Ashtiani and Beheshti (2006), proposed a correction factor (K_{Gmn}) applicable to Equation 2.47 to predict the maximum scour depth around a group of cylindrical columns. The factor K_{Gmn} can be computed using Equation 2.47:

$$K_{Gmn} = 1.11 \frac{m^{0.0396}}{[(n)^{0.5225} (G/D)^{0.1153}]} \quad 2.47$$

The notations of Equation 2.47 are similar to Equation 2.43. This correction factor represents the ratio of scour depth at a particular column group with particular spacing (G/D) to that of the equivalent solid column that has dimension of the group of columns when the columns are touching each other.

2.3.8.4 Sheppard/Melville Equation

Sheppard et al. (2014) proposed a method to predict the equilibrium scour depth combining the previous equations suggested by Sheppard and Miller (2006) and Melville (1997). The equations were slightly modified to form a new equation, referred as the Sheppard/Melville equation or simply the S/M equation. The results from the study show that the S/M equation exhibits the best performance among tested equations and is recommended to be applied in the prediction of equilibrium scour depths. The equations are:

$$\frac{d_s}{D} = 2.5f_1f_2f_3 \quad \text{for } 0.4 \leq \frac{V}{V_c} \leq 1.0 \quad 2.48$$

$$\frac{d_s}{D} = f_1 \left[2.2 \left(\frac{\frac{V}{V_c} - 1}{\frac{V_{lp}}{V_c} - 1} \right) + 2.5f_3 \left(\frac{\frac{V_{lp}}{V_c} - \frac{V}{V_c}}{\frac{V_{lp}}{V_c} - 1} \right) \right] \quad \text{for } 1 \leq \frac{V}{V_c} \leq \frac{V_{lp}}{V_c} \quad 2.49$$

$$\frac{d_s}{D} = 2.2f_1 \quad \text{for } \frac{V}{V_c} > \frac{V_{lp}}{V_c} \quad 2.50$$

$$f_1 = \tanh \left[\left(\frac{h}{D} \right)^{0.4} \right] \quad 2.51$$

$$f_2 = \left\{ 1 - 1.2 \left[\ln \left(\frac{V}{V_c} \right) \right]^2 \right\} \quad 2.52$$

$$f_3 = \left[\frac{\left(\frac{D}{d_{50}} \right)}{0.4 \left(\frac{D}{d_{50}} \right)^{1.2} + 10.6 \left(\frac{D}{d_{50}} \right)^{-0.13}} \right] \quad 2.53$$

where V_{lp} is the live bed peak velocity which can be computed as the larger of the values from following equations:

$$V_{lp} = 0.6\sqrt{gh} \quad 2.54$$

$$V_{lp} = 5V_c \quad 2.55$$

The sediment critical velocity, V_c , used in the above mentioned equations can be computed using Shield's diagram as discussed in Section 2.3.1.1.

2.4 Open Channel Flow and Flow around Bridge Piers

It is essential to understand the hydraulics of open channel flow and sediment transport for the study of flow and scour around the hydraulic structures like bridge piers. The nature of flow in an open channel is highly dependent on the types of boundary. Flow over a moveable boundary behaves differently from the rigid boundary flow. When the bed materials start to move, there is an interaction between flow and the boundary, resulting in a complex nature of flow. However, to understand the flow in moveable boundary channels, the basic concept of flow over rigid boundaries should be reviewed and the hydraulics of moveable boundary channels can be introduced.

2.4.1 Hydraulics of Open Channel Flow

An open channel flow is simply a free surface fluid flow, which describe the fluid motion in open channel for example Chaudhry (2007) and Chanson (2004). The fundamental types of open channel flow are based on the change in velocity of flow with respect to time and space which are described as follows:

Considering time as a criterion, open channel flow can be classified as:

1. **Steady flow:** The flow is considered as steady if the depth of flow and hence the velocity of flow at a point does not change over time. Mathematically it can be expressed as $\partial v/\partial t = 0$, where ∂v is the variation of the flow velocity at a given point over the elapsed time ∂t .
2. **Unsteady flow:** In this type of flow, the depth of flow and the velocity of the flow at a point change with time i.e. $\partial v/\partial t \neq 0$.

On the other hand, open channel flow can be classified according to the space criterion as follows:

1. **Uniform flow:** The flow will be considered uniform if the magnitude and direction of the velocity of flow at a given instant of time is the same at every

section of the channel. To fulfill this condition of flow, the cross section of the channel should be identical in size, shape and orientation. Mathematically it can be expressed as $\partial v/\partial x = 0$ and $\partial v/\partial n = 0$, where ∂x represents the distance travelled by the liquid particles, ∂v is the variation in the velocity while travelling the distance ∂x and ∂n is the direction normal to the flow direction.

2. **Varied flow:** If the flow velocity at a time varies with respect to distance, the flow is known as varied flow or non-uniform flow. Mathematically it is expressed as $\partial v/\partial x \neq 0$ and $\partial v/\partial n \neq 0$. Depending upon the rate of variation of velocity with respect to distance, varied flow in an open channel is classified as gradually varied flow and rapidly varied flow. The flow is said to be gradually varied flow if the flow characteristics varies at a slow rate with respect to the distance. However, if the flow characteristics change significantly over a comparatively short distance, it is known as rapidly varied flow.

Furthermore, there are other types of open channel flow, which are governed to a large degree by viscosity, gravity and inertial forces. Considering the effect of viscosity, the flow may be laminar or turbulent flow; whereas, the flow can be classified as subcritical, supercritical and critical depending upon the effect of gravity relative to inertia.

1. **Laminar and turbulent flows:** The magnitude of viscous force relative to the inertial force determines whether the flow is laminar or turbulent. If the viscous forces are so strong relative to the inertial forces, then the flow is laminar. However, in turbulent flow, viscous forces are weak relative to the inertial forces. The ratio of viscous forces and inertial forces is defined as the Reynolds number and is given by Equation 2.56.

$$R_e = \frac{Vl}{\nu} \quad 2.56$$

where, R_e is Reynolds number; V is the mean velocity of flow, l is the characteristic length and ν is the kinematic viscosity of the fluid.

For laminar flow, the value of R_e is small, normally less than 500. However for turbulent flow the value of R_e is large, usually greater than 2000. When the value of R_e falls between 500 and 2000, the flow is called mixed or transitional flow.

2. **Subcritical, supercritical and critical flows:** When the velocity of flow is equal to the velocity of the gravity wave having small amplitude, the flow is known as critical flow. For subcritical flow, the flow velocity is less than that of critical flow. Whereas, for the supercritical flow, the flow velocity is greater than the critical velocity. The Froude number, F_r , defines the state of the flow as critical, subcritical and supercritical which is equal to the ratio of inertial and gravitational forces. For a rectangular channel, Froude number is defined by Equation 2.57 given as under:

$$F_r = \frac{V}{\sqrt{gh}} \quad 2.57$$

where, F_r is Froude number, h is flow depth, g is acceleration due to gravity and V is velocity of flow.

Depending upon the value of F_r , flow is classified as subcritical if F_r is less than 1; critical if F_r is equal to 1; and supercritical if F_r is greater than 1.

2.4.2 Basic Equations for Flow in Open Channels

Three laws of conservation were reported to describe the steady and free surface flows, which were named as conservation of mass, conservation of momentum and conservation of energy. Based on these laws, important basic equations governing the open channel flow have been derived and presented.

2.4.2.1 Continuity Equation

Conservation of mass states that the mass rate of steady flow is the same at all sections of the channel. For a constant density of fluid throughout the sections, the mass rate can be interpreted as a volumetric rate, or flow discharge.

In Figure 2.23, consider the flow of an incompressible liquid in a channel with no inflow or outflow across the channel boundaries; the continuity equation is given as:

$$Q = V_1 A_1 = V_2 A_2 \quad 2.58$$

Equation 2.58 is valid for non-uniform mean velocities of V_1 and V_2 at sections 1 and 2 respectively.

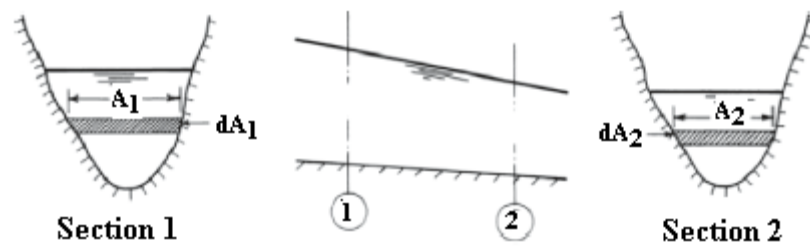


Figure 2.23 Notations for continuity equations; (after Chaudhry, 2007)

2.4.2.2 Momentum Equation

The principle of conservation of momentum is defined as the time rate of change of momentum in the body of water flowing in a channel is equal to the resultant of all the external forces acting on the body. This conservation of momentum is based on Newton's second law of motion.

As shown in Figure 2.24, consider that V_1 and P_1 are the velocity of flow and the pressure force in Section 1 respectively and V_2 and P_2 are the velocity of flow and Pressure force acting at Section 2 respectively, then according to the principle of conservation of momentum, total resultant force acting on a body of water is given by Equation 2.59.

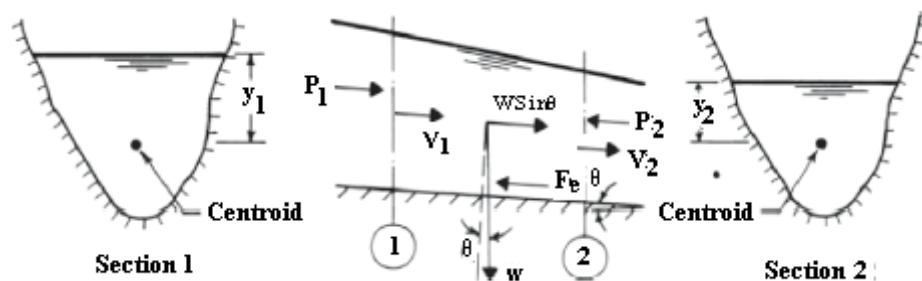


Figure 2.24 Notations for momentum equations and application; (after Chaudhry, 2007)

$$F_T = \rho Q(\beta_2 V_2 - \beta_1 V_1) \quad 2.59$$

where, F_T is the total external forces acting on a body of water, β is momentum coefficient.

If W is the weight of water between Section 1 and 2, θ is the slope of the channel and F_e is the external force due to shear between the liquid and the channel sides, then the resultant force acting on a body of water along direction of flow is given by Equation 2.60

$$F_T = P_1 - P_2 + W \sin \theta - F_e \quad 2.60$$

$$\text{or, } F_T = \rho g A_1 y_1 - \rho g A_2 y_2 + W \sin \theta - F_e \quad 2.61$$

Now from Equations 2.59 and 2.61,

$$\rho Q(\beta_2 V_2 - \beta_1 V_1) = \rho g A_1 y_1 - \rho g A_2 y_2 + W \sin \theta - F_e \quad 2.62$$

Equation 2.62 is the momentum equation for steady flow.

2.4.2.3 Energy Equation

The principle of conservation of energy states that total energy of the closed system cannot change, though it can be conserved over time. According to this principle, in Figure 2.25, the total energy head at Section 1 should be equal to the total energy head at Section 2 plus the head loss between these two sections. Mathematically it is expressed in Equation 2.63 as presented in Simons and Senturk (1992).

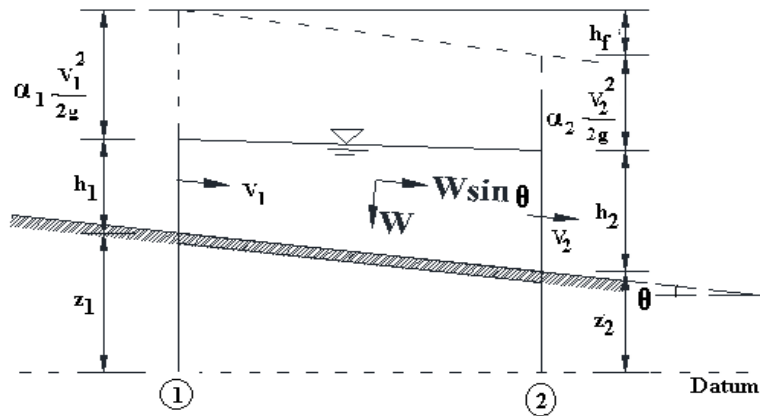


Figure 2.25 Notations for energy equations

$$z_1 + h_1 \cos^2 \theta + \alpha_1 \frac{V_1^2}{2g} = z_2 + h_2 \cos^2 \theta + \alpha_2 \frac{V_2^2}{2g} + h_f \quad 2.63$$

where z is the elevation of the channel bed, h is the depth of flow, α is the energy coefficient and h_f is the loss of energy. The subscripts 1 and 2 represent the flow conditions at Sections 1 and 2. All the notations are clearly shown in Figure 2.25. For a small channel slope, Equation 2.63 can be reduced to:

$$z_1 + h_1 + \alpha_1 \frac{V_1^2}{2g} = z_2 + h_2 + \alpha_2 \frac{V_2^2}{2g} + h_f \quad 2.64$$

2.4.3 Boundary Layer in Open Channel Flow

In the field of fluid mechanics and hydraulic engineering, a boundary layer is defined as the layer of fluid close to the bounding surface, where the flow experiences a significant effect of viscosity. Figure 2.26 schematically shows a boundary layer development in an open channel flow with an ideal entrance condition. The development of a boundary layer in open channel is clearly presented by Simons and Senturk (1992). As shown in Figure 2.26, it can be considered that flow at the upstream of point A is uniform where the velocity of flow, V , is constant. As the flow enters the channel, the friction between flow and the bottom of the channel alters the flow pattern with the development of laminar

flow between the boundary and the line AB. The velocity distribution above the laminar boundary line AB remains uniform downstream of point A. Due to the surface roughness of the boundary, small eddies appear at the top of the rough layer. However they are suppressed in laminar flow. As the flow velocity increases in the downstream direction, the size of eddies increases; and at the downstream of point B they reach to the top of the laminar flow region. After point B, eddies are stronger so that there is a generation of turbulence along line BC. The thickness of the laminar layer decreases as the turbulence increases. Now the resulting velocity distribution is parabolic in the laminar flow region and logarithmic in the turbulent flow region.

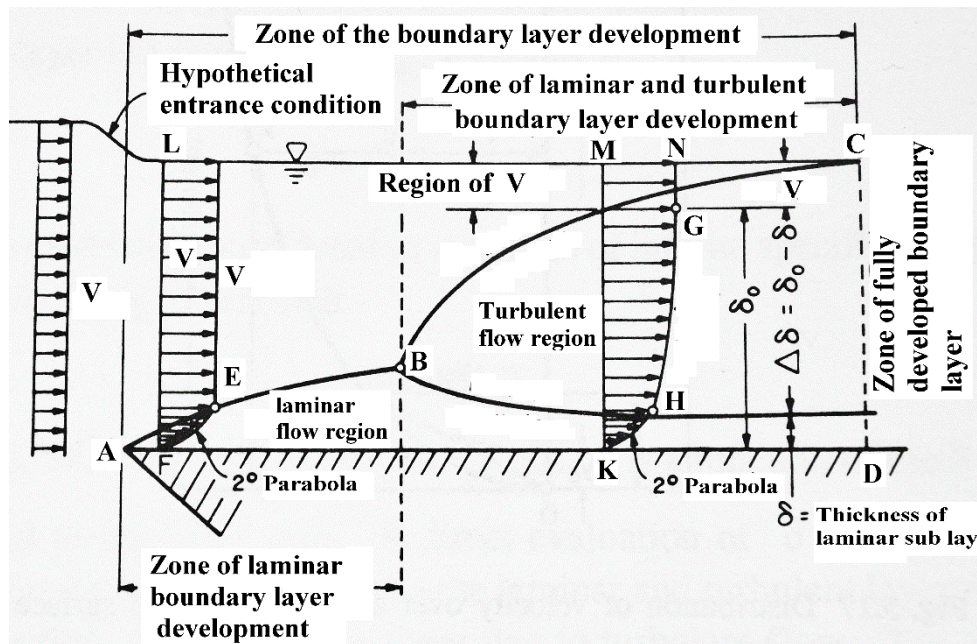


Figure 2.26 Development of boundary layer in open channel (Simons, 1992)

The thickness of the boundary sub layer, δ , is defined as the distance between the boundary and the point at which the viscous flow velocity is 99% of the free-stream velocity. According to Schlichting and Gersten (1999), the laminar boundary layer thickness for a flat plate of length of l can be estimated by considering the equilibrium condition of inertial forces and frictional forces and is represented by Equation 2.65.

$$\frac{\delta}{l} = \frac{5}{\sqrt{Re_l}} \sqrt{\bar{x}} \quad 2.65$$

where R_{el} is the Reynolds number with respect to the plate length and x is the distance from the leading edge along the flat plate.

Similarly the turbulence boundary layer is the turbulent flow region, the thickness of which is called the thickness of turbulence boundary layer. In Figure 2.26, it is represented by δ_o . The flow downstream side of the section CD is the zone of fully developed turbulent flow. Simons and Senturk (1992) further presented three different regimes of roughness with different values of δ . The first roughness regime is a hydraulically smooth regime for which $0 \leq k_s V_* / \nu \leq 3.63 - 5$, where k_s = the roughness of the sand, which is also known as Nikuradse sand roughness and is equal to the mean diameter of the sands. In this regime, the size of the roughness of elements is small and all the protrusions are contained within the laminar sub layer. The second roughness regime is the transition regime for which $3.68 - 5 \leq k_s V_* / \nu \leq 68 - 70$. In this regime, the roughness partly extends through the laminar sub layer, causing additional resistance to flow. The last regime is the hydraulically rough regime for which $k_s V_* / \nu > 68 - 70$. In this regime all protrusions extend through the laminar sub layer, causing the largest part of resistance to flow. According to Schlichting and Gersten (1999), the boundary layer on a plate remains laminar close to the leading edge and becomes turbulent at the downstream side. At the transition from laminar to turbulent flow, there is significant increase in the boundary layer thickness.

2.4.4 Turbulence in Open Channel Flow

The flows in most of the hydraulic structures such as spillways, weirs, irrigation channel and water supply systems are turbulent. In turbulent flow, the velocity and pressure vary with time and space. If u , v and w are the instantaneous velocity components at a point; \bar{u} , \bar{v} and \bar{w} are the mean components of velocities; and u' , v' and w' are the fluctuating components of velocity in the stream-wise, transverse and vertical directions respectively, then the relating equations can be written as:

$$u = \bar{u} + u' \quad 2.66$$

$$v = \bar{v} + v' \quad 2.67$$

$$w = \bar{w} + w' \quad 2.68$$

The root mean square value of u' , v' and w' are the turbulence intensity components. The turbulence intensity is given by:

$$TI = \sqrt{\frac{1}{3}(\overline{u'^2} + \overline{v'^2} + \overline{w'^2})} \quad 2.69$$

Based on the velocity fluctuation components, the turbulence kinetic energy (TKE) of the flow can be determined. In fluid dynamics, the turbulence kinetic energy is defined as the mean kinetic energy per unit mass associated with eddies in turbulent flow. Generally, the TKE can be determined by taking the mean of the turbulence normal stresses and is expressed as in Equation 2.70.

$$TKE = \frac{1}{2}(\overline{u'^2} + \overline{v'^2} + \overline{w'^2}) \quad 2.70$$

Furthermore the fluctuating parts of the velocity can be used to quantify the Reynolds stress, which is the total stress tensor in a fluid. The components of Reynolds stress tensor are defined by:

$$\tau_{uv} = -\rho\overline{u'v'} \quad 2.71$$

$$\tau_{vw} = -\rho\overline{v'w'} \quad 2.72$$

$$\tau_{uw} = -\rho\overline{u'w'} \quad 2.73$$

2.4.5 Flow around Bridge Piers

Extensive investigations have been carried out on local scour around bridge piers installed in cohesion-less sediments. Based on these investigations large numbers of studies have been published. Most of the investigations until this date are focused on the bridge piers with a single column. Very limited studies have been made on the piers with multiple in-

line columns. In the previous publications, it was reported that the flow structure around the bridge piers is very complicated and hence the accurate prediction of scour depth is a very challenging task. In the following sections, review of flow structures around the bridge piers and scour around the bridge piers are presented.

Scouring around the bridge piers is considered one of the main reasons for bridge failure. Hence, it creates a great threat to the stability of a bridge structure and the load carrying capacity of the bridge. It can be noticed from the previous investigations on scour around bridge piers, most of the studies were based on behaviour of a single pier. However, in actual practice, the bridge piers in rivers are generally installed in the form of two or more sequential columns aligned in the flow direction. When the flow of the river is obstructed by a hydraulic structure such as bridge piers, there is the formation of a complex three dimensional flow structure. Because of the complex characteristics of the three dimensional flow structures around the piers, it is difficult to predict the maximum scour depth. Therefore, to estimate scour depth precisely, it is necessary to understand the mechanism of flow structure around the bridge piers. Many investigators, such as Melville (1975); Melville and Raudkivi (1977a); Baker (1979); Dargahi (1989); Salim and Jones (1996); Ahmed and Rajaratnam (1997); Richardson and Panchang (1998); Meneghini et al. (2001); Muzzammil and Gangadhariah (2003); Raben et al. (2010); Shrestha et al. (2012); Kumar and Kothiyari (2012a); Shrestha et al. (2013), Ataie-Ashtiani and Aslani-Kordkandi (2013) among others have conducted research on flow structures around bridge piers.

As described in Section 2.3.3, the flow-field around a bridge pier is characterized by the vortex system which consists of a horseshoe vortex system that wraps around the base of the pier, the bow wave near the free surface at the upstream face of the pier, and the wake vortex system behind the pier that extends over the depth of flow. According to Dey and Bose (1994), these flow features have very complex flow structure, which makes it more complicated to understand the flow field around bridge piers.

2.4.5.1 Horseshoe Vortex System

Two types of horseshoe vortex system namely: a laminar horseshoe vortex system and a turbulent horseshoe vortex system, were reported in the literature by several investigators,

such as Baker (1979); Baker (1980); Lin et al. (2002a); Muzzammil and Gangadhariah (2003); Kirkil (2008); and Huang et al. (2014). Baker (1979) reported that the horseshoe vortex system will be formed at the junction of obstacles like bridge piers in river flow. This horseshoe vortex system will produce high bed shear stresses on the river bed which will cause the erosion of bed materials and hence there will be formation of scour hole around the base of the bridge piers.

Baker (1979) conducted extensive experiments in a smoke tunnel using flow visualization methods and described the horseshoe vortex system at upstream of the cylinders mounted on a wall where the laminar boundary layer is growing. During the experiments both the steady and oscillating vortex system were observed. It was concluded from the experiments that in steady horseshoe vortex systems, 2, 4 or 6 numbers of vortices were formed. Increase in Reynolds number results in the increase in the number of vortices. He further reported that the horseshoe vortex system exhibit a regular oscillatory motion which was found to be complex. As the Reynolds number increased, steady horseshoe vortex systems began to oscillate intermittently and randomly. For a higher value of Reynolds number, the oscillations became irregular and the horseshoe vortex system became turbulent. Lin et al. (2002a) studied the horseshoe vortex system near the junction of a vertical plate normal to the flow. Depending on the Reynolds number and height to width ratio (H/W) of the vertical plate, the vortex system was classified as steady vortex system, periodic oscillation vortex system with small displacement, periodic break way vortex system, and turbulent like vortex system. It was reported that this classification was independent of the height to boundary layer thickness (H/δ) in the range of $H/W = 0.5 - 4.0$.

On the other hand Baker (1980) conducted an experimental investigation on the horseshoe vortex system inside a turbulent boundary layer at upstream of a circular cylinder. The flow topology on the bed and in the plane of symmetry was studied in that investigation. It was observed from the experiments that the predominant structure of the turbulent horseshoe vortex system contained two primary vortices. One was observed attached to the bed and the other smaller intermittent vortex was observed near the cylinder base. Dargahi (1989) investigated the turbulent horseshoe vortex system for a wide range of Reynolds number (8400 to 46000) and observed that the vortices were shed

from the separation region similar to the laminar horseshoe vortex case. It was reported that in most of the cases, the horseshoe vortex system contained three primary vortices rotating in the same direction and two bed-attached vortices rotating in the opposite direction.

2.4.5.2 Vortex Shedding

Vortex shedding is a phenomenon in which the flow oscillates behind the hydraulic structure. When the flow of fluid is disrupted by an obstruction, vortices are created at the back of the obstruction and detach periodically. Due to this detachment, unsteady flow is created. According to Sumer and Fredsøe (1997), vortex shedding phenomenon is the most important feature of the flow regimes around the bridge piers with Reynolds number (Re) > 40 . The flow regimes changed as the Re increased. Figure 2.27 gives the definition sketch of wake region and boundary layer region. As shown in the Figure 2.27, the wake region extends over a distance at the downstream side of the pier which is comparable to the diameter of the pier, D , while the boundary layer extends over a very small thickness, δ . The dependency of the laminar boundary layer with the Re is given by Schlichting and Gersten (1999) which is expressed in Equation 2.74. From this equation, it can be seen that for Re larger than 100, the value of δ/D is less than 1.

$$\frac{\delta}{D} = \left(\frac{1}{Re} \right) \quad 2.74$$

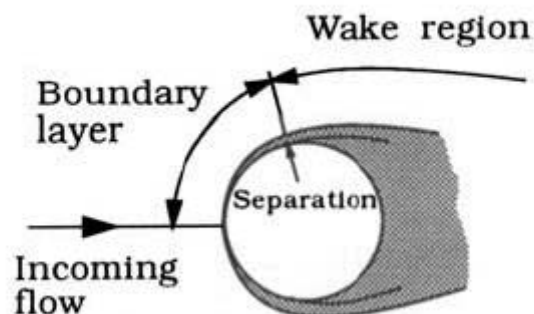


Figure 2.27 Definition sketch of flow regions; (after Sumer and Fredsøe, 1997)

On the other hand Figure 2.28 shows the summarization of changes in flow regimes with increase in Re . The flow regimes around the cylindrical objects with respect to Re are studied by several investigators; for example Bloor (1964); Gerrard (1978); Williamson (1988); Williamson (1989); Sumer and Fredsøe (1997); Batchelor (2000). As reported by Sumer and Fredsøe (1997), it is clear from Figure 2.28 that for $Re < 5$, the boundary layer separation does not occur. When the range of Re is between 5 and 40, a pair of vortices form at the wake of the cylinder. Increase in the value of Re also increases the length of vortex formation. Further increase in the value of Re results in an unstable wake. Eventually other vortices are generated and are shed alternately at either side of the cylinder. When the range of Re is between 40 and 200, the resulting vortex shedding is called laminar vortex shedding. Further increasing the range of Re between 200 and 300, transition to turbulence occurs. For $Re > 300$, the wake is completely turbulent; however the boundary layer over the cylinder remains laminar until the value of Re become less than 3×10^5 . This regime is known as subcritical flow regime. With further increase in Re to 3.5×10^5 , the boundary layer becomes turbulent at only one side of the cylinder and the boundary layer on the other side remains laminar. Such type of flow regime is called critical flow regime. When the Re is between 3.5×10^5 and 1.5×10^6 , this regime is called supercritical flow regime where turbulent boundary layer separation occurs on both sides of the cylinder. Further increase in Re value greater than 1.5×10^6 makes the regime fully turbulent. In this flow regime, the boundary layer is partly laminar and partly turbulent. This regime is called the upper transition flow regime which exists until Re is less than 4.5×10^6 . Finally for the value of Re greater than 4.5×10^6 , the regime is called trans critical flow regime in which the boundary layer on the cylinder surface is virtually turbulent everywhere.

The study on fluid dynamics of multiple cylinder configurations have been carried by several researchers, for example Zdravkovich (1977); Zdravkovich (1987); Gu (1996); Sumner et al. (2000); Lin et al. (2002b) and Sumner (2010). Sumner (2010) reported that when two cylinders are placed in tandem arrangements, the different flow regimes are observed. The complex interactions between the shear layers, vortices, wakes and Karman vortex streets of the flow field are generated due to the configuration of multiple

cylinders. The flow regime in this case basically depends on the spacing between two cylinders, orientation of the cylinders and the Reynolds number.

The fluid behaviour for two cylinders is theoretically approached in a simplified way by Zdravkovich (1987). He classified two basic types of interference which are based on the location of the downstream cylinder with respect to the upstream one. The interference regions are wake interference and proximity interference as shown in Figure 2.29. The wake interference exists when one of the cylinders is partially or completely submerged in the wake of the other i.e. cylinders are placed in tandem or staggered arrangements. While the proximity interference occurs when cylinders are placed in side by side arrangements. In the proximity interference, neither of the cylinders is submerged in the wake of others.





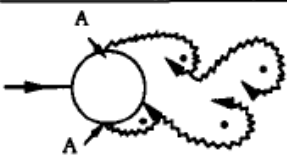
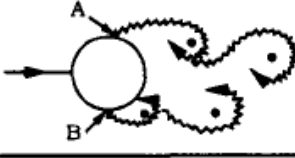
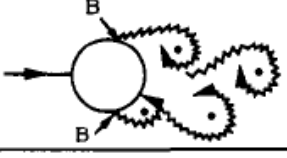


a)		No separation. Creeping flow	$Re < 5$
b)		A fixed pair of symmetric vortices	$5 < Re < 40$
c)		Laminar vortex street	$40 < Re < 200$
d)		Transition to turbulence in the wake	$200 < Re < 300$
e)		Wake completely turbulent. A: Laminar boundary layer separation	$300 < Re < 3 \times 10^5$ Subcritical
f)		A: Laminar boundary layer separation B: Turbulent boundary layer separation; but boundary layer laminar	$3 \times 10^5 < Re < 3.5 \times 10^5$ Critical (Lower transition)
g)		B: Turbulent boundary layer separation; the boundary layer partly laminar partly turbulent	$3.5 \times 10^5 < Re < 1.5 \times 10^6$ Supercritical
h)		C: Boundary layer com- pletely turbulent at one side	$1.5 \times 10^6 < Re < 4 \times 10^6$ Upper transition
i)		C: Boundary layer comple- tely turbulent at two sides	$4 \times 10^6 < Re$ Transcritical

Figure 2.28 Flow regimes around smooth circular cylinder in steady current, (Sumer and Fredsoe, 1997)

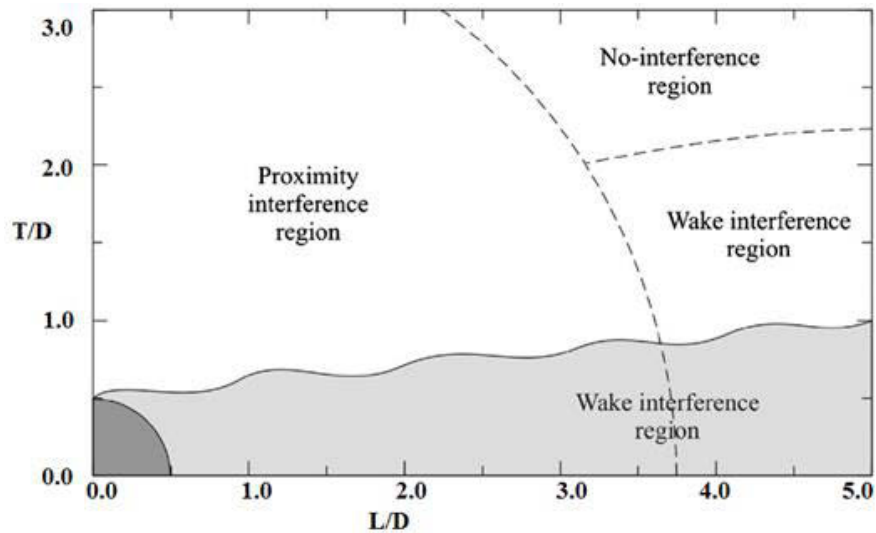


Figure 2.29 Definition sketch of flow interference region for two cylinders arrangements; (after Sumner, 2010)

As reported by Sumner (2010), when two cylinders are arranged in tandem configurations, the downstream cylinder is shielded from the approach flow by the upstream cylinder. The approach flow for the downstream cylinder is modified by the wake of the upstream cylinder. Additionally, the downstream cylinder interferes with the wake and vortex formation region of the upstream cylinder. He further reported that the upstream cylinder behaved as a turbulence generator and the downstream cylinder behaved as a wake stabilizer. The spacing between two cylinders determined whether the cylinders behaved as a single bluff body or as two individual bodies. Sumner (2010) presented a simplified classification of flow regimes for two tandem circular cylinders as shown in Figure 2.30. The flow regimes are basically classified as the extended-body regime, the re-attachment regime and the co-shedding regime.

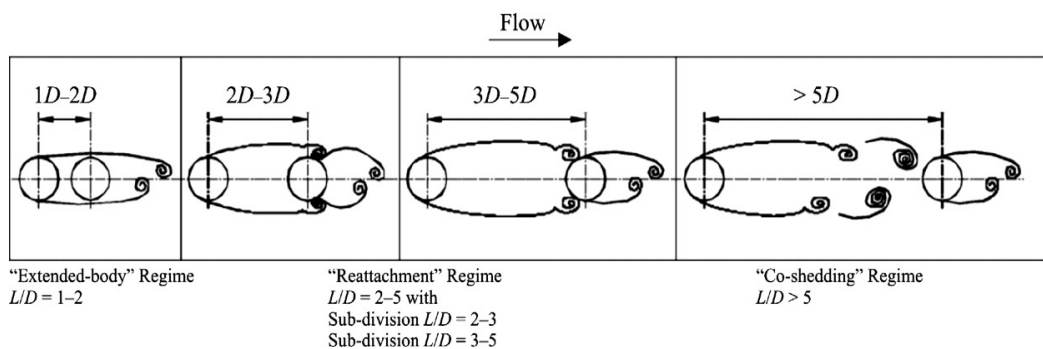


Figure 2.30 Classification of flow regimes for two tandem cylinders; (after Sumner, 2010)

For the condition of extended body regime, Zdravkovich (1987) suggested the ranges of L/D ratios as $1 < L/D < 1.2-1.8$, while Zhou and Yiu (2006) suggested as $1 < L/D < 2$. For these ranges of L/D values, the two cylinders act as a single bluff body in which the free shear layers separated from upstream cylinders wrap around the downstream cylinder, without any re-attachment onto its surface. It was reported by Sumner (2010) that in this regime, the downstream cylinder is positioned inside the vortex formation region of the upstream cylinder. The shear layers detached from the upstream cylinder elongate significantly larger than that of the single cylinder case. The vortex behind the downstream cylinder occurs closer to the cylinder when compared to the single cylinder.

The re-attachment regime occurs in the range of $1.2-1.8 < L/D < 3.4-3.8$ or $2 < L/D < 5$ as reported by Zdravkovich (1987) or Zhou and Yiu (2006), respectively, depending on the value of the Reynolds number. In this regime, the two cylinders are sufficiently far apart that the shear layer detached from the upstream cylinder re-attach on the upstream side of the downstream cylinder. However the vortex street is formed only behind the downstream cylinder. According to Lin et al. (2002b) the re-attachment regime is principally characterized by the re-attachment of the shear layer from the upstream cylinder, and formation and shedding of eddies in the gap between the two cylinders. Eddies in the gap substantially and intermittently vary in terms of their strength, asymmetry, and general behaviour.

The co-shedding regime occurs in the range of $L/D > 3.4 - 3.8$ as reported by Zdravkovich (1987) or $L/D > 5$ as reported by Zhou and Yiu (2006), respectively, in which the two cylinders are placed in such a way that the vortex shedding occur from both upstream and downstream cylinders. Zdravkovich (1987) reported that in this regime, the vortex shedding behind the downstream cylinder is called binary vortices. Furthermore, Sumner (2010) reported that in the co-shedding regime, both the cylinders undergo vortex shedding of the same frequency; and the vortex shedding behind the downstream cylinder is disturbed by the vortices generated by upstream cylinder. The resulting vortices behind the downstream cylinder are larger but weaker than those of the extended-body and re-attachment regimes. Hence the vortices shed from the downstream cylinder dissipate quickly.

2.4.5.3 Vortex Strength and Size

As the horseshoe vortex system at upstream of the bridge pier is the most significant parameter in the scour process, it is very important to analyze its strength and size. It was reported in most of the previous research that the horseshoe vortex system depends on the diameter of the pier and the approach flow velocity. As reported by Lee (2006), the vortex strength is defined as circulation around a vortex core, which can be mathematically expressed as in Equation 2.75:

$$\Gamma = \int \vec{V} \cdot d\vec{s} = \int_0^{2\pi} V_{\theta} r d\theta = 2\pi R V_{\theta} \quad 2.75$$

where,

R = radius of the vortex

V_{θ} = tangential vortex velocity = $\omega_0 R$

ω_0 = angular velocity of revolution

It was experimentally hypothesized by Qadar (1981) that the maximum value of scour depth should necessarily be a function of the initial vortex strength. The initial vortex strength, Γ_0 , can be defined by Equations 2.76 - 2.79.

$$\Gamma_0 = V_{\theta} R \quad 2.76$$

$$R = 0.1 (D + 0.025) \quad \text{for, } D \geq 0.025m \quad 2.77$$

$$R = 0.1 D \quad \text{for, } D \gg 0.025m \quad 2.78$$

$$V_{\theta} = 0.092 D^{-0.5} V^{0.83} \quad 2.79$$

Kothyari et al. (1992) suggested a mathematical expression for the diameter of the primary vortex using the experimental data from other investigators, for example. Baker (1979); Qadar (1981); Muzzamil et al. (1989); and from his own experiments, which is

given in Equation 2.80. Furthermore it was reported that the size of the horseshoe vortex is also affected by the bridge opening ratio, $(W-D)/W$, where W is the width of the flume or span-wise spacing between two piers.

$$R = 0.14 h \left(\frac{D}{h} \right)^{0.85} \quad 2.80$$

where D is the diameter of the bridge pier, h is the depth of flow and R is the radius of the vortex.

According to Muzzammil and Gangadhariah (2003), for higher values of pier Reynolds number, the size of the vortex is only dependent on the diameter of the pier. They suggested that the size and tangential velocity of the vortex are given in Equations 2.81 and 2.82:

$$R = 0.1 D \quad \text{For, } Re \geq 10^4 \quad 2.81$$

$$V_\theta = 2\pi f R \quad 2.82$$

where f is the frequency of rotation of the vortex. Substituting the value of V_θ from Equation 2.82 to Equation 2.75 gives vortex strength as in Equation 2.83.

$$\Gamma = (0.2\pi D)^2 f \quad 2.83$$

2.4.5.4 Frequency of Vortex Shedding

Referring to previous studies it can be found that wake vortices play an important role in the scouring phenomenon in the wake region of the bridge piers. Lee (2006) reported that the wake vortices contribute in the movement of the sediment particles through the process of suspending, sliding, rolling and jumping. Hence, studying the flow structure in the wake region is very important to predict the scour depth around bridge piers. As the detached boundary layers from two sides of the piers are directed towards the

centreline and curl back forming vortices which extend over a distance at the downstream side of the pier which is comparable to the diameter of the pier, D . The vortex is initially formed at one side of the pier, moving to the downstream side becoming larger in size and strength and is finally shed at a constant frequency. The shedding is followed by formation of a vortex on the other side of the piers. This phenomenon of altering of vortices at constant space is called vortex shedding. Figure 2.31 shows the schematics of the of vortex shedding behind the bridge piers.

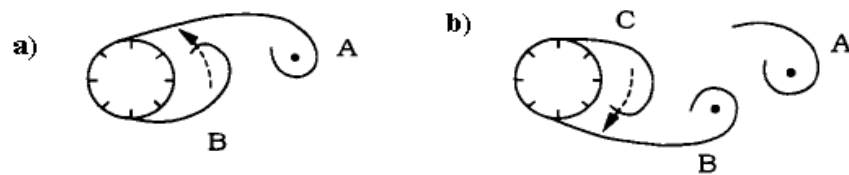


Figure 2.31 Schematics of vortex shedding a) Prior to shedding of Vortex A, Vortex B is being drawn across the wake, b) Prior to shedding of Vortex B, Vortex C is being drawn across the wake (Sumer and Fredsoe, 1997)

The vortex shedding frequency is directly proportional to the flow velocity and inversely proportional to the characteristic length scale (the diameter of the pier). However, it is independent of fluid properties such as density, viscosity. The vortex shedding frequency is related to the Strouhal number, which is given by the following equation:

$$St = \frac{fD}{V} \quad 2.84$$

where, St = the Strouhal number; f = the vortex shedding frequency; D = the diameter of the pier; and V = the velocity of flow.

Sumer and Fredsøe (1997) stated that the Strouhal number is defined as the normalized vortex shedding frequency. They presented the variation of Strouhal number with Reynolds number using the different experimental data from previous researches as shown in Figure 2.32. It is clear from the figure that the St is 0.1 at $Re = 40$ at which the vortex shedding first appears. Then it increases gradually as Re increases and attains a value of about 0.2 when the value of Re is about 300. Further increase in the value of Re

about 3×10^5 , St remains more or less constant at the value of approximately 0.2. After this, St experiences a sudden jump at $Re = 3 - 3.5 \times 10^5$, where St increases from 0.2 to a value of about 0.45. This high value of St is maintained over the range of $Re = 3 \times 10^5$ to 2×10^6 ; subsequently it decreases slightly with increasing the value of Re .

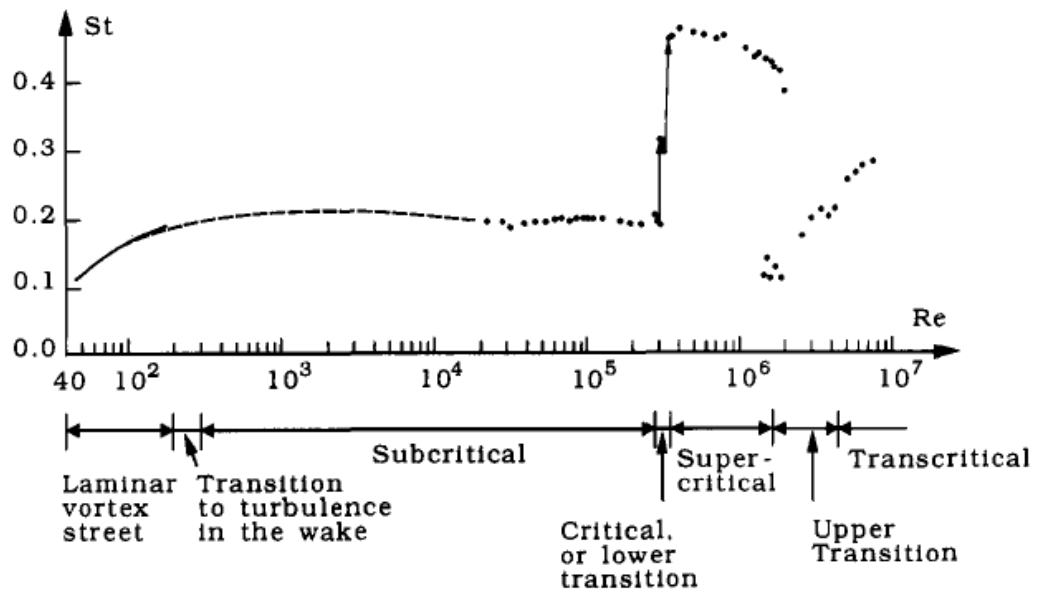


Figure 2.32 Strouhal number as a function of Reynolds number; (Sumer and Fredsoe, 1997)

2.5 Summary and Identification of the Gap in Literature

In this chapter, a detailed review of the available literature related to the scour problem around bridge piers has been presented. Different topics such as the general definition and classification of the scour at the bridge crossings, the mechanism of local scour and the effect of different factors that influence the local scour depth, methods of estimating the scour depth, flow regimes around the bridge piers have been described in detail.

Basically, scour is the consequence of the interaction between flow and hydraulic structures such as bridge piers placed in flowing water in which the sediment material is removed and eroded from the bed and the banks of the streams and also from the vicinity of the hydraulic structures. In Section 2.2 general definitions of scour as presented in various previously published studies have been outlined. Furthermore, the types of scour

are presented in this section according to which scour can occur at a bridge crossing; these types are broadly classified as general scour, contraction scour and local scour.

Section 2.3 describes the local scour, classification of local scour and the mechanism of local scour. The classification of local scour is primarily based on the amount of material supplied into the scour area and the capacity of flow to transport the sediment. According to this, it is described that two types of local scour exist namely: clear water scour and live bed scour. The clear water scour and live bed scour are determined by the critical mean velocity of flow, which can be calculated using Equation 2.12. Additionally, the effect of various parameters (for example the velocity of flow, the depth of flow, the size and shape of piers, the size of bed materials) on the local scour depth around bridge piers has been presented in this section. The general concept of sediment transport phenomenon and beginning of sediment motion has been briefly described, which gives a better understanding of scour around hydraulic structures. In addition, various equations for predicting the scour depth around bridge piers, developed in the past studies have been presented as in Table 2.3. All of these equations were developed for a bridge pier with a single column. Only a few studies have been carried out on the scour around the bridge piers with a group of columns.

The basic mechanism of the local scour around the bridge piers has been identified as a system of vortices developed around the bridge piers. Section 2.4 has been furnished with the basic concept of open channel flow that includes types of open channel flow, basic equations of open channel flow and various turbulence equations. Furthermore, horseshoe vortex and wake vortex have been described as the primary vortex system that causes the scour around bridge piers. Hence, the horseshoe vortex system, vortex shedding, vortex strength and vortex shedding frequency have been presented in section 2.4. Two types of horseshoe vortex system: laminar horseshoe vortex system and turbulent horseshoe vortex system have been reported which depend on the values of the Reynolds number. Moreover, the vortex shedding phenomenon has been identified as an important feature of flow regimes around the bridge piers. Different types of flow regimes that depend on the Reynolds number have been presented in Section 2.4. For the case of two in-line circular cylinders, it has been reported that the flow regimes depend on the spacing between the two cylinders, orientation of the cylinders and the Reynolds number. The

flow regimes for two in-line circular cylinders have also been categorised as the extended body regime, the re-attachment regime and the co-shedding regime.

According to the critical review conducted on previous investigations, it is found that extensive studies have been carried out on scour and flow structure around bridge piers consisting of a single column and numerous equations have been developed to predict the equilibrium scour depth. Only a few studies have been conducted for the bridge pier consisting of a group of piers in a matrix form and are limited to equilibrium scour depth around the piers. However, in a real situation the majority of bridge structures are supported by bridge piers comprising two or more in-line columns. By and large, the scour depth and flow structure behaviour of two in-line columns have not been well investigated in the past. Hence, the present study mainly focuses on the experimental investigation on flow structures and scour depth at bridge piers comprising twin circular columns aligned in the flow direction; and then the effects of spacing between the columns on flow structures and scour depth are evaluated.

CHAPTER 3

**EXPERIMENTAL SETUP AND
METHODOLOGY**



3.1 Introduction

3.2 Experimental Setup and Design

3.3 Velocity Measurement

3.4 Experimental Procedure and Data Acquisition

3.5 Summary

3. EXPERIMENTAL SETUP AND METHODOLOGY

3.1 Introduction

In this chapter, the experimental arrangements, design of hydraulic models, equipment used during experiments, data acquisition methods and variables measured in the study are described. Three sets of laboratory experiments that include flow structure using an acoustic Doppler velocimeter (ADV), local scour around the bridge piers and flow structure using particle image velocimetry (PIV) are carried out in this study. All of the experiments are conducted in the Hydraulics Laboratory at the University of Technology, Sydney (UTS), Australia.

3.2 Experimental Setup and Design

3.2.1 Flume and its Components

Two different flumes were used to conduct the experimental tests. In this dissertation, the flumes are denoted by Flume 1 and Flume 2. Both flumes are recirculating flumes and available in the hydraulics laboratory at UTS. Flume 1 is 19 m long, 0.61 m wide and 0.61 m deep. At the working section of the flume, there is a section in the form of a recess, which is 5.00 m long and 0.15 m deep, located at 9.0 m downstream from the flume inlet section. This recess has been filled by sand; thus called the sand recess. Plexiglass sidewall has been provided along one side of the working section to facilitate visual observations. A settling chamber has been provided upstream to the inlet section of the flume. There is also an overhead tank at the upstream side of the flume, into which the water is pumped from the main reservoir tank. The main function of this overhead tank is to provide a continuous flow of water at constant rate to the flume. Water from this overhead tank is supplied to the settling chamber of the flume. A regulating gate has been provided at the outlet section of the flume, which is used to control the depth of flow in the flume and hence to control the velocity of flow. The used water from the flume is then discharged to the outlet tank, which is again sent to the main reservoir. The schematic diagram of Flume 1 is shown in Figure 3.1. This flume has been used for the study of local scour around bridge piers and flow structure interactions using an acoustic Doppler velocimeter (ADV).

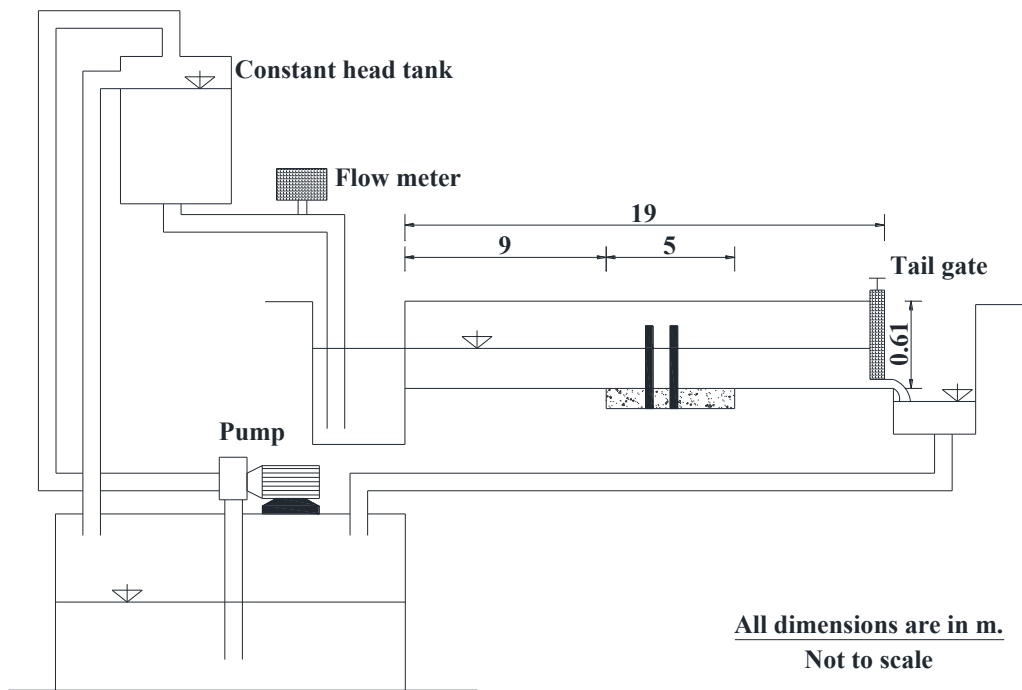


Figure 3.1 Schematic diagram of Flume 1

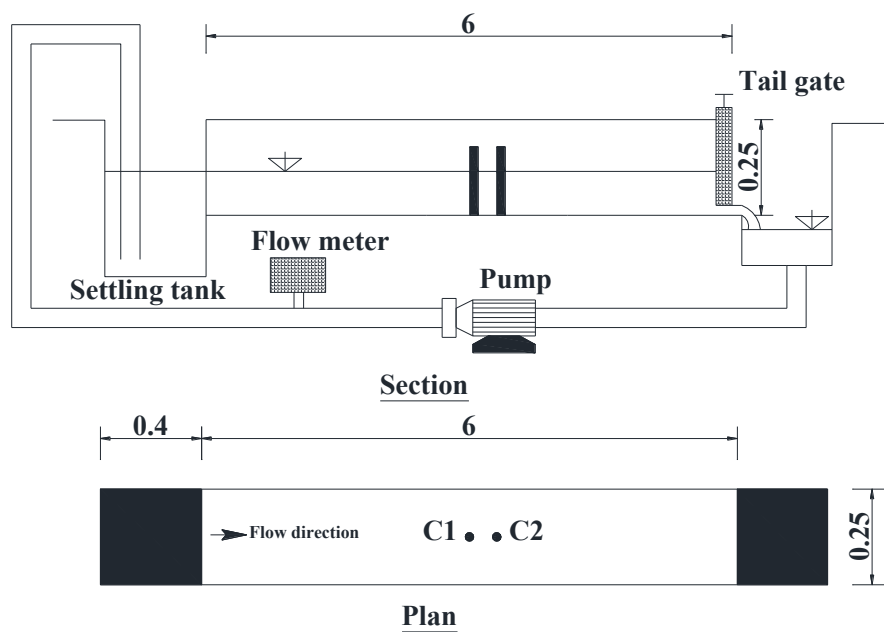


Figure 3.2 Schematic diagram of Flume 2

Another flume with a smaller size (Flume 2) with nominal dimensions of 6 m long, 0.25 m wide and 0.25 m deep as shown in Figure 3.2 has been used for the study of flow structure around the bridge piers under fixed bed condition using particle image velocimetry (PIV). It is made of a plexiglass sidewall so that the experiments can easily be monitored all the time. There is a provision of a settling tank at the inlet section, which supplies water in the flume. There is another tank installed at the outlet section from where the used water is pumped to the settling tank. This flume has also been equipped with a flow meter, a regulating gate and a pump.

3.2.2 Electromagnetic Flow Meter

Siemens, MAG 5000 electromagnetic flow meter has been used to measure the flow rate of water in the flume. The measuring accuracy of the instrument used has been $\pm 0.4\%$ of the flow rate. This instrument has been placed between the inlet section of the flume and the outlet of the constant head tank. Figure 3.3 shows a photograph of this electromagnetic flow meter. As the water flows through this instrument, the amount of flow is displayed on the digital screen, provided at the top of the instrument.



Figure 3.3 Electromagnetic flow meter (courtesy of Siemens)

3.2.3 Vernier Point Gauge

A vernier point gauge with least count of 0.05 mm has been used to measure the bed profile. This vernier point gauge has been mounted in such a way that it can move in all three directions (longitudinal, transverse and vertical directions). Figure 3.4 shows a photograph of the vernier point gauge used.



Figure 3.4 Vernier point gauge to measure the scour depth

3.2.4 Model Columns of Bridge Piers

Experiments were carried out with a single column and two in-line circular columns. When two columns were used, they were arranged in such a way that the flow direction was parallel to the pier alignment i.e. the angle of flow attack was zero. The columns were installed at the centreline of the flume at the same longitudinal section. Figure 3.5 shows a schematic illustration of the two in-line circular column model.

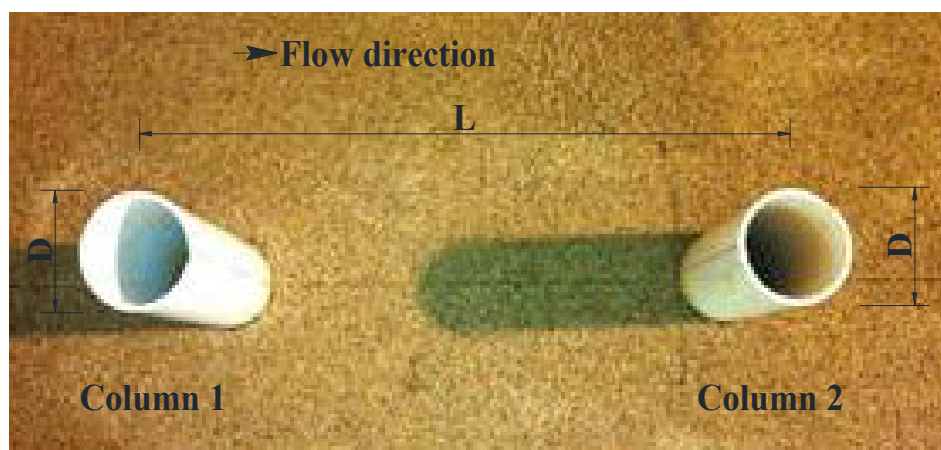


Figure 3.5 Model columns showing the spacing between them

The column diameter was carefully chosen so that there was no contraction effect on the depth of scour. According to Melville and Coleman (2000), in-order to avoid the contraction effect, the flume width should be at least 10 times the column diameter. In this study, columns with diameters of 55 mm were taken for the tests in Flume 1, and for the Flume 2, 16 mm diameter columns were adopted. The flume width to the column diameter ratio (W/D) were 11.27 for Flume 1 and 15.62 for Flume 2, which satisfy the boundary condition recommended by Melville and Coleman (2000).

3.2.5 Bed Materials

In the case of Flume 1, 150 mm thick sand was placed in the recess at the test section of the flume. To find the properties and types of sand used for this study, the soil-grading test (sieve analysis) was carried out in the soils laboratory at UTS. The specification of the sand used is given in Table 3.1

Table 3.1 Specification of bed material

Parameter	Value
Mean particle size, d_{50}	0.85 mm
Specific gravity, s_s	2.60
Geometric standard deviation, σ_g	1.33
Coefficient of uniformity, $C_u = d_{60}/d_{10}$	1.77
Coefficient of curvature, $C_c = (d_{30})^2/(d_{10} \times d_{60})$	1.10

where, d_{60} = grain size at 60% passing, d_{30} = grain size at 30% passing and d_{10} = grain size at 10% passing.

The plot of the grain size distribution (sieve analysis) test is shown in Figure 3.6. The geometric standard deviation of sand is 1.33, the coefficient of uniformity is 1.77 and the coefficient of curvature is 1.08. According to Melville and Coleman (2000), for uniform sand, σ_g should be between 1.3 and 1.5. Additionally, Ameson et al. (2012) reported that the sand will be considered as uniformly graded when $C_u < 6$ and $1 < C_c < 3$, where C_u and C_c are coefficient of uniformity and coefficient of curvature, respectively. The selected

sand satisfies all the condition of uniformity. Once the diameter of the model column was determined, the mean grain size of bed material was verified as per the design criteria developed by Ettema (1976), according to which, the grain size does not affect the depth of scour if the pier width to the grain size ratio exceeds a value of about 50. Based on these design criteria, the mean grain size of the bed material was checked with the adopted bed material. For this study, the ratio was 61.8, satisfying the criterion suggested by Ettema (1976).

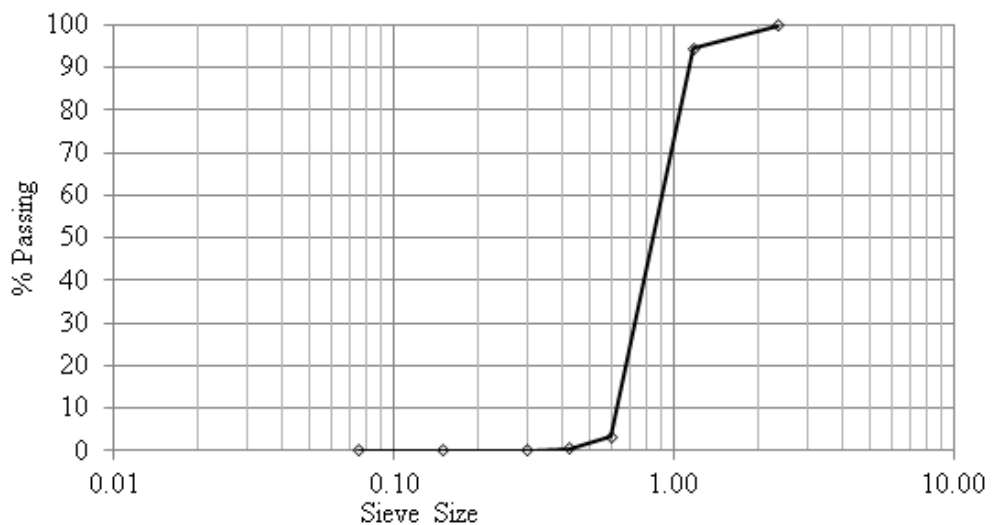


Figure 3.6 Grain size distribution curve of the sand used

3.2.6 Flow Conditions

Two types of flow conditions were chosen for different experimental tests: (1) condition without scouring and (2) condition with scouring.

The condition of no scouring was used to study the flow structure around the bridge piers. Both flumes were used for the experimental tests regarding flow structures. In Flume 1, a small flow rate of 0.0118 m³/s was supplied to the flume and the depth of flow was adjusted in such a way that there was no shallowness effect and no scouring to occur around the columns. To avoid these effects, an approach flow depth of 175 mm was adjusted in the flume. The ratio of flow depth to the diameter of the column (h/D) was 3.18 i.e. $D/h = 0.31$, which is less than 0.7. This condition satisfies the flow shallowness effect given by Melville and Coleman (2000). Temperature and salinity of water were

also measured prior to the starting of the experiments and found to be 20°C and 0, respectively. For each of the flow conditions described above, seven different sets of columns arrangements (different spacing between the piers) were established and the data were captured in three different layers for each setup. For Flume 2 a flow rate of 0.003 m³/s and an approach flow depth of 130 mm were established so that there was no sediment movement around the columns. In this flow condition, the ratio of D/h was calculated as 0.12, satisfying the condition of flow shallowness as described earlier.

Table 3.2 Flow conditions for experimental tests

Tests	Q (m ³ /s)	h (m)	D (mm)	d ₅₀ (mm)	V/V _c	Reynolds No. (Re)	Froude No. (Fr)	Remarks
1	0.0118	0.175	55	0.85	0.38	12500	0.068	Flume 1 Fixed bed
2	0.0185	0.115	55	0.85	0.74	22000	0.19	Flume 1 Mobile bed
3	0.0330	0.160	55	0.85	0.91	35500	0.25	Flume 1 Mobile bed
4	0.0315	0.15	55	0.85	0.93	35000	0.22	Flume 1 Mobile bed
5	0.0350	0.16	55	0.85	0.96	37600	0.23	Flume 1 Mobile bed
6	0.003	0.13	16	0.85	0.38	6000	0.041	Flume 2 Fixed bed

Another flow condition was established for the condition of clear water with local scour around piers. Flow rates, used in this condition, ranged from 0.0185 to 0.033 m³/s and depth of flow was adjusted in the range of 115 to 160 mm, satisfying the condition of flow shallowness so that the pier would be considered as a narrow pier. During the experiments in these conditions, water temperatures were recorded. The temperature

range was between 13°C and 20°C. However, according to the experiments conducted by Melville and Chiew (1999), it was reported that there is no discernible difference in the scour depth development, or equilibrium scour depth due to temperature variation.

In this study, six sets of tests were carried out as shown in Table 3.2. For each test there was different subset of tests including a single column, and twin in-line circular columns with different spacing between them ($L/D = 0$ to 12). Test 1 and Test 6 were designed to study the flow structure around the bridge piers. Tests 2 to 5 were designed to study the scour around bridge piers comprising a single column and twin columns as well as the influence of pier spacing on scour depth. The incipient motion condition of the sediment particle was determined according to the procedure given in Section 2.3.1.1.

3.3 Velocity Measurement

During the experiments on flow structures, three dimensional velocity components were the primary data to be measured. In this study, velocity components were measured using an Acoustic Doppler Velocimetry and a Particle Image Velocimetry measurement technique, which are separately described as follows:

3.3.1 Acoustic Doppler Velocimetry (ADV)

An Acoustic Doppler Velocimeter was used to measure the instantaneous three dimensional velocity components during the experiments on the flow structure in Flume 1. An ADV is a single point current meter that measures the three dimensional velocity components in high and low flow conditions. An ADV uses an acoustic Doppler technology to measure three-dimensional velocity in a small sampling volume located a distance away from the probe head. As per the detail information on SonTek (2001), the SonTek / YSI 16-MHz MicroADV was used as a current meter, which is optimal for using in the laboratory. The velocity range is programmable from ± 1 mm/s to ± 2.50 m/s. Data can be acquired at sampling rates up to 50 Hz. The ADV consists of three basic elements: the probe, the signal-conditioning module, and the processor. The probe is attached to the conditioning module, which contains low noise receiver electronics enclosed in a submersible housing. The ADV conditioning module and probe are connected to the processing module using a custom shielded cable. The ADV field

processor is a set of three printed circuit cards that operates from external DC power and outputs data using serial communication. The ADV field processor is operated from a computer containing special software to record the measured velocities.

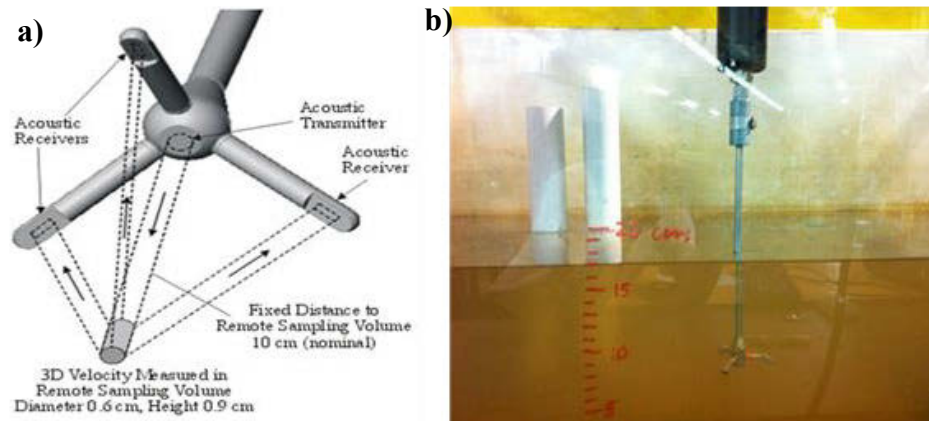


Figure 3.7 Velocity measurement a) Acoustic Doppler Velocimeter (ADV) (SonTek (2012), and b) measuring velocity in laboratory

The probe consists of an emitter and several receivers. A signal is emitted from the centre of the probe head. There are three prongs on the probe head with three receivers. The rate at which the signal is returned to the receivers allows the probe to calculate flow velocities in three dimensions x , y and z . The interpreted velocities are returned as three velocity vectors. Figure 3.7a shows the components of the probe. Another important equipment during the measurement is the signal processing hardware, which performs the signal generation and processing required for the ADV to make velocity measurements. As described in SonTek (2001), the processor generates the electrical signals that are converted to acoustic energy at the transducers. It also digitises the return signal and performs the Doppler processing to calculate velocity. The signal processor is enclosed in a splash proof housing that saves the instrument from incidental water contact. This housing is connected to the probe, computer, and DC power input. The signal processor enclosed in a splash proof housing and ADV probe are shown in Figure 3.8.

A software package named Horizon ADV was used for the data collection using the ADV instrument. This program can be used to configure ADV systems and to display the data files collected from ADV systems. Furthermore, another software package named

WinADV was used for processing and viewing the data collected from ADV signals. Details of this software are provided in Section 3.4.



Figure 3.8 ADV probe and signal processor in splash proof housing (SonTek (2012))

To obtain sufficient time averaged velocities, samples must be recorded over a period of time. Approximately ten to twenty seconds was assumed to be sufficient to plot the variability in the flow. At the default sample rate, measurements are taken at one-second intervals. In order to measure the velocity at different positions and different layers of the flowing water a special arrangement is designed to hold the ADV. With this special arrangement, the ADV is moved along x, y and z directions. For the experimental tests of this research, the sampling duration was more than 60 seconds to achieve a low standard error. As reported by Beheshti and Ataie-Ashtiani (2010), the optimal record length (minimal sampling effort to achieve a low standard error) ranges between 60 to 90 seconds.

3.3.2 Particle Image Velocimetry (PIV)

Particle Image Velocimetry (PIV) was used for the study of flow structure around bridge piers in Flume 2. In this method, a number of images were recorded to measure the displacement of particles moving within a narrow light sheet. According to Westerweel (1997), PIV is an optical flow diagnostics in an optically homogeneous fluid. In an optically homogeneous fluid, there is less interaction such as refraction of the incident

light with the fluid. Due to these lesser interactions, the information of the flow field can be easily retrieved. In Particle Image Velocimetry, the fluid is seeded with small tracer particles, enabling the visibility of fluid motion. The instantaneous displacement of these seeded particles is used to retrieve the information on flow velocity field. Schematic illustration of the PIV system is shown in Figure 3.9, which also shows the components of the PIV system.

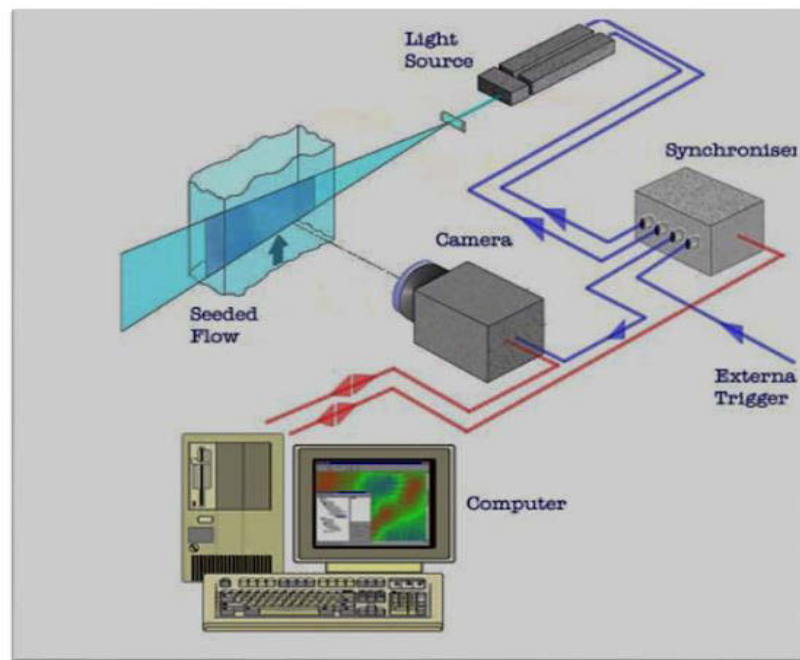


Figure 3.9 Schematic illustration of PIV system, (ILA-GmbH (2004))

The seeding particles are a very important component of the PIV system. In order to get accurate results, the seeded particles must be able to match the properties of the fluid used for the investigation. The ideal seeding particles have the same density as the fluid being used and should be spherical. Additionally the size of the particles should be small enough so that the time to respond the particle motion of the fluid is reasonably short and accurately follows the flow. Accurate visualization of the particles needs sufficient scattered light, which is directly related to the size of the particles. In this study, Polyamide 2070 was used as seeding particles, having an approximate mean diameter of 5 μm and approximate mean density of 1.016 g/cm^3 with a spherical shape. In addition

to this, the possibility of missing data due to reflection was minimised using a dull black paint on the model columns.

A high-resolution PCO-Tech scientific camera, as shown in Figure 3.10, was used to capture the images. It has a 14 bit cooled Charge Coupled Device (CCD) camera system comprising an advanced CCD and electronic technology. This camera consists of a compact camera with an external intelligent power supply. The image data are transferred via standard data interfaces to a computer. This digital CCD camera is a high performance PCO-camera comprising a double shutter function for the PIV.



Figure 3.10 Digital charged coupled device (CCD) camera,(PCO-TECH (2008)

According to the information provided in the VidPIV user manual by ILA-GmbH (2004), the laser source used for PIV was the pulsed double cavity Nd:YAG laser. In this double cavity Nd:YAG laser, two lasers have been inserted into a single compact platform. The laser system provides a symmetrical output beam of 532 nm frequency in the form of visible (green) spectrum. The laser head was interfaced with an articulated mirror arm and ICE 450 power supply as shown in Figure 3.11. The articulated mirror arm guides the light from the laser head to the measurement plane in PIV experiments. The arm delivers the light controlling the laser illumination to the measurement plane. The ICE 450 power supply unit housed all the necessary items to operate the laser heads. Basically, ICE 450 supplies a high current pulse to the flash lamp located in the laser head. Additionally, ICE 450 contains a heat exchanger (water to air) and cooling fans to remove the unwanted heat from the laser head.

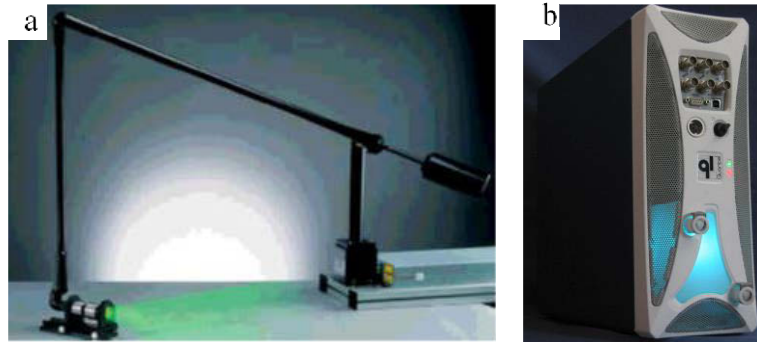


Figure 3.11 Laser source and the controlling system: a) laser head with mirrored arm (ILA-GmbH), and b) ICE450 power supply system (Quantel (2006))

Another important component of the PIV system is its synchronizer, which is a high precision timing unit acting as an external trigger for both the camera and the laser. It is controlled by the computer software known as synchronizer control. It dictates the timing of each image from the CCD camera with a very low jitter down to 0.1 ns so that the PIV measurement can be conducted at a very precise moment.

3.4 Experimental Procedure and Data Acquisition

3.4.1 Procedure for Fixed Bed Experiments in Flume 1

At the very first step of the experiment, the bed material (sand) with a mean grain size (d_{50}) of 0.85 mm was placed in the sand recess. With the help of a long straight edged rectangular wooden bar, the sand in the flume was levelled. On the levelled bed, the initial bed elevations were checked using a vernier point gauge at random points to ensure the proper levelling. After levelling the sand bed, column model with diameter (D) of 55 mm as bridge piers were carefully installed at the centreline of the flume along the longitudinal direction. The columns were installed in such a way that they were positioned exactly at the vertical position. The position and the inclination of the columns were measured using a common measuring tape, bubble level and a tri-square and adjusted to accurate positions. For acquiring better results from the experiments, the position and vertical-ness of columns are very important. It can be noted that significant change in the flow pattern may occur due to column position and orientation disparities. The next step was to fill the flume with water. Keeping the tailgate in closed condition,

the flume was initially filled with water using a very small flow rate. The flow rate was adjusted in such a way that the sand bed was not disturbed by the flow of water. As the depth of water was reached to the designed depth of flow, flow rate was then gradually increased very carefully up to the designed rate ($Q = 0.0118 \text{ m}^3/\text{s}$). The tailgate provided at the downstream end of the flume was moved up and down to maintain the required depth of flow i.e. $h = 175 \text{ mm}$. Since the depth of flow is directly related to the velocity of flow, this step was carried out very carefully.

To study the flow structures around the bridge piers, three-dimensional velocities at several points on the upstream and downstream side of the pier were measured using a micro acoustic Doppler velocimeter. During the experiments, a down looking ADV probe was mounted on special clamps fixed on a steel frame to facilitate the probe to move in longitudinal, transverse and vertical directions. The measurement points on the flume are as shown in Figure 3.12. For each set of experiments, data were captured on three different layers, $z/h = 0.085, 0.26$ and 0.54 measured from the bed of the flume. The reason for taking these levels was due to the high signal quality. After careful inspection of the measured velocity time series, it was observed that the signal quality was sharply decreased in layers between 20 and 40 mm above the bed. While using ADV, measurements closer than 40 mm around the columns were not possible because of the length of the probe arms. The critical flow velocity, V_c , for sediment entrainment was predicted using Equations 2.10 and 2.12 given by Melville and Coleman (2000). The experiments were performed under clear water condition with the flow intensity $V/V_c \approx 0.38$, where V is the free stream velocity of flow and V_c is the critical velocity of sediment. In this experiment, time averaged velocity components (u, v, w) were measured in the Cartesian coordinate system (x, y, z). The origin of the coordinate system was assumed to be on the upstream face of Column 1 and all the measurements were made with reference to that point. The coordinate x indicates the distance along the flow axis, y indicates the transverse distance from the flow axis and z represents the vertical distance from the original sand bed surface.

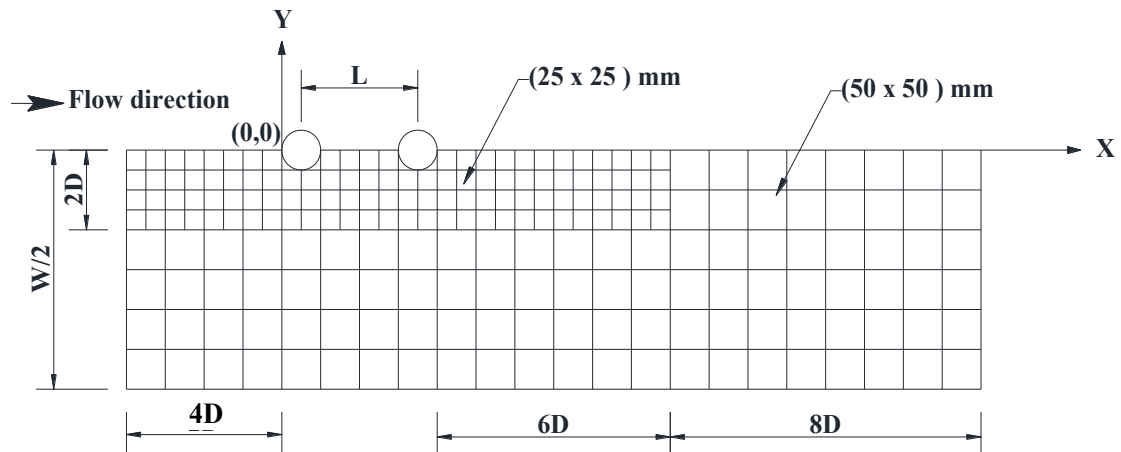


Figure 3.12 Measurement grid in horizontal plane (top view)

As stated earlier, the instantaneous three-dimensional velocity components were measured by MicroADV (SonTek). The employed ADV was a very precise instrument measuring the velocity components at the rate of 50 Hz. The distance of the sample volume from the probe was 50 mm, indicating the necessity of an upward looking probe to measure the data of the upper 50 mm layer of the flow.

The sampling duration was 60 seconds was taken as described in Section 3.3.1. The same procedure as described above was repeated for another set of experiments with different values of L/D ranging from 0 to 6. The data were captured in the computer with the application of a software package called Horizon-ADV. Wahl (2000) presented the minimum recommended value of correlation coefficient and SNR values as 70% and 15, respectively. Furthermore, it is reported that data filtering based on correlation coefficient and SNR value is very useful. Hence, the measurements were further processed using public domain software Win-ADV to obtain the time mean and the root mean square values at each point of the velocity measurements. At the same time of processing, measurements were filtered to reject points with correlation coefficient less than 70% and a Signal to Noise Ratio (SNR) value less than 15. However, during the experiments and data measurement, at all the points, the correlation coefficient was found to be 95% and more, with SNR value not less than 15. For further calculation and analysis purposes, the filtered data were taken to get results that are more precise.

3.4.2 Procedure for Mobile Bed Experiments in Flume 1

In these experiments, three sets of experiments were carried out for different flow conditions. Preparation of the bed was carried out in a similar way as described in fixed bed experiments. A set of 34 numbers of experiments using a single column (4 experiments for four different flow conditions) and two in-line circular columns (10 different $L/D \times 3$ flow conditions = 30 experiments) with different spacing were conducted. The duration of the experiments was taken as 72 to 75 hours because after 75 hours of the test duration, no sediment movement around Column 1 was noticed. The columns were installed in the flume with different spacing between them (for example $L/D=1, 2, 3, 4, 5, 6, 8, 10$ and 12 centre to centre of columns). For each set of column arrangements, three different flow conditions as shown in Table 3.2 were established. Out of these experimental tests, four experiments (the single column and two in-line circular columns with spacing $1D, 2D$ and $3D$) conducted under the flow condition of Test 2 as shown in Table 3.2 were monitored for the development of scour hole and measurements were taken at different elapsed times. At the end of each test, the pump was stopped and all water was carefully drained out from the flume. Measurements of the final bed level were carried out using a vernier point gauge. The scour depth and scour profiles in the upstream side and the downstream side of both the columns were measured. The scour profiles measurements were carried out along the axis of symmetry of the columns and measurement points were about 20 mm apart. Additionally, the maximum scour depth, the minimum scour depth, the size of the scour hole and the angle of repose were measured and recorded for further analysis.

3.4.3 Procedure for Fixed Bed Experiments in Flume 2

In Flume 2, a set of fixed bed experiments were carried out for the study of flow structures around bridge piers consisting of a single column as well as two in-line circular columns. A set of 40 numbers (8 different $L/D \times 5$ different $Y/D = 40$ runs) of experimental runs were carried out for the same flow conditions with different spacing between the columns. The model columns (16 mm in diameter) of bridge piers were painted with dull black paint to minimise the reflection effect during the experiment to avoid the data missing. The columns were installed on the centre line of the flume at a distance of 2 m from the

inlet section of the flume. The flow rate of 3 l/s was supplied to the flume and the depth of flow was maintained at 130 mm. The details of flow condition are presented in Table 3.2. Additionally the flume was equipped with apparatus required for the Particle Image Velocimetry (PIV) as described in Section 3.3.2. The equipment was installed in such a way that detailed data in the vertical plane could readily be measured. The chances of capturing missing data were decreased by manipulating the camera distance, laser width and position of laser head. The laser-guided arm was positioned on the top of the flume and the laser sheet was projected on the required measurement axis. The camera was installed in front of the flume perpendicular to the laser sheet. The measurements were carried out at different vertical planes parallel to the direction of flow as shown in Figure 3.13 i.e. planes at $y/D = 0, 1.25, 2.5, 3.75$ and 5 . For each set of experiment, images were captured for various spacing between the columns i.e. $L/D = 0, 1, 2, 2.5, 3, 4, 5$ and 6 .

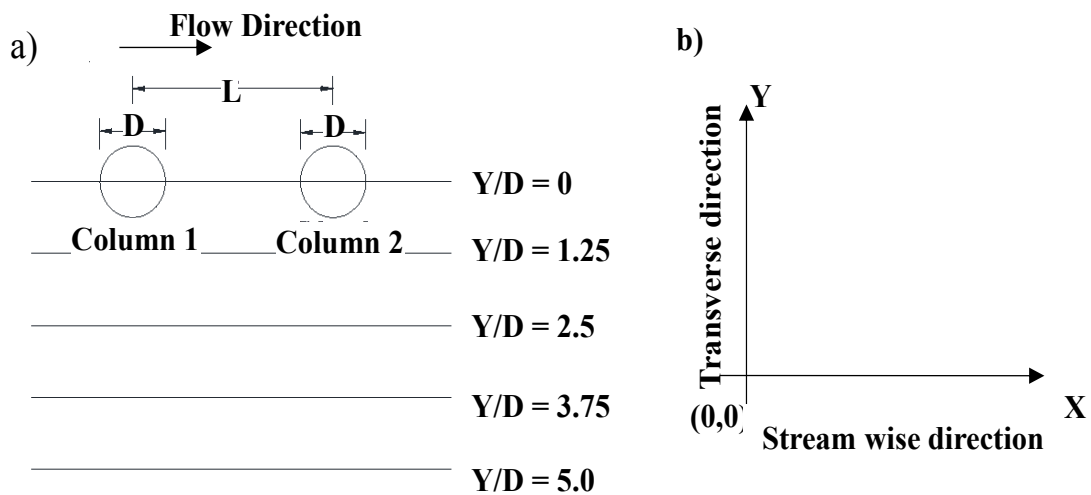


Figure 3.13 Different axes of PIV measurements (top view)

Once the setup was completed, the seeding particles (Polyamide 2070) were added to the flow. These seeding particles were illuminated in the plane of flow at least twice by means of a laser within a short time interval. It was assumed that the seeding particles follow the flow velocity between the two illuminations. The light scattered by seeded particles was acquired by a high-resolution digital camera. The images acquired from camera were stored in the computer. The flow field was measured on a grid of interrogation area of the size 32×32 pixels. It can be noted that the displacement of seeding particles between two consecutive images determines the fluid velocity. To extract displacement

information from the PIV recordings, the stored images were processed using a software package called VidPIV. In the first step of image processing, a spatial calibration was carried out by generating image mapping to map measurements made from the images in the pixel unit. The annotation function was used to exclude the mask areas where no velocity information was present. The cross correlation function was applied to the raw PIV images to extract the most common particle displacement found between two interrogations areas. The vector information extracted was further filtered to remove outliers and interpolated to calculate the missing data. An additional operation was applied using adaptive cross correlation to achieve a higher accuracy improving the correlation coefficient. Vector filters were reapplied, followed by interpolation and finally the vector maps were derived as vector magnitudes. These vector magnitudes were extracted and saved for further analysis of the flow field.

3.5 Summary

A series of laboratory experiments have been conducted on flow structures and scour around bridge piers in the hydraulics laboratory at the University of Technology, Sydney. Two different sized flumes were used for the experimental tests. Flume 1 is 19 m long, 0.61 m wide and 0.61 m deep. At the working section of the flume, there is section in the form of a recess, which is 5.00 m long and 0.15 m deep, located at 9.0 m downstream from the flume inlet section. Another flume with a smaller size (Flume 2) with dimensions of 6 m long, 0.25 m wide and 0.25 m deep was used for the study of flow structures around the bridge piers under fixed bed condition using Particle Image Velocimetry. Both flumes were equipped with a flow meter, a regulating gate and a pump. An electromagnetic flow meter was used to measure the flow rate of water in the flume. The scour depth was measured using a vernier point gauge with least count of 0.05 mm. This point gauge was mounted on the flume in such a way that it could move in all the three directions.

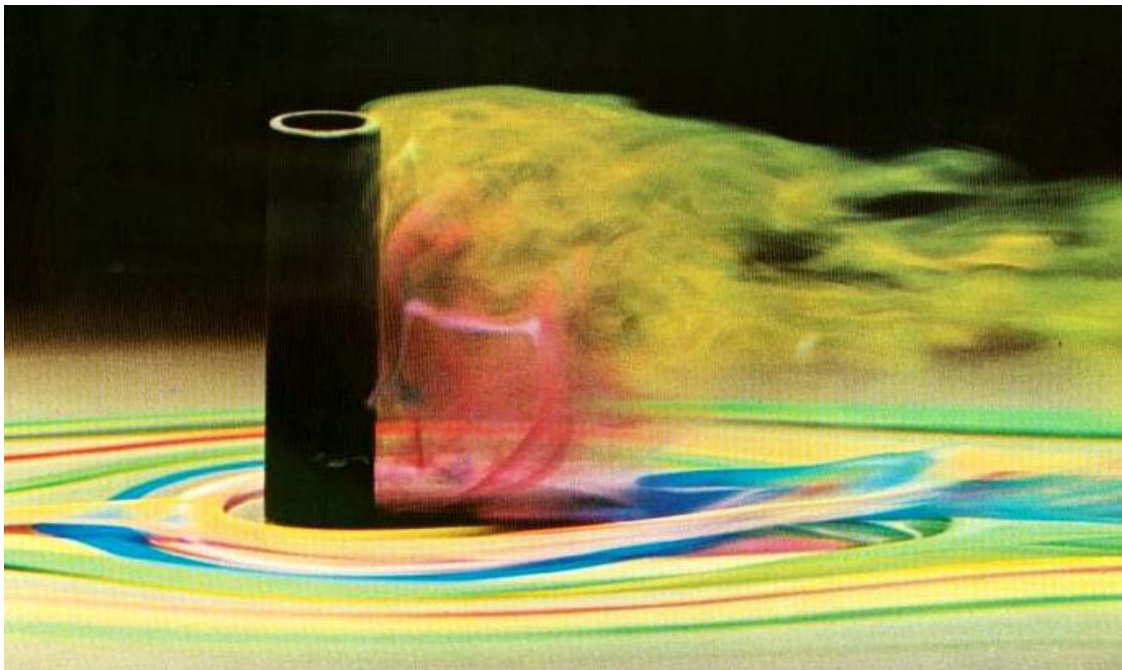
The model columns used for Flume 1 were circular pipes with an external diameter of 55 mm, while for Flume 2 the column diameter was 16 mm. The diameters of the columns were selected in such a way that there was no contraction effect on the depth of the scour. For this reason, the flume width to the column diameter ratio was checked to be greater

than 10. Uniformly graded non-cohesive sand of mean grain size (d_{50}) of 0.85 mm was used as a bed material. The size of the sand was determined in such a way that there was no grain size effect on the scour depth. It was determined using the design criteria developed by Ettema (1976).

All of the experimental tests were conducted under clear water flow condition with different values of the critical velocity ratio (V/V_c). The critical velocity of flow was determined based on the relationships given by Melville and Coleman (2000). For each flow condition, different tests were carried out including a single column, and two in-line circular columns with different spacing between them ($L/D = 0$ to 6). Altogether 64 runs (28 runs for ADV method + 40 runs for PIV method) of fixed bed experiments were carried out for the study of flow structures. Velocity was measured using ADV apparatus and PIV measurement techniques. The ADV apparatus was used to measure the three dimensional velocity components in the horizontal plane and the PIV method was used to measure the two dimensional velocity components in vertical planes. Additionally, 34 numbers of moveable bed experiments under different flow conditions were carried out for the study of scour depth.

CHAPTER 4

RESULTS AND DISCUSSION ON FLOW STRUCTURE



4.1 Introduction

4.2 Previous Investigations on Flow around Bridge Piers

4.3 Flow around Bridge Piers in Horizontal Plane

4.4 Flow around Bridge Piers in Vertical Plane

4.5 Bursting Phenomenon and Quadrant Analysis

4.6 Summary

4. RESULTS AND DISCUSSION ON FLOW STRUCTURE

4.1 Introduction

The flow around bridge piers is one of the most important topics of interest to hydraulic engineers and designers because it will lead to an in-depth understanding of flow and its consequences. As reported by Ahmed and Rajaratnam (1998), numerous studies have been conducted since the late 1950s to understand the flow structure around bridge piers and its relationship with the local scour. However, the complex three dimensional flow structure and its interaction with the sediment transport create great difficulties in analysing the problems. Menna and Pierce (1988), Ahmed and Rajaratnam (1998) and Dey and Raikar (2007) provided a comprehensive understanding of three dimensional turbulent flow structure and the concept of mechanism of scouring process to predict the depth of the scour hole within a high level of precision.

Many tests have been conducted to study the flow structure around a single column and two in-line circular columns with varying spacing between them. An acoustic Doppler velocimeter (ADV) was employed to measure the velocity components of flow in three different horizontal planes, while particle image velocimetry (PIV) was used to measure instantaneous velocity in different vertical planes parallel to the direction of flow. The results are analysed and presented in this chapter.

4.2 Previous Investigations on Flow around Bridge Piers

As presented in Section 2.4, many researchers have conducted extensive investigations on flow structures. A brief review to highlight the main findings of the investigations is presented in this section:

Melville and Raudkivi (1977b) conducted an experimental study on flow around a circular cylinder under flat bed and deformed bed conditions. They measured the flow, turbulence intensity and bed shear stress distribution around the cylinder using a hot film anemometer. The hydrogen bubble technique was used to obtain the flow pattern. Their experiments disclosed that there was the presence of spiral flow in the form of necklace vortices at the base of the cylinder. The weaker necklace vortices and the lower level of

turbulence intensity were reported at equilibrium scour conditions compared to the flat bed condition.

Menna and Pierce (1988) presented the experimental results of the mean flow structure of the upstream and surrounding flow around a teardrop shaped cylinder. Measurements included the mean velocity, Reynolds stresses, turbulent kinetic energy, floor pressure, and wall shear stress. It was observed that the flow was continuously turned down to the wall and its direction near the wall was significantly different from that of the wall shear stress. It was also reported that the boundary layer thickness did not change significantly around the cylinder and the flow observed to be accelerated within the undisturbed boundary layer.

Ahmed and Rajaratnam (1998) conducted an experimental study of the flow and bed shear stress field around a circular cylinder on different types of bed conditions. The experiments were carried out on smooth and rough bed surfaces under flat bed and scoured bed conditions. That study showed the effects of bed roughness and the presence of scour hole on the flow field. It was concluded that the bed roughness induced a steeper pressure gradient resulting in strong down-flow in front of the pier. The maximum down-flow in the absence of scour hole was reported approximately 35% of the approach flow. Additionally they concluded that the magnitude of the bed shear stress was increased due to the bed roughness. It was noticed in the experiments that the skewing of the flow near the bed was resisted by the bed roughness.

Unger and Hager (2007) conducted an experimental study to investigate the internal flow features around circular bridge piers using particle image velocimetry system. They performed the study over a wide range of Reynolds number ($5 \times 10^4 - 3.5 \times 10^6$) and visualised the flow pattern in several horizontal and vertical planes. The temporal evolution of vertical flow in front of the pier and the horseshoe vortex inside the scour hole were investigated measuring the velocity and vorticity profiles. It was identified that the horseshoe vortex system is the main reason for the growth of scour hole. Based on the experimental data, they derived an empirical relation for the temporal evolution of the size and the shape of the primary vortex of the horseshoe vortex system. Additionally,

they found the slight variation of the strength of down flow and the position of the stagnation point during the scour process.

Beheshti and Ataie-Ashtiani (2010) performed an experimental investigation on the three dimensional flow field around a complex bridge pier placed on a rough fixed bed. The pier model consisted of a column, a pile cap, and a 2×4 pile group. The instantaneous three dimensional velocity components were measured using an ADV. The results were presented in the form of profile and contour plots of three dimensional velocity components, turbulent intensity components, turbulent kinetic energy, and Reynolds stresses. In addition to this, the velocity vectors were presented and discussed at different vertical and horizontal planes. It was reported that the approaching boundary layer at the upstream of the bridge piers separated in two vertical directions, with an upward flow towards the column and a contracted flow in the downward direction towards the pile. They found that the main features responsible for the sediment entrainment were the contracted flow below the pile cap and towards the piles, a strong down flow along the side of the piers at the upstream region, and a vortex flow behind the pier and amplification of the turbulence intensity along the side of the piers at the downstream side.

Kumar and Kothyari (2012b) performed an experimental study on the flow pattern and the three dimensional turbulence characteristics around the circular uniform and the compound piers in the presence of scour hole. Four sets of experimental tests were carried out under the clear water flow condition using a uniform circular pier and circular compound pier. The flow field was observed in the pre-developed scour hole and three dimensional velocity components were measured using an ADV. Detailed measurement of time averaged velocities, turbulence intensities and Reynolds shear stresses at eight different vertical profiles for various radial distances from the centre of the piers were examined. In that study, the diameter of the principal vortex at upstream of the pier was expressed in terms of diameter of the pier. It was noticed that the profile of flow velocity, turbulence intensities and Reynolds shear stresses around each of the pier models at different vertical planes were more or less similar. However, the measurements close to the piers showed significant changes in the vertical profile of flow parameters.

An experimental study on turbulence flow and sediment entrainment around a bridge pier was conducted by Izadinia et al. (2013). They reported that the maximum velocity occurred at the edge of the scour hole and the velocity profile became normal outside the scour hole. At the downstream side of the pier, the secondary currents were found more significant because of the occurrence of maximum velocity near the bed. The observed turbulence intensity component in the transverse direction was larger in the downstream side. Similarly, vertical Reynolds stress ($u'w'$) was reported stronger at the downstream side of a pier. They concluded that there was occurrence of heavily fluctuating Reynolds stress at the downstream side and unsteady shedding wake vortices due to flow separation.

Recently, Ataie-Ashtiani and Aslani-Kordkandi (2013) conducted an experimental study on the flow field around a single column and two in-line columns with the spacing of $3D$. That study provided a comparison between the flow pattern around the single pier and two in-line circular columns. During the experiments, the model columns were installed on a moderately rough flatbed laboratory flume. The results were time average velocity components, turbulence intensity components, turbulent kinetic energy, and Reynolds shear stresses and were presented graphically in the form of contour and profile. The power spectra analysis of instantaneous velocity measurements at different points were also presented in this study. It was reported that the results from the experiments showed significant changes in the flow structure, particularly in the near wake region, due to the presence of the downstream pier. Within the gap between the two columns, a stronger up-flow and weaker transverse deflection were formed in comparison with that of the single column case. Sheltering effect was noticed due to which the velocity of flow approaching the downstream pier was decreased to 20% to 30% of the approach mean velocity. Comparing with the results of single pier, considerable decrease in turbulent intensities and turbulent kinetic energy were noticed around two in-line circular columns. Decrease in the strength of vortex structure in the wake of the two-column case in comparison with the single column case was reported as a result of the power spectra analysis.

It is clear from the above review that most of the investigations on flow structure were based on the bridge piers with a single circular column. Apparently, only a few studies were associated with two in-line circular columns. However, effects of spacing between

two in-line columns on flow structures were not well investigated. Hence, in the present study, an in-depth investigation on the effect of spacing between two in-line circular columns on flow structures has been analysed and compared with the findings from previous investigations.

4.3 Flow around the Bridge Piers in Horizontal Plane

In this study, the data acquisition around the bridge piers in horizontal planes was carried out as described in the Section 3.4.1. The three dimensional instantaneous velocity components were measured using an ADV in three different horizontal layers. The first layer was close to the bed with $Z/h = 0.09$, the second layer was at the depth with $Z/h = 0.26$ and the measurement at the third layer was carried out at the depth with $Z/h = 0.54$. The captured data were processed and analysed using Win-ADV software. For the sake of simplicity, in the case of two in-line circular columns, the column at the upstream side is denoted as Column 1 (or C1) and the column at the downstream side is denoted as Column 2 (or C2). The measurements were carried out in Cartesian coordinate system provided that the origin is located at the upstream face of the Column 1. Different notations associated with bridge pier arrangement, used in this thesis, are shown in Figure 4.1. In the figure, X and Y represent the axes along streamwise and transverse direction, respectively; whereas D and L represent the diameter of the column and the centre-to-centre distance between two in-line circular columns.

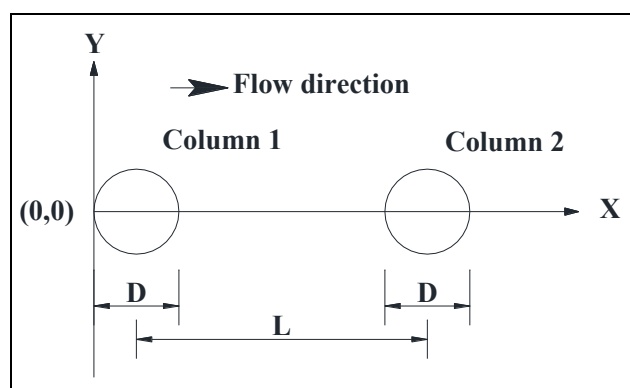


Figure 4.1 Definition sketch of the bridge piers arrangement

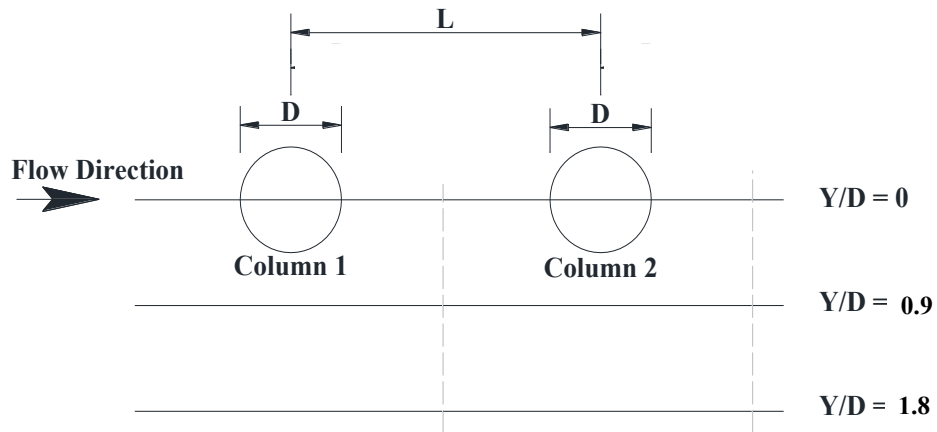


Figure 4.2 Schematic diagram of different axis of data analysis in horizontal planes

The results on the flow field and the turbulence characteristics of the flow around bridge piers and the effects of spacing between two in-line circular columns are presented in the following subsections. The processed and analysed data are presented in contour and profile plots for velocity components (u , v , and w), velocity fluctuation components (u' , v' and w'), turbulence intensity components (TI_u , TI_v and TI_w), turbulent kinetic energy (TKE) and Reynolds stresses. Comparisons have been carried out for different combinations including the single column and the double columns with various L/D ratios (i.e. $L/D = 1.5, 2, 3, 4, 5$ and 6). In addition, for each column arrangement, the three dimensional data along three different lines parallel to the flow direction have been extracted, as shown in Figure 4.2.

4.3.1 Flow Pattern

Vector plots and the stream line plots as shown in Figure 4.3 for the single column case and Figure 4.4 for two in-line circular columns case with $L/D = 3$ clearly represent the flow patterns around the bridge piers. The detailed figures of velocity vectors and streamline plots in planes $Z/h = 0.26$ and 0.54 for different values of L/D are presented in Appendices A.1.1 and A.1.2. In the vector diagram, the length of the vector gives the resultant magnitude of velocity components u and v given by $\sqrt{u^2 + v^2}$, the direction is clearly represented by the inclination of the vectors. For the condition of no piers, it is observed that there is not any deflection in velocity vectors and the magnitude of the vectors is uniform throughout the flow field. When a column was added to the system, flow started deflecting from its original direction. It was common to all the cases that the flow pattern at the upstream side of a column was similar, while at the downstream side

of the columns, the flow pattern was different in various conditions. It is also common to all the cases that the flow was deflected away and accelerated at the side of the columns. At the downstream side, the flow was again directed towards the line of symmetry.

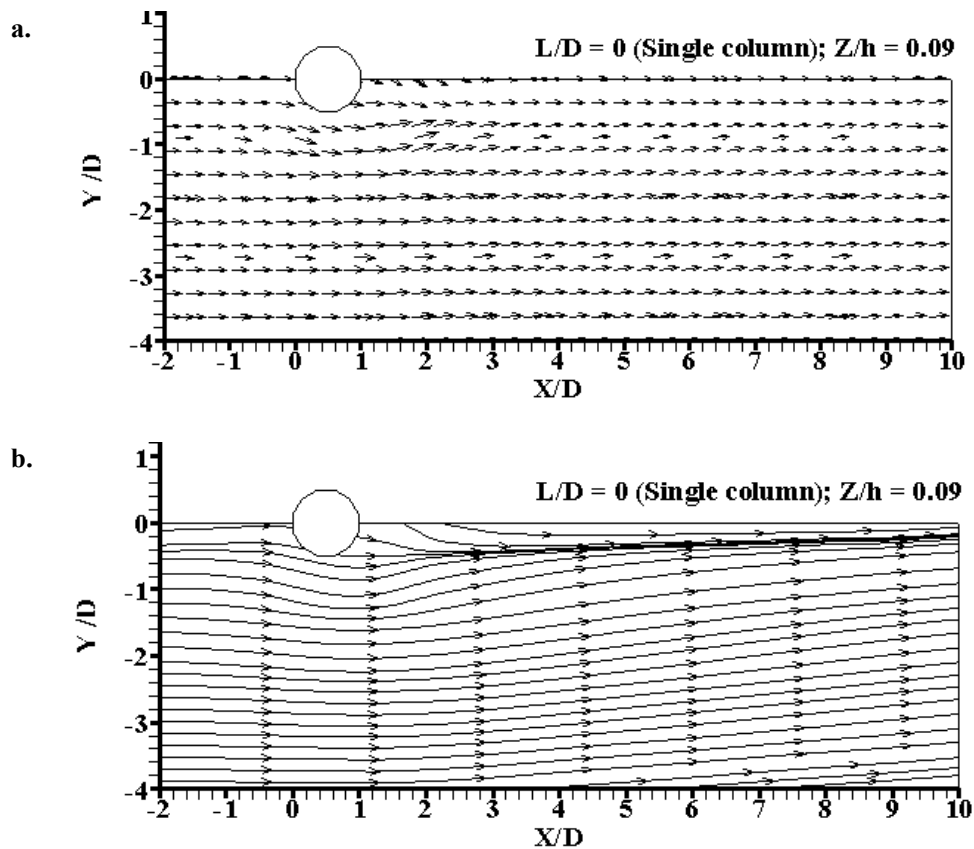


Figure 4.3 Flow pattern around a single column in horizontal plane at $Z/h = 0.09$ a) Vector plot, and b) Streamline plot

For the single column bridge pier, the vector plots and streamline plots for different values of Z/h indicated that in the wake region of the column, the reverse flow and the recirculation of the flow occurred. Furthermore, it is noticed that the size of the recirculation zone increased as the distance from the bed increased. This is due to the effect of roughness close to the bed. In the case of two in-line columns, for $L/D < 2$, reverse flow and recirculation of flow were not observed between the two columns. The shear layer separated from Column 1 wrapped around Column 2. Hence, only one wake was observed at the downstream side of Column 2. However, for $L/D > 2$, two different flow patterns were observed at the downstream side of Column 1 and Column 2. For $L/D = 3$, streamline diagrams show that the wake of Column 1 at $Z/h = 0.09$ is extended almost

throughout the gap. The shear layer, which separated from Column 1 re-attached on the upstream side of Column 2. According to the description of flow regime made on Section 2.4.2, it is called the re-attachment regime, which is principally characterised by formation and shedding of eddies in the gap. As the distance from the bed increased, the shear layer, which separated from Column 1 moved towards the downstream side of Column 2. This nature of flow indicates that there is no vortex shedding between the two columns. Further increase in spacing results in the flow separation at a distance about $2D$ measured from the face of Column 1. There was formation of vortex shedding at the downstream side of both Column 1 and Column 2. As described in Section 2.4.2, it is called the co-shedding regime. In this regime, both the columns undergo vortex shedding of the same frequency and produce weaker vortices behind Column 2 than that in the case of $L/D < 3$. This is attributed to the disturbance of vortex shedding of Column 1 to the vortex shedding behind Column 2.

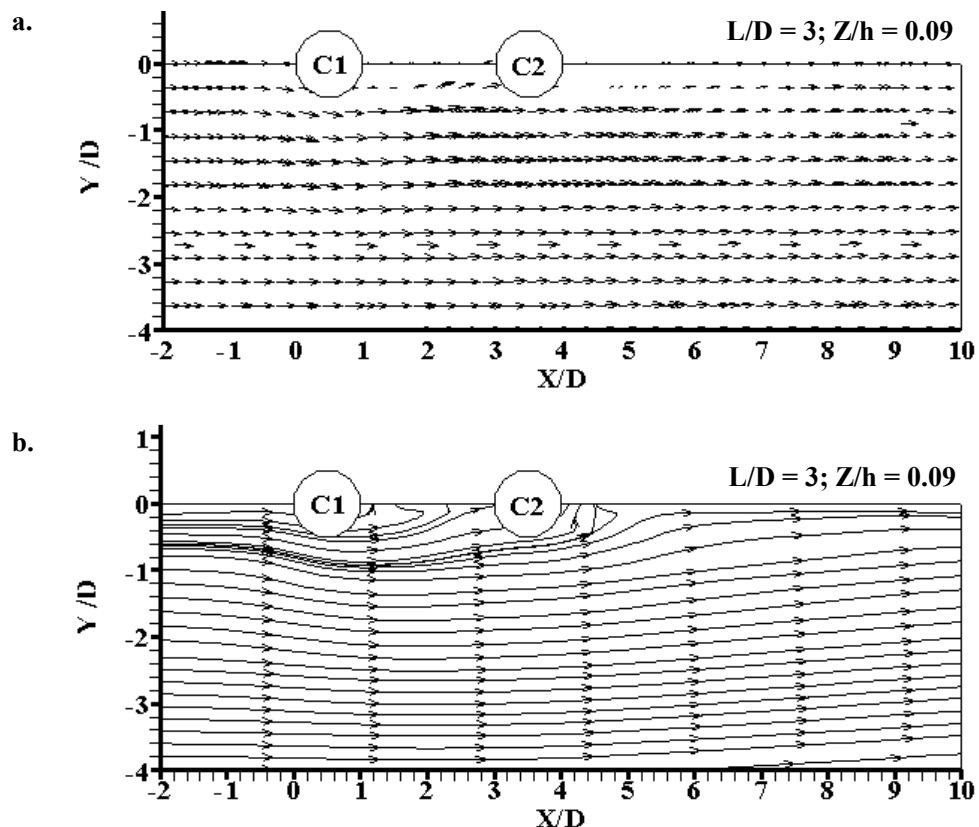


Figure 4.4 Flow pattern around two columns with $L/D = 3$ in horizontal plane at $Z/h = 0.09$ a) Vector plot, and b) Streamline plot

4.3.2 Three Dimensional Velocity Component

Figure 4.5 shows the contour plot of normalised streamwise velocity component, u/V for the single column case at three different horizontal planes $Z/h = 0.09, 0.26$ and 0.54 . Similarly, Figure 4.6 shows the distribution of u/V in horizontal planes along three different longitudinal axes $Y/D = 0, 0.9$ and 1.8 . Contour plots show that pockets of higher and lower values of u/V exist at the side and in the wake of the column, respectively. The increase in the value of u/V at the side of the column is attributed to the obstruction due to the presence of column resulting in flow contraction. The distribution profiles as shown in Figure 4.6 indicated that for $Y/D = 0$, the value of u/V at the wake of the column decreased as the value of Z/h increased. It was also noticed that the value of u/V at the wake increased with increase in the value of X/D . This observed phenomenon was common to all of the horizontal planes. When $Y/D = 0.9$, the maximum value of u/V at the side of a column was approximately equal to 1.2. Gradual decrease in the value of u/V at the side of the column was observed as the value of Y/D increased.

For two in-line columns cases, Figures 4.7 and 4.8 show the contour plot and distribution profile plot, respectively for $L/D = 3$. For other values of L/D , contour plots and profile plots are presented in Appendices A.1.3 and A.1.4. Similar to the single column case, it was noticed in all the cases of two in-line columns that the maximum value of u/V occurred along the side of the columns and the minimum value occurred in the wake. For the spacing $L/D \leq 2$, no reverse flow in the gap could be inferred from the contour plots. This was because Column 2 was positioned inside the vortex formation region of Column 1. This situation is attributed to the extended body regime of the flow. At the downstream side of Column 2, reverse flow was noticed, closer to the column when compared to the single column case and extended up to the distance of about $2D$, measured from the face of Column 2. For $L/D \geq 3$, in the gap region, reverse flow was observed, extending throughout the gap. Moreover, a gradual increase in the strength of reverse flow in the gap occurred as the value of Z/h increased. However, at the downstream side of Column 2, weaker reverse flow in comparison with that of Column 1 was observed. This is because of the sheltering effect of Column 1, resulting in a decrease in approach velocity of flow for Column 2. The contour plots exhibited that the strength of reverse flow at the wake of Column 2 increased with an increase in value of L/D ; however, at the region

beyond the wake zone, it decreased with an increase in the spacing between two piers. Furthermore, it was observed that the magnitude of u/V at the downstream side of the single column was continuously higher than that of the other cases.

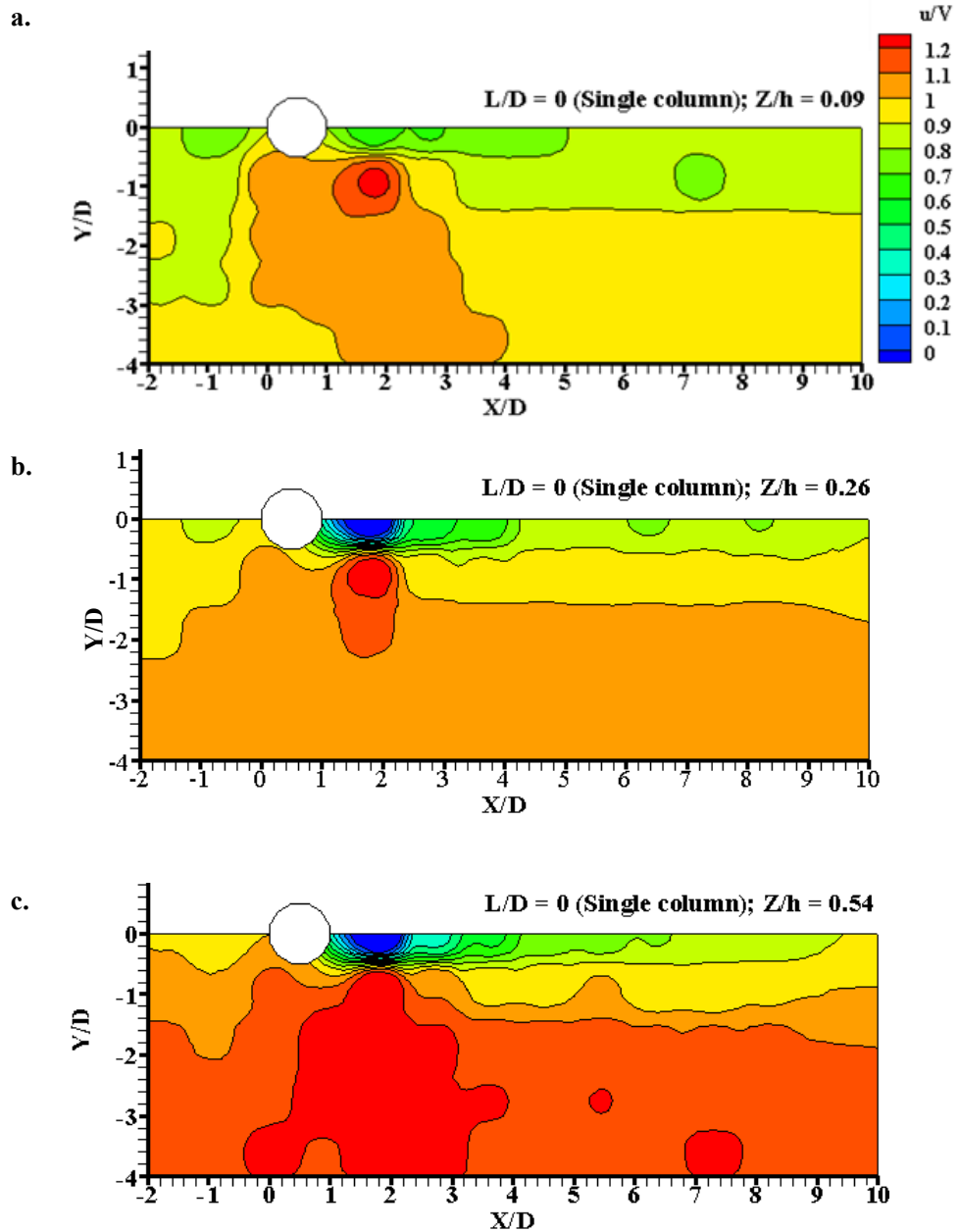


Figure 4.5 Contour plots of streamwise velocity component for the single column case in different horizontal planes a) at $Z/h = 0.09$, b) at $Z/h = 0.26$ and c). at $Z/h = 0.54$

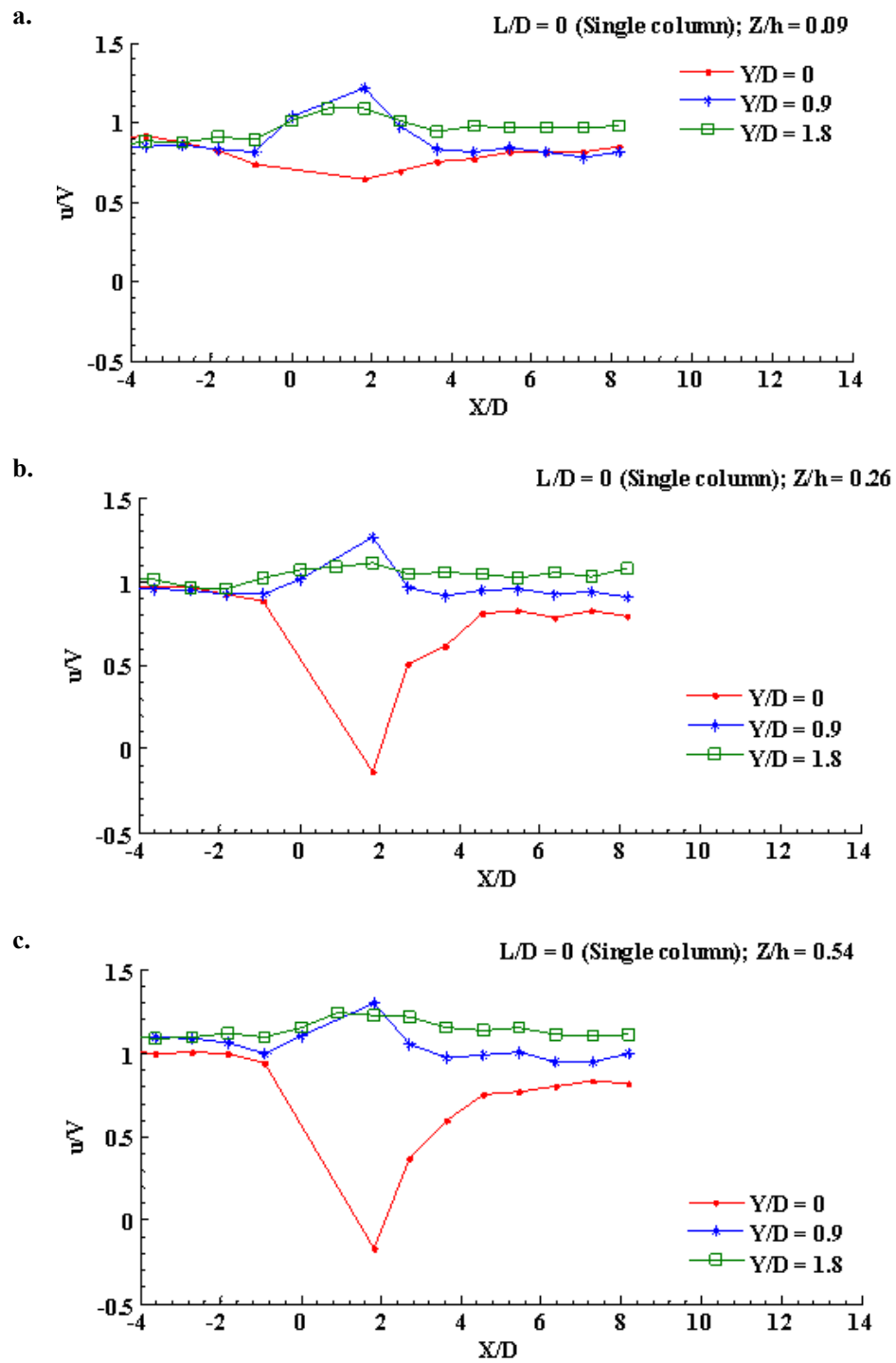


Figure 4.6 Profile plots of streamwise velocity component for the single column case in different horizontal planes along three different longitudinal axes a) at $Z/h = 0.09$, b) at $Z/h = 0.26$ and c). at $Z/h = 0.54$

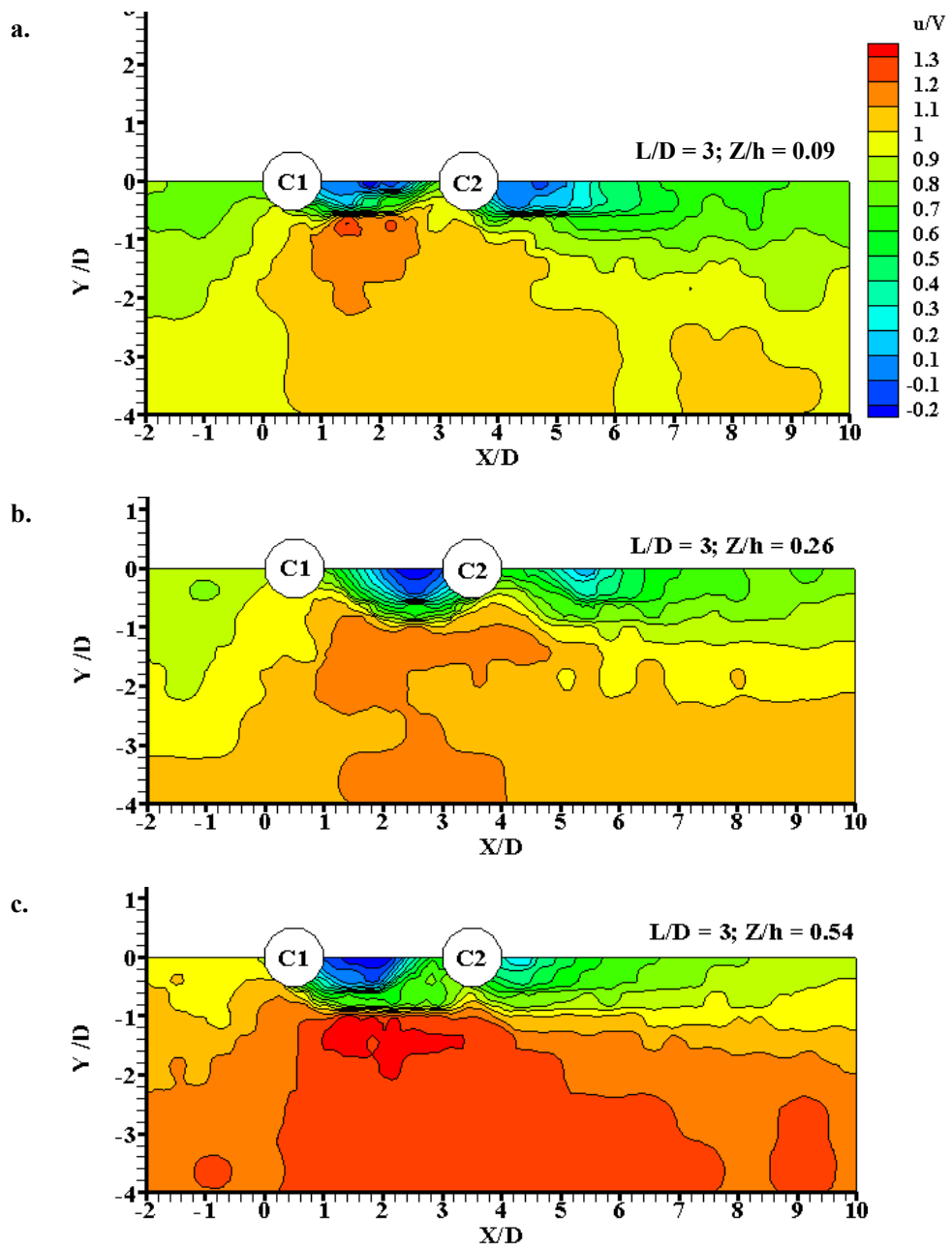


Figure 4.7 Contour plots of streamwise velocity component for two columns case with $L/D = 3$ in different horizontal planes a) at $Z/h = 0.09$, b) at $Z/h = 0.26$ and c). at $Z/h = 0.54$

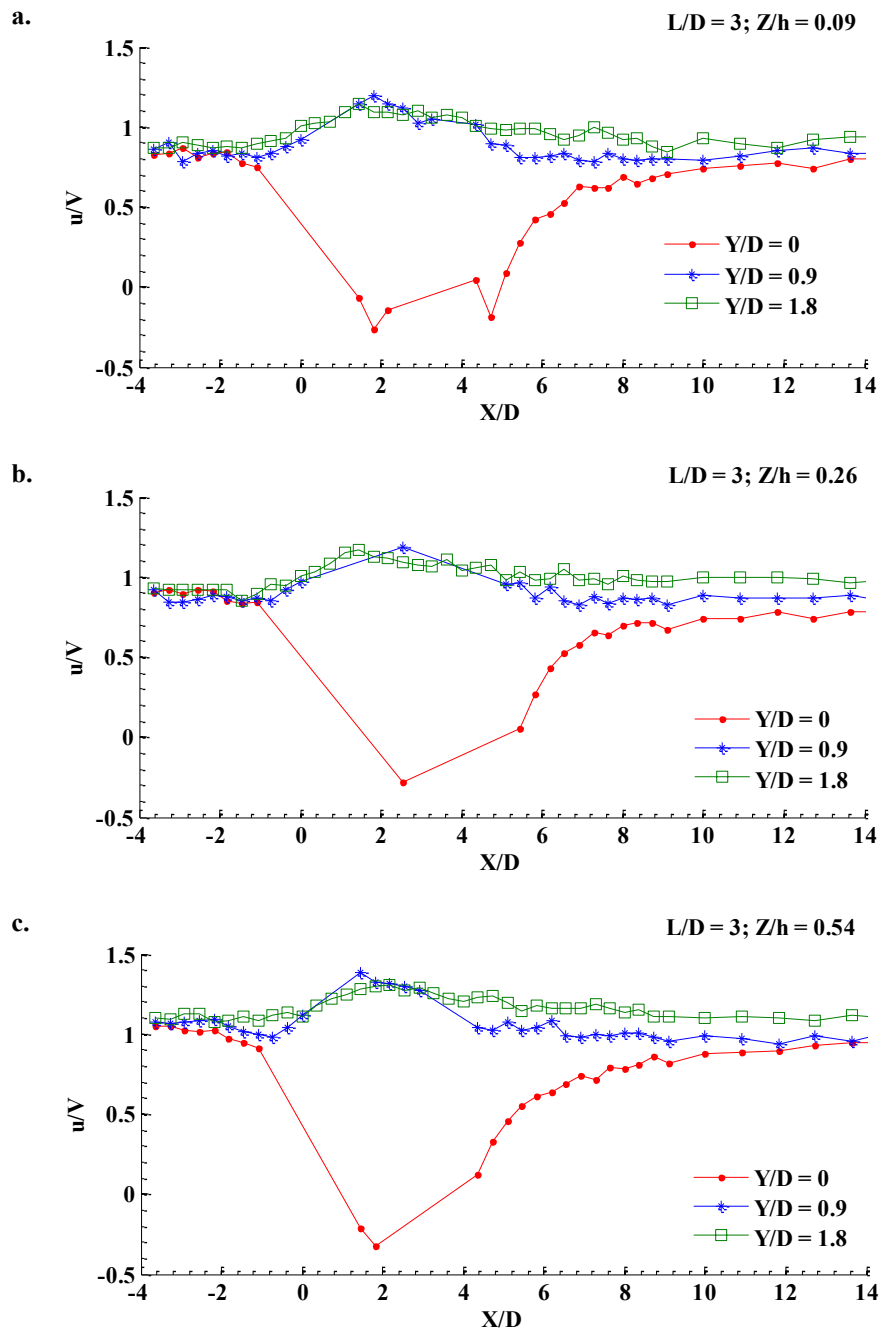


Figure 4.8 Profile plots of the streamwise velocity component for two-column case with $L/D = 3$ in different horizontal planes along three different longitudinal axes a) at $Z/h = 0.09$, b) at $Z/h = 0.26$ and c). at $Z/h = 0.54$

The normalised transverse velocity components, v/V for the single column case and the two-column case $L/D = 3$ are presented in contour plots as in Figures 4.9 and 4.10, respectively. Similarly, the distribution of v/V along three different longitudinal axes $Y/D = 0, 0.9$ and 1.8 for the single column case and the two-column case with $L/D = 3$ are

presented in Figures 4.11 and 4.12, respectively. The detailed contour plots and profile plots for different values of L/D at three different horizontal planes at $Z/h = 0.09$, 0.26 and 0.54 are presented in Appendices A.1.5 and A.1.6.

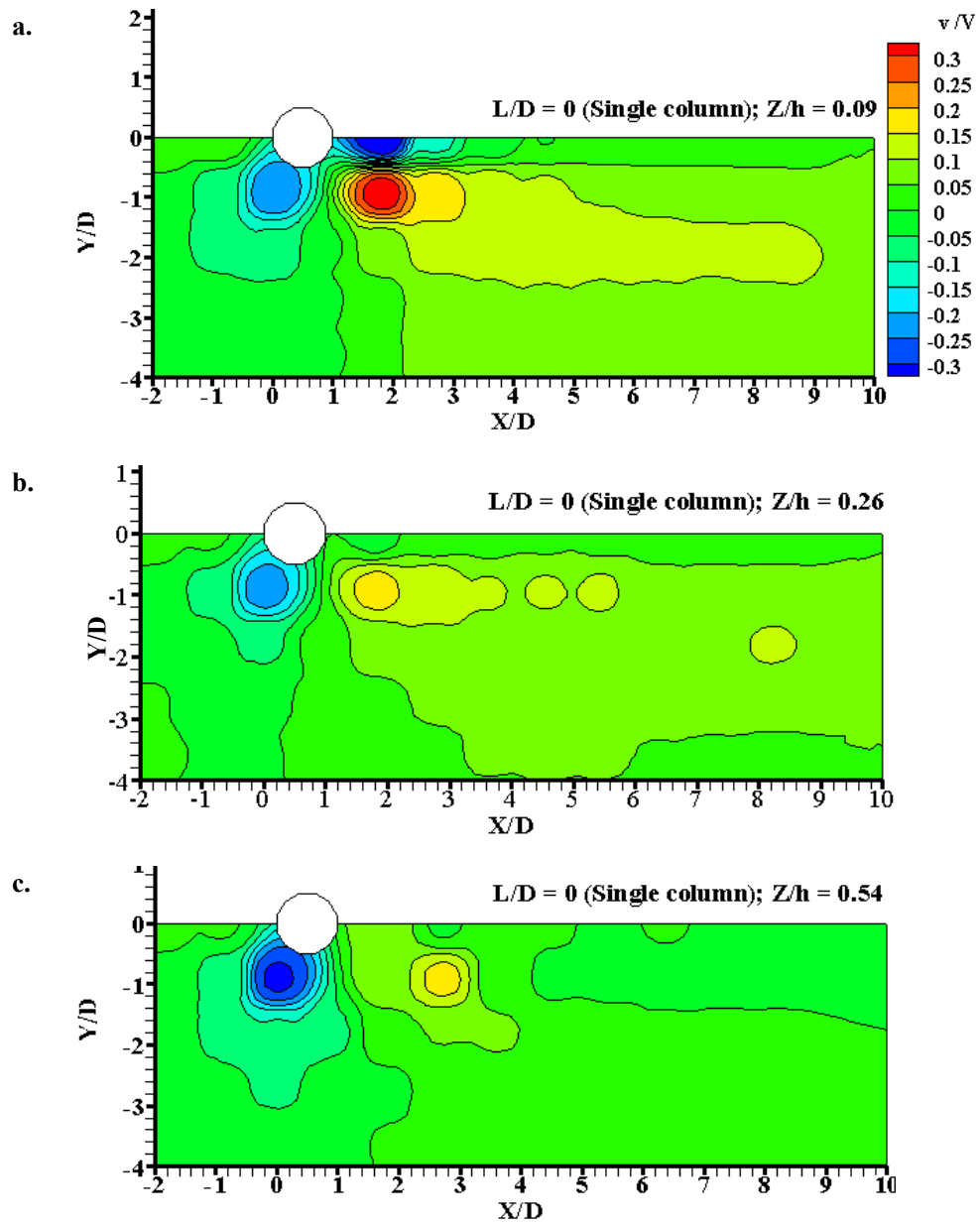


Figure 4.9 Contour plots of transverse velocity component for the single column case in different horizontal planes a) at $Z/h = 0.09$, b) at $Z/h = 0.26$ and c). at $Z/h = 0.54$

The contour plots for the single column case in Figure 4.9 indicate that the pocket of higher value of negative v/V happens at the upstream side near the zone of shear layer separation. The negative value of v/V indicates the deviation of flow away from the

column. At the downstream side, a positive value of v/V was observed i.e. the flow converged in the wake of a column. The magnitude of v/V in the wake near the bed was the highest and it decreased as the distance from the bed increased.

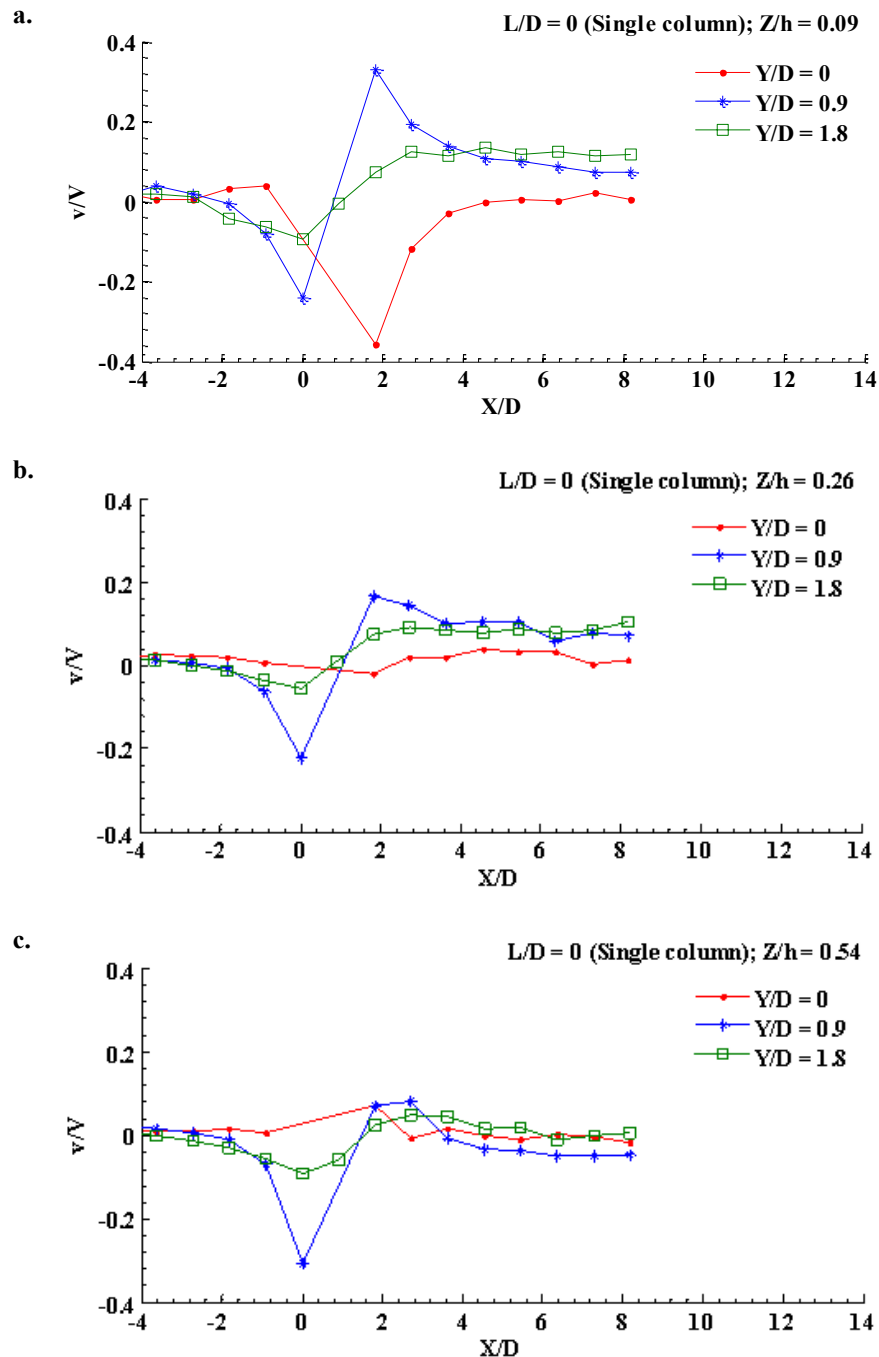


Figure 4.10 Profile plots of transverse velocity component for the single column case in different horizontal planes along three different longitudinal axes a) at $Z/h = 0.09$, b) at $Z/h = 0.26$ and c). at $Z/h = 0.54$

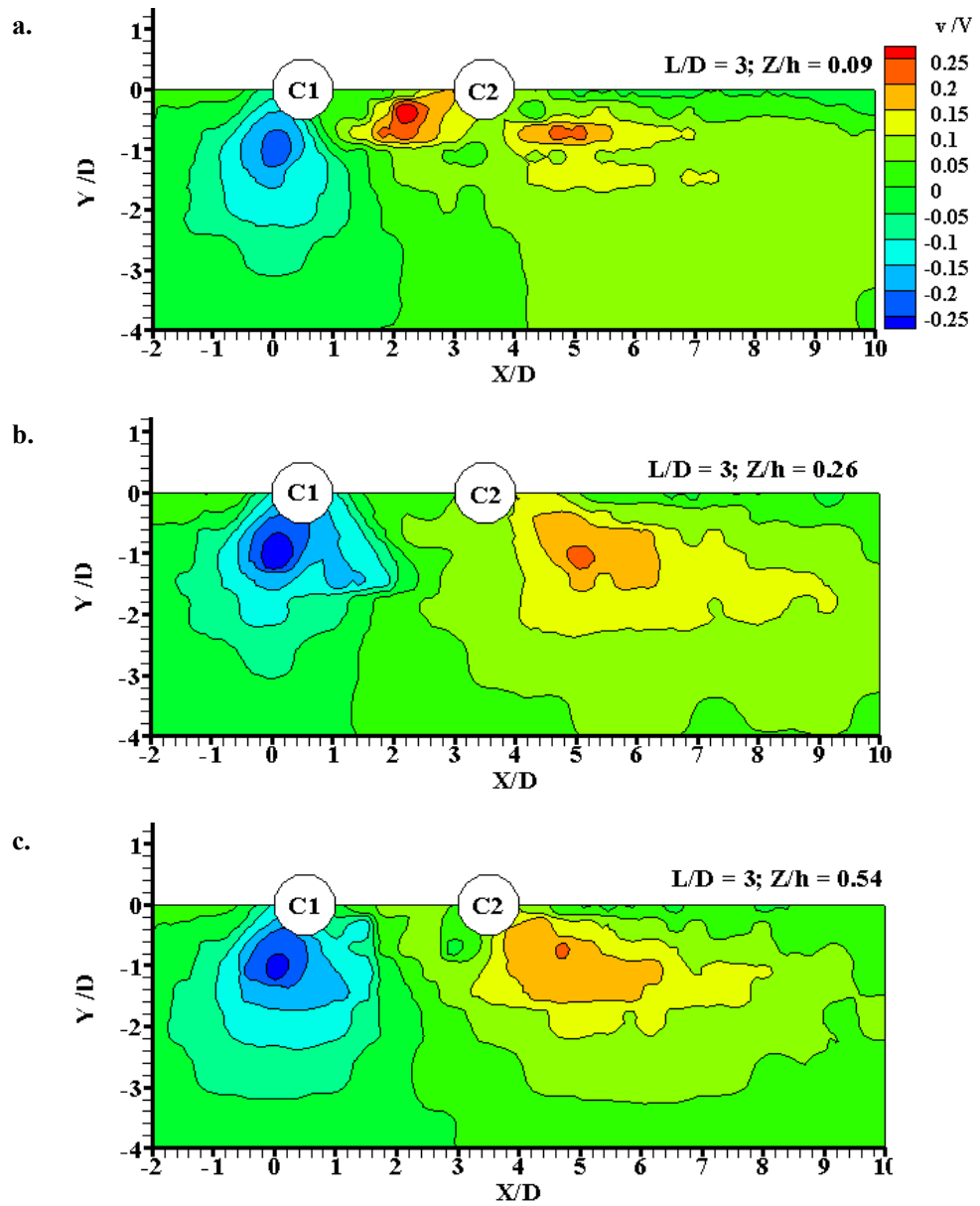


Figure 4.11 Contour plots of transverse velocity component for the two-column case with $L/D = 3$ in different horizontal planes a) at $Z/h = 0.09$, b) at $Z/h = 0.26$ and c). at $Z/h = 0.54$

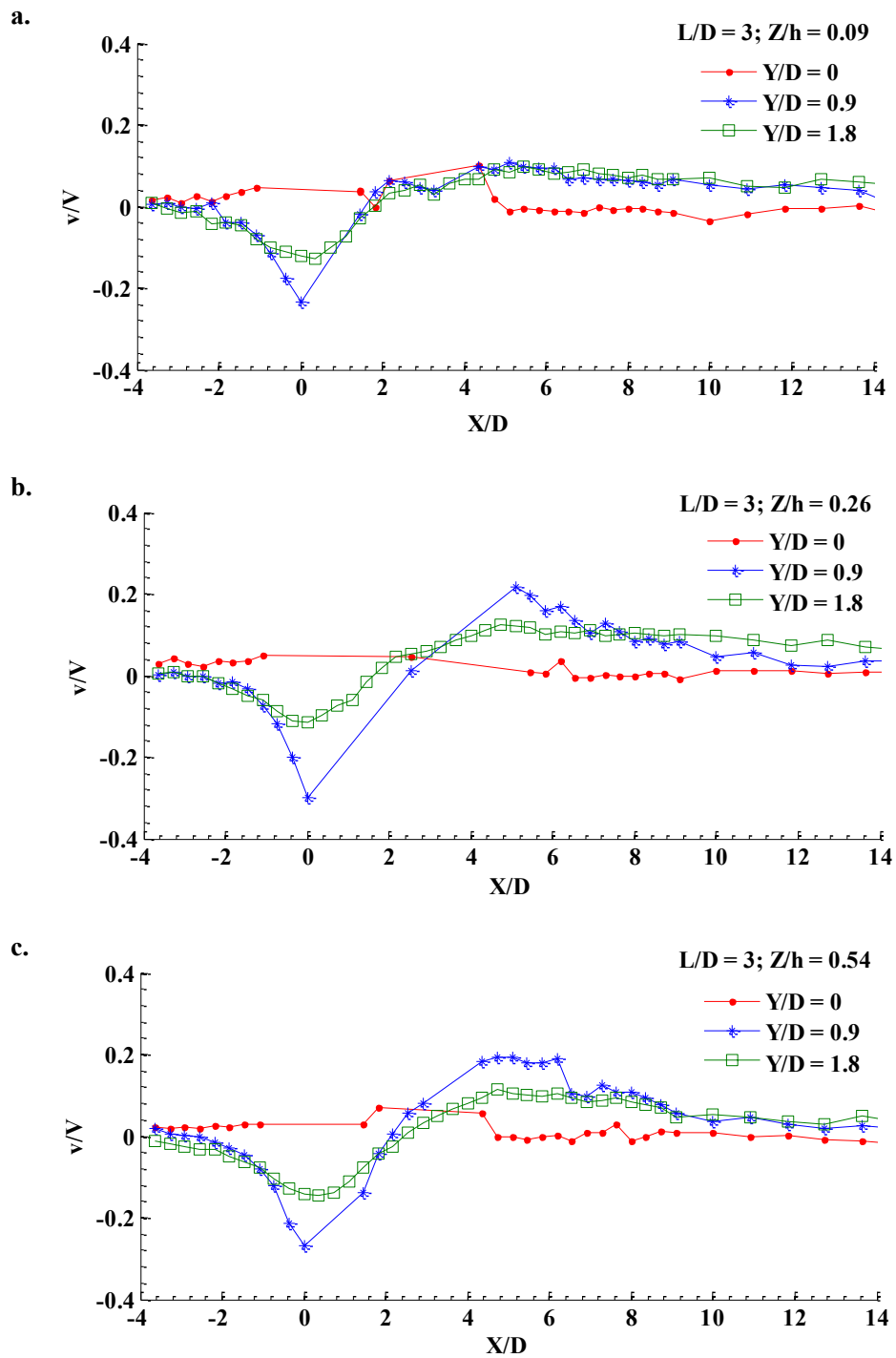


Figure 4.12 Profile plots of transverse velocity component for the two-column case with $L/D = 3$ in different horizontal planes along three different longitudinal axes a) at $Z/h = 0.09$, b) at $Z/h = 0.26$ and c). at $Z/h = 0.54$

For the two in-line columns case with $L/D \leq 2$, the minimum and maximum values of v/V were similar to those of the single column case. In the gap between the two columns, no deflection of the flow was noticed. The contour plots indicated that the pocket of higher values of v/V occurred at the downstream side of Column 2. Furthermore, the value of v/V was stronger in the upper level than near the bed. When $L/D = 3$ at $Z/h = 0.09$, a higher value of v/V was observed in the gap, which decreased as the value of Z/h increased. This can be due to the generation of the re-attachment regime close to the bed. However, for the upper level, the shear layer separated from Column 1 converged at the downstream side of Column 2, resulting in a small deflection of flow inside the gap. Additionally, the figures reveal that the observed transverse velocity in the downstream side of Column 2 is stronger than that of the case $L/D < 2$. For $L/D > 3$, similar results can be seen from the contour plots. However, the pocket of higher value of v/V occurred close to Column 1 in its wake. As the flow approached Column 2, the value of v/V became approximately equal to 0.

The contour plots of normalised velocity component, w/V for the single column and two in-line columns with $L/D = 3$ are shown in Figures 4.13 and 4.15, respectively in three different horizontal planes at $Z/h = 0.09, 0.26$ and 0.54 . Figures 4.14 and 4.16 show the distribution of w/V along three different longitudinal axes at $Y/D = 0, 0.9$ and 1.8 in horizontal planes for single column and two columns with $L/D = 3$ respectively. Contour plots and profile plots for other values of L/D in different horizontal planes are presented in Appendices A.1.7 and A.1.8.

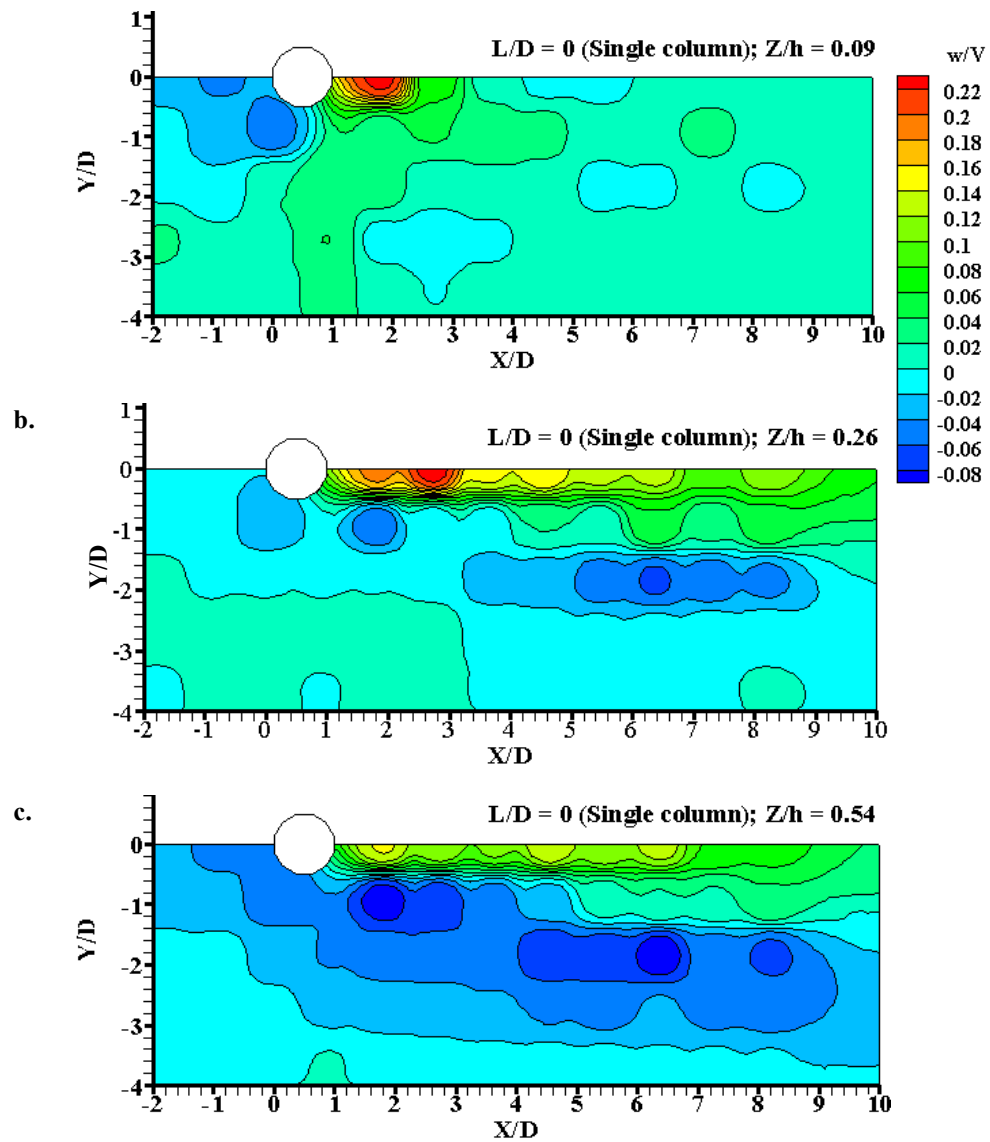


Figure 4.13 Contour plots of vertical velocity component for the single column case in different horizontal planes a) at $Z/h = 0.09$, b) at $Z/h = 0.26$ and c). at $Z/h = 0.54$

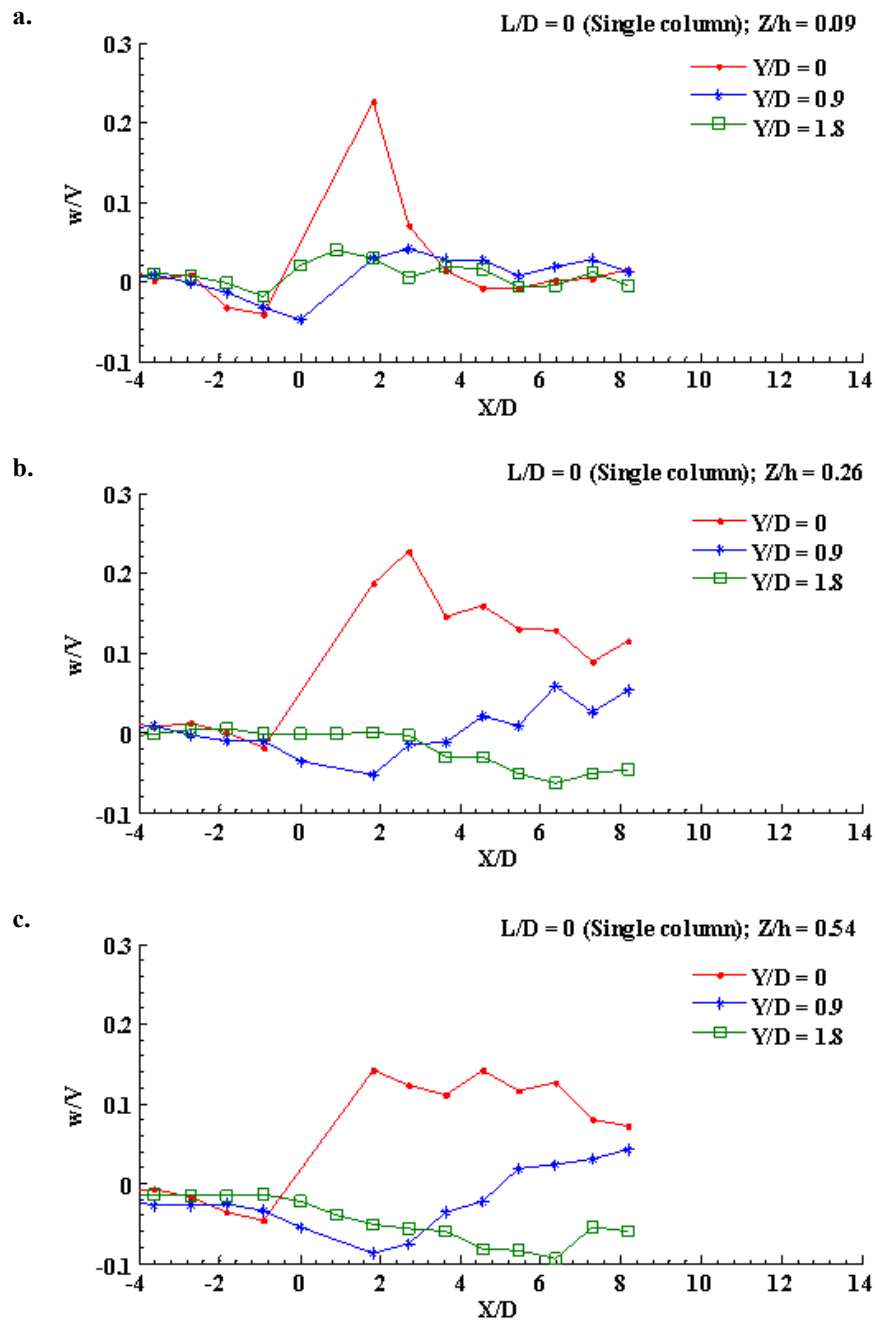


Figure 4.14 Profile plots of vertical velocity component for the single column case in different horizontal planes along three different longitudinal axes a) at $Z/h = 0.09$, b) at $Z/h = 0.26$ and c). at $Z/h = 0.54$

For the single column case as shown in Figure 4.13, a negative value of w/V was observed close to the column at the upstream side. It is clear from Figure 4.14 that at the upstream side of a column, the negative value of w/V increases as the flow approaches the column. The negative value of w/V is indication of the down flow, which is due to the pressure

difference at the stagnation point. The occurrence of down flow was common to all the cases of two in-line columns. Furthermore, the profile plots for different cases indicate that the down flow is stronger close to the bed than that in the upper levels. At the downstream side of the columns, a positive value of w/V is observed i.e. an up flow was noticed for all cases. In the case of the single column, the pocket of higher values of w/V occurred close to the bed, while the extent of up flow increased as the value of Z/h increased.

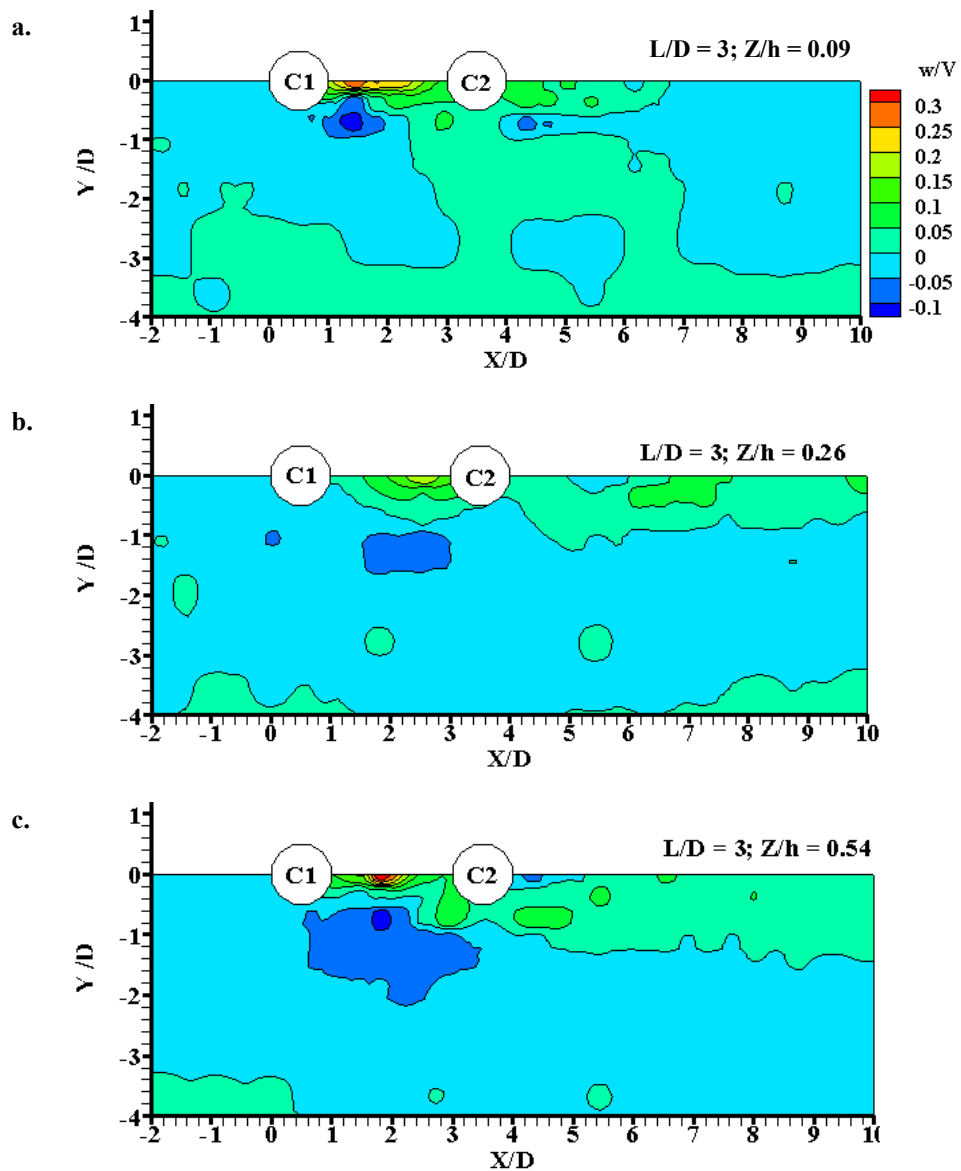


Figure 4.15 Contour plots of vertical velocity component for the two-column case with $L/D = 3$ in different horizontal planes a) at $Z/h = 0.09$, b) at $Z/h = 0.26$ and c). at $Z/h = 0.54$

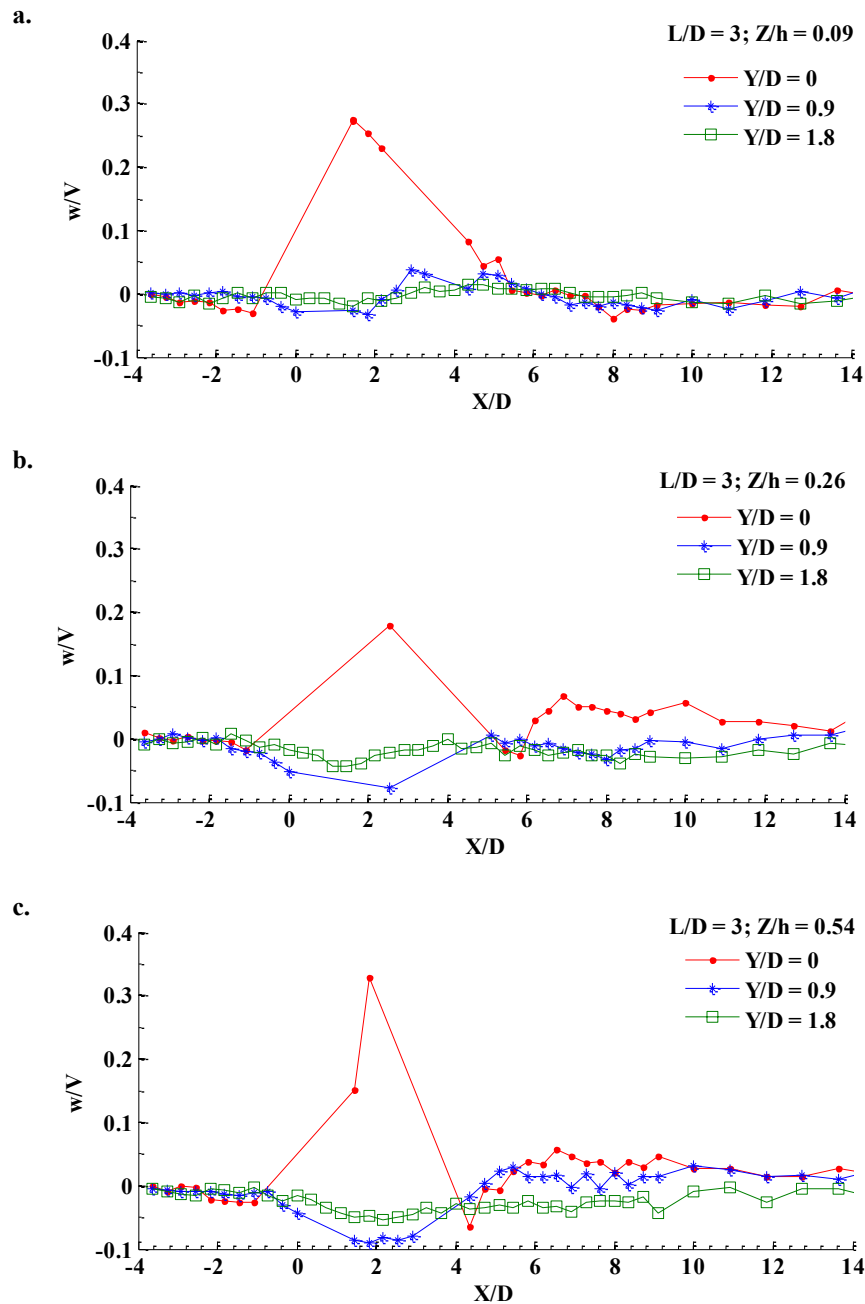


Figure 4.16 Profile plots of vertical velocity component for the two-column case with $L/D = 3$ in different horizontal planes along three different longitudinal axes a) at $Z/h = 0.09$, b) at $Z/h = 0.26$ and c). at $Z/h = 0.54$

In the case of two in-line columns, for $L/D \leq 2$, the weak up flow were noticed inside the gap. As the spacing between two columns increased, intensity of up flow increased in the wake of Column 1. At the downstream side of Column 2, weaker up flow than that of single column was observed close to the bed. However, a small down flow was noticed behind Column 2 at mid depth. Similar results were reported by Ataie-Ashtiani and

Aslani-Kordkandi (2013). It can be clearly seen from the contour plots for $L/D \geq 3$ that, as the flow approaches the Column 2, intensity of up flow decreases. On the other hand, the down flow at the upstream side of Column 2 interacts with the up flow close to the bed and hence the development of the horseshoe shoe vortex was not expected in front of Column 2.

4.3.3 Turbulence Intensity

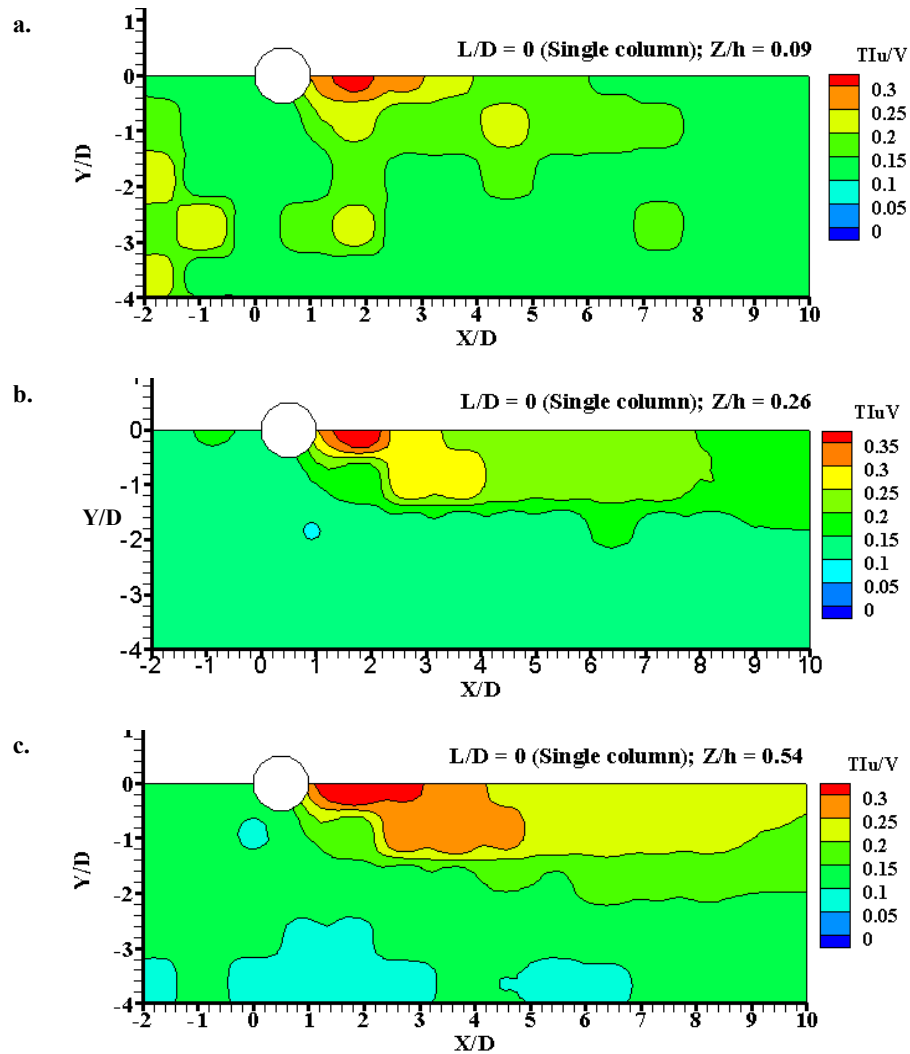


Figure 4.17 Contour plots of streamwise turbulence component for the single column case in different horizontal planes a) at $Z/h = 0.09$, b) at $Z/h = 0.26$ and c). at $Z/h = 0.54$

Three dimensional turbulence intensity components in the streamwise direction (TIu), in the transverse direction (TIv), and in the vertical direction (TIw) have been obtained by calculating the root mean square values of the velocity fluctuation components u' , v' and

w' , respectively. To analyse the turbulence intensity, it has been normalised using the free stream velocity (V). The normalised turbulence intensity components Tl_u/V , Tl_v/V and Tl_w/V are presented in contour plots and profile plots in different horizontal planes.

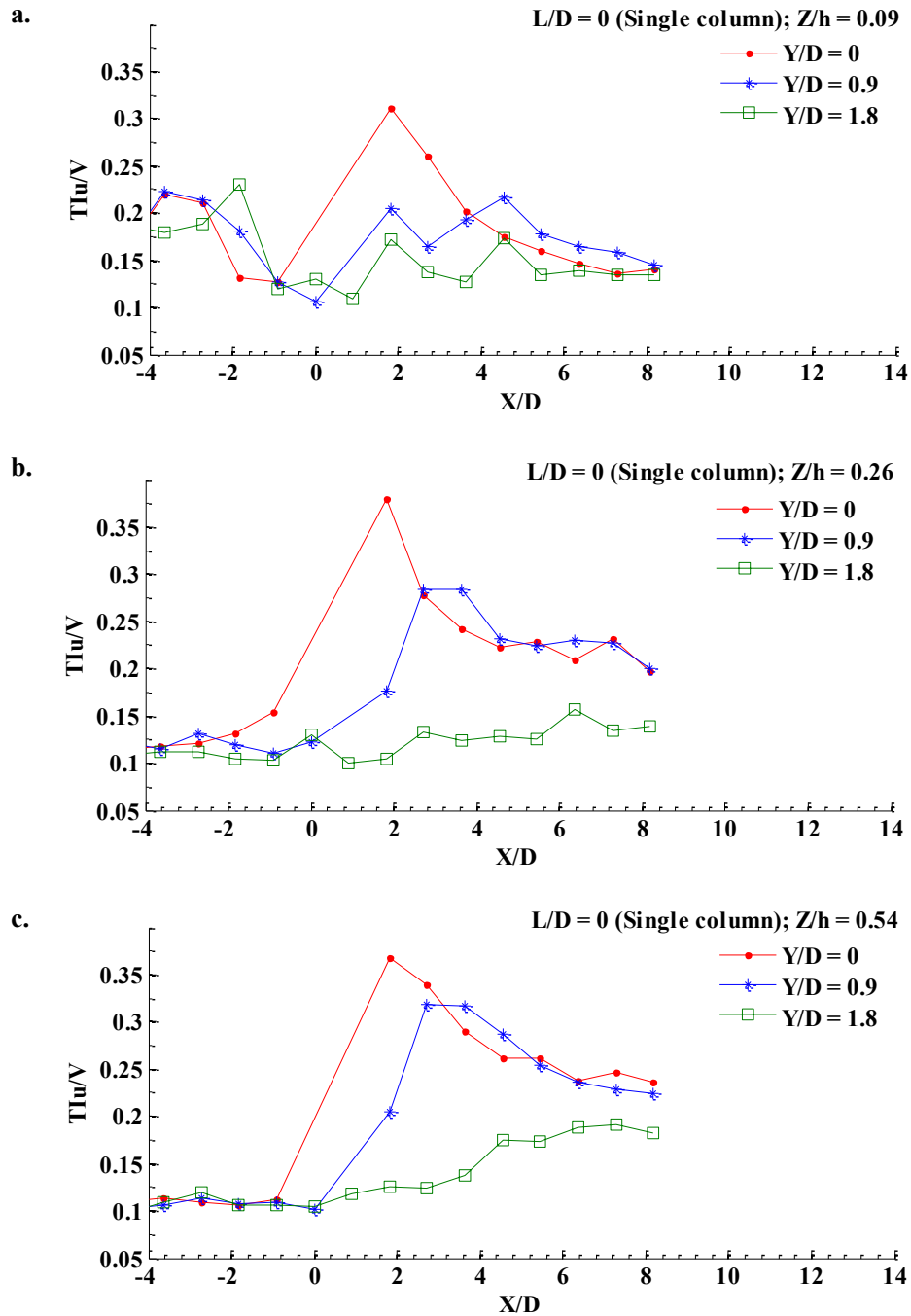


Figure 4.18 Profile plots of streamwise turbulence intensity component for the single column case in different horizontal planes along three different longitudinal axes a) at $Z/h = 0.09$, b) at $Z/h = 0.26$ and c). at $Z/h = 0.54$

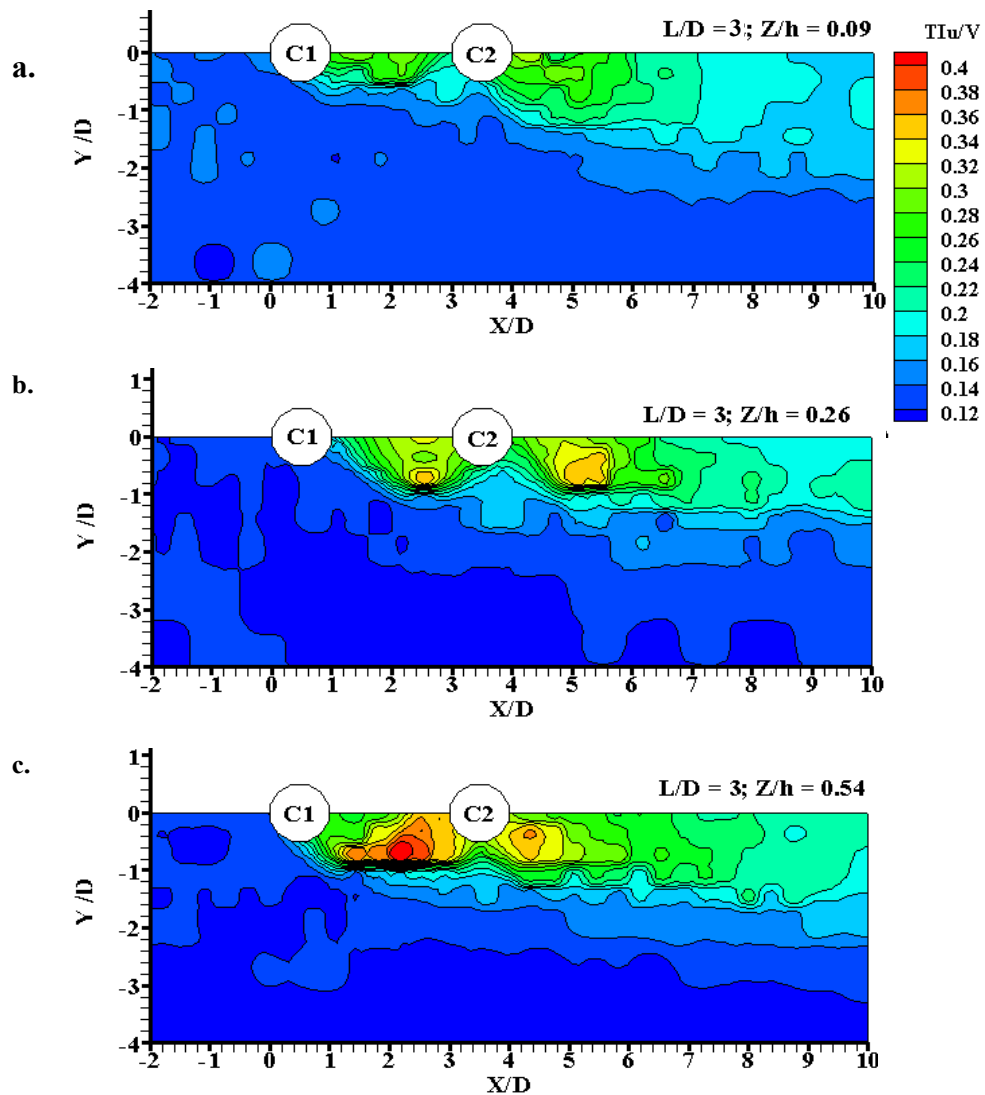


Figure 4.19 Contour plots of streamwise turbulence intensity component for the two-column case with $L/D = 3$ in different horizontal planes a) at $Z/h = 0.09$, b) at $Z/h = 0.26$ and c). at $Z/h = 0.54$

Figures 4.17 and 4.19 show the contour and profile plots, respectively for the single column case in three different horizontal planes at $Z/h = 0.09, 0.26$ and 0.54 . The profile plots, shown in Figures 4.18 and 4.20, are generated along three different longitudinal axes at $Y/D = 0, 0.9$ and 1.8 . The figures illustrate that higher values of TIu/V are observed in the wake of a column and it is common to all the horizontal planes. However, the magnitude of TIu/V is observed higher at upper levels than at levels close to the bed. For two in-line columns cases, contour plots and profile plots are presented in Figures 4.19 and 4.20, and Appendices B.1.1 and B.1.2. The results indicated that for $L/D \leq 2$, the pocket of higher value of TIu/V happened in the wake of Column 2. When $L/D = 3$, a

higher value of Tl_u/V close to the bed was observed in the wake of both columns with approximately the same intensity. The value of Tl_u/V increased as the value of Z/h increased. Furthermore, the figures exhibit that the value of Tl_u/V in the gap is higher than that behind Column 2.

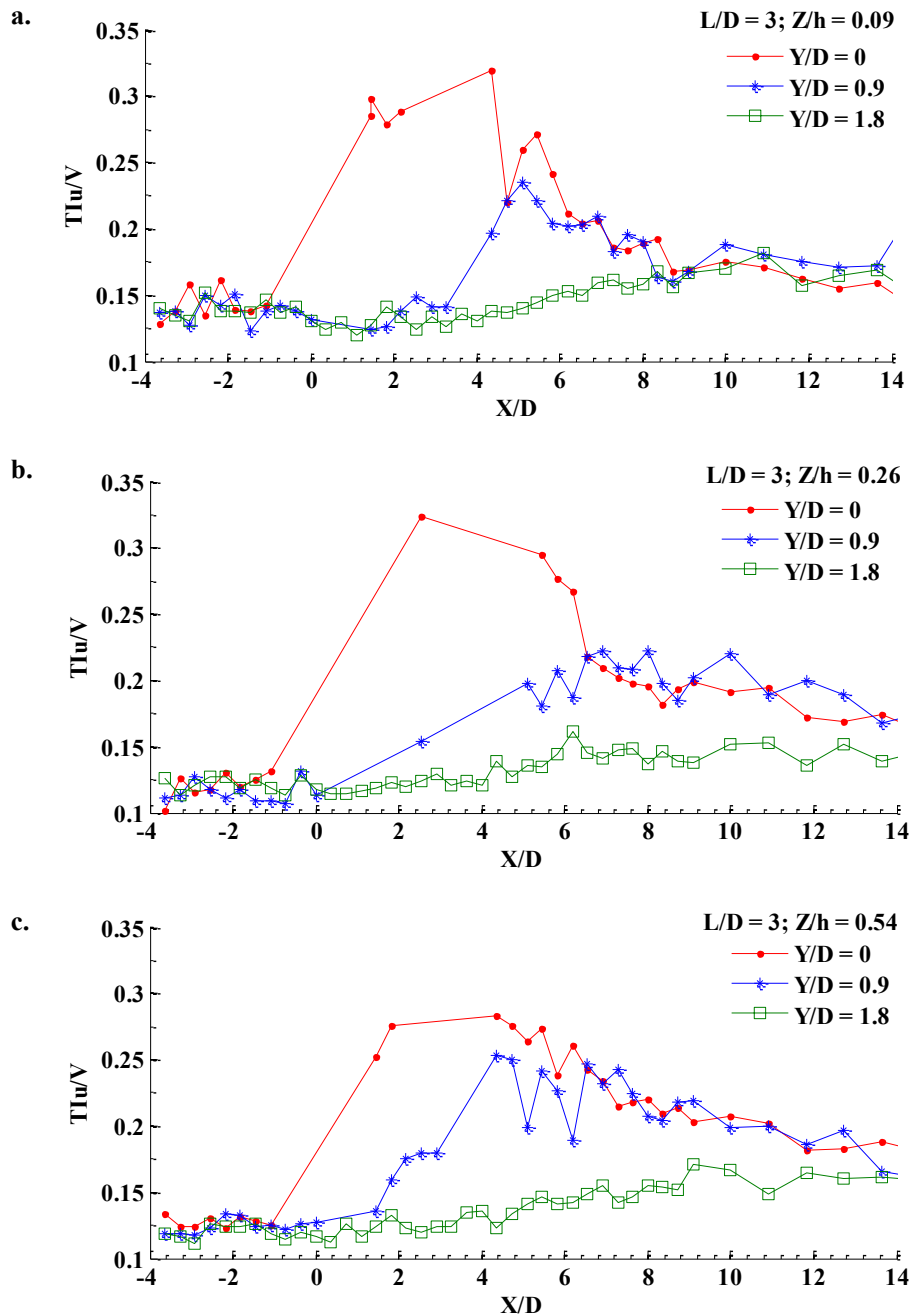


Figure 4.20 Profile plots of streamwise turbulence intensity component for the two-column case with $L/D = 3$ in different horizontal planes along three different longitudinal axes a) at $Z/h = 0.09$, b) at $Z/h = 0.26$ and c). at $Z/h = 0.54$

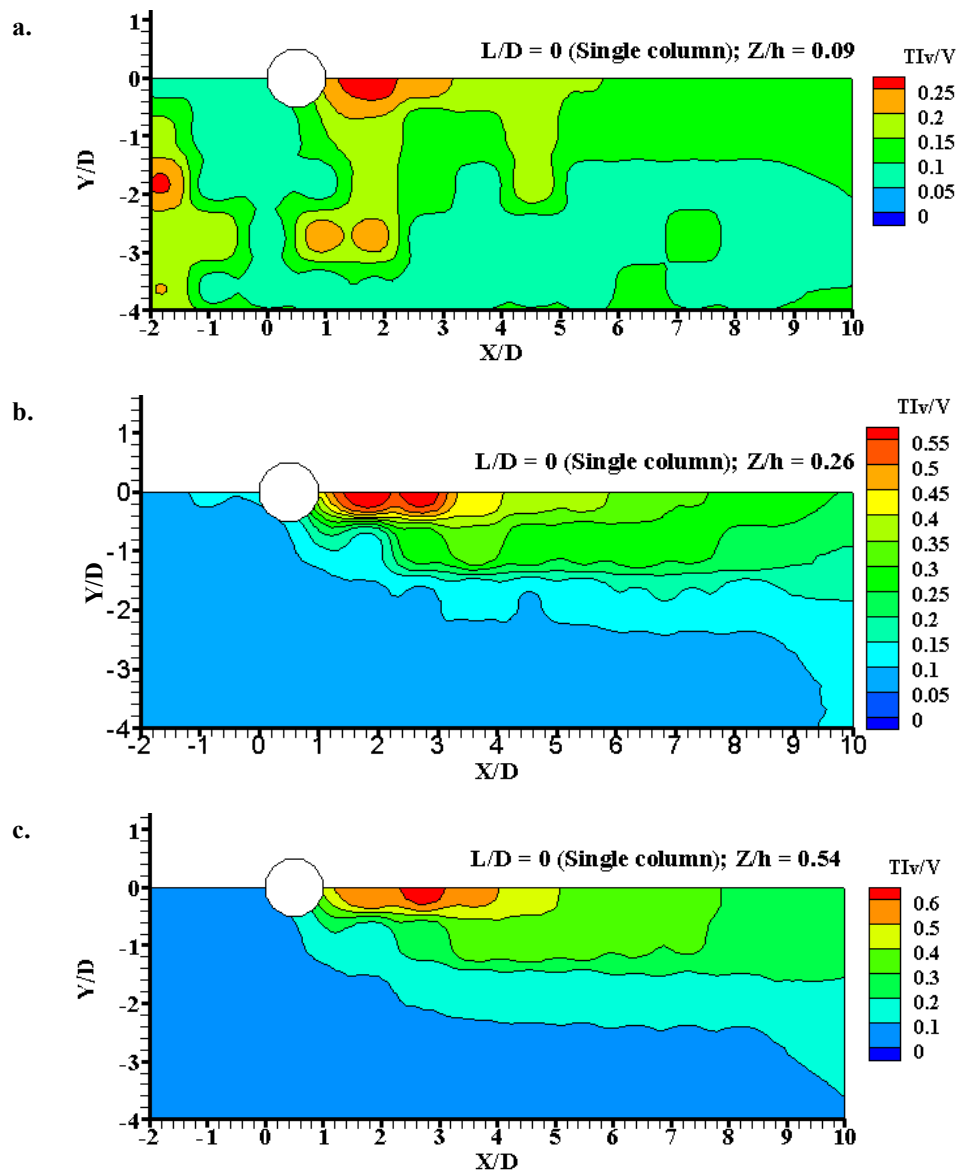


Figure 4.21 Contour plots of transverse turbulence intensity component for the single column case in different horizontal planes a) at $Z/h = 0.09$, b) at $Z/h = 0.26$ and c). at $Z/h = 0.54$

The distribution of normalised components of turbulence intensity in the transverse direction, TIv/V in contour plots are shown in Figures 4.21, Figure 4.22 and Appendix B.1.3 and in profile plots along three different longitudinal axes are shown in Appendix B.1.4. For the single column case, the contour plots, shown in Figure 4.21 indicate that the maximum value of TIv/V occurs in the wake of the column, which is approximately equal to 0.6. Comparing this results with the maximum value of TIu/V , it can be seen that the maximum value of TIv/V is about 2 times higher than that of TIu/V . Furthermore, it

can be clearly seen from the contour plots and profile plots that the value of Tl_v/V increases as the distance from the bed increases towards the free surface. Additionally the contour plots, depicted in Figure 4.21a, close to the bed at $Z/h = 0.09$ exhibits that the upstream portion of column experiences a small pocket of higher value of Tl_v/V . The reason behind this could be the effect of bed roughness.

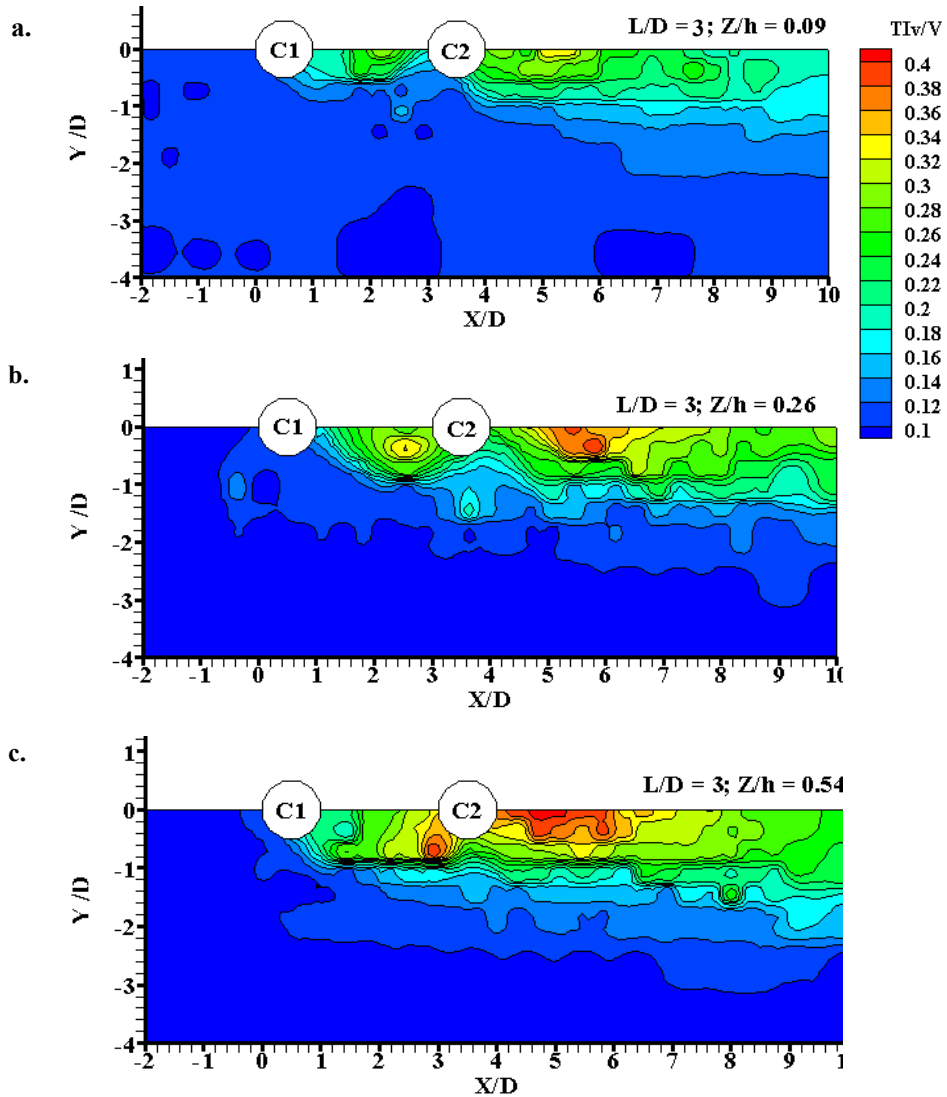


Figure 4.22 Contour plots of transverse turbulence intensity component for the two-column case with $L/D = 3$ in different horizontal planes a) at $Z/h = 0.09$, b) at $Z/h = 0.26$ and c). at $Z/h = 0.54$

Figure 4.23 shows the contour plots of Tl_v/V for two in-line columns with $L/D = 3$ at horizontal planes. In order to compare the results, other figures for different values of L/D are referenced from Appendix B.1.3. Referring to the contour plots for two in-line

columns cases, for $L/D < 2$, it was noticed that the pocket of higher values of TI_v/V was present only in the wake of Column 2. However, the maximum value of TI_v/V was about 50% smaller than that of the single column case. For $L/D = 3$ as shown in Figure 4.23, it can be clearly seen that both the columns experience the higher values of TI_v/V . However, the magnitude of TI_v/V behind the Column 2 is higher than that in the gap, found to be approximately equal to 0.4, which is about 0.66 times of the values in the single column case.

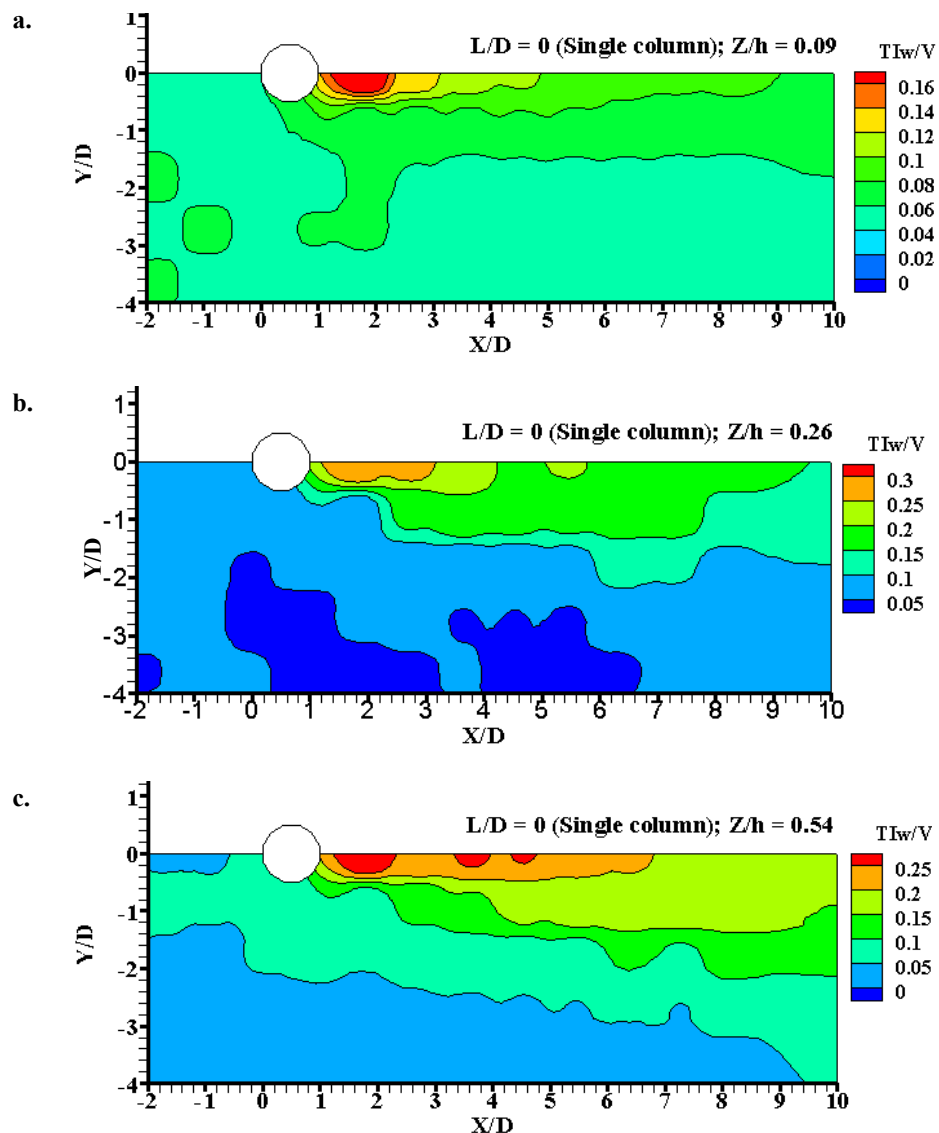


Figure 4.23 Contour plots of vertical turbulence intensity component for the single column case in different horizontal planes a) at $Z/h = 0.09$, b) at $Z/h = 0.26$ and c). at $Z/h = 0.54$

Figure 4.23 shows the contour plots of the normalised vertical component of turbulence intensity, TI_w/V for the single column cases. Similarly, the profile plots are presented in Appendix B.1.6. The results from the figures indicate that the higher values of TI_w/V have occurred in the wake of column. The maximum value of TI_w/V was found to be about 0.3 at $Z/h = 0.26$.

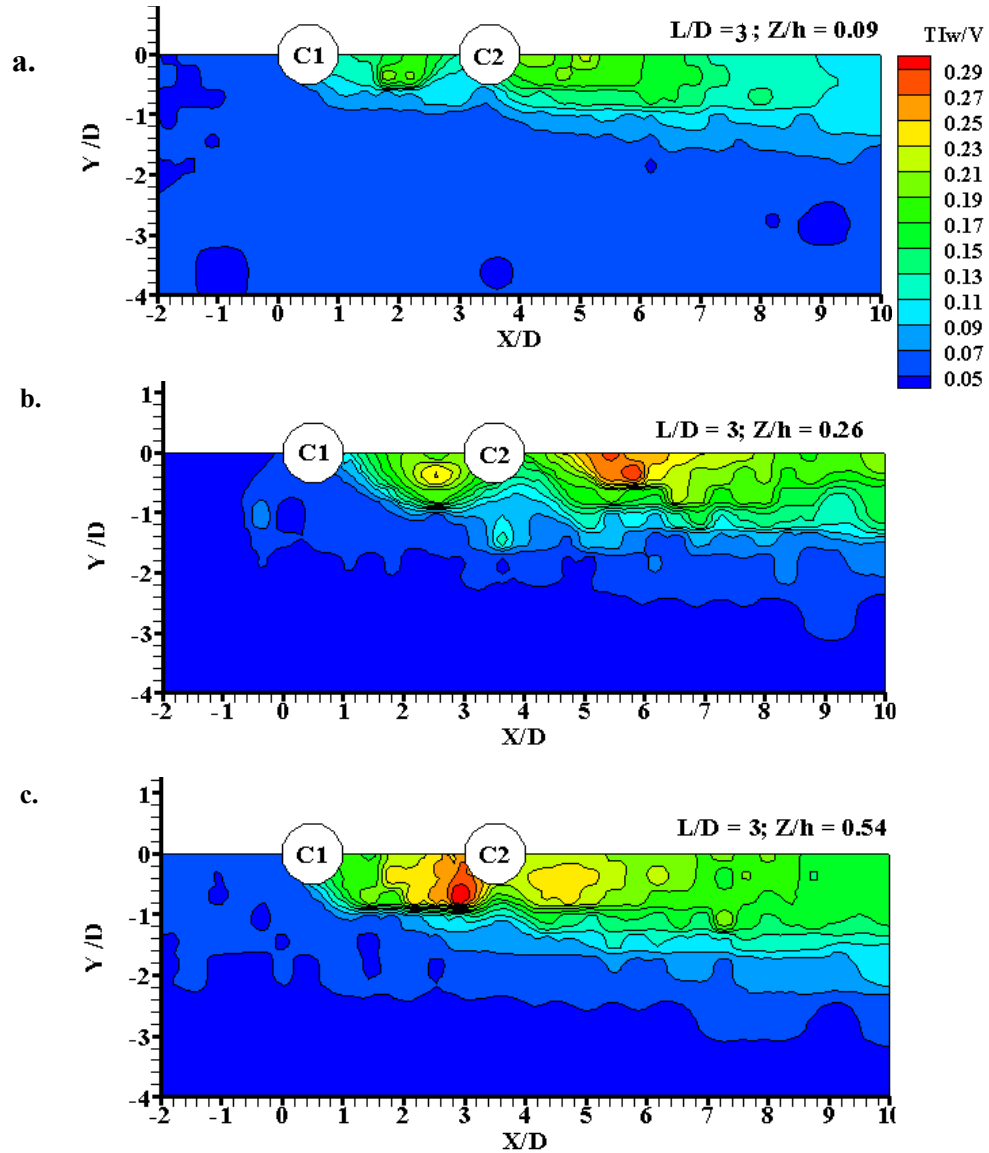


Figure 4.24 Contour plots of vertical turbulence intensity component for the two-column case with $L/D = 3$ in different horizontal planes a) at $Z/h = 0.09$, b) at $Z/h = 0.26$ and c). at $Z/h = 0.54$

For two in-line columns cases, the contour plots and profile plots are presented in Appendices B.1.5 and B.1.6. Contour plots of TI_w/V for $L/D = 3$ in various horizontal planes at $Z/h = 0.09, 0.26$ and 0.54 are shown in Figure 4.24. The figure for $L/D < 2$ shows the maximum value of TI_w/V is about 40% smaller than that in the single column case. The figures reveal that the values of TI_w/V increase as the spacing between two columns increases. For $L/D \leq 2$, higher values of TI_w/V occurred only in the wake of Column 2. When $L/D \geq 3$, both the columns experienced a pocket of higher values of TI_w/V at the mid-depth of flow. Increase in the value of TI_w/V is noticed as the distance from the bed increases. At upper levels, it was observed that the value of TI_w/V in the gap was higher than behind Column 2.

4.3.4 Turbulent Kinetic Energy

The turbulent kinetic energy (TKE) at a point is determined by taking the mean of the turbulence normal stresses as given in Equation 2.14. In this study TKE has been calculated and then normalized by the square of free stream velocity (V^2). The results are presented in contour plots for the single column and the two-column cases with different spacing between columns in three different horizontal planes at $Z/h = 0.09, 0.26$ and 0.54 . Additionally, profiles of TKE/V^2 along three different longitudinal axes at $Y/D = 0, 0.9$ and 1.8 have been generated to study the distribution behavior.

Figure 4.25 shows the contour plots of TKE/V^2 for the single column case, showing high values at the downstream side of the column. Referring to this figure, the distribution of TKE is more or less similar to the distribution of turbulence intensities. The value of turbulent kinetic energy close to the bed was smaller than in the higher level at $Z/h = 0.26$. As the value of Z/h increased further, decrease in the value of TKE/V^2 was noticed. Figures reveals that the greatest values of TKE/V^2 appear at $Z/h > 0.26$ just in the downstream of the column, with values reaching 5 times greater than the values in the upstream side. For two in-line columns cases with $L/D \leq 2$ as shown in the figures of Appendix C.1.1 and Figure 4.26, the maximum value of TKE/V^2 was in the wake of Column 2, with its value similar to the single column case. For $L/D \leq 2$, the results could not be interpreted between two columns due to complication of taking proper measurements. For all the cases, longitudinal profiles, as shown in Appendix C.1.2,

showed that the distribution was similar to the distribution of turbulence intensity component in the transverse direction. Furthermore, the figures show that the turbulent kinetic energy in the wake zone increases as the spacing between columns increases. Likewise in turbulence intensity, the value of turbulent kinetic energy decreases when the distance at the downstream side from the pier face increased. Additionally, the turbulent kinetic energy for the single column case was observed to be higher than that for the two in-line columns cases. This could be due to the influence of Column 2. However, for any values of L/D , the same magnitude of TKE/V^2 was observed in the gap and behind Column 2.

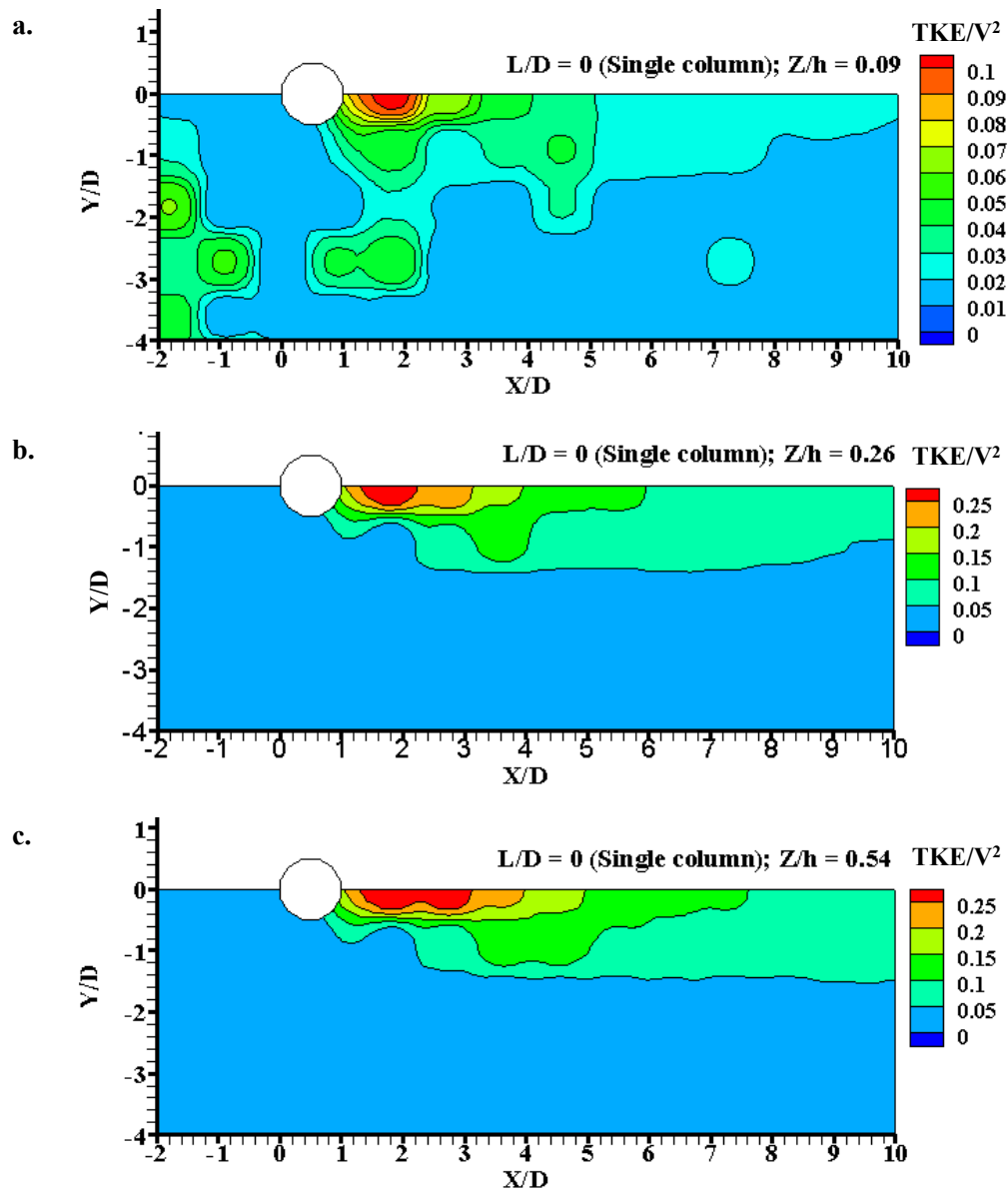


Figure 4.25 Contour plots of turbulent kinetic energy for the single column case in different horizontal planes a) at $Z/h = 0.09$, b) at $Z/h = 0.26$ and c). at $Z/h = 0.54$

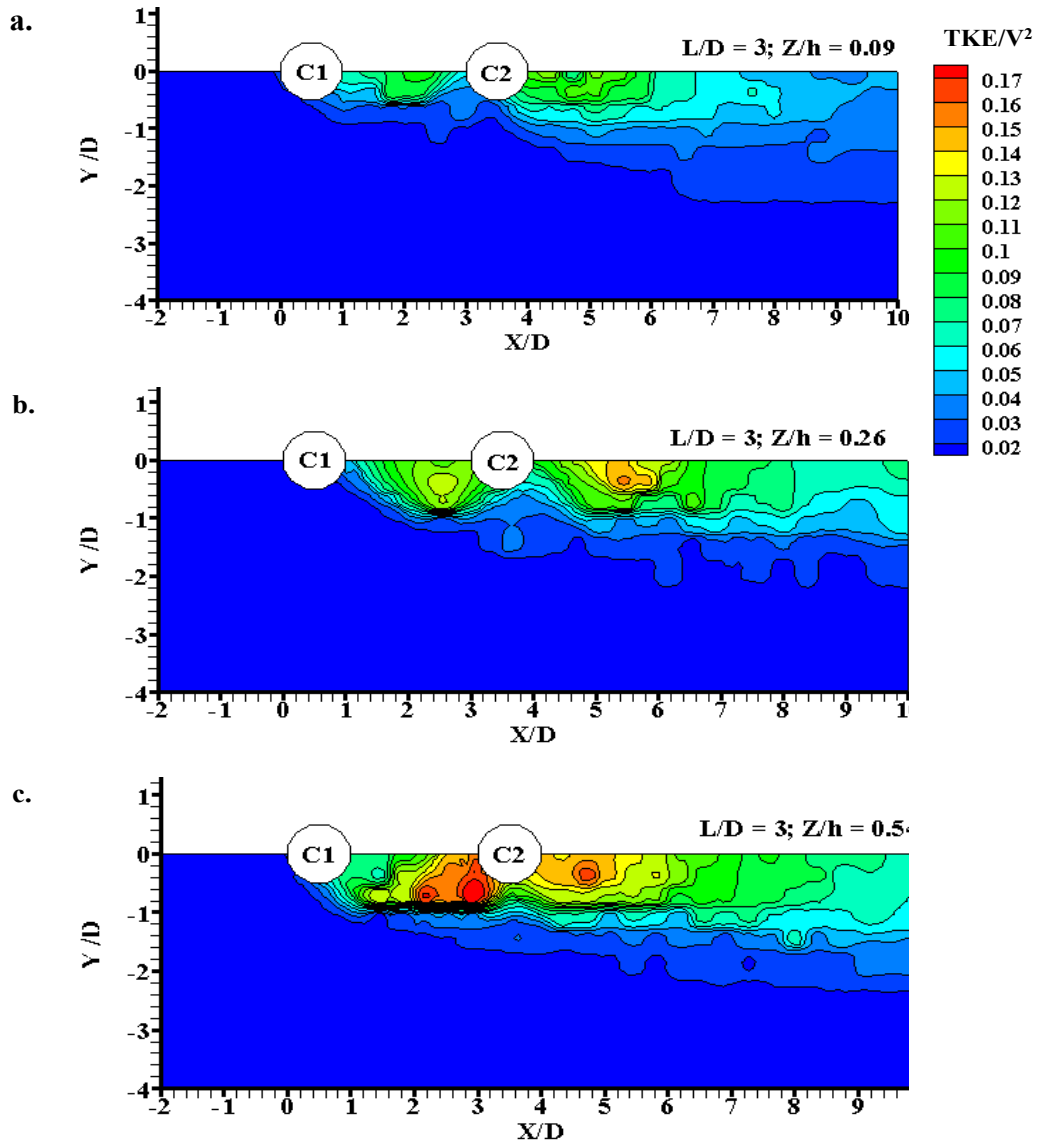


Figure 4.26 Contour plots of turbulent kinetic energy for the two-column case with $L/D = 3$ in different horizontal planes a) at $Z/h = 0.09$, b) at $Z/h = 0.26$ and c). at $Z/h = 0.54$

4.3.5 Reynolds Shear Stresses

Three-dimensional Reynolds shear stresses have been calculated using only the streamwise, transverse and vertical components of velocity fluctuation and are given by $-\rho \overline{u'v'}$, $-\rho \overline{u'w'}$, and $-\rho \overline{v'w'}$. For the presentation of results, the Reynolds stress components have been normalised by ρV^2 , where, ρ represents the mass density of water. The results have been presented in profile plots of $-\overline{u'v'}/V^2$, $-\overline{u'w'}/V^2$ and $-\overline{v'w'}/V^2$ for the single column and the two-column cases along three different horizontal planes at

$Z/h = 0.09, 0.26$ and 0.54 . Reynolds shear stresses have been analyzed along the axis of symmetry i.e. at $Y/D = 0$.

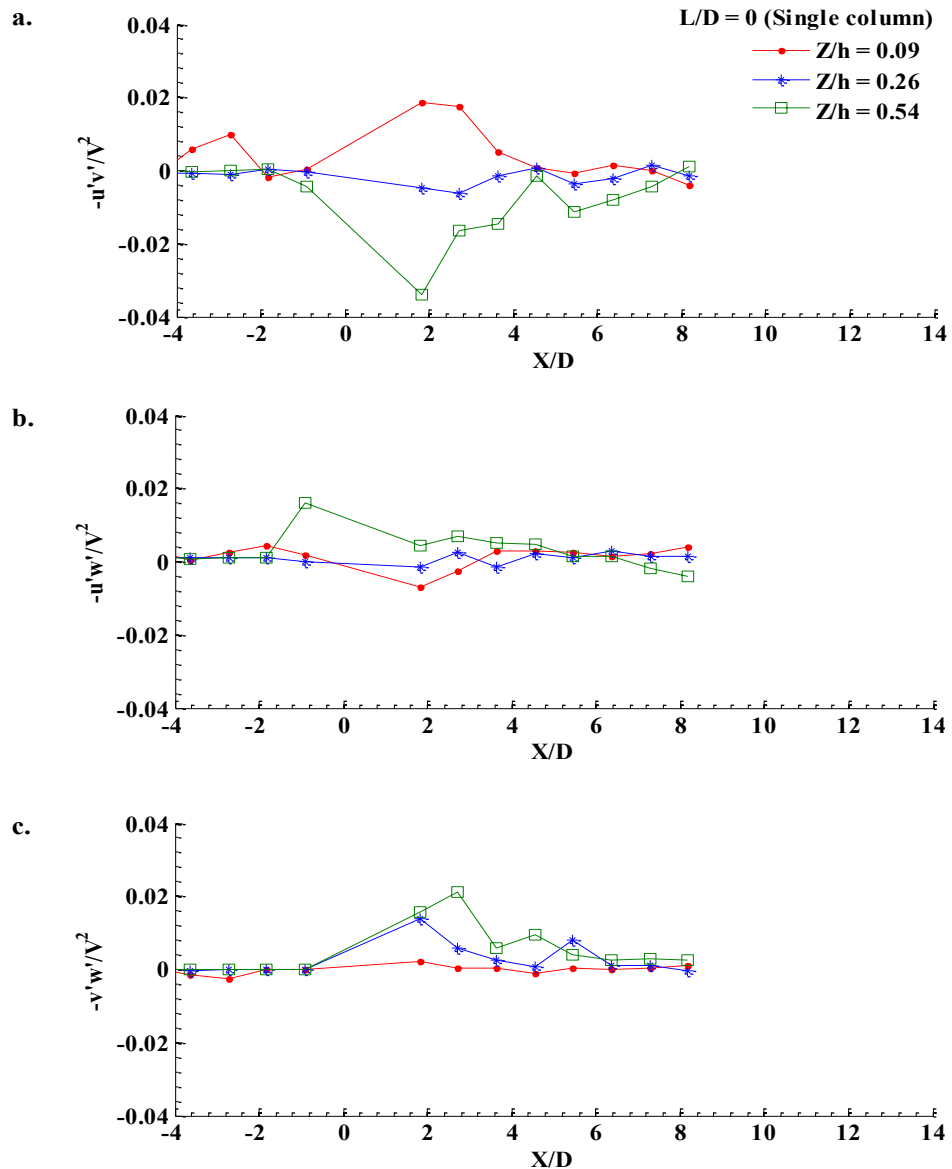


Figure 4.27 Profile plots of Reynold shear stresses for the single column case in different horizontal planes along axis of symmetry a) in $u-v$ plane, b) in $u-w$ plane, and c) in $v-w$ plane

Figure 4.27 shows the distribution of $-\overline{u'v'}/V^2$, $-\overline{u'w'}/V^2$ and $-\overline{v'w'}/V^2$ at different horizontal planes for the single column case. The figures indicate that at the upstream side of the column, the distributions of all the components of Reynolds stresses are similar with their values approximately equal to 0. The maximum positive value of $-\overline{u'v'}/V^2$ was observed close to the bed in the wake of a column. Gradual decrease in the value of

$-\overline{u'v'}/V^2$ was noticed as the distance to the downstream side increases. However, at upper levels ($Z/h = 0.54$), the maximum negative value of $-\overline{u'v'}/V^2$ was observed in the wake. Furthermore the results indicated that the absolute values $-\overline{v'w'}/V^2$ were very small, compared to $-\overline{u'v'}/V^2$ and $-\overline{u'w'}/V^2$.

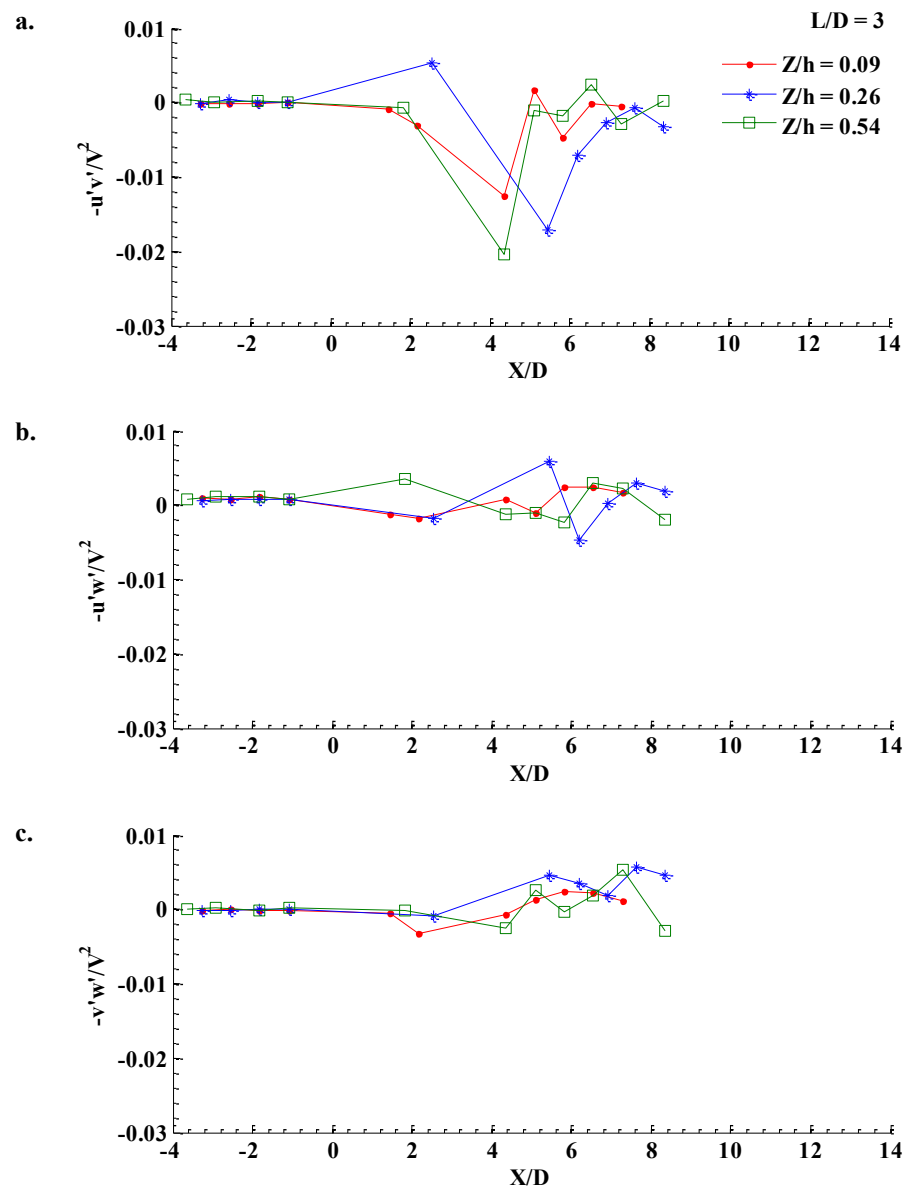


Figure 4.28 Profile plots of Reynolds shear stresses for two-column case with $L/D = 3$ in different horizontal planes along axis of symmetry a) in $u-v$ plane, b) in $u-w$ plane, and c) in $v-w$ plane

For two in-line columns cases, Figure 4.28 shows the distributions of Reynolds stress components for $L/D = 3$. The remaining figures for other values of L/D can be found in

Appendix D.1. Comparing the profile plots for two columns cases, it is noticed that the distribution trends of Reynolds stresses at the upstream side of Column 1 are similar as in the case of a single column. The figures reveal that the absolute values of $-\overline{u'v'}/V^2$ in the wake of two columns are smaller than that in the case of a single column. For $L/D < 3$, the wake of Column 1 experienced a very weak value of $\overline{u'v'}/V^2$. However, in the wake of Column 2, the absolute values of $-\overline{u'v'}/V^2$ were observed increasing with increase in the spacing until $L/D = 3$. Further increase in spacing resulted in a decrease in the absolute value of $-\overline{u'v'}/V^2$ in the wake of Column 2. The reason behind this could be the convergence of shear layer separated from Column 1 in the gap and weak flow velocity approaching the Column 2. Comparing the profile plots for $-\overline{u'w'}/V^2$, indicated that its magnitude close to the bed was approximately the same for all the cases. However, the absolute value of $-\overline{u'w'}/V^2$ was observed increasing at the wake zones as the value of Z/h increases. Distribution of $-\overline{v'w'}/V^2$ shows that its magnitude in the wake of Column 1 is very small. However, in the wake of Column 2, the values of $-\overline{u'w'}/V^2$ and $-\overline{v'w'}/V^2$ were observed to be approximately the same, which was about 50% smaller than that in the single column case. Comparing all figures confirms that Reynolds stress components in the wake of the columns have a non-linear distribution. As suggested by Nakagawa and Nezu (1993), this non-linear distribution of Reynolds stresses is an indication of the oscillatory behaviour of the flow generated by the secondary currents.

4.4 Flow around the Bridge Piers in Vertical Plane

As described in Section 3.4.3, flow structures around bridge piers in different vertical planes were studied using the PIV method. PIV measurements were taken at different vertical planes positioned at $Y/D = 0, 1.25, 2.5, 3.75$ and 5.0 as shown in Figure 4.13. For each plane, the experiments were carried out with a single column as well as two in-line circular columns with $L/D = 1, 2, 2.5, 3, 4, 5,$ and 6 . The instantaneous velocity components u and w were determined by processing and analysing the PIV images.

The results on the flow field and the turbulence characteristics of the flow around bridge piers and the effects of spacing between two in-line columns are presented in contour and profile plots for velocity components (u , and w), velocity fluctuation components (u' , and w'), turbulence intensity components (TI_u and TI_w), turbulence kinetic energy (TKE) and

Reynolds stresses (RS_{uw}). The results have been compared for different combinations including the single column and the two in-line columns with various L/D ratios. For each plane of measurement, the data along different vertical lines perpendicular to the flow direction have been extracted. The positions and the notations of extraction lines are clearly shown in Figure 4.29. At the upstream of Column 1, US1 and US2 represent the positions of the extraction line, which are at the distance of D and $2D$, respectively from the upstream face of Column 1. Similarly, DS1, DS2 and DS4 represent the position of extraction line located at a distance of D , $2D$ and $4D$ respectively from the downstream face of Column 2. In the case of extraction lines between two in-line columns, a typical case of column arrangement of $L/D = 6$ is shown in Figure 4.29 and is represented by B1, B2, B3 and B4 at a distance of D from each other. However, the numbers of extraction lines between two columns depend upon the distance between them. In this chapter, only the figures for the cases $L/D = 0$ and 3 (the single column and two in-line columns with spacing $3D$) along two vertical planes at $Y/D = 0$ and 1.25 are presented and the rest of the figures for other cases are presented in appendices. The following subsections give the detailed results and discussions on the flow structures around bridge piers in different vertical planes.

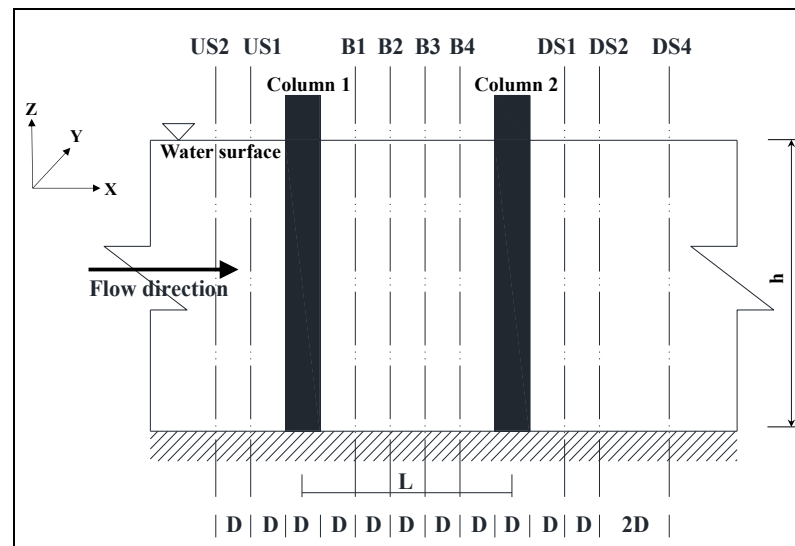


Figure 4.29 Schematic diagram of different axis of data analysis at upstream and downstream side of the columns in vertical planes (US, B and DS stand for upstream side, between and downstream side of the columns, respectively)

4.4.1 Flow Pattern

The flow patterns around the bridge piers at a vertical plane are clearly represented by vector diagrams and the streamline diagrams shown in Figures 4.30 – 4.33. In the vector diagrams as shown in Figures 4.30 and 4.31, the magnitude of the velocity vector is given by $\sqrt{u^2 + w^2}$ where u is the velocity component in the direction of flow and w is the velocity component in the vertical direction. Additionally, the direction is clearly represented by the inclination of the vectors. Figures 4.30 a, and b represent the velocity vector diagram for the single column case at two different vertical planes $Y/D = 0$ and 1.25 respectively. For the condition of no piers, it is observed that there is not any deflection in velocity vectors and the magnitude of the vectors is uniform throughout the flow field. It is clear from the figures that, when a column is added to the system, flow started to separate from its original direction. Considering the plane at $Y/D = 0$, as the flow approaches the bridge pier, there is a generation of downward flow due to the pressure gradient induced at the upstream face of the bridge pier. This downward flow forms a clockwise vortex at the base of the bridge pier. The similar flow pattern has been observed and reported in the previous literatures by Melville and Raudkivi (1977b); Dargahi (1989); Sumer et al. (1997); Ahmed and Rajaratnam (1998); Richardson and Panchang (1998) and Graf and Istiarto (2002). At the immediate downstream side, reversal as well as upward flow are observed, which can be clearly seen in vector and streamline diagrams. This result is in good agreement with the experimental results of Sahin et al. (2007) and Ataie-Ashtiani and Aslani-Kordkandi (2013). The flow at the wake of the pier is observed to be in a random direction, which gives a good indication of the complexity of the flow structure. Furthermore, it is observed that the flow is separated at around $2D$ on the downstream side measured from the downstream face of the column. At this separated region, the intensity of up flow is observed to be a maximum.

Figures 4.31a, and b represent the vector diagrams for the two in-line columns case of $L/D = 3$. For other values of L/D , figures were presented in Appendix A.2.1. For the case of $L/D = 1$, there is not any space between the columns. Hence, the wake is formed only behind the column 2. For $L/D = 2$, existence of wake is not noticed behind column 1. However, most of the velocity vectors between the two columns represent the existence

of reverse and upward flow. As the spacing increases to $L/D = 3$, flow separation was observed at a distance of around $1.5D$ from the downstream face of Column 1. Ataie-Ashtiani and Aslani-Kordkandi (2013) reported upward flow everywhere in the gap for $L/D = 3$ except near the bed just in front of the downstream column. Additionally, rotation of the flow was clearly observed at the immediate downstream side of column 1. On analysing the vector and streamline diagrams for $L/D = 4, 5$ and 6 , a similar flow pattern was observed. Considering the vector diagrams, it is evident that the flow between two columns is separated at a distance of $2.5D$ measured from the downstream face of Column 1 and the rotation of the flow exists. Comparing the vector diagrams in all the cases, it is evident that recirculation of the flow exists behind Column 2. The anticlockwise recirculation of the flow starting from near the bed level close to the column diminishes towards the downstream at the middle layer of the depth of flow. For all sets of combination, the flow patterns at the upstream side of the bridge piers are found to be almost similar, while at the downstream side of the pier, the flow pattern is different in various conditions. Comparing the flow behind the single column and two in-line columns, it is observed that wake behind the single column is larger than that of the two columns cases.

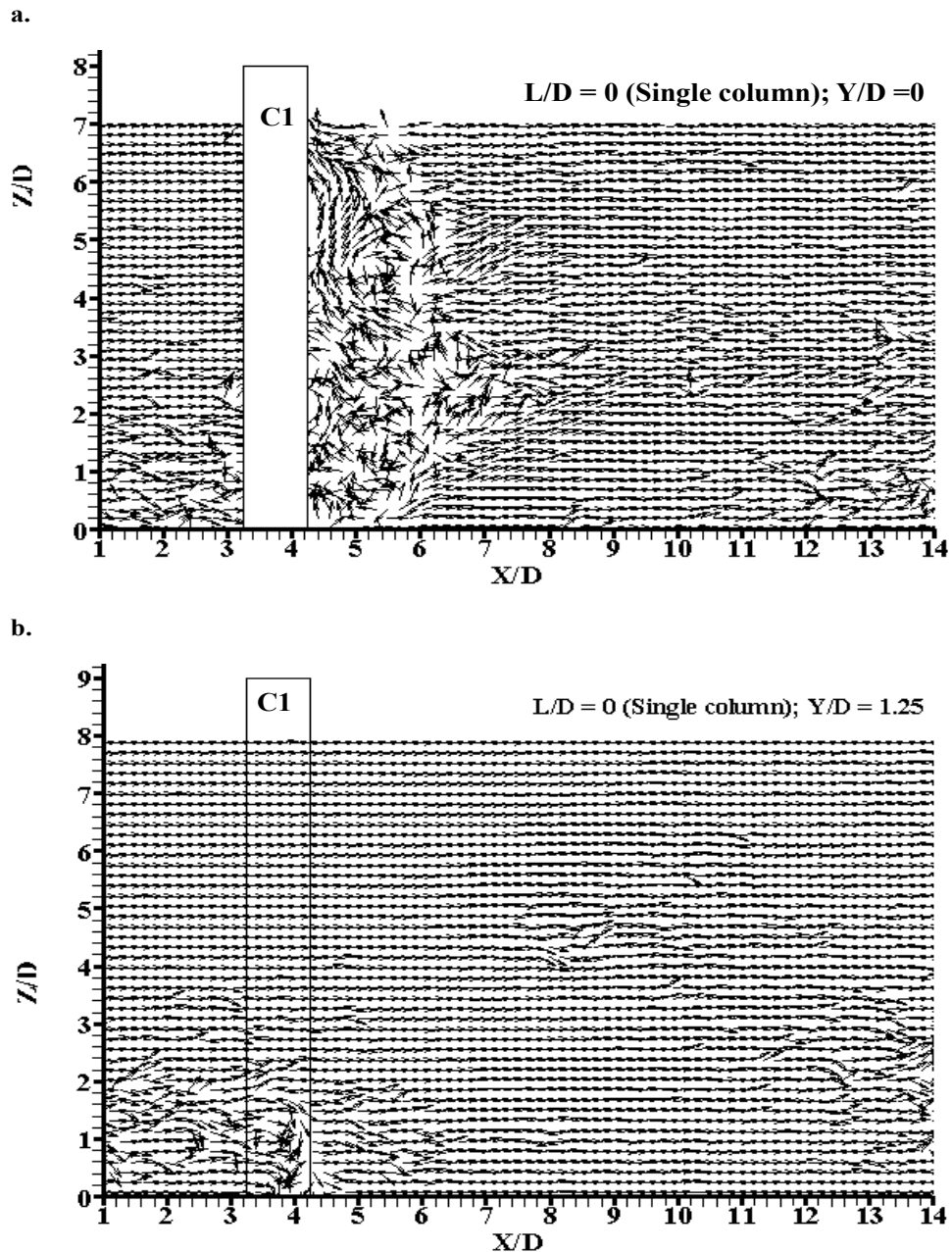


Figure 4.30 Vector plots for single column a) vertical plane at $Y/D = 0$, and b) vertical plane at $Y/D = 1.25$

For all the cases of $Y/D = 1.25$, the vector diagrams and the streamline diagrams exhibit very small deflection and separation of flow in the vertical plane. The effect of columns diminishes as the value of Y/D increases. The flow patterns around the bridge piers were more clearly presented in the streamline diagrams as shown in Figures 4.32 and 4.33 and Appendix A.2.2.

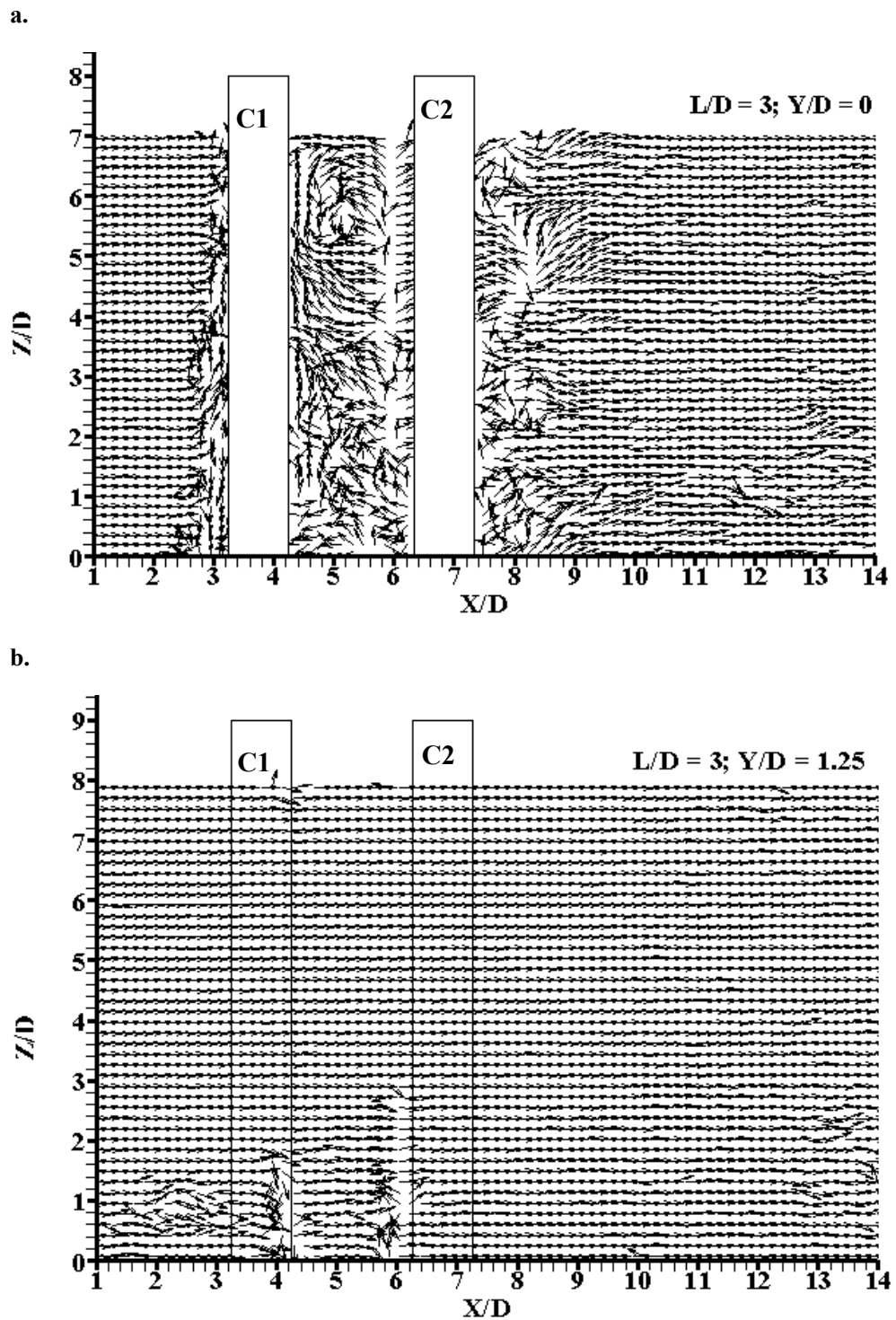


Figure 4.31 Vector plots for two columns cases with $L/D = 3$ a) vertical plane at $Y/D = 0$, and b) vertical plane at $Y/D = 1.25$

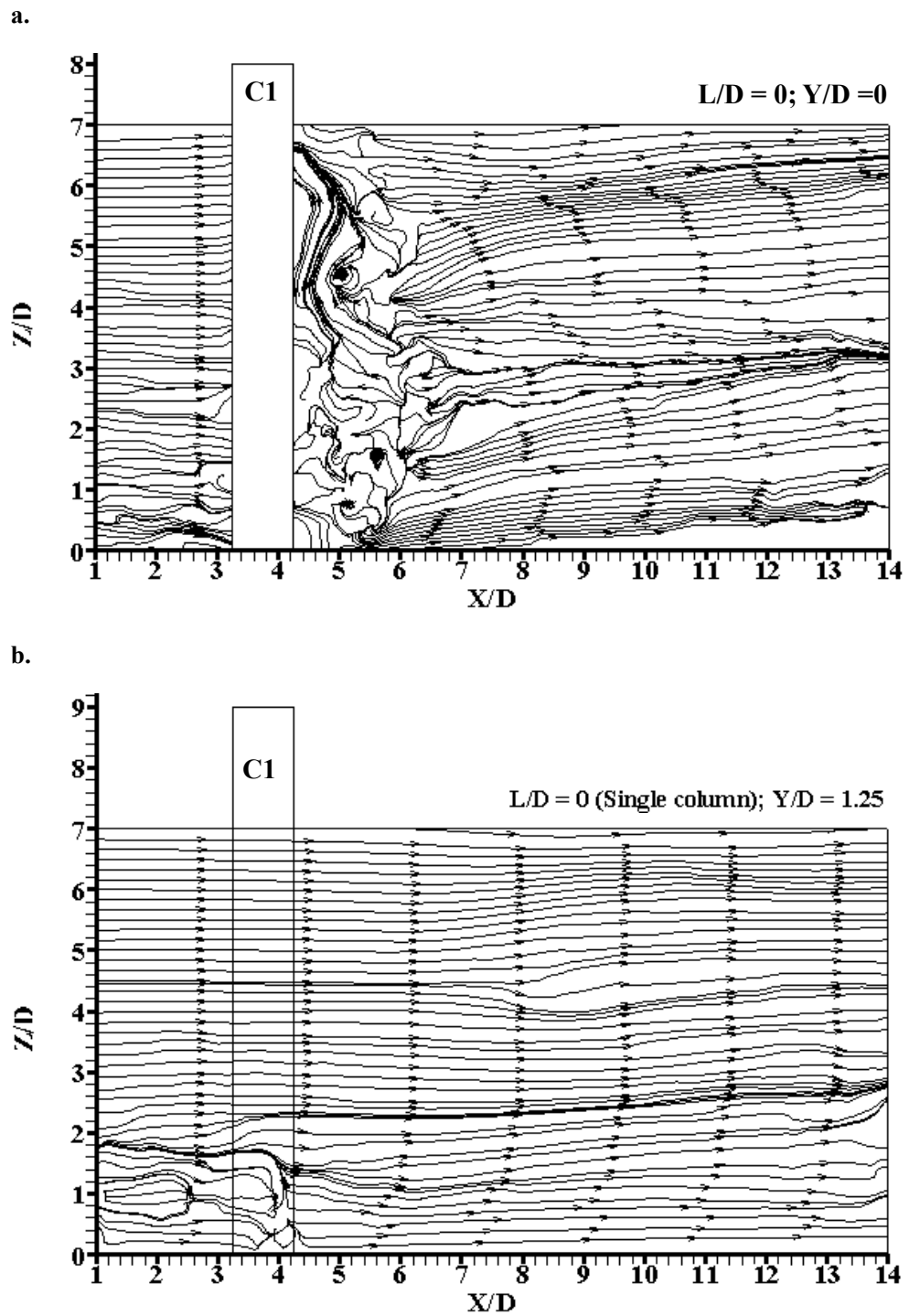


Figure 4.32 Streamline plots for single column a) vertical plane at $Y/D = 0$, and b) vertical plane at $Y/D = 1.25$

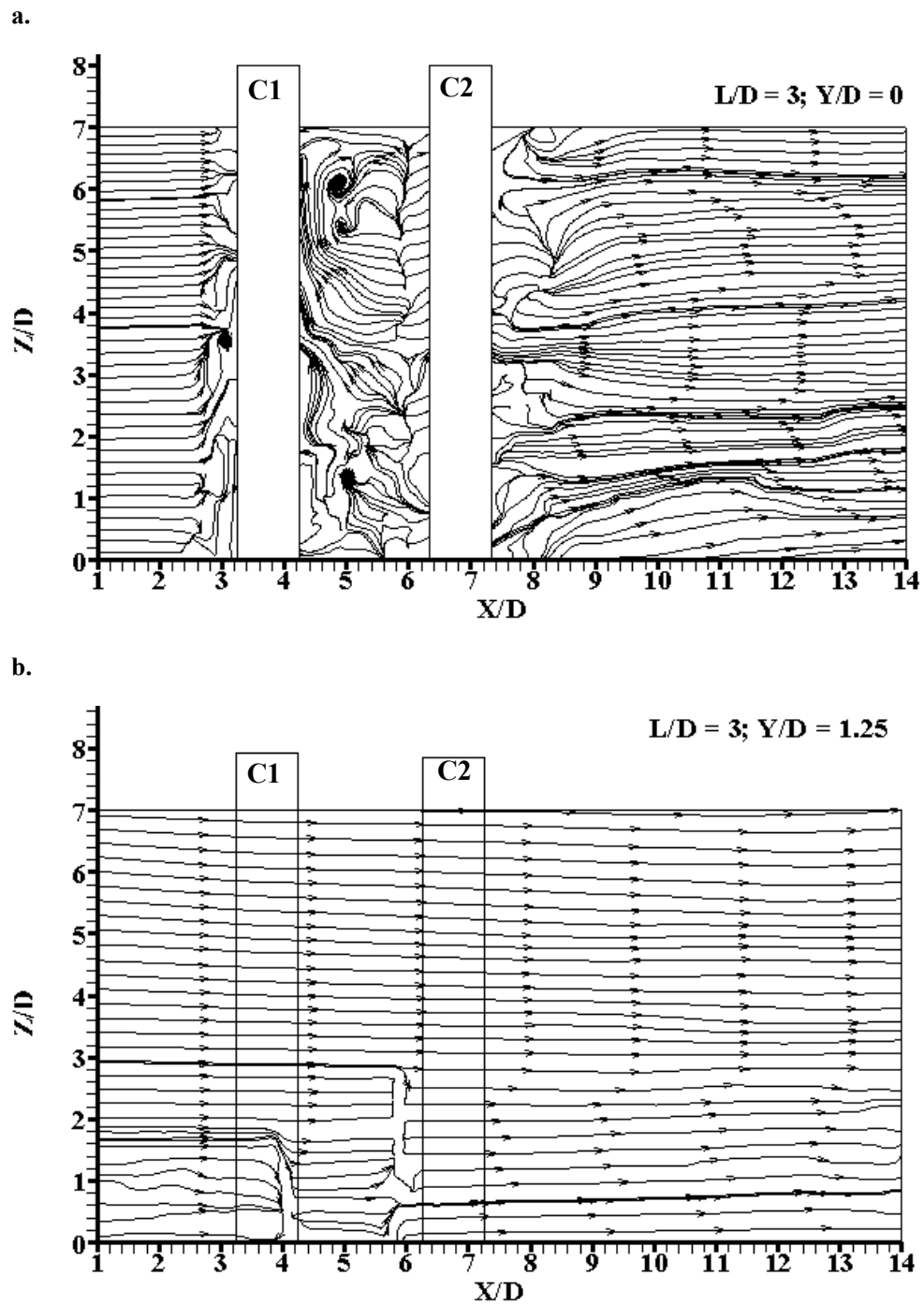


Figure 4.33 Streamline plots for two columns cases with $L/D = 3$ a) vertical plane at $Y/D = 0$, and b) vertical plane at $Y/D = 1.25$

4.4.2 Time Average Velocity Components

Figures 4.34 to 4.41 show the contour plots and profile plots of velocity components in the vertical plane, in which the streamwise velocity component (u) and the vertical

velocity component (w) are normalised by the free stream flow velocity, (V). These figures give a clear picture of the distribution of velocity components in vertical planes.

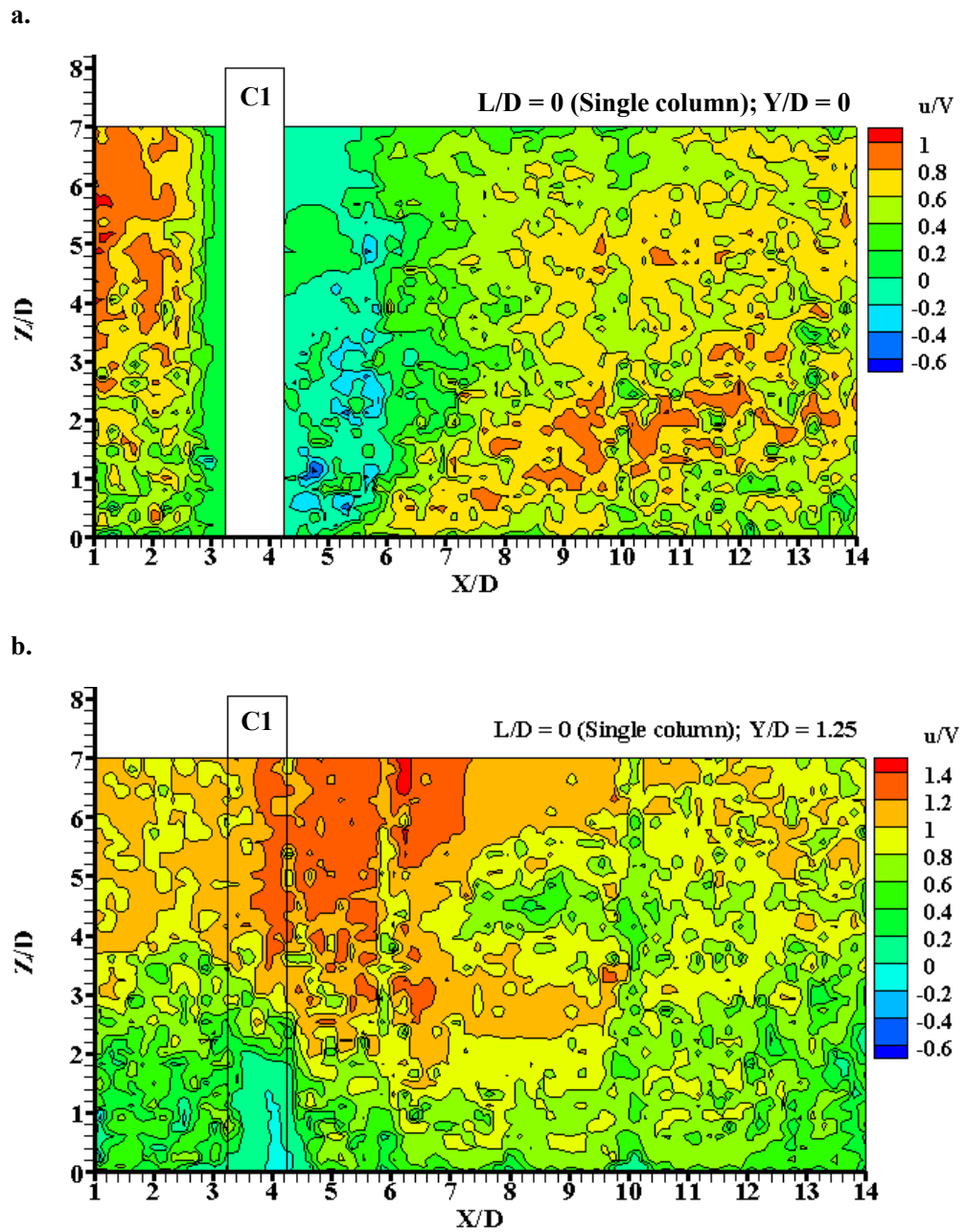


Figure 4.34 Contour plots of streamwise velocity component for the single column case in different vertical planes a) at $Y/D = 0$, and b) at $Y/D = 1.25$

For the case of a single column in the plane at $Y/D = 0$, the contour of u/V is shown in Figure 4.34a and distribution of u/V at different points of the vertical plane are shown in Figure 4.35. It is clear from the contour diagram that the value of u/V at the upstream

side of the column is approximately equal to 1 at a distance $X/D \geq 1.25$ measured from the upstream face of the column. As the flow approaches the column, the value of u/V becomes smaller and finally reduces to zero at the face of the column. Figure 4.35a shows that at the upstream side of the column, the values of u/V are decreasing gradually towards the bed. It was also noticed that u/V for US1 was less than that for US2. This demonstrates that the u/V diminished gradually as the column was approached. At the downstream side of the column, it is clear from the contour plot that the value of u/V ranged from -0.6 to 0 at the wake close to the downstream face of the column. The profile plot in Figure 4.35b for the downstream side of the column shows that the value of $u/V \leq 0$ at DS1. The negative value of u/V indicates the presence of the reverse flow in this region (see Figure 4.34a). The figures exhibit that the value of u/V increases as the flow moves further downstream and ultimately comes to the normal flow condition. The contour plot of u/V at the plane $Y/D = 1.25$ is shown in Figure 4.34b. This figure shows that the maximum value of u/V occurs at the side of the column, which is approximately equal to 1.2.

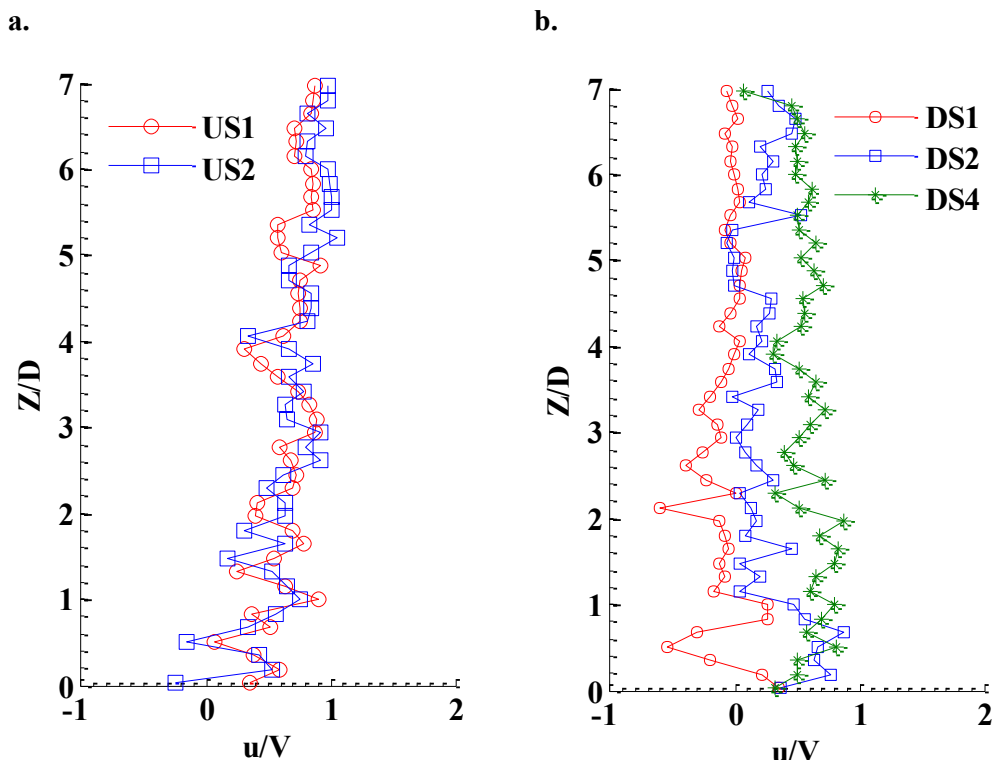


Figure 4.35 Profile plots of streamwise velocity component for the single column case in vertical plane at axis of symmetry a) upstream side; b) downstream side

For the case of two in-line columns, contour plots of u/V for $L/D = 3$ at $Y/D = 0$ and 1.25 are shown in Figure 4.36. For the rest of the columns arrangements, contour plots are presented in Appendix A.2.3. Similarly, Figures 4.37 and 4.38a show the velocity profiles of u/V at different positions of the upstream and downstream sides of the columns for $L/D = 3$. Figures in Appendix A.2.5 show the profiles for other arrangements of two columns. According to the contour plots and the profile plots at the upstream side of Column 1, the distribution of u/V are almost the same for all the column arrangements. The value of u/V remains 1 when the flow reaches about $1D$ distance, measured from the upstream face of the Column 1; u/V then decreases gradually as the flow moves towards the column. This type of distribution was also observed in the single column case. However, for the downstream side of Column 2 and between the two columns, the distribution of u/V varied with respect to the spacing between the two columns. When $L/D = 1$, at the downstream side of Column 2 very close to the column, the minimum u/V was approximately equal to -0.2, quite similar to the value obtained for the single column case. A gradual increase in the value of u/V was noticed with increase in the distance from the downstream face of column 2. This condition applied to all of the arrangements of two in-line columns. For the spacing $L/D \geq 2$, it was observed that the value of $u/V < 0.5$ was reached within the zone of around $2D$, measured from the downstream face of Column 2.

Considering the flow between two in-line columns, the contour plots and the profile plots, presented in Appendices A.2.3 and A.2.5 indicate that the value of u/V for the case of $L/D = 2$ varies between -0.5 and 0. The negative value of u/V indicates the reverse flow within the region. Velocity vector diagrams give the evidence of this type of reverse flow. As the spacing between the two columns increased, the value of the streamwise component of the flow velocity approaching Column 2 was observed positive. For $L/D > 3$, the maximum value of the streamwise component of approach flow for Column 2 was $u/V = 0.4$. Ataie-Ashtiani and Aslani-Kordkandi (2013) reported that for the case of $L/D = 3$, the velocity of flow approaching the downstream column was equal to 0.2-0.3 times the free stream flow velocity, V , which is consistent with the present study results. On the other hand, the contour plots of the plane at $Y/D = 1.25$ show that all the arrangements of columns experience the maximum value of $u/V = 1.2$ at the side of the columns. In this plane, for $L/D \leq 3$, the maximum value of u/V was at the side of both

columns including the gap between the two columns. However, for $L/D \geq 4$, the value of u/V decreased to approximately equal to 1 as the flow approached the Column 2.

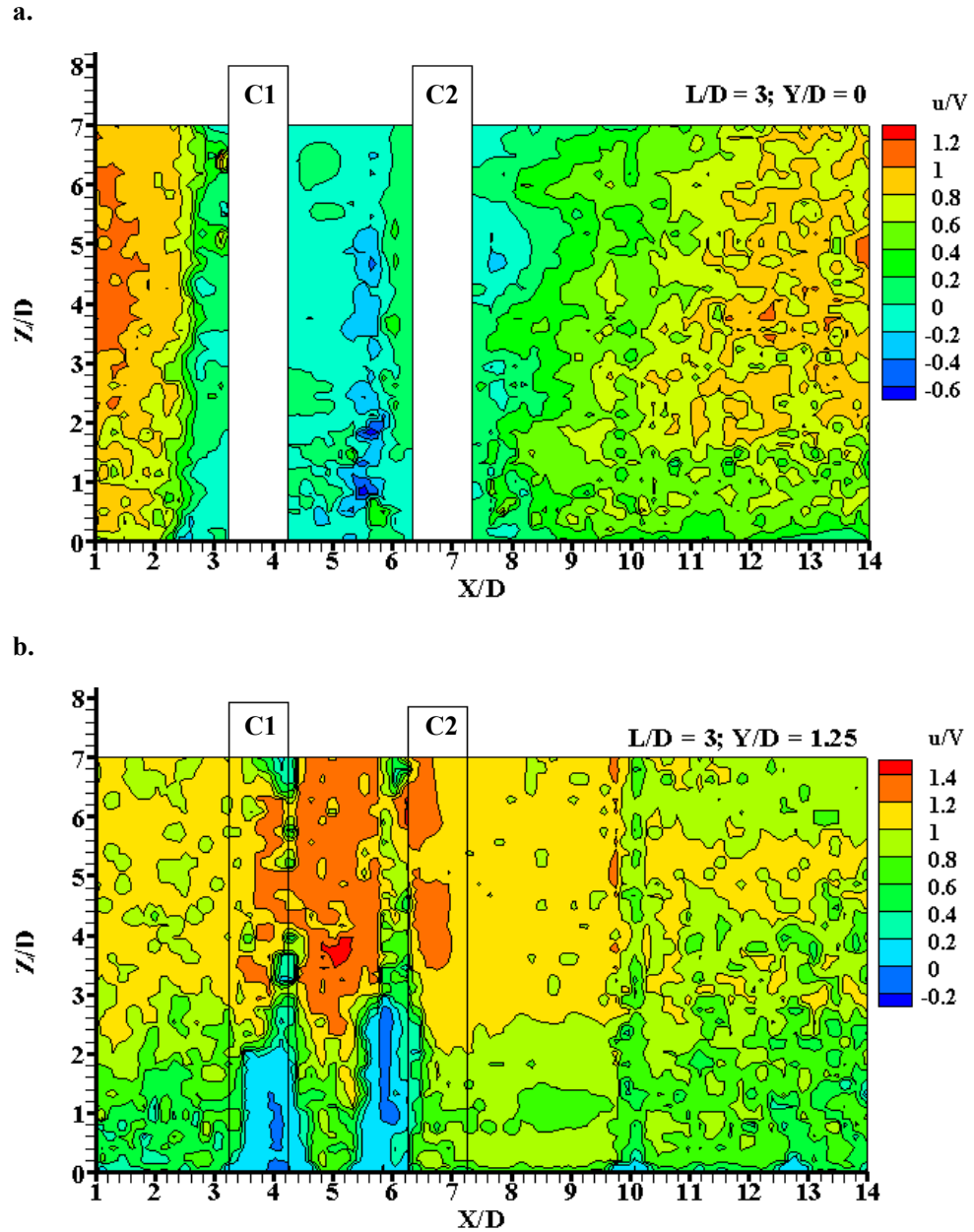


Figure 4.36 Contour plots of streamwise velocity component for the case of two in-line columns with $L/D = 3$ in different vertical planes a) at $Y/D = 0$, and b) at $Y/D = 1.25$

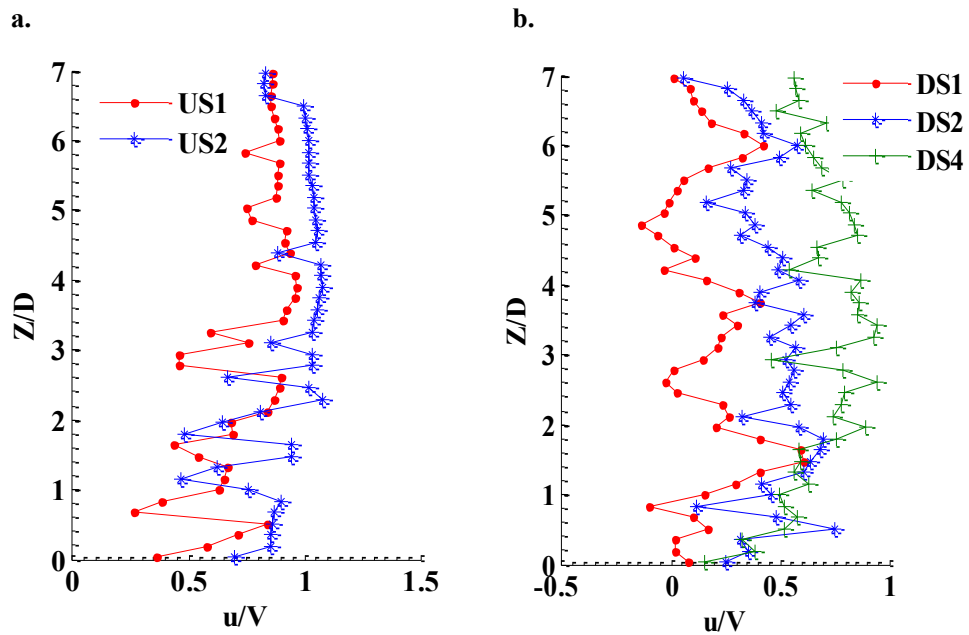


Figure 4.37 Profile plots of streamwise velocity component for two columns case with $L/D = 3$ in vertical plane at axis of symmetry a) upstream side; b) downstream side

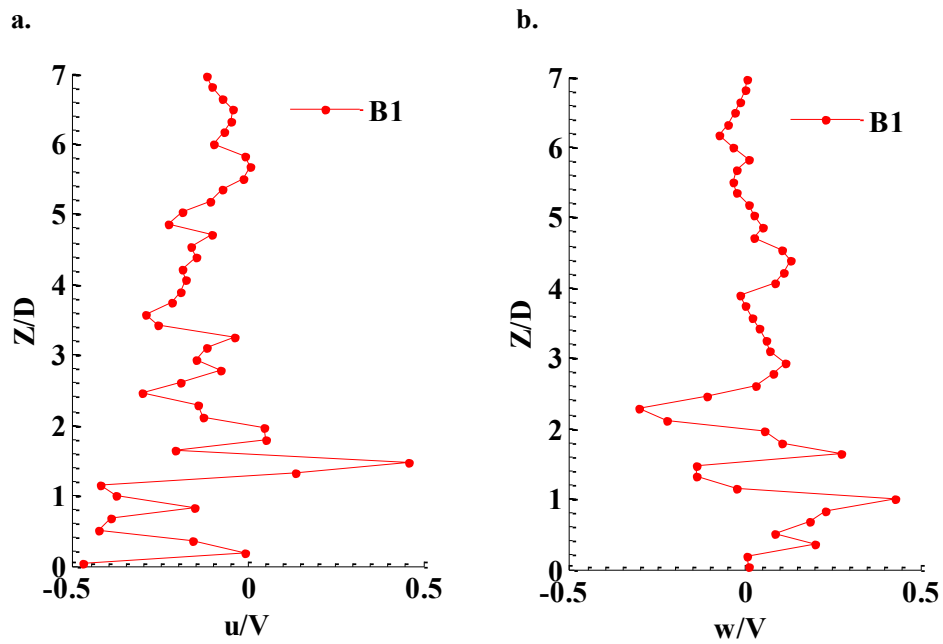


Figure 4.38 Profile plots of velocity components between two columns with $L/D = 3$ in vertical plane at axis of symmetry a) streamwise component, b) vertical component

The contour plots for the vertical velocity components (w/V) for the single column in the plane at $Y/D = 0$ and 1.25 are presented in Figure 4.39 and the distribution profile of w/V

at different positions of the upstream and downstream sides of the column are presented in Figure 4.40. At the upstream side of the column, the range of vertical velocity component (w/V) was from -0.3 to 0.2. The negative value represents the down flow. The maximum value of this down flow was observed at the upstream side. It is in good agreement with the experimental values observed by Ahmed (1995). As this down flow interacts with the boundary layer, a horseshoe vortex was formed at the base just upstream of a column. As per Dargahi (1989), this is the primary horseshoe vortex. This horseshoe vortex system interacts with the bed resulting in the more turbulence near the bed. Distribution of w/V at US1 and US2 of the upstream side of the column is shown in Figure 4.37a. It indicates the generation of high turbulence near the bed, which is evident from more fluctuation of w/V . At the downstream side of the column, the upward flow region extending towards the free surface was observed. The maximum value of w/V was found to be approximately equal to 0.5 at a distance of about $1.5D$ measured from the downstream face of the column. Furthermore, it is clear from the figure that the maximum and minimum value of w/V occurred close to the bed within the wake. Distribution of w/V in different positions DS1, DS2 and DS4 at the downstream side of the column as shown in Figure 4.37b shows that the vertical velocity component was heavily fluctuate near the bed. Significant fluctuation of w/V was observed up to the distance of $4D$ measured from the downstream face of a column.

Figure 4.34b shows the contour plot of w/D in the $Y/D = 1.25$ plane. It shows that down flow of magnitude 0.2 was observed just upstream from a column and at the side of the column. The vector diagram in Figure 4.30b and the streamline diagram in Figure 4.31b give a clear picture of down flow in this region. At the downstream side of this plane, no significant down flow or up flow was noticed. In the case of the bridge piers with two in-line columns, Figure 4.41 and Appendix A.2.4 show the contour plot of w/V at the planes $Y/D = 0$ and 1.25 . In these figures for $L/D > 3$, at the immediate upstream side of Column 1, poor quality of distribution of w/V is observed, which could be due to the reflection during the imaging process. However, at a distance of about $1D$ measured from the upstream face of Column 1, the flow is observed as expected. Hence, considering the flow in this region, at the upstream side of Column 1, the down flow is observed in all the cases of two in-line columns arrangements. The maximum value of down flow with

w/V was approximately equal to 0.2 observed close to the bed near the column base. This is also clearly presented in Figure 4.41a. Furthermore, the distribution of w/V at US2, shown in Figure 4.42a, indicates no down flow throughout the flow depth. In the plane $Y/D = 1.25$ as shown in Figure 4.41, down flow with w/V is approximately equal to 0.1, observed at the upstream and at the side of Column 1. Similar flow is observed at the upstream side of Column 1 for all the values of L/D .

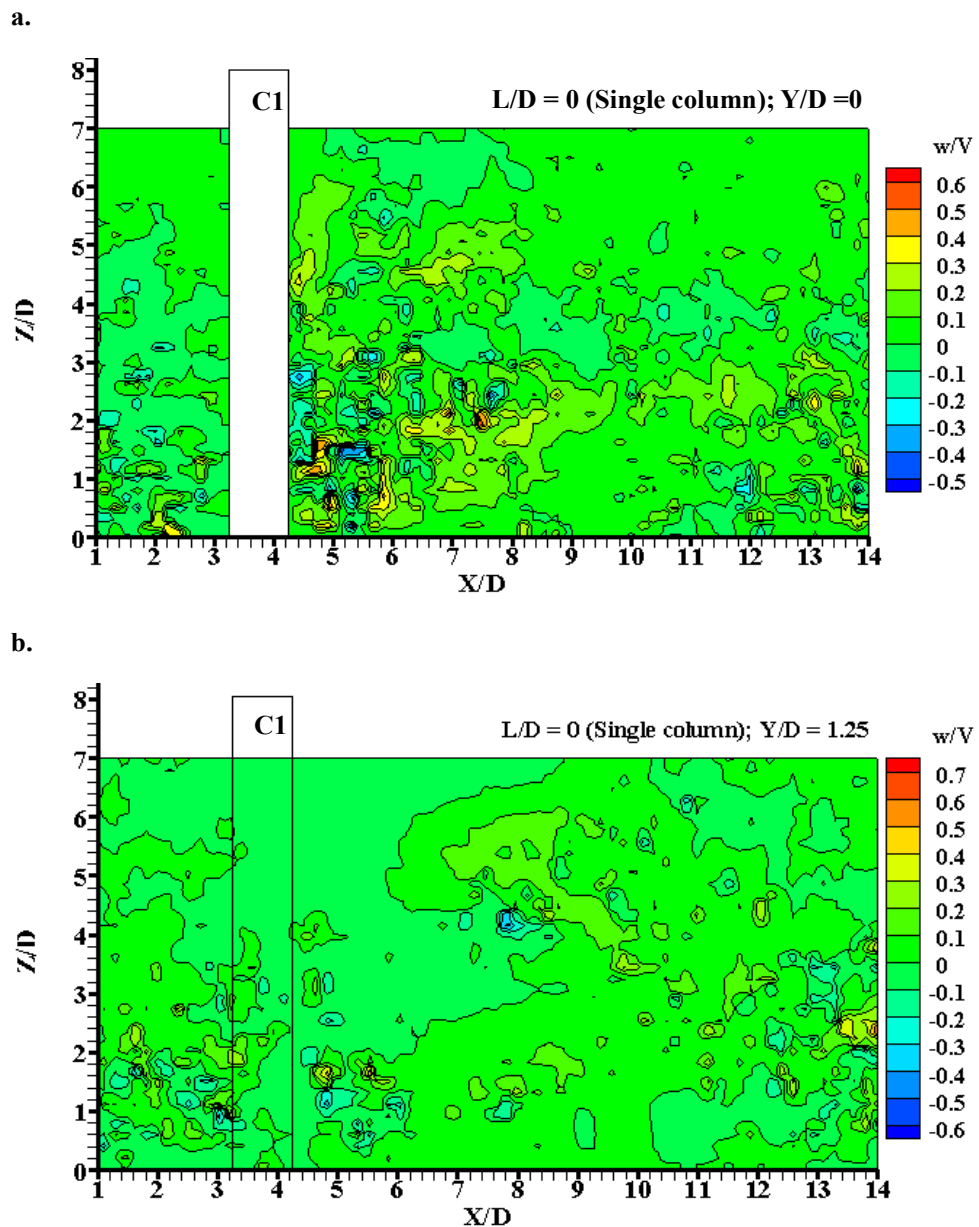


Figure 4.39 Contour plots of vertical velocity component for single column case in different vertical planes a) at $Y/D = 0$, and b) at $Y/D = 1.25$

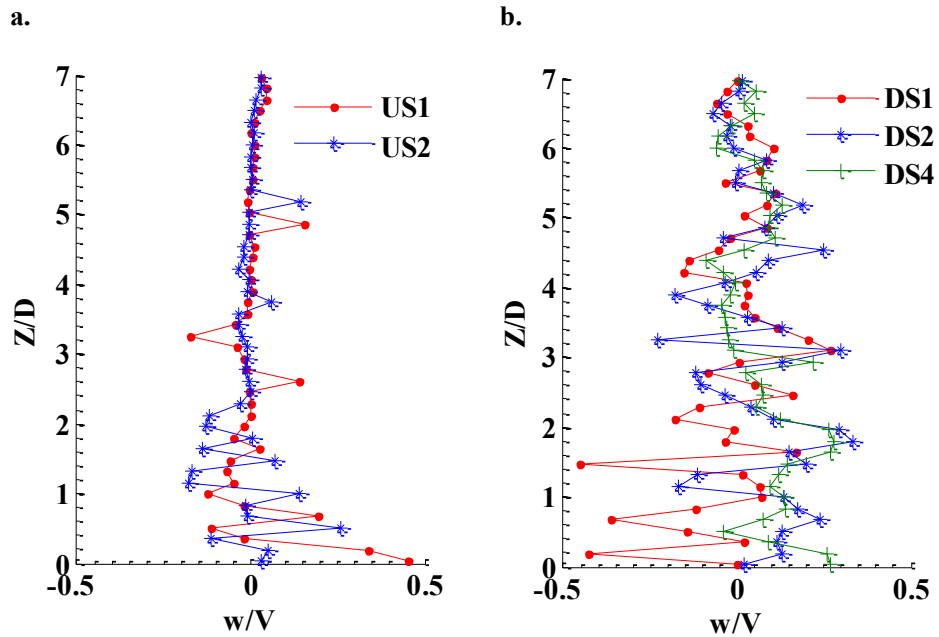


Figure 4.40 Profile plots of vertical velocity component for single column case in vertical plane at axis of symmetry a) upstream side; b) downstream side

Considering the flow between two in-line columns, for $L/D = 2$, the gap experiences positive values of w/V ranging from 0.1 to 0.3. This shows the existence of up flow throughout the gap. Since no down flow is noticed at the upstream side of Column 2, the horseshoe vortex in this region is not formed. According to Sumer and Fredsoe (2002), for small spacing the horseshoe vortex in front of Column 2 is destroyed. For $L/D = 3$, stronger up flow is noticed than that of $L/D = 2$. However, the horseshoe vortex at the base of Column 2 is not noticed. For $L/D \geq 4$, the maximum value of w/V is approximately equal to 0.5, which is observed about $2D$ downstream measured from the face of Column 1. As the flow approaches Column 2, intensity of upward flow decreases and eventually down flow is noticed. The horseshoe vortex in front of Column 2 is expected to form near the base of the Column 2. However, the size of the horseshoe vortex is smaller than that of Column 1. Sumer and Fredsoe (2002) reported that the horseshoe vortex for Column 2 existed only when $L/D > 4$ and the size of the horseshoe vortex is smaller than that of the single column case due to the shielding effect of Column 1. For $L/D = 3$, Ataie-Ashtiani and Aslani-Kordkandi (2013) observed a small rotation near the bed just in front of the downstream column. They further reported that such flow structure could not be a

horseshoe vortex because of the suppression of down flow due to the formation of the reattachment regime.

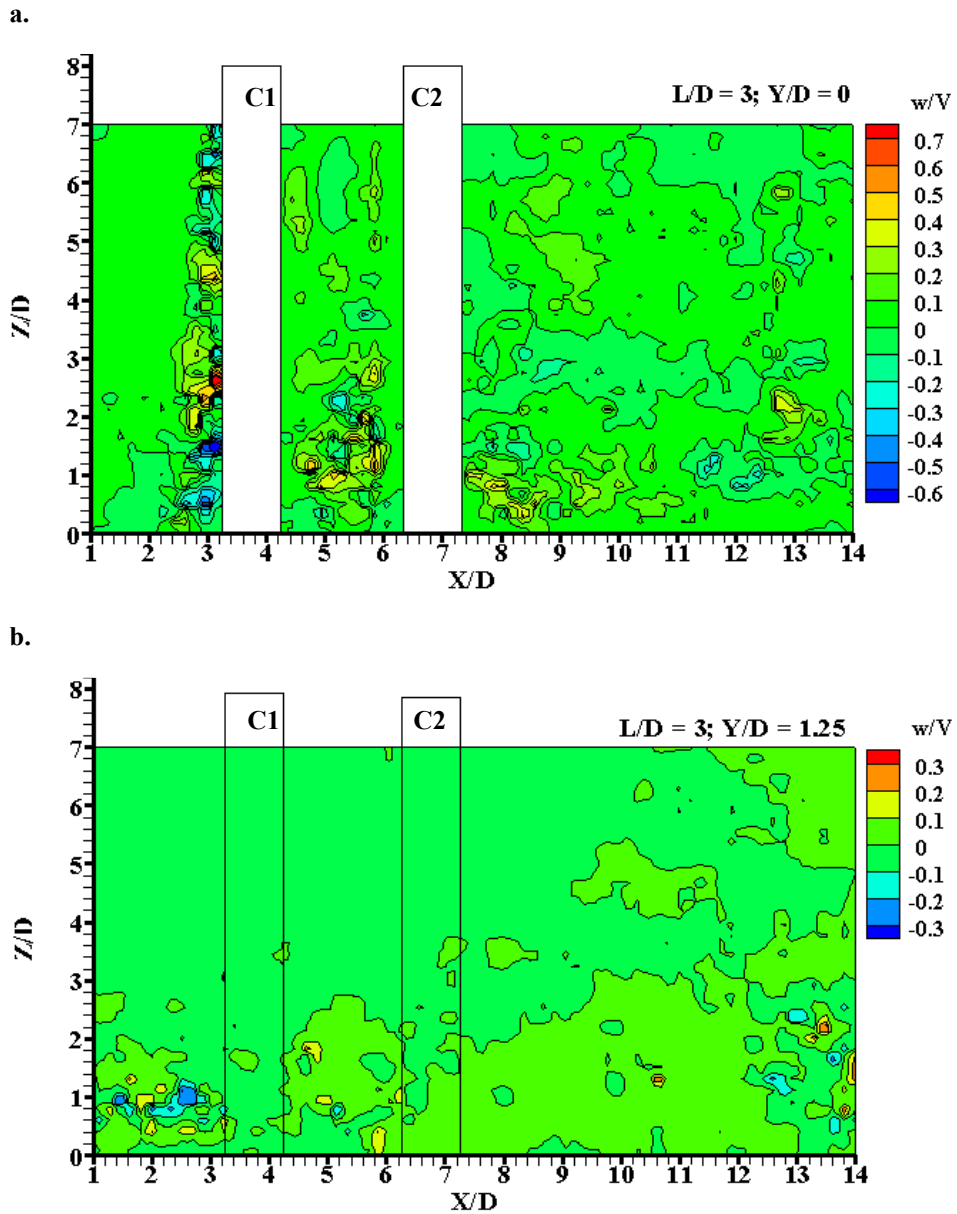


Figure 4.41 Contour plots of vertical velocity component for the two-column case with $L/D = 3$ in different vertical planes a) at $Y/D = 0$, and b) at $Y/D = 1.25$

At the downstream side of Column 2, for all columns arrangements, upward flow exists with the maximum value of $w/V = 0.2$, which is about 50% smaller than that of the single column case and about 30% smaller than the case of Column 1 in the two-column case.

This is due to the sheltering effect of Column 1. According to the contour plots and vector plots, one can easily see that the flow structures at the wake of Column 2 are totally different from the single column case. For $L/D \leq 4$, a small zone of recirculation was observed close to the free surface. Similar results were observed by Ataie-Ashtiani and Aslani-Kordkandi (2013) for $L/D = 3$. According to the profile plots, the distributions of w/V at DS1, DS2, and DS4 for $L/D \leq 4$ were observed to be similar. However, for $L/D > 4$ the distribution of w/V at DS1 was observed with a significant negative value close to the bed. Distribution of w/V at DS2 and DS4 were observed to be similar in all the cases of two column arrangements.

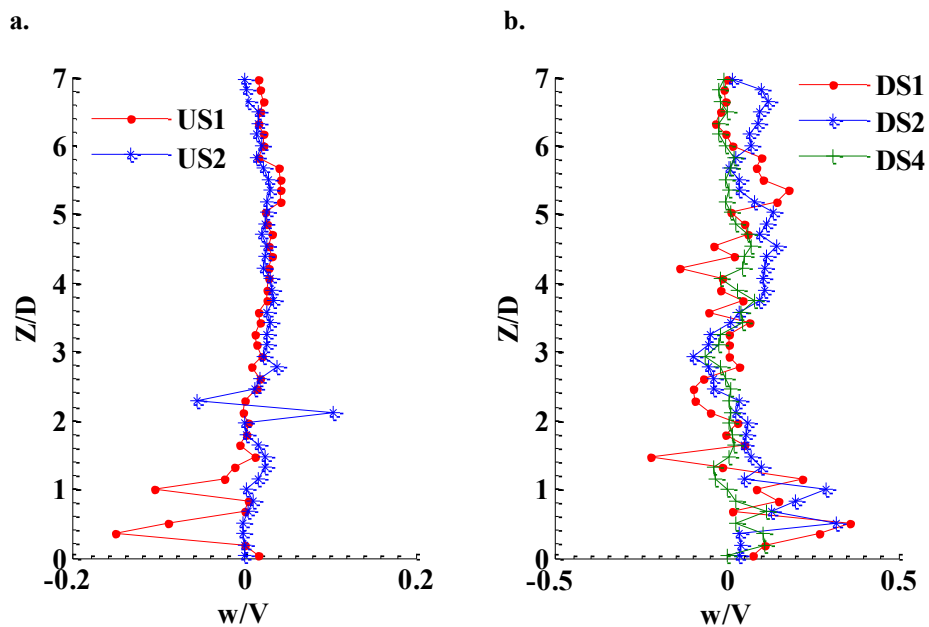


Figure 4.42 Profile plots of vertical velocity component for the two-column case with $L/D = 3$ in vertical plane at axis of symmetry a) upstream side; b) downstream side

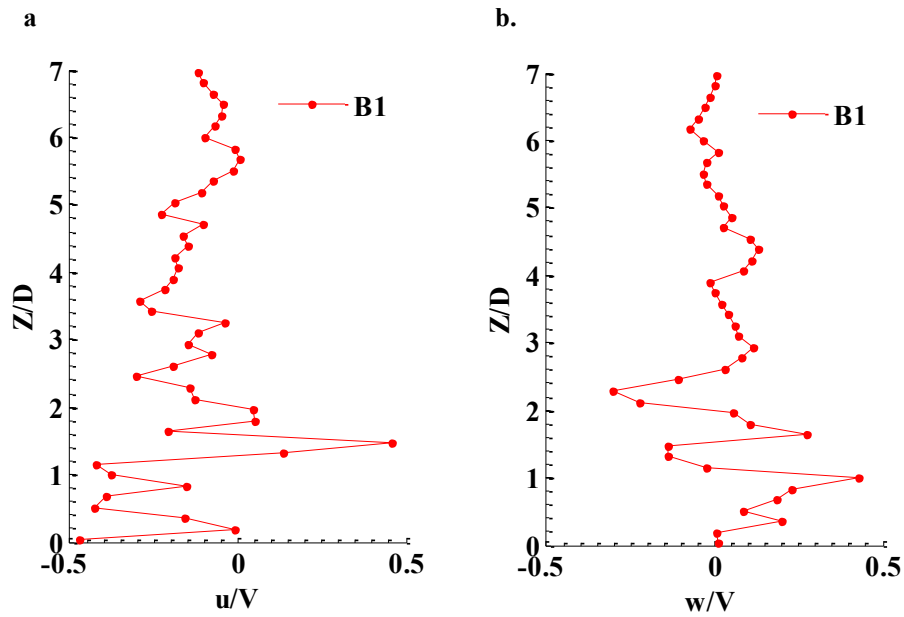


Figure 4.43 Profile plots of velocity components between two columns with $L/D = 3$ in vertical plane at axis of symmetry a) streamwise component, b) vertical component

According to the streamline plots and contour plots of u/V and w/V for two in-line columns with various spacing, upward and reverse flow are observed between two columns for $L/D = 2$. Pockets of strong upward and reverse flow occurred close to the bed. As the spacing increased to $L/D = 3$, stronger upward flow and reversed flow than in the case of $L/D = 2$ was identified close to the bed which was observed at the flow separation zone. As the flow separation for $L/D = 3$ occurred close to Column 2, strength of flow (upward and reverse) at downstream side close to Column 1 was higher in the case of $L/D = 2$ than that of $L/D = 3$. When the spacing between two columns increased, the strength of reverse and upward flow in the wake of Column 1 decreased. As the flow moves towards Column 2, gradual increase in streamwise velocity and decrease in vertical velocity component were observed. At the wake of column 2, a very weak streamwise velocity component of magnitude $u/V < 0.2$ was noticed for all the cases. However, the magnitude of upward flow increased with increase in the spacing between two columns.

4.4.3 Turbulence Intensity Components

The root mean square (rms) values of the components of velocity fluctuations (u' and w') give the turbulence intensity components. In this study, Tl_u and Tl_w in the streamwise

direction and the vertical direction, respectively, are normalised using the free stream velocity, V . The results are presented in contour plots and the distribution profiles at different positions of upstream, downstream and between the columns (in the case of two in-line columns).

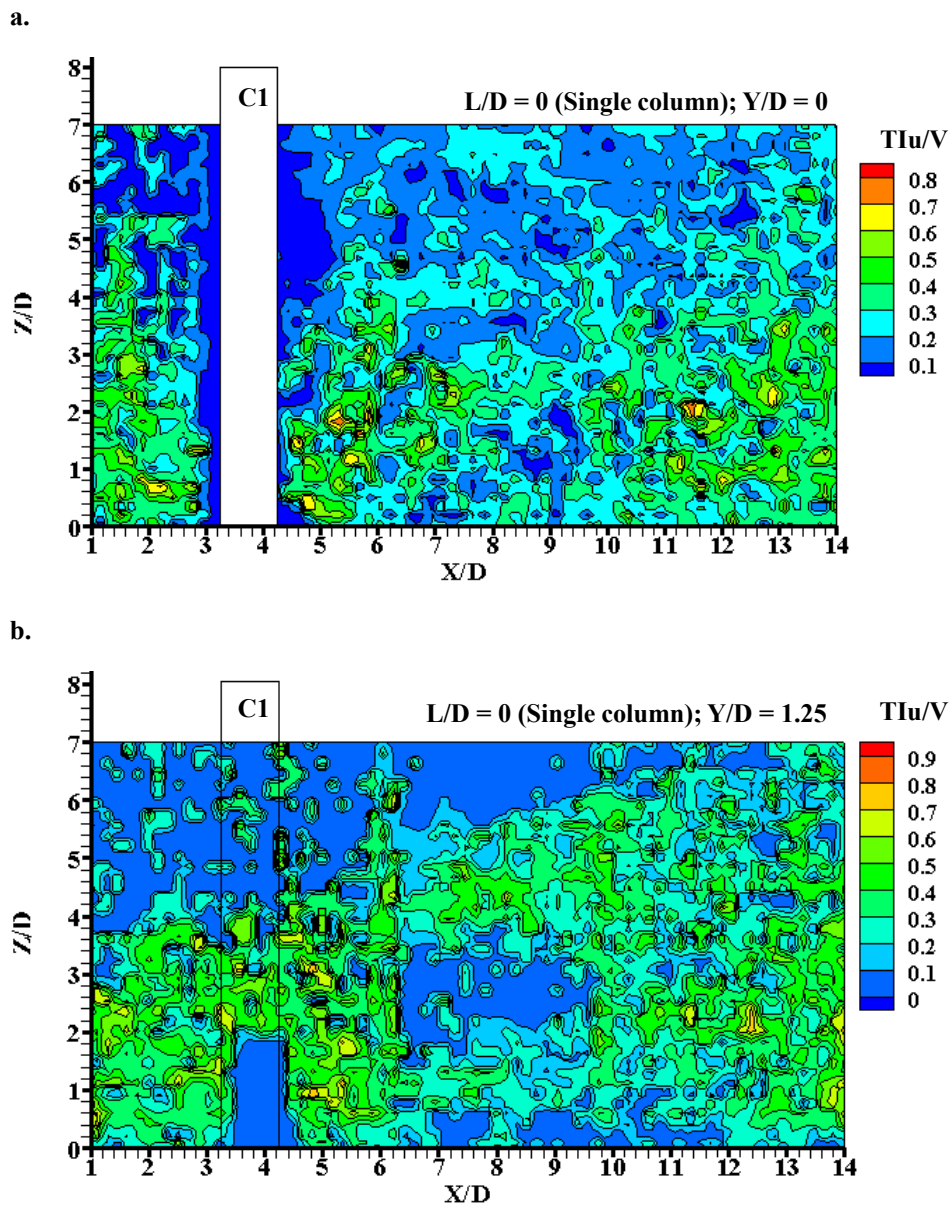


Figure 4.44 Contour plots of streamwise turbulence intensity component for the single column case in different vertical planes a) at $Y/D = 0$, and b) at $Y/D = 1.25$

The contour plots of Tiu/V for the single column for the planes $Y/D = 0$ and 1.25 are shown in Figure 4.44. Additionally the distribution profiles of Tiu/V in the $Y/D = 0$ plane

at different positions of the upstream side and the downstream side of a column are shown in Figure 4.45. At the upstream side of a column in plane $Y/D = 0$, the contour plot and profile plot show that the pocket of higher value of Tl_u/V exists close to the bed and decrease with increasing the distance towards the free surface. Similar results from the experiments was reported by Beheshti and Ataie-Ashtiani (2010). In the case of the plane at $Y/D = 1.25$, a similar distribution of Tl_u/V is noticed at the upstream and side of a column. At the downstream side of a column for a plane $Y/D = 0$, maximum value of $Tl_u/V = 0.8$ was observed close of the column within the distance of about $1.5D$ measured from the downstream face of a column. The pocket of higher value of Tl_u/V was extended to the mid-depth of the flow. For a plane $Y/D = 1.25$, slightly weaker Tl_u/V was noticed at the downstream side. However, the zone of higher value of Tl_u/V was observed approximately at the same positions as that in the $Y/D = 0$ plane.

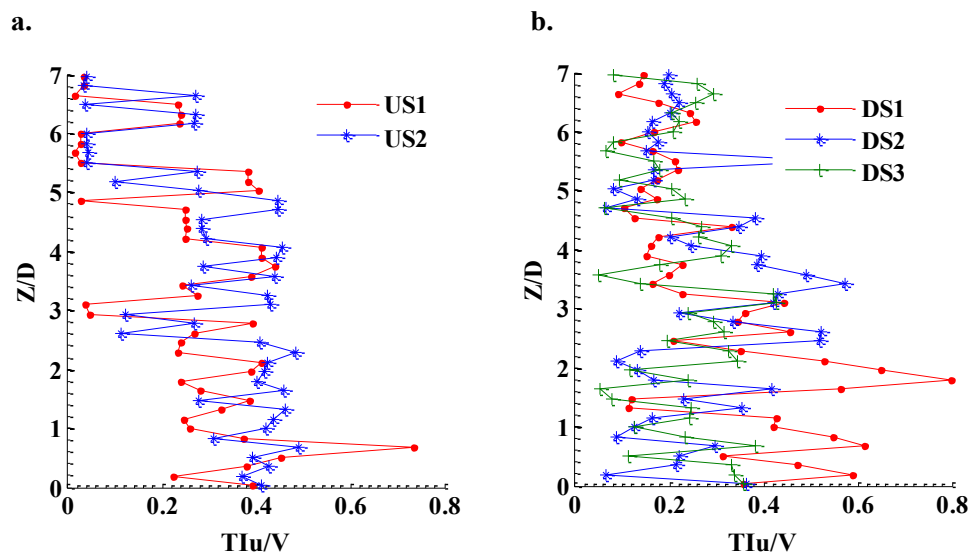


Figure 4.45 Profile plots of streamwise turbulence intensity component for the single column case in vertical plane at axis of symmetry a) upstream side; b) downstream side

For the two in-line column cases, Figure 4.46 show the contour plots and Figure 4.47 shows the profile plots of Tl_u/V for $L/D = 3$. The rest of the figures for different arrangements of two columns are referenced from Appendices B.2.1 and B.2.3. The profile plots for Tl_u/V for different values of L/D show that at the upstream side of

Column 1, the maximum value of $Tl u/V = 0.5$ is observed in the zone close to the bed for the case of a single column. The same result was reported by Ataie-Ashtiani and Aslani-Kordkandi (2013). Careful analysis of the flow between two columns for $L/D \leq 4$ shows that the higher values of $Tl u/V$ exist close to the bed. It can be noted that the higher value zone is extended throughout the gaps. For $L/D = 6$, the maximum value of $Tl u/V$ occurs close to Column 1 at a distance of about $1.5D$ measured from the face of Column 1. As the flow approached Column 2, $Tl u/V$ was reduced by about 60% of the maximum value, observed at the downstream side of Column 1.

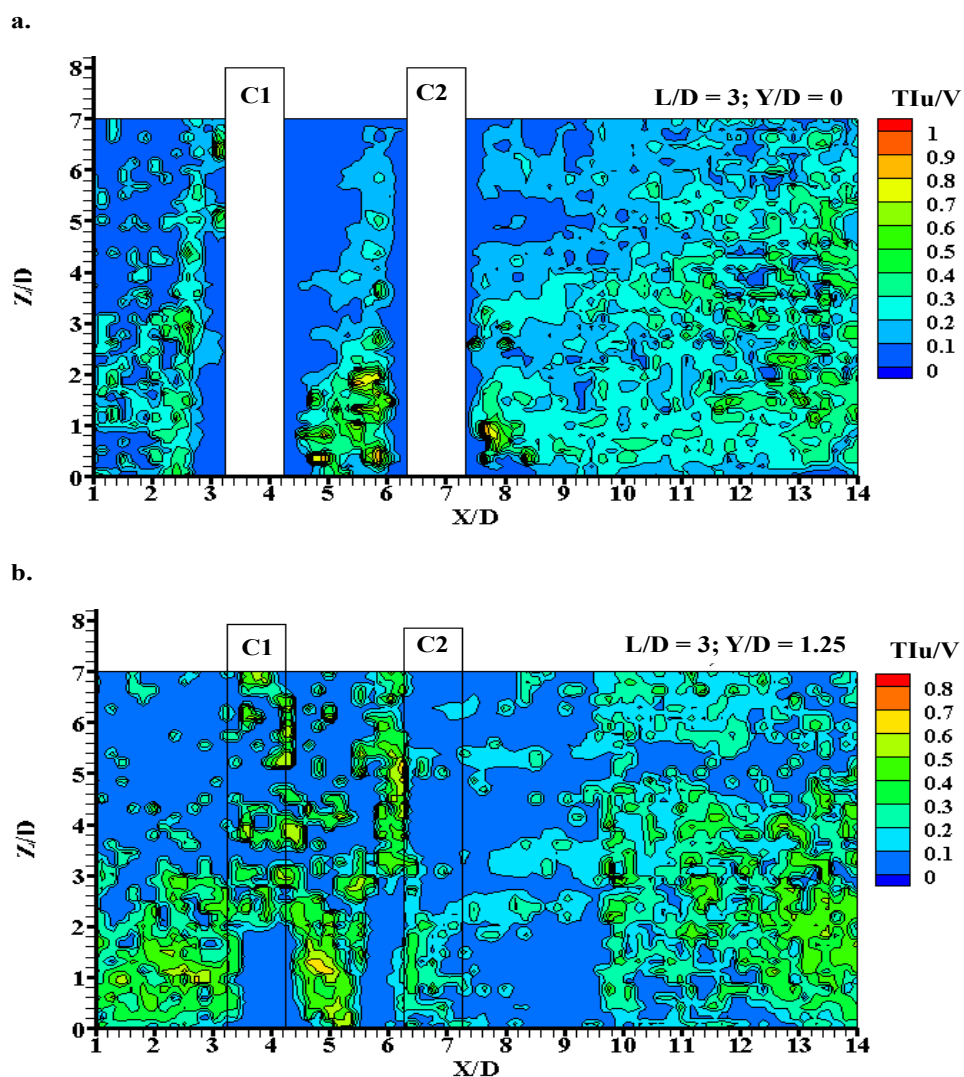


Figure 4.46 Contour plots of streamwise turbulence intensity component for two columns case with $L/D = 3$ in different vertical planes a) at $Y/D = 0$, and b) at $Y/D = 1.25$

At the downstream side of Column 2, decrease in the values of Tl_u/V was noticed, while comparing the values at the downstream side of Column 1. However, the distribution profile exhibits a similar pattern as in the upstream side and between two in-line columns. Furthermore, the figures reveal that the value of Tl_u/V at the downstream side of Column 2 increases with increase in the spacing between the two columns. Comparison of the figures for $L/D \leq 3$ at the plane $Y/D = 1.25$ reveals that significant reduction in the value of Tl_u/V can be seen at the downstream side of Column 2. However, for $L/D \geq 4$, it was observed that the distribution of Tl_u/V at the downstream side of Column 2 is similar to that of the single column case.

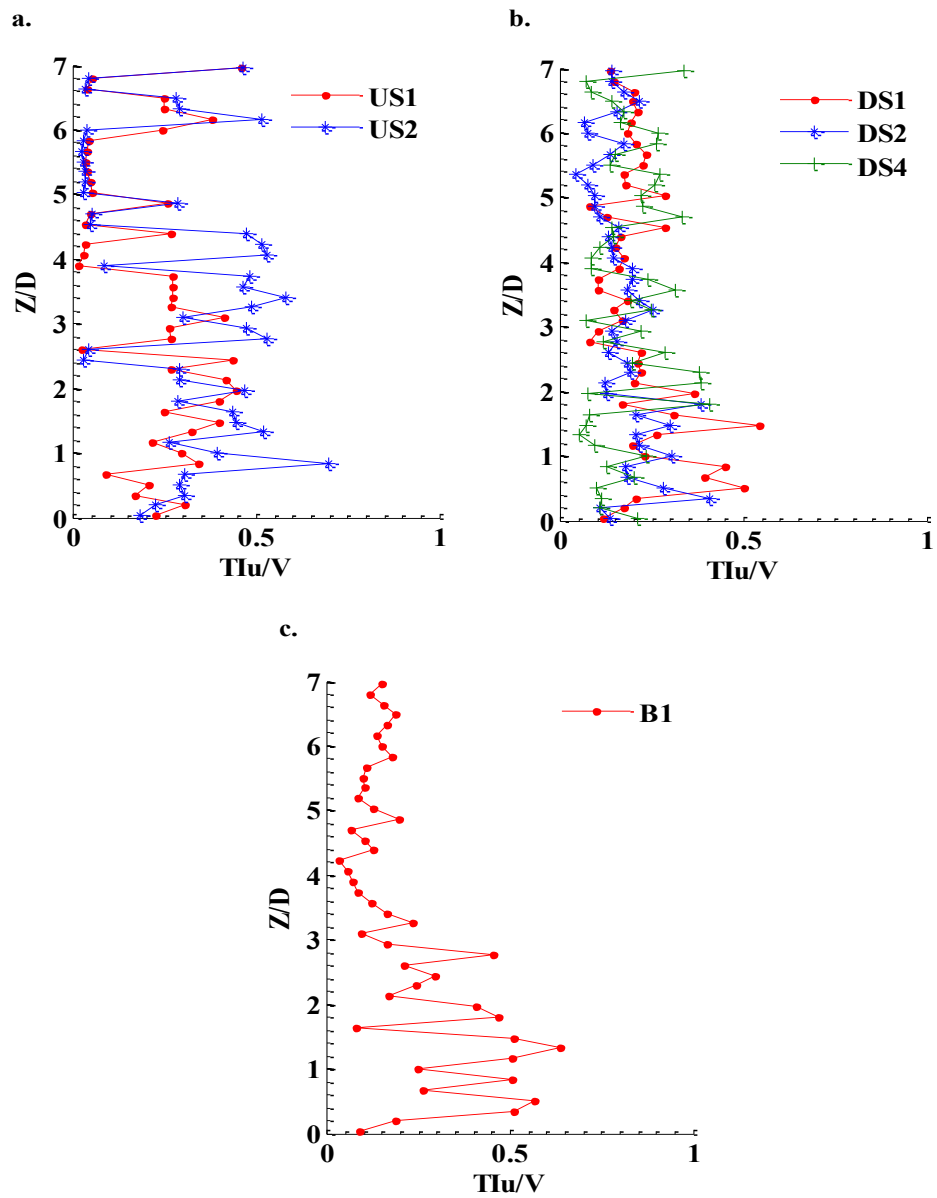


Figure 4.47 Profile plots of streamwise turbulence intensity component for two-column case with $L/D = 3$ in vertical plane at axis of symmetry a) upstream side, b) downstream side, and c) between two columns

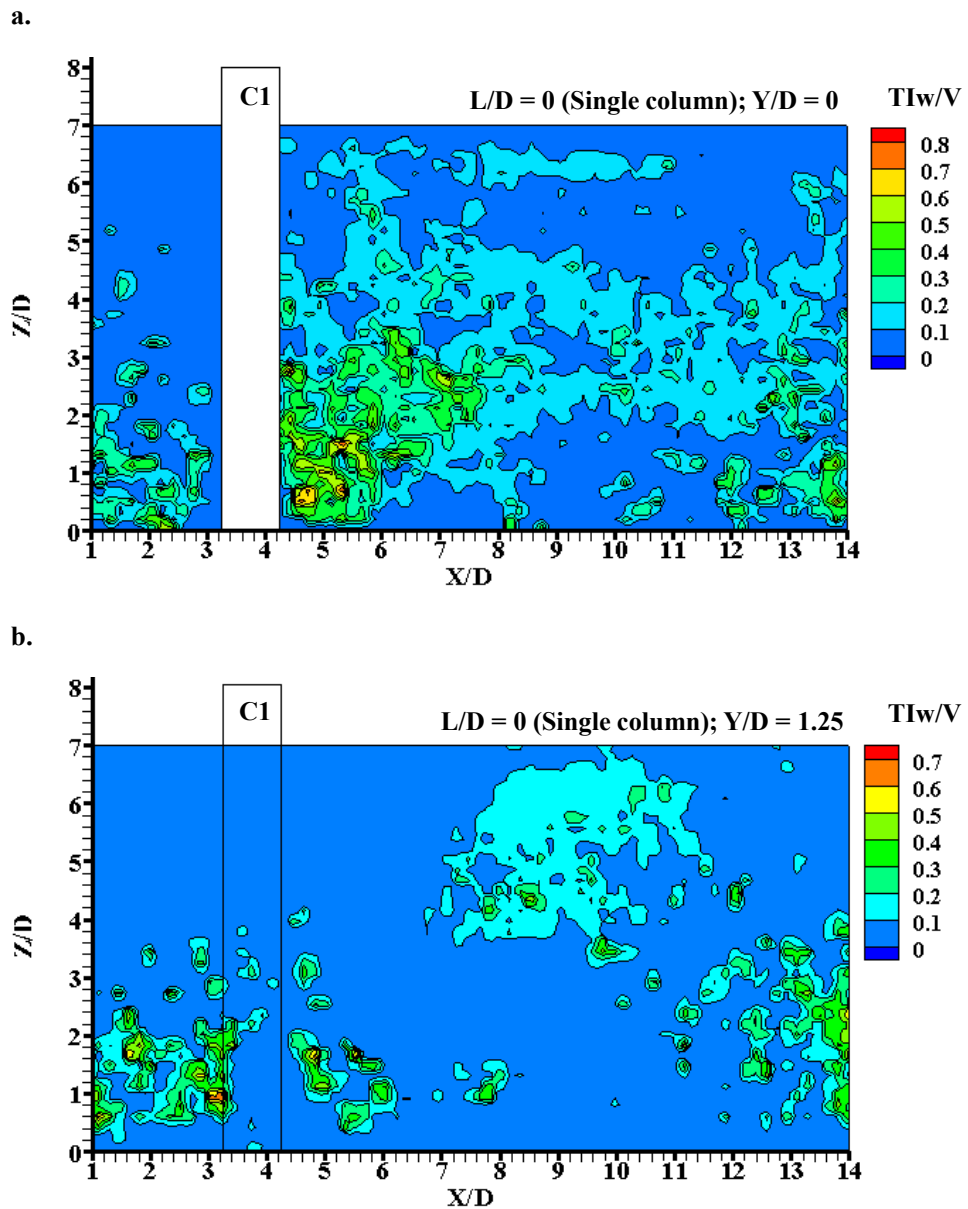


Figure 4.48 Contour plots of vertical turbulence intensity component for the single column case in different vertical planes a) at $Y/D = 0$, and b) at $Y/D = 1.25$

Distribution of the vertical component of normalised turbulence intensity TIw/V for the single column case in two different vertical planes at $Y/D = 0$ and 1.25 is presented in Figures 4.48 and 4.49. The contour plots and the profile plots at the upstream side of the column show that the magnitude of TIw/V is significantly smaller than that of TIu/V . The profile plot in Figure 4.49a shows that the maximum value of TIw/V is about 0.2 and occurred close to the bed at US1. Then it decreases with increase of the distance towards the free surface. At the downstream side of the column, the distribution of TIw/V is similar

to the distribution of TIu/V with approximately the same value. However, for the contour plot in the plane $Y/D = 1.25$, the distribution of TIw/V is different in both magnitude and order than in the case of TIu/V . From the figure, very weak vertical turbulence intensity can be noticed in the plane at $Y/D = 1.25$, except close to the bed.

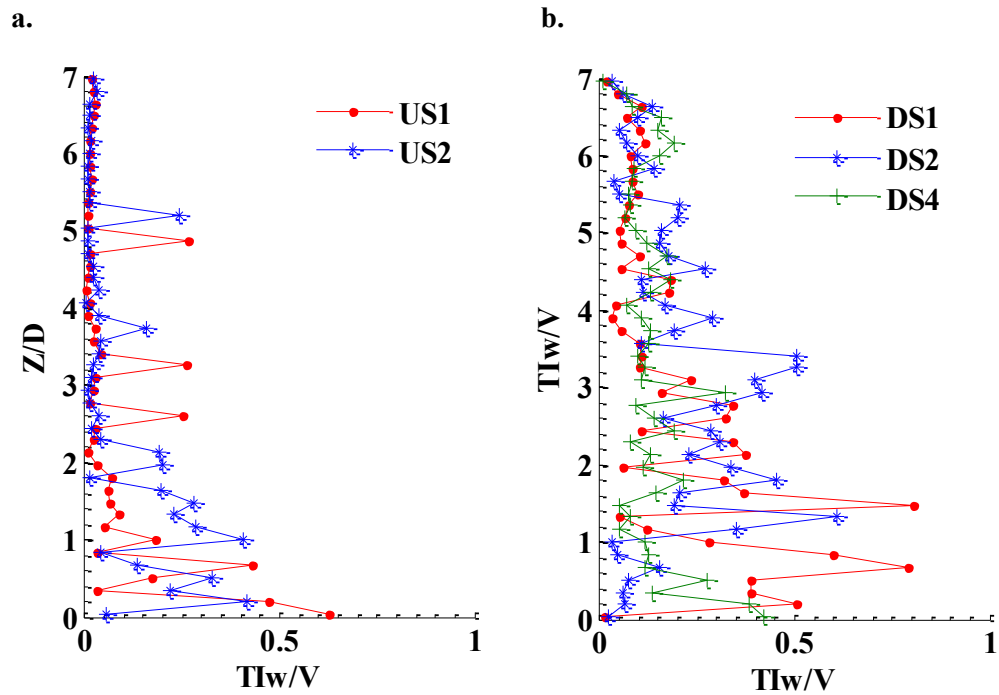


Figure 4.49 Profile plots of vertical turbulence intensity component for the single column case in vertical plane at axis of symmetry a) upstream side; b) downstream side

For the case of two in-line columns, the distribution of TIw/V for $L/D = 3$ is presented in Figures 4.50 and 4.51. For other values of L/D contour plots and profile plots are presented in Appendices B.2.2 and B.2.4. According to the figures for all the values of L/D , approximately the same order and distribution of TIw/V is observed at the upstream side of Column 1. Similarly, for the plane $Y/D = 1.25$, the distribution of vertical turbulence intensity at the upstream side of the Column 1 for all values of L/D is almost constant.

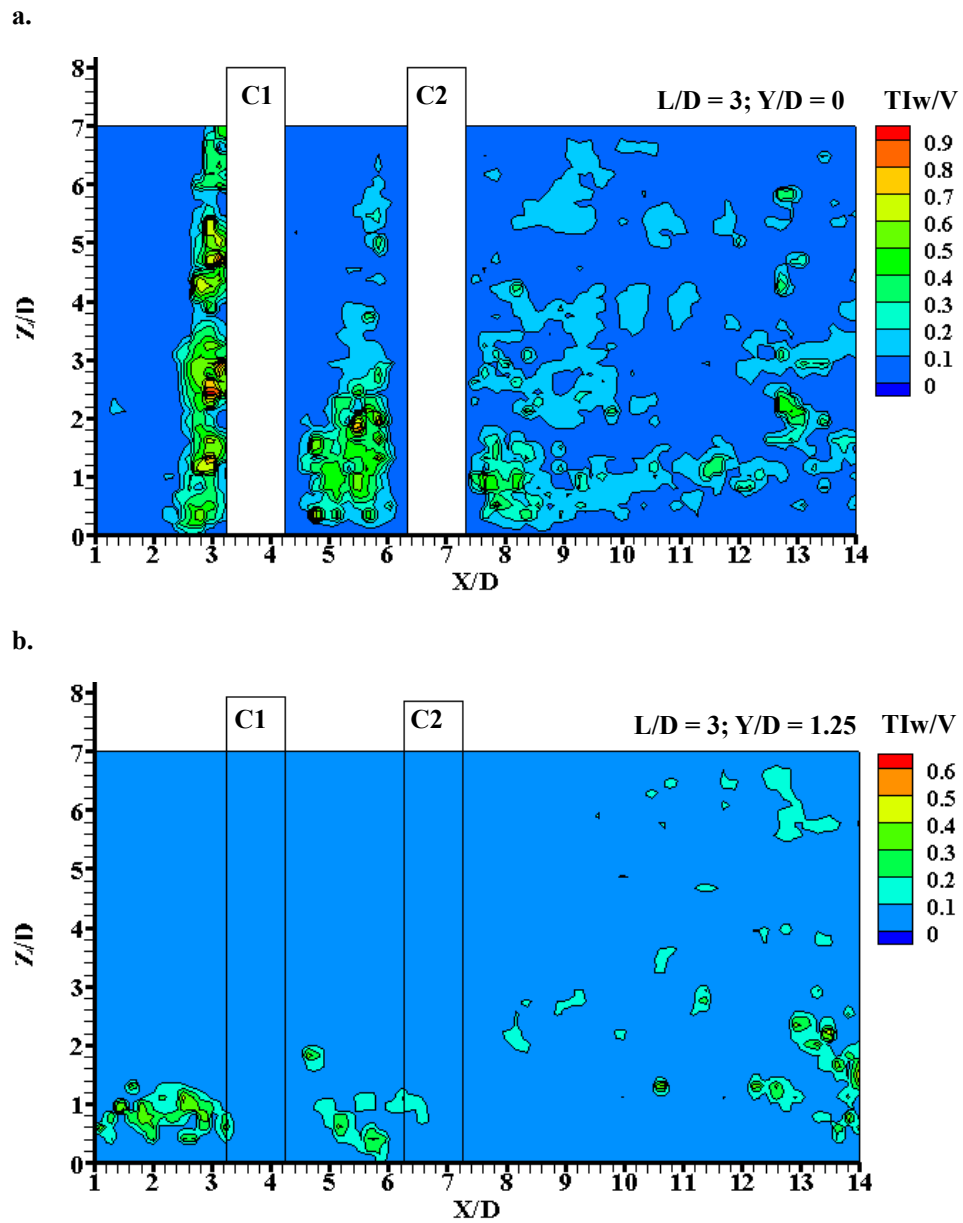


Figure 4.50 Contour plots of vertical turbulence intensity component for two columns case with $L/D = 3$ in different vertical planes a) at $Y/D = 0$, and b) at $Y/D = 1.25$

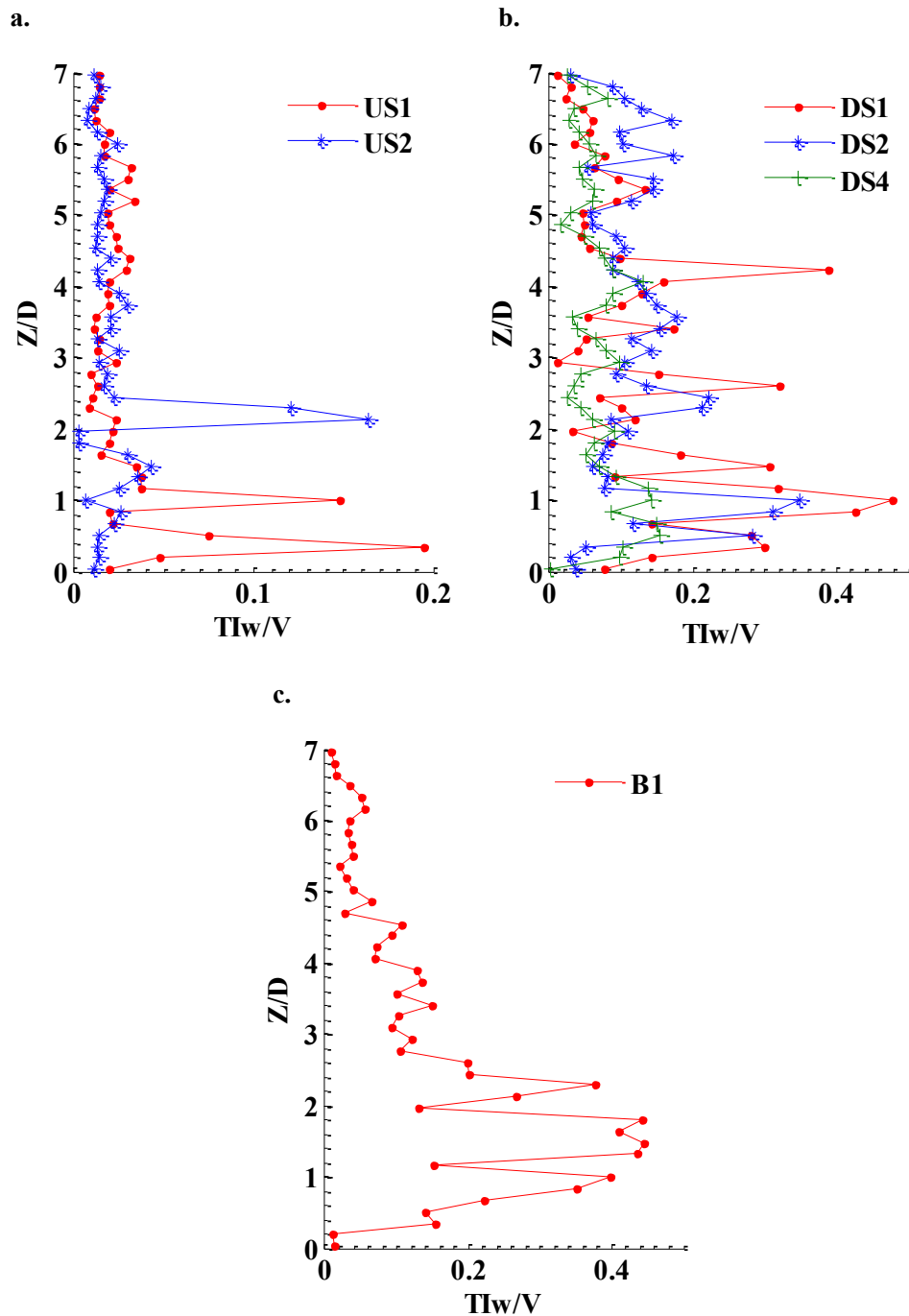


Figure 4.51 Profile plots of vertical turbulence intensity component for the case of two in-line columns with $L/D = 3$ in vertical plane at axis of symmetry a) upstream side, b) downstream side, and c) between two columns

Between two in-line columns, higher values of TIw/V were observed, close to the bed. The value decreased towards the free surface as in the case of TIu/V . When $L/D \leq 3$, the vertical turbulence intensity in the gap near the bed was observed with the maximum

value lying in the range of 0.4 to 0.5. While for $L/D \geq 4$, the maximum value of TI_w/V was approximately equal to 0.4 close to the Column 1 and gradually decreased as the flow approached Column 2 and eventually reaches the condition similar to the upstream side of Column 1. It was noticed that the maximum values of TI_u/V and TI_w/V between the two columns for all the values of L/D were approximately the same.

Referring to the profile plots for $Y/D = 0$ plane, shown in Appendix B.2.4, the maximum value of TI_w/V for $L/D = 1$ at the downstream side of Column 2 was about 50% less than that of the single column case. The profile plots further revealed that the value of TI_w/V increased as the spacing between the two columns increased. It was also common to observe that TI_w/V gradually decreased in the downstream direction in all the cases of L/D . For the plane $Y/D = 1.25$, when $L/D \leq 3$, a similar distribution of TI_w/V was observed with a value approximately equal to 0.1. However, for $L/D > 3$ a slight increase in TI_w/V was noticed at the bank of the downstream side of Column 2, which was further extended towards the downstream side.

4.4.4 Turbulent Kinetic Energy

The results of turbulent kinetic energy (TKE) in the vertical plane parallel to the flow direction are presented in this section. It can be noted that the transverse component of velocity fluctuation has not been considered. Contour plots of TKE/V^2 for the single column case in the vertical planes at $Y/D = 0$ and 1.25 are presented in Figure 4.52. Similarly the distribution of TKE/V^2 at different positions of the upstream and downstream side in a plane $Y/D=0$ is presented in Figure 4. The results from the contour plots and profile plots indicate that the distribution of TKE/V^2 is similar to the distribution of turbulence intensity. At the upstream side of a column, higher values of turbulent kinetic energy were observed close to the bed and gradually decreased towards the free surface. The maximum value of TKE/V^2 was approximately equal to 0.3 for both US1 and US2 at the upstream side of a column. At the downstream side of a column, the maximum value of TKE/V^2 was observed close to the column near the bed. It was about 2 times greater than that of the upstream side. The profile plot at the downstream side of a column as shown in Figure 4.53b indicates that the value of turbulence kinetic energy decreases as the distance increases to further downstream side direction.

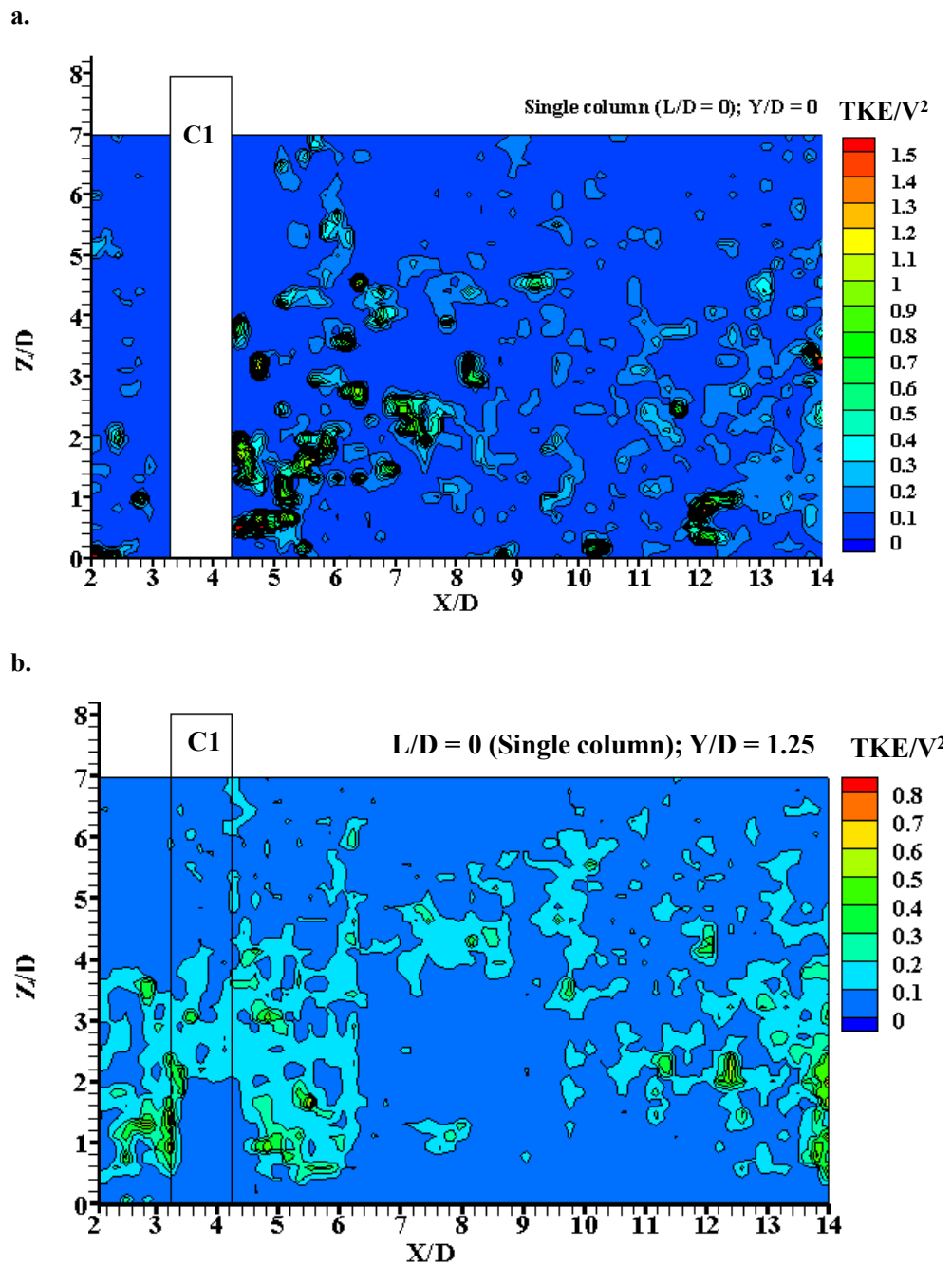


Figure 4.52 Contour plots of turbulent kinetic energy for the single column case in different vertical planes a) at $Y/D = 0$, and b) at $Y/D = 1.25$

For two in-line column cases contour plots of TKE/V^2 are presented in Figure 4.54 for $L/D = 3$. Plots for other values of L/D are given in Appendix C.2.1. Furthermore, in Figure 4.55 and Appendix C.2.2, the distributions of TKE/V^2 at different positions of the upstream and downstream side of the columns are presented. Results from the contour

plots and profile plots for various L/D indicate that there is significant change in the turbulence kinetic energy from upstream to downstream of the columns. At the upstream side of Column 1, the distributions of TKE/V^2 for all the cases of L/D were similar to the single column case. Between the two columns and at the downstream side of Column 2, the contour plots show that the distribution of TKE/V^2 is more or less similar to that of the turbulence intensity. The figures exhibit an increase in turbulence kinetic energy behind the Column 1 as the spacing between the two column increases. For the case of $L/D = 3$ and 4, the pocket of higher value of turbulent kinetic energy occurred close to the Column 2. However, for $L/D > 4$, the value of turbulent kinetic energy decreased as flow approached Column 2. For example, in the case of $L/D = 6$, the value of TKE/V^2 close to Column 2 at the upstream side was approximately equal to 0.1, about 70% less than that of the downstream side of Column 1. At the downstream side of Column 2, the figures indicate that the value of TKE/V^2 increases as the spacing between the two columns increases up to $L/D = 3$. Further increase in spacing results in the decrease in the value of TKE/V^2 .

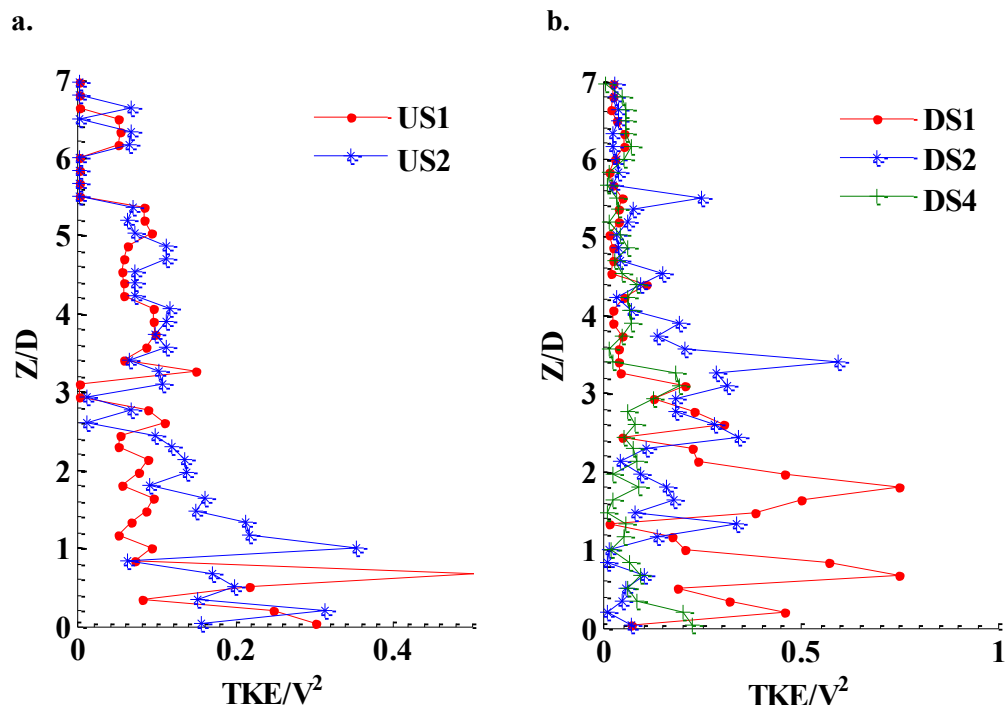


Figure 4.53 Profile plots of turbulent kinetic energy for the single column case in vertical plane at axis of symmetry a) upstream side; b) downstream side

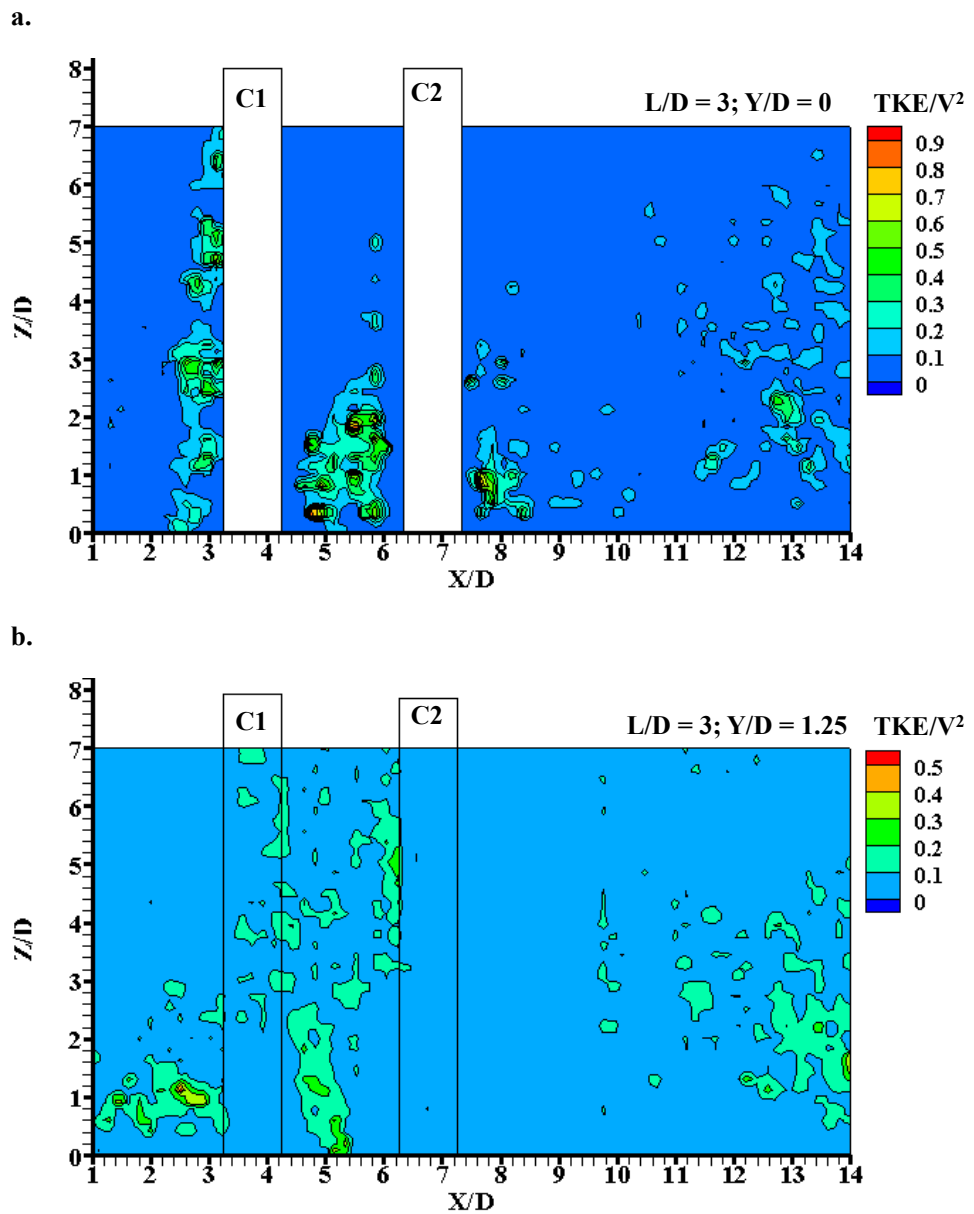


Figure 4.54 Contour plots of turbulent kinetic energy for the two-column case with $L/D = 3$ in different vertical planes a) at $Y/D = 0$, and b) at $Y/D = 1.25$

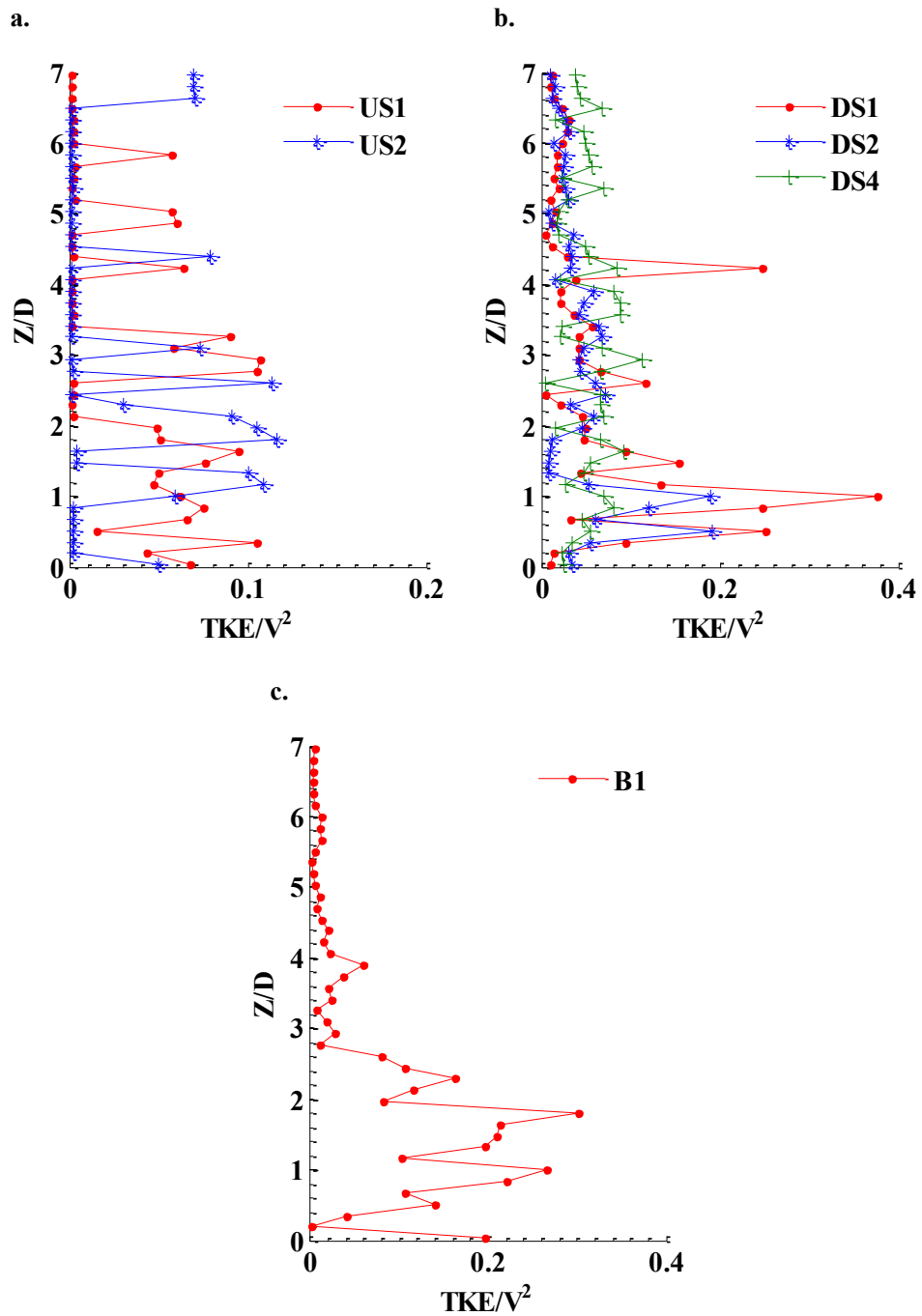


Figure 4.55 Profile plots of turbulent kinetic energy for the case of two in-line columns with $L/D = 3$ in vertical plane at axis of symmetry a) upstream side, b) downstream side, and c) between two columns

4.4.5 Reynolds Shear Stresses

In this study, for the vertical planes parallel to the flow direction, Reynolds shear stresses are calculated using only the streamwise and vertical components of velocity fluctuation and are denoted by $-\overline{\rho u'w'}$. For the presentation of results, $-\overline{\rho u'w'}$ have been normalised by ρV^2 . Here, ρ represents the mass density of water.

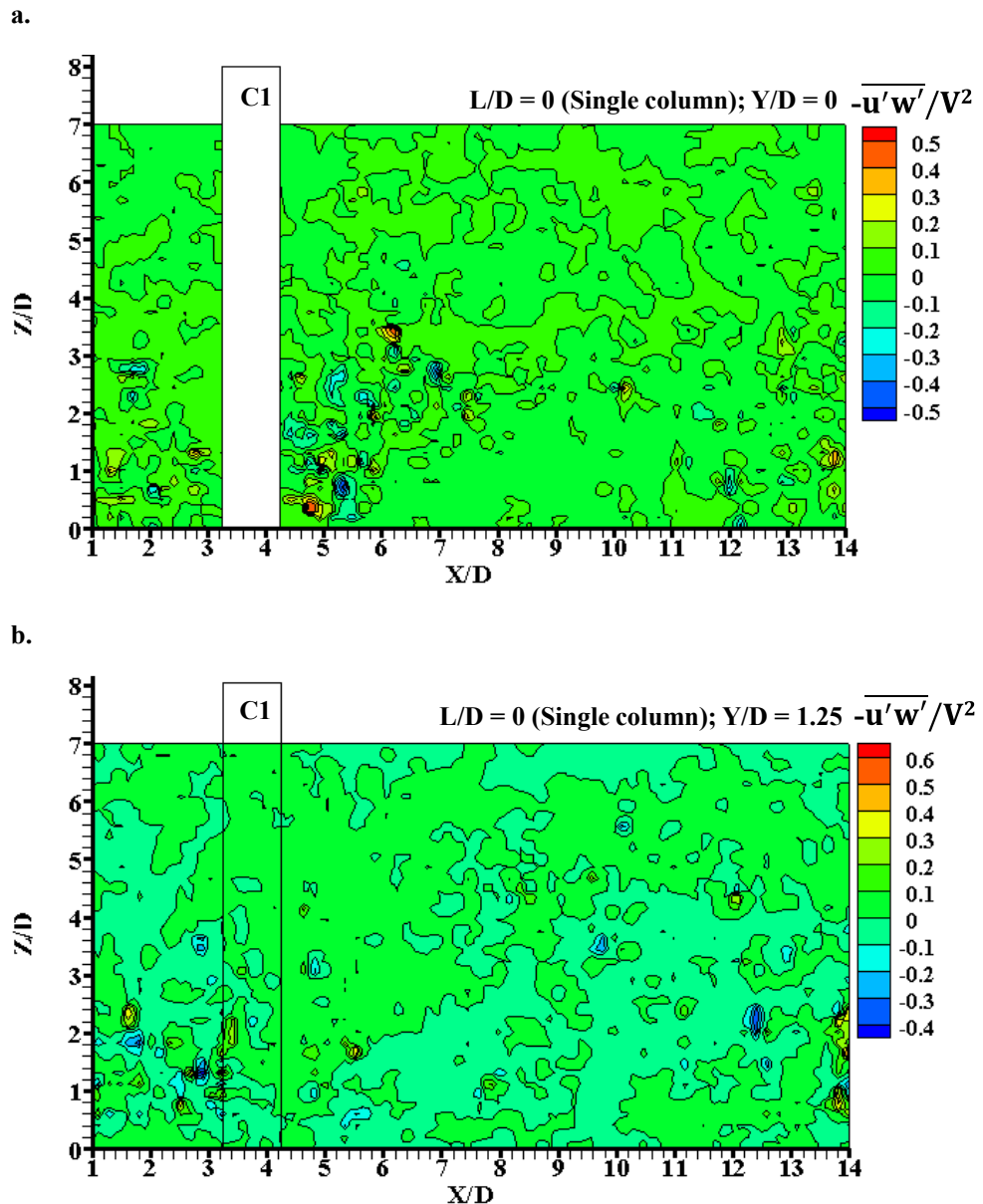


Figure 4.56 Contour plots of Reynolds shear stress for the single column case in different vertical planes a) at $Y/D = 0$, and b) at $Y/D = 1.25$

The contour plots of $-\overline{u'w'}/V^2$ on two different longitudinal planes $Y/D = 0$ and 1.25 for the single column case is shown in Figure 4.56. Similarly, Figure 4.57 shows the profiles of $-\overline{u'w'}/V^2$. The contour plots indicate that at the upstream side of a column, $-\overline{u'w'}/V^2$ considerably increases as the flow approaches close to the column. Small pockets of positive as well as negative values of $-\overline{u'w'}/V^2$ were observed near the bed close to the column. The normalised Reynolds stress values at the upstream side were in the range of $-0.3 < -\overline{u'w'}/V^2 < 0.2$. At the downstream side of a column, a similar trend of distribution of $-\overline{u'w'}/V^2$ was observed with higher values close to the bed. In $Y/D = 0$ plane, the pocket of positive and negative values in the range of $-0.5 < -\overline{u'w'}/V^2 < 0.5$ was observed close to the column and extended up to a distance of $3D$ downstream, measured from the face of the column. However, in the plane $Y/D = 1.25$, a positive value of $-\overline{u'w'}/V^2$ approximately equal to 0.3 was observed throughout the depth.

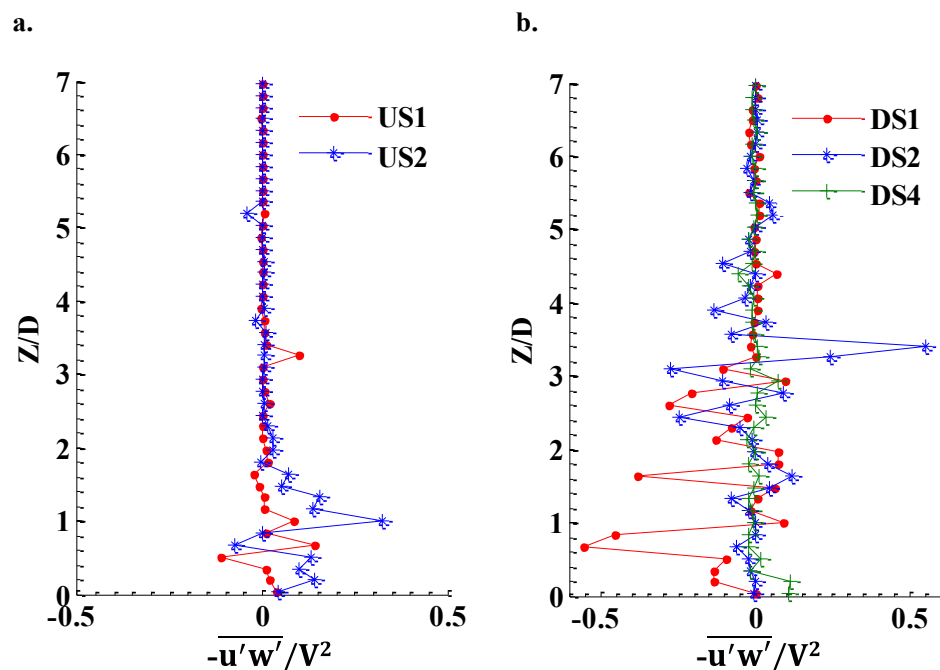


Figure 4.57 Profile plots of Reynolds shear stress for the single column case in vertical plane at axis of symmetry a) upstream side; b) downstream side

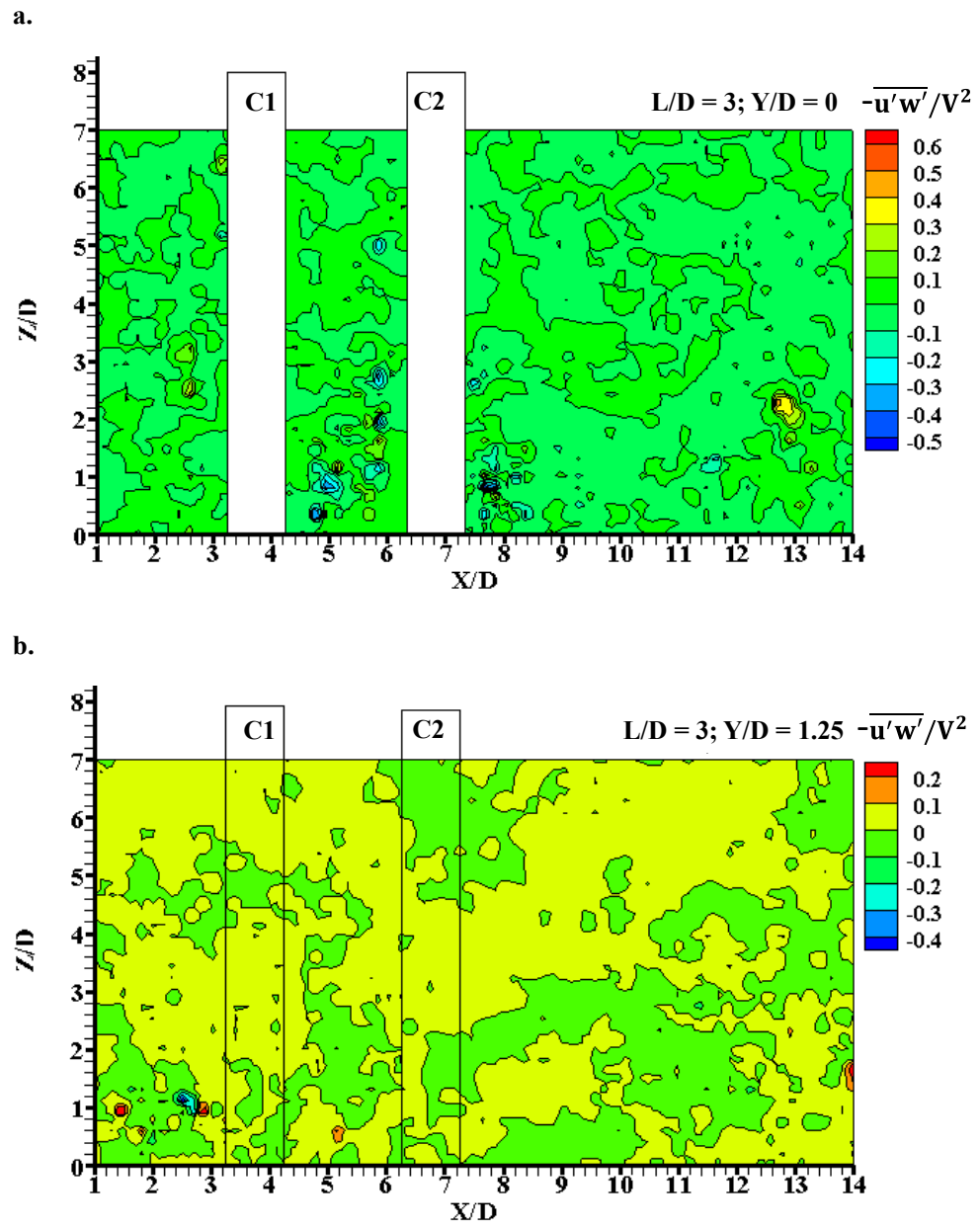


Figure 4.58 Contour plots of Reynolds shear stress for the case of two in-line columns with $L/D = 3$ in different vertical planes a) at $Y/D = 0$, and b) at $Y/D = 1.25$

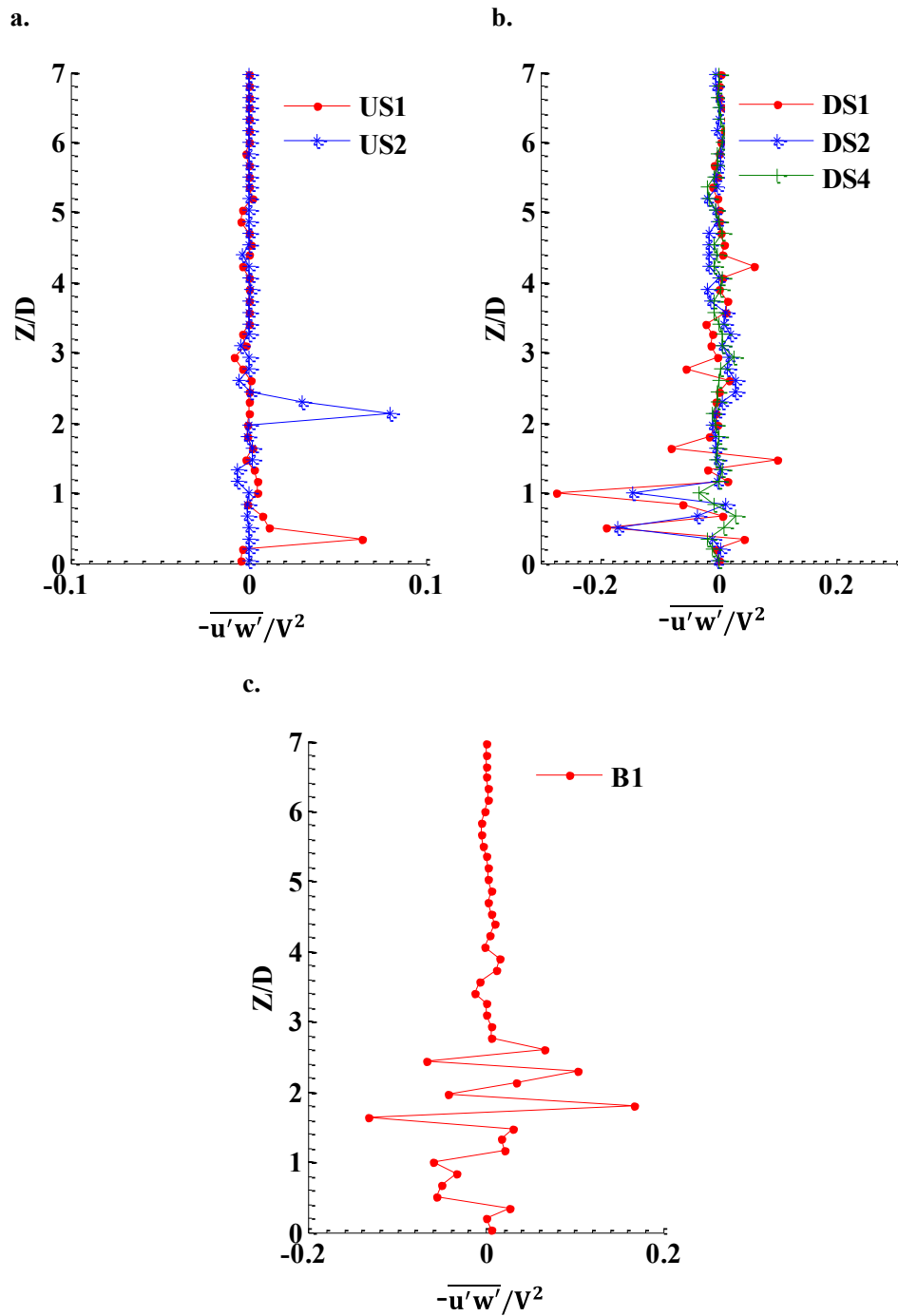


Figure 4.59 Profile plots of Reynolds shear stress for the two-column case with $L/D = 3$ in vertical plane at axis of symmetry a) upstream side, b) downstream side, and c) between two columns

For the two in-line columns cases, contour plots and profile plots of $-\overline{u'w'}/V^2$ for $L/D = 3$ are presented in Figures 4.58 and 4.59. Contour plots for other values of L/D are

presented in Appendix D.2.1. Similarly, the figures in Appendix D.2.2 show the profile of $-\overline{u'w'}/V^2$ in vertical sections at different positions. The contour plots and profile plots at the upstream side of Column 1 for all values of L/D indicate similar trends of $-\overline{u'w'}/V^2$ distribution. However, at the downstream side of Column 2 and between the two columns, significant increase in the values of $-\overline{u'w'}/V^2$ have been observed. Between the two columns, it was common to observe the higher negative values of $-\overline{u'w'}/V^2$ close to the bed. Moreover, it was observed that the value of $-\overline{u'w'}/V^2$ decreased with increase in the spacing between the two in-line columns. Higher values of $-\overline{u'w'}/V^2$ were observed close to Column 1 and gradually decreased as the flow approached Column 2. For example in the case of $L/D = 6$, $-\overline{u'w'}/V^2$ was in the range of -0.1 to 0.1 close to Column 1, while it was approximately equal to zero close to Column 2. In the wake of Column 2, increase in the value of $-\overline{u'w'}/V^2$ was noticed with increase in the distance between the two columns until $L/D = 3$. Further increase in the value of L/D decreased $-\overline{u'w'}/V^2$ at the wake of Column 2. For $L/D \leq 3$, the maximum negative value of $-\overline{u'w'}/V^2$ was approximately equal to 0.2 at the wake of Column 2. For $L/D > 3$, an approximate range of $-0.1 < -\overline{u'w'}/V^2 < 0.1$ was observed.

4.5 Bursting Phenomenon and Quadrant Analysis

4.5.1 Introduction

Nakagawa and Nezu (1993) defined the coherent structure as the organized motion of the fluid parcels that have life cycles, including birth, development, interaction and breakdown. Bursting phenomena and the large scale vertical motion were two types of coherent structures reported by them.

In the field of hydrodynamics of open channel flows, bursting phenomenon received more attention for the analysis of turbulence flow structures in the boundary layer zone. Kline et al. (1967); Corino and Brodkey (1969); and Kim et al. (1971) were the first investigators who introduced the concept of bursting phenomenon. Kline et al. (1967) conducted an experimental investigation on the coherent structures in turbulent boundary layers using a hydrogen bubble visualization and found that the sub-layer structure consisted of low speed and high speed streaks with relatively regular spacing in the span-wise direction. It was noticed that the low speed streaks were gradually lifted away from

the wall and then began to oscillate and finally were ejected from the wall. It was observed that these processes occurred intermittently and randomly over the surface.

4.5.2 Review on Quadrant Analysis

Corino and Brodkey (1969) investigated the turbulent flow near the solid boundary and observed the generation and transport processes. It was found that the sub layer was continuously disturbed by small scale velocity fluctuation and the fluid elements were periodically ejected outwards from the wall which interacted with the mean flow resulting in velocity fluctuation. These ejections and resulting fluctuations were believed to be a factor in the generation of turbulence

Kim et al. (1971) conducted an experimental study on the turbulence structure of a smooth surface boundary layer in a low speed water flow using hydrogen bubble measurements and hot wire measurements with dye visualization. They focused on the process of production of turbulence near the wall. It was discovered that the turbulence energy and the Reynolds stresses were generated during an intermittent bursting process. Furthermore, they describe the overall behavior of a flow model during bursting. It was summarized that the overall model of bursting can be described by three stages of flow namely: slow lifting of low speed streaks, rapid growth of oscillatory motion, and break up of oscillation. After completion of these cycles, the velocity profile returns to a form generally like the mean profile shape.

Many experimental investigations have been conducted on the mechanism of turbulence production and bursting phenomenon in smooth-wall boundary layers and have produced an outline of bursting phenomenon which are well accepted at the present time. The bursting phenomena in smooth boundary layers was described in several comprehensive reviews by Willmarth (1975); Wallace (1985); Kim (1987); Kline and Afgan (1990); and Smith et al. (1991). Lu and Willmarth (1973) developed the quadrant technique for the better understanding of the contribution to Reynolds stresses. According to quadrant analysis of two dimensional velocity fluctuations u' , and w' (or v'), the bursting process can be classified in four different classes of events such as: outward interaction ($u'>0$, $w'>0$), ejection ($u'<0$, $w'>0$), inward interaction ($u'<0$, $w'<0$) and sweep ($u'>0$, $w'<0$) in

four different quadrant zones denoted by Q1, Q2, Q3 and Q4 respectively as shown in Figure 4.60.

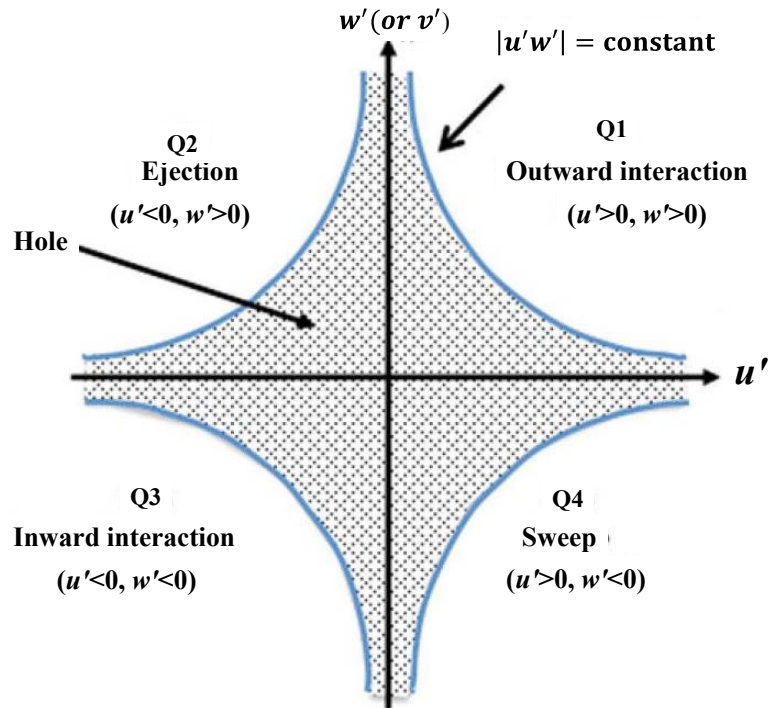


Figure 4.60 Definition sketch of four quadrant zones in u - w plane

As reported in Nakagawa and Nezu (1993), the instantaneous Reynolds- stress signal $u'(t)w'(t)$ is directly related to bursting phenomena. For the generation of turbulence, ejection and sweep motions are the main events. Hence, sorting functions $I_e(t)$ for ejection and $I_s(t)$ for sweeps are introduced to detect the basic features of the bursting phenomena and are defined by the following equations:

$$I_e(t) = \begin{cases} 1, & u'(t) < 0 \text{ and } w'(t) > 0 \\ 0, & \text{otherwise} \end{cases} \quad 4.1$$

$$I_s(t) = \begin{cases} 1, & u'(t) > 0 \text{ and } w'(t) < 0 \\ 0, & \text{otherwise} \end{cases} \quad 4.2$$

As there are interaction motions contained in ejection and sweep motions, the sorting functions cannot be used directly to detect the bursting motion. Thus, Lu and Willmarth

(1973) introduce a threshold level, H (also called the hole size) in u' - w' quadrant analysis. They assumed that ejection and sweep motions occur under the following condition:

$$|u'(t)w'(t)| \geq H(RMS_{u'}RMS_{w'}) \quad 4.3$$

where, H is the hole size (0, 1, and 2), $RMS_{u'}$ and $RMS_{w'}$ are the local root mean square values of velocity fluctuation in stream-wise and vertical direction respectively

Lu and Willmarth (1973) presented a method to analyse the structure of instantaneous Reynolds stress, according to which, the Reynolds stresses at a point in the u' - w' plane are equal to the sum of contributions measured in four quadrants. The contributions to Reynolds stresses from four quadrants were computed from the following equation:

$$(u'w')_i = \lim_{T \rightarrow \infty} \frac{1}{T} \int_0^T u'w' I_i dt \quad 4.4$$

where, I_i ($i = 1, 2, 3$ and 4) is an indicator that detects the production of turbulence. $I_i = 1$, if $|u'(t)w'(t)| \geq H(RMS_{u'}RMS_{w'})$ and the point (u', w') in the u' - w' plane is in the i^{th} quadrant; and $I_i = 0$, otherwise.

Shiau (1999) applied the concept of stress fraction, S_i , to analyse the contribution to Reynolds stress. Stress fraction is defined as the contribution ratio between $(u'w')_i$ and total Reynolds stress at a point in u' - w' plane, which is given by:

$$S_i = \frac{(u'w')_i}{-u'w'}, \quad (i = 1, 2, 3 \text{ and } 4) \quad 4.5$$

For hole size $H=0$, the sum of fractional contributions from all bursting events is equal to 1.

Another way of analysing the organization of coherent structure is the probability of occurrence of bursting events in each quadrant. Keshavarzi and Shirvani (2002) and Keshavarzi and Gheisi (2006) performed a probability analysis to examine the

organization of coherent structure using the conditional probability analysis. In order to estimate the probability of occurrence of each event, the following equations have been proposed:

$$P_i = \frac{n_i}{N}, \quad (i = 1, 2, 3 \text{ and } 4) \quad 4.6$$

$$N = \sum_{i=1}^4 n_i \quad 4.7$$

where, P_i is the probability of occurrence of each event, n_i is the number of events in each class and N is the total number of bursting events.

In recent years, quadrant analysis based on two dimensional velocity information has been extensively used to analyse the contribution of bursting events for the generation of turbulence structure. Nakagawa and Nezu (1978); Nakagawa and Nezu (1993); and Keshavarzy and Ball (1997) investigated two dimensional quadrant analysis of the bursting process and reported that the sweep and ejection events have higher contribution for the production of turbulence than outward interaction and inward interaction. Furthermore, Keshavarzi and Gheisi (2006) proposed a three dimensional quadrant analysis for the study of the bursting process addressing the effect of transverse velocity components.

Roussinova et al. (2009) reported the analysis of the instantaneous velocity field measured by particle image velocimetry (PIV) in a smooth open channel flow using proper orthogonal decomposition (POD) to expose the vertical structure. The results from the POD analysis were combined with the results from momentum analysis and conditional quadrant analysis performed at three different threshold level. It was reported that the results from quadrant analysis cannot provide useful information about the extreme events when using the threshold level, $H = 0$. On the other hand, while using the larger threshold, i.e. $H \geq 0$, there could be significant loss of information about flow events. However, the quadrant analysis provides the spatial distribution of the important events such as ejection and sweep. In that study, the effect of flow structure on the mean

flow, the contribution of each event to the Reynolds stress was presented analysing the profile of stress fractions at each quadrant. It was concluded from this analysis that ejection and sweep events were the larger contributors to the mean Reynolds stresses. Furthermore, it was reported that the inward and outward interaction generate about three times smaller stress fraction than that of ejection and sweep events.

Yang (2010) has theoretically investigated conditionally averaged turbulent structures in two dimensional uniform flow considering the momentum flux caused by upward and downward velocity. It was reported that, this momentum flux generated results in deviation of conditional Reynolds shear stress from expected linear distribution. Furthermore, the results indicated that the conditional Reynolds stress produced by the contribution of ejection event is always greater than the classical Reynolds stress, whereas the Reynolds stress produced by the contribution of sweep event is always less than the classical Reynolds stress. Additionally, it was reported that the deviation of conditional turbulence intensities is similar to the deviation of conditional Reynolds stress.

Izadinia et al. (2013) conducted an experimental investigation on the stochastic nature of instantaneous shear stresses over the scour hole and its influences on sediment entrainment and transport. It was reported that the probability distribution of instantaneous Reynolds stresses were distributed in such a way that the tails of the distribution decayed to zero slower than the Gaussian distribution. On the other hand, the quadrant analysis indicated that outward and inward interactions were dominant near the bed at the upstream side of the bridge pier. As the distance from the bed increased, ejection and sweep events became dominant. The reason behind this was reported as due to the velocity reversal phenomenon, which occurs near the bed at the upstream side of the pier. Furthermore, it was indicated that the occurrence probability of sweep events is more than other events at the upstream side. Dominant sweep events at the upstream side were reported as the cause of maximum scour depth at this region and transportation of sediments to the downstream side. The assessment of stress fraction revealed that contributions of each events to Reynolds stress production are stronger at the downstream side of the piers.

Keshavarzi et al. (2014) performed three dimensional analysis of turbulent flow structures around a single circular bridge pier by measuring the instantaneous three dimensional velocity components using an ADV. In that study, the velocity data were analysed using the Markov process to investigate the probability of occurrence of bursting events. Three dimensional octant analysis was used for the better understanding of the bursting events during sediment entrainment. The concept of conditional transitional probability was applied for the analysis of coherent turbulent structures. It was concluded from the results that the external sweep and internal ejection events primarily contribute the sediment entrainment around a single circular bridge pier.

4.5.3 Results of Quadrant Analysis

In this study, quadrant analysis has been employed to analyse the structure of instantaneous Reynolds stresses measured around bridge piers consisting of a single column and two in-line columns. The Reynolds stress at a point is presented as the sum of contributions measured in four quadrants. The results are analysed based on the probability of occurrence (P_i) of each quadrant and contribution ratio (stress fraction, S_i) for the production of Reynolds stresses. In this section, the results are analysed for the flow in $u-w$ plane at the plane of symmetry i.e. $Y/D = 0$. The results for the single column and two in-line column cases are presented in this section as given in Figures 4.61 to 4.70 and Appendices E.1 and E.2. In this section, the results associated with the single column and two columns with $L/D = 3$ are presented, while the rest of the results are referenced from figures given in Appendices E.1 and E.2.

The probability of occurrence (P_i) of each of the four quadrants ($i = 1, 2, 3$ and 4) is determined from the experimental data using Equations 4.6 and 4.7. P_i , which is plotted against the normalised depth of flow and the results are shown in Figures 4.61 to 4.65. For the single column case, P_i at the upstream side (US1) is shown in Figure 4.61. Referring to this figure, it can be seen that the probability of occurrence of each event varies with depth of flow. The figure exhibits that the highest value of the depth-averaged probability of occurrence is in the sweep event (Q4) followed by the outward interaction (Q1), the inward interaction (Q3) and the ejection events (Q2). This maximum value of sweep event occurred at the upstream side of a column where the horseshoe vortex and

strong down flow took place. According to Lu and Willmarth (1973), sweep event is associated with high speed flow that is faster than the average streamwise velocity and slower than the average vertical velocity. Hence, the excavated bed material from the upstream side is easily transported to the downstream side. This shows that the bridge piers experience the maximum scour depth at the upstream side. Furthermore, the maximum values of P_i close to the bed at $Z/D < 2$ have been observed in the sweep and ejection events. Additionally, the results from for the upstream side of the single column indicate that the value of P_i of ejection event decreases as the distance from the bed increases towards the free surface.

This trend is consistent with the results presented by Keshavarzy and Ball (1997) and Izadinia et al. (2013). Probability of occurrence profile of sweep event for the upstream side of the single column case shows the higher values of P_i throughout the flow depth. The above results indicate that the sweep event is the most important bursting events for the entrainment of sediment particles. At the downstream side of the single column case, profile plots of probability of occurrence of each quadrant are presented in Figure 5.62. The figure reveals that P_i for ejection event in the wake is observed at a maximum close to the bed. A similar result is also reported by Izadinia et al. (2013). As discussed in Section 4.4.1, strong upward flow exists at the wake of the column. Occurrence of a maximum value of the probability of occurrence of ejection event and strong upward flow in the wake of a column make the sediments become suspended. However, comparing the depth average probability of occurrence, the outward interaction was the dominant event, followed by the ejection, the sweep and the inward interaction events. As reported by Keshavarzi et al. (2014), outward interaction results in the force vectors being directed towards the water surface and inward interaction results in the force vectors directed opposite to the mean flow direction. Hence, outward and inward interactions were not effective for the entrainment of sediment.

L/D = 0, Y/D = 0, US1

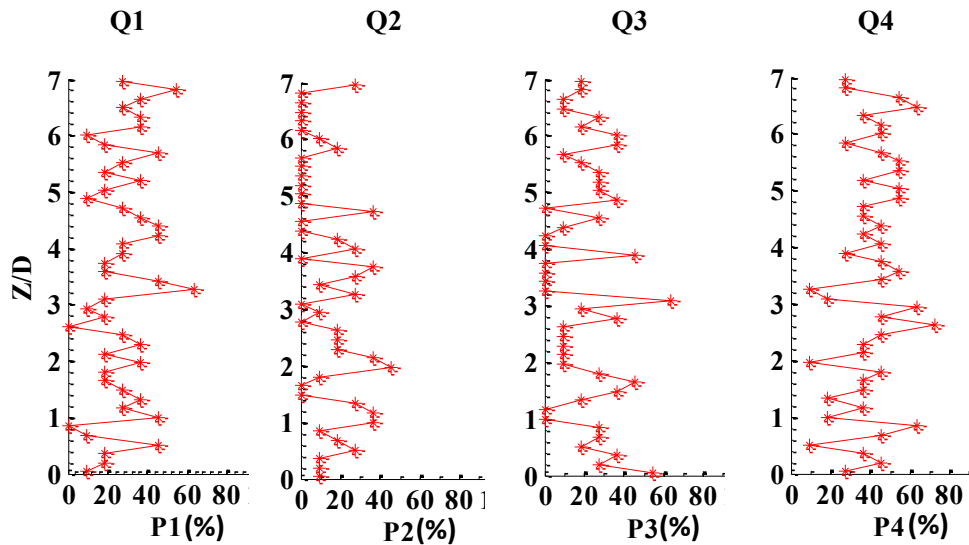


Figure 4.61 Profile plots of probability of occurrence of different quadrants at upstream side (US1) for single column case

L/D = 0, Y/D = 0, DS1

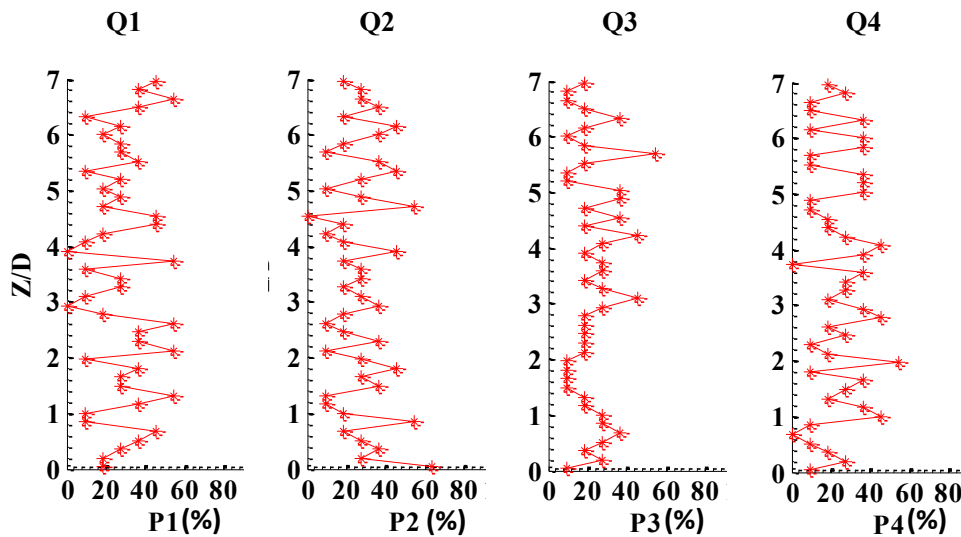


Figure 4.62 Profile plots of probability of occurrence of different quadrants at downstream side (DS1) for single column case

Figures 5.63 to 4.65 show the profile plots of the probability of occurrence of each of the four events for the two in-line columns case with $L/D = 3$. Considering these figures along with the figures presented in Appendix E.1, the results indicate that at the upstream side

of Column 1 for all values of L/D , the highest value of P_i occurs in a sweep event as in the single column case. Comparing the depth average probability of occurrence of a sweep event for different values of L/D indicates that the value of P_i at the upstream side of Column 1 increases as the spacing between the two columns increases until $L/D = 3$. Further increase in the spacing results in a decrease in the value of P_i of a sweep event. However, the values of P_i of a sweep event at the upstream side for two column cases were higher than those for the single column case. As described in Section 4.3.1, in the two in-line column cases, the shear layer separated from Column 1 was extended more than that of the single column case to the downstream side. This is the indication of a larger extension of horseshoe vortex legs towards the downstream side. According to the simulation results observed by Kirkil et al. (2008), transport of bed sediment is associated with the motion of the vortical structure detached from the leg of the primary horseshoe vortex and the sweep event of turbulent burst phenomenon close to the bed. This supports the fact that the higher scour depth is observed for the two-column case rather than for the single column. While considering the ejection event at the upstream side of Column 1, it is observed that for $L/D = 1$, the average value of P_i is similar to the single column case. For $L/D > 1$, a significant decrease in the average value of P_i for ejection event was observed. However, gradual increase in the value of P_i of ejection event was noticed with increase in the spacing between the two columns. Considering the distribution of P_i in outward and inward interaction events, for all values of L/D at the upstream side of Column 1, the average value of P_i in outward interaction was higher than in inward interaction. Furthermore, it was common to all of the cases that the value of P_i in inward interaction event increased with increase in the distance from the bed towards the free surface.

Between two columns, the profile plots for the case of $L/D = 2$ and 3, only one point was selected to analyse the probability of occurrence of events. However, for $L/D > 4$, two points, one at the downstream side of Column 1 and another point at the upstream side of Column 2, were selected for analysis. For $L/D = 2$, the probability of occurrence of ejection and sweep events (dominant events) were approximately the same. Similar results were observed in the case of $L/D = 3$. However, the value of P_i in sweep event decreased as the spacing increased from $L/D = 2$ to 3, whereas, the value of P_i in ejection

event increased. For $L/D = 2$, P_i of outward interaction and inward interaction were similar. Further increase in the spacing resulted in a decrease in P_i of sweep event. The probability of occurrence of ejection event at the downstream side of Column 1 increased until $L/D = 3$. For $L/D > 3$, a gradual decrease in the value of P_i was observed. Comparing these results with the single column case shows that P_i of ejection event remains approximately the same for the downstream side of a single column and Column 1 of the two columns cases. However, the value of P_i in sweep event at the downstream side of Column 1 is higher than that of the single column case. As the flow approaches Column 2 for $L/D > 3$, a decrease in P_i of sweep event and an increase in ejection event can be observed.

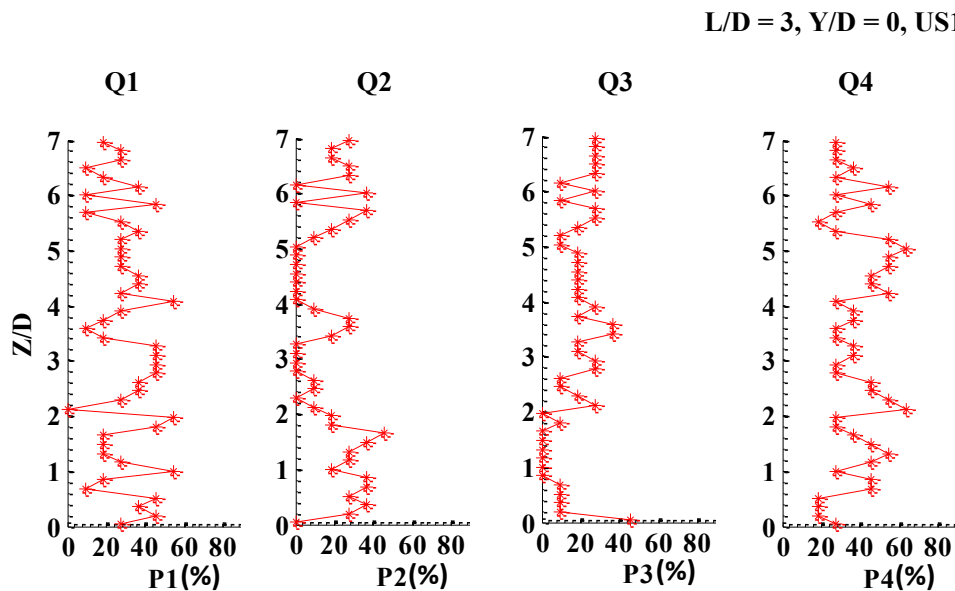


Figure 4.63 Profile plots of probability of occurrence of different quadrants at upstream side (US1) of Column 1 for the twocolumn case with $L/D = 3$

At the downstream side of Column 2 in two-column cases, the results reveal that inward interaction is dominant. Considering ejection and sweep events for all values of L/D , reveals that the probability of occurrence of ejection event is higher than that of sweep event. Furthermore, the results indicate that increase in the spacing between two columns results in decrease in the probability of occurrence of ejection and sweep events. While comparing the results with the single column case, for $L/D = 1$, slight increase in P_i of

sweep and ejection events occurred. However, for $L/D > 1$, the values of P_i in sweep and ejection events were observed significantly less than those of the single column case.

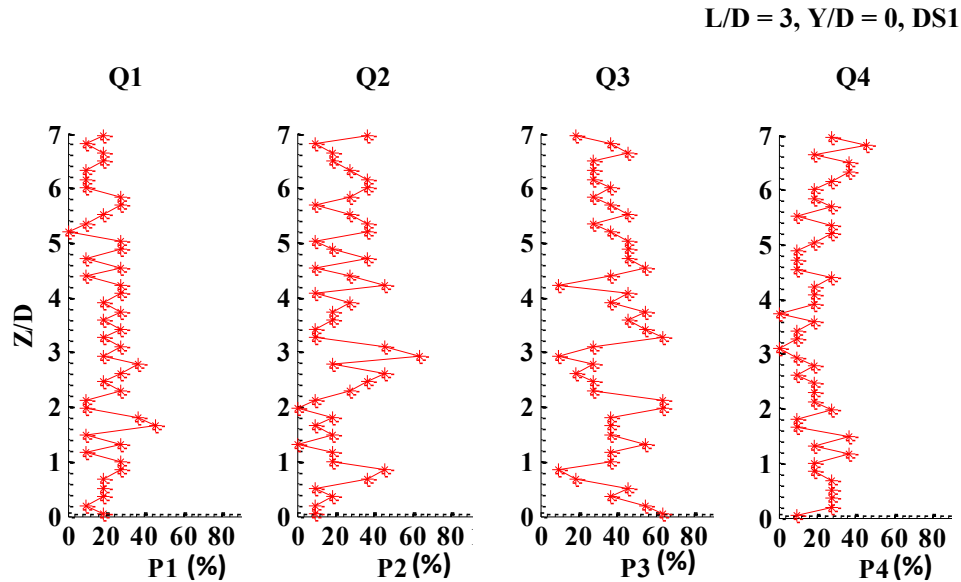


Figure 4.64 Profile plots of probability of occurrence of different quadrants at downstream side (DS1) of Column 2 for two columns case with $L/D = 3$
 $L/D = 3, Y/D = 0, B1$

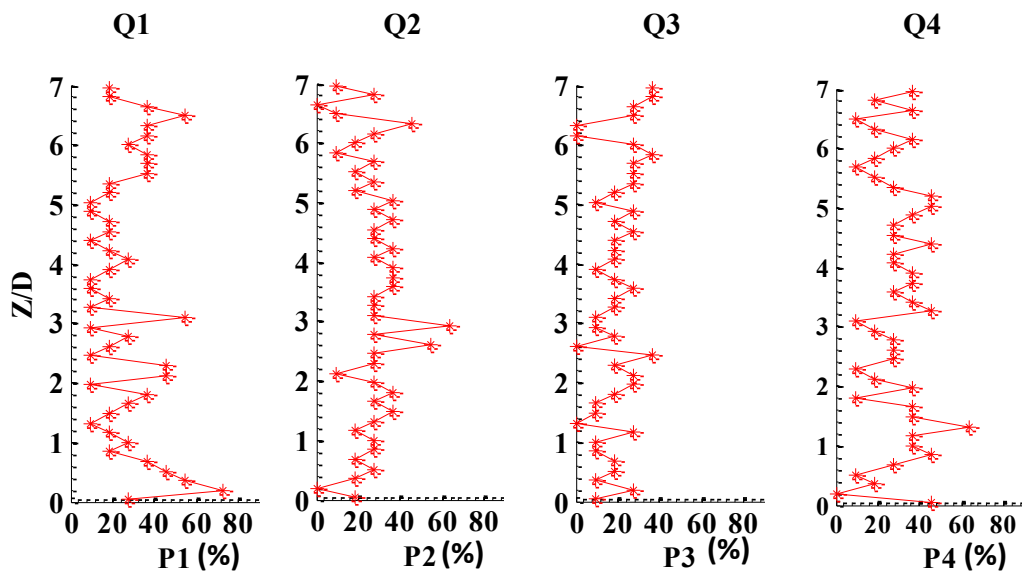


Figure 4.65 Profile plots of probability of occurrence of different quadrants between two columns (at B1) with $L/D = 3$

The contribution of each quadrant for production of Reynolds stresses has also been analysed based on the stress fraction. Contribution of shear stress fractions of four events

are presented in Figures 4.66 to 4.70 and Appendix E.2. Figure 4.66 shows the profile plots of the stress fraction of each event at the upstream side of a single column bridge pier. The results at the upstream side (US1) of the single column case indicate that the depth-average stress fraction for sweep events has a higher contribution in the production of Reynolds stresses than the ejection event. This is because of the existence of down flow at the upstream side of the column and the result is consistent with the findings by Yang (2010). He reported that down flow is associated with sweep event. Furthermore, the figures exhibit that contribution of S_i for sweep and ejection events decreases towards the free surface. At the downstream side of the single column case, S_i for ejection event is observed higher than that of sweep event. This is due to the strong upward flow in the wake of a column. According to Yang (2010) ejection is associated with upward flow and produces higher Reynolds stresses than sweep event. Lu and Willmarth (1973) also reported that about 77% of the contribution to the Reynolds stress is produced by the ejection event. They further reported that the sweep event also significantly contributes to the production of Reynolds stress. It was found that the distribution trend and magnitude of S_i for the sweep and ejection events were similar. Additionally, it is clear from the figures that at the downstream side of the column, S_i fluctuates more strongly than at the upstream side.

For two in-line columns cases, the contribution of S_i of each event for the production of Reynolds stresses at the upstream side of Column 1 are presented in Figure 4.68 and Appendix E.2. As in the case of the single column, S_i of ejection and sweep events close to the bed at the upstream side of Column 1 are dominant for all values of L/D . However, at higher depth, outward interaction and inward interaction are associated with higher values of S_i . Similar results were also reported by Izadinia et al. (2013).

L/D = 0, Y/D = 0, US1

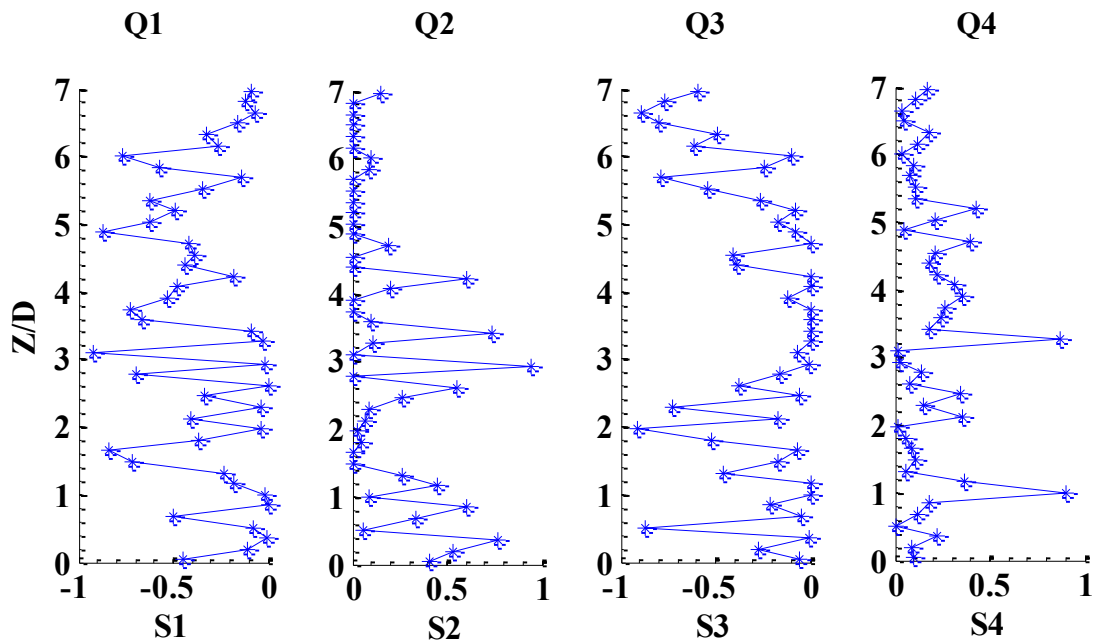


Figure 4.66 Profile plots for contribution of stress fraction of different quadrants for the production of Reynolds stress at upstream side of single column

L/D = 0, Y/D = 0, DS1

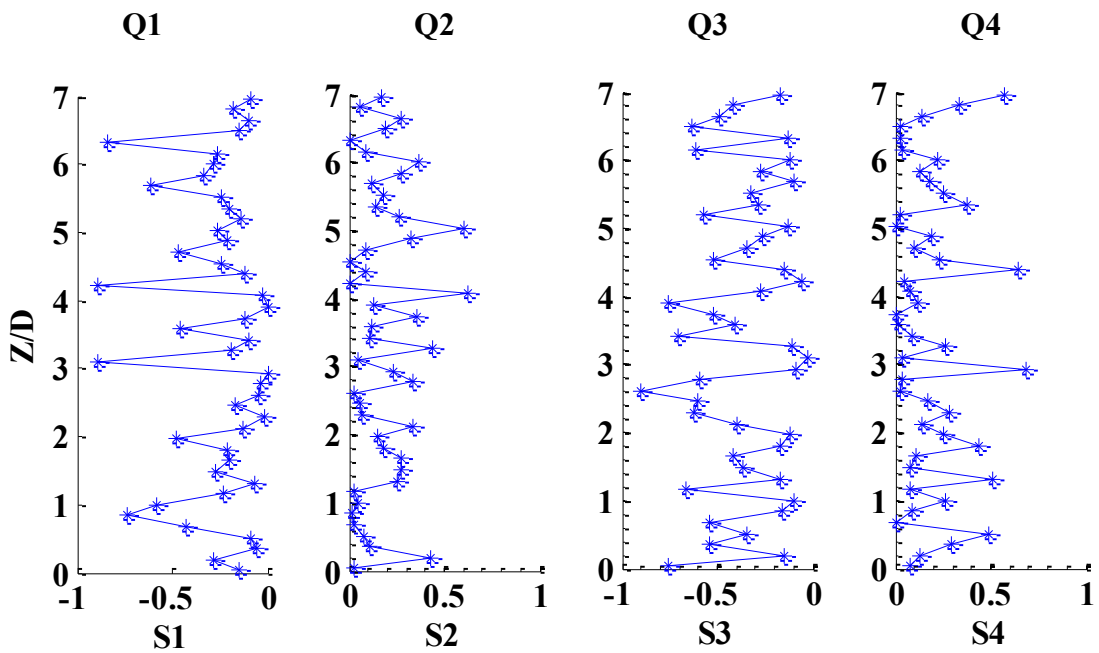


Figure 4.67 Profile plots for contribution of stress fraction of different quadrants for the production of Reynolds stress at downstream side of single column

At the downstream side of Column 1, the value of S_i was higher for the ejection event. Comparing this value with the single column case, the value of S_i for the ejection event at the downstream side of Column 1 was higher for all values of L/D . Furthermore, the maximum value of S_i is observed for $L/D = 2$. This is due to strong turbulence in the wake of Column 1, as described in Section 4.4.2. As suggested by Yang (2010), strong turbulence intensities and hence the maximum Reynolds shear stress are associated with upward flow, particularly in the wake of a column. Hence, the high values of turbulence characteristics keep the sediments in suspended form. Gradual decrease in the value of S_i for an ejection event at the downstream side of Column 1 was observed while increasing the value of L/D . For $L/D > 3$, at the upstream side of Column 2, outward interaction and inward interaction became dominant. According to Mianaei and Keshavarzi (2010), domination of outward interaction and inward interaction is associated with the deposition of sediment. Hence, the suspended sediments are expected to deposit at the upstream side of Column 2. However, down flow and horseshoe vortex close the upstream face of Column 2 keep the sediments entrained. Similar to the downstream side of Column 1, the maximum value of S_i for the ejection event occurred close to the bed at the downstream side of Column 2. However, considering the depth average value of S_i for the sweep and ejection events at the downstream side of Column 2 indicated a significant contribution in production of Reynolds stress. As the spacing between two columns increased, contribution of the ejection and sweep events in the production of Reynolds stress increased. Comparison revealed that the value of S_i of the ejection and sweep events at the downstream side of Column 2 for all values of L/D was less than that of Column 1.

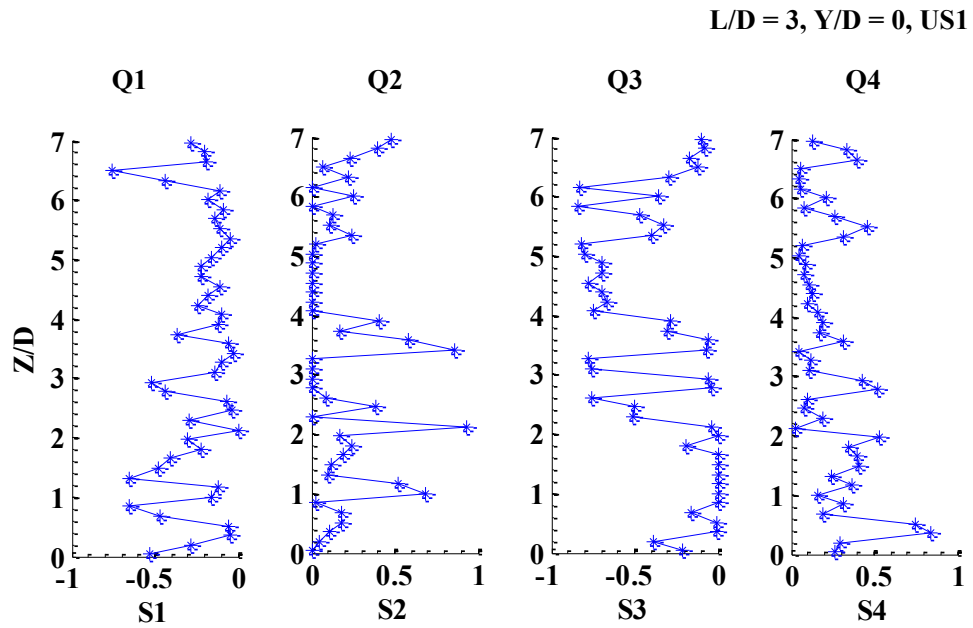


Figure 4.68 Profile plots for contribution of stress fraction of different quadrants for the production of Reynolds stress at upstream side of Column 1 for two columns case with $L/D = 3$

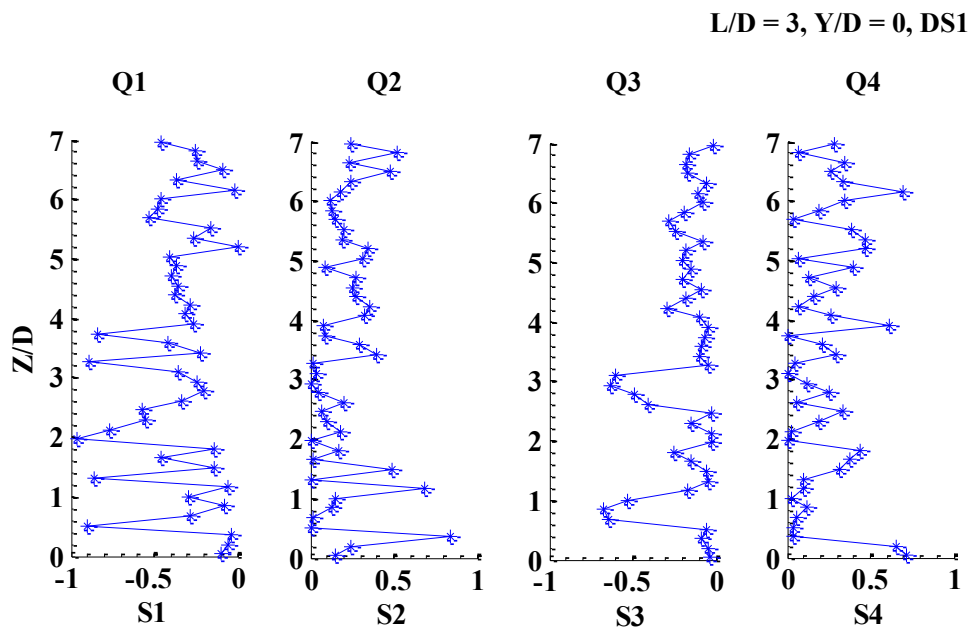


Figure 4.69 Profile plots for contribution of stress fraction of different quadrants for the production of Reynolds stress at downstream side of Column 2 for two columns case with $L/D = 3$

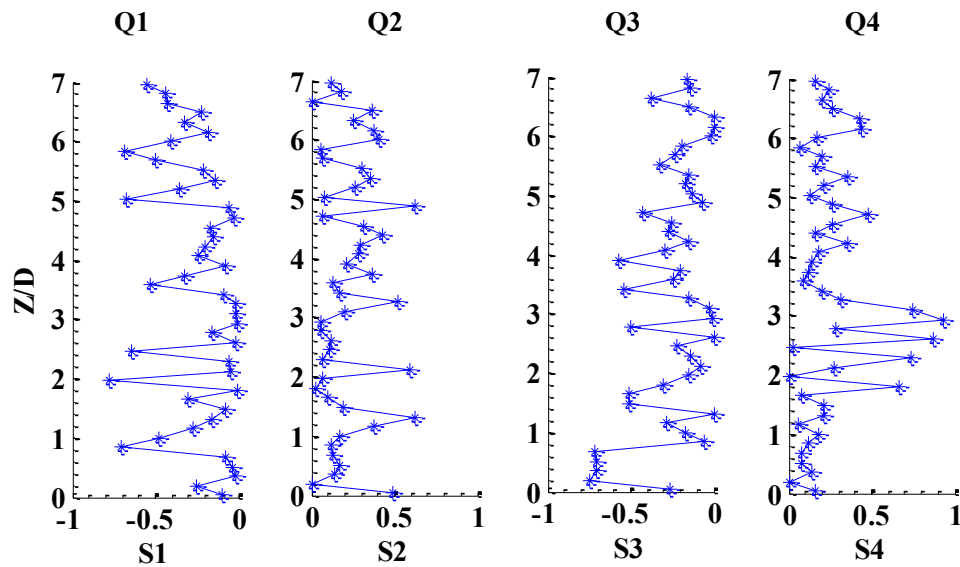


Figure 4.70 Profile plots for contribution of stress fraction of different quadrants for the production of Reynolds stress between two columns with $L/D = 3$

4.6 Summary

The detailed results from the experimental study of flow structures around bridge piers comprising a single column and two in-line columns with varying spacing between them have been presented in this chapter. The measured instantaneous velocity components were analysed and the results for flow field and turbulence characteristics have been presented in graphical forms using vector plots, streamline plots, contour plots and profile plots.

The vector plots and the streamline plots in horizontal planes for the single column case indicated that the wake of the column experienced reverse flow and recirculation. Close to the bed, the shear layer, which had separated from the side of the column, converged at farther distance than that in the upper levels. At the upstream side of the column, there was a generation of down flow. At the immediate downstream side, reversal and upward flows were observed. The maximum value of up flow was at a distance of $2D$ from the downstream side of column at which the flow was separated. In the two in-line columns case, for $L/D < 2$, reverse flow and recirculation was observed only in the wake of Column 2. The shear layer separated from Column 1 wrapped around Column 2 and the horseshoe vortex was formed only in the front of Column 1. When $L/D \geq 3$, it was found that the

flow between the two columns was separated at a distance of $2.5D$, measured from the downstream face of Column 1. Two separate horseshoe vortices were observed in front of both Column 1 and Column 2, and the rotation of flow occurred behind both columns. Furthermore, it was noted that the wake behind the single column was larger than that of the two-column cases.

The results from the contour and profile plots of three dimensional velocity components in horizontal and vertical planes for the single column case indicated that higher values of the streamwise velocity component (u/V) occurred at the side of the columns. Negative values of u/V were observed in the wake of the column, exhibiting the reverse flow in this region. The maximum transverse velocity component (v/V) was observed at the upstream side of the column near the zone of shear layer separation. At the upstream side of the column, a negative value of vertical velocity component (w/V) was observed, indicating the down flow. Significant fluctuation of w/V occurred up to the distance of $4D$ measured from the downstream face of the column. For the two in-line columns case with $L/D \leq 3$, in the gap region, reverse flow was extended throughout the gap between the two columns. Very small deflection of flow was noticed inside the gap. However, at the downstream side of Column 2, higher values of v/V were recorded with values approximately equal to those of the single column case. The contour plots demonstrate that the strength of reverse flow at the wake of Column 2 increases with an increase in the value of L/D . Furthermore, it was observed that the magnitude of u/V at the downstream side of the single column was constantly higher than that of the other cases. Considering the w/V component of flow for the two-column case with $L/D = 2$, the gap experienced positive values of w/V , showing the existence of up flow throughout the gap. As the spacing between the two columns increased, a stronger up flow occurred compare to that of $L/D = 2$. For $L/D > 3$, a horseshoe vortex in front of Column 2 was formed near the base of the column. However, the size of the horseshoe vortex was smaller than that of Column 1, which could be due to the shielding effect of Column 1.

The results on turbulence intensity in three different horizontal planes showed that the columns experienced very weak turbulence intensity at the upstream side of the columns with similar behaviour for all cases of column arrangements. The maximum value of turbulence intensity occurred in the wake of the columns. For all combinations of the

columns, the value of Tl_u/V was greater than the component Tl_w/V , whereas the turbulence intensity in the transverse direction, Tl_v/V , was much larger than Tl_u/V and Tl_w/V . The value of turbulence components increased with an increase in the spacing between the two columns. At the downstream side of Column 2, the values of turbulence intensity components were smaller than the values measured in the single column case and between two-column cases with different spacing. This could be due to sheltering by Column 1 resulting the reduction in effective approach velocity for Column 2. The distribution of turbulent kinetic energy (TKE) was similar to the distribution of turbulence intensities. The maximum value of TKE/V^2 took place between the gap, when $L/D = 3$. The results indicated that the value of TKE/V^2 increased as the spacing between the two columns increased up to $L/D = 3$. Further increase in spacing resulted in a decrease in the value of TKE/V^2 .

The results on the Reynolds shear stresses in different horizontal planes along the axis of symmetry indicated that the absolute value of $-\overline{u'v'}/V^2$ was higher than that of $\overline{u'w'}/V^2$ and $-\overline{v'w'}/V^2$. The maximum values of Reynolds shear stresses were observed close to the bed in the wake of the columns. Absolute values of $-\overline{u'v'}/V^2$ in the wakes for both columns in the two-column cases were smaller than those in the case of the single column. In the wake of Column 2, absolute values of $-\overline{u'v'}/V^2$ were observed increasing with increase in the spacing until $L/D = 3$. Further increase in spacing resulted in a decrease in the absolute value of $-\overline{u'v'}/V^2$ in the wake of Column 2. The values of $-\overline{u'w'}/V^2$ and $-\overline{v'w'}/V^2$ in the wake of Column 2 were approximately the same, about 50% smaller than the values of the single column case. Furthermore, absolute values of $-\overline{u'w'}/V^2$ were higher close to the bed in the wake and decreased to zero towards the free surface. It was noticed that the value of $-\overline{u'w'}/V^2$ decreased with increase in the spacing between two columns. Higher values of $-\overline{u'w'}/V^2$ were observed close to Column 1 and gradually decreased as the flow approached Column 2.

The quadrant analysis technique was employed to explore the contribution of each quadrant for the production of Reynolds shear stresses. Analysis was carried out based on the probability of occurrence and the stress fraction of each quadrant. According to the probability of occurrence at the upstream side of the single column case, the sweep

event was dominant. Hence, a sweep event was considered as one of the most important bursting events. The depth average probability of occurrence in the wake of a column showed that the outward interaction was the dominating event. However, the probability of occurrence of the ejection event was higher than that of the sweep event. Hence, sediments in the wake of the column were expected to be in the suspended form. The results for the two-column cases indicated that at the upstream side of column 1, the sweep event was dominant. The probability of occurrence of the sweep event increased with increase in the spacing between the two columns until $L/D = 3$. Further increase in the spacing resulted in a decrease in the value of P_i of the sweep event. However, the values of P_i of the sweep event at the upstream side for two in-line columns cases were higher than that of the single column case. For $L/D > 1$, the values of P_i in the sweep and ejection events behind Column 2 were significantly less than those of Column 1 and the single column case. The stress fraction analysis indicated that outward and inward interactions were contributed strongly to the production of Reynolds stresses at the upstream side of all columns arrangements. For the two in-line column cases, behind Column 1, the ejection event was dominant and reached the maximum value when $L/D = 2$. Considering the sweep and ejection events at the downstream side of Column 2, contribution of S_i for the ejection event was higher than that of the sweep event. As the spacing between the two columns increased, the contribution of the sweep event in the production of Reynolds stresses increased. Hence, it can be concluded that between and at the downstream side of the two columns arrangements, there was a significant contribution of the stress fraction of all quadrants to the production of Reynolds stresses.

CHAPTER 5

RESULTS AND DISCUSSION ON LOCAL SCOUR



5.1 Introduction

5.2 Review on Scour around Bridge Piers

5.3 Temporal Development of Scour Depth

5.4 Equilibrium Scour Depth for Two-Column Case

5.5 Comparison of Observed and Predicted Maximum Scour Depth

5.6 Scour Profile along Line of Symmetry of Bridge Piers

5.7 Width of the Scour Hole

5.8 Summary

5. RESULTS AND DISCUSSION ON LOCAL SCOUR

5.1 Introduction

In this chapter local scour around a bridge pier with a single column and two in-line circular columns with different spacing are analyzed and presented. Local scour depths around two in-line circular columns are compared with the scour depth around a single column. Furthermore, this chapter exhibits the description on the temporal variation of scour depth, bed profile after scouring and characteristics of scour hole. Additionally, a semi-empirical equation is developed to capture the effect of spacing between two in-line circular columns on the scour depth.

5.2 Previous Investigations on Scour around Bridge Piers

In the history of bridge collapse, local scour around bridge piers is found to be one of the main causes of failure. Local scour around bridge piers has been extensively studied and numerous scour prediction equations have been developed by several investigators. Most of the previous studies were based on scour prediction around a single column and the process has been studied extensively, for example Laursen and Toch (1956); Melville (1975); Raudkivi and Ettema (1985); Melville and Sutherland (1988); Breusers and Raudkivi (1991); Yanmaz and Altinbilek (1991); Dey et al. (1995); Melville and Coleman (2000); Khwairakpam et al. (2012) Radice and Tran (2012). However, in real situations, employing two or more columns are very common in practice. Only a few investigations have been made on the group of columns providing little knowledge on scour patterns. Hannah (1978); Salim and Jones (1998); Richardson and Davis (2001); Sumer et al. (2005); Ataie-Ashtiani and Beheshti (2006); Mubeen-Beg (2010); Domenech et al. (2011); and Amini et al. (2012) have conducted various investigations on scour around bridge piers consisting of multiple columns.

Laursen and Toch (1956) conducted experimental studies on different models of bridge piers and abutments. The model bridge pier consisted of two shafts joined with a web. Three-hour long experiments were conducted both in the absence and in presence of webs at different values of the angle of flow attack. In the case of the pier without a web, it was concluded that for small angles of approach (0 to 10 degrees) the downstream shaft was

shielded by the upstream shaft resulting in smaller scour depth at the downstream shaft. Additionally, it was suggested that a separate scour hole for each shaft was formed. On comparison of scour depth results for circular and rectangular shape piers, it was reported that the equivalent rectangular pier produced about 15% more scour depth than that of the circular pier.

Hannah (1978) conducted a series of experimental investigation on scour around single and multiple columns with tandem and side by side arrangements for different spacing between the columns. He has conducted seven-hour experiments for the scour depth and proposed an adjustment factor of 1.25, which was multiplied to seven hours scour depth to extrapolate the equilibrium scour depth. Furthermore, he conducted two- column experiments, varying both the spacing and the angle of attack. It was concluded from those experiments that the equilibrium scour depth first attained at the upstream column followed by the downstream column. It was reported that when $L/D = 1$ i.e. two columns were attached to each other, the scour depth around the two-column system was equal to the scour depth around the single column case. Furthermore, it was reported that an increase in spacing between two columns resulted in increase in experience of reinforcing effect, reaching a maximum at $L/D = 2.5$ and is evident up to $L/D = 11$. Reinforcing effect occurs when the downstream column is placed so that the columns' scour holes overlap. This aids in the sediment removal around the upstream column increasing its scour depth. Additionally he proposed the coefficients to be applied to the single pier scour depth for the determination of scour depth around two columns.

Nazariha (1996) conducted a series of experimental tests for the study on local scour around bridge piers consisting of single and two columns. The experimental tests were conducted for 2 hours duration and clear water flow conditions were applied for all tests. Additionally an experiment with 90 hours duration was carried out for the study of temporal variation of the scour depth. It was reported that more than 83% of total scouring occurred within the first two hours. Hence, equilibrium scour depth was determined using a factor of 1.4, applied to the observed scour depths after 2 hours duration. For the two-column cases, the effects of different angle of attack and spacing between two columns were investigated. According to the experimental results, it was concluded that the greater the value of angle of attack, the larger were the equivalent diameter of the pier and the

scour depth consequently. On the other hand, from the experiments of two columns with zero angle of flow attack, it was reported that for the spacing of $L/D = 1$, the scour depth was equal to that of the single column case. An increasing trend of scour depth was reported for the range of $1 < L/D \leq 4$. After this, the scour depth was decreased and ultimately reached the value of scour depth for the single column case. Furthermore it was reported that a separate scour hole was formed around the two columns when $L/D > 5$.

Salim and Jones (1998), studied the scour around pile groups and observed that the scour depth around the pile group decreased as the spacing between the piles increased. According to Sumer et al. (2005), scour around piles group was caused by the local scour mechanism around an individual pile and generated by the global scour mechanism over the entire area of the pile group. They further described the geometrical characteristics of the scour hole. Ataie-Ashtiani and Beheshti (2006), conducted an experimental investigation on scour around a group of piles including two piles in tandem arrangement and concluded that the maximum scour depth around two piles arranged in tandem arrangement increases with increase in the spacing between the piles. They observed that the maximum scour depth occurs at the upstream pile when the value of $L/D = 3$. In the case of scour depth at the downstream pile, scour depth at this pile is always smaller than the single pile case. The reason behind this condition was explained by the fact that the horseshoe vortex at the downstream side pile was smaller than the single pile case and the existing live bed conditions. Furthermore, it was reported that the scour depth at the piles with spacing of $3D$ was 20% more than the scour around a single pier. In this study, a number of correction factors to predict the maximum local scour depth for the pile group were developed considering the base equations given by Melville and Coleman (2000) and Richardson and Davis (2001).

Hager and Unger (2010) investigated the effect of a single-peaked flood wave on pier scour under clear water scour of a cohesion-less material. In this study, temporal scour development along with the end scour depth were presented in terms of particle Froude number based on the maximum approach flow velocity and the mean sediment size. The results of that study indicated that the end scour depth depended on the peak approach flow velocity.

Amini et al. (2012) investigated the clear water local scour for a range of submerged and unsubmerged pile groups (Submerged pile group: the pile groups are capped below the water surface. Unsubmerged pile group: the pile groups are capped above the water surface, only pile groups obstruct the flow.) in different configurations and concluded that the scour depth was dependent on the pier diameter, the pile spacing and the submergence ratio (the ratio of approach flow depth to the height of pile relative to the undisturbed streambed). An empirical relationship to predict the local scour depth was developed, giving the effect of pile group arrangements, pile spacing and submergence ratio on local scour.

It is clear from the above review that only a few studies have been carried out on scour around bridge piers consisting of multiple columns and have not provided the correlation of the flow structure and the scour depth. Reliable equations have not been well developed for the prediction of scour depth around the bridge piers with multiple columns. Hence, in this study, detailed investigation on local scour around bridge piers comprising two in-line circular columns are carried out which is applicable and useful for practicing bridge engineers. The results of this study quantify the effects of the spacing between two columns on the maximum scour depth by an appropriate equation. Meanwhile, the results obtained are correlated with the flow structures around single and two in-line circular columns. The results can be used to facilitate the position of piers when scouring is a design concern.

5.3 Temporal Development of Scour Depth

The measured data of the experiments as described in Section 3.4.2 are plotted in Figures 5.1 and 5.2. These figures show the temporal development of scour depths around the upstream column (Column 1) and the downstream column (Column 2) for test duration up to 75 hours. The temporal development of the scour depth for a single column and two in-line circular columns with different spacing ($1D$, $2D$ and $3D$) are monitored and plotted as shown in Figures 5.1 and 5.2.

Analysing the scour depth results, illustrated in Figure 5.1 revealed that the scour depth was rapidly developed for the first ten hours of the test duration. Approximately 90% of the total scour depth was achieved in this duration. The scour depth after 72 hours

duration was about 99% of equilibrium scour depth, calculated using Equations 2.12-2.14. The rate of scouring continuously reduced with time, and after 72 hours, the development of scour was very slow. Hence, the maximum duration of the tests was between 72 and 75 hours.

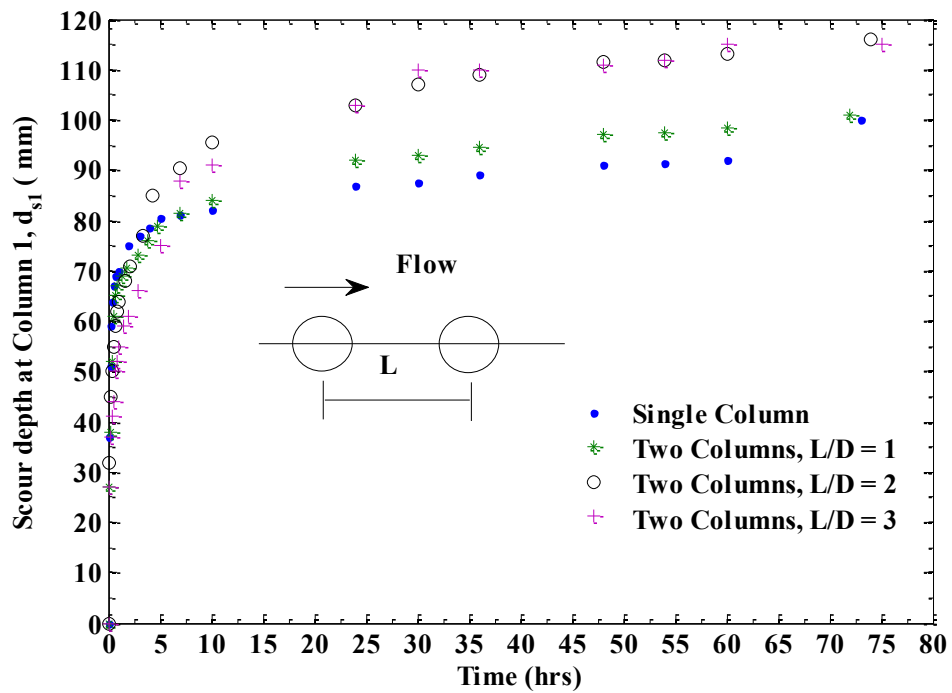


Figure 5.1 Temporal development of scour depth at Column 1 for a single column and two columns with $L/D = 1, 2$ & 3 ; Time, $t = 72-75$ hours and $V/V_c = 0.74$.

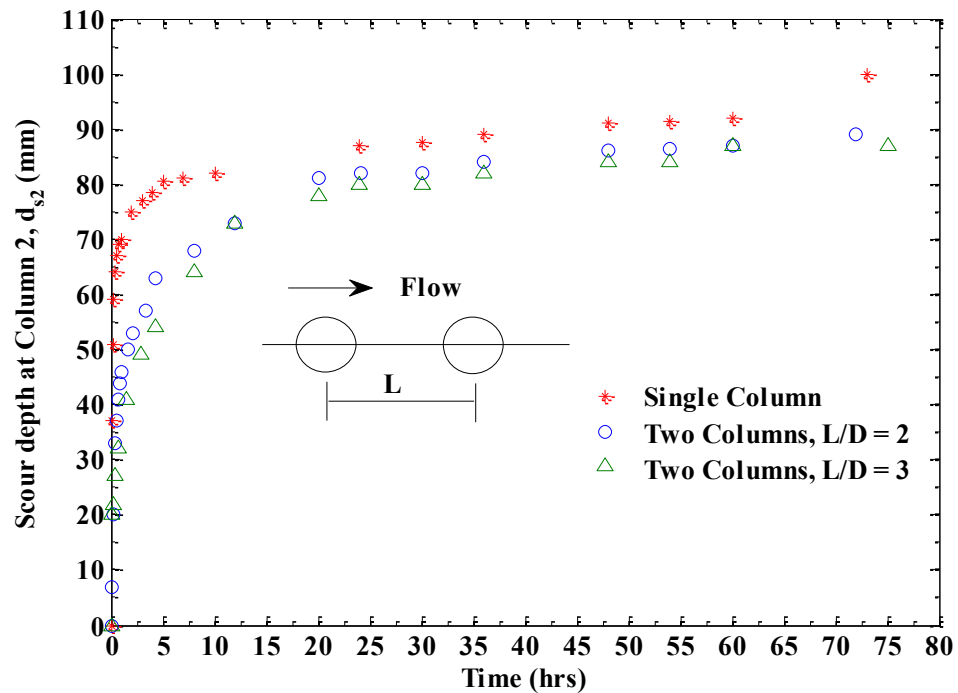


Figure 5.2 Temporal development of scour depth at Column 2 for a single column and two columns with $L/D = 2$ & 3 ; Time, $t = 72-75$ hours and $V/V_c = 0.74$.

In order to determine the equilibrium scour depth, a time factor (K_t) has been applied to extrapolate the scour depth. The time factor has been calculated using the expressions developed by Melville and Coleman (2000) as presented in Equations 2.34 – 2.36.

The time factor K_t (72 hours) was calculated as 0.99, i.e. 99% of the equilibrium scour depth. The present study satisfies the condition of Equation 2.36. Hence, Equations 2.14 and 2.36 have been used to calculate t_e and K_t (72 hours), respectively and presented in Table 5.1. In order to compare the present results with the scour depth predicted using existing equations, a factor ($1/K_t$) is applied to the scour depth d_s , obtained from this study in 72 hours. The value of scour depth thus obtained is extrapolated equilibrium scour depths, which are comparable to the predicted scour depth.

Table 5.1 Time for equilibrium scour depth and time factor K_t

Test No.	h/D	V/V_c	t_e days	K_t (72 hours)
1	2.09	0.74	3.34	1.002
2	2.91	0.91	3.34	1.001
3	2.73	0.93	3.36	1.001

Figure 5.2 shows the temporal scour development for a single column and two in-line circular columns with $L/D = 2$ and 3. During the experiment, continuous scour development at Column 2 was observed even after 72 hours. However, the rate of scour development was very slow. This demonstrates that the equilibrium scour hole around Column 2 is achieved in a longer duration than Column 1 (in the two-column case) and the single column case. Furthermore, it was observed that the scour depth at the downstream column is continuously less than the scour depth at the single column case. Similar results were observed by Hannah (1978). Furthermore, the results from the temporal development of the scour depth around Column 2 indicated that for the first 20 hours of test duration, the rate of scour development was high. It was observed that about 90% of the maximum scour depth was attained after 20 hours.

5.4 Equilibrium Scour Depth for Two-Column Case

In total 34 test runs were conducted for a single column (4 experiments) and two in-line circular columns (30 experiments) under different flow conditions; the results are presented in Table 5.2. In this table, the observed scour depths around Column 1 and 2 are expressed in a dimensionless parameter using the observed scour depth for the single column at the same flow condition. Similarly, the spacing between two columns (L) is normalised by dividing L by the diameter of the column (D).

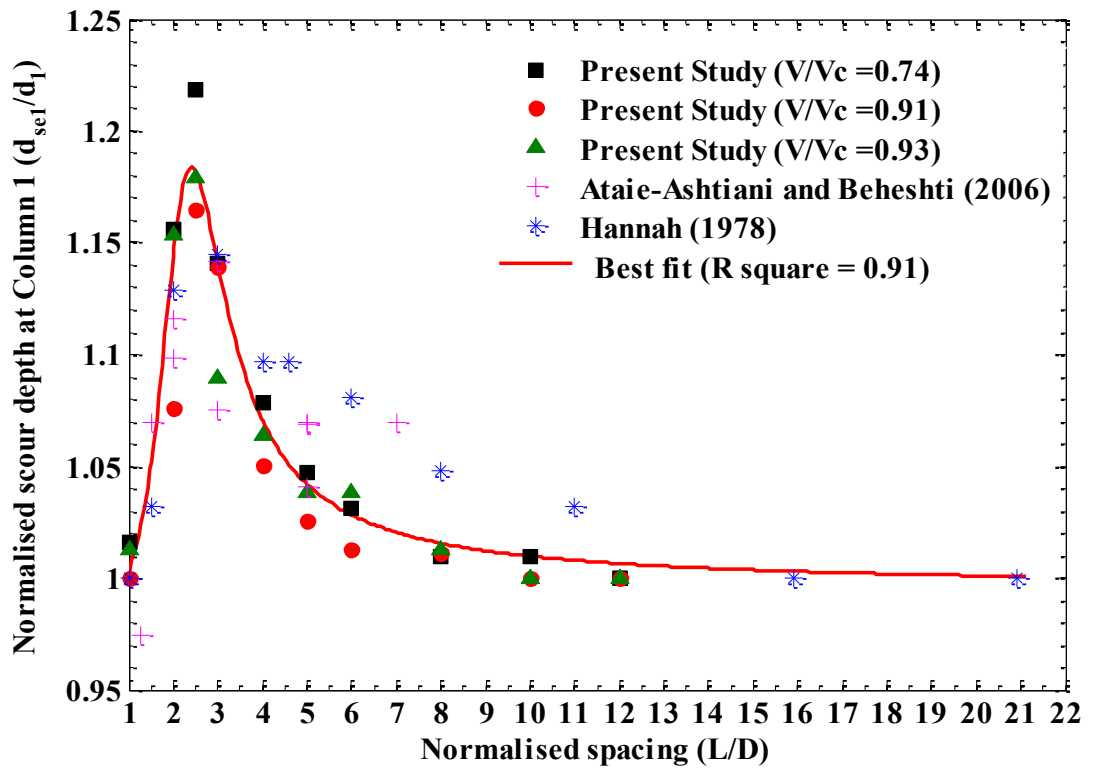


Figure 5.3 Scour depths at upstream column (Column 1) for different spacing between two columns

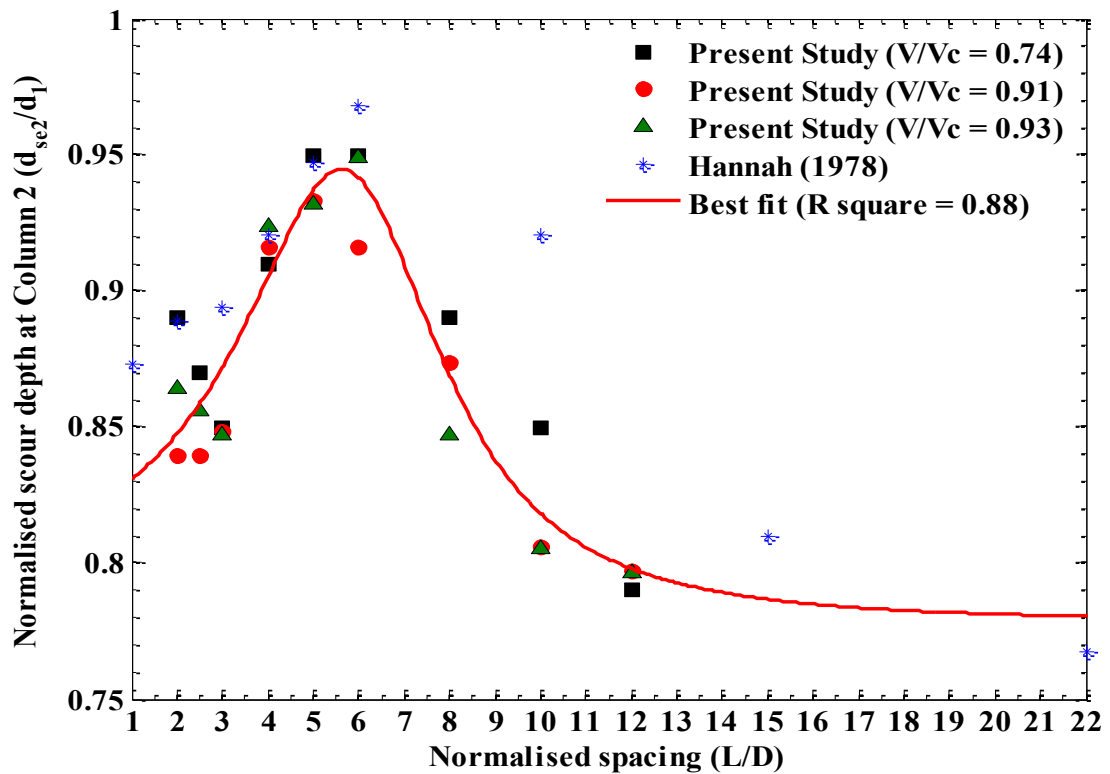


Figure 5.4 Scour depths at downstream column (Column 2) for different spacing between two columns

Figure 5.3 displays the data for the scour depth at Column 1 obtained from experiments of 3 different flow conditions including 34 experimental tests from this study, two sets of experimental data from Hannah (1978) and Ataie-Ashtiani and Beheshti (2006). In Figure 5.3, the equilibrium scour depth, normalised by the equilibrium scour depth at the upstream side of the single column (d_{se1}/d_1), is plotted against the spacing between two columns, normalised by the diameter of a column (L/D). Similarly, Figure 5.4 shows the plots of scour depth data for Column 2 from the present study under different flow conditions. In this figure, the normalised maximum scour depth at Column 2 (d_{se2}/d_1) is plotted against normalised spacing (L/D).

Table 5.2 Test results for different piers arrangements

Run No.	V/V _c	L/D	d ₁ (mm)	d _{se1} (mm)	d _{se2} (mm)	d _{se1} /d ₁	d _{se2} /d ₁
1	0.74	0	100			-	
2	0.91	0	117.9			-	
3	0.93	0	118.5			-	
4	0.93	0	118.0			-	
5	0.74	1		101.5		1.02	
6	0.74	2		115.6	89.5	1.15	0.90
7	0.74	2.5		121.9	87.9	1.22	0.88
8	0.74	3		114.6	85.6	1.15	0.86
9	0.74	4		107.8	91.5	1.08	0.92
10	0.74	5		104.7	96.0	1.05	0.96
11	0.74	6		103.1	96.0	1.03	0.96
12	0.74	8		101.0	89.7	1.01	0.90
13	0.74	10		101.0	85.5	1.01	0.86
14	0.74	12		100.0	79.8	1.00	0.80
15	0.91	1		118.5		1.01	
16	0.91	2		127.5	99.2	1.08	0.84
17	0.91	2.5		138.0	99.5	1.17	0.84
18	0.91	3		135.0	100.0	1.14	0.85
19	0.91	4		124.0	108.5	1.05	0.92
20	0.91	5		121.5	110.4	1.03	0.94
21	0.91	6		120.0	108.0	1.02	0.92
22	0.91	8		119.8	103.2	1.02	0.88
23	0.91	10		118.5	95.4	1.00	0.81
24	0.91	12		118.5	94.1	1.00	0.80
25	0.93	1		119.5		1.01	
26	0.93	2		136.1	102.5	1.15	0.86
27	0.93	2.5		139.2	101.9	1.17	0.86
28	0.93	3		128.6	100.5	1.09	0.84
29	0.93	4		125.5	109.5	1.06	0.92
30	0.93	5		122.5	110.5	1.03	0.93
31	0.93	6		122.5	112.6	1.03	0.95
32	0.93	8		119.5	100.8	1.01	0.85
33	0.93	10		118.0	95.5	0.99	0.81
34	0.93	12		118.0	94.0	0.99	0.79

For Column 1, an equation (a rational second-degree quadratic equation, Rat22) for the best-fit line as shown in Figure 5.3 was derived using the nonlinear least square method with goodness of fit of 0.91 as an R-square value. This relationship is presented in Equation 5.1. Similarly, an equation for the best-fit line of Column 2 was derived with goodness of fit of 0.88 as an R-square value and presented in Equation 5.2.

For Column 1

$$\frac{d_{se1}}{d_1} = \frac{a_1s^2 + a_2s + a_3}{s^2 + a_4s + a_5} \quad 5.1$$

For Column 2

$$\frac{d_{se2}}{d_1} = \frac{b_1s^2 + b_2s + b_3}{s^2 + b_4s + b_5} \quad 5.2$$

where,

a_1, a_2, a_3, a_4 and a_5 , = the model constants for Column 1 obtained experimentally, which are presented in Table 5.3.

b_1, b_2, b_3, b_4 and b_5 , = the model constants for Column 2 obtained experimentally, which are presented in Table 5.3.

d_{se1} = the maximum scour depth at upstream side of Column 1 in the case of two in-line circular columns

d_{se2} = the maximum scour depth at upstream side of Column 2 in the case of two in-line circular columns

d_1 = the equilibrium scour depth at upstream side of the pier in the case of single column

s = the normalised spacing between two columns = L/D

L = the centre to centre distance between two columns

D = the diameter of a column

Table 5.3 Model constants

Column 1		Column 2	
Model Constant	Value	Model Constant	Value
a_1	0.995	b_1	0.780
a_2	-4.165	b_2	-9.155
a_3	5.249	b_3	34.010
a_4	-4.286	b_4	-11.650
a_5	5.360	b_5	41.510

The right hand sides of Equations 5.1 and 5.2 are expressions of column-spacing factor between two columns. Thus the equations can simply be expressed as:

For Column 1

$$d_{se1} = K_{s1}d_1 \quad 5.3$$

For Column 2

$$d_{se2} = K_{s2}d_1 \quad 5.4$$

where, K_{s1} and K_{s2} are the column-spacing factors for Columns 1 and 2, respectively, considering the effect of spacing between two columns, which are functions of s ($=L/D$).

Referring to Figure 5.3, the best-fit line shows the maximum scour depth at Column 1 occurs when the spacing between columns was $2.5D$, which was about 18% higher than the value obtained for the single column. It can be noted that, in actual practice the maximum scour might occur at the spacing between $2D$ and $3D$. When the spacing between columns was $1D$, i.e. two columns touching each other, the scour depth was observed to be approximately the same as the scour depth for the single column case. The

scour depth increased as the spacing between the columns increased up to $2.5D$, and then started to decrease with an increase in the spacing between the columns of the bridge pier. According to Hannah (1978), the reason behind this could be due to the reinforcing effect of Column 2. He further reported that, for the spacing around $2.5D$, the Column 1 experienced the maximum reinforcing effect and this effect existed until the spacing between the two columns was less than or equal to $10D$. In the present study, the experiments were conducted for the spacing up to $12D$. It was observed that the scour depth at Column 1 for spacing more than $10D$ was nearly equal to the scour depth for the single column case. According to Sumer and Fredsoe (2002), the increase in the scour depth around Column 1 can partly be due to the increase in horseshoe vortex flow. It was reported that for $L/D < 3$, the presence of the downstream column caused blockage of flow, resulting in an increase in the size of lee-wake vortices. Hence, a larger horseshoe vortex, formed in front of Column 1, can cause a larger scour depth.

Recalling the results on the flow structures around bridge piers from Chapter 4, it was observed that for $L/D < 3$, vortex shedding occurred only behind Column 2. Hence, the flow pattern was more or less similar to the single column case. However, the turbulence characteristics such as turbulence intensity, turbulent kinetic energy and Reynolds shear stresses were notably different from the single column case. When the spacing was in the range of $2 \leq L/D \leq 3$, stronger turbulence structures were noticed behind Column 1. Generally, more sediments are expected to remain in suspended form, which can easily be washed to the downstream side. Hence, a higher scour depth can be expected at Column 1. Moreover, the results from bursting analysis indicates that the probability of occurrence (P_i) of a sweep event at the upstream side of Column 1 increases as the spacing between two columns increases up to $L/D = 3$. Further increase in the spacing results in decrease in the value of P_i of a sweep event. In addition to this, the values of P_i of a sweep event at the upstream side for two in-line columns cases were observed higher than that of the single column case. This result strongly supports the fact that for the two in-line circular column case, the maximum scour depth can be observed at the upstream side of Column 1, when L/D is approximately equal to 2.5. This shows that the maximum scour depth results obtained in the present study are consistent with the results on flow structures as summarised above.

Figure 5.4 shows the effect of spacing between two in-line circular columns on the maximum scour depth around Column 2. Comparing the results, as indicated in Figures 5.3 and 5.4, clearly illustrates that the scour depth at Column 2 is constantly smaller than the single column case. This is due to the destruction of the horseshoe vortex in front of Column 2. The results on flow structures in Chapter 5 indicated that for $L/D < 3$, only one horseshoe vortex was formed. Two separate horseshoe vortices were generated only when $L/D > 3$. On the other hand, reduction in the velocity approaching Column 2 decreases the effect of horseshoe vortex at Column 2 due to sheltering by Column 1. In addition to this, the results from the bursting analysis indicated that the probability of occurrence of sweep and ejection events at the upstream side of Column 2 were significantly less than that of the single column case. Hence, the above results clearly show a sound correlation between the results on flow structures and scour around Column 2. Furthermore, the results on scour depths indicated that at spacing of $L/D = 2.5$, the scour depth observed at Column 2 was about 75% of the maximum scour depth at Column 1. Additionally, Figure 5.4 indicates that the maximum value of scour depth at Column 2 can be spotted when $5 < L/D < 6$.

5.5 Comparison of Observed and Predicted Maximum Scour Depths

Based on the single column scour depth, Equation 5.3 can be used to predict the maximum scour depth around bridge piers consisting of two in-line circular columns. In this study, different existing equations to predict the maximum scour depth for a single pier as presented in Section 2.3.8 were used to calculate the scour depths for a single column, which is multiplied by column-spacing factors K_{s1} and K_{s2} to predict the corresponding scour depths for two in-line columns cases. However, for the case of predicted scour depth from this study, the observed scour depths around a single column from different sets of experiments were taken and multiplied by column-spacing factors to calculate the predicted scour depths for two in-line columns cases.

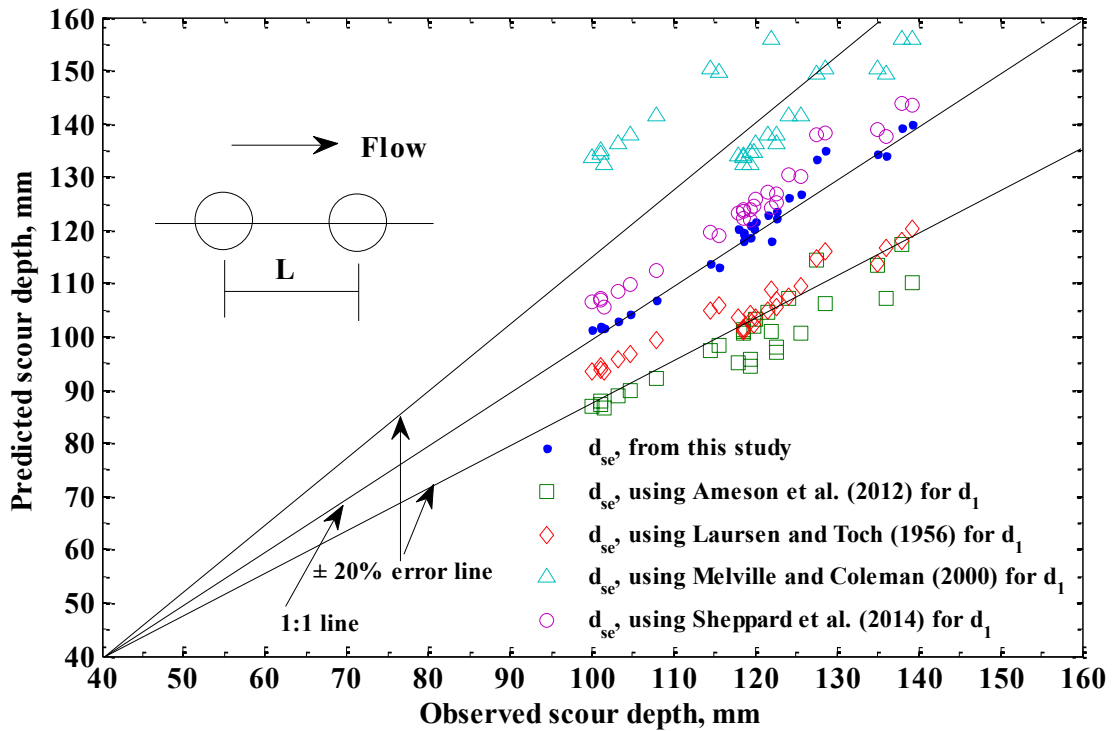


Figure 5.5 Comparison of predicted and observed scour depths for two-column bridge piers

For the comparison of the predicted and the observed scour depths, Equations 2.37, 2.38, 2.44 and 2.48 given by Laursen and Toch (1956), Melville and Coleman (2000), Ameson et al. (2012) and Sheppard et al. (2014), respectively were used to calculate the scour depth around single column and modified by multiplying by the column-spacing factors, K_{s1} and K_{s2} . The predicted scour depths were calculated using the above-mentioned modified equations and the results were compared with the observed scour depths. Figure 5.5 shows the comparison of the predicted and observed maximum scour depths at Column 1. The figure shows that the predicted scour depths using the equation given by Laursen and Toch (1956) consistently under-predict the scour depths. However, the prediction falls within the $\pm 20\%$ error lines. Similarly, the predicted scour depths using the equation proposed by Ameson et al. (2012) also under-predict the results, falling outside the $\pm 20\%$ error lines. Results of the experimental study conducted by Ferraro et al. (2013) also show that the HEC-18 methodology, developed by Ameson et al. (2012), under-predicts when estimating the maximum scour depth around bridge piers. On the other hand, Figure 5.5 exhibits that the scour depths predicted, based on the equations

developed by Melville and Coleman (2000) and Sheppard et al. (2014), are consistently over the experimental results. However, the prediction using the equation by Sheppard et al. (2014) is closer to the line of perfect agreement, which is less than 12% over prediction. Hence, it is clear from the above the comparison suggests that the equation by Sheppard et al. (2014) can be considered the most appropriate equation that can be used for reasonable prediction of the maximum scour depth at bridge piers comprising two in-line circular columns.

5.6 Scour Profile along Centerline of the Bridge Piers

Hannah (1978) conducted an experimental study of the bed profile after scouring at the downstream side of the bridge pier. He found that aggraded materials flattened with time. The zone of influence of bridge piers was extended approximately to $3D$ upstream of the front column and $25D$ behind the downstream column and reached the maximum width of $10D$ across the flume at the downstream end of the aggradation zone. Additionally it was reported that the shape of the zone of influence around the bridge pier was similar in both single column and two-column cases.

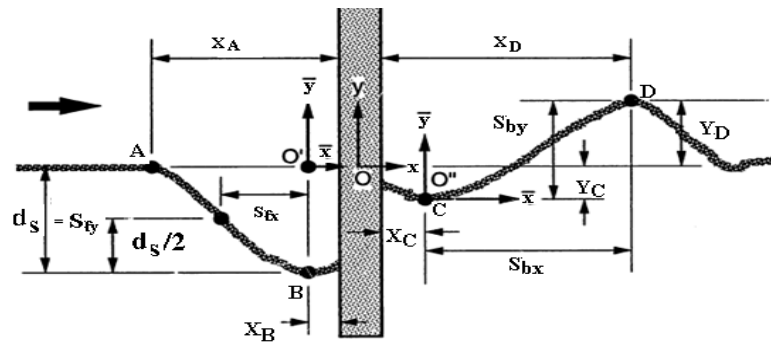


Figure 5.6 Length scale of scour profile (Ahmed (1995))

Ahmed (1995) reported that most of the models of scour developments observed by earlier investigators are primarily based on the similarity of the scour profile. Ahmed (1995) conducted a series of laboratory experiments to study the behaviour of length scale of scour profile as defined in Figure 5.6. He reported that at the upstream side of the bridge pier, the average slope of the scour hole was observed about 35° , which is approximately equal to the angle of repose of bed materials. Furthermore, the upstream extent of the scour hole was reported larger for the finer bed material and smaller for the

coarser material. Similarly, it was concluded that the extent of the scour hole at the downstream side of the bridge pier depended on the size of the pier. The smaller pier size results in the larger extent of the scour hole at the downstream side.

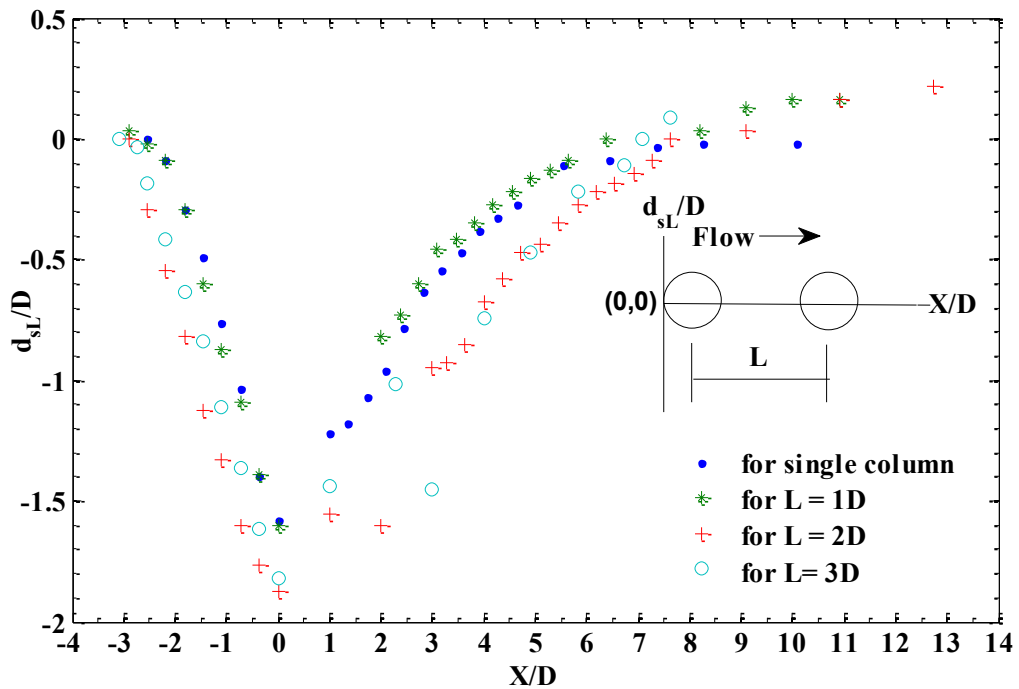


Figure 5.7 Scour profile for different column spacing

Figure 5.7 shows the profile of scour hole for the single column case and two in-line column cases with different spacing. In this figure, d_{sL} represents the scour depth at different positions along the line of symmetry (x-axis) for different values of L . The profile measurement was carried out along the centreline of the two in-line columns arrangement. In the figure, the scour depth and the distance along the centreline were normalised by the diameter of the column. The figure reveals that at the upstream side of Column 1, the scour holes begin at approximately the same point. However, at the downstream side of Column 2, the scour holes extended more as the spacing between the two columns increased. Furthermore, it was observed that the maximum slope of the scour occurs at the upstream side of the column at an angle approximately equal to 32° . Additionally the deposition of the bed material downstream of Column 2 varies with the variation of spacing between the piers. The results also clearly show the variation of scour

depth with respect to the spacing between columns, which was described in detail in Section 5.4.

5.7 Width of the Scour Hole

Hannah (1978) observed in his experiments that the width of the scour hole remains constant with a value of approximately $9D$, while the length of influence zone changed linearly until two independent holes are formed. It was reported that two independent scour holes were established at $L/D = 8$ after 2 hours and $L/D = 10$ after 7 hours.

Richardson and Abed (1993) reported that the knowledge of the top width of the scour hole at piers is important to design the scour countermeasures (for example extent of rip rap needed as a scour countermeasure) and to design the spacing of bridge piers to ensure there is not any overlapping of the scour holes. According to the authors, the top width of the scour holes at piers is a function of the depth of the scour hole and the angle of repose of bed material in water. The equation for predicting the width of the scour hole is given as:

$$w_s = d_{se} (K + \cot \theta) \quad 5.5$$

where,

w_s = the top width of the scour hole measured from each side of column

d_{se} = the maximum scour depth

K = the bottom width of the scour hole related to the depth of scour

θ = the angle of repose of the bed material ranging from 30° to 44°

If the bottom width of the scour hole is equal to the scour depth (d_{se}), the value of K is equal to 1. Hence the top width of the scour hole in cohesion-less material would vary from 2.07 to 2.8 d_{se} . On the other hand, for $K=0$, the top width of the scour hole would vary from 1.07 to 1.8 d_s . Hence the top width of the scour hole ranges from 1.07 to 2.8 d_{se} .

In the present study, the maximum widths of scour hole were measured for the different values of L/D between two in-line columns of bridge piers. Figure 5.8 shows the plot of

the normalised width of the scour hole (w_s/D) against the spacing between the piers (L/D). The variation of the width of the scour hole for different spacing between columns under different flow condition was clearly presented in this figure. In the figure width of scour hole was denoted by w_{sL} , where $L = 0, 1, 2, 3 \dots$. It is clear from the figure that the width of the scour hole varies from $6D$ to $9D$. The width of scour hole for the single column was less than that for the two in-line columns cases. However for $L/D = 1$, w_s was observed to be almost equal to the single column case. For $L/D \leq 3$, w_s was observed increasing with increase in the spacing between the two columns. For the range $3 < L/D < 5$, very small fluctuation of w_s was noticed. Furthermore, the figure reveals that when the value of L/D is around 3, the maximum value of w_s can be around $9D$. When $L/D > 5$, significant decrease in w_s was noticed. For $L/D \geq 10$, it was observed that two separate scour holes were developed around each column. Additionally, it was observed that the width across the midpoint between the two piers was larger than the widths across the piers.

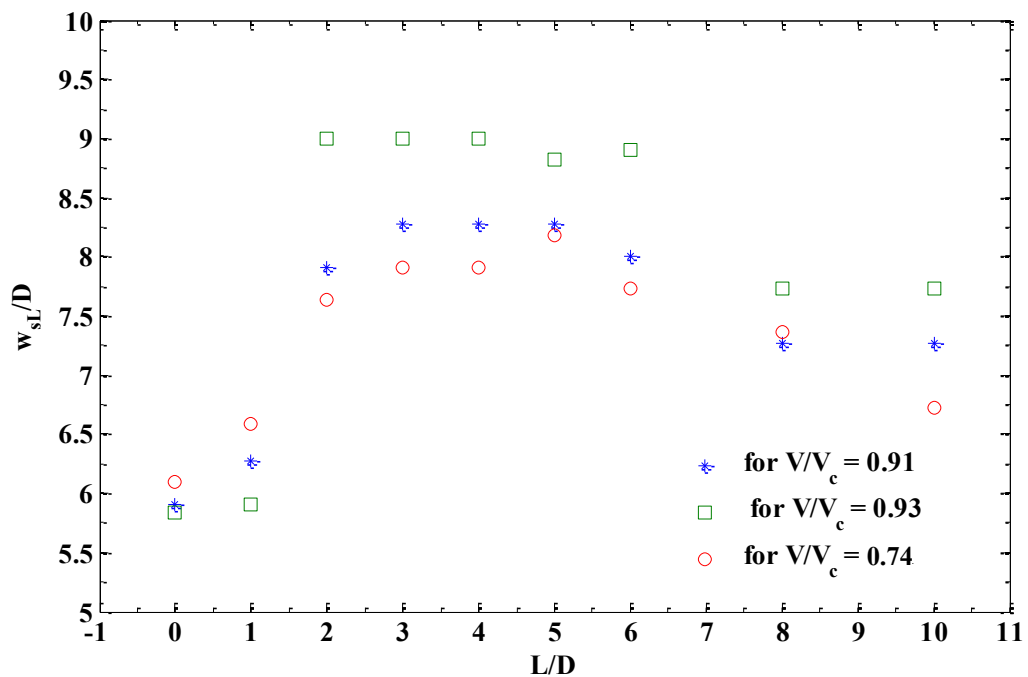


Figure 5.8 Variation of width of the scour hole for different spacing between two columns

Figure 5.9 shows the comparison of observed top width of scour hole and that of the predicted values using the Equation 6.5 for different scour depths around the columns at various spacing. It can be clearly seen in the Figure 5.9 that few values of observed top widths were falling within $\pm 20\%$ error lines. This shows that when the bridge pier consists of two in-line columns, the Equation 5.5 consistently under-predicts the width of the scour hole. However, the top width predicted for the single column case was found to be in good agreement with the observed value. Furthermore, it was noticed that the maximum top width of the scour hole for the two columns case is about 1.5 times the top width of the scour hole for the single column case.

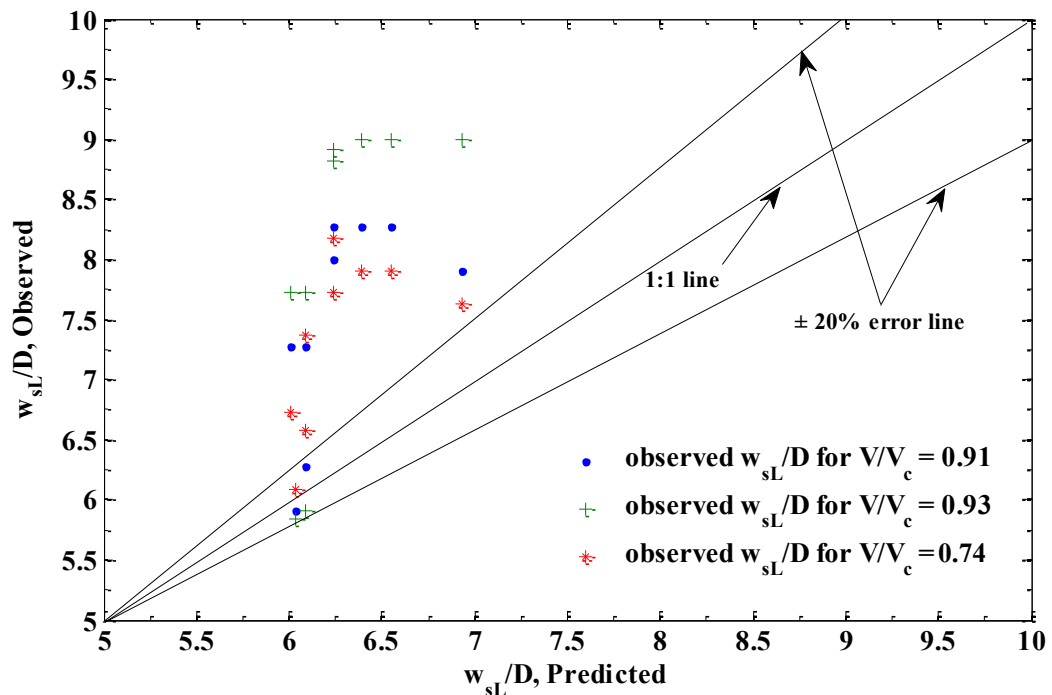


Figure 5.9 Predicted and observed to width of the scour hole

5.8 Summary

A series of laboratory experiments have been carried out to study the local scour around bridge pier consisting of a single column and twin columns. For the case of two-column bridge piers, the columns were placed in tandem arrangements with varying spacing between the columns. At the end of each experiment, the final bed profile and the

geometry of the scour holes were measured and the results were presented in tabular as well as in graphical forms.

Experiments on temporal development of scour depths around bridge piers were conducted for a period of 72 or 75 hours. The experiments were carried out for a single and two column bridge piers with spacing $1D$, $2D$ and $3D$. The scour depths at different elapsed time were monitored and recorded for further analysis. It was observed that approximately 90% of the total scour depth was achieved within the first 10 hours of the experiments. After 72 hours, the equilibrium scour depth was achieved at the upstream column. For the downstream column, continuous scour development was observed even after 72 hours. This shows that the equilibrium scour depth at the downstream column is attained in a longer duration than that for the upstream column (two in-line circular columns) as well as for the single column case.

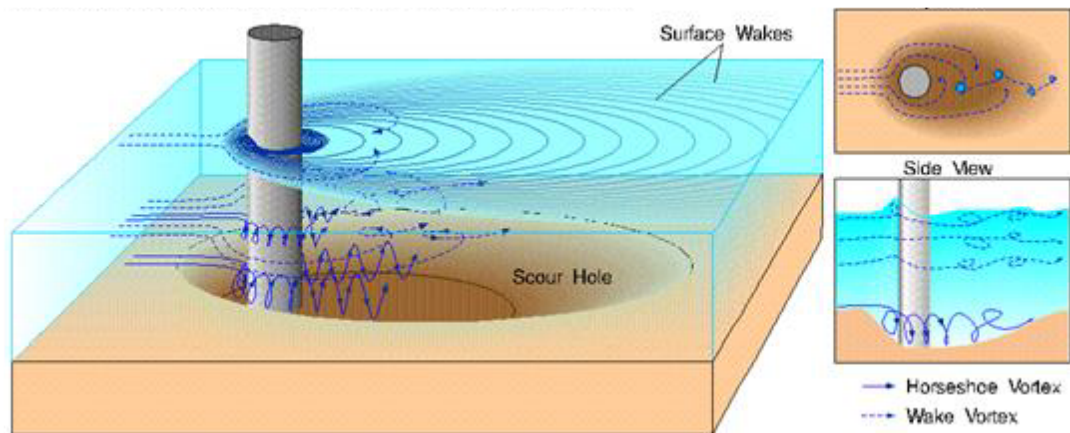
Overall 34 experiments were carried out for the local scour measurement around bridge piers. Using these local scour depth data along with the maximum scour depth data from the past investigations, the equations for the best fit line for Columns 1 and 2 have been derived using the nonlinear least square method with a goodness of fit of 0.91 and 0.88 as an R-square values which were given by Equations 5.1 and 5.2, respectively. From Equations 5.3 and 5.4, column-spacing factors, K_{s1} and K_{s2} , were proposed that could be used with the existing scour depth equations to predict the maximum scour depth for two in-line column cases. Furthermore, it was observed from the experiments that the maximum scour depth occurred at Column 1 when the spacing between the two columns was $2.5D$. The maximum observed value of local scour depth for the two in-line circular columns was around 18% higher than the value obtained for the single column case. The reasons for maximum scour depth at the spacing of $2.5D$ were found to be associated with the reinforcing effect of Column 2, the strong horseshoe vortex at Column 1, strong turbulence characteristics at the wake of Column 1, and the highest probability of occurrence of sweep events at the upstream side of Column 1.

Furthermore, the final bed profiles were measured, and the results were presented in Figure 5.5. It is clear from the figure that at the upstream side of the columns, the scour holes begin approximately at the same point. However, at the downstream side, the scour

hole was extended more as the spacing between the two columns increased. Additionally, the slope of the scour hole was found to be approximately 32° . Another important geometric parameter of the scour hole, the width of the scour hole, was measured for each experiment. It was observed that the width of the scour hole varied from $6D$ to $9D$. When the spacing between the two columns was about $3D$ then the maximum value of the width of the scour hole was observed, which was equal to $9D$. Furthermore, it was noticed that the maximum top width of the scour hole for the two-column case was about 1.5 times the top width of the scour hole for the single column case.

CHAPTER 6

CONCLUSION AND RECOMMENDATIONS



6.1 Introduction

6.2 Conclusions

6.3 Recommendations for Future Research

6. CONCLUSION AND RECOMMENDATIONS

6.1 Introduction

In the history of bridge failure, scour around the bridge piers has been reported as the main cause of failure. More than 60% of bridge failures are associated with the scour and other hydraulic reasons. The effect of bridge failure is directly reflected in the social and economic development of a nation. The main reason behind the bridge failure due to scour is poor design of pier foundations. Many investigations have been made attempting to estimate the maximum scour depth and to understand the mechanism of scour around bridge piers. Most of the previous investigations were based on the scour and the flow structure around a single pier. This is reflected in the wide range of equations developed by several investigators for the estimation of local scour depth around bridge piers. There are limited studies on scour around the bridge piers comprising a group of columns. Additionally, the flow around the bridge piers comprising two or more in-line columns is not well investigated. However, in practice, bridge piers often consist of multiple columns in tandem arrangement to support the loading of the structure. Thus a detailed study on scour and flow around bridge piers with two in-line circular columns has been experimentally carried out. This study has presented the efforts made for advanced understanding of research and practice on flow structures and the scour depth around bridge piers by addressing the challenges related to the aforementioned problems.

6.2 Conclusions

The main contribution of this research is the detailed study on the flow structure interaction and quantifying the maximum local scour depth around bridge piers consisting of one circular column or two in-line circular columns. In this study, the effects of spacing between the two columns on the flow structure and the scour depth around bridge piers have been thoroughly investigated. The work consisted of the design of the physical model and experimental tests for the study of flow structures and scour around bridge piers. A series of experimental tests were conducted using a single column and two cylindrical columns with circular cross sections. The tests comprised of measuring instantaneous three dimensional velocity components, experimental investigation of temporal variation of the scour depth around a single column and two-column bridge

piers, and analysis of the equilibrium scour depth under various conditions of column arrangements. An acoustic Doppler velocimetry (ADV) and particle image velocimetry (PIV) techniques were employed to measure the instantaneous three dimensional velocity components. To measure the scour depth and the final bed profile, a Vernier depth gauge with a least count of 0.1 mm was used. Similarly, to measure the flow rate, an electromagnetic flow meter with an accuracy of $\pm 0.4\%$ was used.

Two flumes with different sizes were employed for the experimental tests, including Flume 1 (19 m long, 0.61 m wide and 0.61 m deep) and Flume 2 (6 m long, 0.25 m wide and 0.25 m deep). Flume 1 was used for the study of flow structures in different horizontal planes using ADV. This flume was also used for the experimental tests on scouring profiles. The other flume with a smaller size (Flume 2) was used for investigating flow structures in vertical planes using the PIV technique. Both flumes were equipped with an electromagnetic flow meter, regulating the gate and the pump. Based on the width of the flume, the diameter of model column was selected in such a way that there was no contraction effect on the depth of scour. The diameters of the adopted model columns were 55 mm and 16 mm for Flume 1 and Flume 2, respectively. The flume width to the column diameter ratios was checked, ensuring they were greater than 10. Uniformly graded non-cohesive sand of mean grain size (d_{50}) of 0.85 mm was used as a bed material. The size of the bed material was determined in such a way that there was no grain size effect on the scour depth. All tests were conducted under the clear water condition with different values of critical velocity ratios ($V/V_c = 0.38, 0.74, 0.91, 0.93$ and 0.96). For each flow condition, different tests were carried out including a single column and two in-line circular columns with different spacing between them ($L/D = 0$ to 12). Altogether 28 tests of fixed bed experiments were carried out for the study of flow structures. Additionally, 34 moveable bed experiments were conducted for the study of the scour depth.

The measured instantaneous velocity components were analysed and the results for flow field and turbulence characteristics were presented in graphical forms using vector plots, streamline plots, contour plots and profile plots. The results from the vector plots and streamline plots for single column case indicated that there is a generation of down flow due to the pressure gradient induced at the upstream face of column. At the immediate

downstream side, reversal, rotational as well as upward flows were observed. For the two-column cases, the maximum value of up flow was observed at a distance of $2D$ from the downstream side of the column at which the flow was found to be separated. For $L/D < 2$, reverse flow and recirculation was observed only in the wake of Column 2. The flow regime in this situation is called “extended body regime”. When $L/D = 3$, the shear layer separated from Column 1 re-attached on the upstream side of Column 2, which is known as “re-attachment regime”. This regime is principally characterised by formation and shedding of eddies in the gap between two columns. Further increase in spacing resulted in the formation of vortex shedding at the downstream side of both Column 1 and Column 2. Hence, it is called “co-shedding regime”. Comparison of the flow behind the single column and the two in-line columns reveals that the wake behind the single column case was larger than that of the two-column cases.

The results from the contour and profile plots of three dimensional velocity components in horizontal and vertical planes indicated that higher and lower values of streamwise velocity component (u/V) were observed at the side and in the wake of a column, respectively. Higher values of negative transverse velocity component (v/V) were observed at the upstream side near the zone of shear layer separation. At the downstream side positive values of v/V were observed i.e. the flow converged in the wake of the column. Negative values of vertical velocity components (w/V) observed at the upstream face of the column, and indicated the presence of down flow. As this down flow interacted with the boundary layer, a horseshoe vortex was formed at the base just upstream of the column. At the downstream side of the column, significant fluctuation of w/V was observed up to the distance of $4D$ measured from the downstream face of the column. For the two-column cases, when $L/D \leq 3$, the reverse flow was extended throughout the gap. Furthermore, the results revealed that the strength of reverse flow at the wake of Column 2 increased with increase in the value of L/D . For $L/D = 2$, no down flow was noticed at the upstream side of Column 2. Hence, the horseshoe vortex in this region was not formed. As the spacing between two columns increased, stronger up flow was observed. For $L/D > 3$, the horseshoe vortex in the front of Column 2 was formed near the base of Column 2. However, the size of the horseshoe vortex at the upstream side of Column 2 was smaller than that of Column 1, which could be due to shielding effect of Column 1.

The three dimensional turbulence intensity components of the flow around the bridge piers were determined by calculating the root mean square value of velocity fluctuations. The results indicated that weak turbulence intensity occurred at the upstream side of bridge piers. However, the maximum values of turbulence intensity were observed in the wake of the columns. Furthermore, it was noticed that the turbulence intensity in the transverse direction was much larger than that of streamwise and vertical directions. For two-column cases, the values of turbulence intensity components were found to increase with increase in the spacing between two columns. Additionally, the results revealed that the magnitudes of turbulence intensity in the wake of Column 2 are smaller than in the single column case and in the gap of the two-column cases. This is due to the sheltering effect of Column 1 that resulted in the reduction of flow velocity approaching Column 2. Furthermore, the turbulent kinetic energy of the flow was determined by taking the mean of the turbulence normal stresses. The results indicated that the distribution of turbulent kinetic energy was similar to the distribution pattern of turbulence intensities. It was common to all the cases that higher values of turbulence kinetic energy were observed close to the bed and gradually decreased towards the free surface. The results from the two-column cases with $L/D = 3$ showed that the maximum value of turbulence kinetic energy occurred between the gap. However, the values of turbulent kinetic energy in the wake of Column 2 increased as the spacing between the two columns increased up to $L/D = 3$. Further increase in spacing resulted in a decrease in the value of turbulence kinetic energy.

Using the three dimensional data of velocity fluctuations, normalised Reynolds stresses on three different planes (u - v , u - w and v - w planes) were calculated as $-\overline{u'v'}/V^2$, $-\overline{u'w'}/V^2$ and $-\overline{v'w'}/V^2$. Based on analysing the Reynolds stresses in horizontal planes along the axis of symmetry, it was observed that the absolute value of $-\overline{u'v'}/V^2$ was constantly higher than that of $-\overline{u'w'}/V^2$ and $-\overline{v'w'}/V^2$. For all the cases, maximum values of Reynolds stresses were observed close to the bed. Furthermore, it was observed that the absolute value of $-\overline{u'v'}/V^2$ in the wake for the two-column cases were smaller than that in the case of the single column. According to the results obtained in vertical planes, the absolute values of $-\overline{u'w'}/V^2$ were higher close to the bed in the wake and decreased to zero towards the free surface. Comparing the results for the two-column

cases, it was found that the value of $-\overline{u'w'}/V^2$ decreased with increase in the spacing between the two columns. Higher values of $-\overline{u'w'}/V^2$ were observed in the wake of Column 1 and gradually decreased as the flow approached Column 2.

In order to analyse the structure of instantaneous Reynolds stresses measured around the bridge piers, the quadrant analysis based on the probability of occurrence (P_i) of each quadrant and the contribution ratio (stress fraction, S_i) for the production of Reynolds stresses were employed. The results indicated that at the upstream side of the single column, based on the probability of occurrence, sweep event was dominant. Higher values of sweep and ejection events occurred close to the bed and gradually decreased towards the free surface. In the single column case, at the downstream side, outward interaction was the dominant event, followed by ejection, sweep and inward interaction events. Considering the results for ejection and sweep events, higher values of P_i occurred in the ejection event. Hence, the sediments were expected to remain in the suspended form at the downstream side of the column. For the two in-line columns cases, at the upstream side of Column 1, P_i increased as the spacing between the two columns increased until $L/D = 3$. Further increase in the spacing resulted in a decrease in the value of P_i of sweep event. However, the values of P_i of sweep event at the upstream side for two-column cases were observed higher than that of the single column case. This is the reason, which supports higher scour depth for the two-column case rather than the single column. Behind Column 2, for all values of L/D , probability of ejection event was observed higher than sweep event. For the two columns cases, both ejection and sweep events around Column 2 were observed significantly less than that of the single column case. The results support the fact that the scour depth around Column 2 is less than that of Column 1 and the single column case. On the other hand, the results on stress fraction indicated that outward interaction and inward interaction contributed strongly in the production of Reynolds stress at the upstream side of all of the two-column arrangements. For the two-column cases, behind Column 1, the ejection event was dominant and reached the maximum value when $L/D = 2$. However, at Column 2, outward interaction and inward interaction were dominant. Comparing the results for all events, it was found that the stress fraction of all quadrants contributed significantly to the production of the Reynolds stress.

A series of experimental tests for the study of the local scour profile around bridge piers was carried out under different flow conditions. Four tests including a single column, and two in-line columns with spacing 1D, 2D and 3D were conducted for studying the temporal development of local scour depths. The results revealed that approximately 90% of the total scour depth at Column 1 was achieved within the first 10 hours of the experiments. After 72 hours, the equilibrium scour depth was achieved at the upstream column. For Column 2, around 90% of the maximum scour depth was achieved after 20 hours. Furthermore, it was observed that the maximum scour depth at Column 2 was continuously smaller than that of the single column case. In addition, altogether 34 experiments were carried out under different flow conditions for the study of local scour around bridge piers. *The results indicated that the maximum scour depth occurred at Column 1 when the spacing between two columns was 2.5D.* The maximum value of local scour depth for the two-column case was about 18% higher than the value obtained for the single column case. Furthermore, an equation for the best-fit line was derived using the nonlinear least square method, given by Equations 5.1 and 5.3. Similarly, an equation of the best-fit line for Column 2 is given by Equations 5.2 and 5.4. The coefficients of spacing between columns, K_{s1} and K_{s2} were proposed for Column 1 and Column 2, respectively that could be used with the existing scour-depth prediction equations to calculate the maximum scour depth for two in-line column cases. Additionally, the results from final bed profiles indicated that at the upstream side of Column 1, the scour holes began approximately at the same point. However, at the downstream side of Column 2, the scour hole was extended more as the spacing between two columns increased. The width of the scour hole was measured for all experiments and it was observed that the width of the scour hole varied from 6D to 9D. The maximum width of the scour hole for the two-column cases was observed at a spacing of 3D, which was approximately 1.5 times more than the width of the scour hole for the single column case.

In summary, it is clearly demonstrated that the flow structures around the two in-line cylindrical columns of bridge piers is more complex than that of the single column case. Furthermore, the spacing between two columns significantly affect the flow structures particularly in the wake of the columns. The results indicated that, for $L/D < 3$, vortex shedding occurred only behind Column 2. Hence, the flow pattern is more or less similar

to the single column case. However, the turbulence characteristics such as turbulence intensity, turbulent kinetic energy and Reynolds shear stresses are notably different from for the single column. When the spacing is in the range of $2 \leq L/D \leq 3$, stronger turbulence structures were noticed behind Column 1. More sediments are expected to remain in suspended form, which can easily be washed to the downstream side. Hence, a higher scour depth can be expected at Column 1. Moreover, the results from the local scour tests exhibit that the maximum scour depth occurred at Column 1 when the spacing between two columns is $L/D = 2.5$. The above results of flow structures and local scour are highly correlated. *Hence, it can be concluded that for tandem arrangements of two in-line cylindrical columns, the spacing in the range of $2 < L/D < 3$ is the most critical at which the columns experience the highest turbulence and hence the maximum scour depth.*

6.3 Recommendations of Future Research

The main aim of this research was to study the flow structure interaction in the process of scouring around bridge piers consisting of two in-line circular columns. To meet the main objective of this research, the present study acted as a fundamental investigation. Notwithstanding the fact that the present study confirmed a notable progress in understanding the flow structure around two cylindrical columns, thorough investigation on this topic is still not complete. Based on the findings of this study, the following recommendations are made for further understanding and clarification of the flow structures and scour around bridge piers with two in-line cylindrical columns:

1. In the present study, all the experiments on flow structures were conducted under flatbed conditions with a steady flow situation. However, effects of scour on flow structures have not been investigated. Although the present results give very good information on the flow structures before commencement of scour, an additional set of experiments are required to be conducted under moveable bed conditions to study the effect of scour hole on flow structures.
2. Experiments in the present study were conducted using only cylindrical columns with circular cross-sections. However, in real situations many different shapes exist. Hence, experiments with different shapes of columns can be carried out for better understanding of the shape effect. In addition, experiments with varied

width of column would be useful. Effect of dune and anti-dune, water depth and vegetation are other conditions arise in real situation, which is recommended for the future research.

3. For deep understanding of vortex shedding events, which are the main contributor to the turbulent kinetic energy, PIV measurements on the horizontal planes would be useful. By conducting these measurements, the relationship between the shedding events in the upstream side and in the wake could be investigated.
4. A single set of uniform sediment as the bed material was used in this study, which is an ideal condition in the lab. However, non-uniform sediment has more practical significance. Therefore, for future research, it is recommended that non-uniform sediments be used for more accurate and practical results.
5. In this study, all the experiments on scouring were conducted under clear water condition. In reality, bridge sites experience different types of flow conditions especially during floods or rainy seasons; scouring often happens under live bed conditions. Hence, a well-designed physical model is recommended to investigate the scour characteristics under live bed conditions.
6. Angle of attack is another important parameter and needs to be considered during the experiments. In the present study, only zero angle of attack was employed. However, the variation of the angle of attack is strongly recommended to be taken into account for future research to investigate its interference effects on the horseshoe vortex system.
7. Although the experimental investigations can provide comparatively more precise and accurate results, they are costly and more time consuming. From the economic point of view, research on bridge scouring based on the finite element numerical modelling using verified software packages is highly recommended for future research in this area. Nonetheless selected field results or laboratory tests are required to validate the numerical outputs.

REFERENCES

2005. Bridge Scour Manual. *Florida Department of Transportation*.
- A KESHAVARZI & A SHIRVANI. 2002. Probability analysis of instantaneous shear stress and entrained particles from the bed. Proceedings of the CSCE/EWRI of ASCE Environmental engineering conference, Niagara.
- A KESHAVARZY & JE BALL 1997. An analysis of the characteristics of rough bed turbulent shear stresses in an open channel. *Stochastic Hydrology and Hydraulics*, 11, 193-210.
- A. KUMAR & U. KOTHYARI 2012b. Three-Dimensional Flow Characteristics within the Scour Hole around Circular Uniform and Compound Piers. *Journal of Hydraulic Engineering*, 138, 420-429.
- A. MELIH YANMAZ & H. DOGAN ALTINBILEK 1991. Study of Time-Dependent Local Scour around Bridge Piers. *Journal of Hydraulic Engineering*, 117, 1247-1268.
- A. QADAR. 1981. The Vortex Scour Mechanism at Bridge Piers ICE Proceedings. Thomas Telford, 71, 3.
- A.A. BEHESHTI & B. ATAIE-ASHTIANI 2010. Experimental study of Three-Dimensional Flow Field around a Complex Bridge Pier. *Journal of Engineering Mechanics, ASCE*, 136, 143-154.
- ALESSIO RADICE & CHAU K TRAN 2012. Study of sediment motion in scour hole of a circular pier. *Journal of Hydraulic Research*, 50, 44-51.
- ALI REZA KESHAVARZI & ALI REZA GHEISI 2006. Stochastic nature of three dimensional bursting events and sediment entrainment in vortex chamber. *Stochastic Environmental Research and Risk Assessment*, 21, 75-87.
- ALIREZA KESHAVARZI, BRUCE MELVILLE & JAMES BALL 2014. Three-dimensional analysis of coherent turbulent flow structure around a single circular bridge pier. *Environmental Fluid Mechanics*, 1-27.

- ANDRES DOMENECH, F.J. VALLES MORAN, G. PALAU SALVADOR & HANS BIHS. 2011. Experimental and numerical modelling of scour at bridge piers 10th Hydraulic Conference, Brisbane, Australia. Engineers Australia.
- ARVED J RAUDKIVI & ROBERT ETTEMA 1983. Clear-water scour at cylindrical piers. *Journal of Hydraulic Engineering*, 109, 338-350.
- ARVED J. RAUDKIVI & ROBERT ETTEMA 1985. Scour at Cylindrical Bridge Piers in Armored Beds. *Journal of Hydraulic Engineering*, 111, 713-731.
- ARVED J. RAUDKIVI 1998. *Loose Boundary Hydraulics*, Rotterdam, Netherlands/ Brookfield, USA, A.A. Balkema.
- ASHISH KUMAR & UMESH C. KOTHYARI 2012a. Three-Dimensional Flow Characteristics within the Scour Hole around Circular Uniform and Compound Peirs. *Journal of Hydraulic Engineering*, 138, 420-429.
- ATA AMINI, BRUCE W. MELVILLE, THAMER M. ALI & ABDUL H. GHAZALI 2012. Clearwater Local Scour around Pile Groups in Shallow-Water Flow. *Journal of Hydraulic Engineering*, 138, 177-185.
- B. ATAIE-ASHTIANI & A. A. BEHESHTI 2006. Experimental Investigation of Clear-Water Local Scour at Pile Groups. *Journal of Hydraulic Engineering*, 132, 1100-1104.
- B. DARGAHI 1989. The Turbulent flow field around a circular cylinder. *Experiments in fluids*, 8, 1-12.
- B. M. SUMER, K. BUNDGAARD & J. FREDSOE. 2005. Global and Local Scour at Pile groups Fifteenth International Offshore and Polar Engineering Conference, Seoul, Korea.
- B. MUTLU SUMER & JØRGEN FREDSE 1997. *Hydrodynamics around cylindrical structures*, Advance Series on Ocean Engineering, 12, World Scientific.
- B. MUTLU SUMER & JORGEN FREDSOE 2002. *The Mechanics of Scour in the Marine Environment*, Advance Series on Ocean Engineering, Toh Tuck Link, Singapore, World Scientific Publishing Co. Pte. Ltd.

- B. W. MELVILLE & A. J. SUTHERLAND 1988. Design Method for Local Scour at Bridge Piers. *Journal of Hydraulic Engineering*, 114, 1210-1226.
- B. W. MELVILLE 1992. Local Scour at Bridge Abutments. *Journal of Hydraulic Engineering*, 118, 615-631.
- B.M. SUMER, N. CHRISTIANSEN & J. FREDSOE 1997. The horseshoe vortex and vortex shedding around vertical wall-mounted cylinder exposed to waves. *Journal of Fluid Mechanics*, 332, 41-70.
- B.W. MELVILLE & A.J. RAUDKIVI 1977a. Flow characteristics in local scour at bridge piers. *Journal of Hydraulic Research IAHR*, 15, 373-380.
- BAO-SHI SHIAU 1999. Ejection and sweep of the Reynolds stress for a turbulent boundary layer flow past windscreen. *Journal of Wind Engineering and Industrial Aerodynamics*, 83, 493-502.
- BEHZAD ATAIE-ASHTIANI & ABOLFAZL ASLANI-KORDKANDI 2013. Flow Field Around Single and Tandem Piers. *Flow, turbulence and combustion*, 90, 471-490.
- BESIR SAHIN, N ADIL OZTURK & HÜSEYİN AKILLI 2007. Horseshoe vortex system in the vicinity of the vertical cylinder mounted on a flat plate. *Flow Measurement and Instrumentation*, 18, 57-68.
- BIG SKY LASER QUANTELL 2006. ICE 450 Power Supply User Manual.
- Bridge Scour Manual* 2013. Department of Transport and Main Roads, Queensland Government, Australia
- BRUCE W. MELVILLE & ARVED J. RAUDKIVI 1977b. FLOW CHARACTERISTICS IN LOCAL SCOUR AT BRIDGE PIERS. *Journal of Hydraulic Research*, 15, 373-380.
- BRUCE W. MELVILLE & STEPHEN E. COLEMAN 2000. *Bridge Scour*, Water Resource Publications, LLC, Colorado, USA.
- BRUCE W. MELVILLE & YEE-MENG CHIEW 1999. Time Scale for Local Scour at Bridge Piers. *Journal of Hydraulic Engineering*, 125, 59-65.

- BRUCE W. MELVILLE 1975. Local Scour at Bridge Sites. Auckland, New Zealand: School of Engineering, University of Auckland.
- BRUCE W. MELVILLE 1997. Pier and Abutment Scour: Integrated Approach. *Journal of Hydraulic Engineering*, 123, 125-136.
- C RT SMITH, JDA WALKER, AH HAIDARI & U SOBRUN 1991. On the dynamics of near-wall turbulence. *Philosophical Transactions: Physical Sciences and Engineering*, 131-175.
- C. H. K WILLIAMSON 1989. Oblique and parallel modes of vortex shedding in the wake of a circular cylinder at low Reynolds numbers. *Journal of Fluid Mechanics*, 206, 579-627.
- C. H. WILLIAMSON 1988. The existence of two stages in the transition to three-dimensionality of a cylinder wake. DTIC Document.
- C. J. BAKER 1980. The turbulent horseshoe vortex. *Journal of Wind Engineering and Industrial Aerodynamics*, 6, 9-23.
- C.J. BAKER 1979. The laminar horseshoe vortex. *Journal of Fluid Mechanics*, 95, 347-367.
- C.R. HANNAH 1978. Scour at Pile Groups. Christchurch, New Zealand: Department of Civil Engineering, University of Canterbury.
- CHANG LIN, PENG-HAO CHIU & SHYH-JIUNN SHIEH 2002a. Characteristics of horseshoe vortex system near a vertical plate–base plate juncture. *Experimental Thermal and Fluid Science*, 27, 25-46.
- CHIJ KUMAR SHRESTHA, ALIREZA KESHAVARZI & HADI KHABBAZ. 2013. Flow Structure at Downstream Side of Two Sequential Bridge Piers. *In: Shoji Fukuoka, Hajime Nakagawa, Tetsuya Sumi & Hao Zhang, eds. International Symposium on River Sedimentation (ISRS 2013), Kyoto, Japan. CRC Press/Balkema, 199.*
- CHIJ KUMAR SHRESTHA, ALIREZA KESHAVARZI, HADI KHABBAZ & JAMES BALL. 2012. Experimental Study of the Flow Structure Interactions between

Bridge Piers 34th Hydrology and Water Resources Symposium (HWRS 2012), Sydney, Australia.

- D. M. SHEPPARD 2004. Overlooked Local Sediment Scour Mechanism. *Transportation Research Record: Journal of the Transportation Research Board*.
- D. SHEPPARD & W. MILLER 2006. Live-Bed Local Pier Scour Experiments. *Journal of Hydraulic Engineering*, 132, 635-642.
- D. SUMNER 2010. Two circular cylinders in cross-flow: a review. *Journal of Fluids and Structures*, 26, 849-899.
- D. SUMNER, S. J. PRICE & M. P. PAIDOUSSIS 2000. Flow-pattern identification for two staggered circular cylinders in cross-flow. *Journal of Fluid Mechanics*, 411, 263-303.
- D.M. SHEPPARD, B. MELVILLE & H. DEMIR 2014. Evaluation of Existing Equations for Local Scour at Bridge Piers. *Journal of Hydraulic Engineering*, 140, 14-23.
- DARYL B. SIMONS & FUAT SENTURK 1992. *Sediment Transport Technology*, Water and Sediment Dynamics, Colorado, USA, Water Resources Publications.
- DAVID S MUELLER. 1997. Field-based research on channel scour at bridges. Proceedings of the US Geological Survey Sediment Workshop, February 4-7.
- DOMENICO FERRARO, ALI TAFAROJNORUZ, ROBERTO GAUDIO & ANTÓNIO H CARDOSO 2013. Effects of pile cap thickness on the maximum scour depth at a complex pier. *Journal of Hydraulic Engineering*, 139, 482-491.
- DW SMITH. 1976. Bridge failures. ICE Proceedings. Thomas Telford, 367-382.
- E.M. LAURSEN & A. TOCH 1956. Scour around bridge piers and abutments. *Bulletin No. 4*. Iowa Highway Research Board, Bureau of Public Roads, Iowa.
- EDWARD R CORINO & ROBERT S BRODKEY 1969. A visual investigation of the wall region in turbulent flow. *Journal of Fluid Mechanics*, 37, 1-30.
- ELHAM IZADINIA, MANOUCHEHR HEIDARPOUR & ANTON J SCHLEISS 2013. Investigation of turbulence flow and sediment entrainment around a bridge pier. *Stochastic Environmental Research and Risk Assessment*, 27, 1303-1314.

- EMMETT M LAURSEN & ARTHUR TOCH. 1953. A generalized model study of scour around bridge piers and abutments. *Proceedings@ sMinnesota International Hydraulic Convention*. ASCE, 123-131.
- Evaluating Scour at Bridges* 2001. Federal Highway Administration Department of Transportation,
- FERDOUS AHMED & NALLAMUTHU RAJARATANAM 1997. The three dimensional turbulent boundary layer flow around bridge piers. *Journal of Hydraulic Research*, 35 209-224.
- FERDOUS AHMED & NALLAMUTHU RAJARATNAM 1998. Flow around Bridge Piers. *Journal of Hydraulic Engineering*, 124, 288-300.
- FERDOUS AHMED. 1995. *Flow and Erosion Around Bridge Piers*. PhD Thesis, Department of Civil Engineering, University of Alberta.
- G. KIRKIL, S. CONSTANTINESCU & R. ETTEMA 2008. Coherent Structures in the Flow Field around a Circular Cylinder with Scour Hole. *Journal of Hydraulic Engineering*, 134, 572-587.
- G. OLIVETO & W. HAGER 2002. Temporal Evolution of Clear-Water Pier and Abutment Scour. *Journal of Hydraulic Engineering*, 128, 811-820.
- G. OLIVETO & W. HAGER 2005. Further Results to Time-Dependent Local Scour at Bridge Elements. *Journal of Hydraulic Engineering*, 131, 97-105.
- GEORGE KEITH BATCHELOR 2000. *An introduction to fluid dynamics*, Cambridge university press.
- GOKHAN KIRKIL. 2008. *Numerical study of the flow field at cylindrical piers in an alluvial bed*. PhD Thesis, Graduate College of Civil and Environmental Engineering, University of Iowa.
- H. NAKAGAWA & I. NEZU 1993. *Turbulence in Open Channel Flows*, Taylor & Francis.
- HANS ALBERT EINSTEIN 1950. *The bed-load function for sediment transportation in open channel flows*, US Department of Agriculture.

- HERRMANN SCHLICHTING & KLAUS GERSTEN 1999. *Boundary-layer theory*, Springer.
- HIROJI NAKAGAWA & IEHISA NEZU 1978. Bursting phenomenon near the wall in open-channel flows and its simple mathematical model. *Kyoto University Faculty Engineering Memoirs*, 40, 213-240.
- HOT KIM, SJ KLINE & WC REYNOLDS 1971. The production of turbulence near a smooth wall in a turbulent boundary layer. *Journal of Fluid Mechanics*, 50, 133-160.
- HOWARD H. CHANG 1988. *Fluvial Processes in River Engineering*, Krieger.
- HUBERT CHANSON 2004. *Hydraulics of open channel flow*, Butterworth-Heinemann.
- ILA-GMBH 2004. Introduction to VidPIV User Manual. Juelich, Germany: ILA GmbH.
- ILA-GMBH Articulated Light Arm User Manual. Juelich, Germany: ILA-GmbH.
- J WESTERWEEL 1997. Fundamentals of digital particle image velocimetry. *Measurement science and technology*, 8, 1379.
- J. - C. LIN, Y. YANG & D. ROCKWELL 2002b. Flow past two cylinders in tandem: instantaneous and averaged flow structure. *Journal of Fluids and Structures*, 16, 1059-1071.
- J. CHABERT & P. ENGELDINGER 1956. Etude des affouillements autour des piles de ponts. Chatou, France.
- J. H. GERRARD 1978. The wakes of cylindrical bluff bodies at low Reynolds number. *Philosophical Transactions of the Royal Society of London. Series A, Mathematical and Physical Sciences*, 288, 351-382.
- JAMES M WALLACE 1985. The vortical structure of bounded turbulent shear flow. *Flow of Real Fluids*. Springer.
- JD MENNA & FJ PIERCE 1988. The Mean Flow Structure Around and Within a Turbulent Junction or Horseshoe Vortex—Part I: The Upstream and Surrounding Three-Dimensional Boundary Layer. *Journal of fluids engineering*, 110, 406-414.

- JENS UNGER & WILLI H HAGER 2007. Down-flow and horseshoe vortex characteristics of sediment embedded bridge piers. *Experiments in Fluids*, 42, 1-19.
- JOHN E. RICHARDSON & VIJAY G. PANCHANG 1998. Three-Dimensional Simulation of Scour-Inducing Flow at Bridge Piers. *Journal of Hydraulic Engineering*, 124, 530-540.
- JOHN KIM 1987. Evolution of a vortical structure associated with the bursting event in a channel flow. *Turbulent Shear Flows 5*. Springer.
- JR MENEGHINI, F SALTARA, CLR SIQUEIRA & JA FERRARI JR 2001. Numerical simulation of flow interference between two circular cylinders in tandem and side-by-side arrangements. *Journal of fluids and structures*, 15, 327-350.
- JS JONES, K ALQALAM, B GRATTON & B SUMMERS. 1995. Effect of the 1994 Southeast Flooding on the Highway System in Georgia. unpublished handout presented at the 1995 ASCE Hydraulics Division Conference, San Antonio, TX.
- KUMALASARI WARDHANA & FABIAN C HADIPRIONO 2003. Analysis of recent bridge failures in the United States. *Journal of Performance of Constructed Facilities*, 17, 144-150.
- L. A. AMESON, L. W. ZEVENBERGEN, P.F. LAGASSE & P.E. CLOPPER 2012. Evaluating Scour at Bridges, Fifth Edition. *FHWA-HIF-12-003, HEC-18*. Washington, D. C.: U. S. Department of Transportation, Federal Highway Administration.
- LEO C VAN RIJN 1984a. Sediment transport, part I: bed load transport. *Journal of hydraulic engineering*, 110, 1431-1456.
- LEO C VAN RIJN 1984b. Sediment transport, Part II: Suspended load transport. *Journal of Hydraulic Engineering*, 110, 1613-1641.
- LEONARDUS CORNELIS VAN RIJN 1993. *Principles of sediment transport in rivers, estuaries and coastal seas*, 1006, Aqua publications Amsterdam.
- LES HAMILL 1999. *Bridge Hydraulics*, USA and Canada, Routledge 29 West 35th Street, New York, NY 10001.

- Local Scour Around Cylindrical Bridge Pier* 1985. Ministry of Works and Development for the National Water and Soil Conservation Authority Hydrology Centre,
- M HANIF CHAUDHRY 2007. *Open-channel flow*, Springer.
- M. M. ZDRAVKOVICH 1977. REVIEW—Review of flow interference between two circular cylinders in various arrangements. *Journal of Fluids Engineering*, 99, 618-633.
- M. M. ZDRAVKOVICH 1987. The effects of interference between circular cylinders in cross flow. *Journal of Fluids and Structures*, 1, 239-261.
- M. MIA & H. NAGO 2003. Design Method of Time-Dependent Local Scour at Circular Bridge Pier. *Journal of Hydraulic Engineering*, 129, 420-427.
- M. MUZZAMIL, KAILASH GUPTA, T. GANGADHARAIHAH & K. SUBRAMANYA. 1989. Vorticity characteristics of scouring horseshoe vortex. Proc. of 3rd Int. Workshop on Alluvial River Problems. 19-26.
- M. MUZZAMMIL & T. GANGADHARAIHAH 2003. The mean characteristics of horseshoe vortex at a cylindrical pier. *Journal of Hydraulic Research*, 41, 285-297.
- M. R. CARSTEN. 1966. Similarity Laws for Localised Scour. *Journal of Hydraulics Division*. ASCE, 13-16.
- M. SUSAN BLOOR 1964. The transition to turbulence in the wake of a circular cylinder. *Journal of Fluid Mechanics*, 19, 290-304.
- MADELINE NOVEY. 2013. CDOT assessing 'millions and millions' in road bridge damage. *coloradoan.com*, Sep. 15 2013.
- MEHRDAD NAZARIHA. 1996. *Design Relationship for Maximum Local Scour Depth for Bridge Pier Groups*. PhD Thesis, Department of Civil Engineering, University of Ottawa.
- MOHAMMAD SALIM & J. STERLING JONES. 1996. Scour around exposed pile foundations. *Compilation of conference papers (1991-1998)*, Reston, VA. ASCE.

- MOHAMMAD SALIM & J. STERLING JONES. 1998. Scour around exposed pile foundations. Compilation of conference papers (1991-1998), Reston, VA.
- MUBEEN-BEG. 2010. Characteristics of Developing Scour Holes around Two Piers Placed in Transverse Arrangement Fifth International Conference on Scour and Erosion (ICSE-5), San Francisco, CA. ASCE.
- N.H.C. BREUSERS & A.J. RAUDKIVI 1991. IAHR, hydraulic structure design manual: Scouring. Balkema Rotterdam, Netherlands.
- N.H.C. BREUSERS, G NICOLLET & H.W. SHEN 1977. Local scour around cylindrical piers. *Journal of Hydraulic Research IAHR*, 15, 211-252.
- NERMIN SARLAK & SAHNAZ TIGREK 2011. Analysis of experimental data sets for local scour depth around bridge abutments using artificial neural networks. *Water Sa*, 37, 595-602.
- P.F. LAGASSE & E.V. RICHARDSON 2001. ASCE compendium of stream stability and bridge scour papers. *Journal of Hydraulic Engineering, ASCE*, 127, 531-533.
- P.N. CHEREMISINOFF, N. P. CHEREMISINOFF & S.L. CHENG 1987. Hydraulics Mechanics 2. *Civil Engineering Practice, Technomic Publishing Company, Inc., Pennsylvania, USA*, 780.
- PADMINI KHWAIRAKPAM, SOUMENDU SINHA RAY, SUBHASISH DAS, RAJIB DAS & ASIS MAZUMDAR 2012. Scour hole characteristics around a vertical pier under clear water scour conditions. *ARPN Journal of Engineering and Applied Sciences*, 7, 649-654.
- PCO-TECH. 2008. <http://www.pco-tech.com/overview/> [Online]. Michigan USA: PCO-TECH Inc.
- R. E. BAKER 1986. Local Scour at bridge piers in non-uniform sediment. *Report No. 402*. School of Engineering, The University of Auckland, Auckland, New Zealand.
- R. ETTEMA 1976. Influence of bed material gradation on local scour. *Report No. 124*, *School of Engineering, the University of Auckland, New Zealand*, 226.

- R. ETTEMA. 1980. *Scour at Bridge Piers*. PhD Thesis, Department of Civil Engineering, University of Aucland.
- RA BAGNOLD 1966. An approach to the sediment transport problem from general physics. *US Geol. Surv. Prof. Pap.*, 422, 1, 231-291.
- RAHUL BHATIA. 2013. *The Emergency: Does anyone know the state of India's bridges?* [Online]. The Caravan. Available: <http://caravanmagazine.in/reportage/emergency>.
- ROBERT ETTEMA, BRUCE W. MELVILLE & BRIAN BARKDOLL 1998. Scale Effect in Pier-Scour Experiments. *Journal of Hydraulic Engineering*, 124, 639-642.
- ROBERT ETTEMA, GEORGE CONSTANTINESCU & BRUCE MELVILLE 2011. Evaluation of Bridge Scour Research: Pier Scour Process and Predictions. *NCHRP Report 175*. Transportation Research Board of the National Academies, Washington D.C.
- ROBERT ETTEMA, GOKHAN KIRKIL & MARIAN MUSTE 2006. Similitude of Large-Scale Turbulence in Experiments on Local Scour at Cylinders. *Journal of Hydraulic Engineering*, 132, 33-40.
- RONG FUNG HUANG, CHING MIN HSU & WEI CHENG LIN 2014. Flow characteristics around juncture of a circular cylinder mounted normal to a flat plate. *Experimental Thermal and Fluid Science*, 55, 187-199.
- RW PRITCHARD 2013. 2011 to 2012 Queensland floods and cyclone events: Lessons learnt for bridge transport infrastructure. *Australian Journal of Structural Engineering*, 14, 167.
- S. E. COLEMAN, C. S. LAUHLAN & B. W. MELVILLE 2003. Clear water scour development at bridge abutment. *Journal of Hydraulic Research*, 41, 521-531.
- S. G. RABEN, P. DIPLAS, N. APSILIDIS, C. L. DANCEY & P. P. VLACHOS. 2010. Local Scour at Bridge Piers: The Role of Reynolds Number on Horseshoe Vortex Dynamics International Conference on Scour and Erosion (ICSE-5) San Francisco, California, United States. American Society of Civil Engineers.

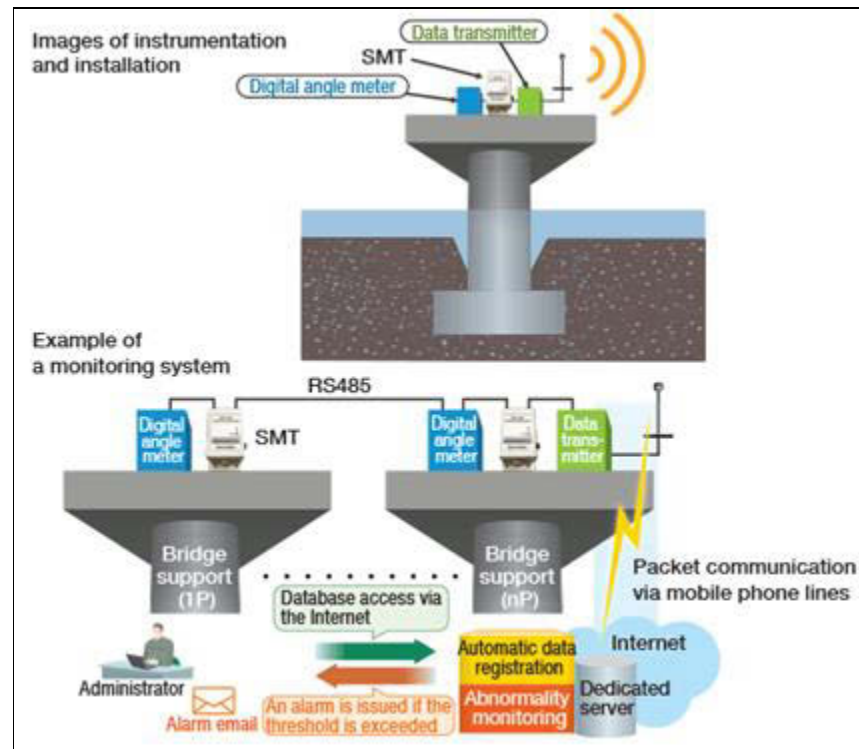
- SAEED JAFARI MIANAIE & ALI REZA KESHAVARZI 2010. Study of near bed stochastic turbulence and sediment entrainment over the ripples at the bed of open channel using image processing technique. *Stochastic Environmental Research and Risk Assessment*, 24, 591-598.
- SEUNG OH LEE. 2006. *Physical modeling of local scour around complex bridge piers*. PhD Thesis, School of Civil and Environmental Engineering, Georgia Institute of Technology, School of Civil and Environmental Engineering, Georgia Institute of Technology, Atlanta, US.
- SHERBAHADUR KC. 2014. Bed of Tinau River Deepen by 1.5 m. *Nagariknews*, 06 Feb. 2014.
- SJ KLINE, WC REYNOLDS, FA SCHRAUB & PW RUNSTADLER 1967. The structure of turbulent boundary layers. *Journal of Fluid Mechanics*, 30, 741-773.
- SONTEK 2001. ADV Field Technical Manual. San Diego, CA: SonTek/YSI, Inc.
- SONTEK. 2012. <http://www.sontek.com/microadv.php> [Online]. San Diego, CA: Son Tek.
- S-Q YANG 2010. Conditionally averaged turbulent structures in 2D channel flow. *Proceedings of the ICE-Water Management*, 163, 79-88.
- SS LU & WW WILLMARTH 1973. Measurements of the structure of the Reynolds stress in a turbulent boundary layer. *Journal of Fluid Mechanics*, 60, 481-511.
- STEPHEN JAY KLINE & NAIM HAMDIA AFGAN 1990. Near-wall turbulence. *Near-Wall Turbulence*, 1.
- SUBHASISH DEY & RAJKUMAR V. RAIKAR 2007. Characteristics of Horseshoe Vortex in Developing Scour Holes at Piers. *Journal of Hydraulic Engineering*, 133, 399-413.
- SUBHASISH DEY & SUJIT K BOSE 1994. Bed shear in equilibrium scour around a circular cylinder embedded in a loose bed. *Applied mathematical modelling*, 18, 265-273.

- SUBHASISH DEY, SUJIT K. BOSE & GHANDIKOTA L. N. SASTRY 1995. Clear Water Scour at Circular Piers: a Model. *Journal of Hydraulic Engineering*, 121, 869-876.
- TONY L WAHL. 2000. Analyzing ADV data using WinADV. Proc., Joint Conf. on Water Resources Engineering and Water Resources Planning and Management. ASCE Reston, Va., 1-10.
- UMESH C. KOTHYARI, RAM CHANDRA J. GARDE & KITTUR G. RANGA RAJU 1992. Temporal Variation of Scour Around Circular Bridge Piers. *Journal of Hydraulic Engineering*, 118, 1091-1106.
- UMESH C. KOTHYARI, WILLI H. HAGER & GIUSEPPE OLIVETO 2007. Generalized Approach for Clear-Water Scour at Bridge Foundation Elements. *Journal of Hydraulic Engineering*, 133, 1229-1240.
- USGS. 2014. *Investigation and Analysis of Floods from Drainage Areas in New Mexico* [Online]. Albuquerque, New Mexico: New Mexico Water Science Centre. Available: <http://nm.water.usgs.gov/projects/floodanalysis/>.
- VESSELINA ROUSSINOVA, A-M SHINNEEB & RAM BALACHANDAR 2009. Investigation of fluid structures in a smooth open-channel flow using proper orthogonal decomposition. *Journal of Hydraulic Engineering*, 136, 143-154.
- W. HAGER & J. UNGER 2010. Bridge Pier Scour under Flood Waves. *Journal of Hydraulic Engineering*, 136, 842-847.
- WH GRAF & I ISTIARTO 2002. Flow pattern in the scour hole around a cylinder. *Journal of Hydraulic Research*, 40, 13-20.
- WIKIPEDIA-CONTRIBUTORS 2015. List of bridge failures. https://en.wikipedia.org/wiki/List_of_bridge_failures. Wikipedia, The Free Encyclopedia.
- WW WILLMARTH 1975. Structure of turbulence in boundary layers. *Advances in applied mechanics*, 15, 159-254.
- Y. M. CHIEW. 1984. *Local Scour at Bridge Piers*. PhD Thesis, Department of Civil Engineering, Auckland University.

Y. ZHOU & M. W. YIU 2006. Flow structure, momentum and heat transport in a two-tandem-cylinder wake. *Journal of Fluid Mechanics*, 548, 17-48.

ZHIFU GU 1996. On interference between two circular cylinders at supercritical Reynolds number. *Journal of Wind Engineering and Industrial Aerodynamics*, 62, 175-190.

APPENDICES



Appendix-A: Plots for Velocity Components

Appendix-B: Plots of Turbulence Intensity

Appendix-C: Plots for Turbulence Kinetic Energy

Appendix-D: Plots for Reynolds Stresses

Appendix-E: Plots for Quadrant Analysis

APPENDIX-A: PLOTS FOR VELOCITY COMPONENTS

A.1 Plots of Velocity Components in Horizontal Plane

A.1.1 Velocity Vector Plots in Horizontal Plane

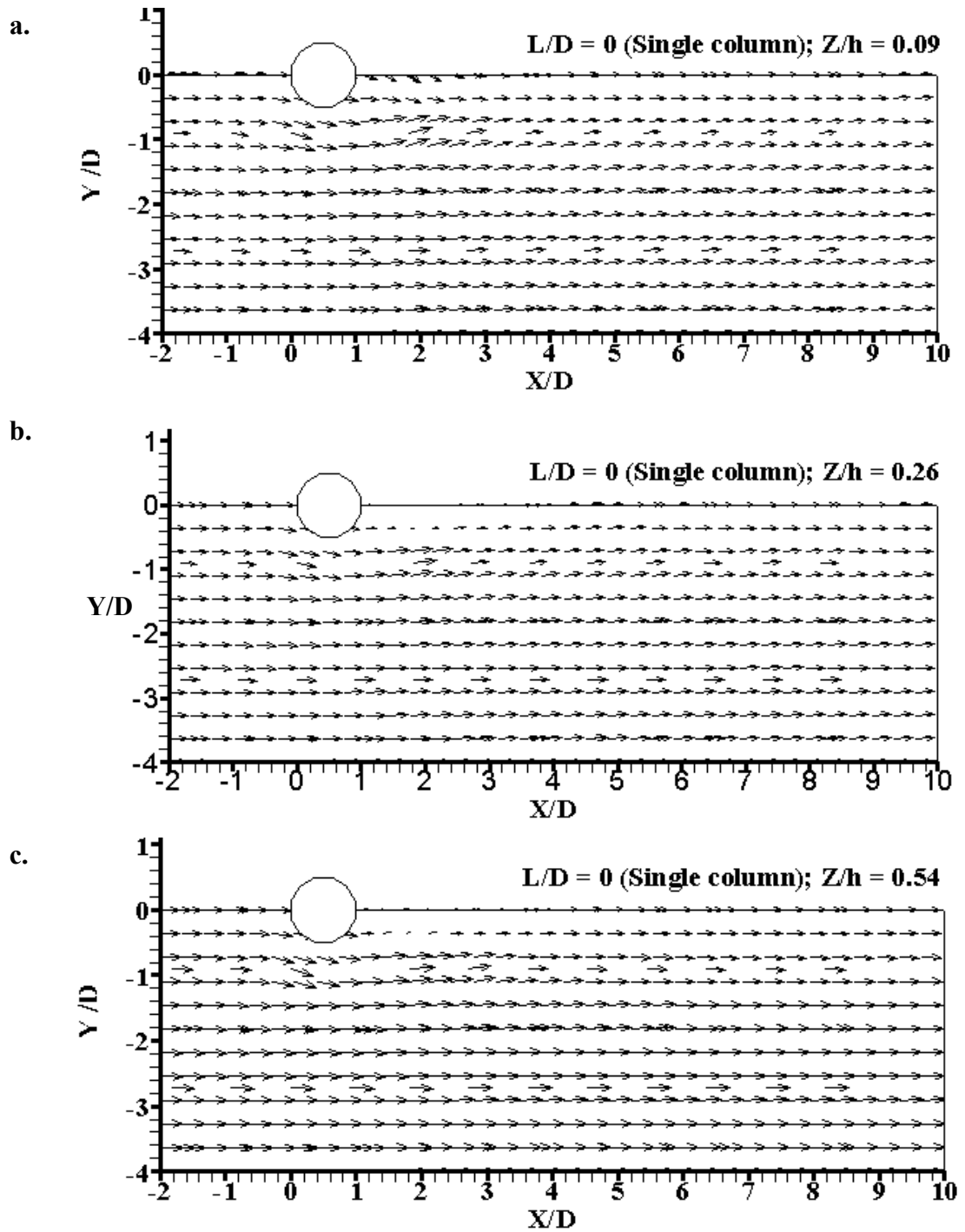


Figure A.1 Velocity vector plots for single column in different horizontal planes; a.) at $Z/h = 0.09$, b.) at $Z/h = 0.26$, and c.) at $Z/h = 0.54$

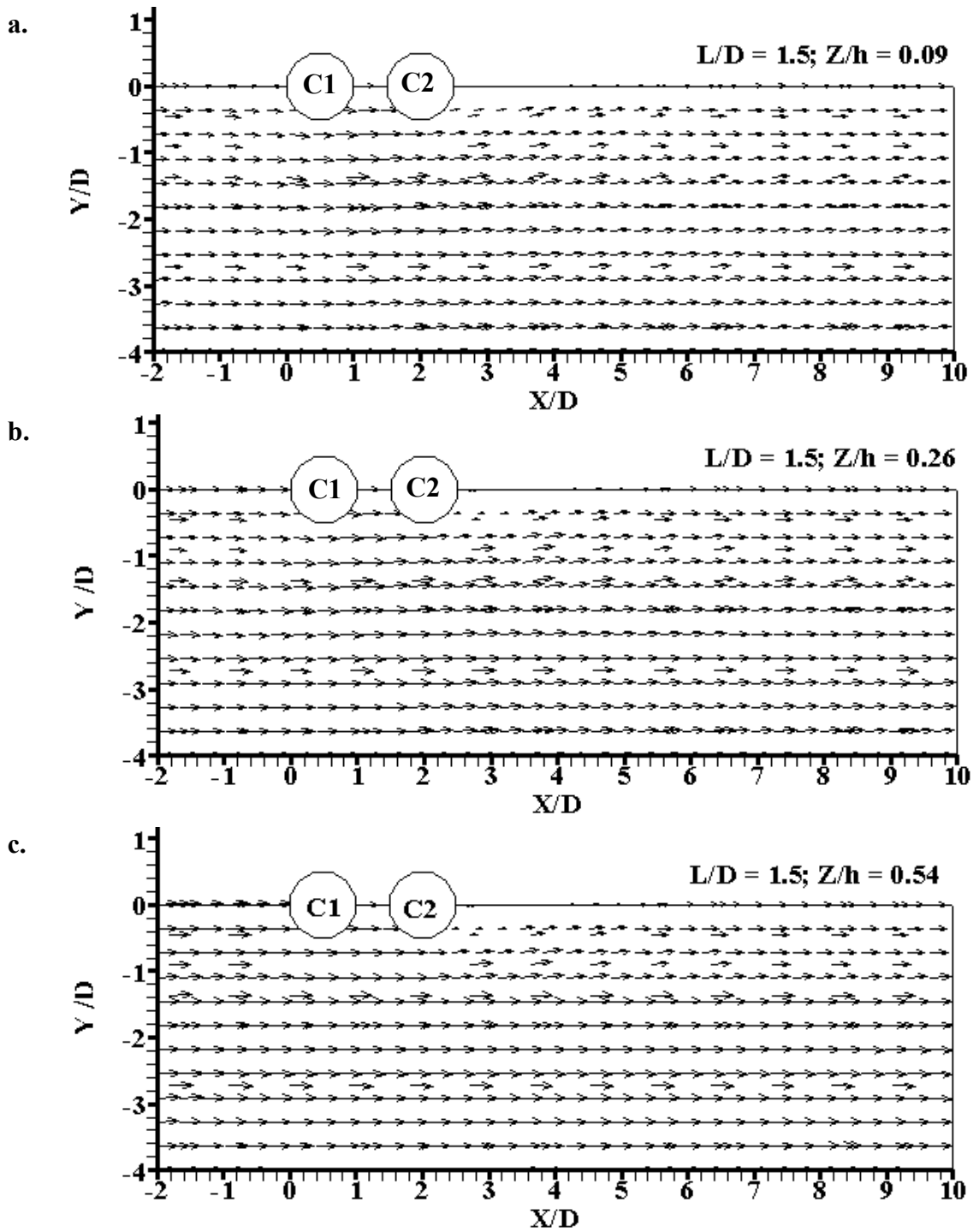


Figure A.2 Velocity vector plots for two columns with $L/D = 1.5$ in different horizontal planes; a.) at $Z/h = 0.09$, b.) at $Z/h = 0.26$, and c.) at $Z/h = 0.54$

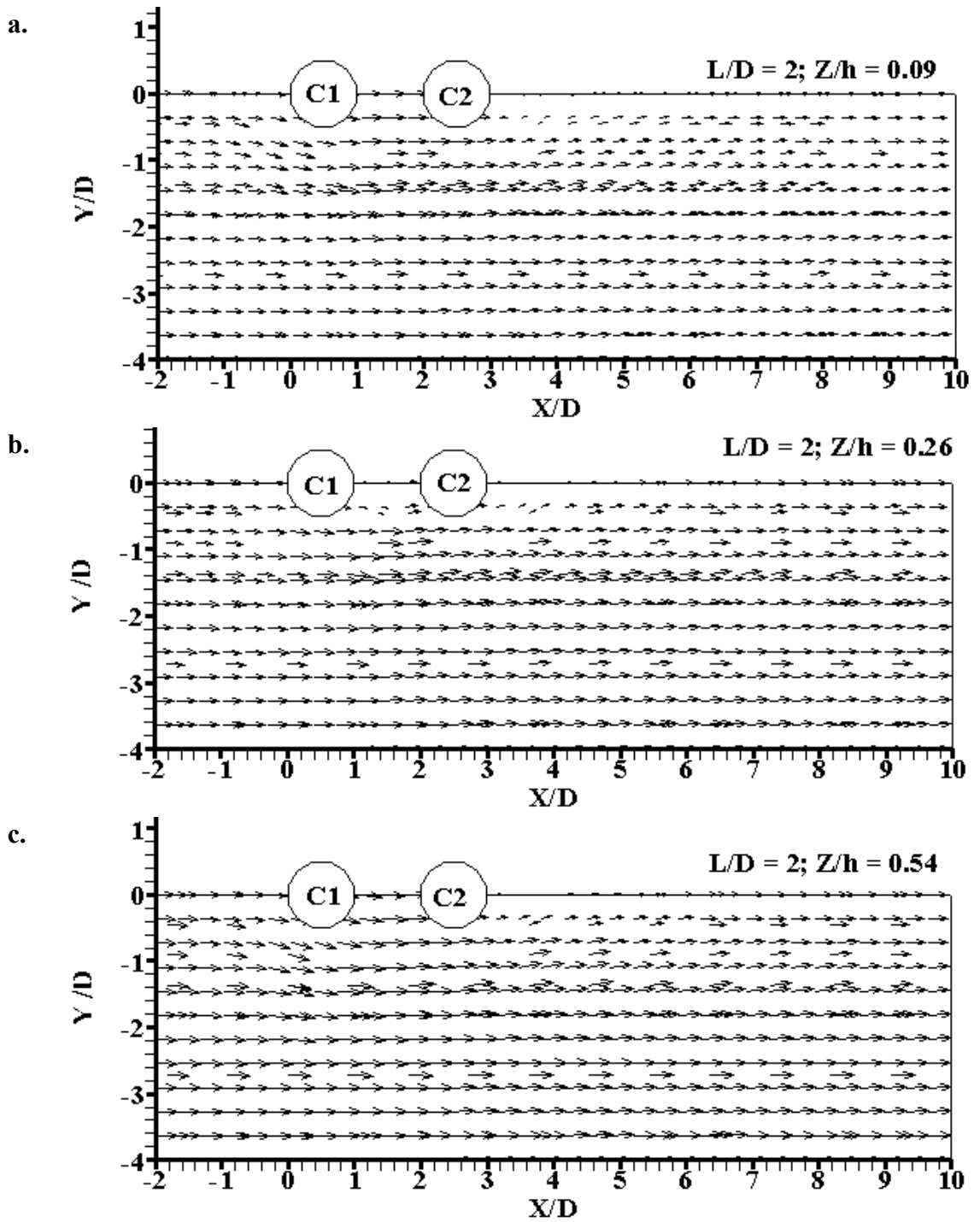


Figure A.3 Velocity vector plots for two columns with $L/D = 2$ in different horizontal planes; a.) at $Z/h = 0.09$, b.) at $Z/h = 0.26$, and c.) at $Z/h = 0.54$

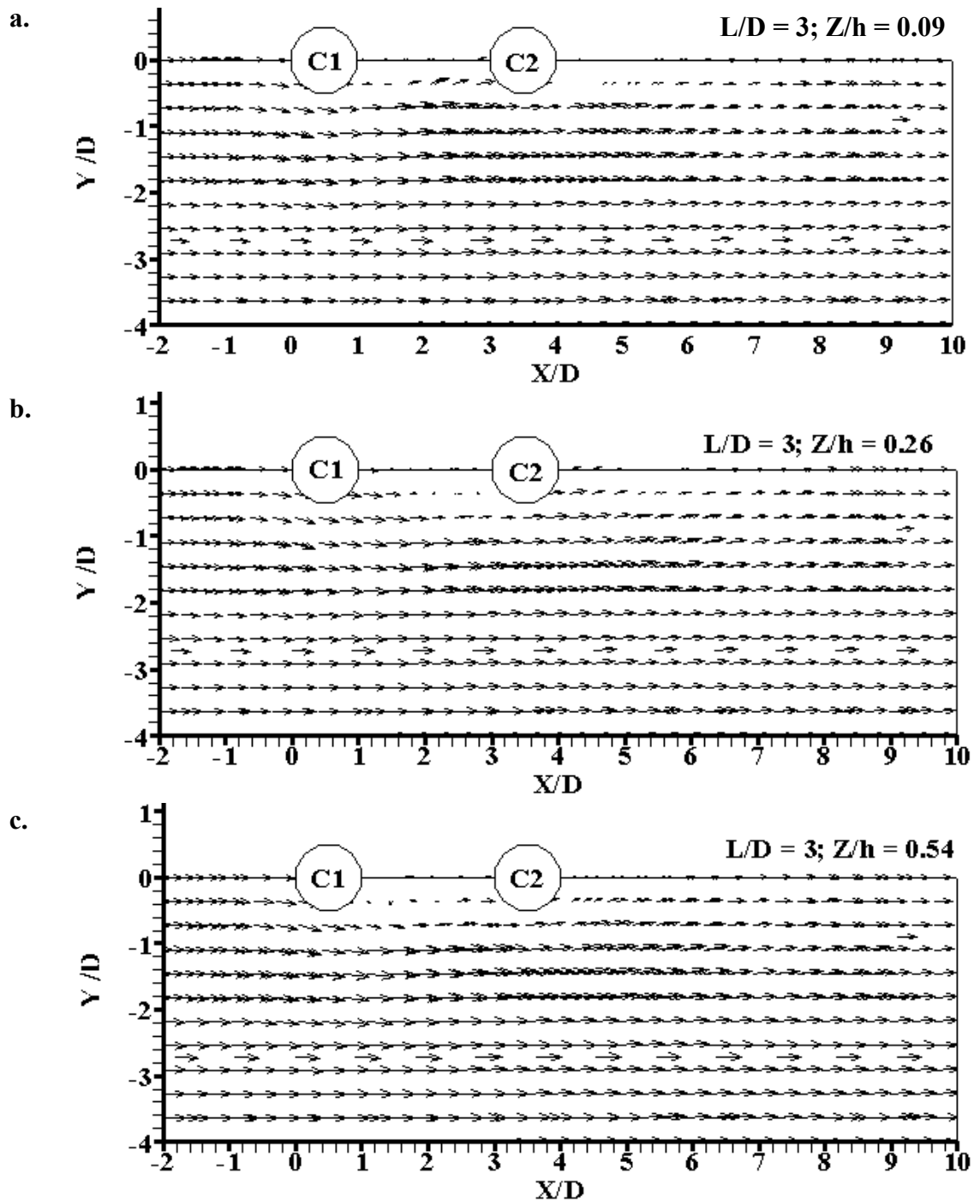


Figure A.4 Velocity vector plots for two columns with $L/D = 3$ in different horizontal planes; a.) at $Z/h = 0.09$, b.) at $Z/h = 0.26$, and c.) at $Z/h = 0.54$

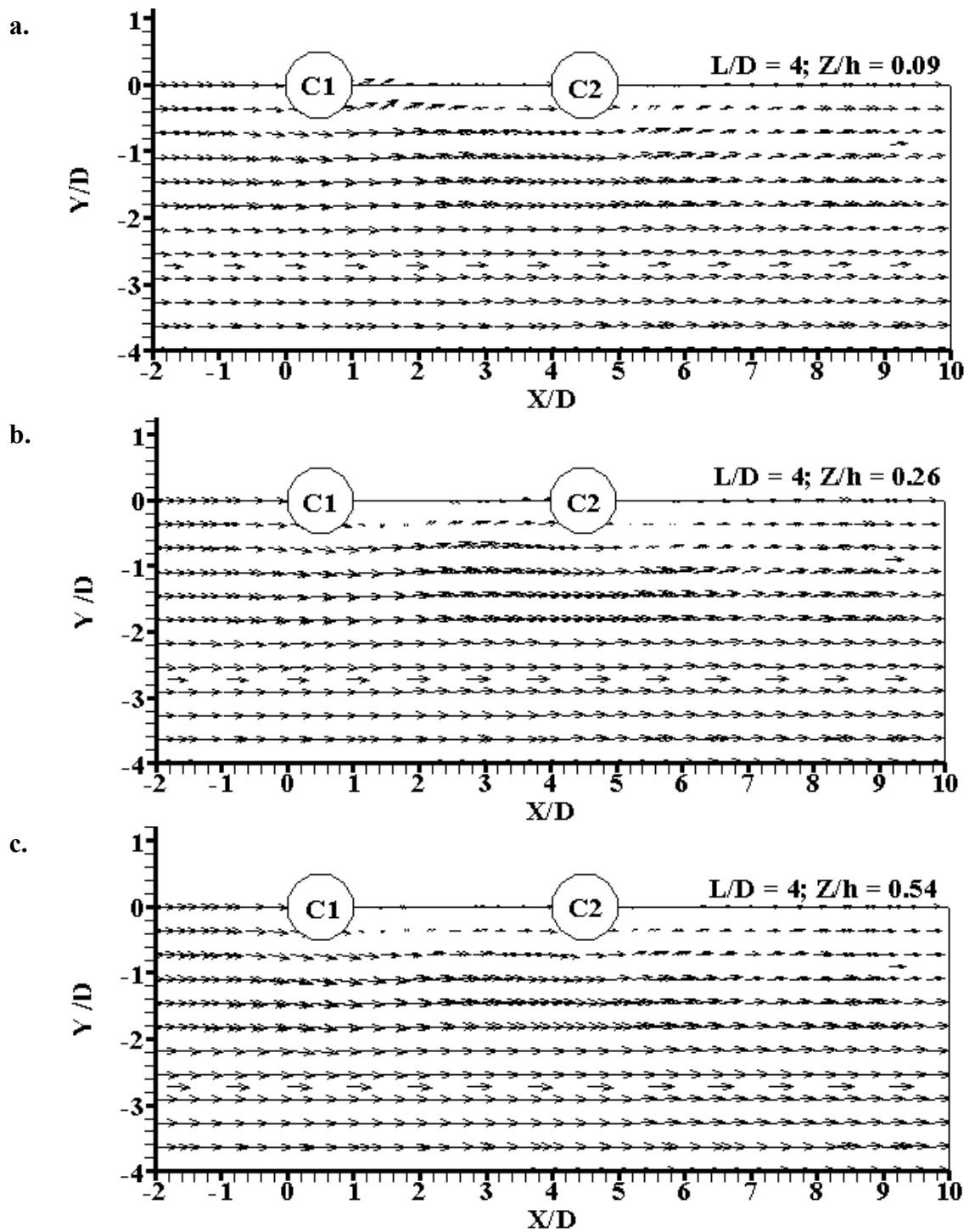


Figure A.5 Velocity vector plots for two columns with $L/D = 4$ in different horizontal planes; a.) at $Z/h = 0.09$, b.) at $Z/h = 0.26$, and c.) at $Z/h = 0.54$

A.1.2 Streamline Plots in Horizontal Plane

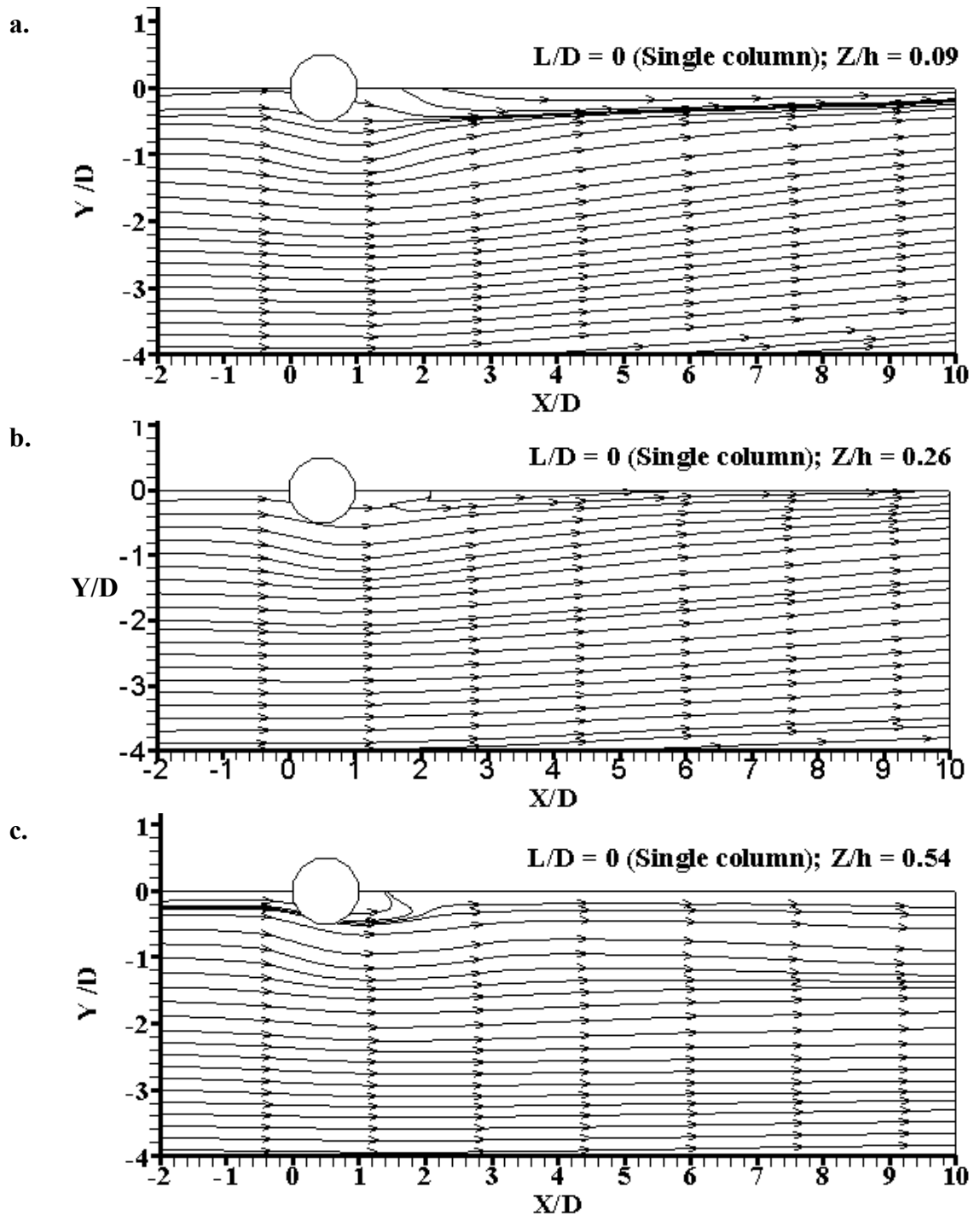


Figure A.6 Streamline plots for single column in different horizontal planes; a.) at $Z/h = 0.09$, b.) at $Z/h = 0.26$, and c.) at $Z/h = 0.54$

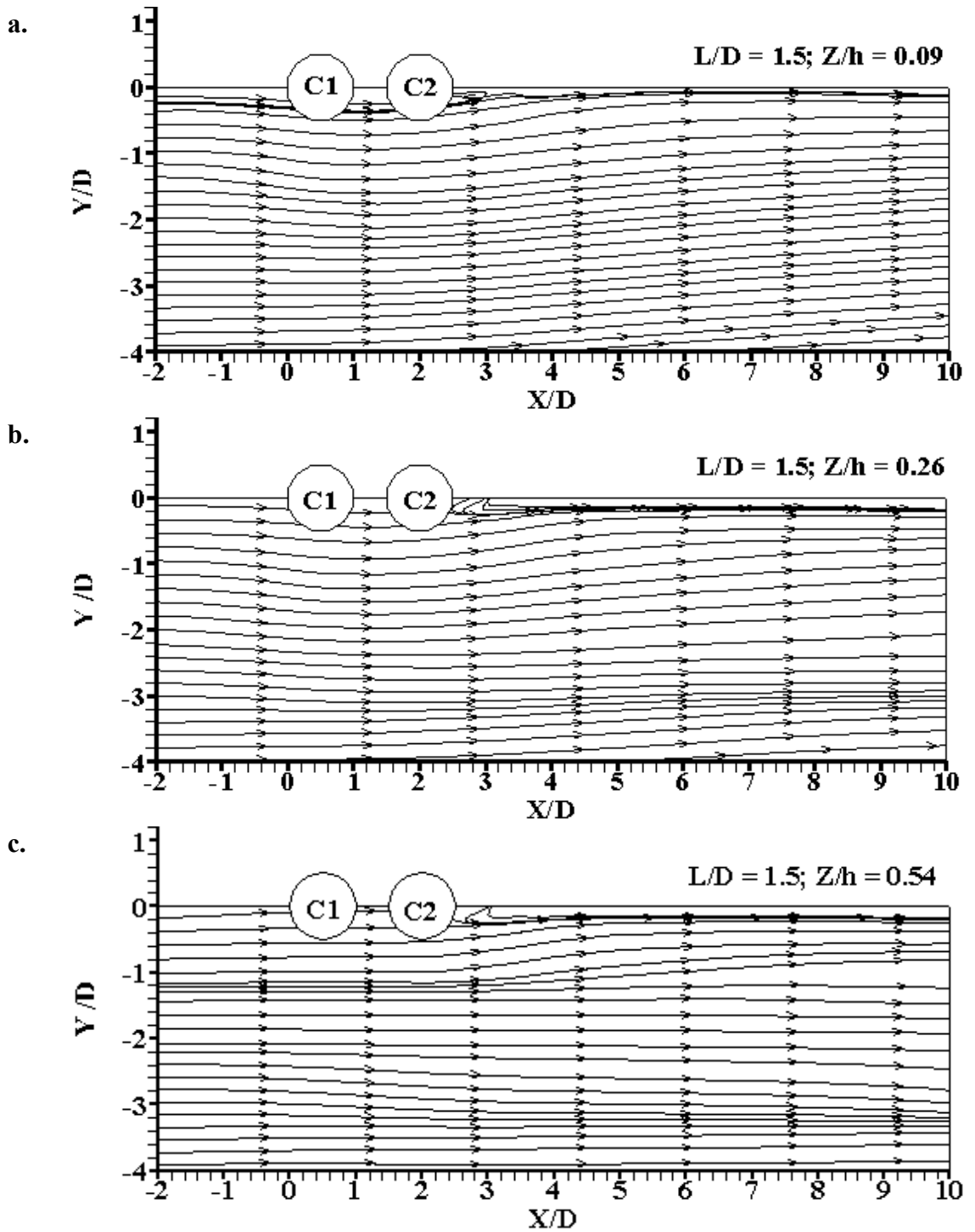


Figure A.7 Streamline plots for two columns with $L/D = 1.5$ in different horizontal planes; a.) at $Z/h = 0.09$, b.) at $Z/h = 0.26$, and c.) at $Z/h = 0.54$

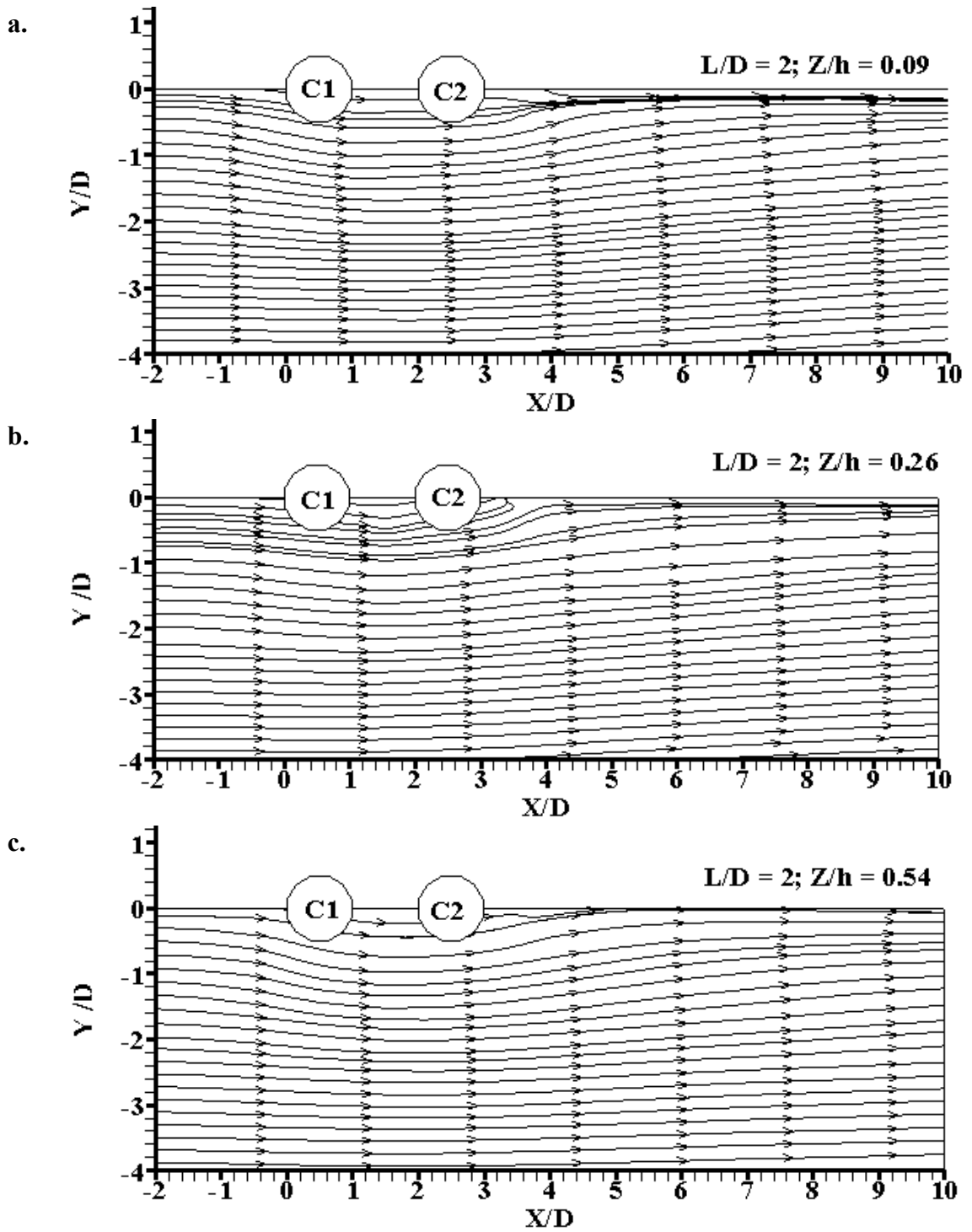


Figure A.8 Streamline plots for two columns with $L/D = 2$ in different horizontal planes; a.) at $Z/h = 0.09$, b.) at $Z/h = 0.26$, and c.) at $Z/h = 0.54$

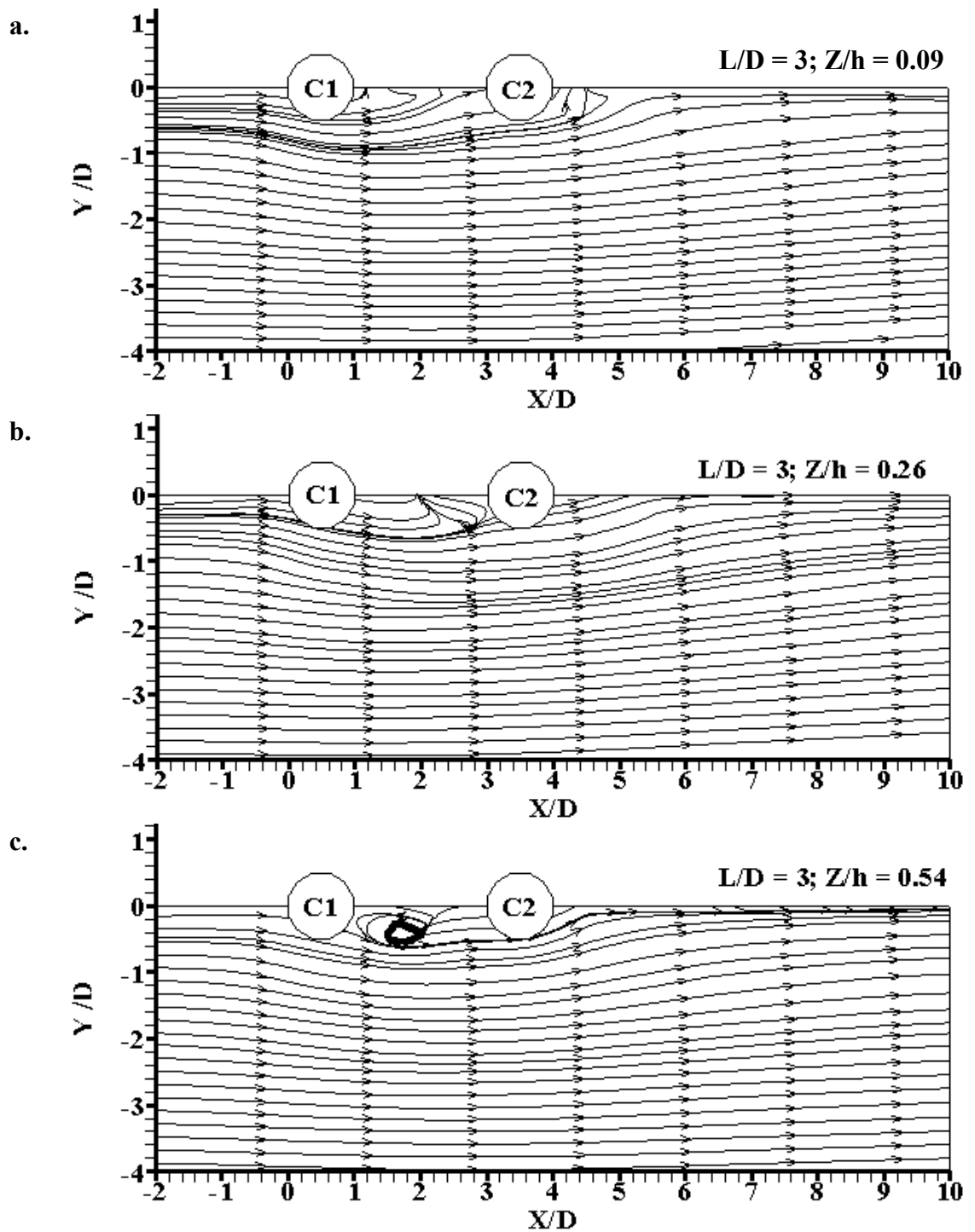


Figure A.9 Streamline plots for two columns with $L/D = 3$ in different horizontal planes; a.) at $Z/h = 0.09$, b.) at $Z/h = 0.26$, and c.) at $Z/h = 0.54$

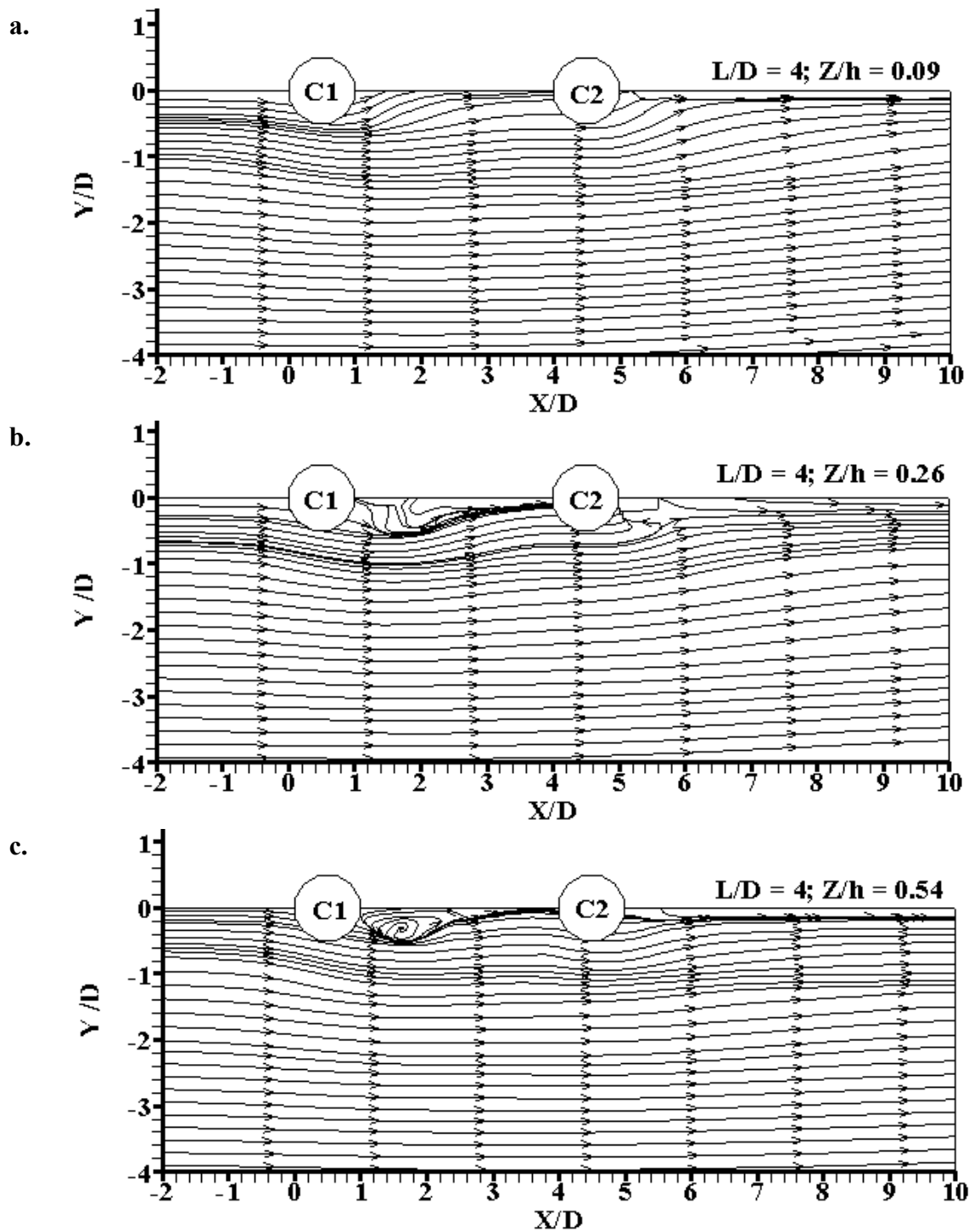


Figure A.10 Streamline plots for two columns with $L/D = 4$ in different horizontal planes; a.) at $Z/h = 0.09$, b.) at $Z/h = 0.26$, and c.) at $Z/h = 0.54$

A.1.3 Contour Plots of Streamwise Velocity Component (u) in Horizontal Plane

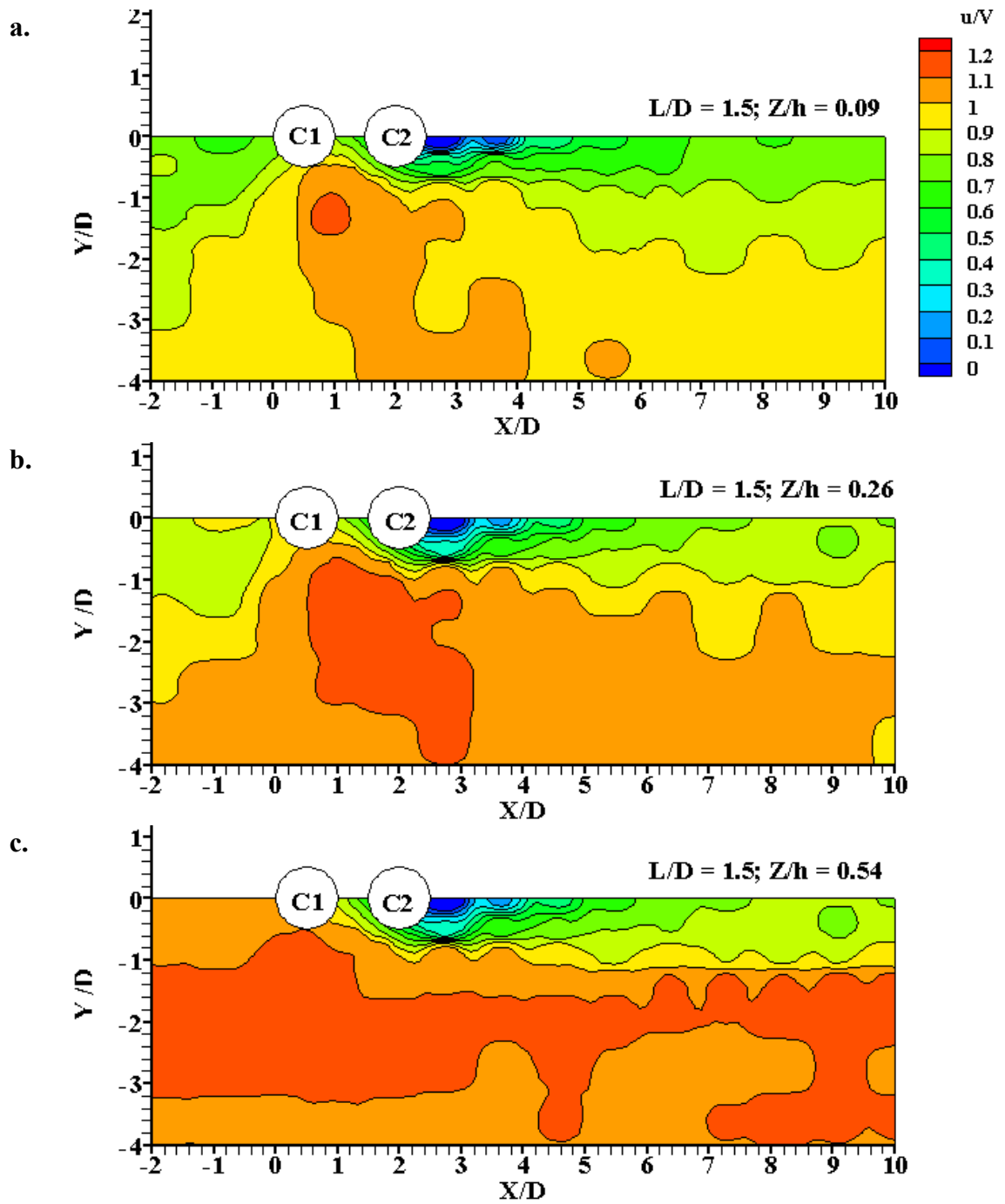


Figure A.11 Contour plots of streamwise velocity component (u/V) for two columns with $L/D = 1.5$ in different horizontal planes; a.) at $Z/h = 0.09$, b.) at $Z/h = 0.26$, and c.) at $Z/h = 0.54$

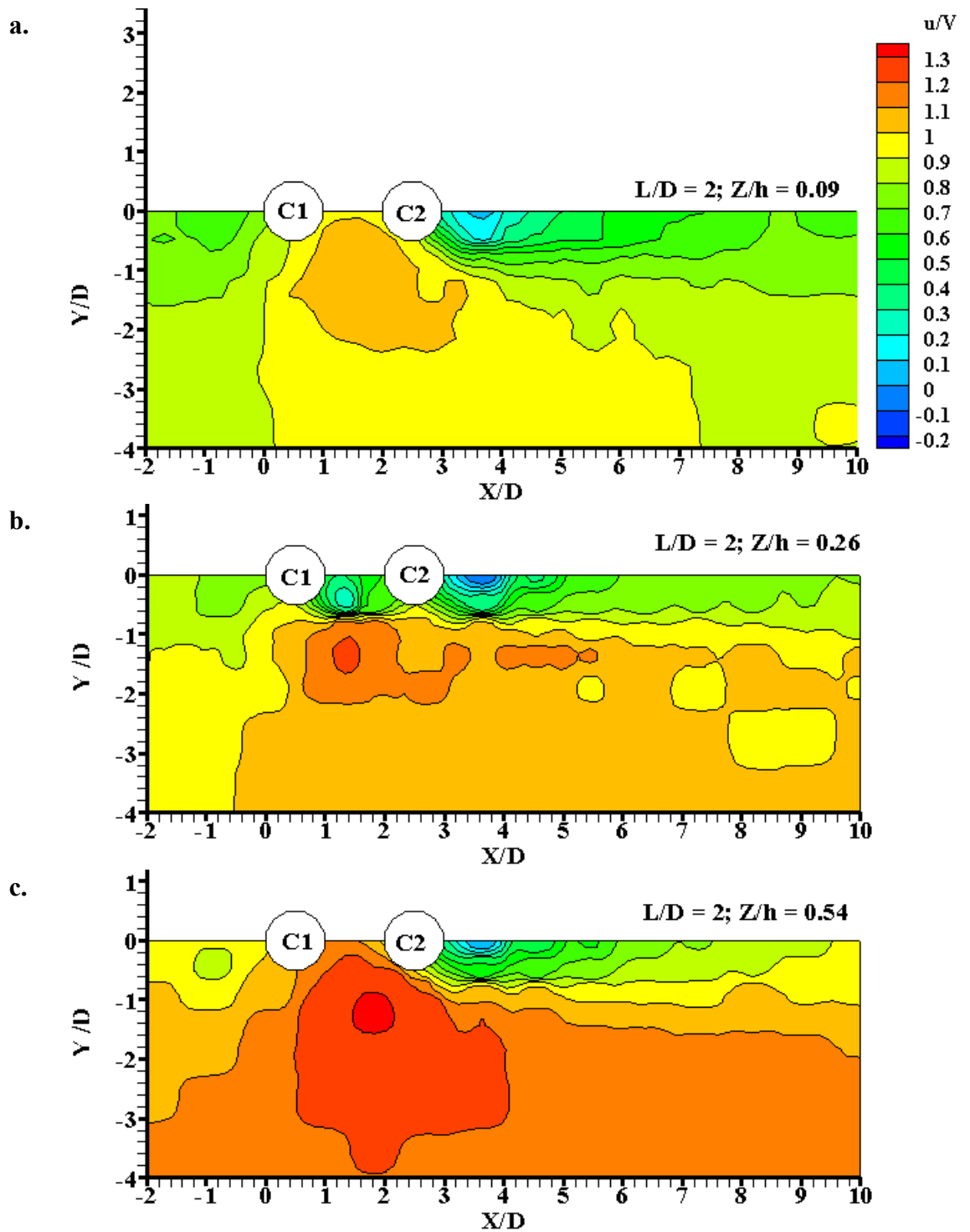


Figure A.12 Contour plots of streamwise velocity component (u/V) for two columns with $L/D = 2$ in different horizontal planes; a.) at $Z/h = 0.09$, b.) at $Z/h = 0.26$, and c.) at $Z/h = 0.54$

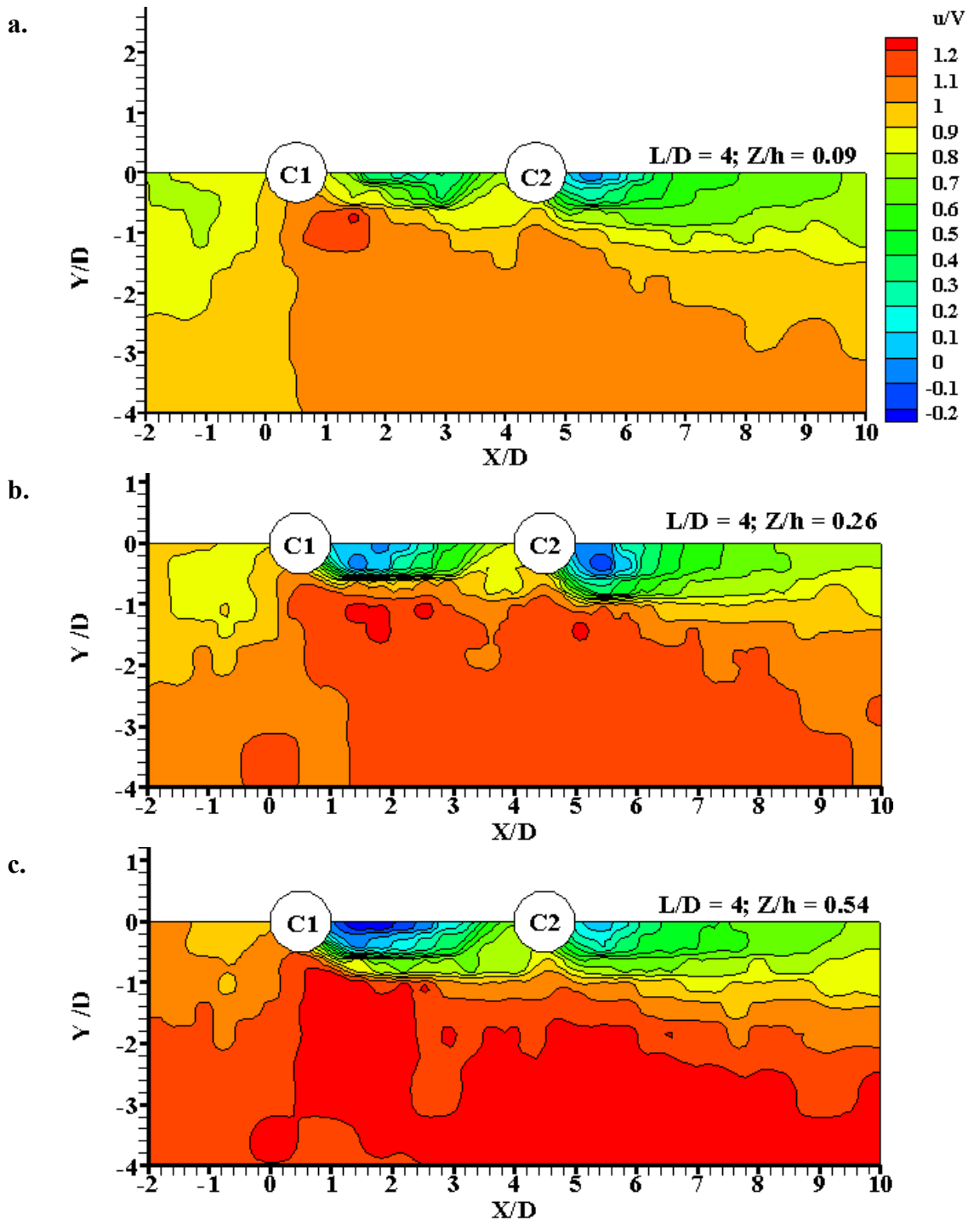


Figure A.13 Contour plots of streamwise velocity component (u/V) for two columns with $L/D = 4$ in different horizontal planes; a.) at $Z/h = 0.09$, b.) at $Z/h = 0.26$, and c.) at $Z/h = 0.54$

A.1.4 Profile Plots of Streamwise Velocity Component (u) in Horizontal Plane

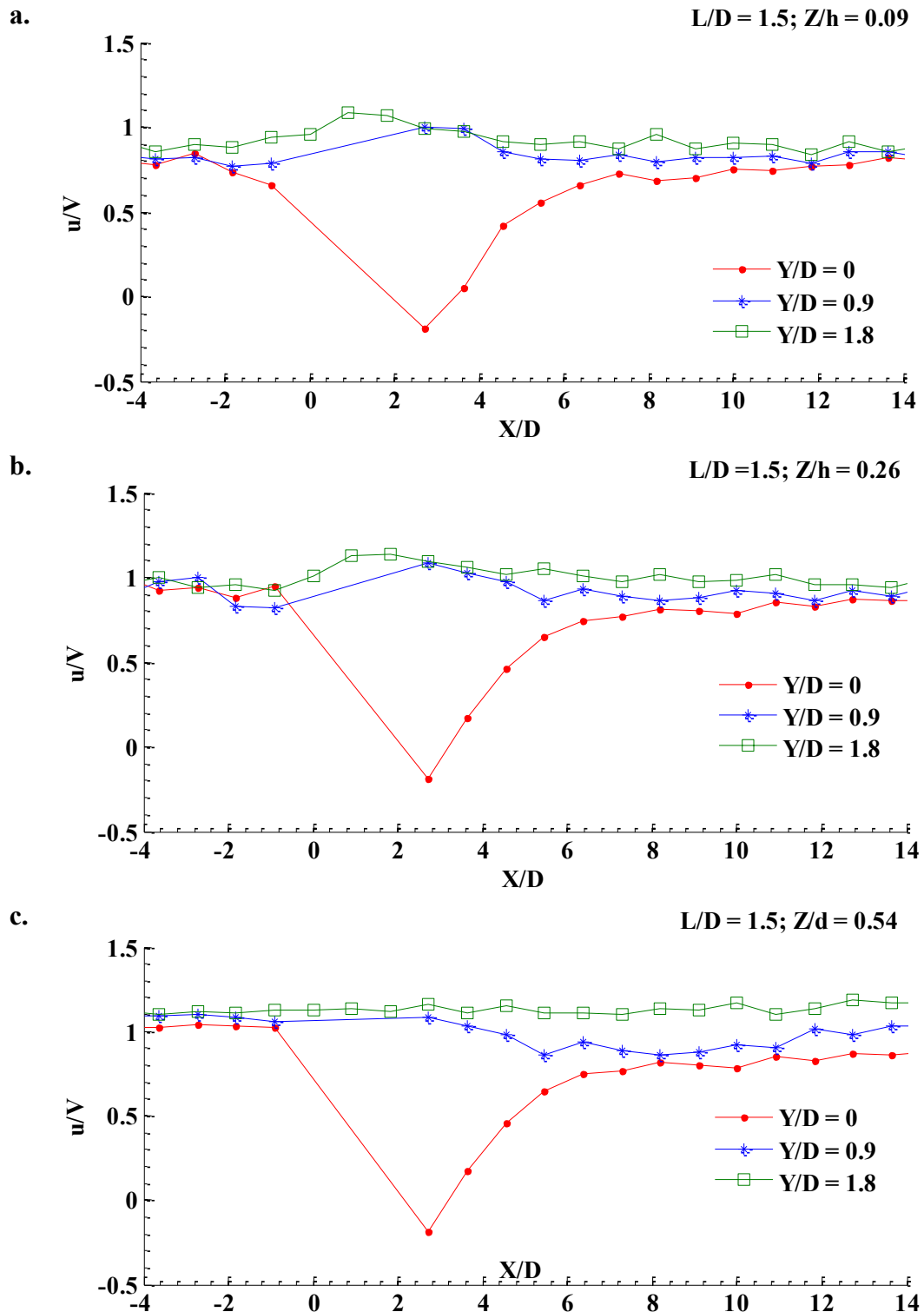


Figure A.14 Profile plots of streamwise velocity component for two columns with $L/D = 1.5$ along three different longitudinal axes in different horizontal planes a) at $Z/h = 0.09$, b) at $Z/h = 0.26$ and c). at $Z/h = 0.54$

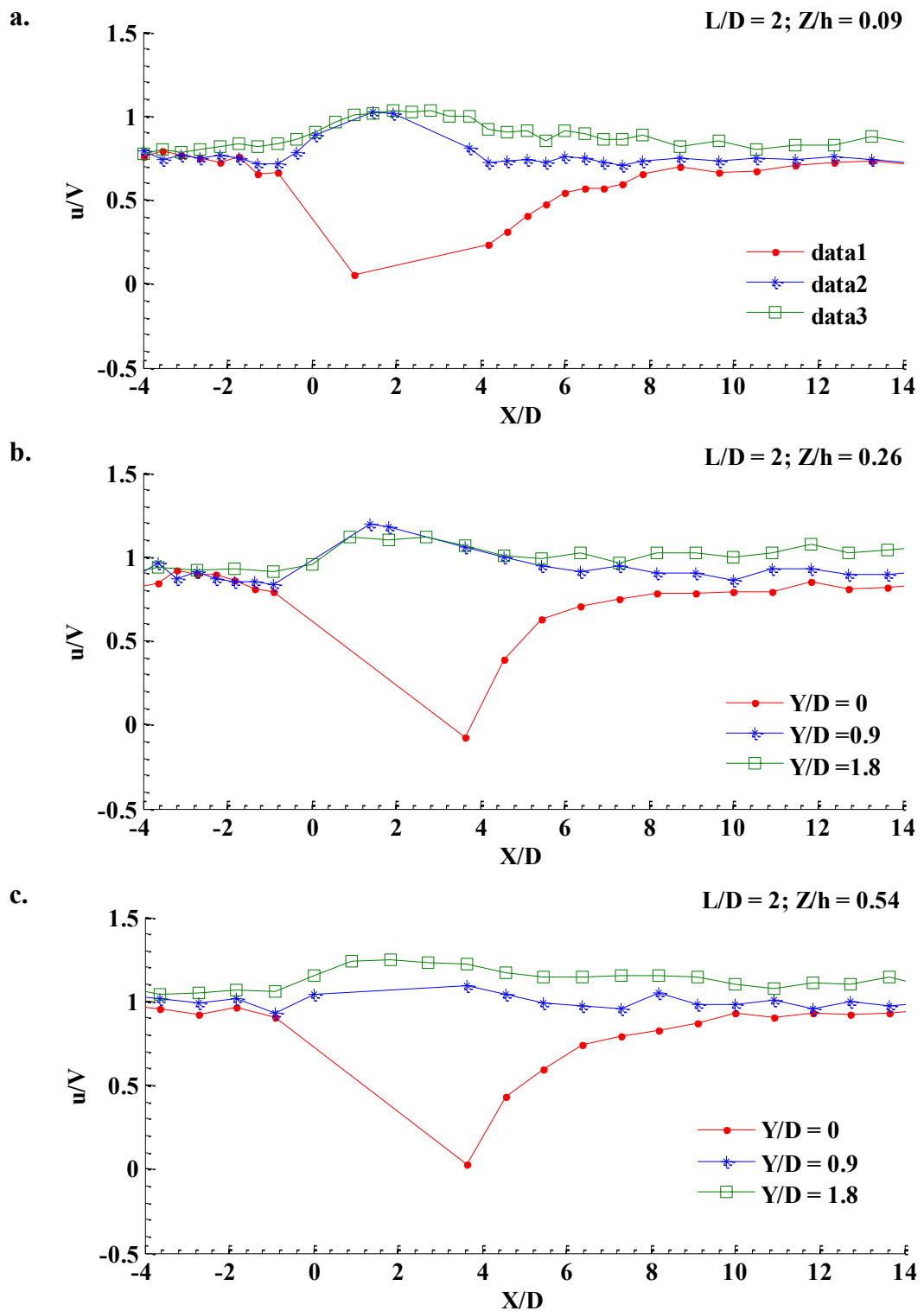


Figure A.15 Profile plots of streamwise velocity component for two columns with $L/D = 2$ along three different longitudinal axes in different horizontal planes a) at $Z/h = 0.09$, b) at $Z/h = 0.26$ and c). at $Z/h = 0.54$

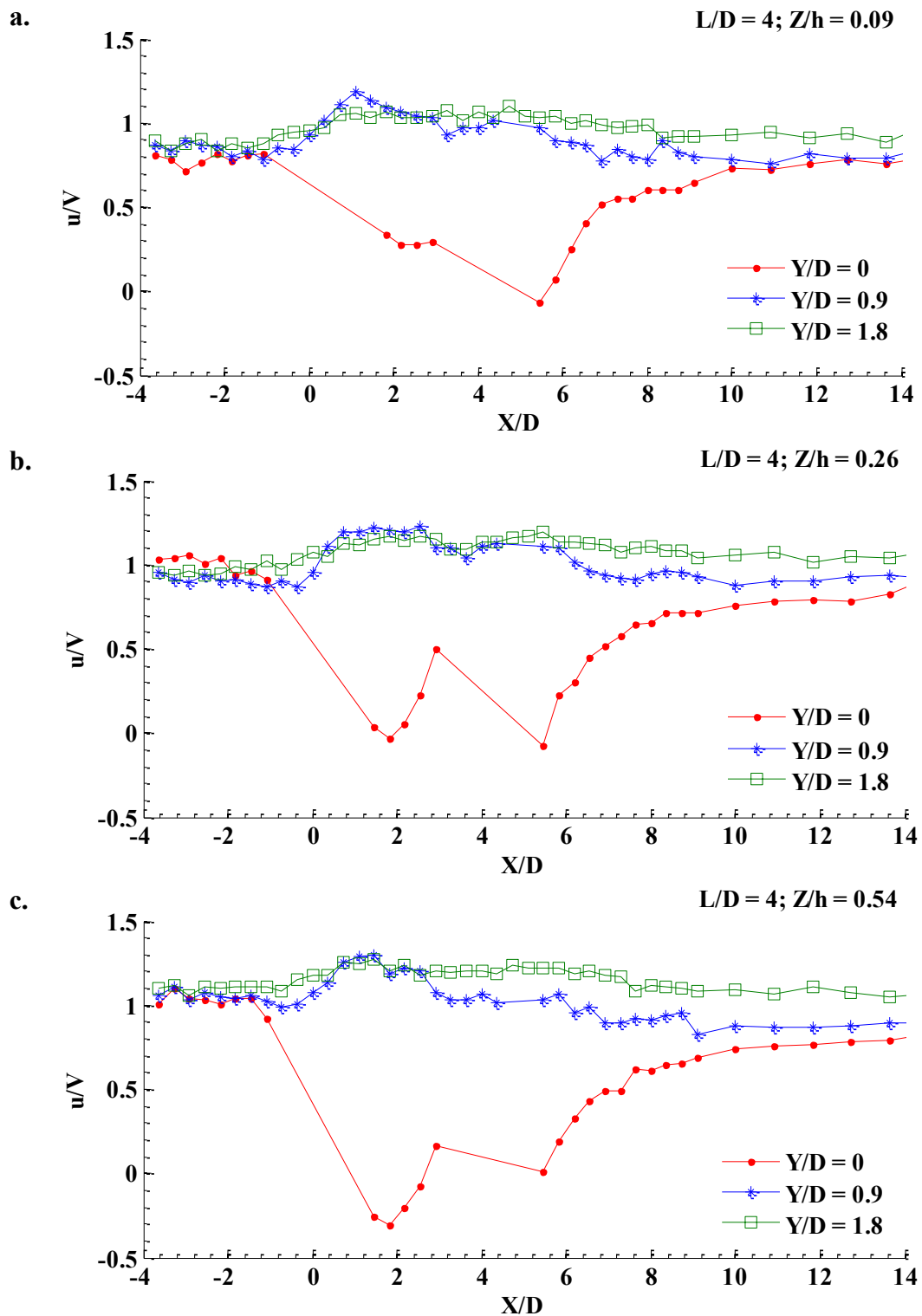


Figure A.16 Profile plots of streamwise velocity component for two columns with $L/D = 4$ along three different longitudinal axes in different horizontal planes a) at $Z/h = 0.09$, b) at $Z/h = 0.26$ and c). at $Z/h = 0.54$

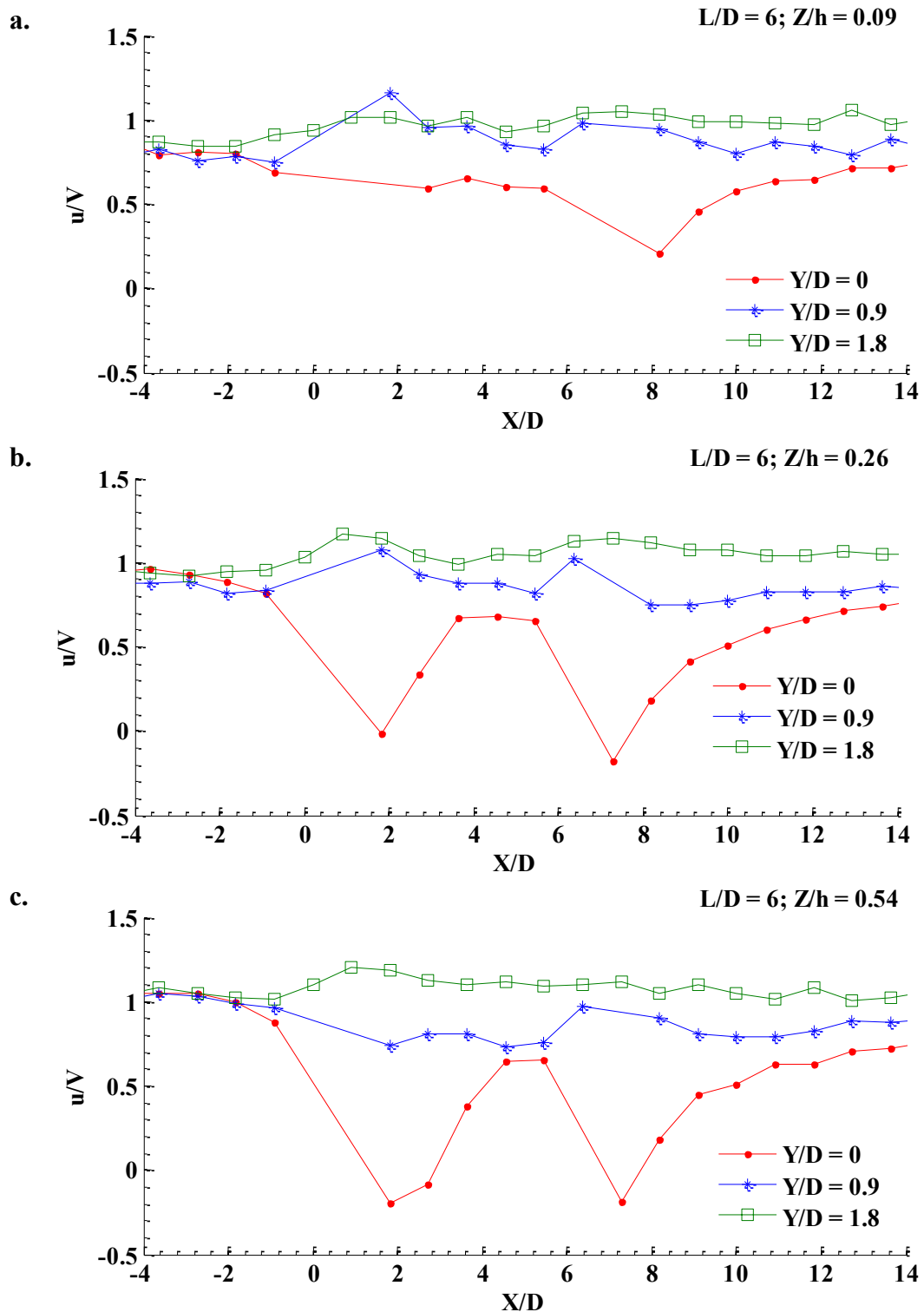


Figure A.17 Profile plots of streamwise velocity component for two columns with $L/D = 6$ along three different longitudinal axes in different horizontal planes a) at $Z/h = 0.09$, b) at $Z/h = 0.26$ and c). at $Z/h = 0.54$

A.1.5 Contour Plots of Transverse Velocity Component (v) in Horizontal Plane

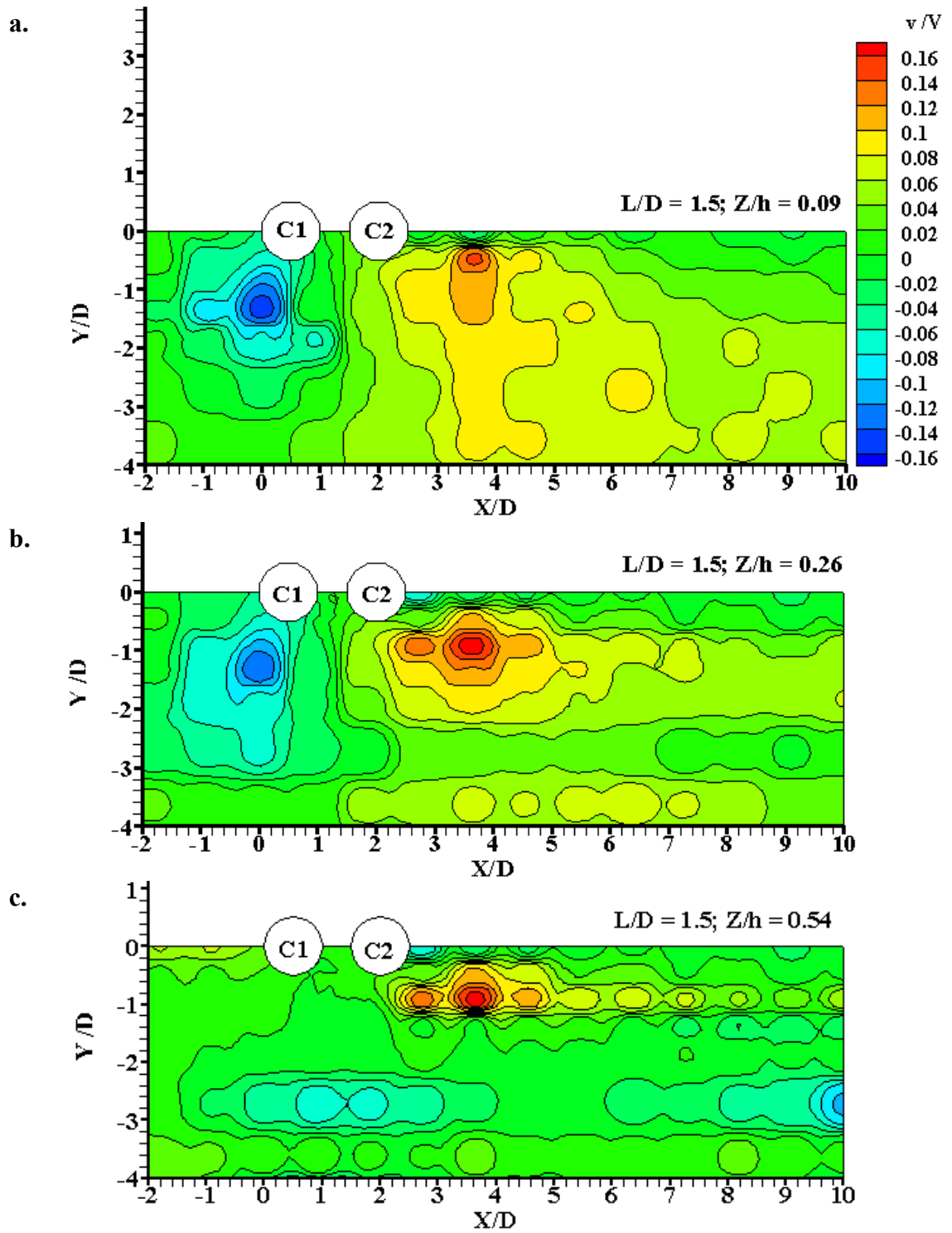


Figure A.18 Contour plots of transverse velocity component (v/V) for two columns with $L/D = 1.5$ in different horizontal planes a) at $Z/h = 0.09$, b) at $Z/h = 0.26$ and c) at $Z/h = 0.54$

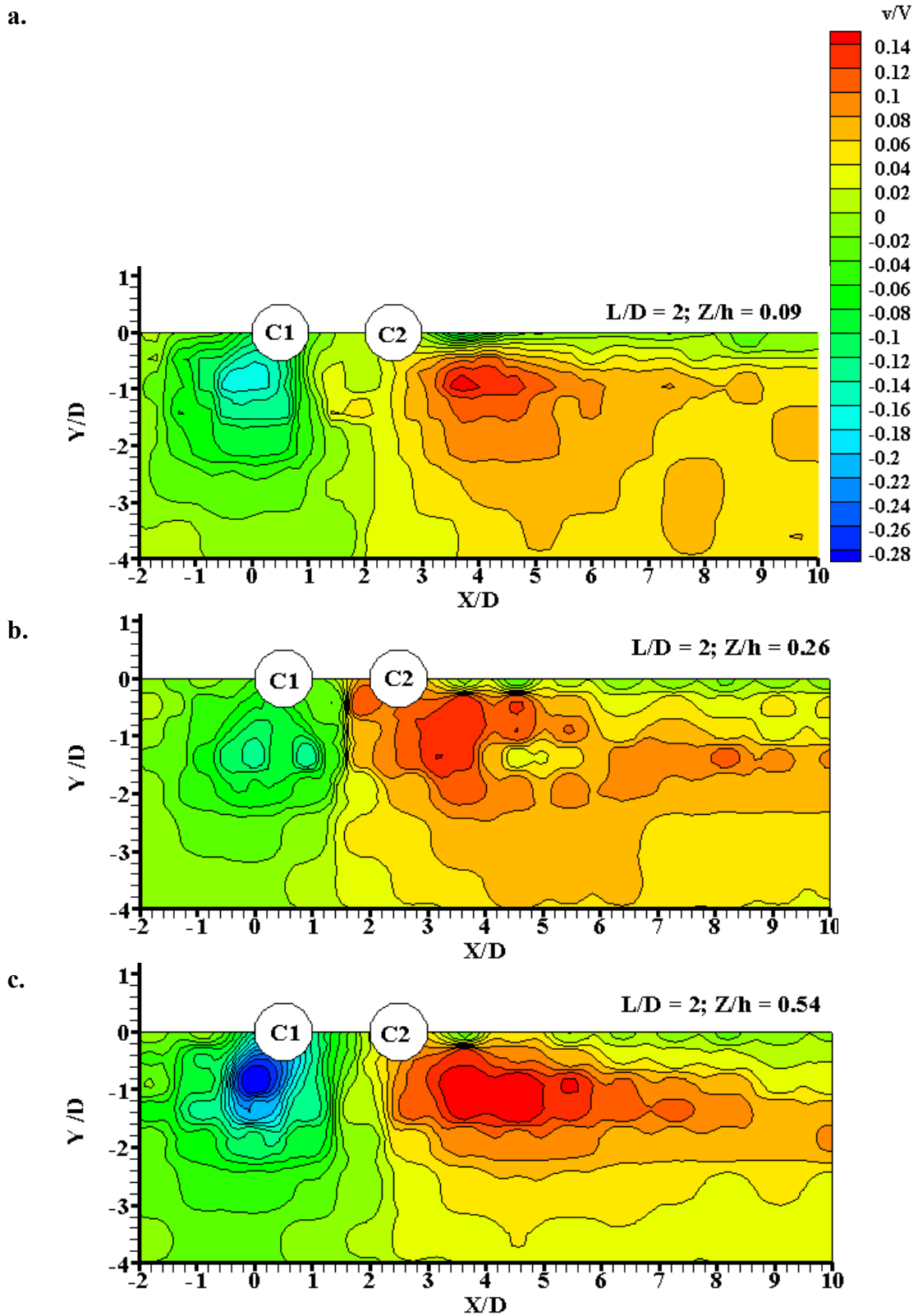


Figure A.19 Contour plots of transverse velocity component (v/V) for two columns with $L/D = 2$ in different horizontal planes a) at $Z/h = 0.09$, b) at $Z/h = 0.26$ and c). at $Z/h = 0.54$

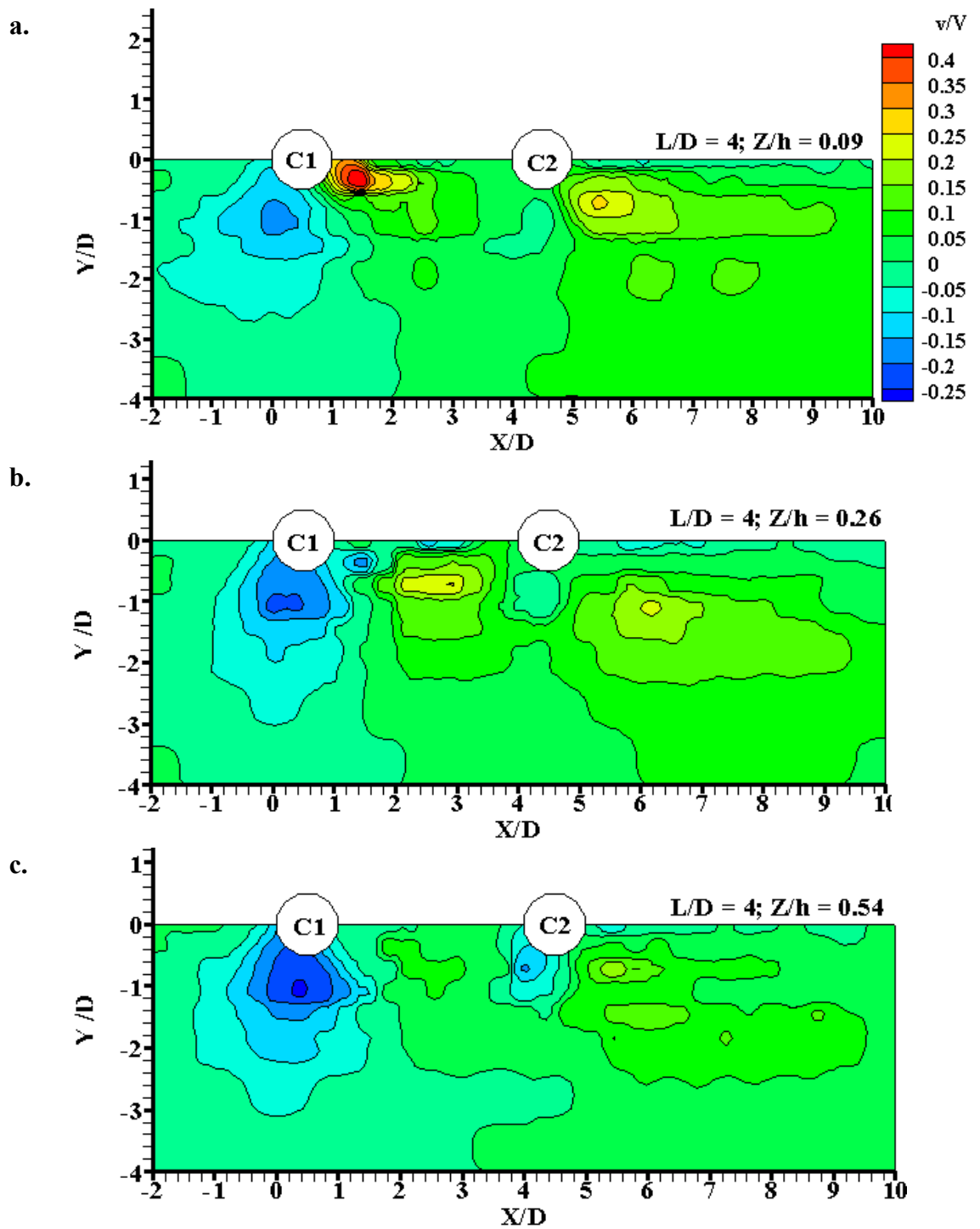


Figure A.19 Contour plots of transverse velocity component (v/V) for two columns with $L/D = 4$ in different horizontal planes a) at $Z/h = 0.09$, b) at $Z/h = 0.26$ and c). at $Z/h = 0.54$

A.1.6 Profile Plots of Transverse Velocity Component (v) in Horizontal Plane

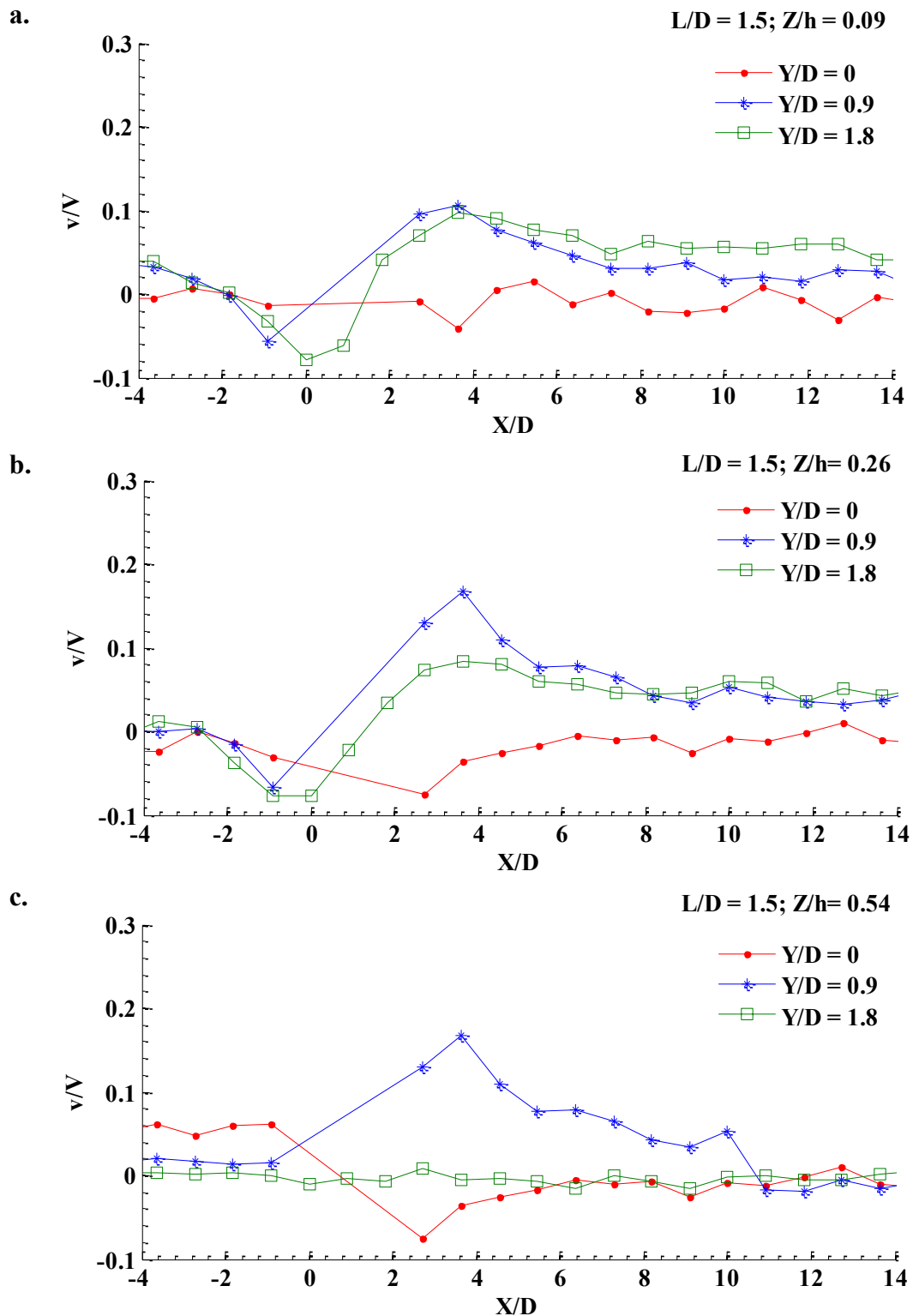


Figure A.20 Profile plots of transverse velocity component for two columns with $L/D = 1.5$ along three different longitudinal axes in different horizontal planes a) at $Z/h = 0.09$, b) at $Z/h = 0.26$ and c). at $Z/h = 0.54$

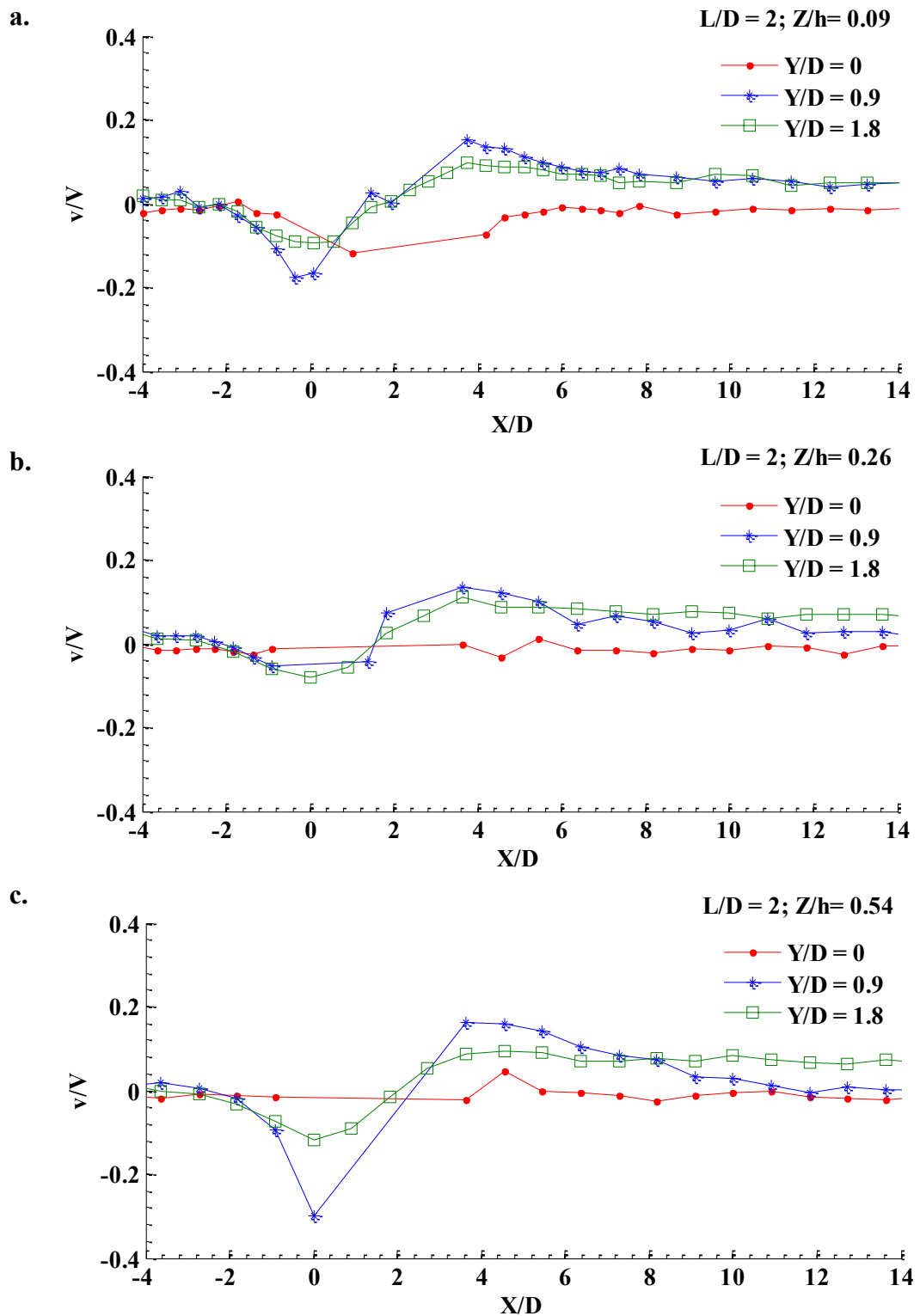


Figure A.21 Profile plots of transverse velocity component for two columns with $L/D = 2$ along three different longitudinal axes in different horizontal planes a) at $Z/h = 0.09$, b) at $Z/h = 0.26$ and c). at $Z/h = 0.54$

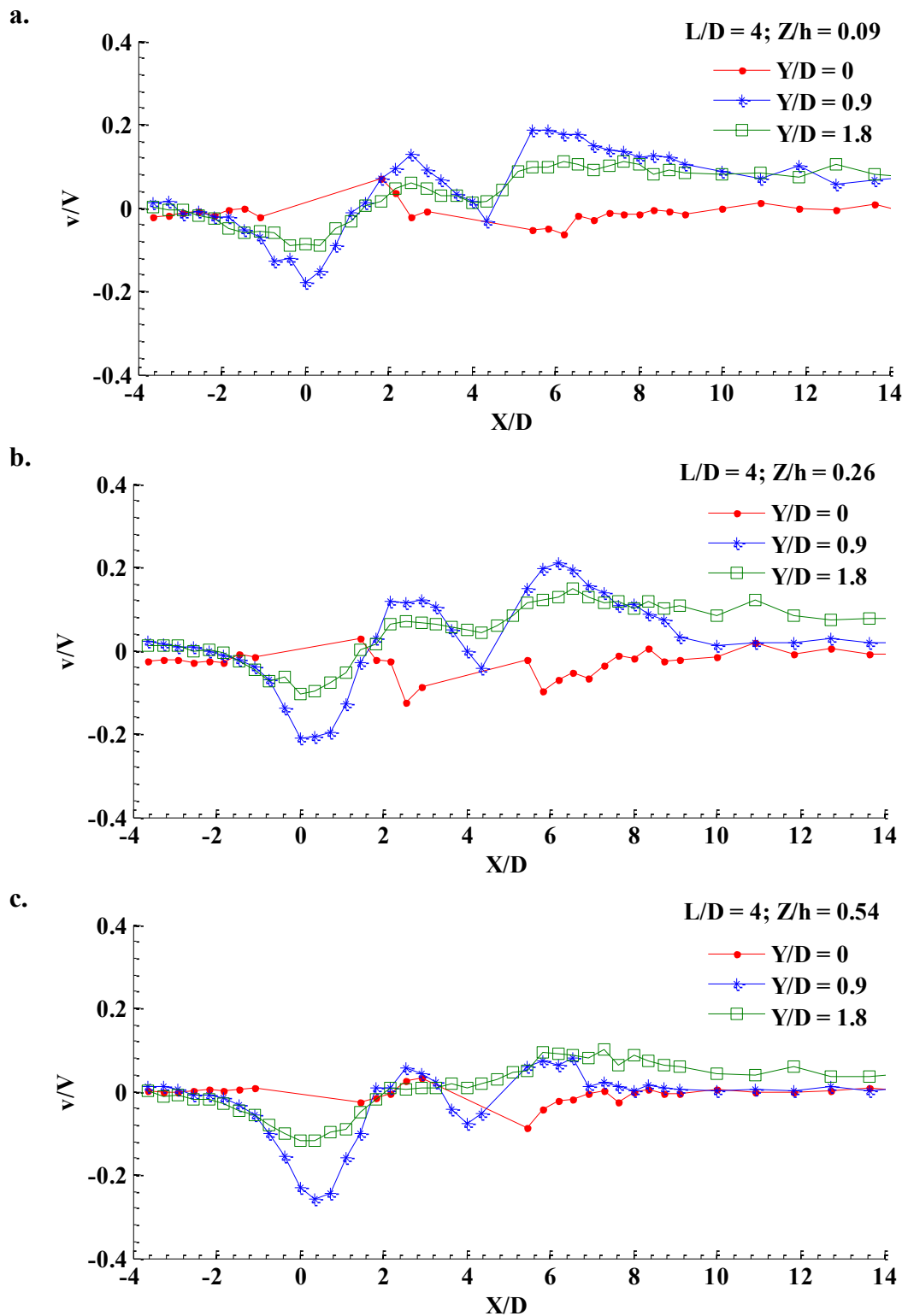


Figure A.23 Profile plots of transverse velocity component for two columns with $L/D = 4$ along three different longitudinal axes in different horizontal planes a) at $Z/h = 0.09$, b) at $Z/h = 0.26$ and c). at $Z/h = 0.54$

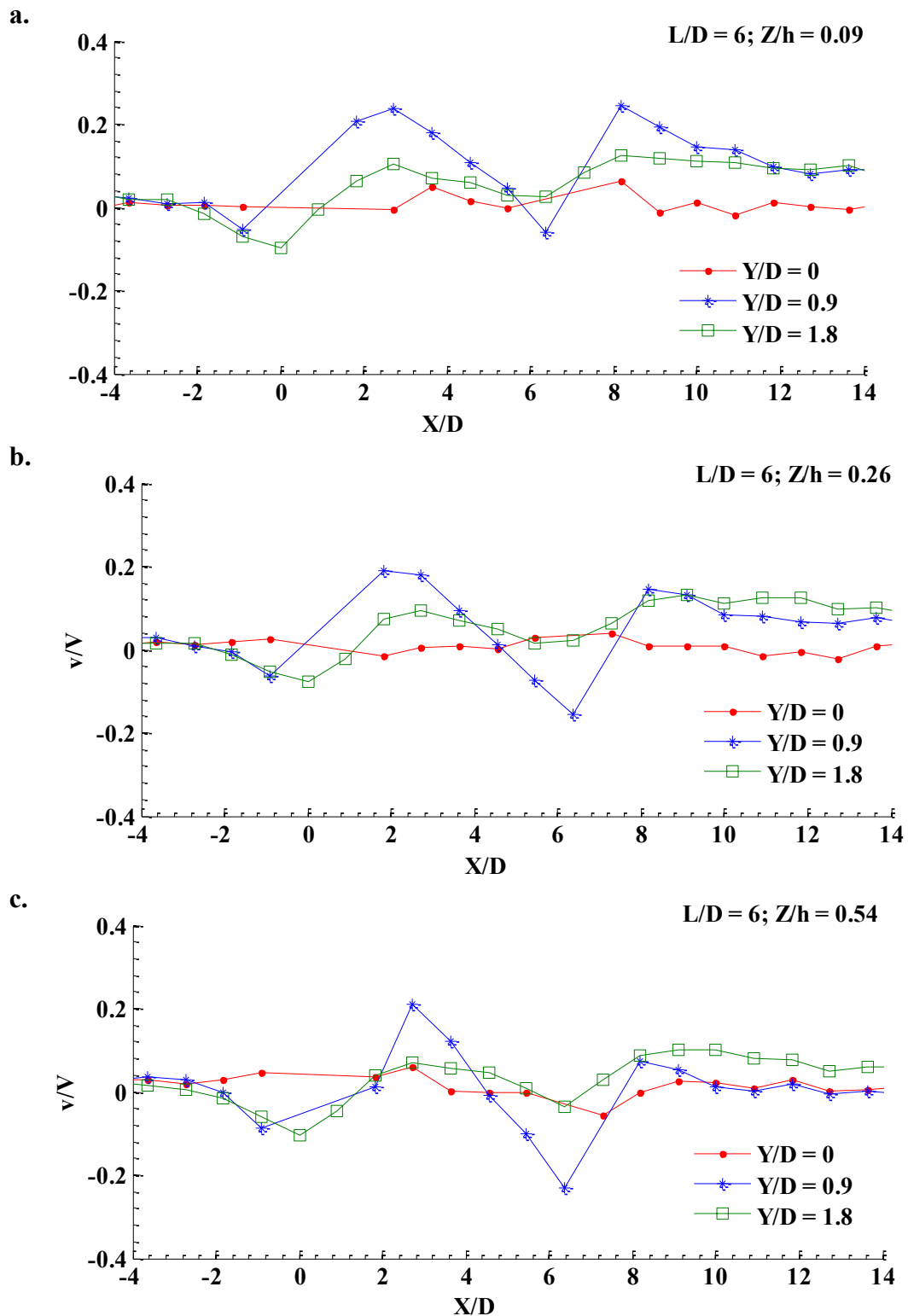


Figure A.24 Profile plots of transverse velocity component for two columns with $L/D = 6$ along three different longitudinal axes in different horizontal planes a) at $Z/h = 0.09$, b) at $Z/h = 0.26$ and c). at $Z/h = 0.54$

A.1.7 Contour Plots of Vertical Velocity Component (w) in Horizontal Plane

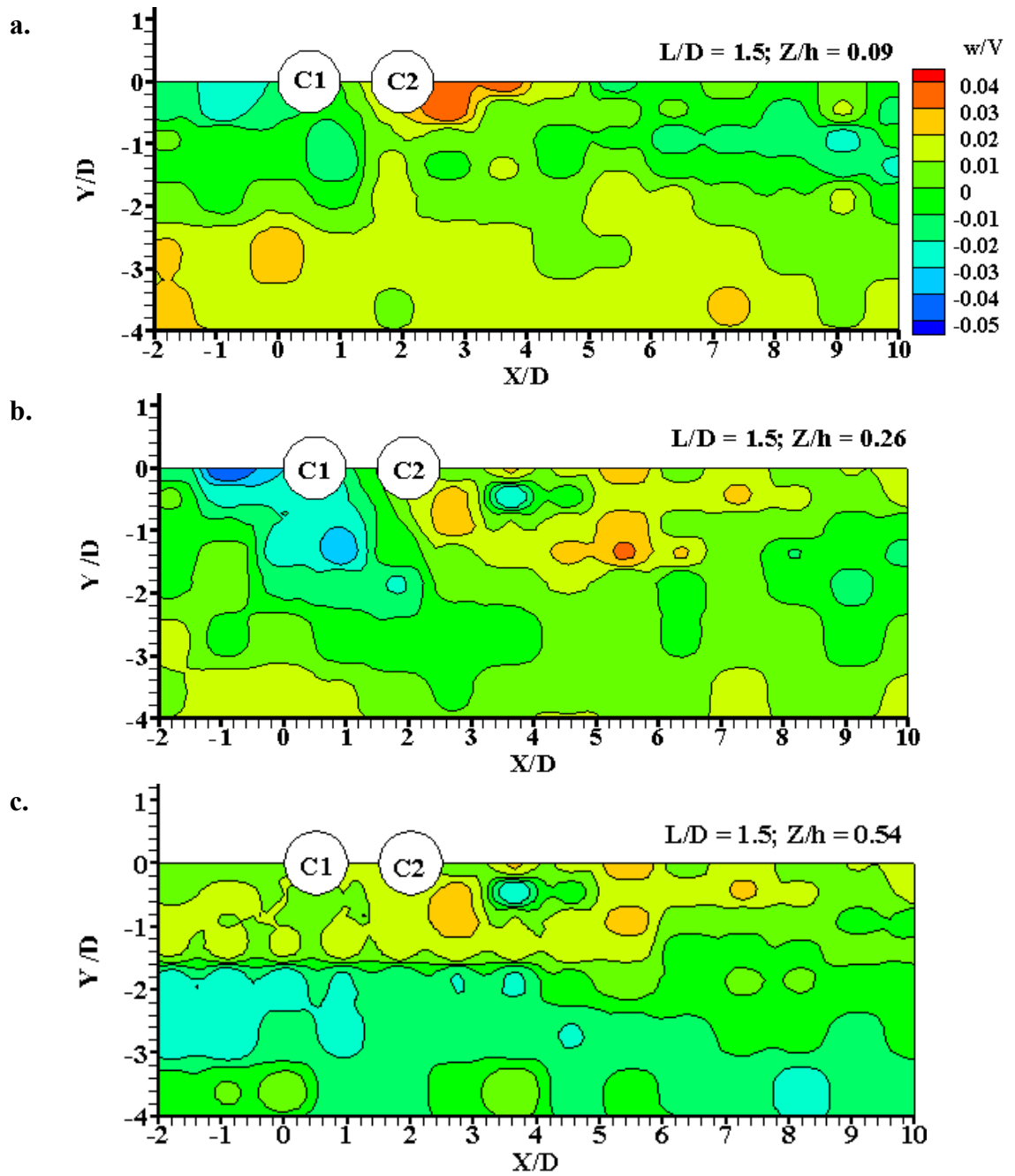


Figure A.25 Contour plots of vertical velocity component (w/V) for two columns with $L/D = 1.5$ in different horizontal planes a) at $Z/h = 0.09$, b) at $Z/h = 0.26$ and c). at $Z/h = 0.54$

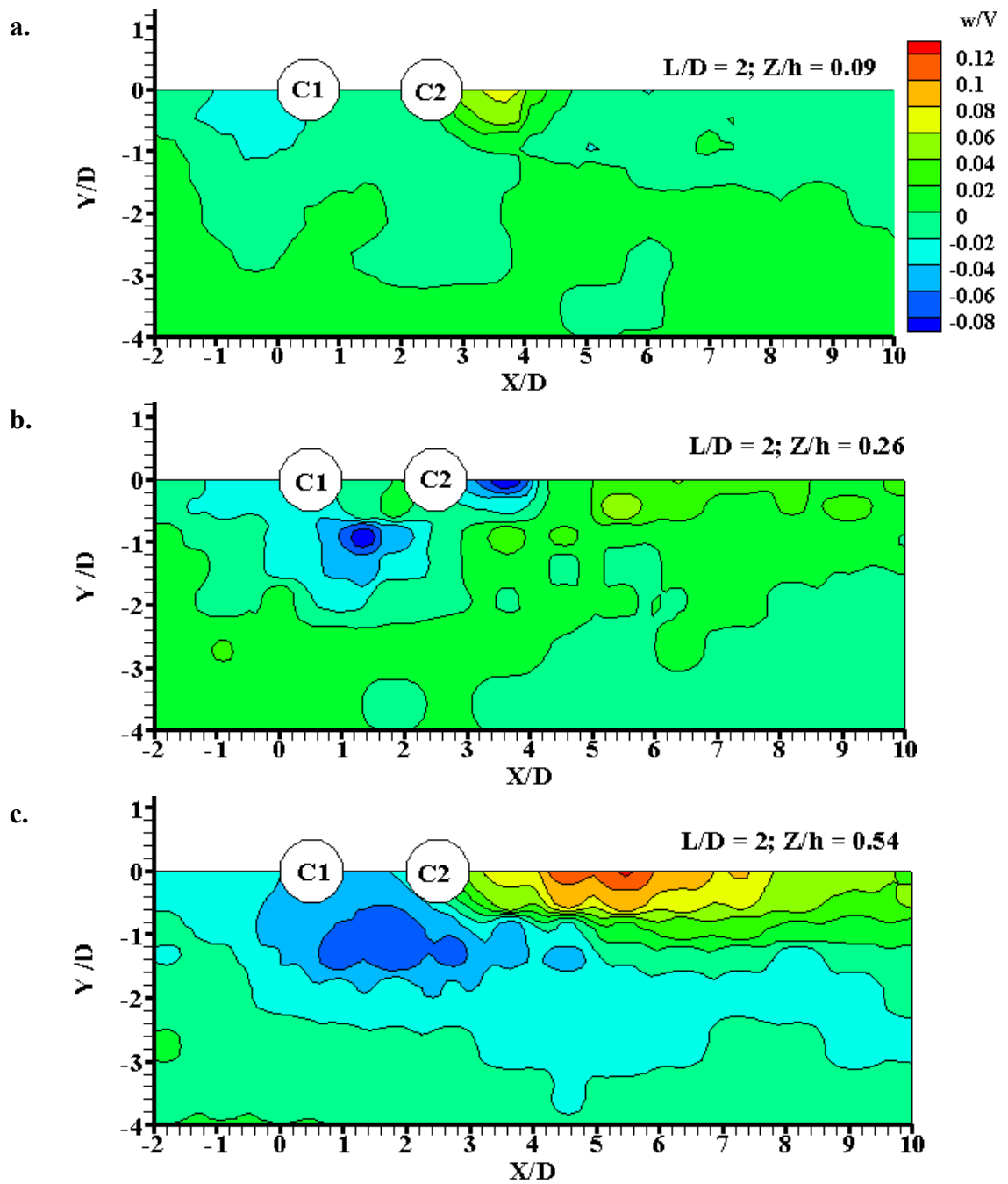


Figure A.26 Contour plots of vertical velocity component (w/V) for two columns with $L/D = 2$ in different horizontal planes a) at $Z/h = 0.09$, b) at $Z/h = 0.26$ and c). at $Z/h = 0.54$

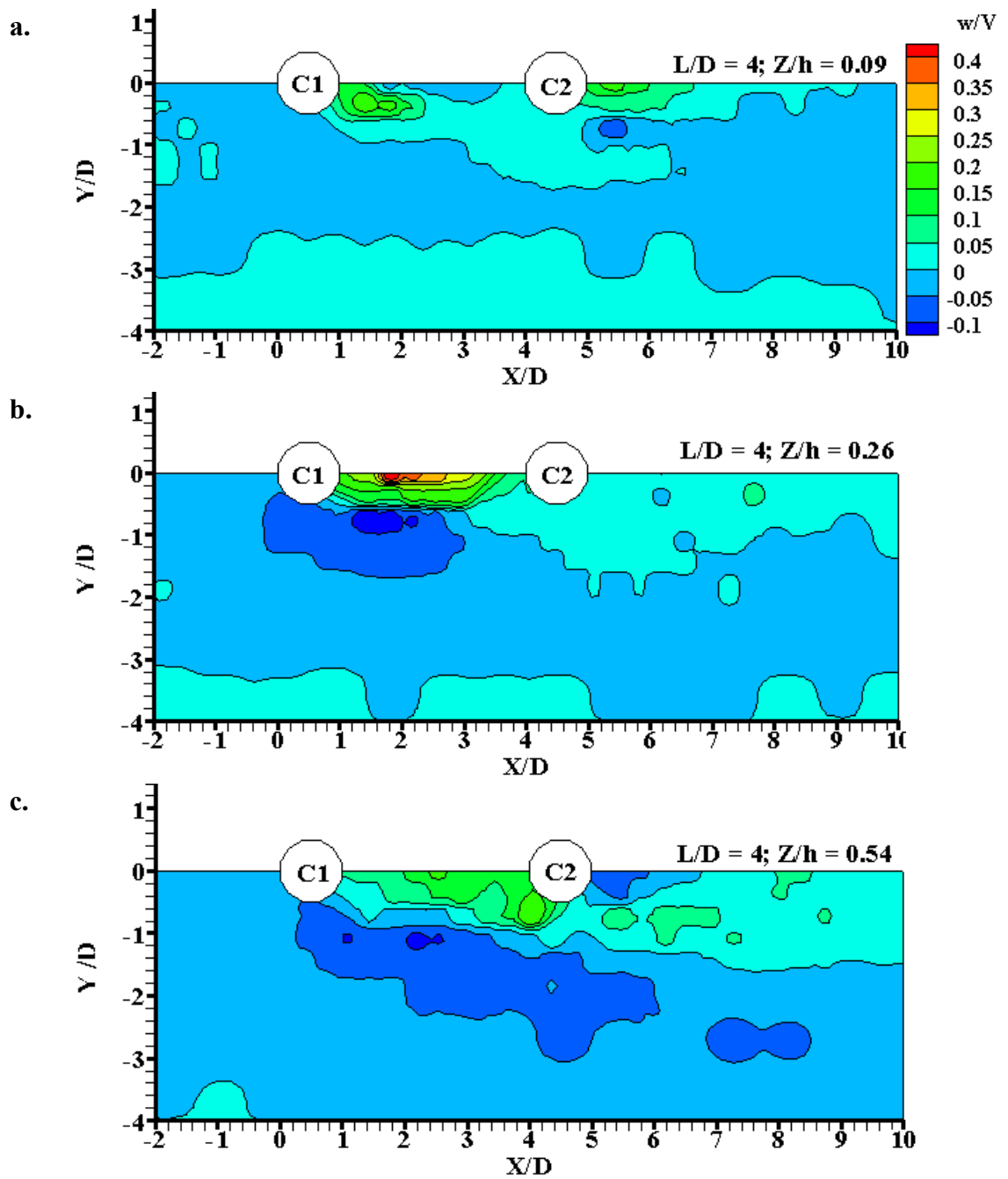


Figure A.27 Contour plots of vertical velocity component (w/V) for two columns with $L/D = 4$ in different horizontal planes a) at $Z/h = 0.09$, b) at $Z/h = 0.26$ and c). at $Z/h = 0.54$

A.1.8 Profile Plots of Vertical Velocity Component (w) in Horizontal Plane

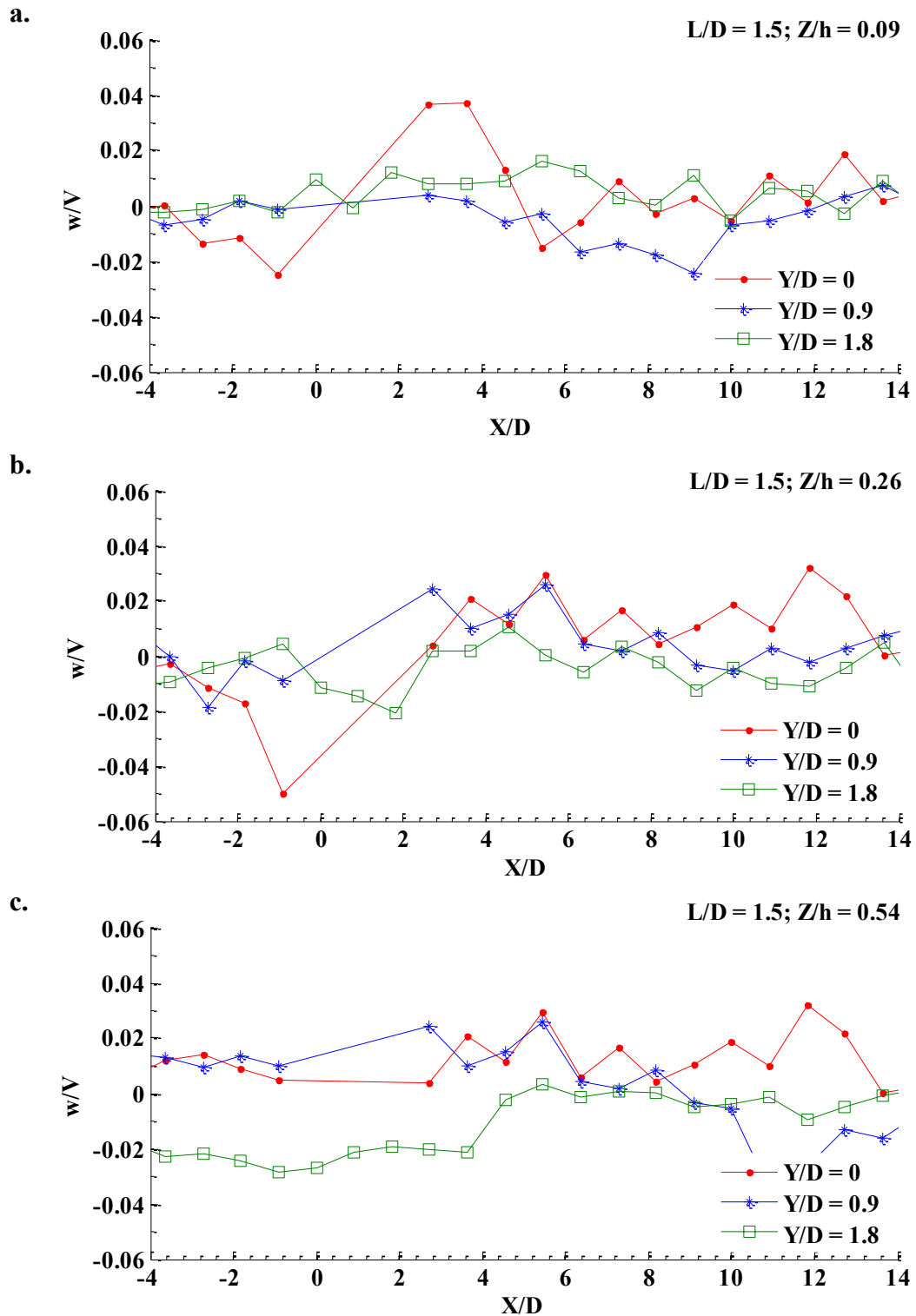


Figure A.28 Profile plots of vertical velocity component for two columns with $L/D = 1.5$ along three different longitudinal axes in different horizontal planes a) at $Z/h = 0.09$, b) at $Z/h = 0.26$ and c). at $Z/h = 0.54$

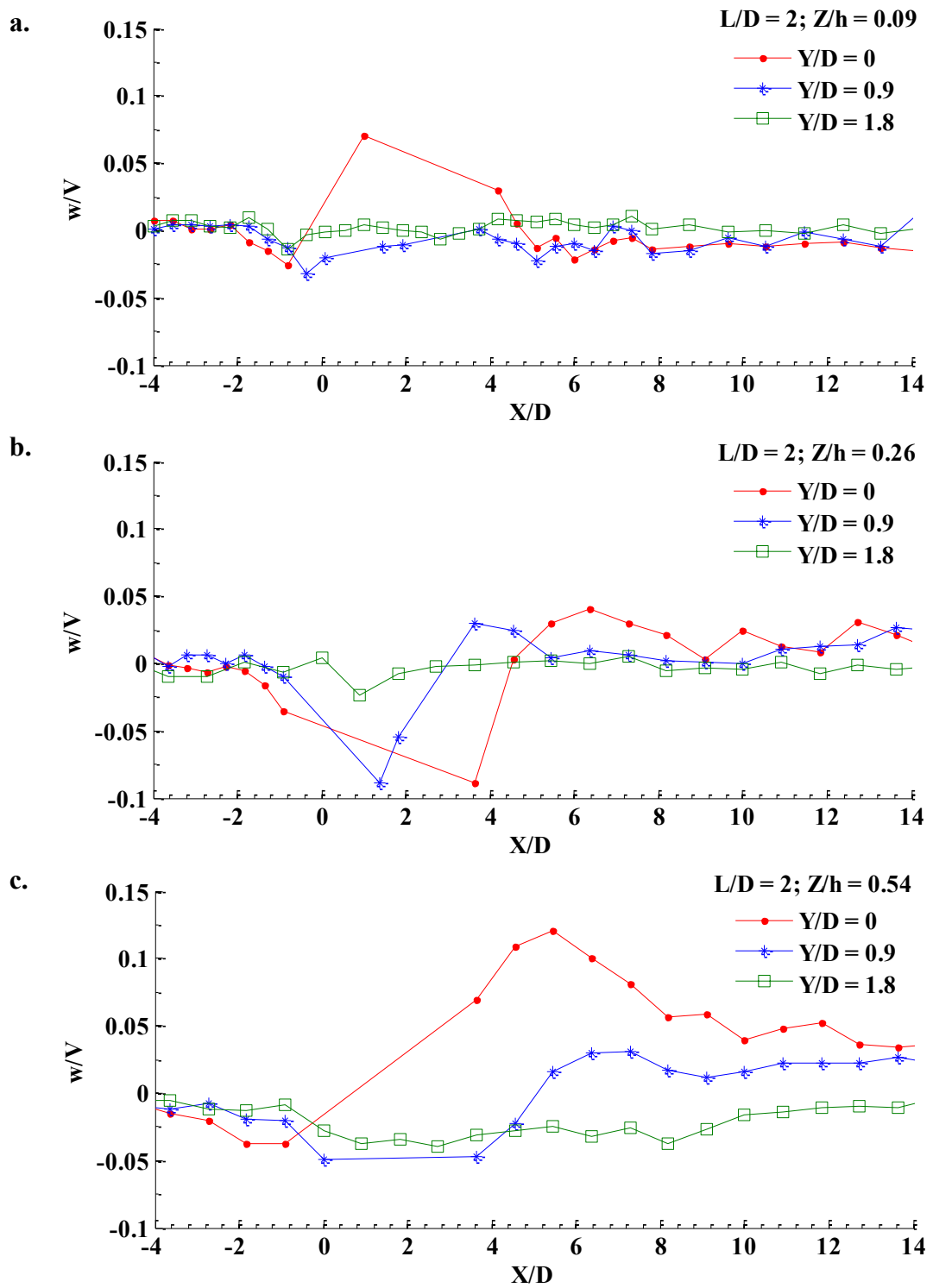


Figure A.29 Profile plots of vertical velocity component for two columns with $L/D = 2$ along three different longitudinal axes in different horizontal planes a) at $Z/h = 0.09$, b) at $Z/h = 0.26$ and c). at $Z/h = 0.54$

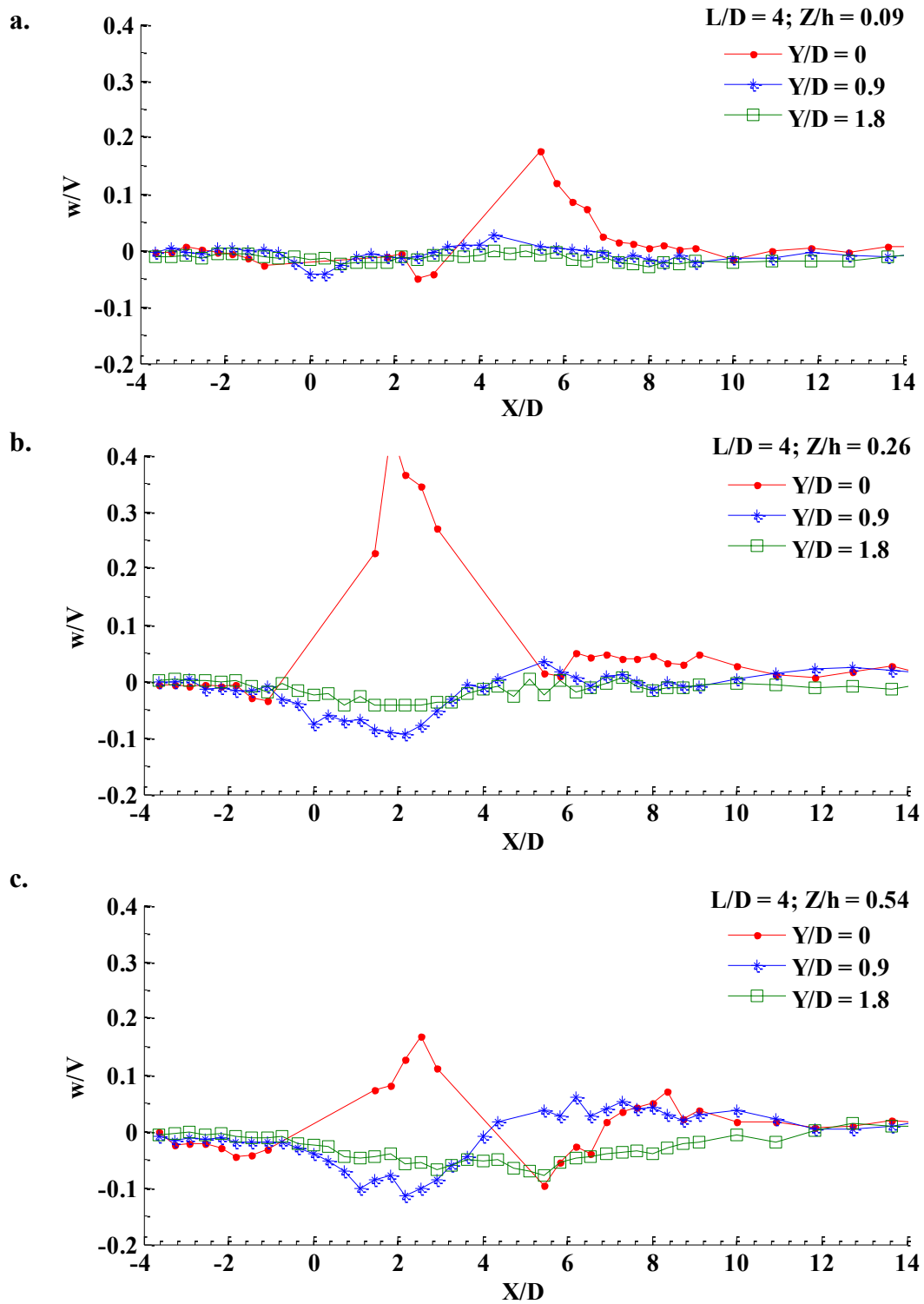


Figure A.30 Profile plots of vertical velocity component for two columns with $L/D = 4$ along three different longitudinal axes in different horizontal planes a) at $Z/h = 0.09$, b) at $Z/h = 0.26$ and c). at $Z/h = 0.54$

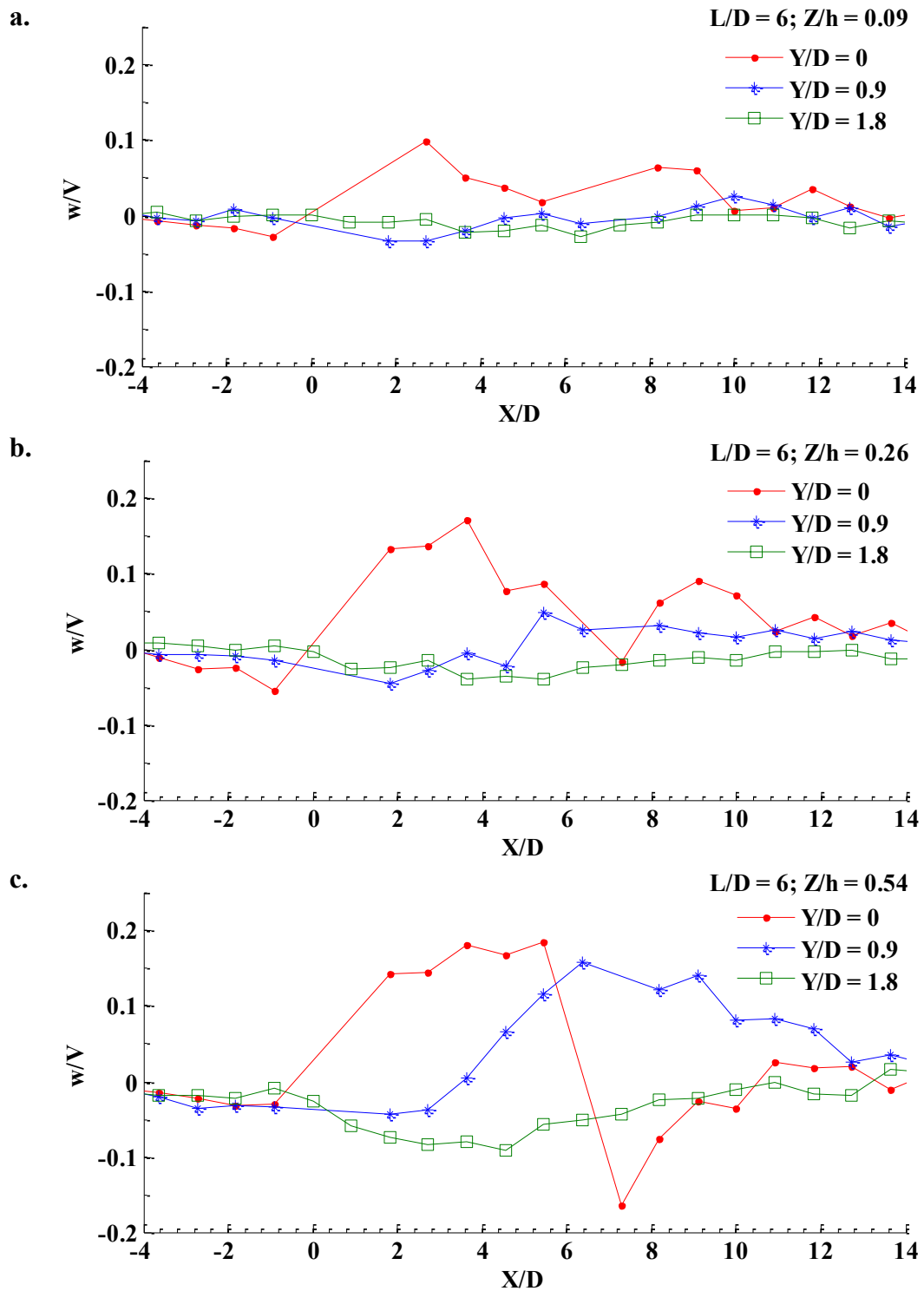


Figure A.31 Profile plots of vertical velocity component for two columns with $L/D = 6$ along three different longitudinal axes in different horizontal planes a) at $Z/h = 0.09$, b) at $Z/h = 0.26$ and c). at $Z/h = 0.54$

A.2 Plots of Velocity Components for Vertical Plane.

A.2.1 Velocity Vector Plots in Vertical Plane

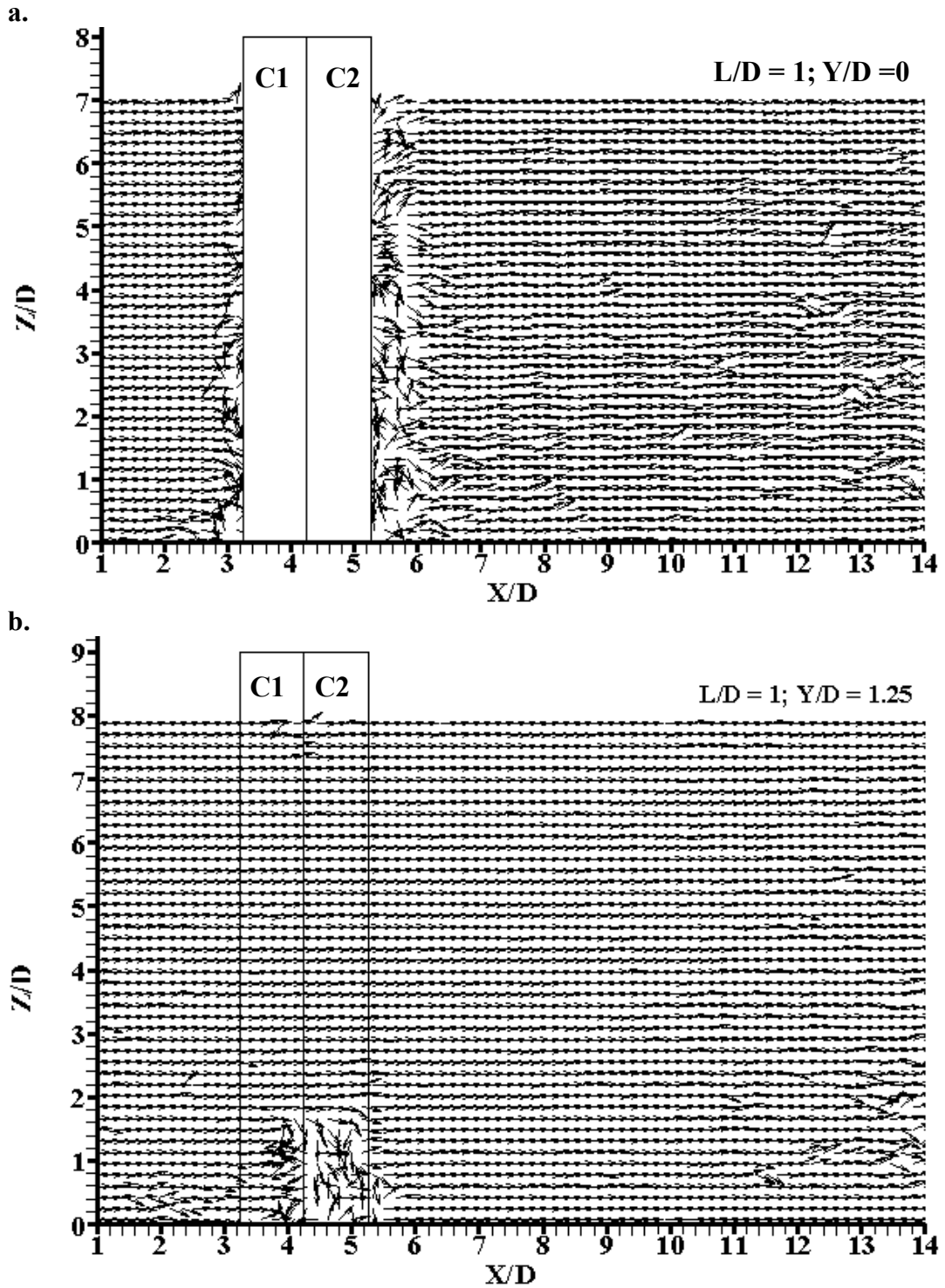


Figure A.32 Vector plots for two columns case with $L/D = 1$ in different vertical planes; a.) at $Y/D = 0$, and b.) at $Y/D = 1.25$

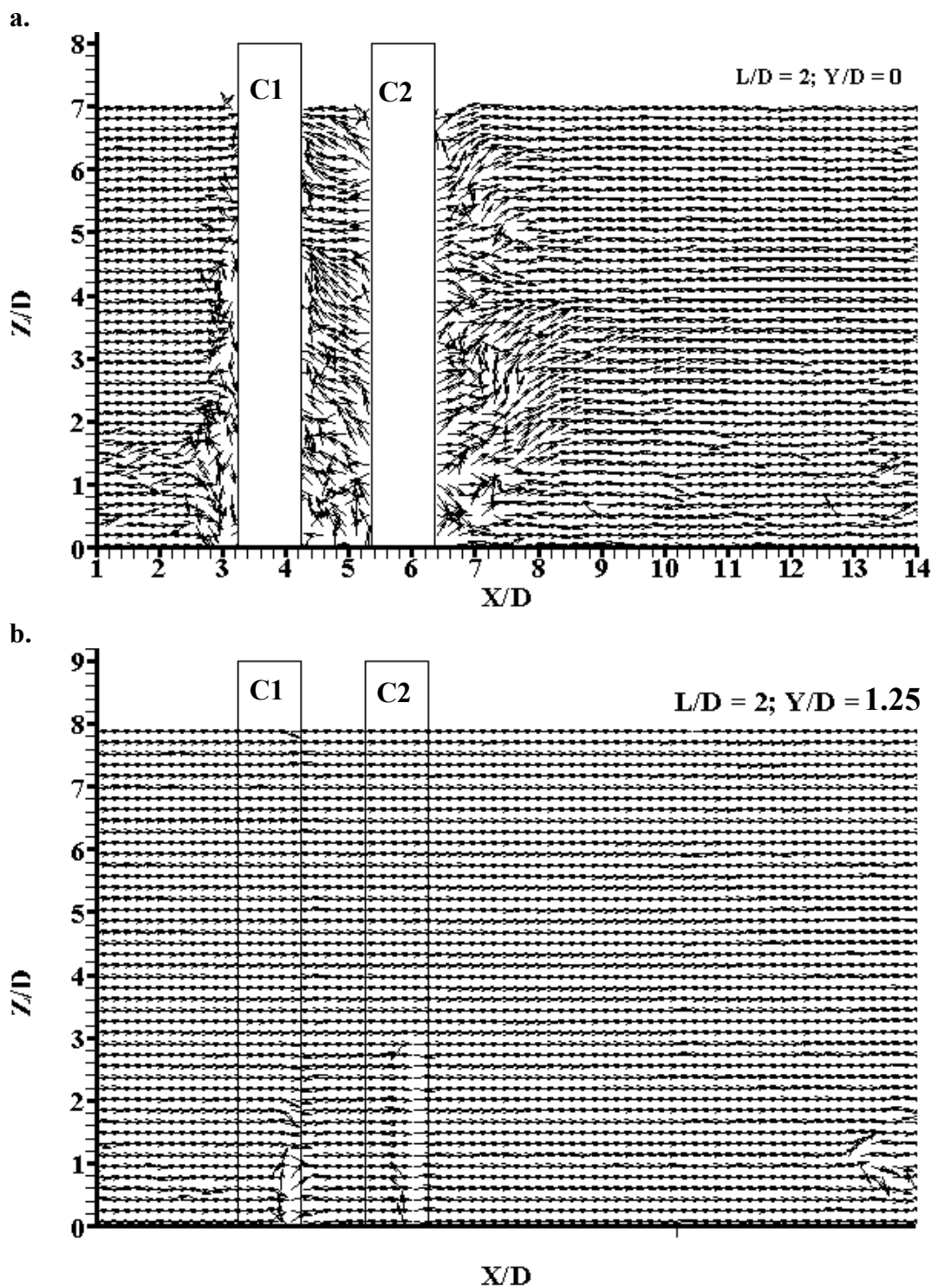


Figure A.33 Vector plots for two columns case with $L/D = 2$ in different vertical planes; a.) at $Y/D = 0$, and b.) at $Y/D = 1.25$

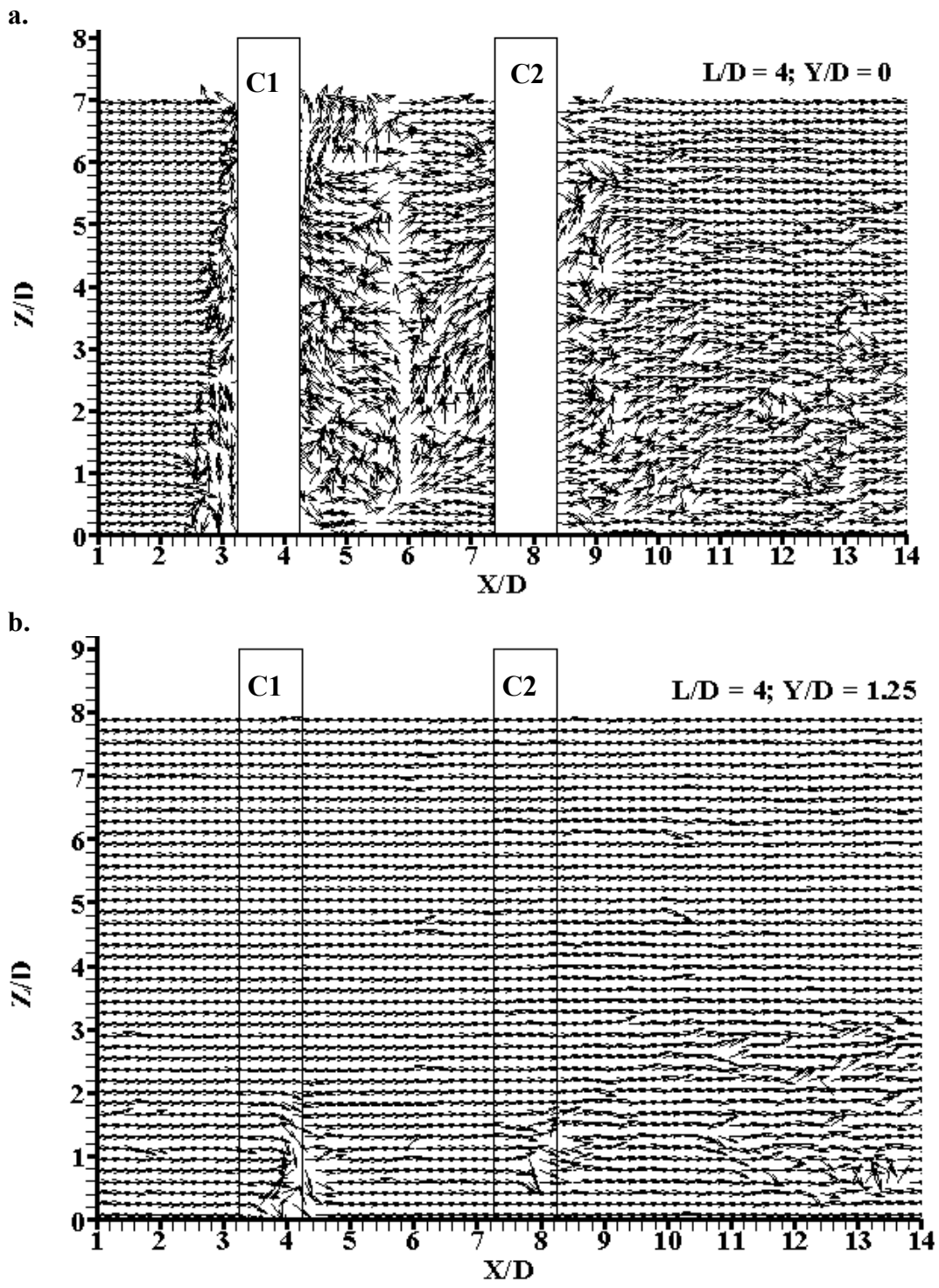


Figure A.34 Vector plots for two columns case with $L/D = 4$ in different vertical planes; a.) at $Y/D = 0$, and b.) at $Y/D = 1.25$

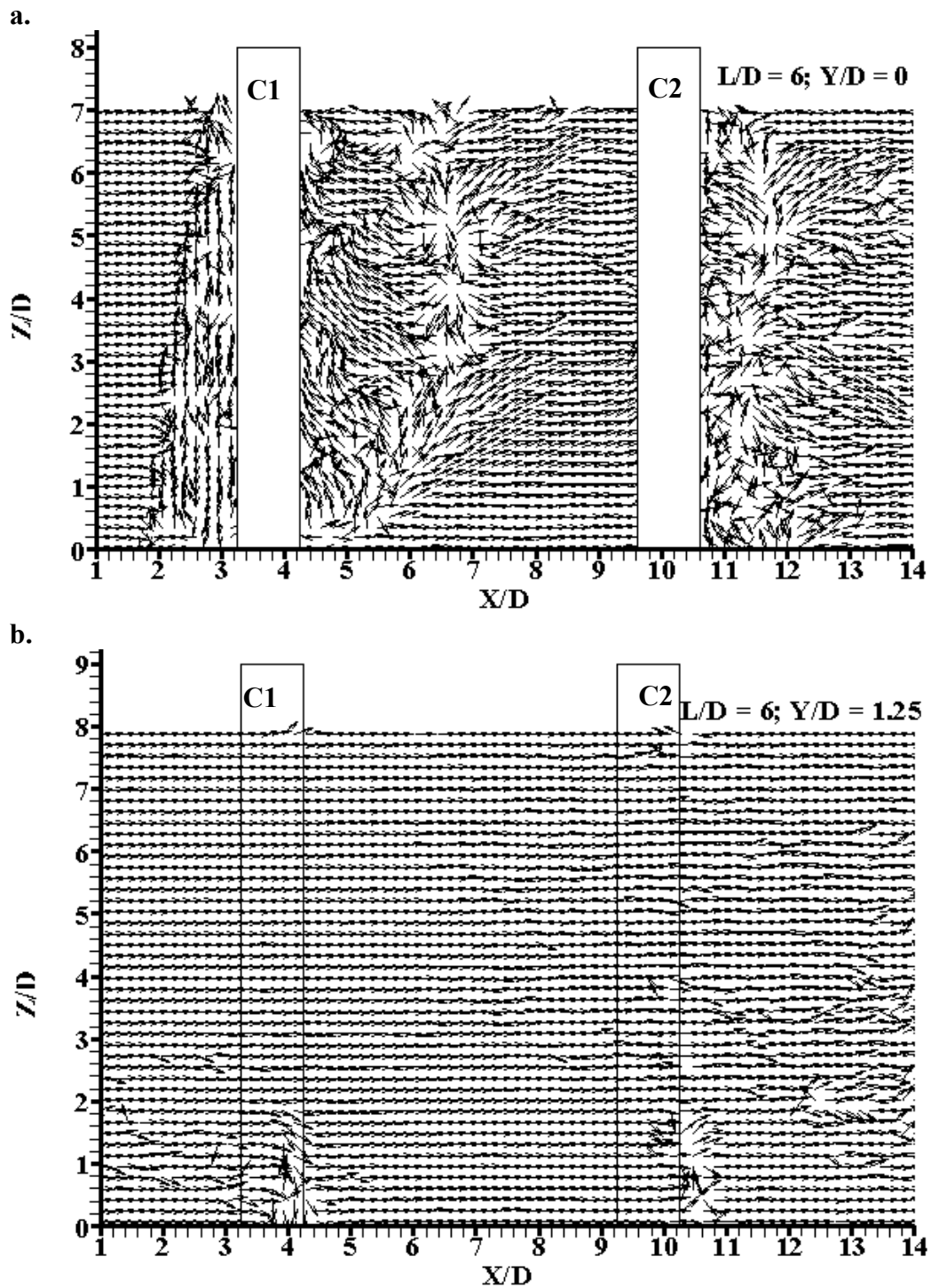


Figure A.35 Vector plots for two columns case with $L/D = 6$ in different vertical planes; a.) at $Y/D = 0$, and b.) at $Y/D = 1.25$

A.2.2 Stream Line Plots in Vertical Plane

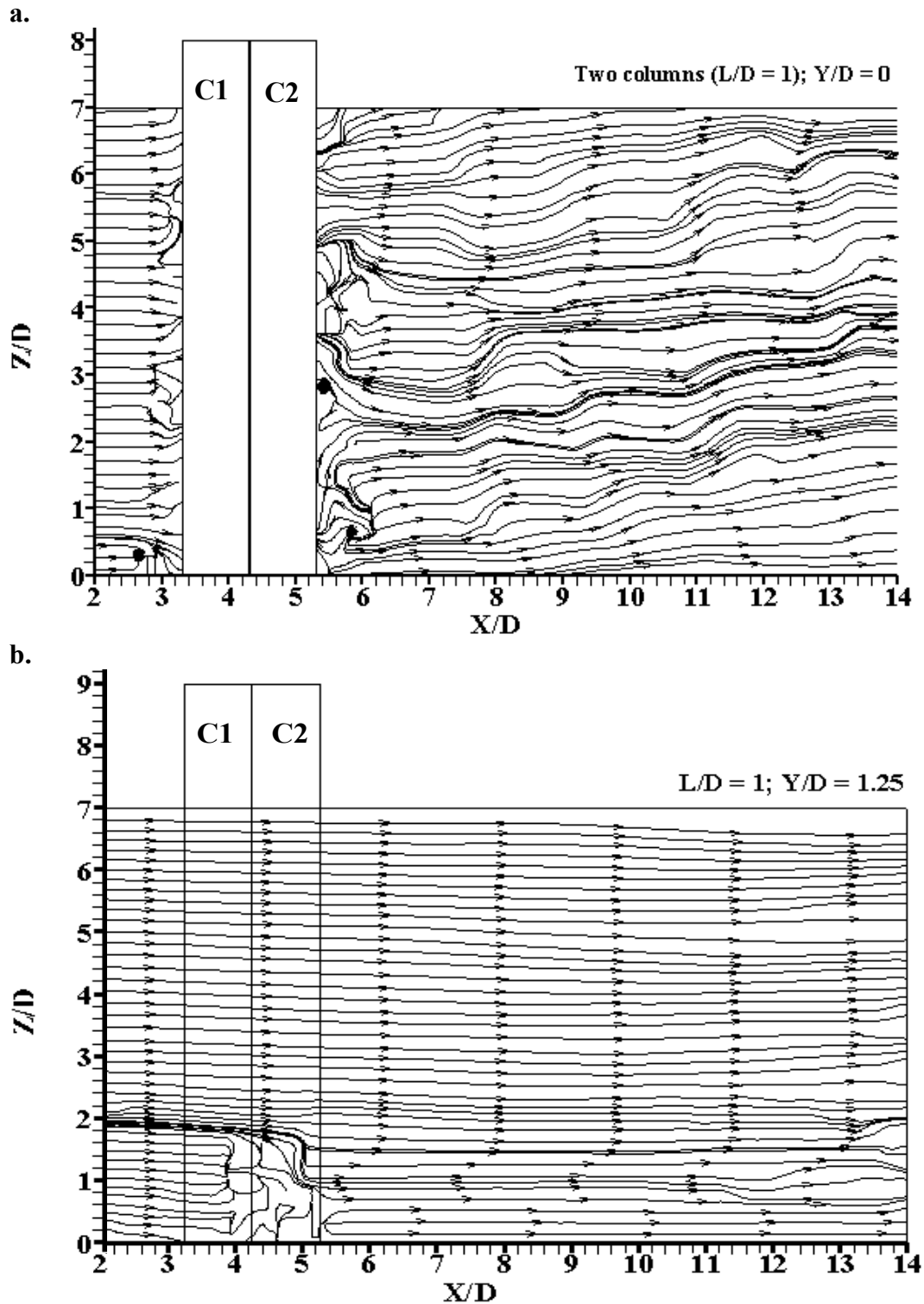


Figure A.36 Streamline plots for two columns case with $L/D = 1$ in different vertical planes; a.) at $Y/D = 0$, and b.) at $Y/D = 1.25$

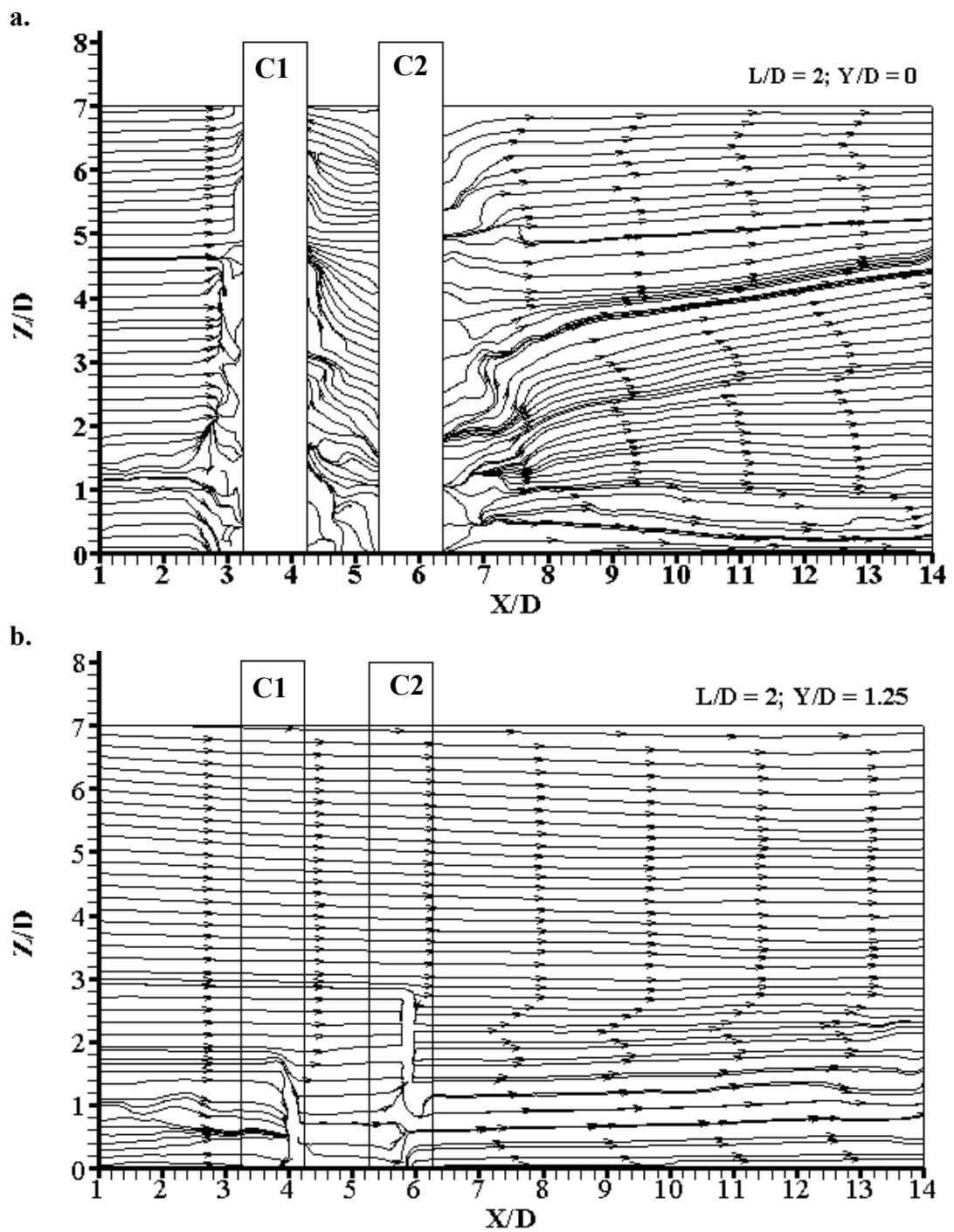


Figure A.37 Streamline plots for two columns case with $L/D = 2$ in different vertical planes; a.) at $Y/D = 0$, and b.) at $Y/D = 1.25$

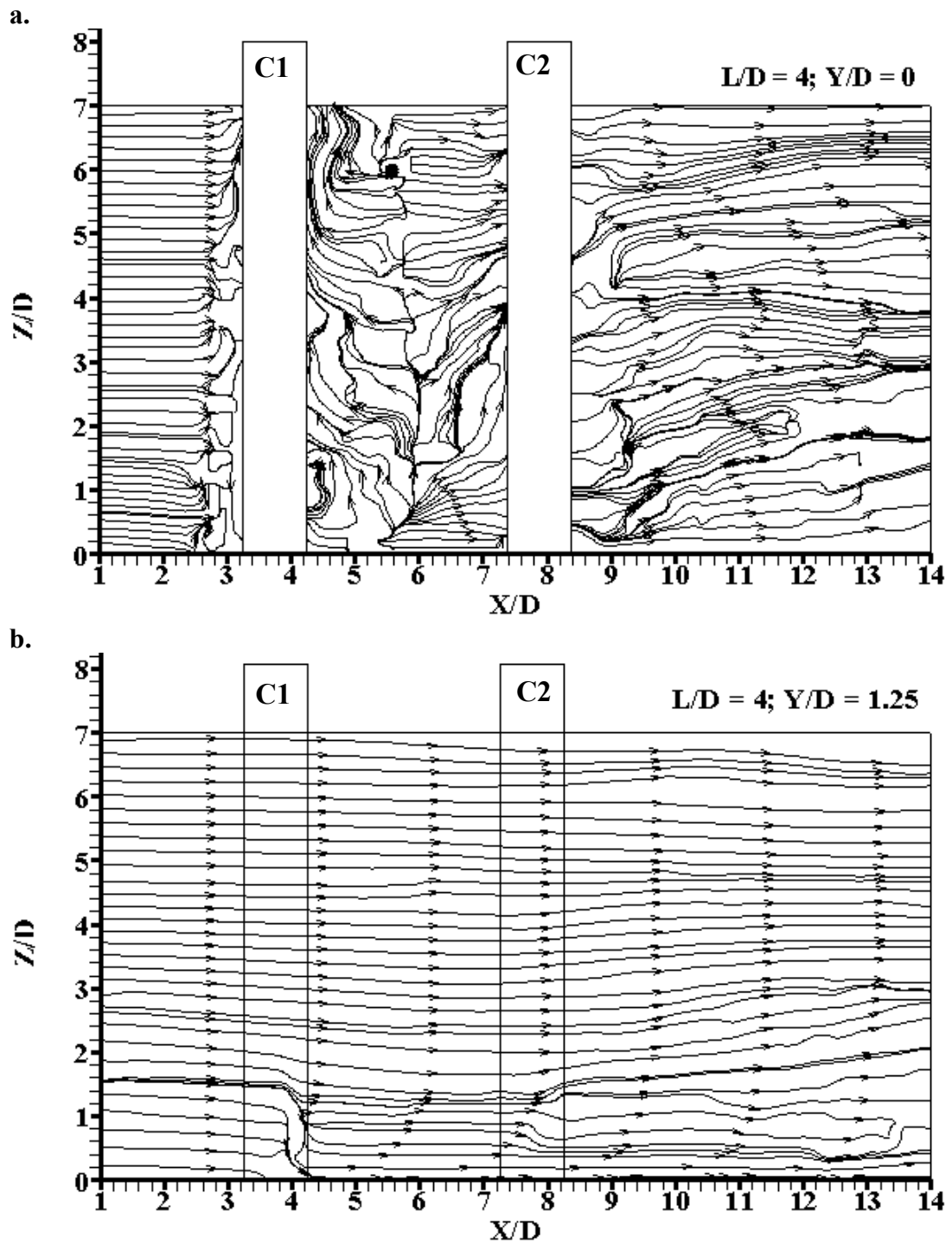


Figure A.38 Streamline plots for two columns case with $L/D = 4$ in different vertical planes; a.) at $Y/D = 0$, and b.) at $Y/D = 1.25$

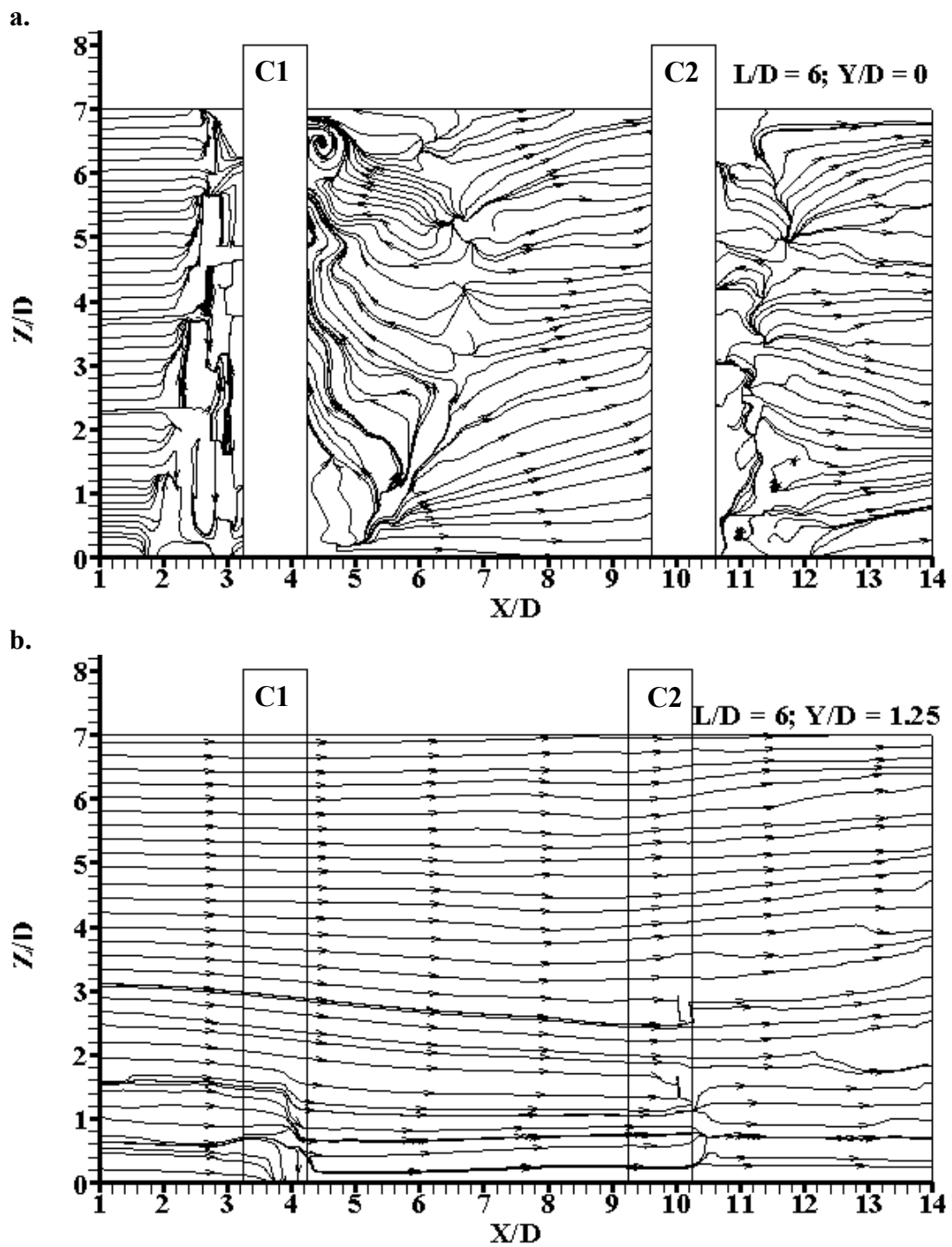


Figure A.39 Streamline plots for two columns case with $L/D = 6$ in different vertical planes; a.) at $Y/D = 0$, and b.) at $Y/D = 1.25$

A.2.3 Contour Plots of Streamwise velocity components (u) in Vertical Plane

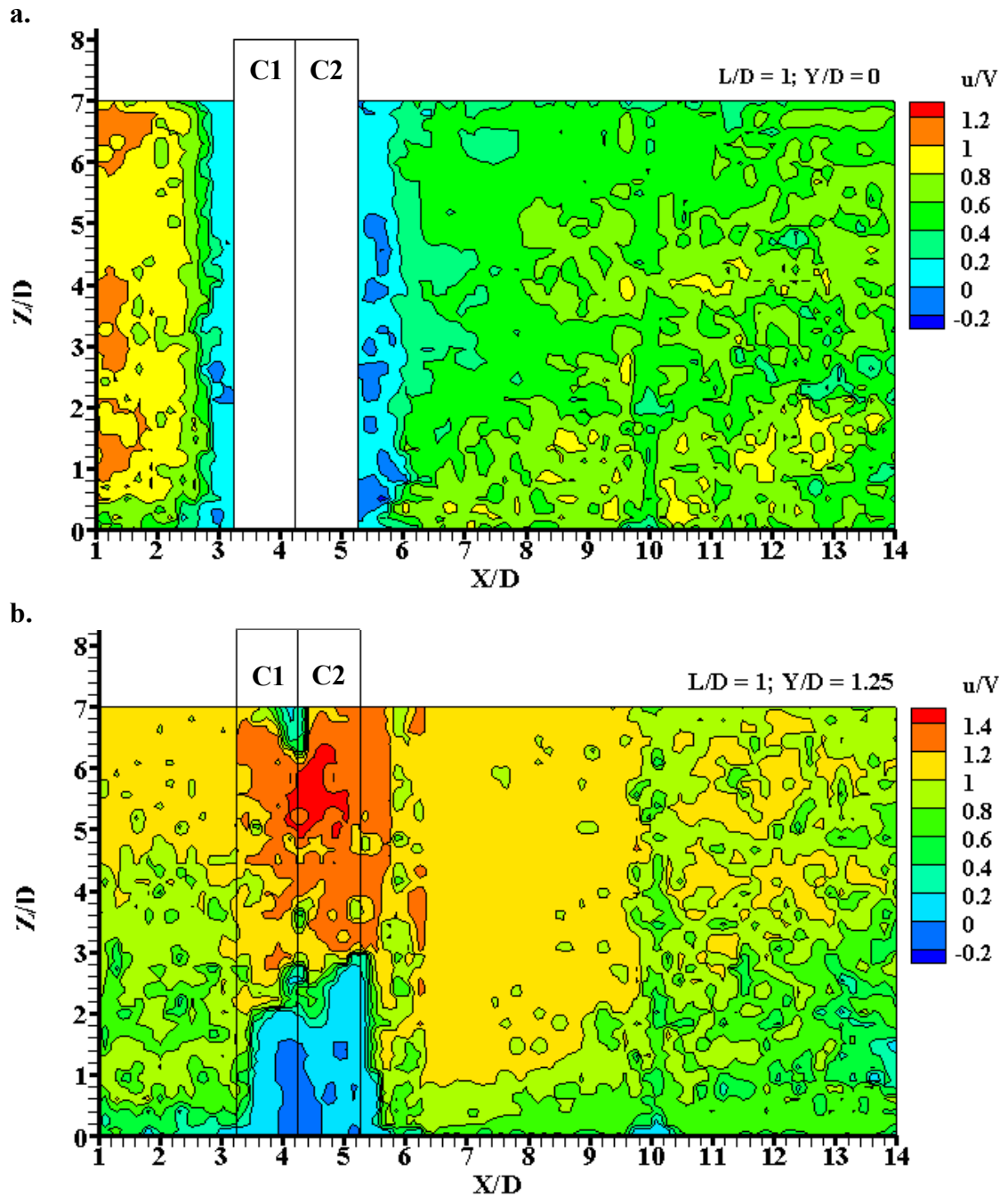


Figure A.40 Contour plots of streamwise velocity component (u/V) for two columns with $L/D = 1$ in different vertical planes a) at $Y/D = 0$, b) at $Y/D = 1.25$

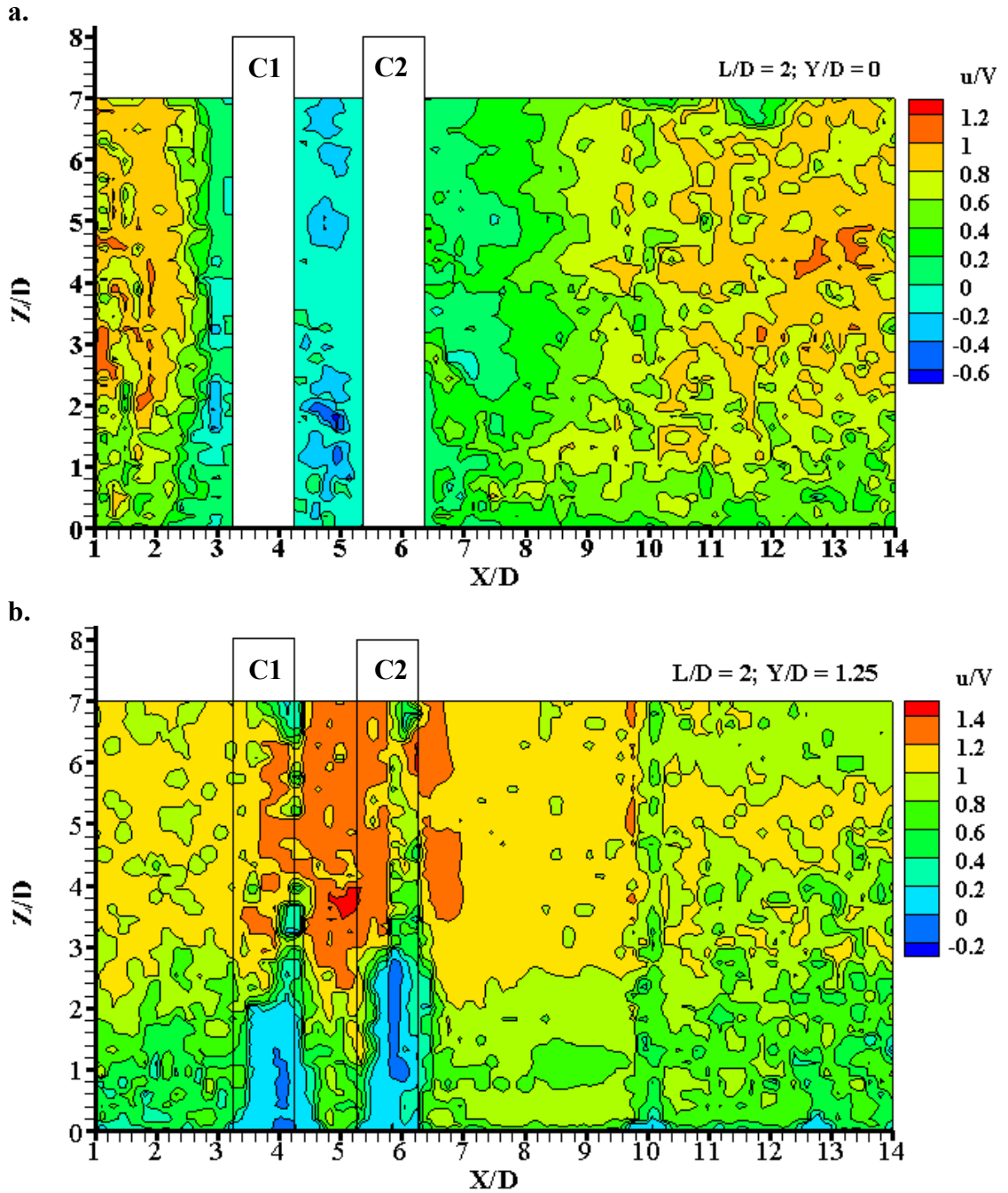


Figure A.41 Contour plots of streamwise velocity component (u/V) for two columns with $L/D = 2$ in different vertical planes a) at $Y/D = 0$, b) at $Y/D = 1.25$

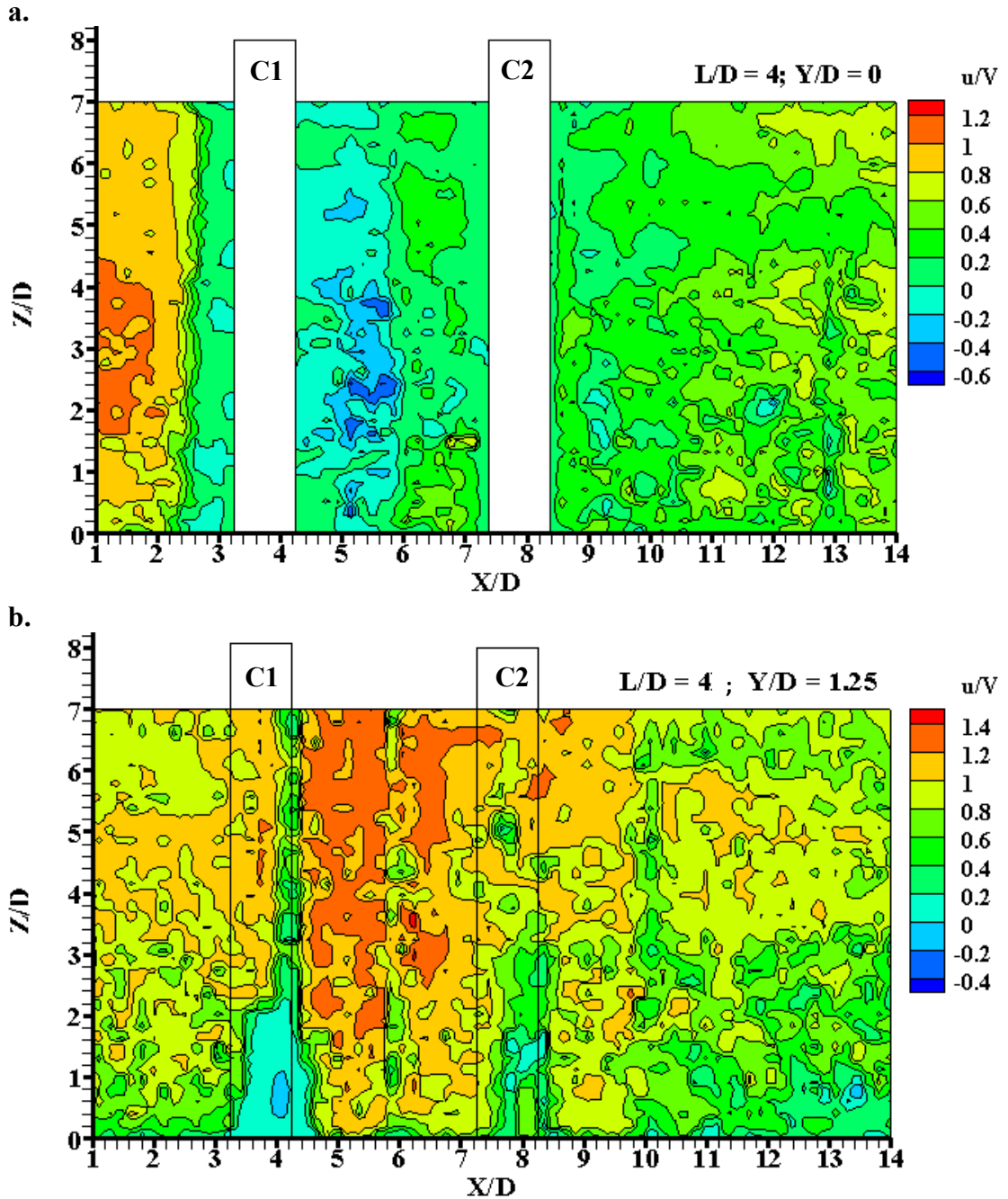


Figure A.42 Contour plots of streamwise velocity component (u/V) for two columns with $L/D = 4$ in different vertical planes a) at $Y/D = 0$, b) at $Y/D = 1.25$

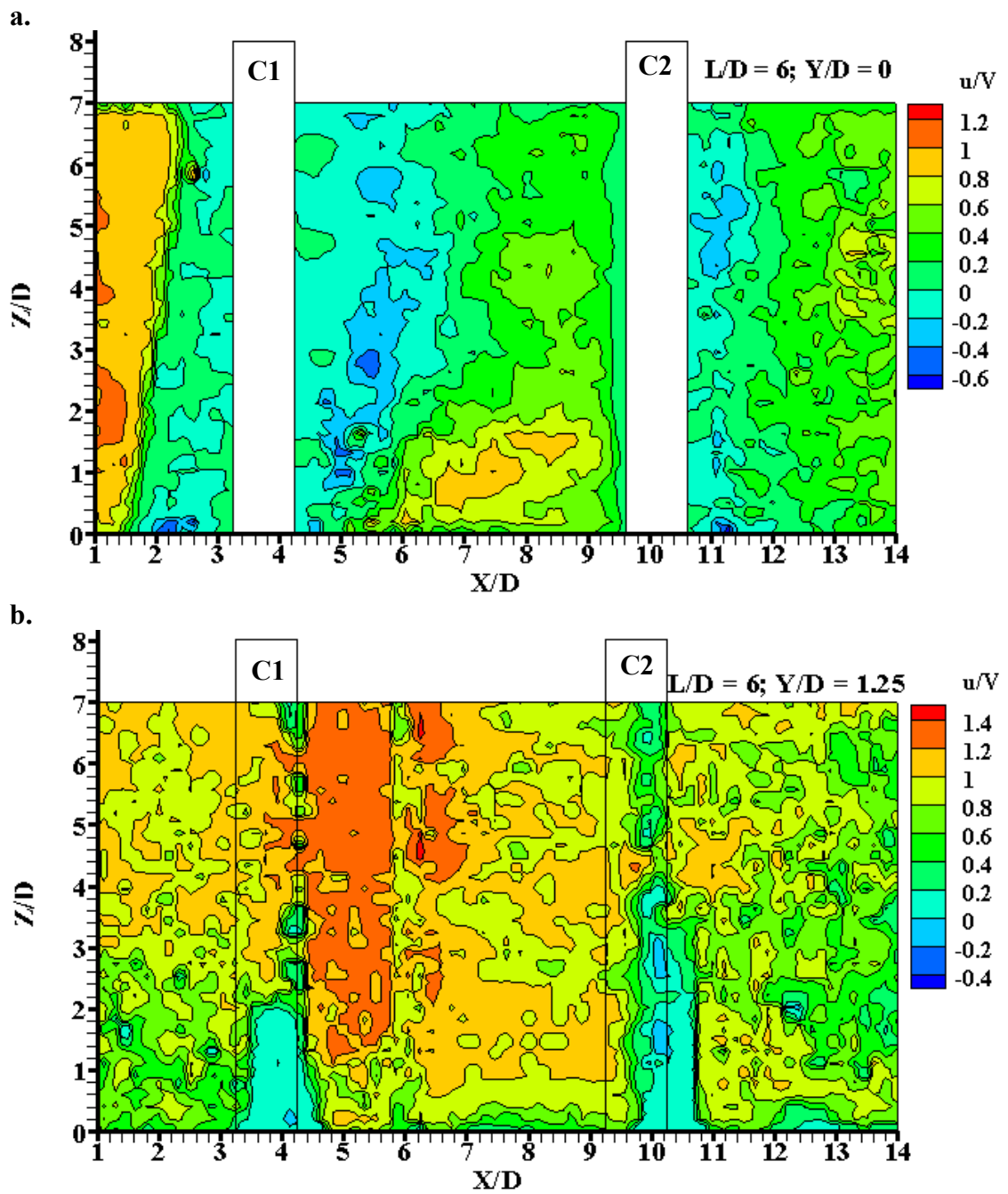


Figure A.43 Contour plots of streamwise velocity component (u/V) for two columns with $L/D = 6$ in different vertical planes a) at $Y/D = 0$, b) at $Y/D = 1.25$

A.2.4 Contour Plots of Vertical velocity components (w) in Vertical Plane

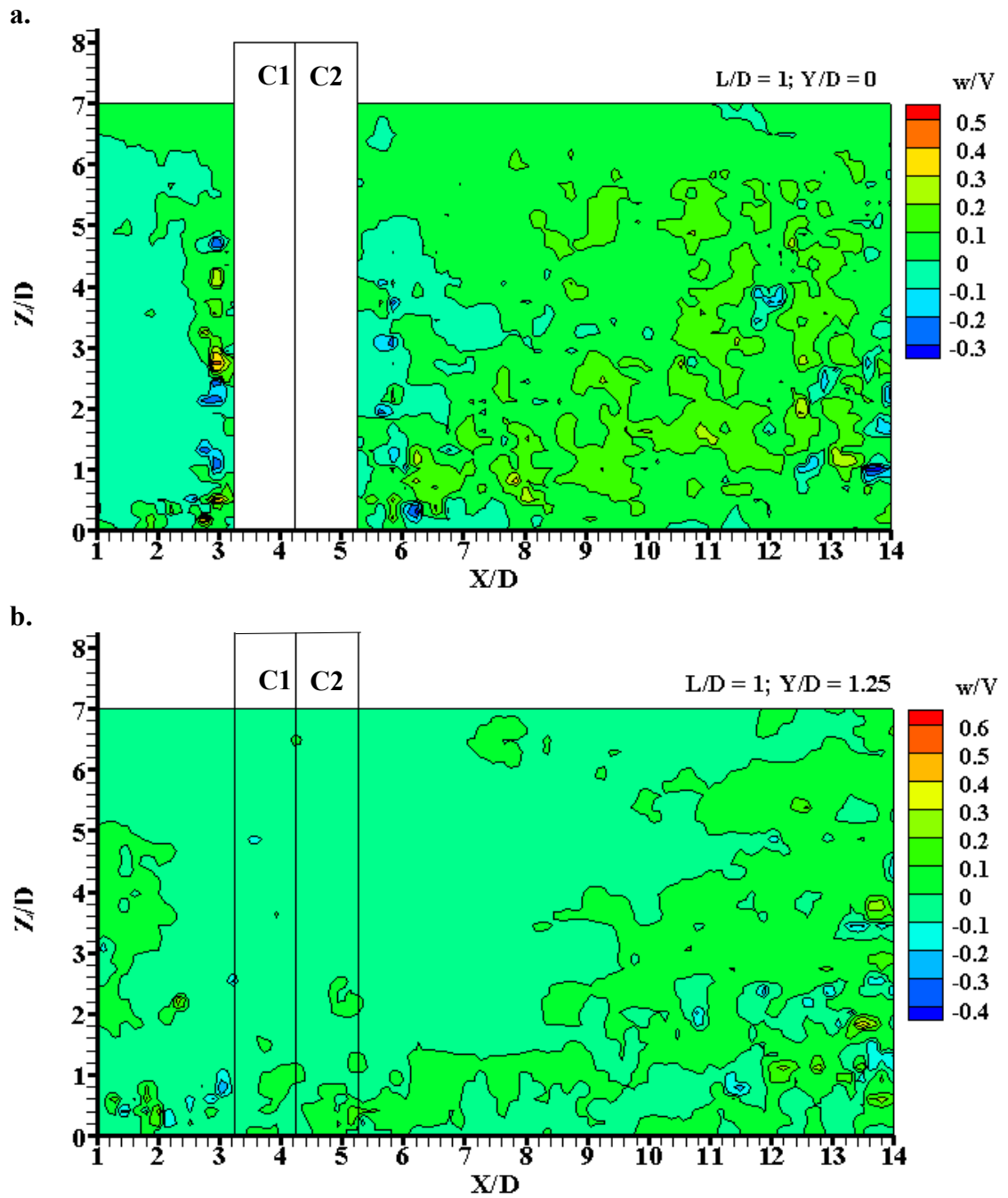


Figure A.44 Contour plots of vertical velocity component (w/V) for two columns with $L/D = 1$ in different vertical planes a) at $Y/D = 0$, b) at $Y/D = 1.25$

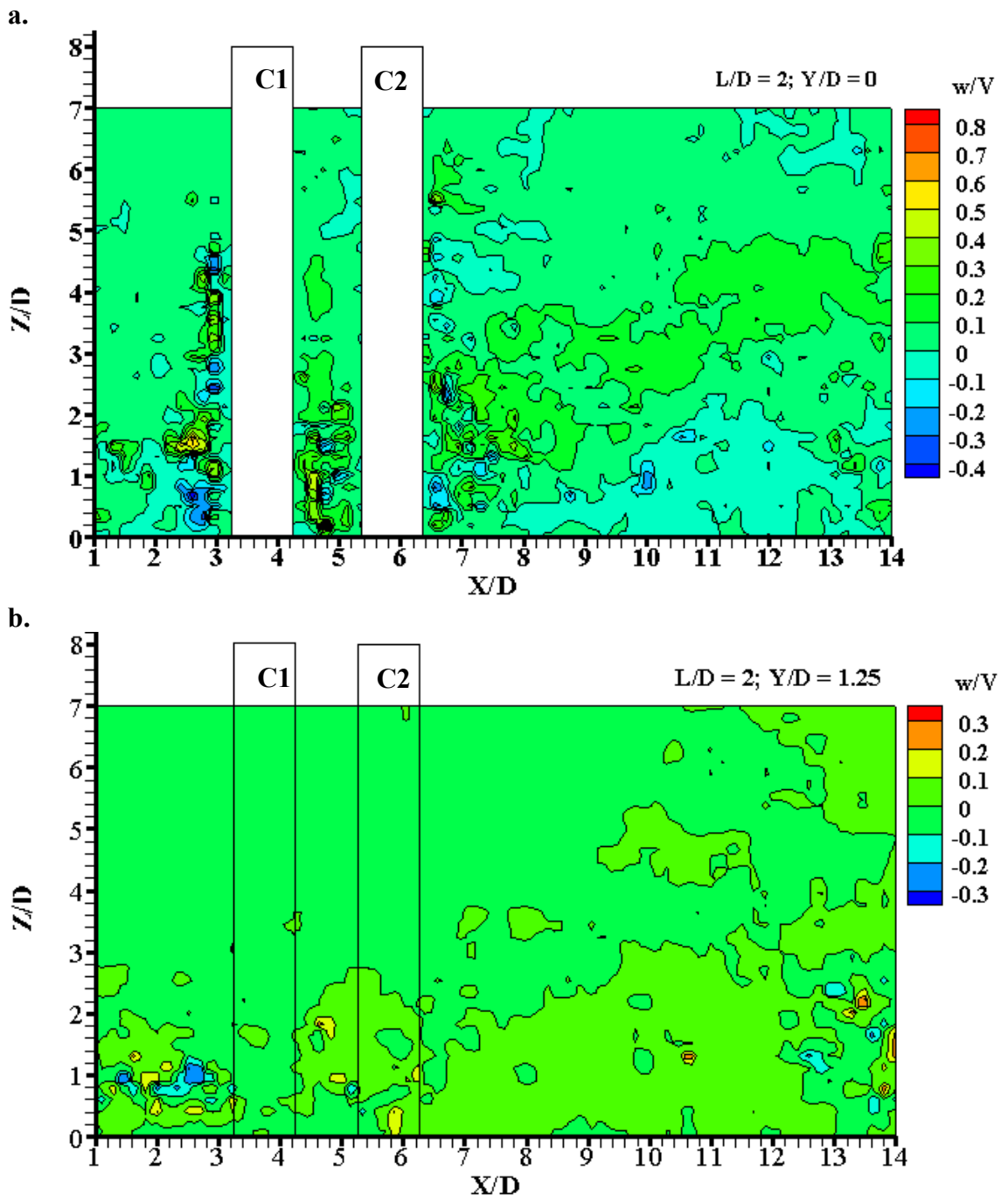


Figure A.45 Contour plots of vertical velocity component (w/V) for two columns with $L/D = 2$ in different vertical planes a) at $Y/D = 0$, b) at $Y/D = 1.25$

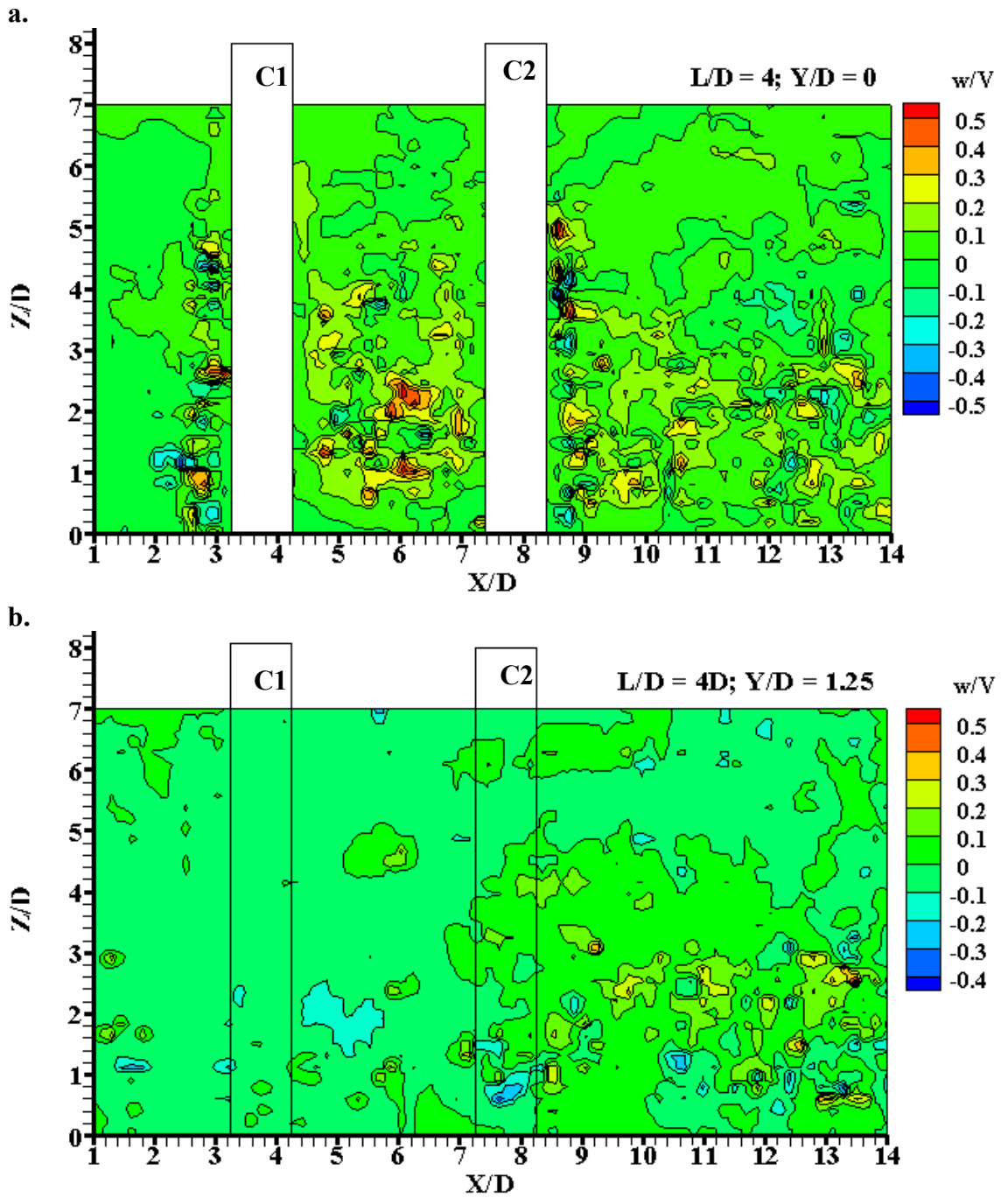


Figure A.46 Contour plots of vertical velocity component (w/V) for two columns with $L/D = 4$ in different vertical planes a) at $Y/D = 0$, b) at $Y/D = 1.25$

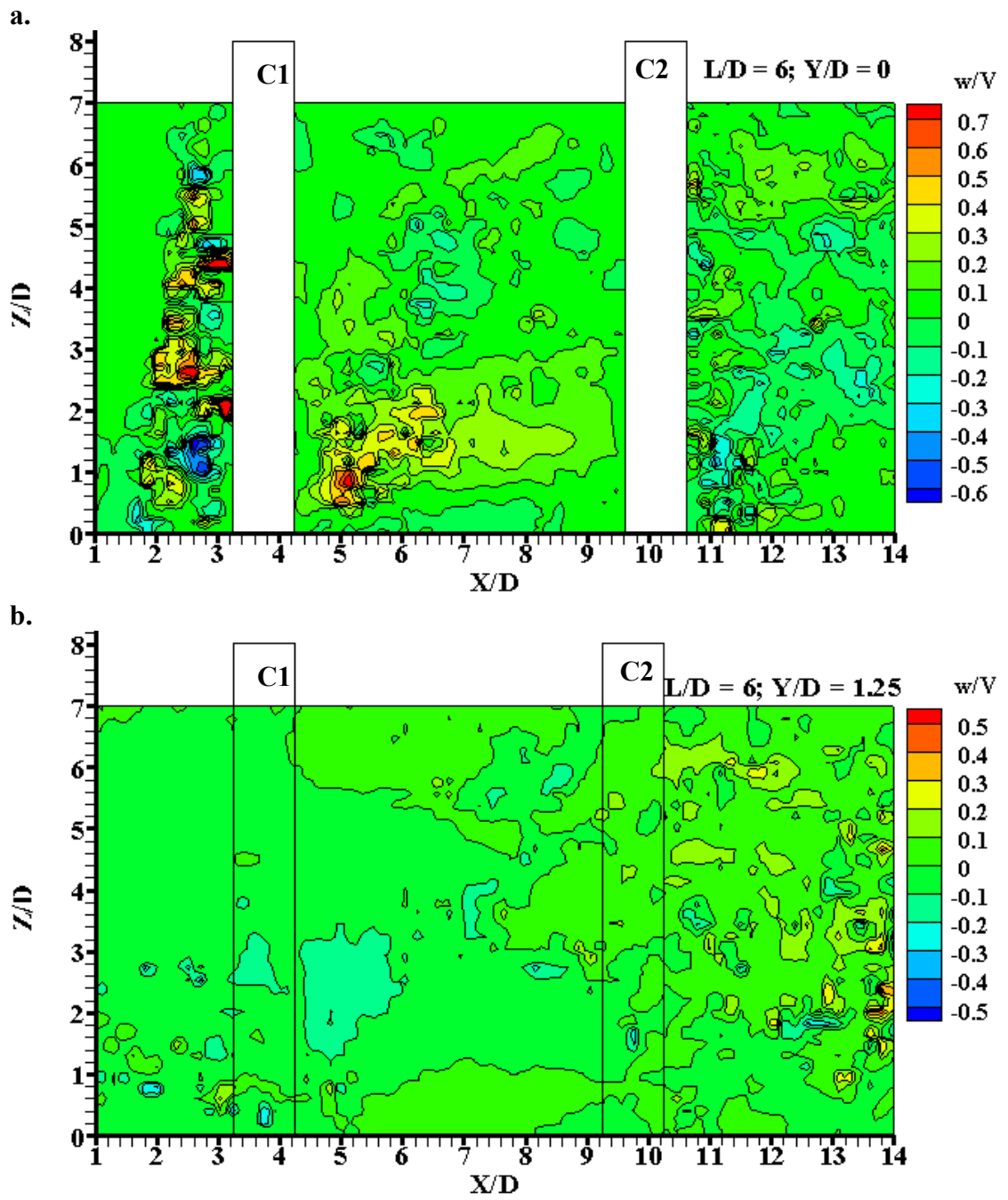


Figure A.47 Contour plots of vertical velocity component (w/V) for two columns with $L/D = 6$ in different vertical planes a) at $Y/D = 0$, b) at $Y/D = 1.25$

A.2.5 Profile Plots of Velocity Components at Upstream and Downstream Side (at $Y=0$) in Vertical Plane

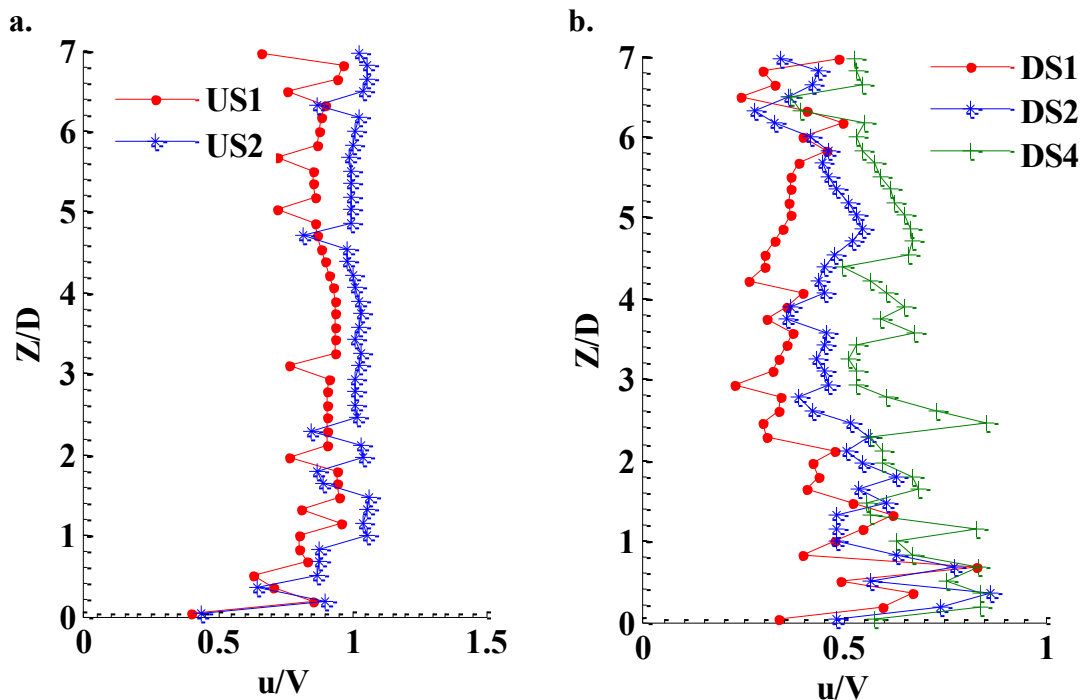


Figure A.48 Profile plots of streamwise velocity component for two columns case with $L/D = 1$ a) in vertical plane at axis of symmetry a) upstream side; b) downstream side

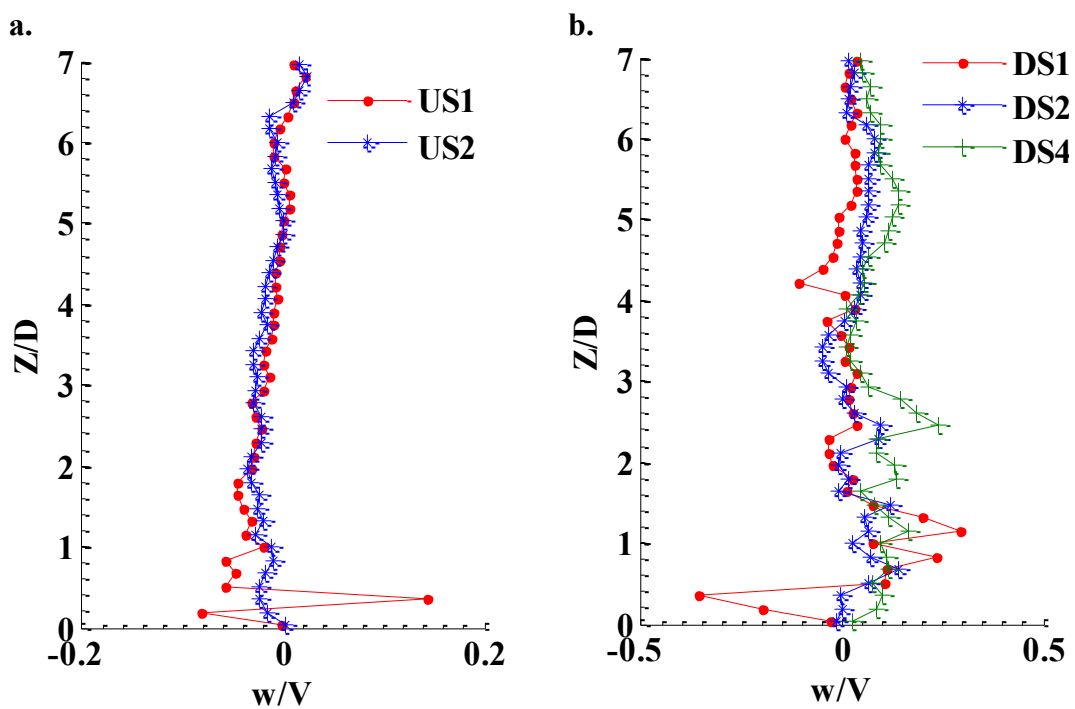


Figure A.49 Profile plots of vertical velocity component for two columns case with $L/D = 1$ a) in vertical plane at axis of symmetry a) upstream side; b) downstream side

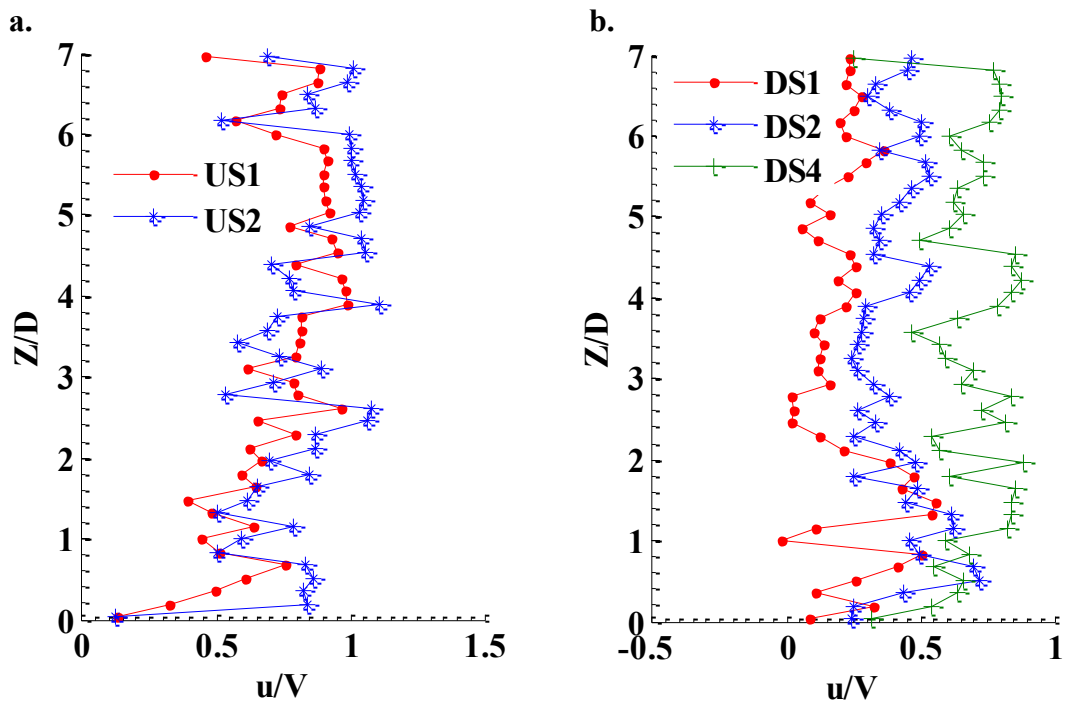


Figure A.50 Profile plots of streamwise velocity component for two columns case with $L/D = 2a$ in vertical plane at axis of symmetry a) upstream side; b) downstream side

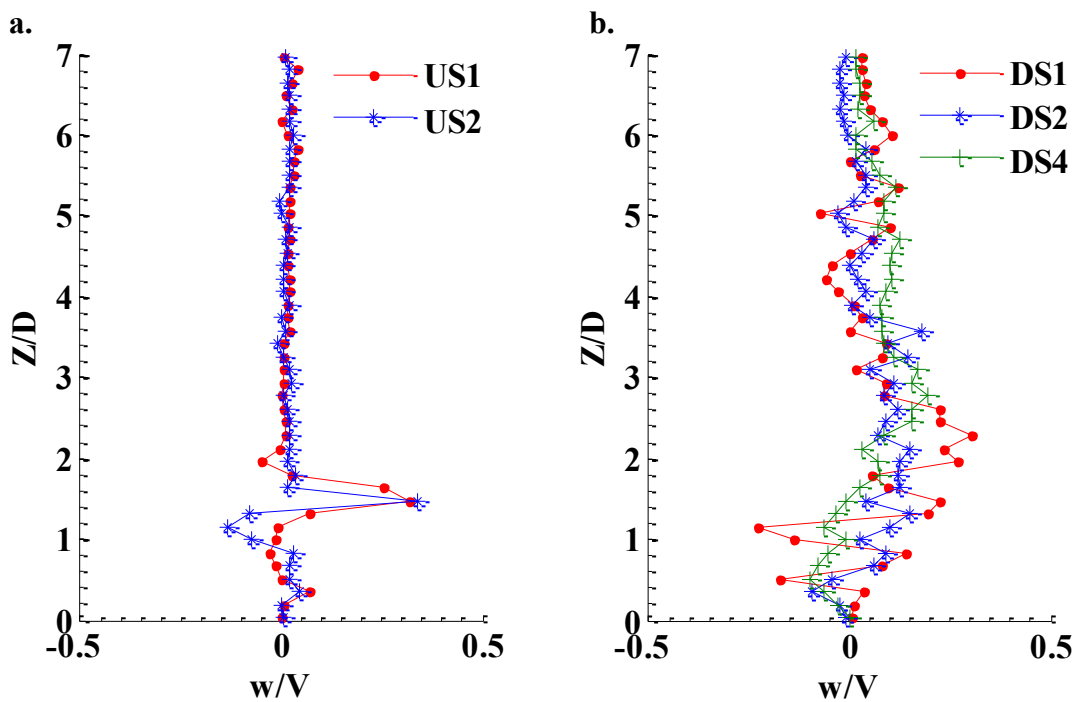


Figure A.51 Profile plots of vertical velocity component for two columns case with $L/D = 2a$ in vertical plane at axis of symmetry a) upstream side; b) downstream side

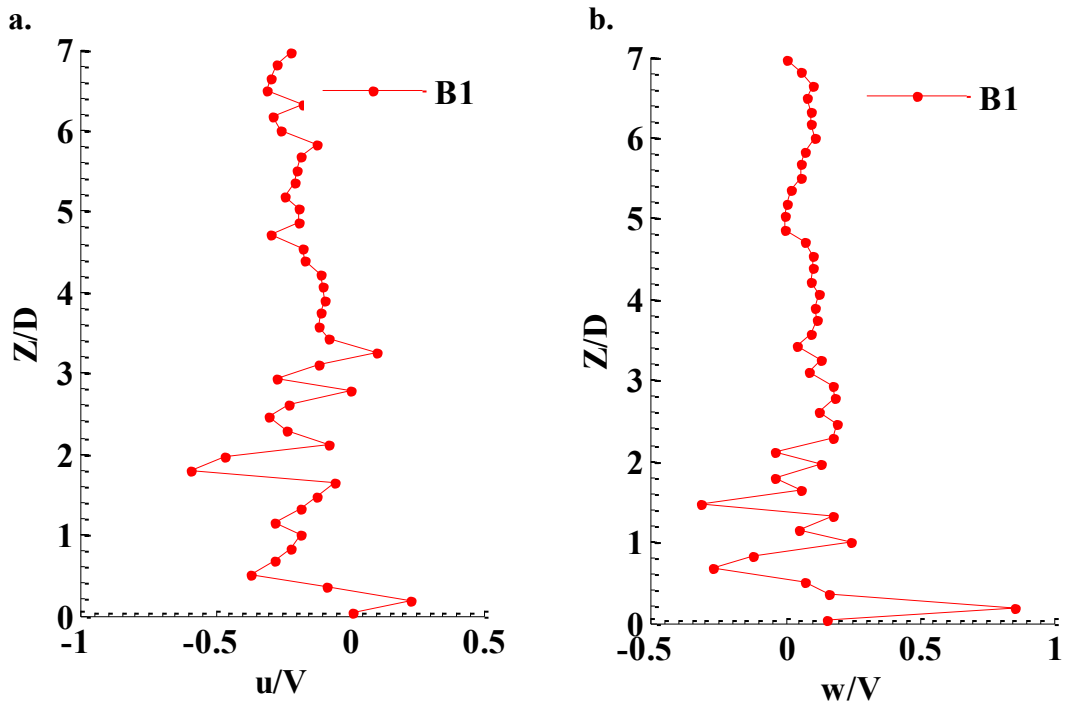


Figure A.52 Profile plots of velocity components between two columns with $L/D = 2$ in vertical plane at axis of symmetry a) stream wise component, b) vertical component

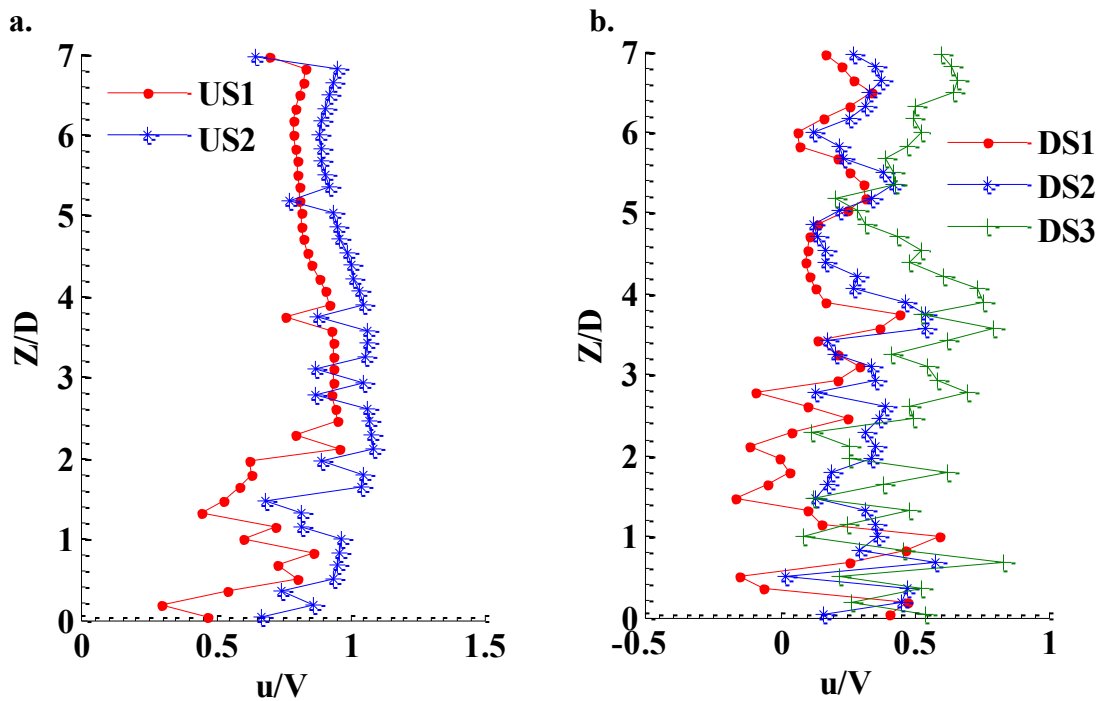


Figure A.53 Profile plots of streamwise velocity component for two columns case with $L/D = 4$ a) in vertical plane at axis of symmetry a) upstream side; b) downstream side

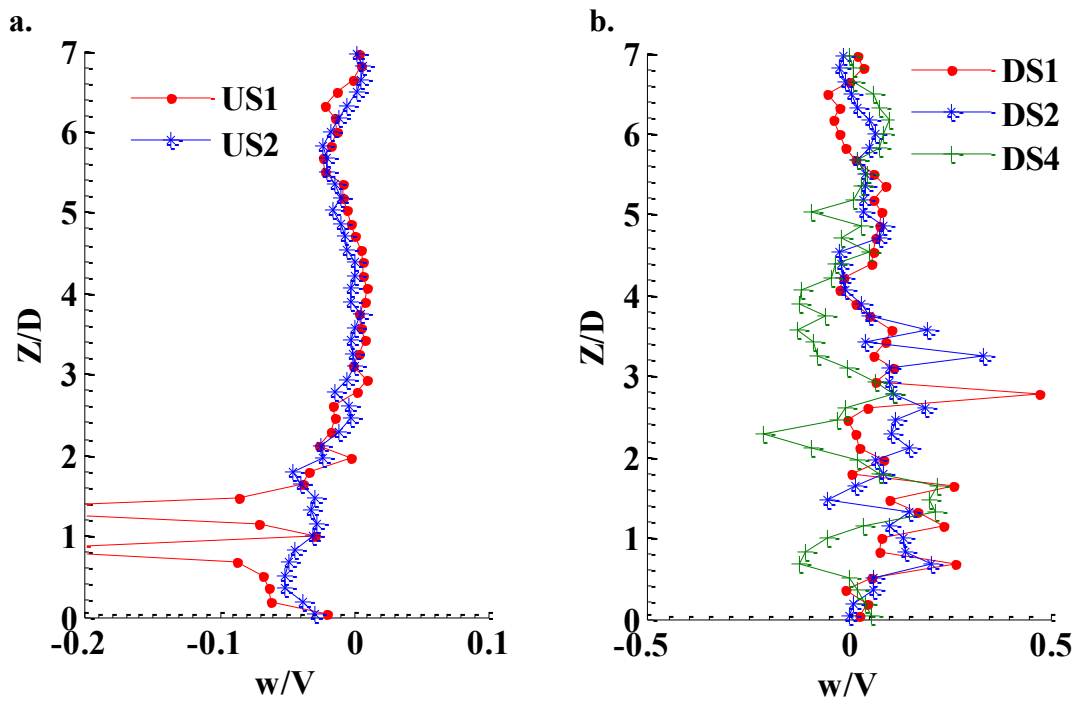


Figure A.54 Profile plots of vertical velocity component for two columns case with $L/D = 4$ a) in vertical plane at axis of symmetry a) upstream side; b) downstream side

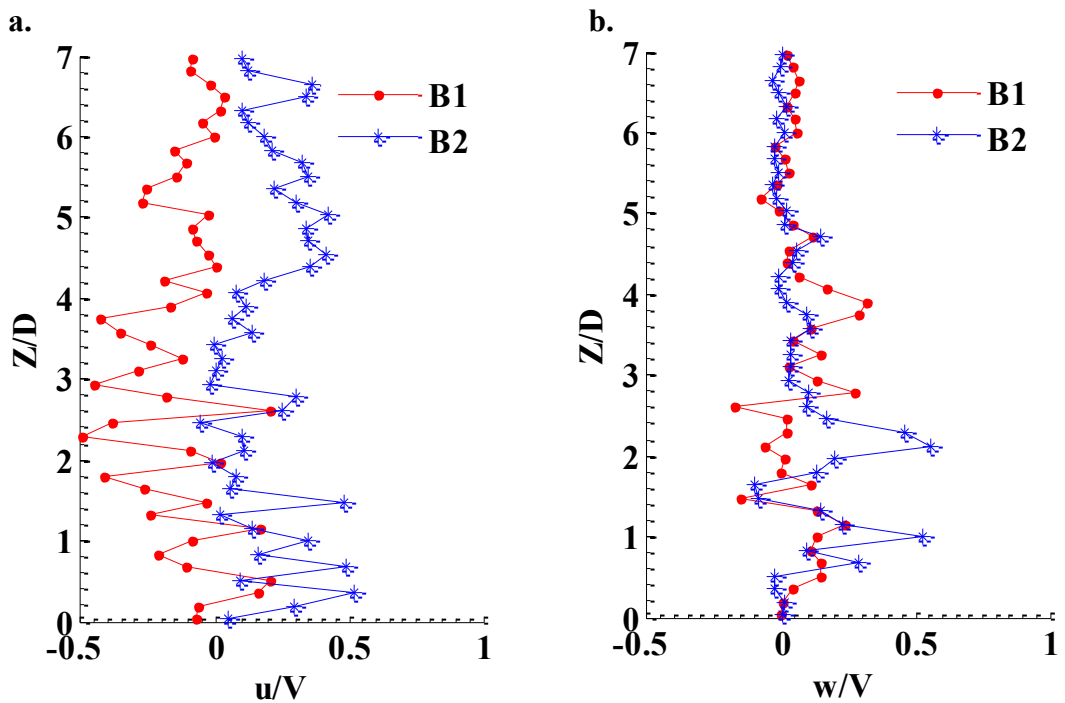


Figure A.55 Profile plots of velocity components between two columns with $L/D = 4$ in vertical plane at axis of symmetry a) stream wise component, b) vertical component

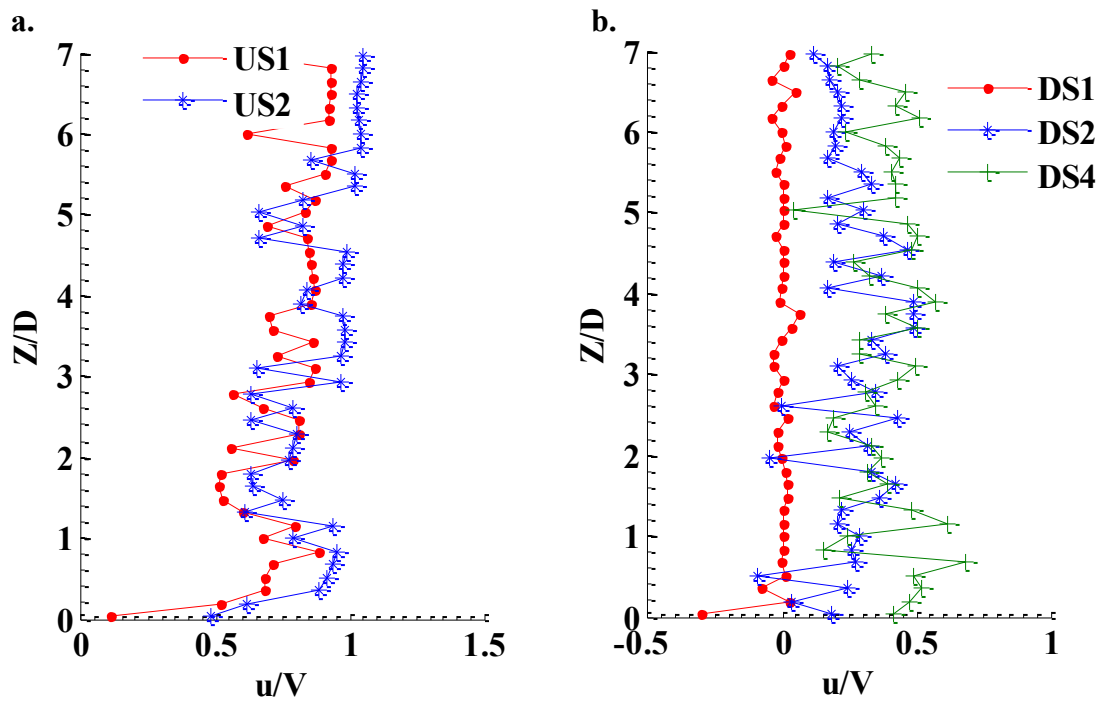


Figure A.56 Profile plots of streamwise velocity component for two columns case with $L/D = 5$ a) in vertical plane at axis of symmetry a) upstream side; b) downstream side

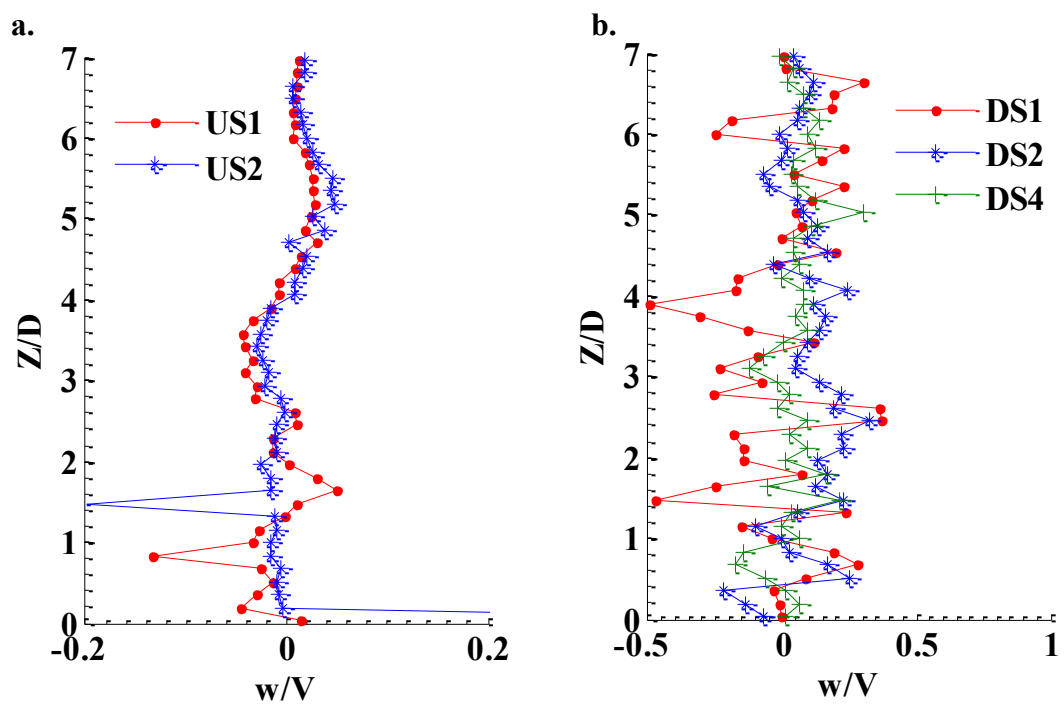


Figure A.57 Profile plots of vertical velocity component for two columns case with $L/D = 5$ in a vertical plane at axis of symmetry a) upstream side; b) downstream side

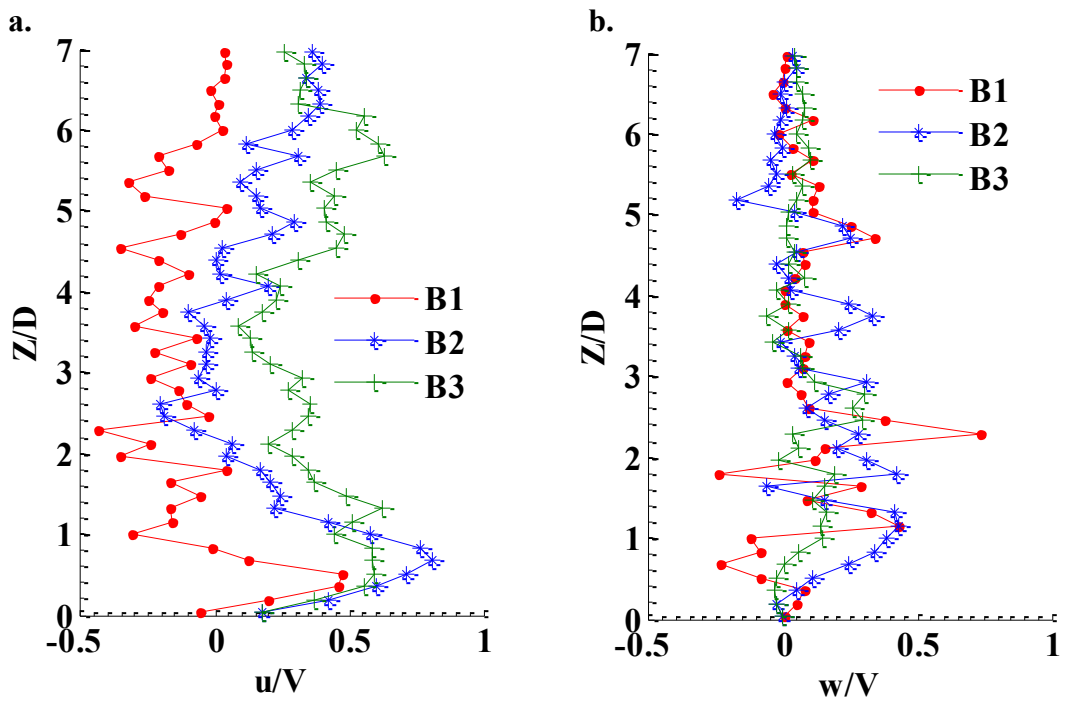


Figure A.58 Profile plots of velocity components between two columns with $L/D = 5$ in vertical plane at axis of symmetry a) streamwise component, b) vertical component

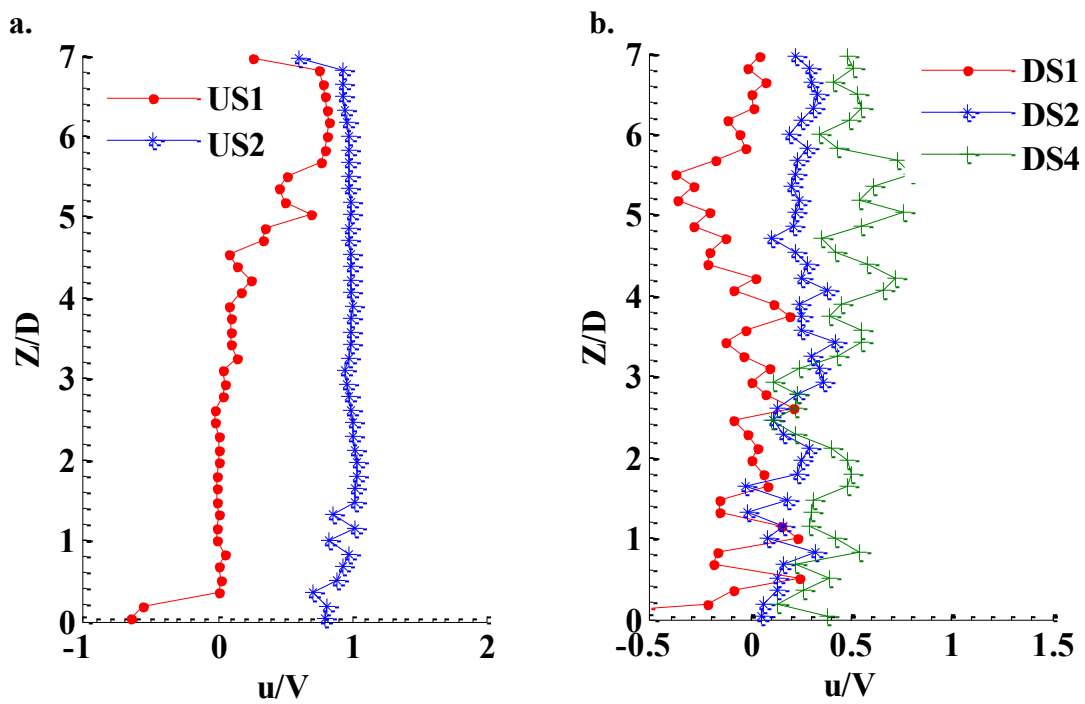


Figure A.59 Profile plots of streamwise velocity component for two columns case with $L/D = 6$ a) in vertical plane at axis of symmetry a) upstream side; b) downstream side

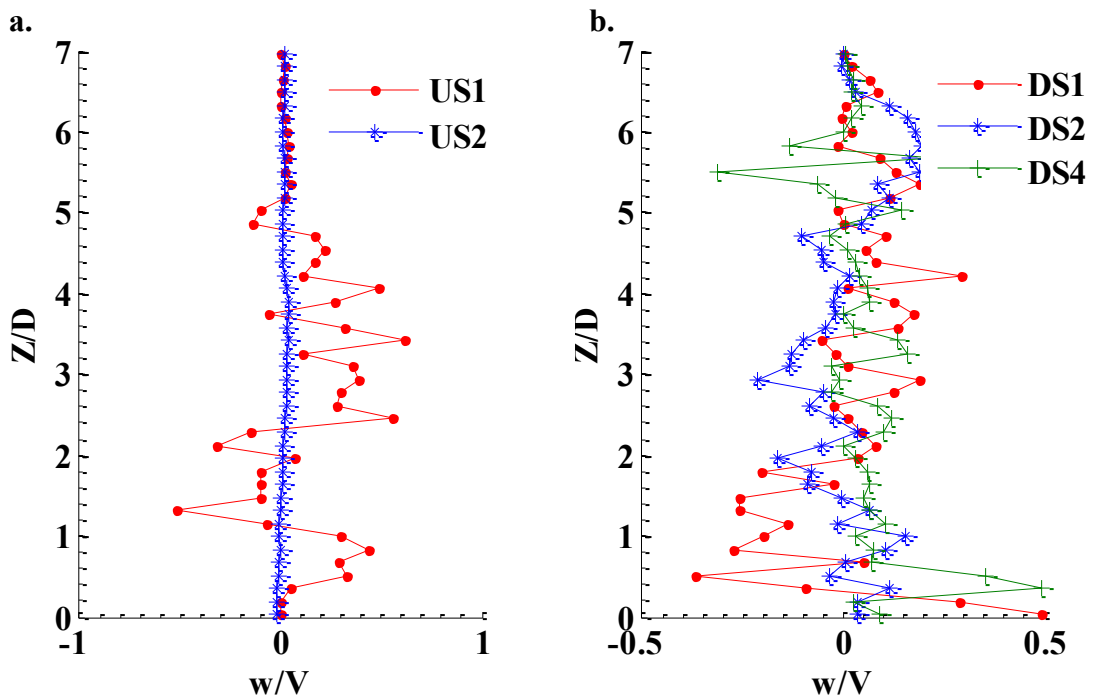


Figure A.60 Profile plots of vertical velocity component for two columns case with $L/D = 6$ in a vertical plane at axis of symmetry a) upstream side; b) downstream side

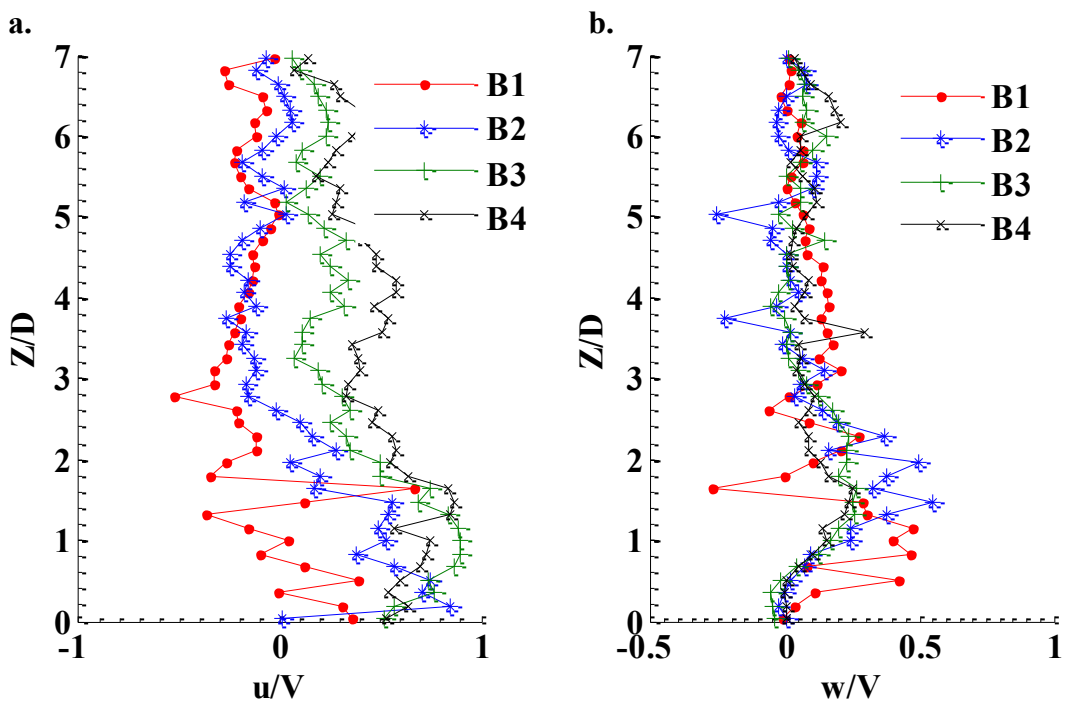


Figure A.61 Profile plots of velocity components between two columns with $L/D = 6$ in vertical plane at axis of symmetry a) streamwise component, b) vertical component

A.3 Table of Results on Velocity Components

Table A. 1 Maximum and minimum values of streamwise velocity components

Test No.	L/D	Z/h	Y/D	u_{max}/V	X/D	u_{min}/V	X/D
1	0	0.09	0	0.9	-4	0.65	2
			0.9	1.2	2	0.6	-1
			1.8	1.1	1	0.9	-1
		0.26	0	0.9	-4	-0.1	2
			0.9	1.3	2	0.9	3.5
			1.8	1.1	2	0.9	-2
		0.54	0	1	-4	-0.2	2
			0.9	1.3	2	1	3.5
			1.8	1.2	2	1	3.5
2	1.5	0.09	0	0.9	-4	-0.2	3
			0.9	1	3	0.8	6.5
			1.8	1.1	1	0.9	7
		0.26	0	0.9	-4	-0.2	3
			0.9	1.1	3	0.9	5.5
			1.8	1.15	1.5	0.9	7
		0.54	0	1	-4	-0.2	3
			0.9	1.1	3	0.8	6
			1.8	1.2	3	1	6
3	2	0.09	0	0.8	-4	0.1	1
			0.9	1.1	2	0.7	4
			1.8	1	2	0.8	7
		0.26	0	0.9	-4	-0.1	3.5
			0.9	1.2	1.5	0.9	9
			1.8	1.1	2	0.9	7
		0.54	0	0.9	-4	0	3.5
			0.9	1.1	2.5	0.9	7.5
			1.8	1.25	2	1.1	11
4	3	0.09	0	0.9	-4	-0.25	2
			0.9	1.2	2	0.8	5.5
			1.8	1.15	1.5	0.75	9
		0.26	0	1	-4	-0.3	2.5
			0.9	1.2	2.5	0.8	7
			1.8	1.2	1.5	0.9	5.5
		0.54	0	1	-4	-0.3	2
			0.9	1.4	1.5	0.9	9
			1.8	1.2	2	1.1	12
5	4	0.09	0	0.9	-4	-0.1	5.5
			0.9	1.2	1	0.8	11
			1.8	1.1	1	0.95	9
		0.26	0	1	-4	-0.1	5.5

			0.9	1.25	2	0.9	10
			1.8	1.15	2	1	12
		0.54	0	1	-4	-0.3	2
			0.9	1.3	1.5	0.8	9
			1.8	1.2	1	1	11
6	6	0.09	0	0.9	-4	0.2	8
			0.9	1.2	2	0.8	-1
			1.8	1	2	0.9	-2
		0.26	0	1	-4	-0.2	7
			0.9	1.1	2	0.8	-2
			1.8	1.2	1	0.9	-2
		0.54	0	1	-4	-0.2	2, 7
			0.9	1	7	0.7	2
			1.8	1.2	1	1	-1

Table A. 2 Maximum and minimum values of transverse velocity components

Test No.	L/D	Z/h	Y/D	v_{max}/V	X/D	v_{min}/V	X/D
1	0	0.09	0	0	-4	-0.15	2
			0.9	0.35	2	-0.2	0
			1.8	0.15	3	-0.1	0
		0.26	0	0	-4	-0.1	2
			0.9	0.18	2	-0.2	0
			1.8	0	-4	-0.1	0
		0.54	0	0	-4	0.02	2
			0.9	0.1	3	-0.3	3
			1.8	0.05	3	-0.05	0
2	1.5	0.09	0	0.02	5.5	0	-4
			0.9	0.1	4	-0.05	-1
			1.8	0.1	4	-0.08	0
		0.26	0	0	-4	-0.08	3
			0.9	0.18	4	-0.07	-1
			1.8	0.1	4	-0.08	0
		0.54	0	0.05	-4	-0.08	2.5
			0.9	0.18	4	0	-1
			1.8	0		0	
3	2	0.09	0	0	-4	-0.1	1
			0.9	0.18	4	-0.21	0
			1.8	0.1	4	-0.1	1
		0.26	0	0		0	
			0.9	0.15	4	-0.02	-1
			1.8	0.1	4	-0.04	0
		0.54	0	0.03	5	3	
			0.9	0.18	4	-0.3	0
			1.8	0.1	5	-0.1	0
4	3	0.09	0	0.1	4	0	
			0.9	0.1	5	-0.22	0
			1.8	0.1	5.5	-0.1	0
		0.26	0	0		0	
			0.9	0.2	5	-0.3	0
			1.8	0.15	5	-0.1	0
		0.54	0	0		0	
			0.9	0.2	5	-0.25	0
			1.8	0.15	4	-0.18	0
5	4	0.09	0	0.04	2	0	
			0.9	0.2	5.5	-0.18	0
			1.8	0.15	6	-0.1	0
		0.26	0	0		-0.1	3
			0.9	0.2	6	-0.2	0
			1.8	0.18	6.5	-0.1	0

		0.54	0	0		-0.1	5.5
			0.9	0.08	6.5	-0.28	0
			1.8	0.1	7	-0.1	0
6	6	0.09	0	0		0	
			0.9	0.24	8	-0.05	6
			1.8	0.12	8	-0.08	0
		0.26	0	0		0	
			0.9	0.2	2	-0.18	6
			1.8	0.15	8	-0.06	8
		0.54	0	0		0	
			0.9	0.22	3	-0.24	6
			1.8	0.1	9	-0.1	0

Table A. 3 Maximum and minimum values of vertical velocity components

Test No.	L/D	Z/h	Y/D	w _{max} /V	X/D	w _{min} /V	X/D
1	0	0.09	0	0.22	2	-0.05	-1
			0.9	0.05	3	-0.05	0
			1.8	0.05	1	-0.02	-1
		0.26	0	0.23	2.5	-0.02	-1
			0.9	0.06	6	-0.05	2
			1.8	0		-0.06	6
		0.54	0	0.14	4	-0.04	-1
			0.9	0.05	8	-0.08	2
			1.8	0		-0.1	6
2	1.5	0.09	0	0.04	3	-0.025	-1
			0.9	0.01	13	-0.02	9
			1.8	0.015	5.5	0	-4
		0.26	0	0.03	5.5	-0.05	-1
			0.9	0.03	6	-0.02	-3
			1.8	0.01	4.5	-0.02	2
		0.54	0	0.03	5.5	0	3
			0.9	0.03	5.5	0	3
			1.8	0	5.5	-0.03	-1
3	2	0.09	0	0.08	1	-0.03	-1
			0.9	0	4	-0.03	-1
			1.8	0		0	
		0.26	0	0.04	6	-0.1	3.5
			0.9	0.03	3.5	-0.08	1.5
			1.8	0		0	
		0.54	0	0.12	5.5	-0.03	-1
			0.9	0.03	6	-0.05	0
			1.8	0	-1	-0.04	3
4	3	0.09	0	0.27	3.5	-0.02	-1
			0.9	0.05	3	-0.03	0
			1.8	0		0	
		0.26	0	0.18	2.5	-0.01	-1
			0.9	0		-0.07	2.5
			1.8	0		0	
		0.54	0	0.35	2	0	
			0.9	0.03	5.5	-0.1	2
			1.8	0		0	
5	4	0.09	0	0.18	5.5	-0.05	2.5
			0.9	0.02	4	-0.05	0
			1.8	0		0	
		0.26	0	0.35	2	-0.05	-1
			0.9	0.02	5.5	-0.1	2
			1.8	0		0	

		0.54	0	0.18	2.5	-0.1	5.5
			0.9	0.07	6	-0.1	2
			1.8	0		0	
6	6	0.09	0	0.1	2.5	-0.02	-1
			0.9	0		0	
			1.8	0		0	
		0.26	0	0.17	3.5	-0.05	-1
			0.9	0.05	5.5	-0.05	2
			1.8	0		0	
		0.54	0	0.18	5.5	-0.16	7
			0.9	0.15	6	0.05	2
			1.8	0		-0.1	4.5

APPENDIX-B: PLOTS FOR TURBULENCE INTENSITIES

B.1 Plots of Turbulence Intensity in Horizontal Plane

B.1.1 Contour Plots of Stream-wise Turbulence Intensity Component (TI_u) in Horizontal Plane

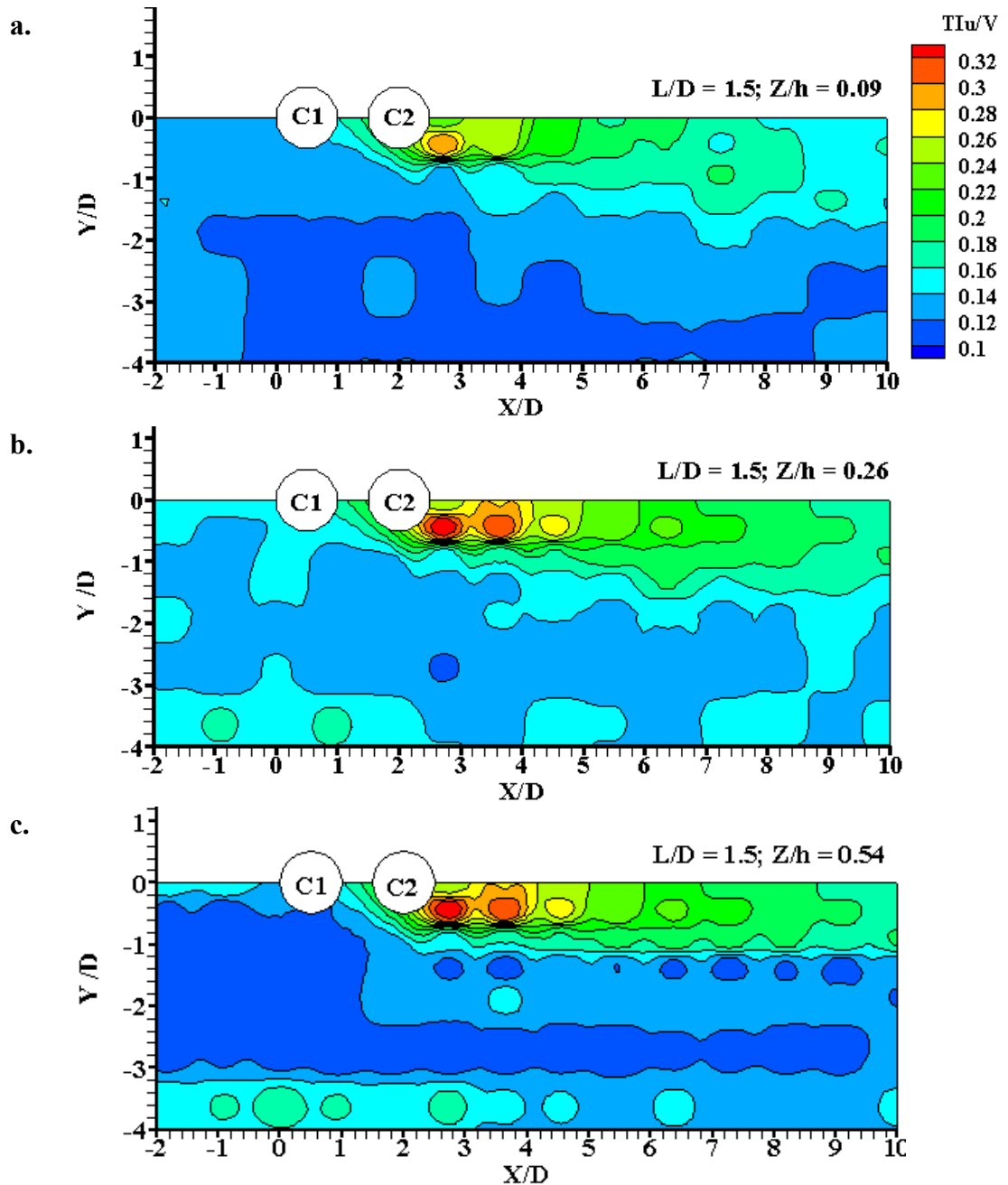


Figure B.1 Contour plots of streamwise turbulence intensity component for two columns case with $L/D = 1.5$ in different horizontal planes a) at $Z/h = 0.09$, b) at $Z/h = 0.26$ and c). at $Z/h = 0.54$

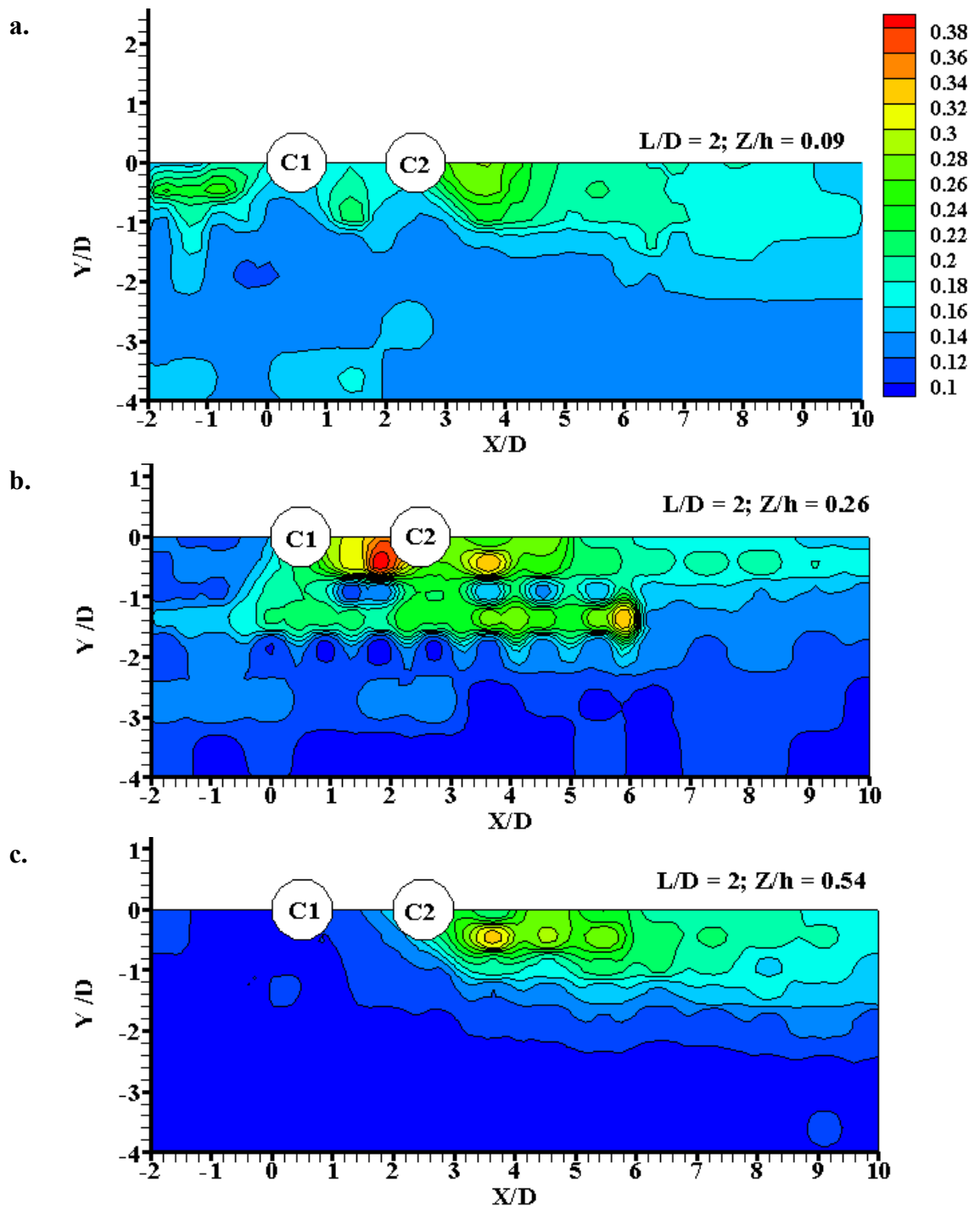


Figure B.2 Contour plots of streamwise turbulence intensity component for two columns case with $L/D = 2$ in different horizontal planes a) at $Z/h = 0.09$, b) at $Z/h = 0.26$ and c). at $Z/h = 0.54$

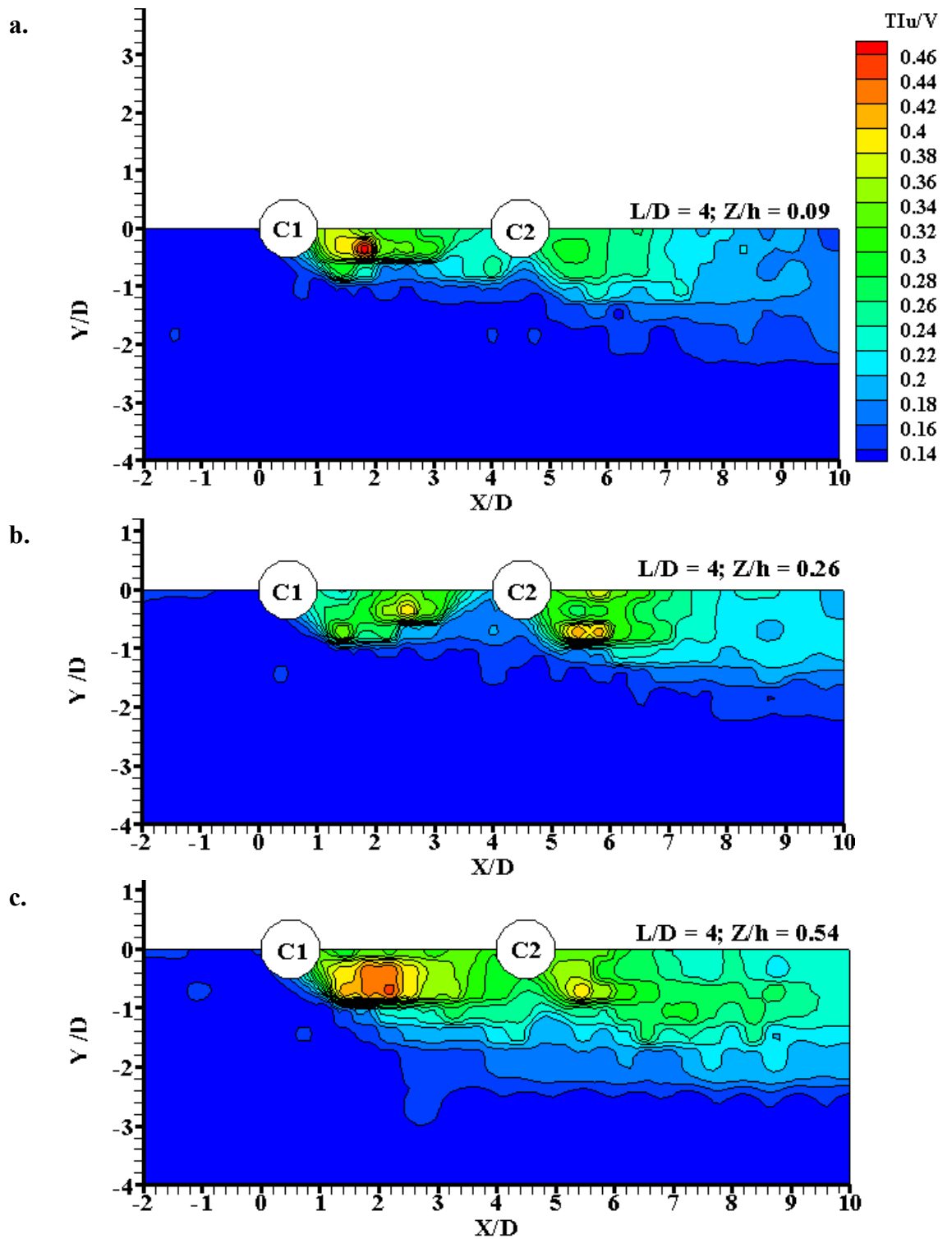


Figure B.3 Contour plots of streamwise turbulence intensity component for two columns case with $L/D = 4$ in different horizontal planes a) at $Z/h = 0.09$, b) at $Z/h = 0.26$ and c). at $Z/h = 0.54$

B.1.2 Profile Plots of Stream-wise Turbulence Intensity Component (TI_u) in Horizontal Plane

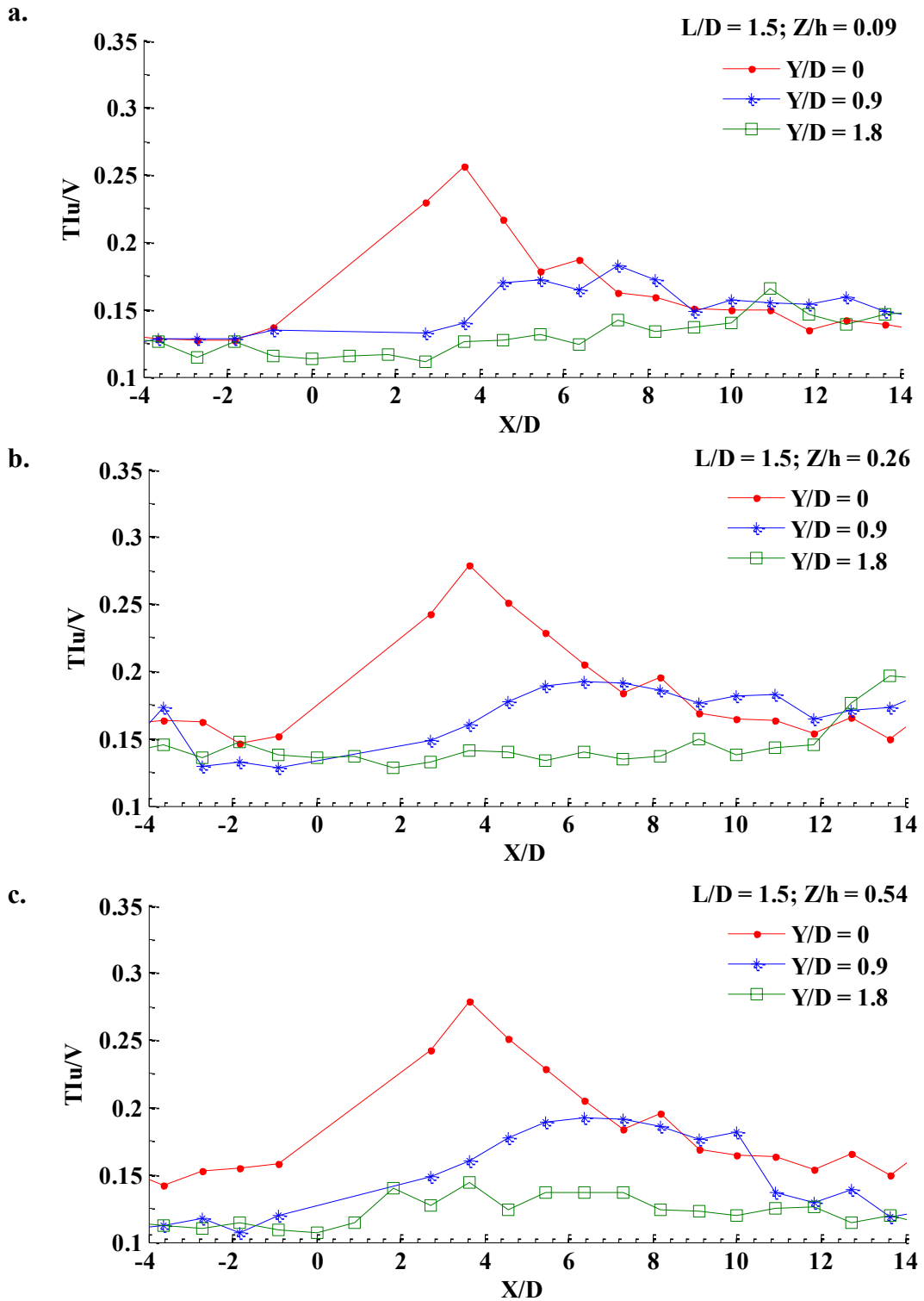


Figure B.4 Profile plots of streamwise turbulence intensity component for two columns case with $L/D = 1.5$ in different horizontal planes along three different longitudinal axes a) at $Z/h = 0.09$, b) at $Z/h = 0.26$ and c). at $Z/h = 0.54$

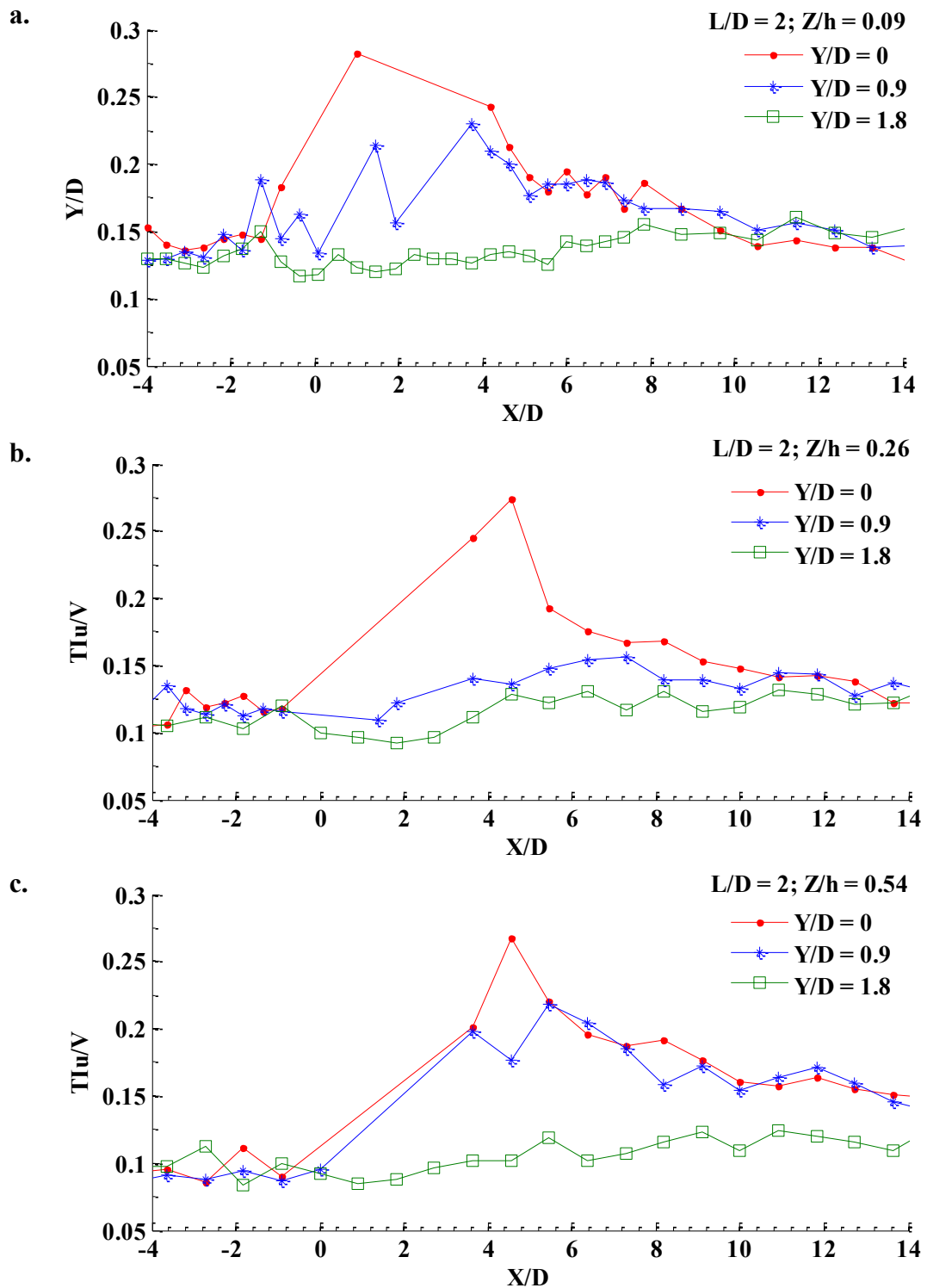


Figure B.5 Profile plots of streamwise turbulence intensity component for two columns case with $L/D = 2$ in different horizontal planes along three different longitudinal axes a) at $Z/h = 0.09$, b) at $Z/h = 0.26$ and c). at $Z/h = 0.54$

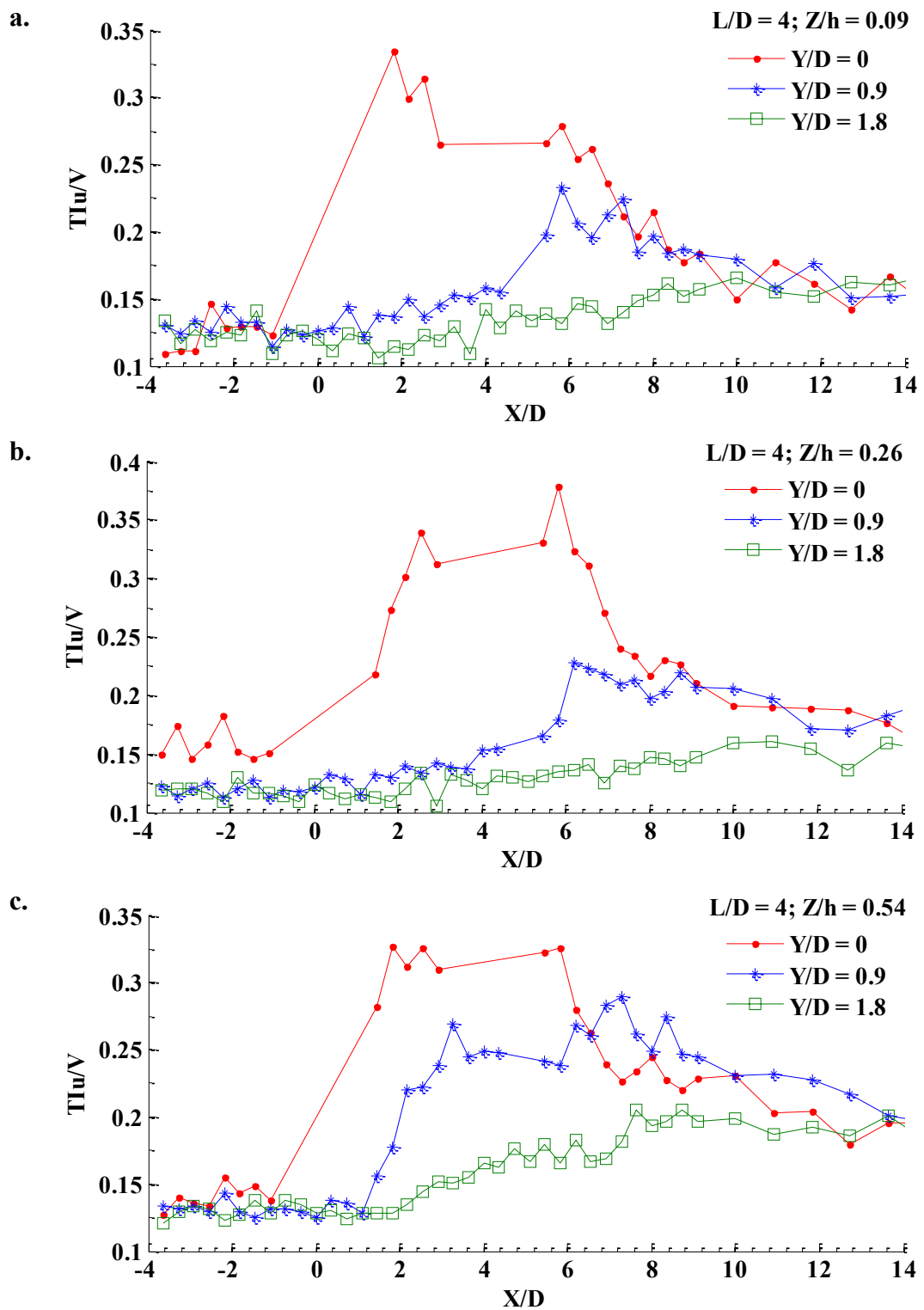


Figure B.6 Profile plots of streamwise turbulence intensity component for two columns case with $L/D = 4$ in different horizontal planes along three different longitudinal axes a) at $Z/h = 0.09$, b) at $Z/h = 0.26$ and c). at $Z/h = 0.54$

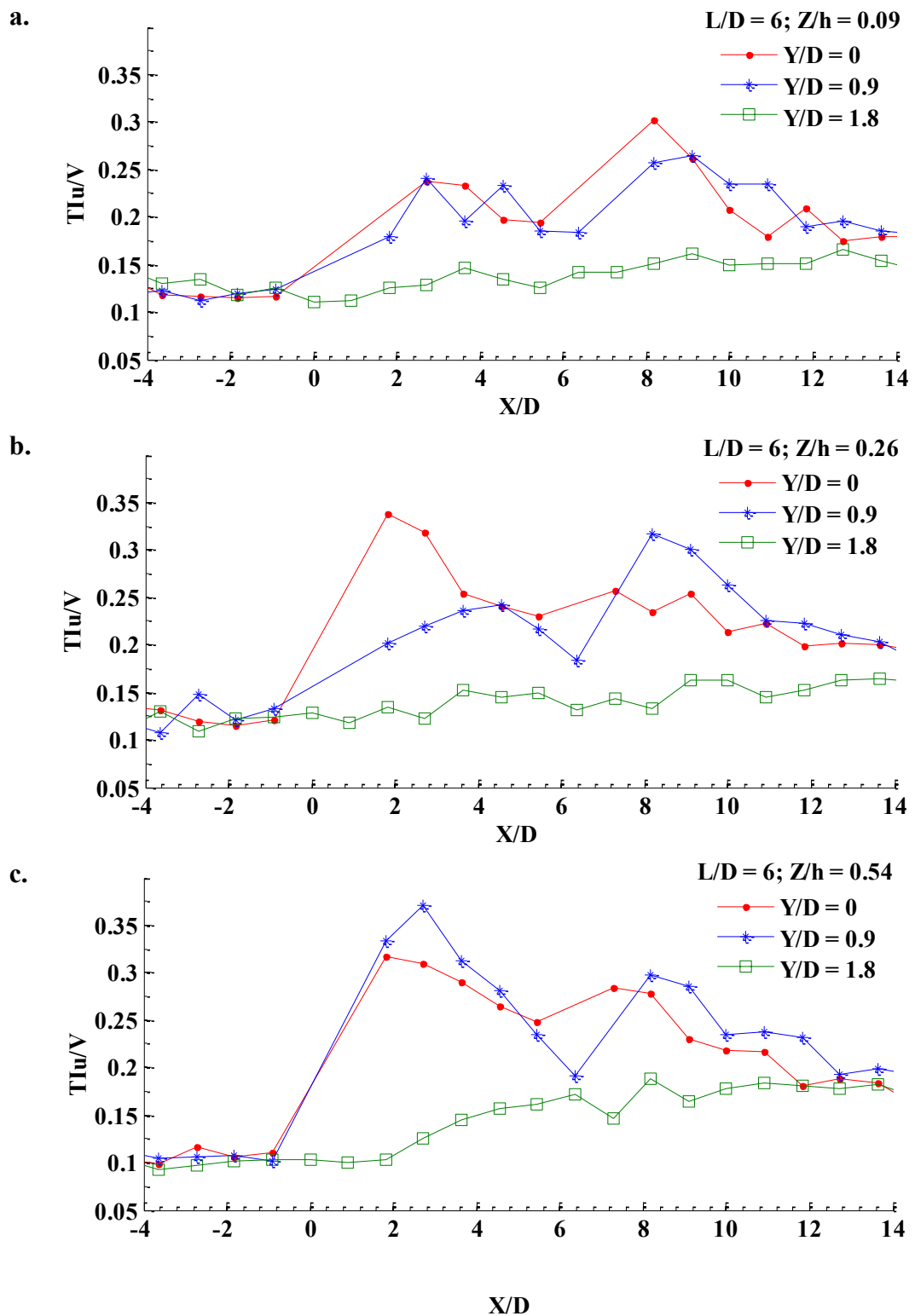


Figure B.7 Profile plots of streamwise turbulence intensity component for two columns case with $L/D = 6$ in different horizontal planes along three different longitudinal axes a) at $Z/h = 0.09$, b) at $Z/h = 0.26$ and c). at $Z/h = 0.54$

B.1.3 Contour Plots of Transverse Turbulence Intensity Component (TI_v) in Horizontal Plane

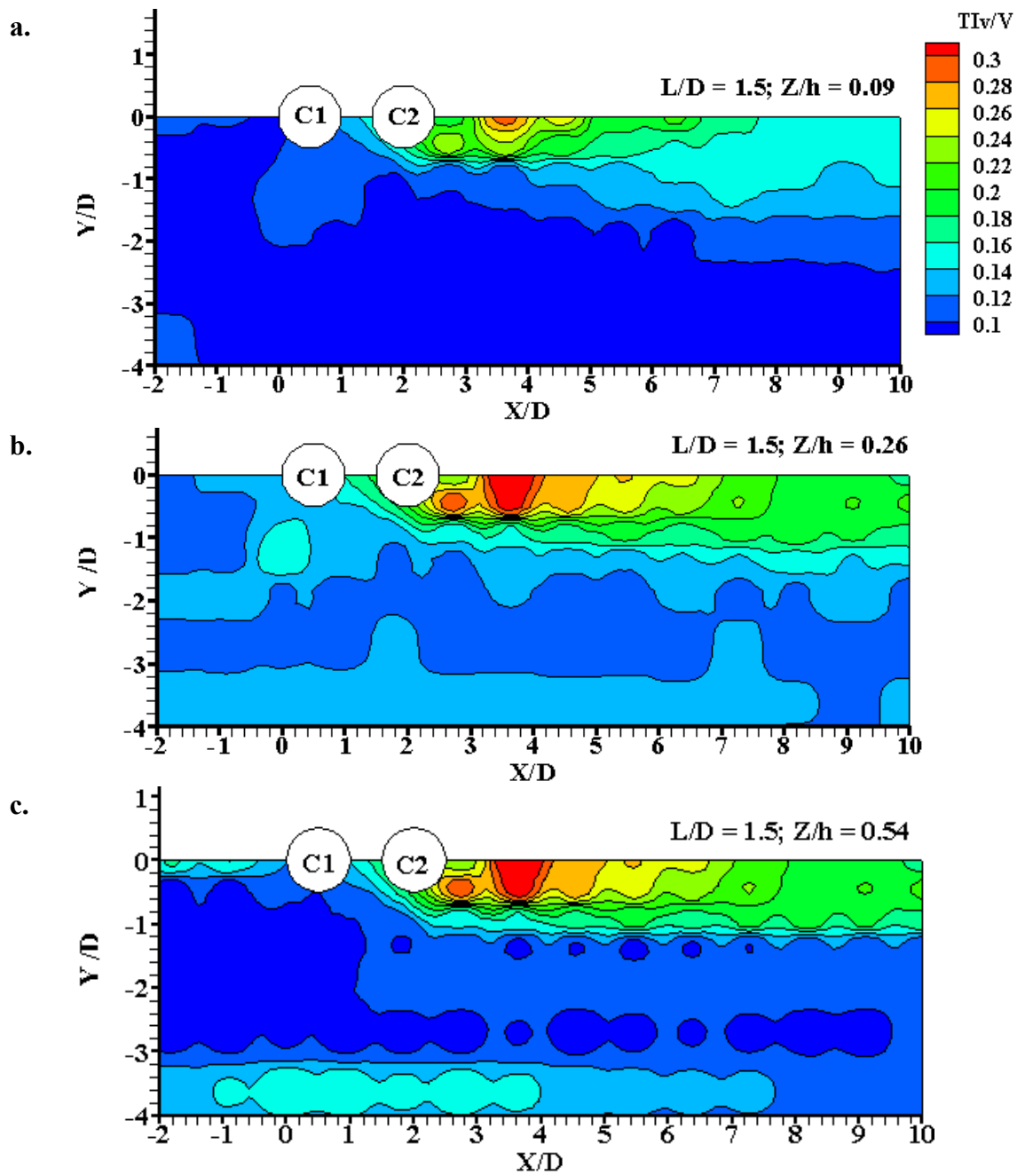


Figure B.8 Contour plots of transverse turbulence intensity component for two columns case with $L/D = 1.5$ in different horizontal planes a) at $Z/h = 0.09$, b) at $Z/h = 0.26$ and c). at $Z/h = 0.54$

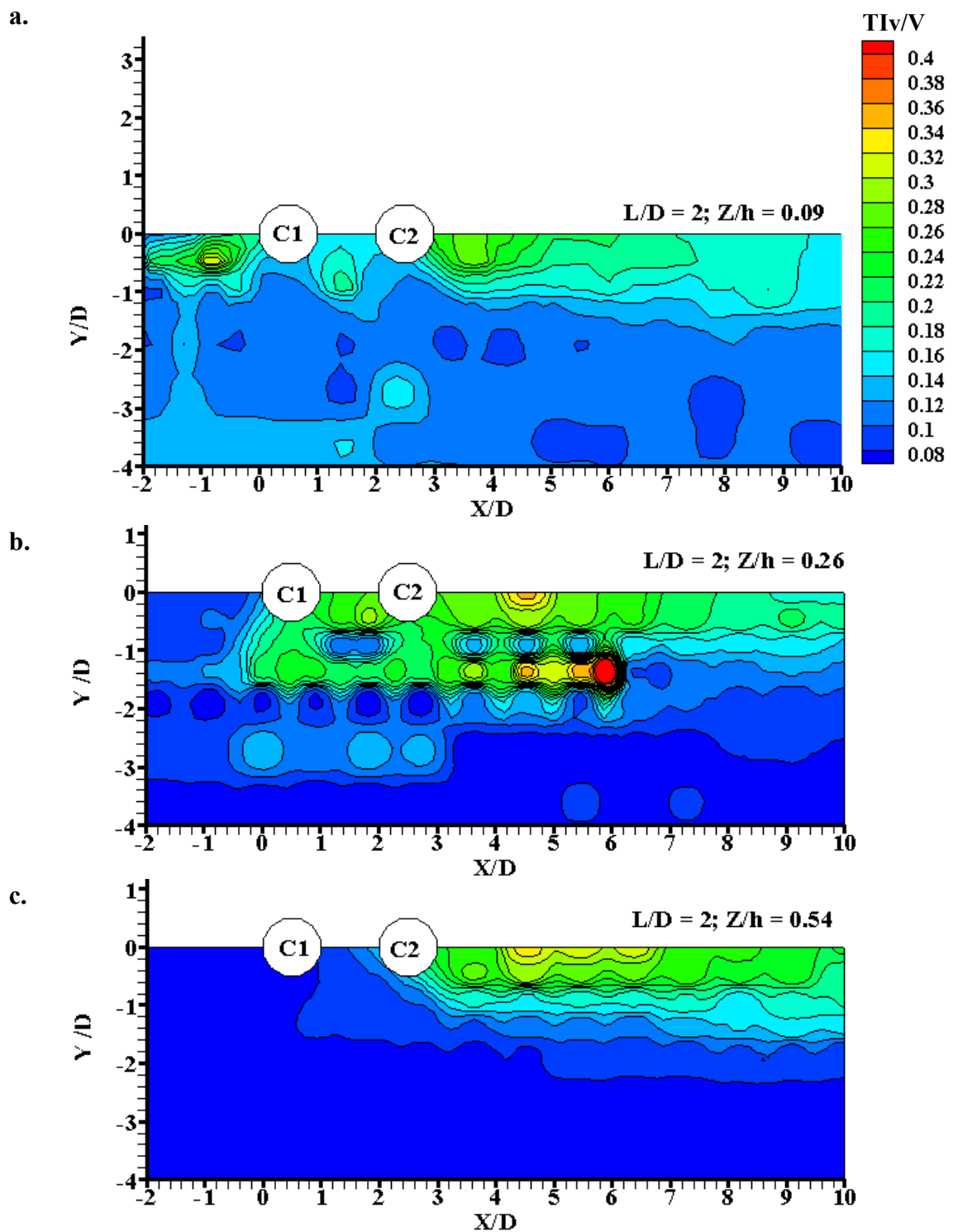


Figure B.9 Contour plots of transverse turbulence intensity component for two columns case with $L/D = 2$ in different horizontal planes a) at $Z/h = 0.09$, b) at $Z/h = 0.26$ and c). at $Z/h = 0.54$

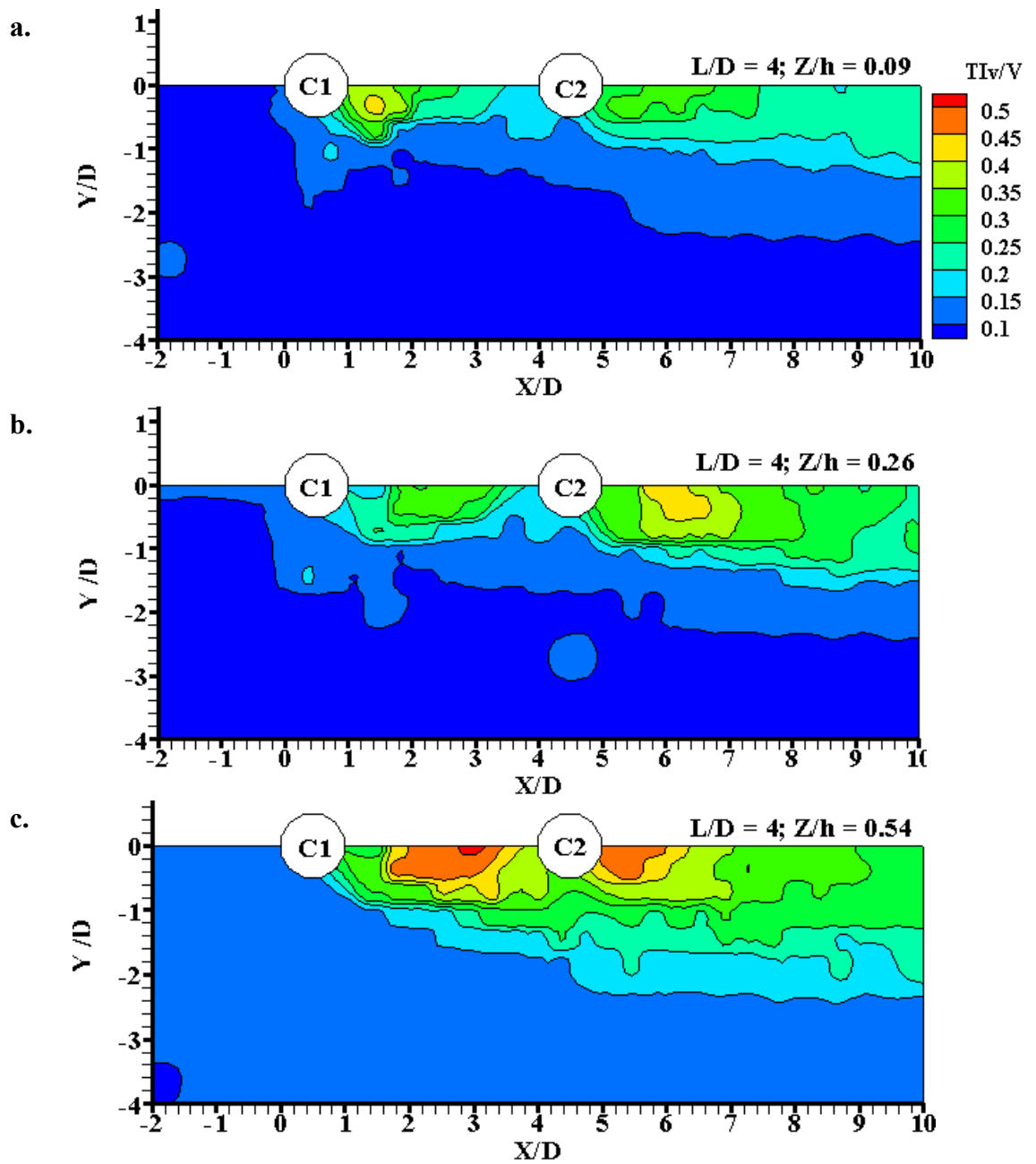


Figure B.10 Contour plots of transverse turbulence intensity component for two columns case with $L/D = 4$ in different horizontal planes a) at $Z/h = 0.09$, b) at $Z/h = 0.26$ and c). at $Z/h = 0.54$

B.1.4 Profile Plots of Transverse Turbulence Intensity Component (TI_v) in Horizontal Plane

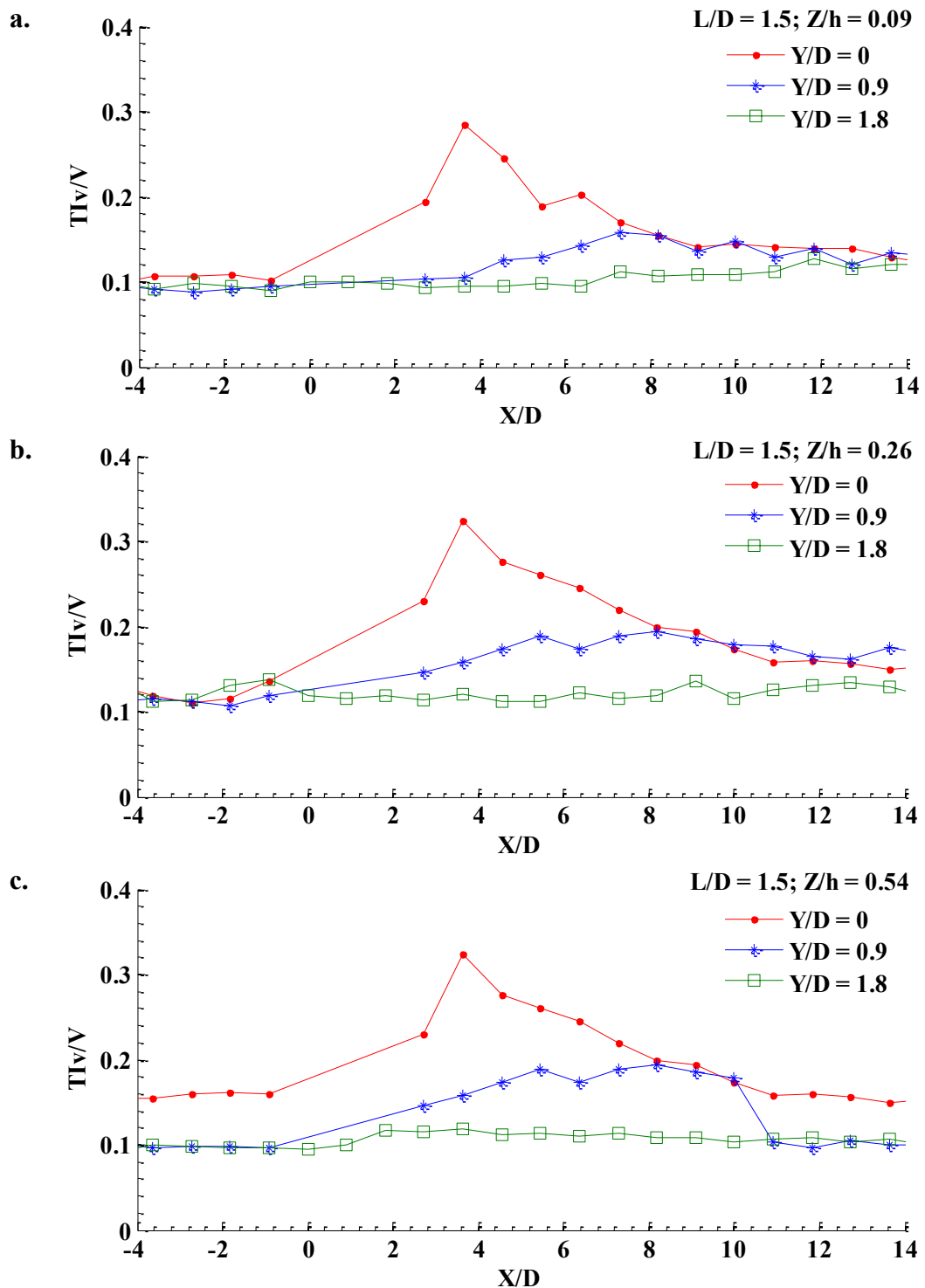


Figure B.11 Profile plots of transverse turbulence intensity component for two columns case with $L/D = 1.5$ in different horizontal planes along three different longitudinal axes a) at $Z/h = 0.09$, b) at $Z/h = 0.26$ and c). at $Z/h = 0.54$

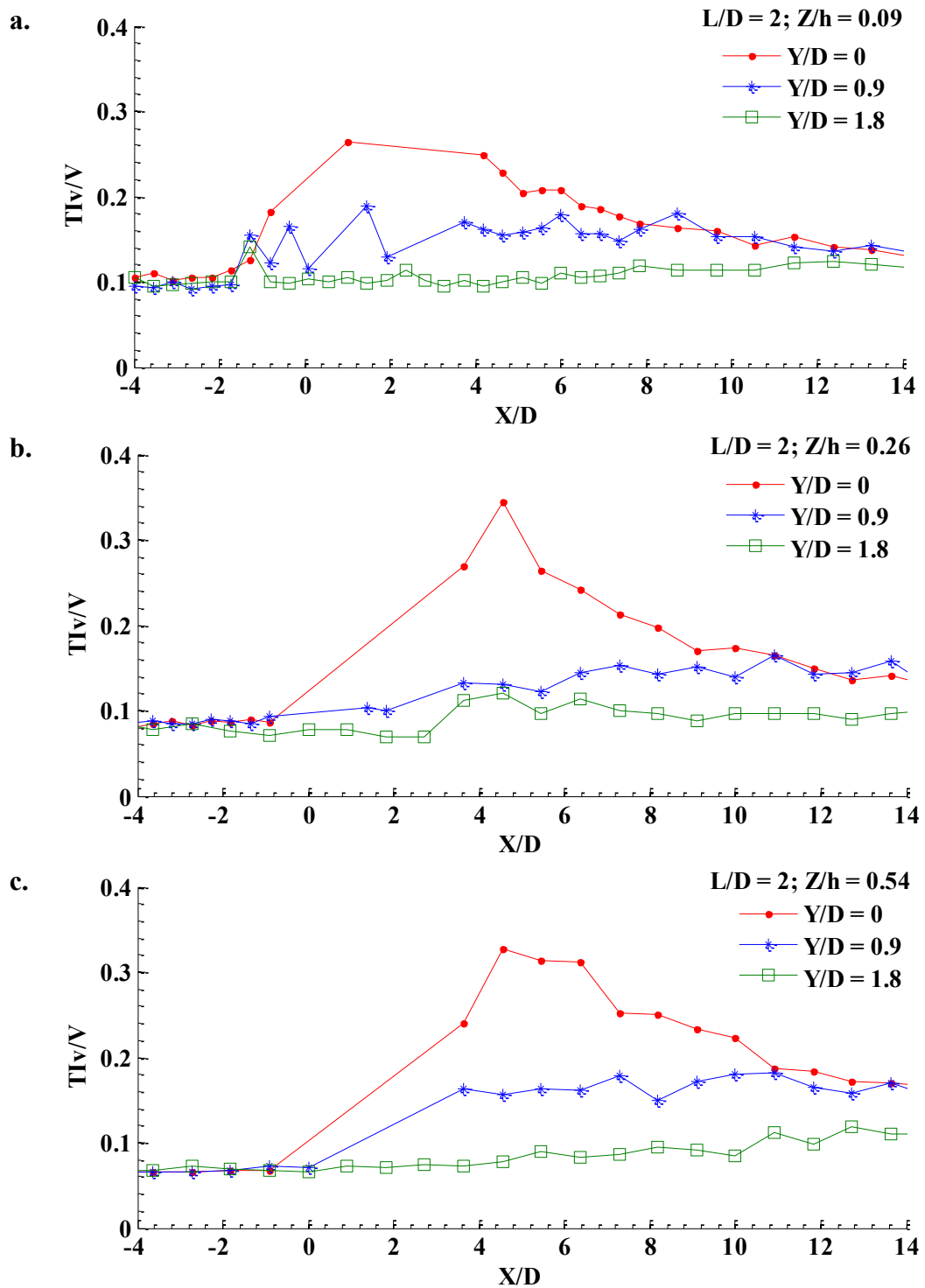


Figure B.12 Profile plots of transverse turbulence intensity component for two columns case with $L/D = 2$ in different horizontal planes along three different longitudinal axes a) at $Z/h = 0.09$, b) at $Z/h = 0.26$ and c). at $Z/h = 0.54$

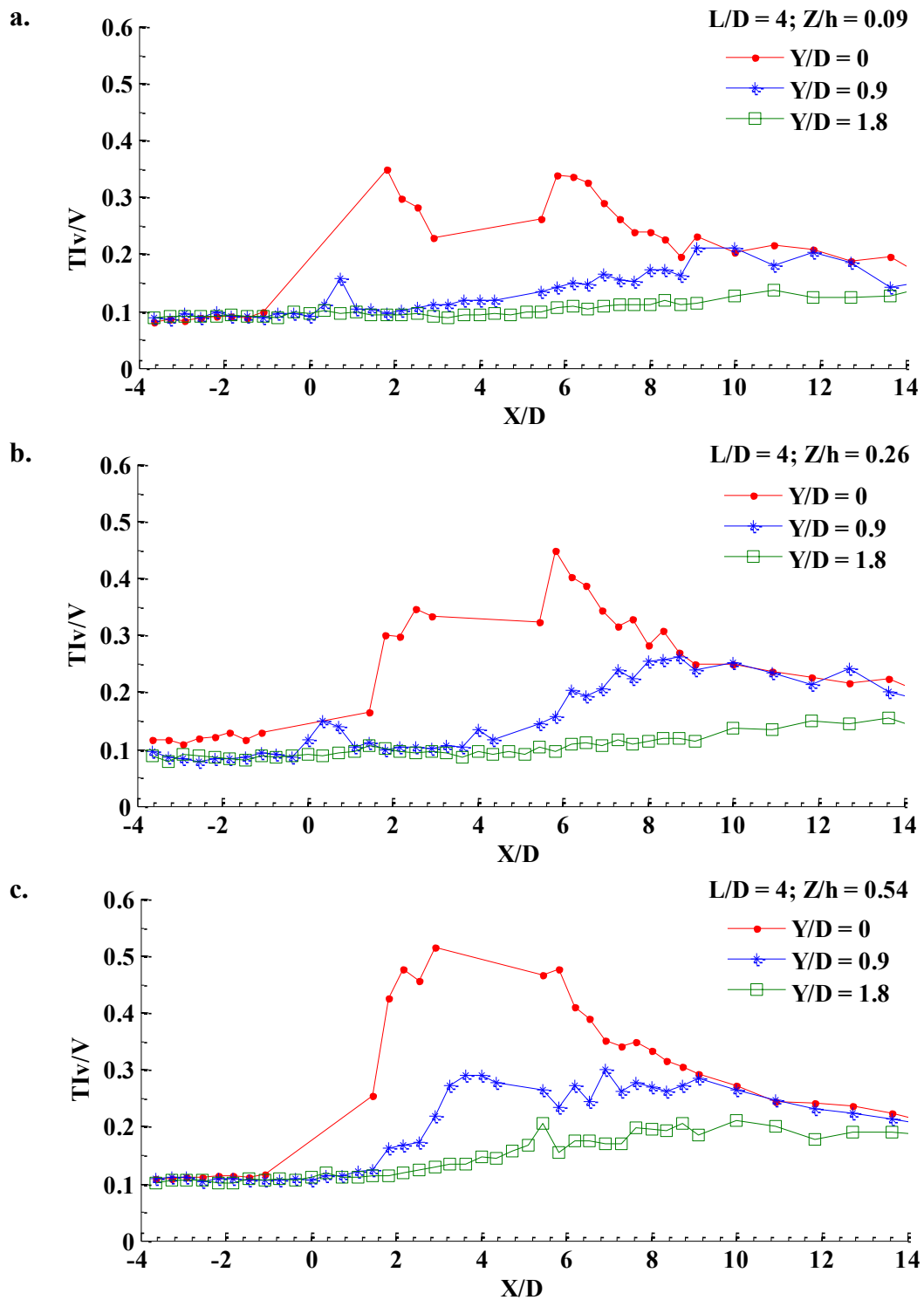


Figure B.13 Profile plots of transverse turbulence intensity component for two columns case with $L/D = 4$ in different horizontal planes along three different longitudinal axes a) at $Z/h = 0.09$, b) at $Z/h = 0.26$ and c). at $Z/h = 0.54$

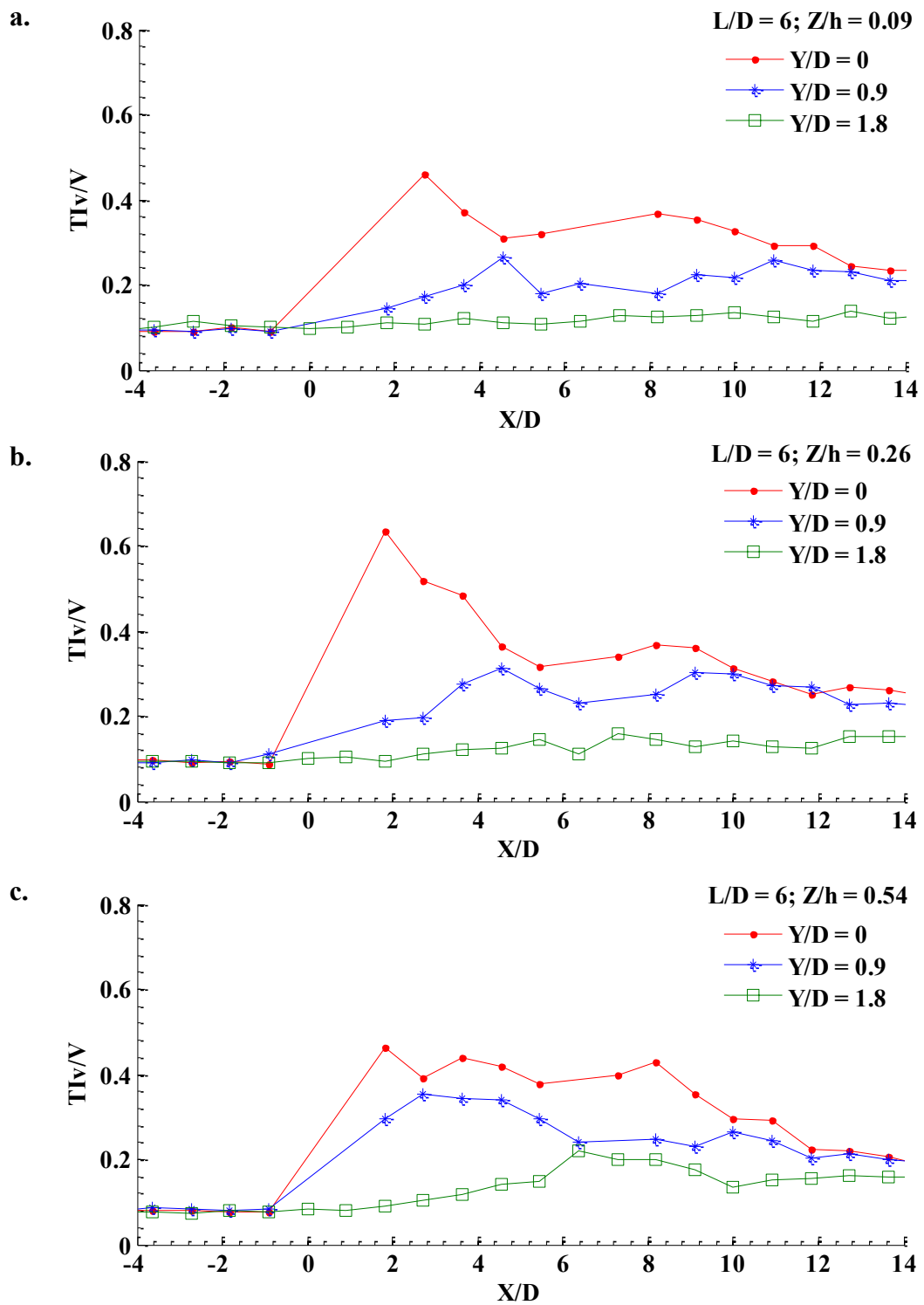


Figure B.14 Profile plots of transverse turbulence intensity component for two columns case with $L/D = 6$ in different horizontal planes along three different longitudinal axes a) at $Z/h = 0.09$, b) at $Z/h = 0.26$ and c). at $Z/h = 0.54$

B.1.5 Contour Plots of Vertical Turbulence Intensity Component (TI_w) in Horizontal Plane

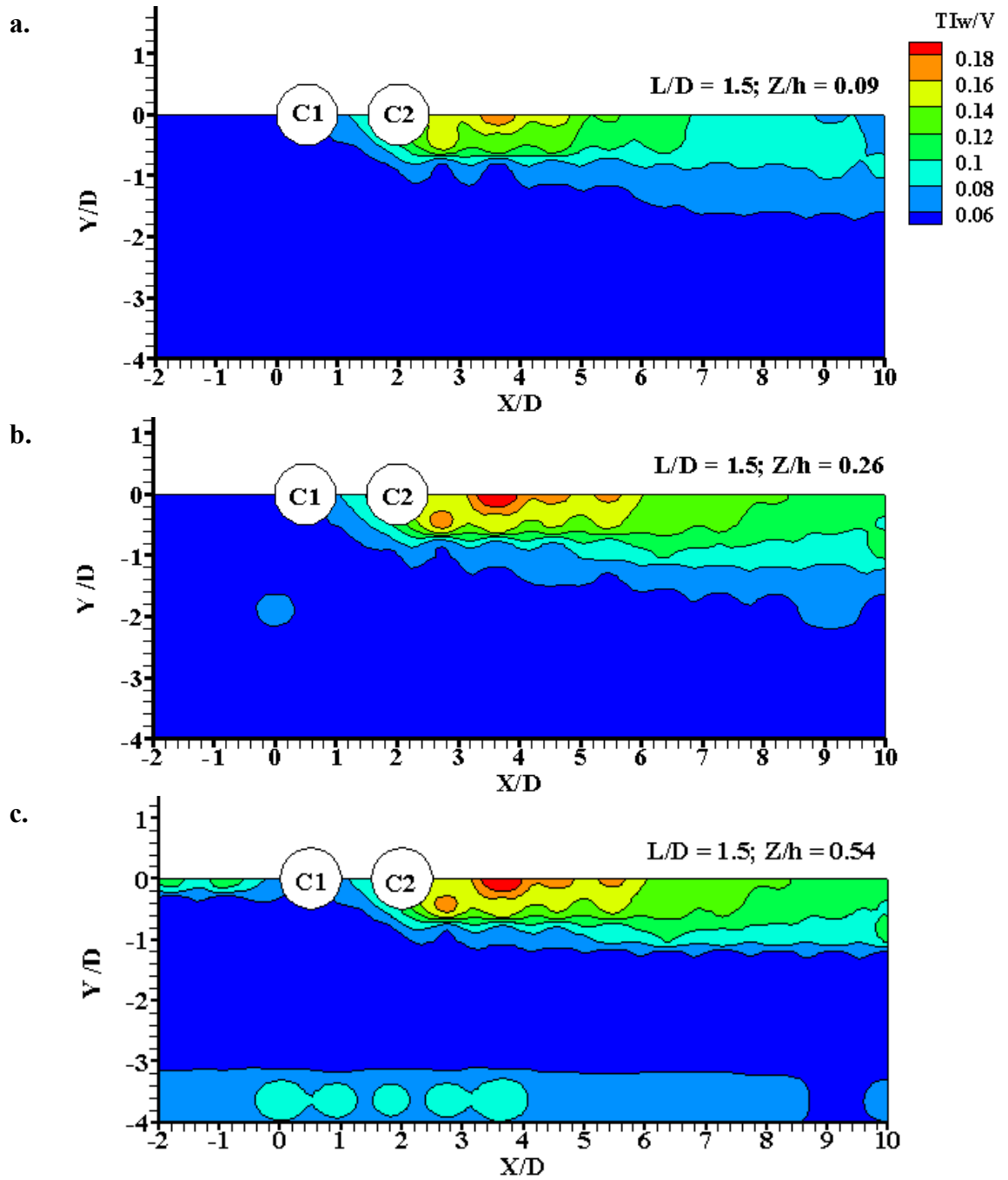


Figure B.15 Contour plots of vertical turbulence intensity component for two columns case with $L/D = 1.5$ in different horizontal planes a) at $Z/h = 0.09$, b) at $Z/h = 0.26$ and c). at $Z/h = 0.54$

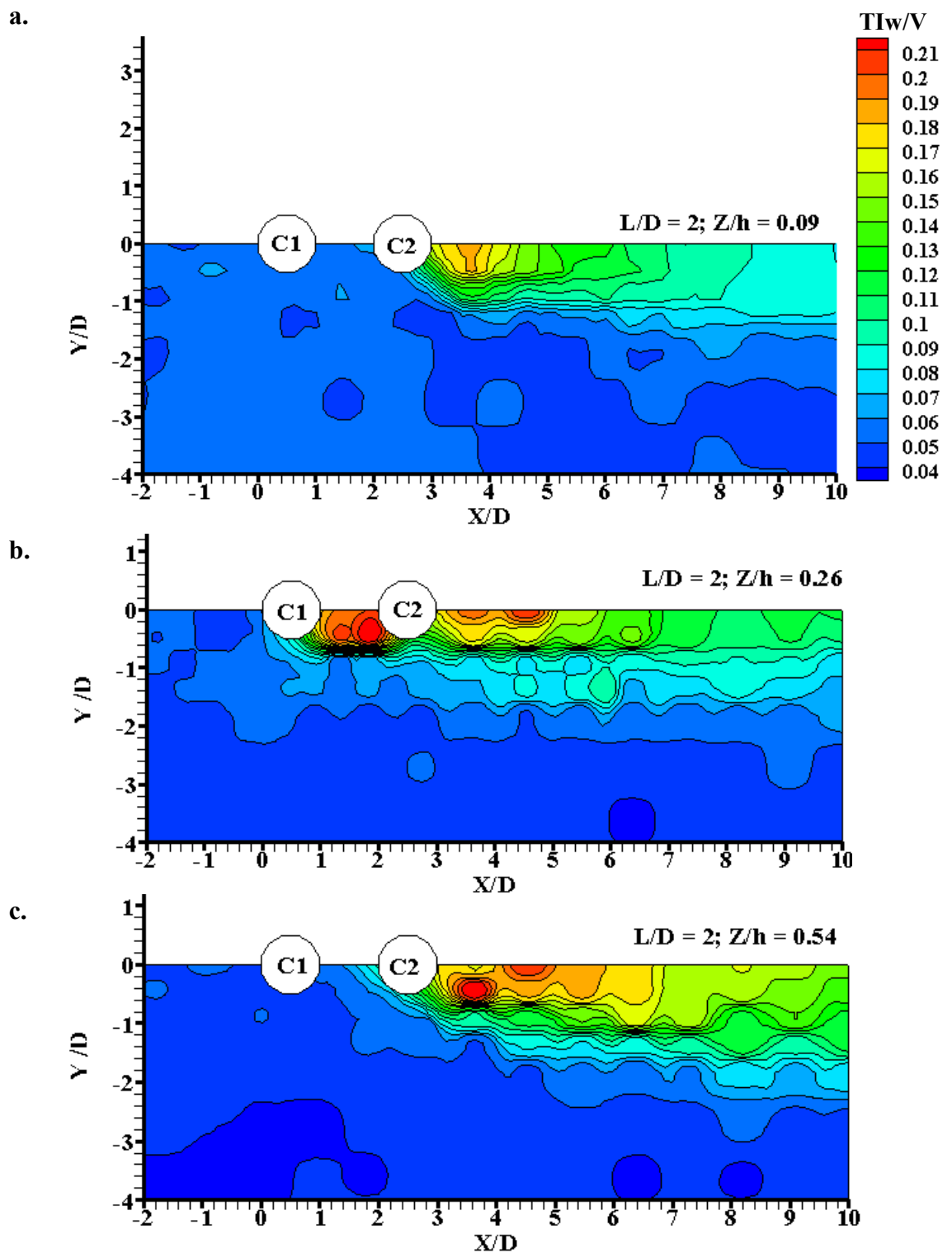


Figure B.16 Contour plots of vertical turbulence intensity component for two columns case with $L/D = 2$ in different horizontal planes a) at $Z/h = 0.09$, b) at $Z/h = 0.26$ and c). at $Z/h = 0.54$

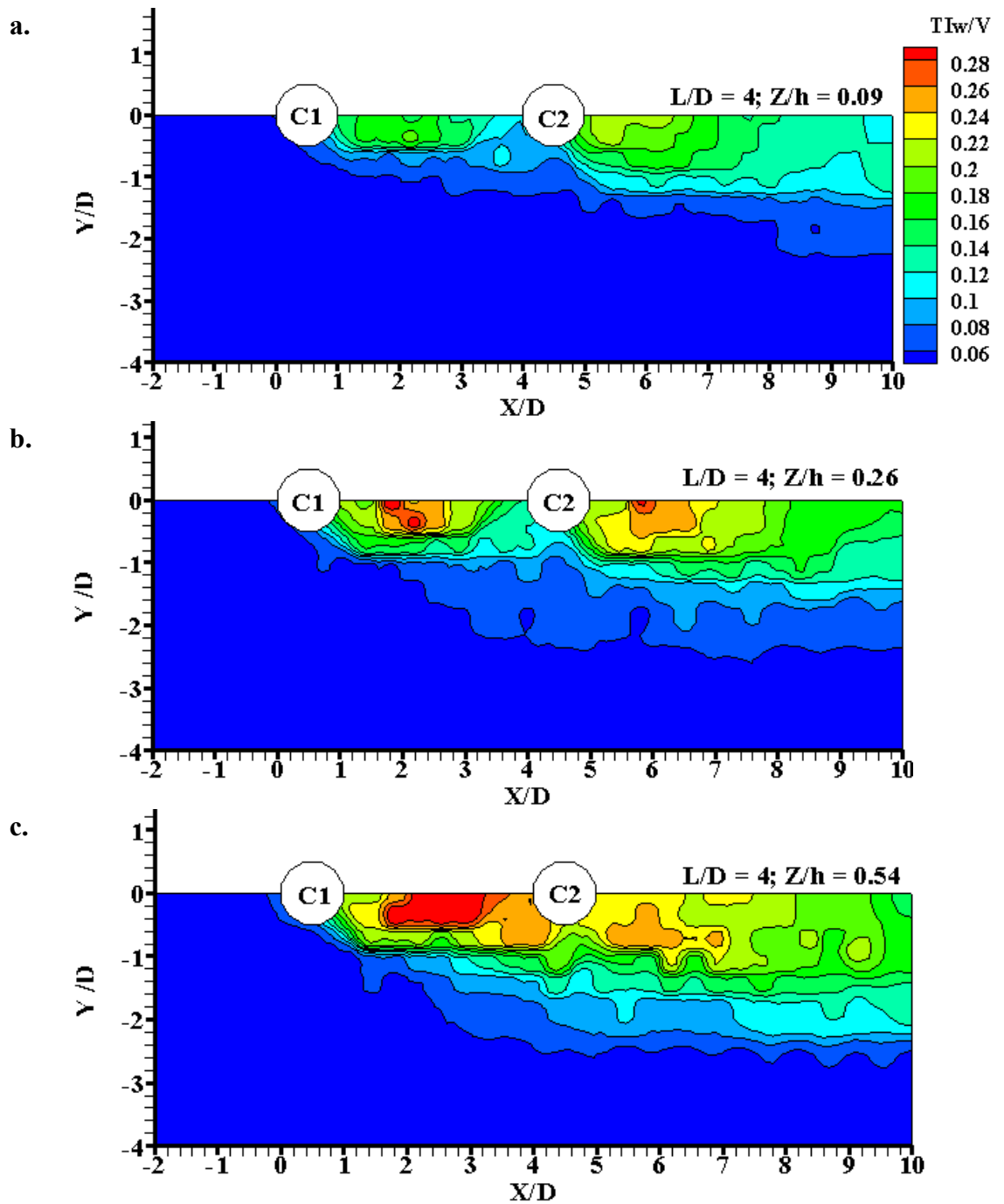


Figure B.17 Contour plots of vertical turbulence intensity component for two columns case with $L/D = 4$ in different horizontal planes a) at $Z/h = 0.09$, b) at $Z/h = 0.26$ and c). at $Z/h = 0.54$

B.1.6 Profile Plots of Vertical Turbulence Intensity Component (TI_w) in Horizontal Plane

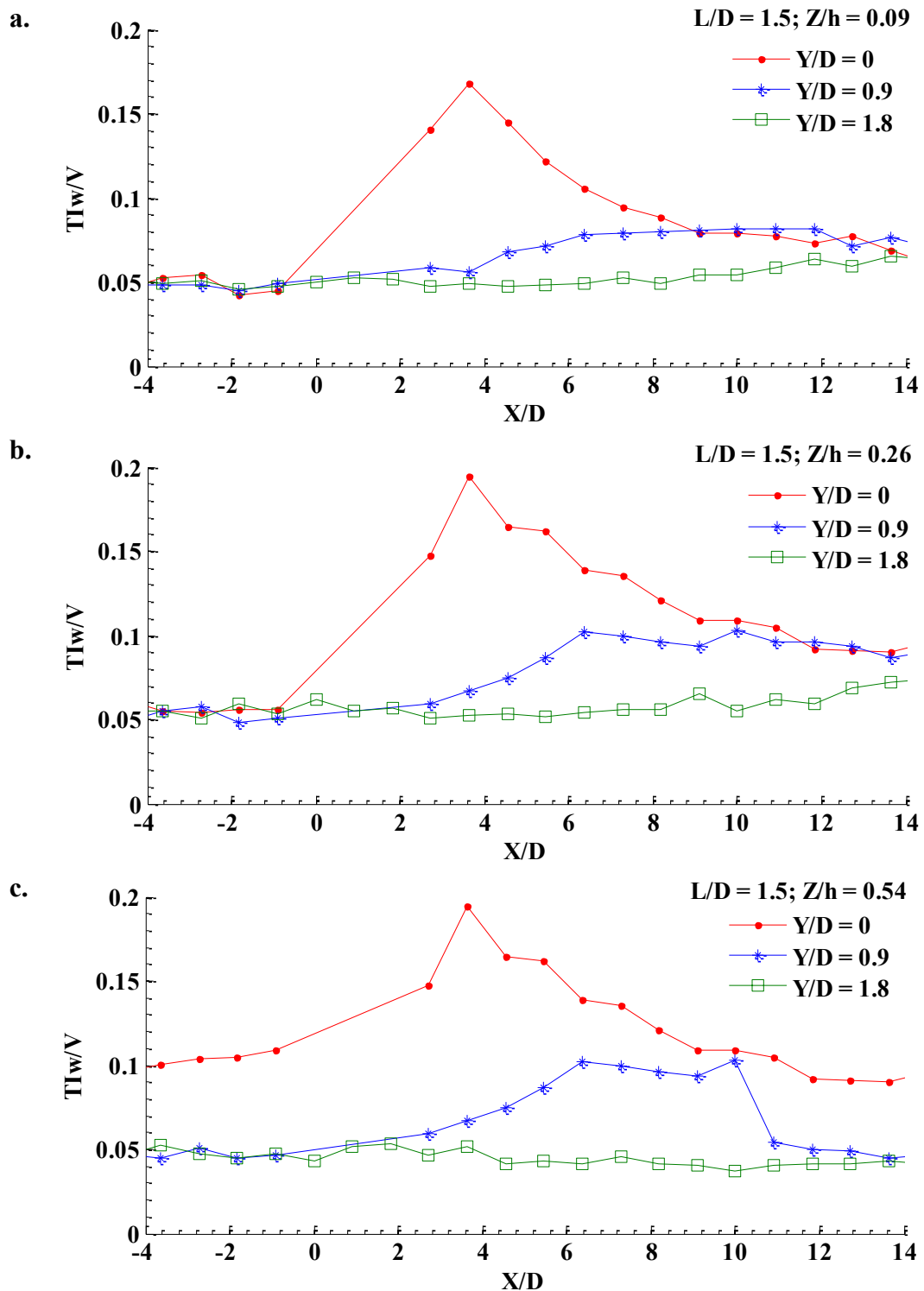


Figure B.18 Profile plots of vertical turbulence intensity component for two columns case with $L/D = 1.5$ in different horizontal planes along three different longitudinal axes a) at $Z/h = 0.09$, b) at $Z/h = 0.26$ and c). at $Z/h = 0.54$

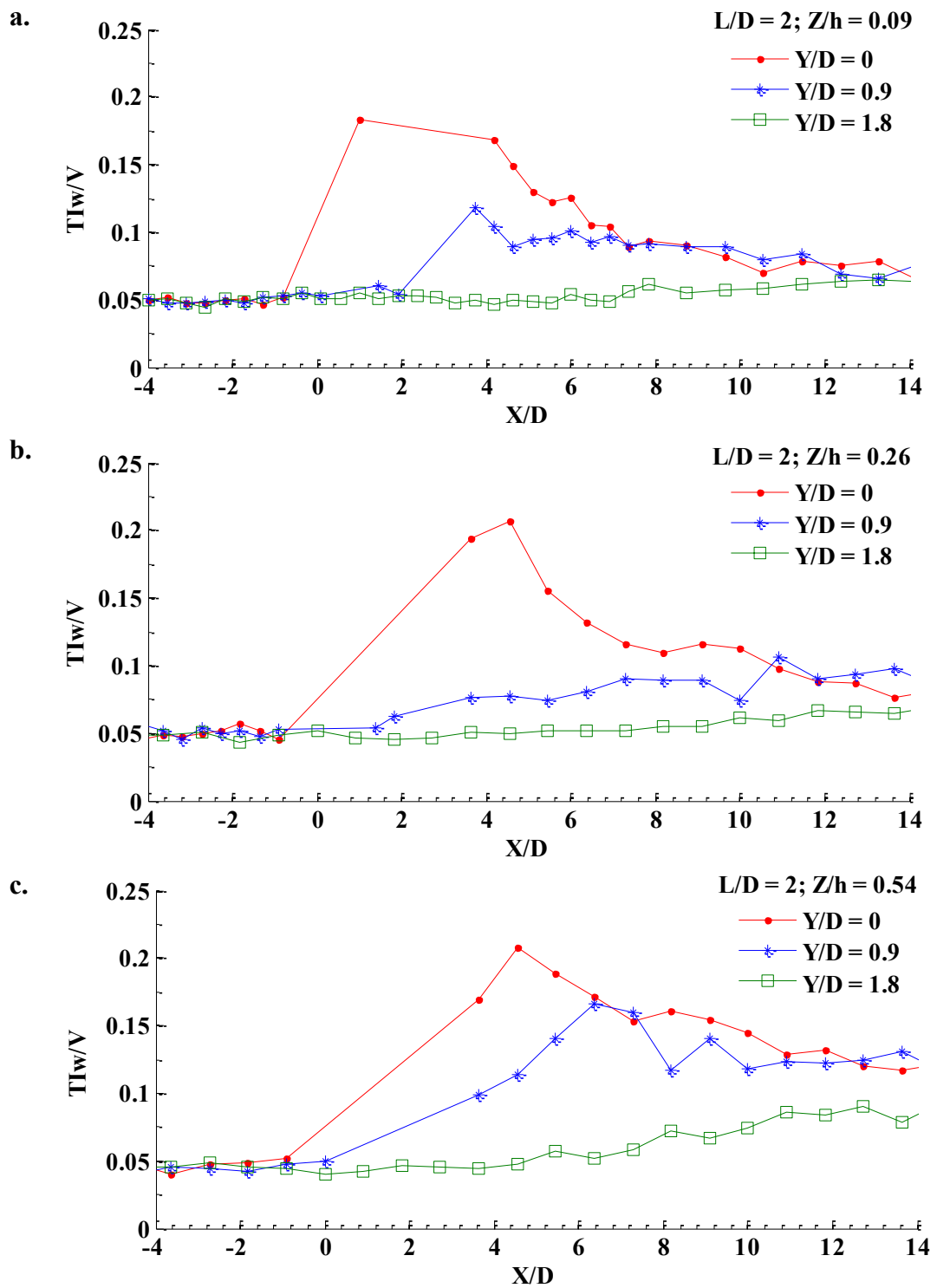


Figure B.19 Profile plots of vertical turbulence intensity component for two columns case with $L/D = 2$ in different horizontal planes along three different longitudinal axes a) at $Z/h = 0.09$, b) at $Z/h = 0.26$ and c). at $Z/h = 0.54$

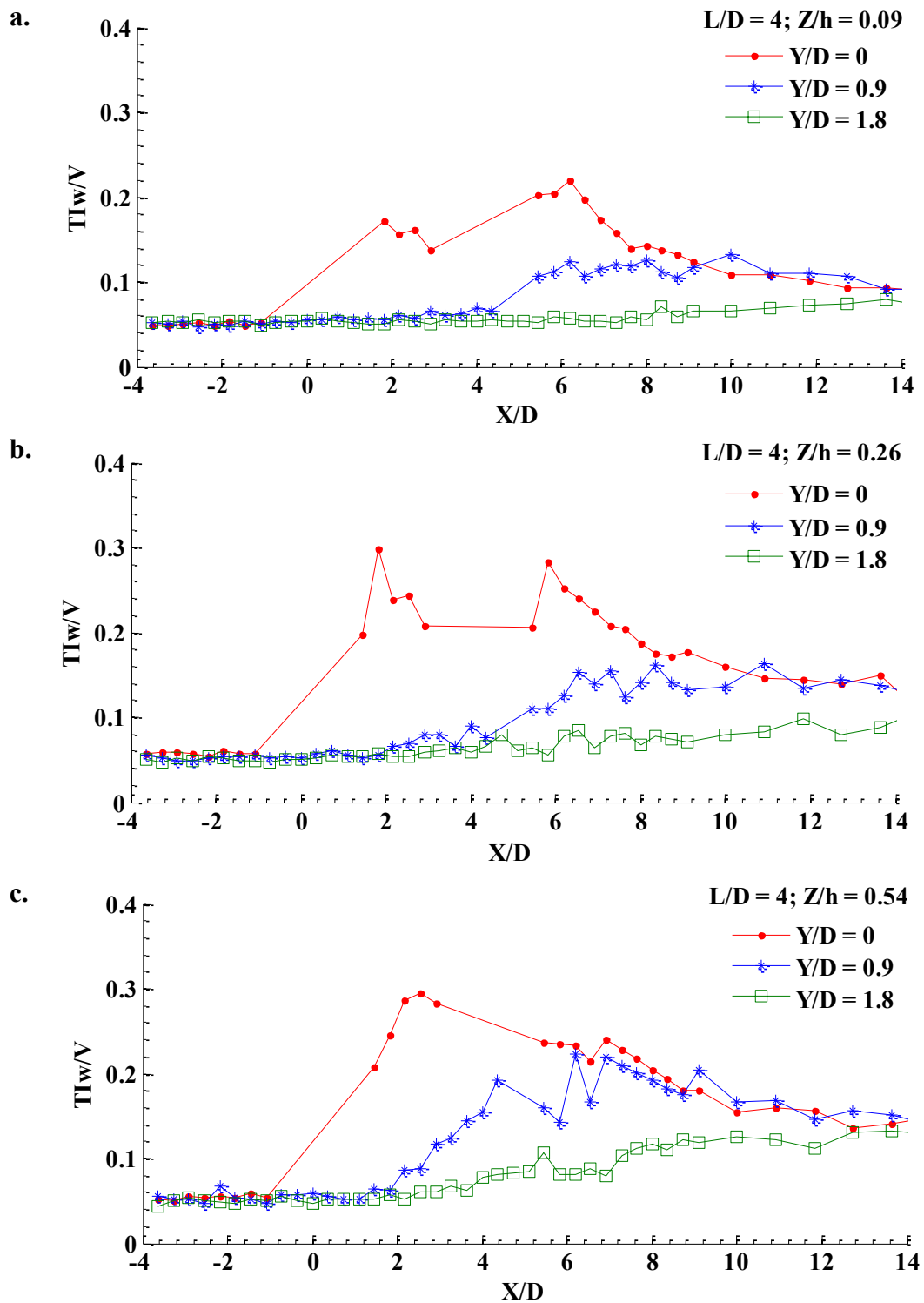


Figure B.20 Profile plots of vertical turbulence intensity component for two columns case with $L/D = 4$ in different horizontal planes along three different longitudinal axes a) at $Z/h = 0.09$, b) at $Z/h = 0.26$ and c). at $Z/h = 0.54$

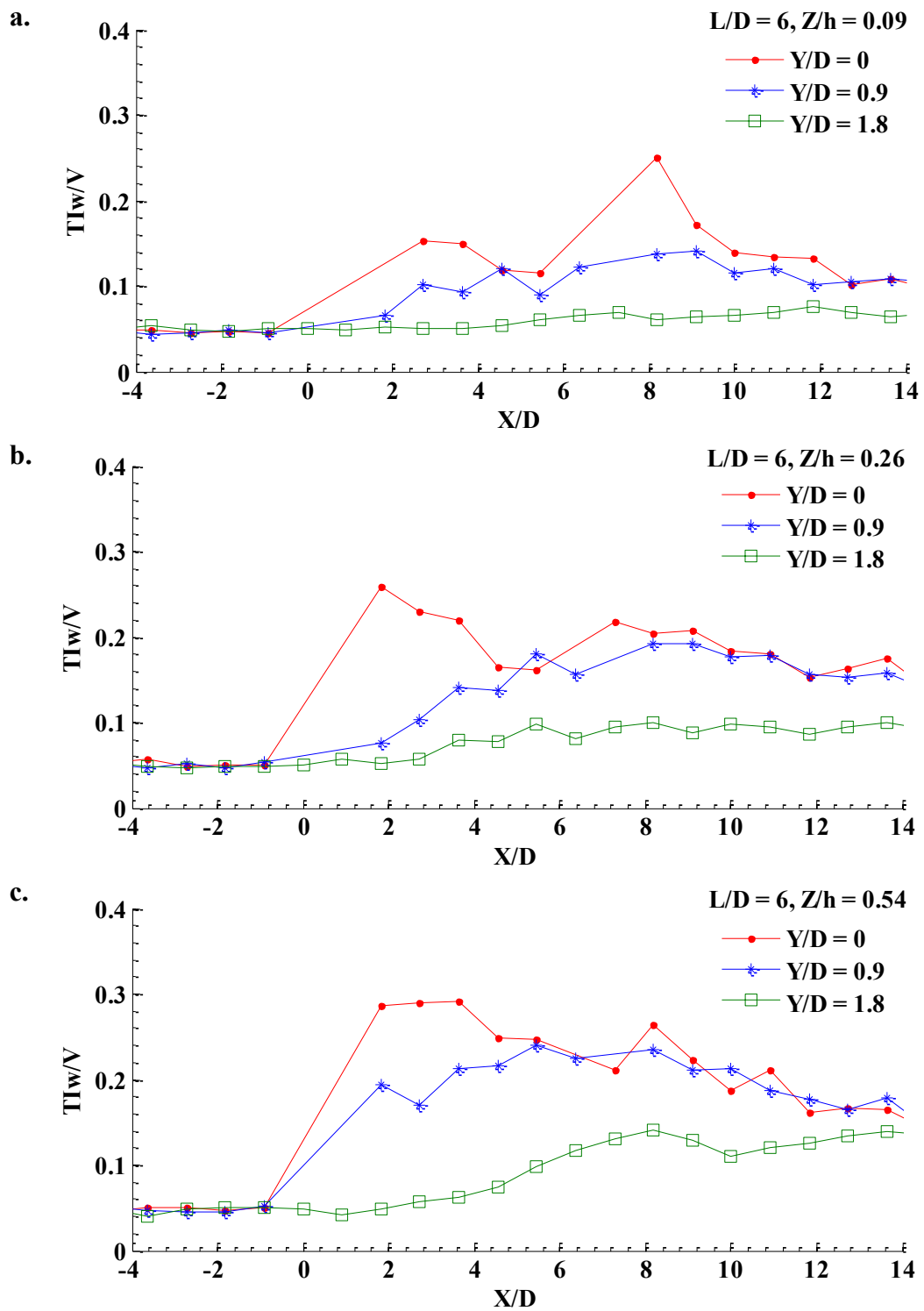


Figure B.21 Profile plots of vertical turbulence intensity component for two columns case with $L/D = 6$ in different horizontal planes along three different longitudinal axes a) at $Z/h = 0.09$, b) at $Z/h = 0.26$ and c). at $Z/h = 0.54$

B.2 Plots of Turbulence Intensity in Vertical Plane

B.2.1 Contour Plots of Stream-wise Turbulence Intensity Component (TI_u) in Vertical Plane

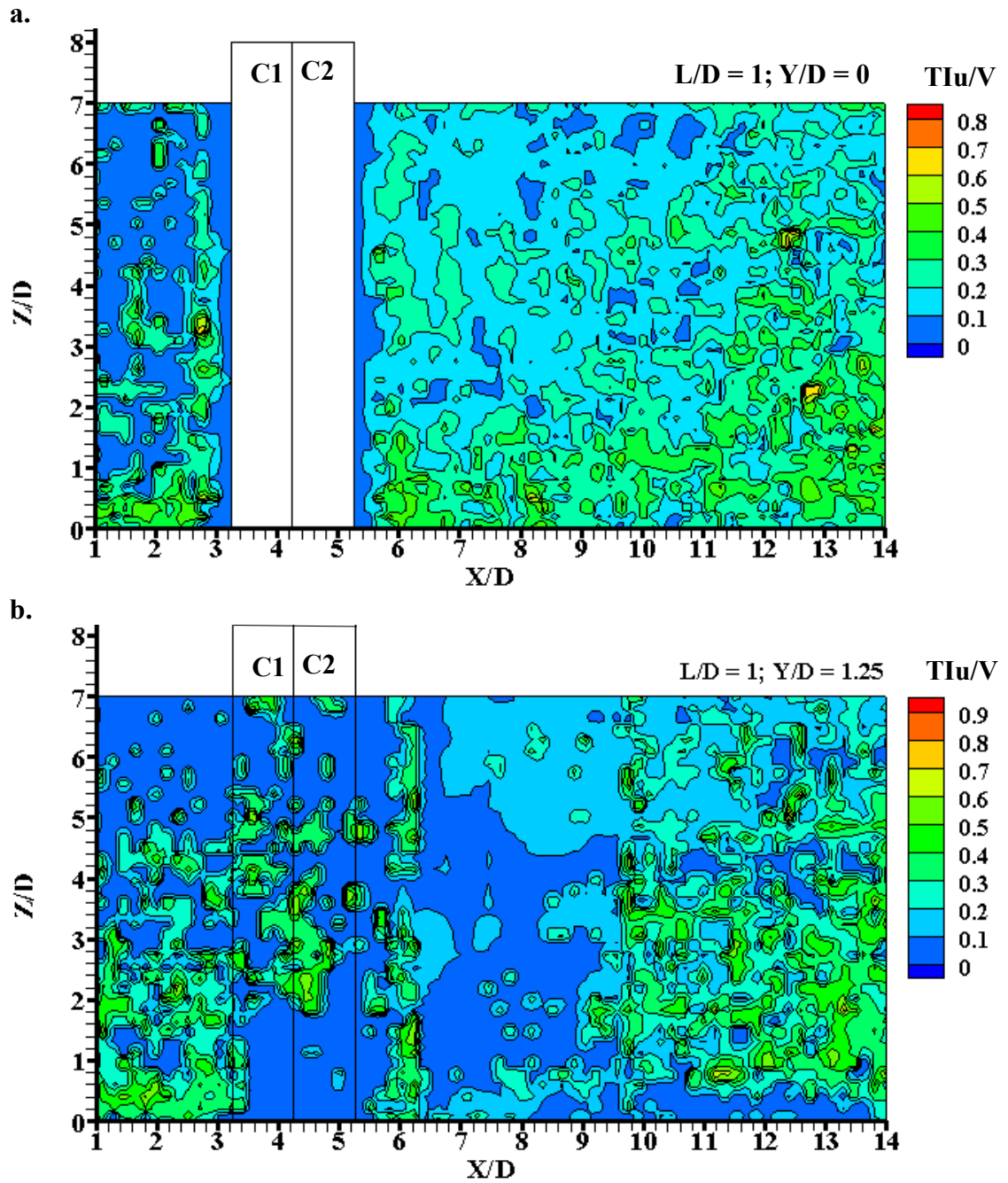


Figure B.22 Contour plots of streamwise turbulence intensity component for two columns case with $L/D = 1$ in different vertical planes a) at $Y/D = 0$, and b) at $Y/D = 1.25$

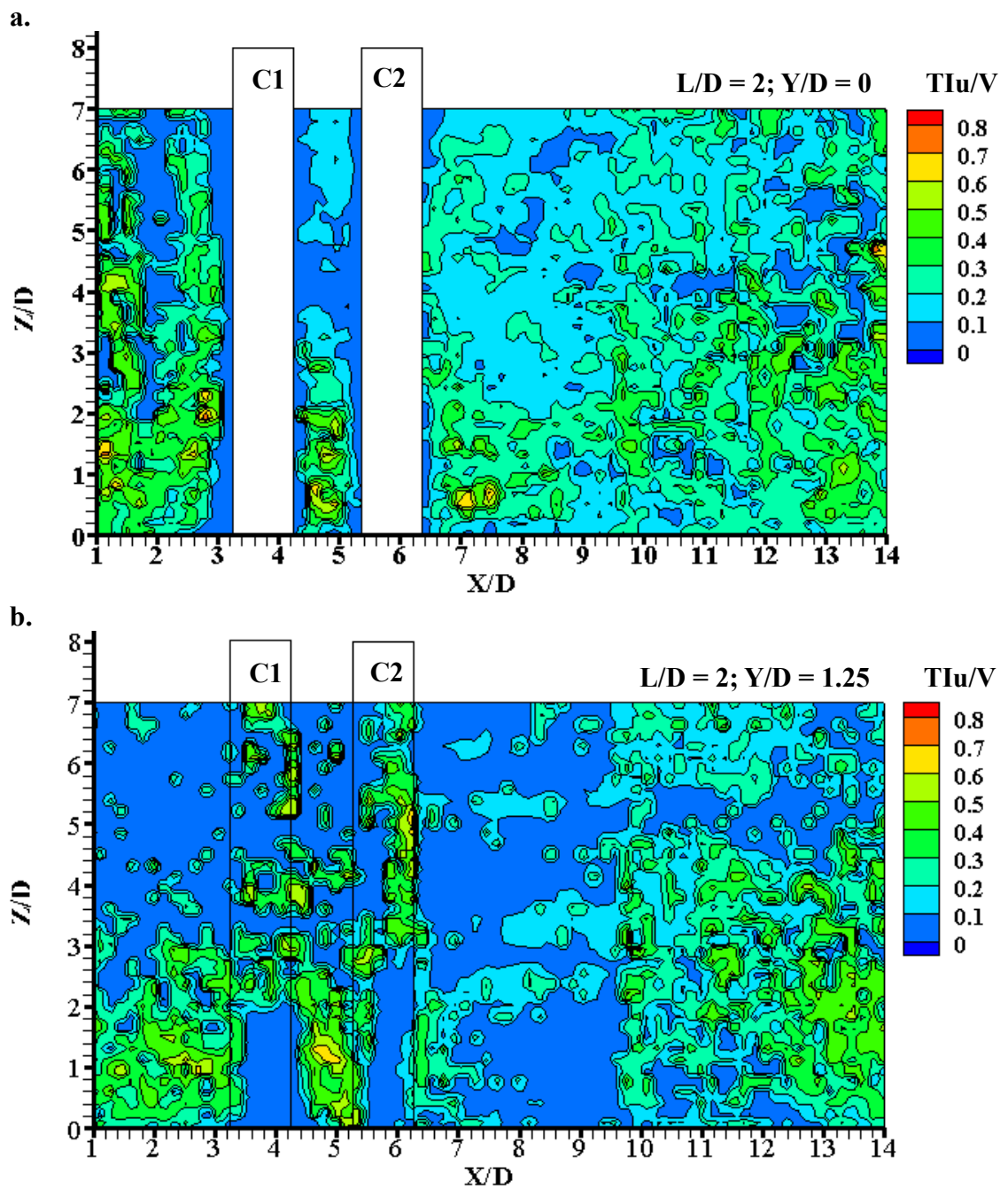


Figure B.23 Contour plots of streamwise turbulence intensity component for two columns case with $L/D = 2$ in different vertical planes a) at $Y/D = 0$, and b) at $Y/D = 1.25$

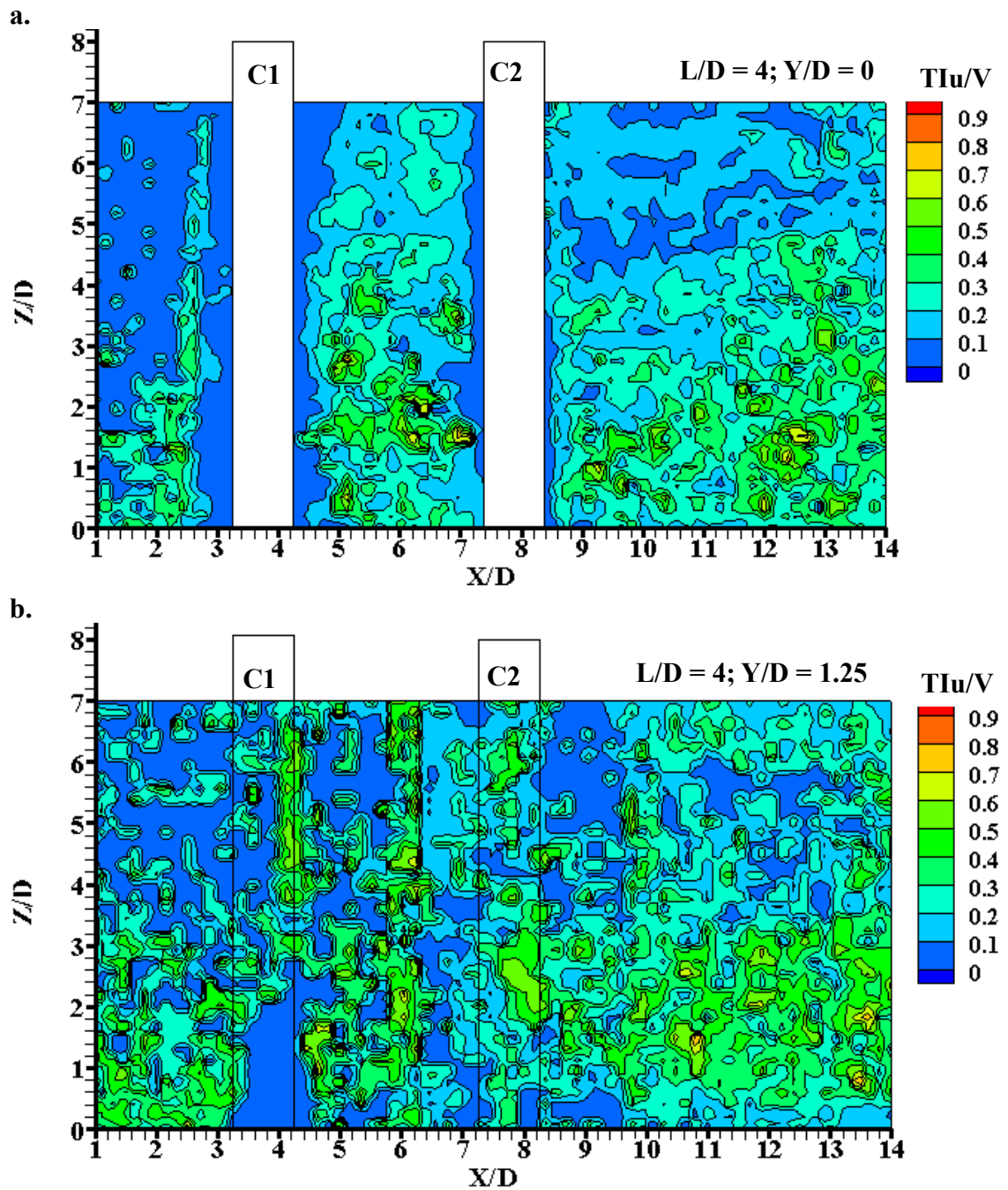


Figure B.24 Contour plots of streamwise turbulence intensity component for two columns case with $L/D = 4$ in different vertical planes a) at $Y/D = 0$, and b) at $Y/D = 1.25$

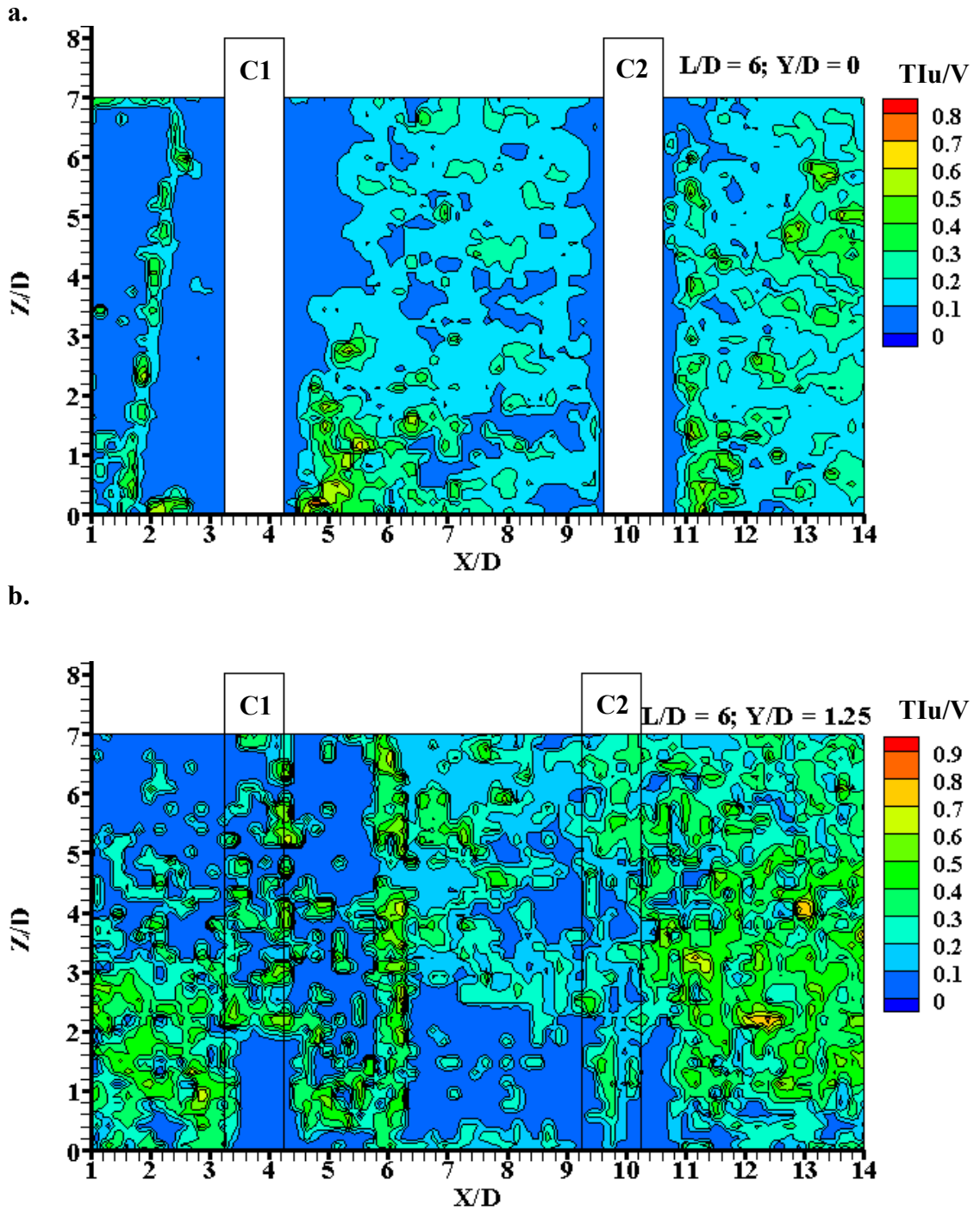


Figure B.25 Contour plots of streamwise turbulence intensity component for two columns case with $L/D = 6$ in different vertical planes a) at $Y/D = 0$, and b) at $Y/D = 1.25$

B.2.2 Contour Plots of Vertical Component of Turbulence Intensity (TI_w) in Vertical Plane

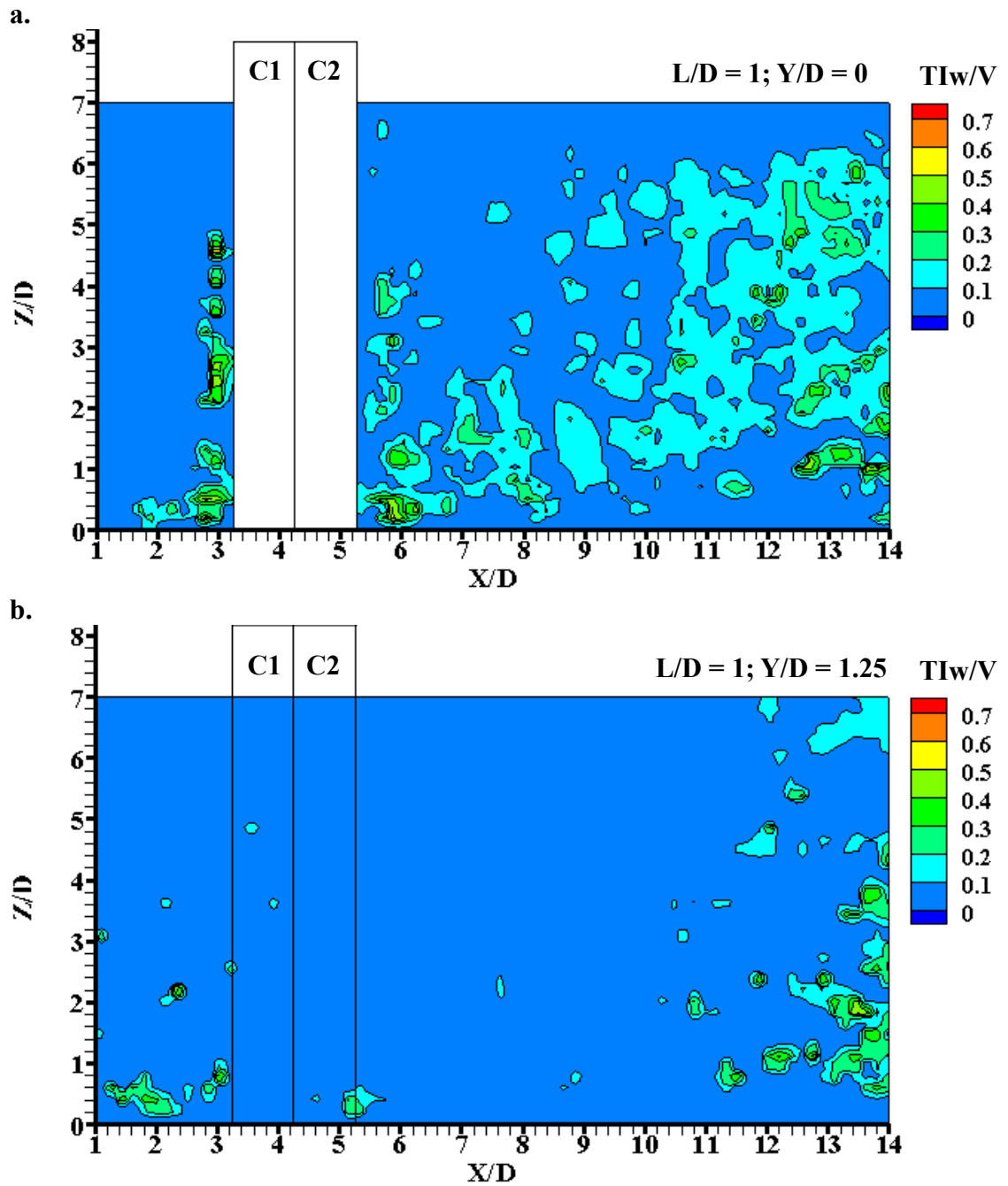


Figure B.26 Contour plots of vertical turbulence intensity component for two columns case with $L/D = 1$ in different vertical planes a) at $Y/D = 0$, and b) at $Y/D = 1.25$

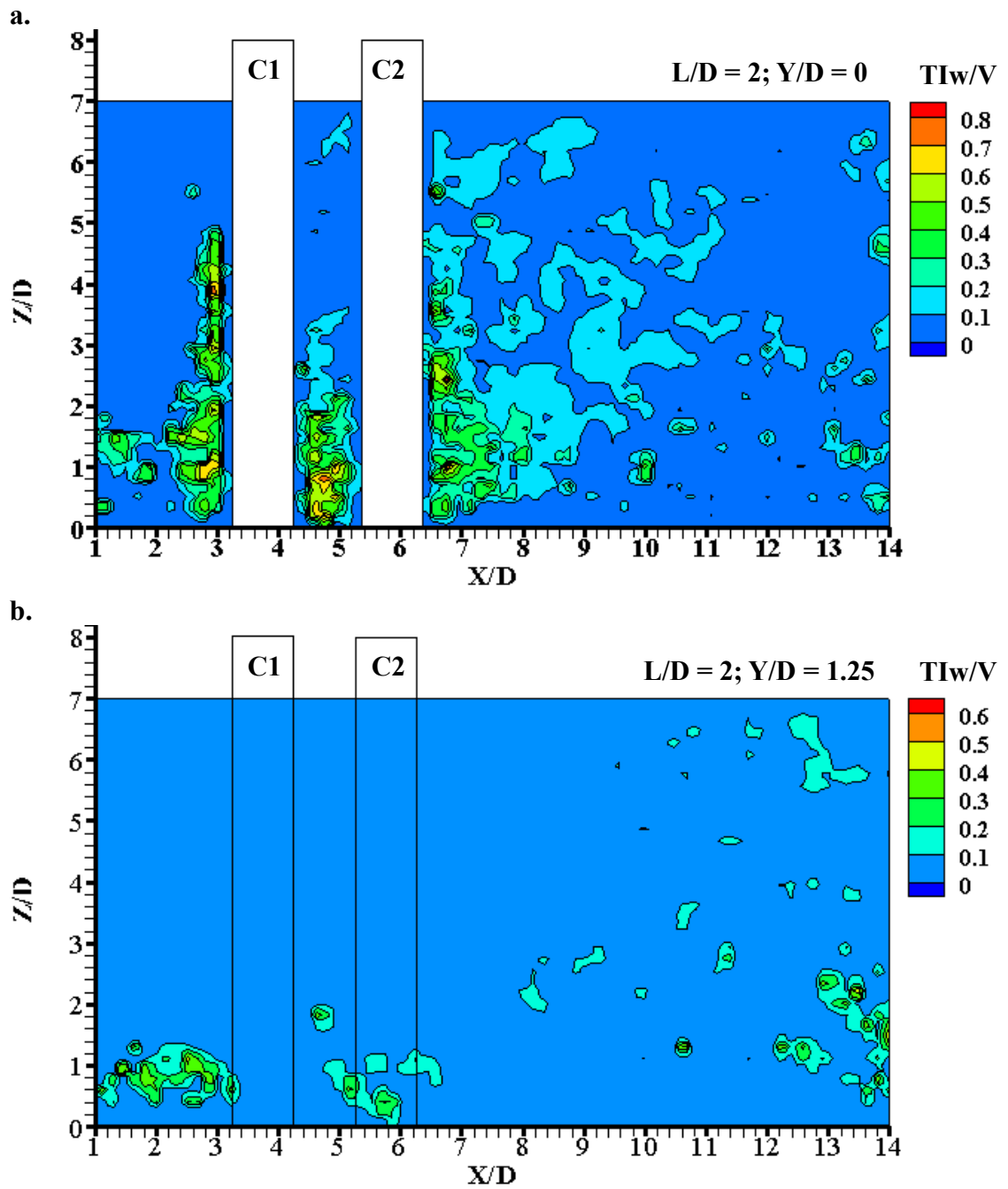


Figure B.27 Contour plots of vertical turbulence intensity component for two columns case with $L/D = 2$ in different vertical planes a) at $Y/D = 0$, and b) at $Y/D = 1.25$

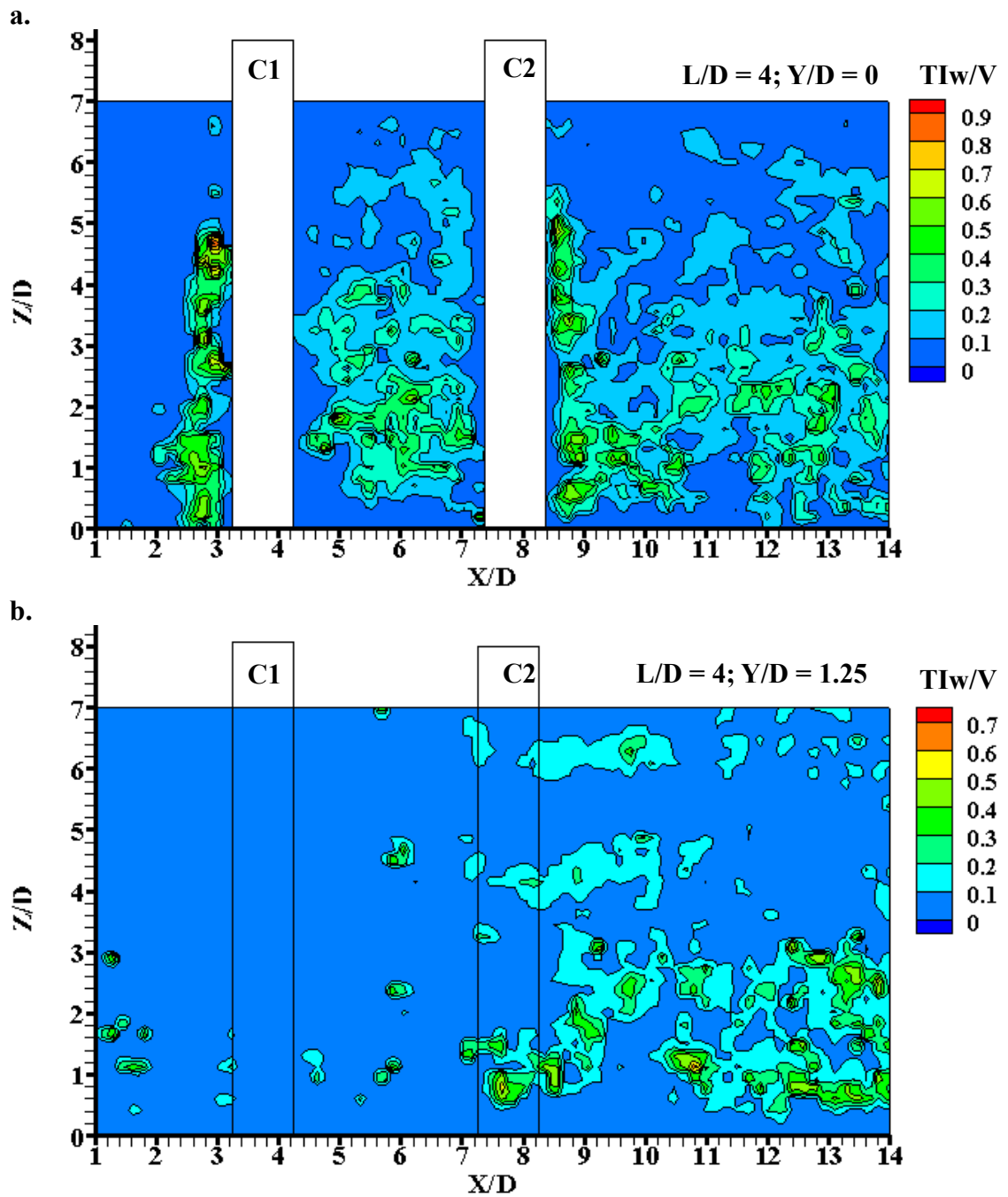


Figure B.28 Contour plots of vertical turbulence intensity component for two columns case with $L/D = 4$ in different vertical planes a) at $Y/D = 0$, and b) at $Y/D = 1.25$

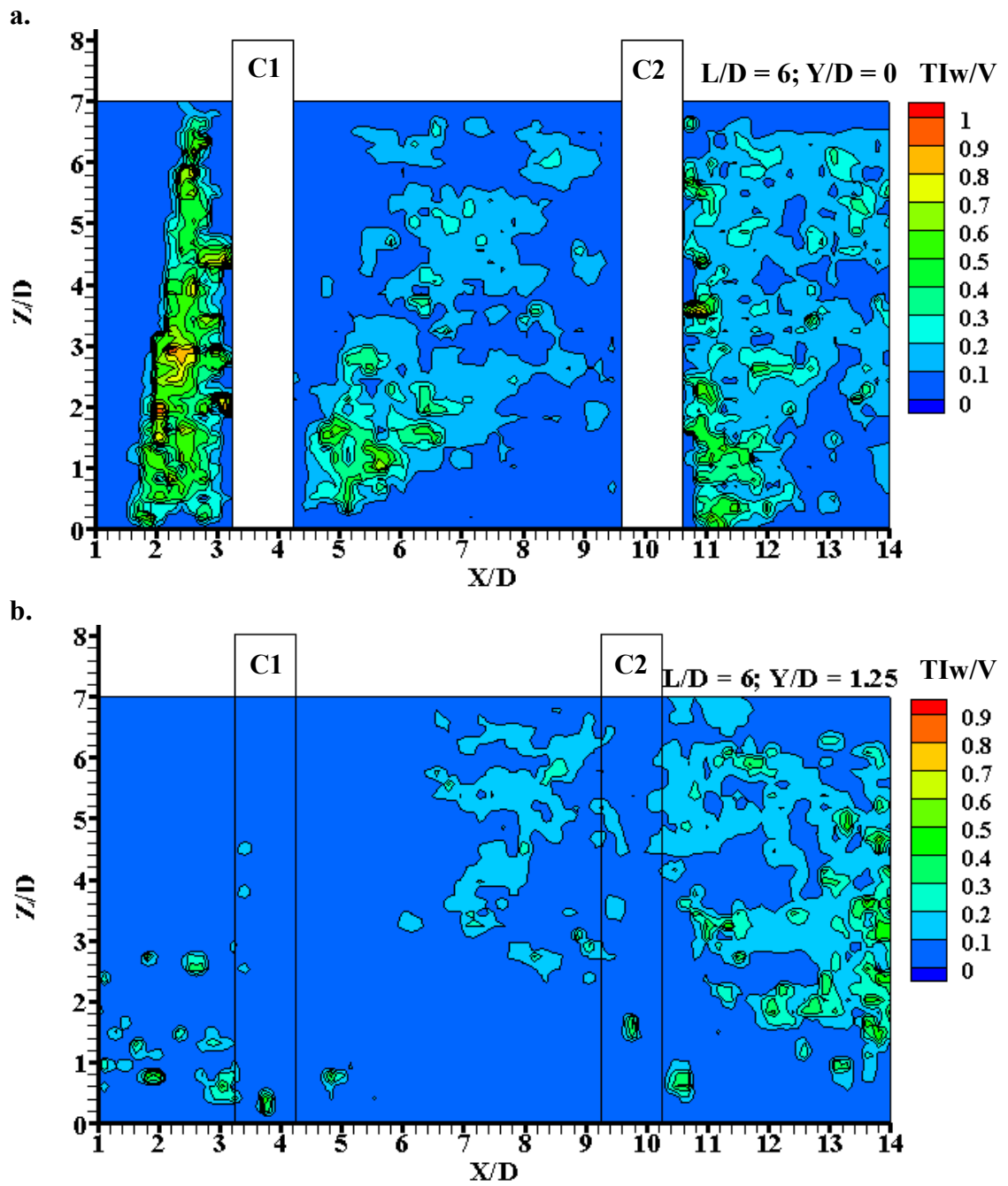


Figure B.29 Contour plots of vertical turbulence intensity component for two columns case with $L/D = 6$ in different vertical planes a) at $Y/D = 0$, and b) at $Y/D = 1.25$

B.2.3 Profile Plots of Streamwise Turbulence Intensity Component (TI_u) in Vertical Plane

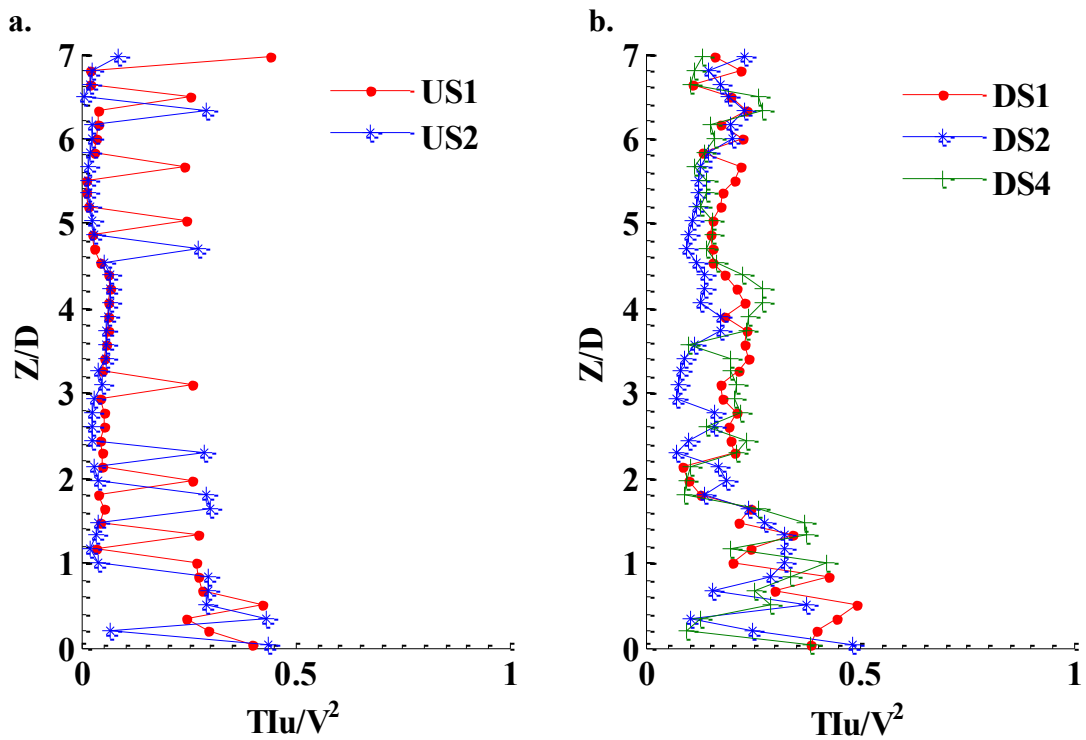


Figure B.30 Profile plots of streamwise turbulence intensity component for two columns with $L/D = 1$ in a vertical plane at axis of symmetry a) upstream side; b) downstream side

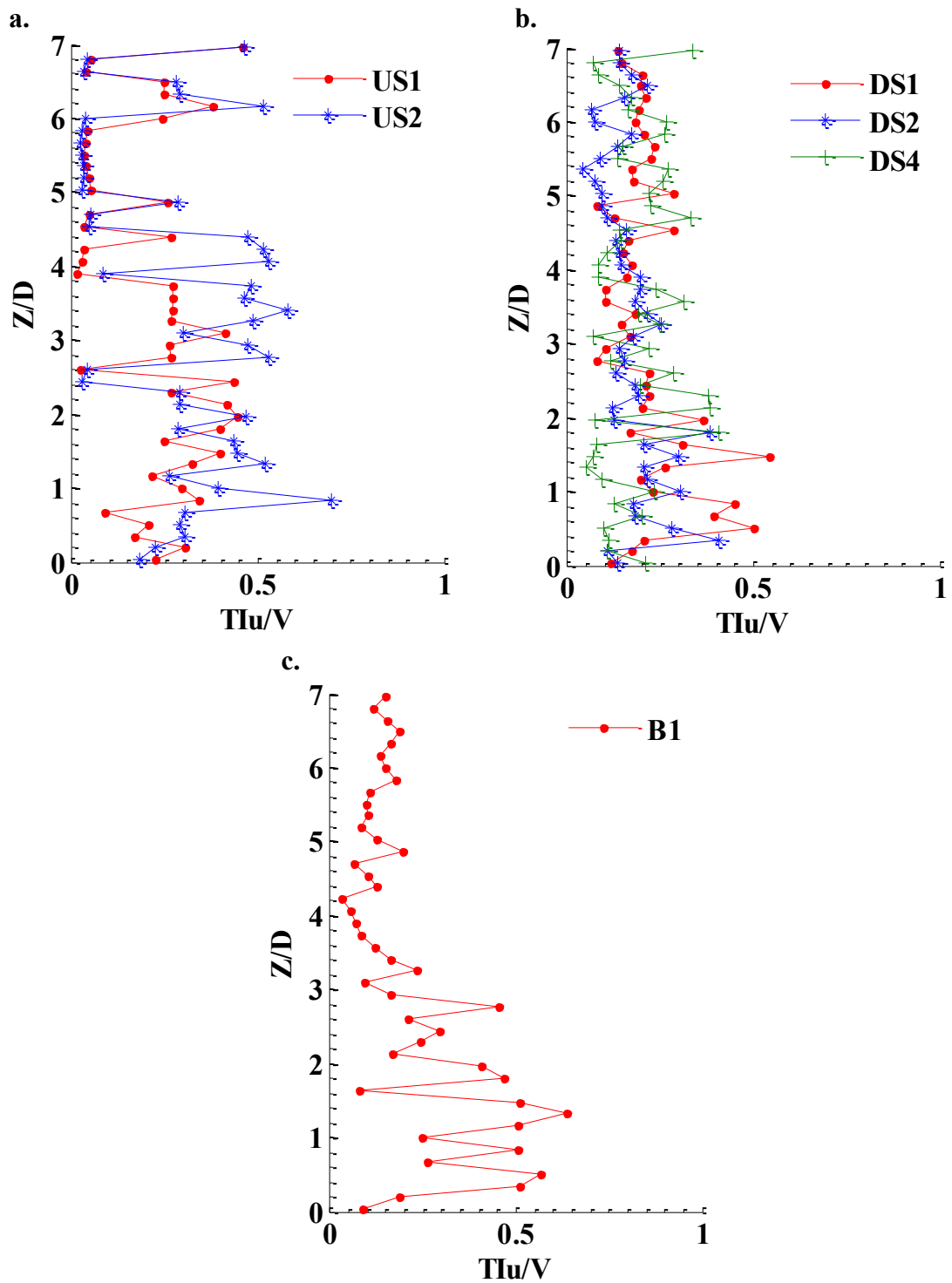


Figure B.31 Profile plots of streamwise turbulence intensity component for two columns with $L/D = 2$ in a vertical plane at axis of symmetry a) upstream side; b) downstream side; and c) between two columns

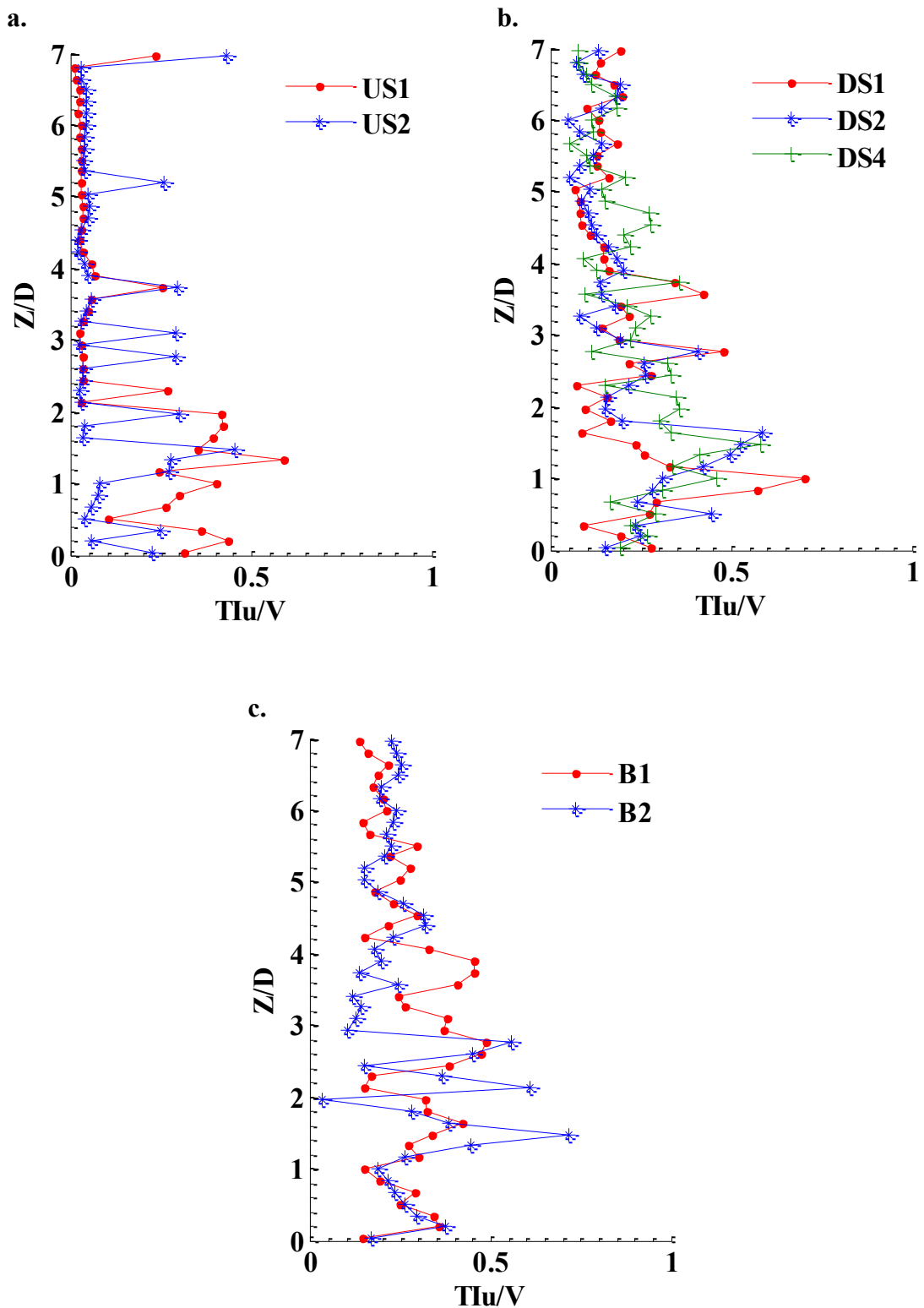


Figure B.32 Profile plots of streamwise turbulence intensity component for two columns with $L/D = 4$ in a vertical plane at axis of symmetry a) upstream side; b) downstream side; and c) between two columns

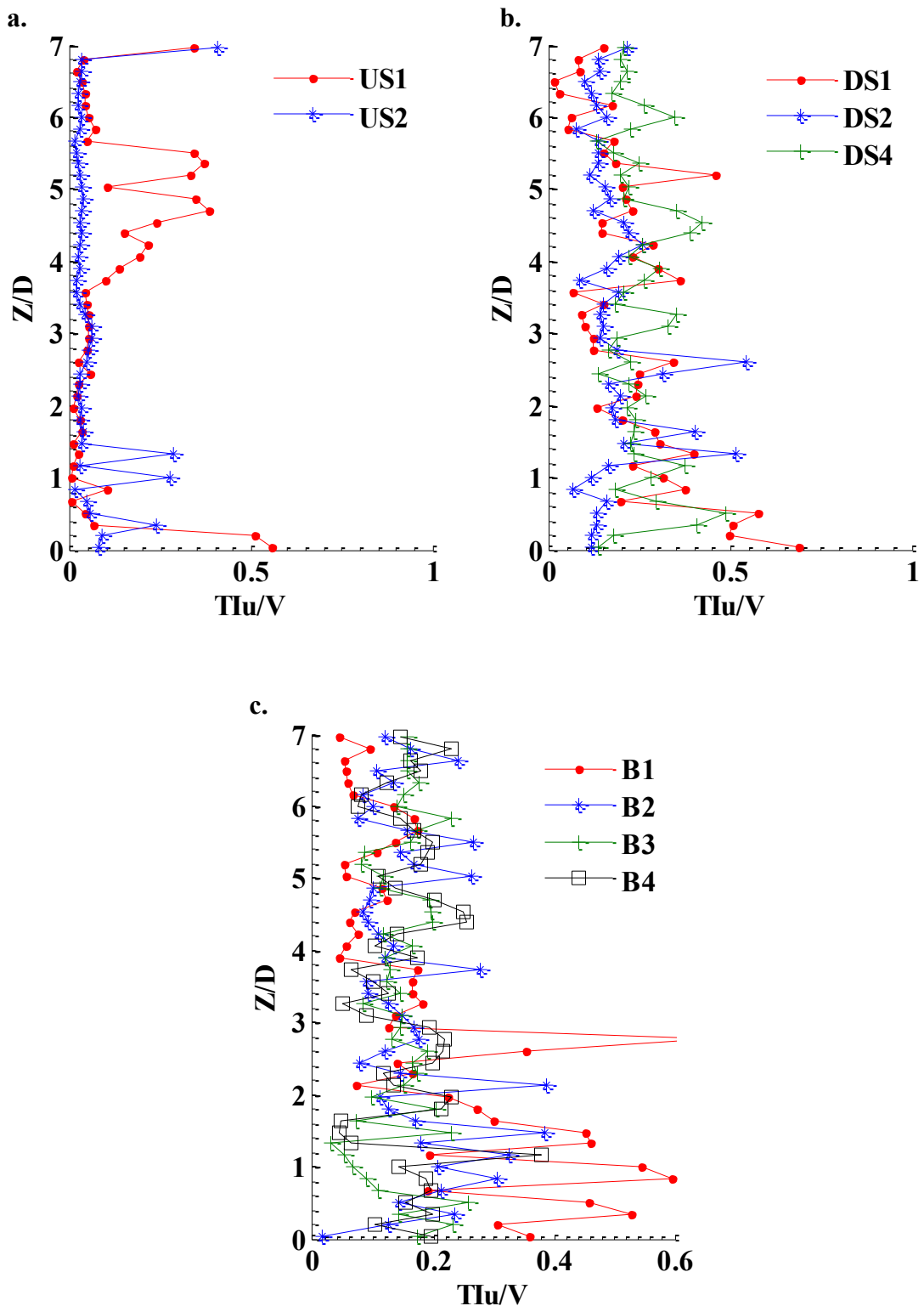


Figure B.33 Profile plots of streamwise turbulence intensity component for two columns with $L/D = 6$ in a vertical plane at axis of symmetry a) upstream side; b) downstream side; and c) between two columns

B.2.4 Distribution of Vertical Turbulence Intensity Component (TI_w) in Vertical Plane

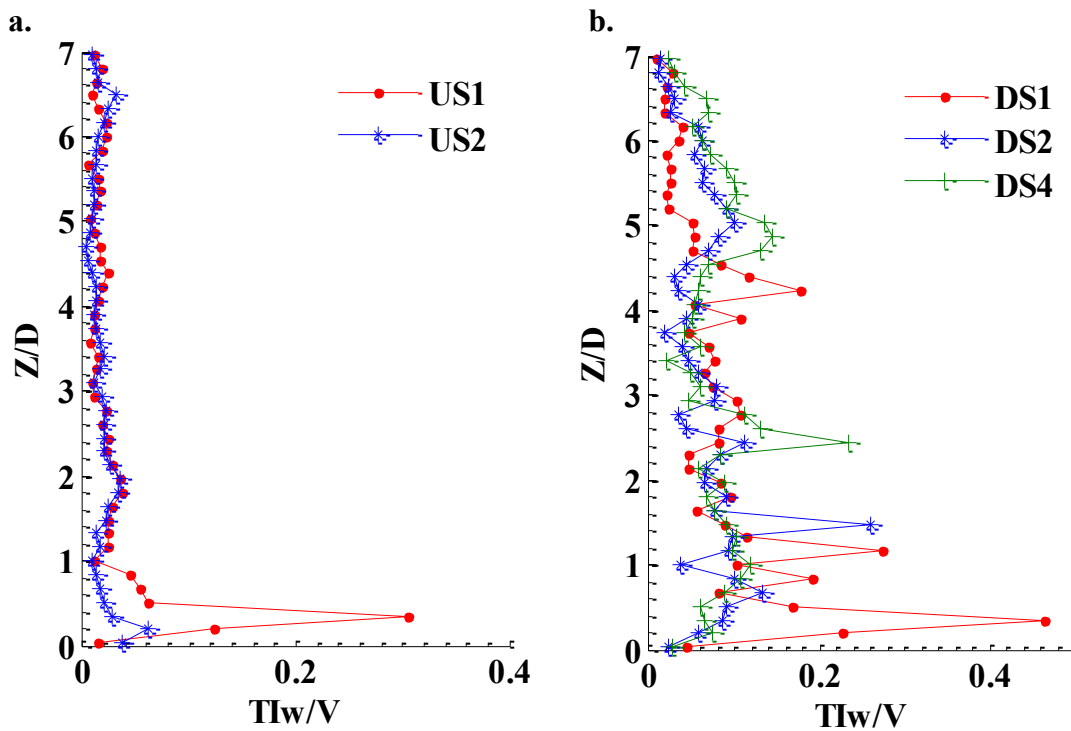


Figure B.34 Profile plots of vertical turbulence intensity component for two columns with $L/D = 1$ in a vertical plane at axis of symmetry a) upstream side; b) downstream side

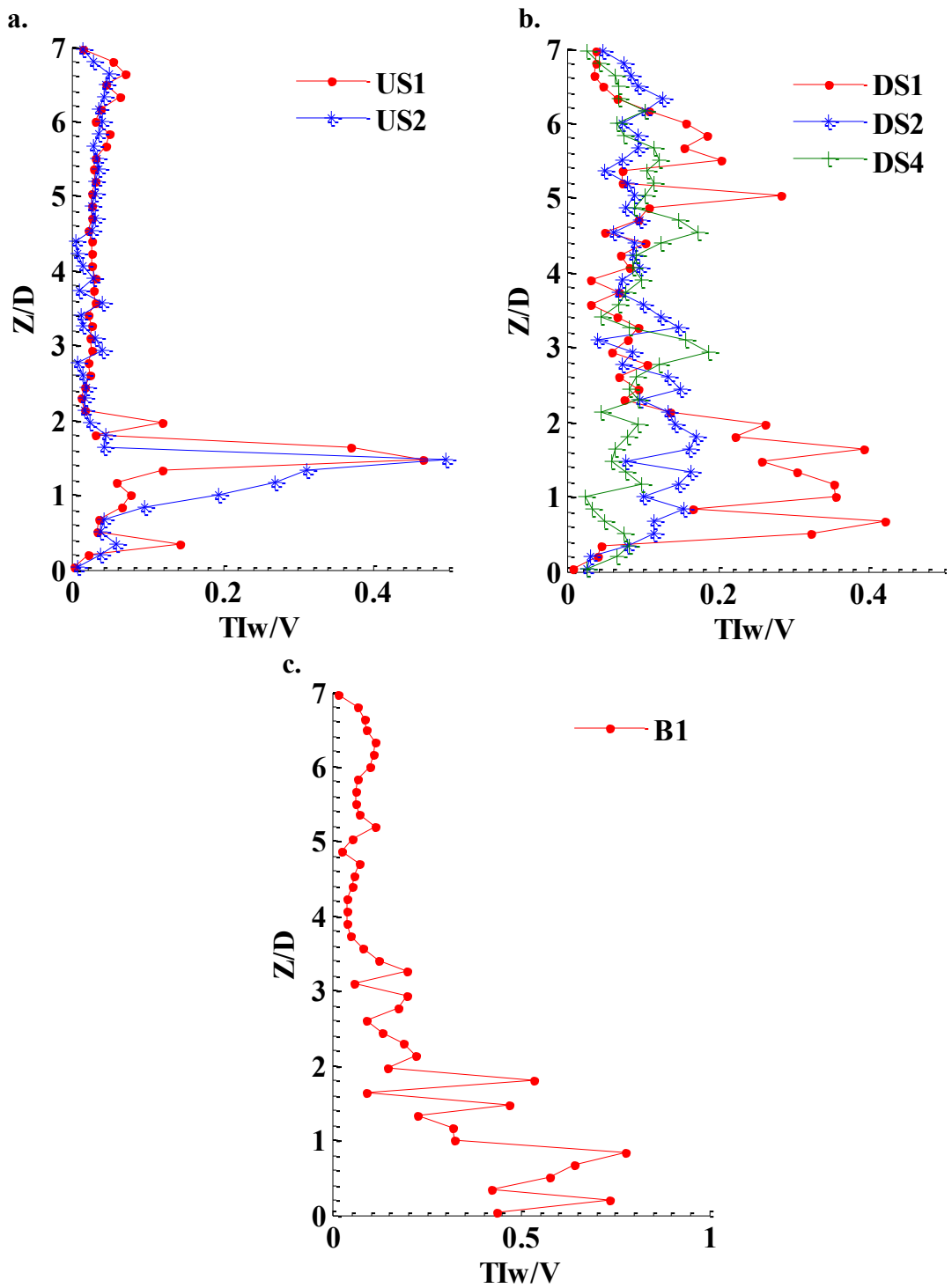


Figure B.35 Profile plots of vertical turbulence intensity component for two columns with $L/D = 2$ in a vertical plane at axis of symmetry a) upstream side; b) downstream side; and c) between two columns

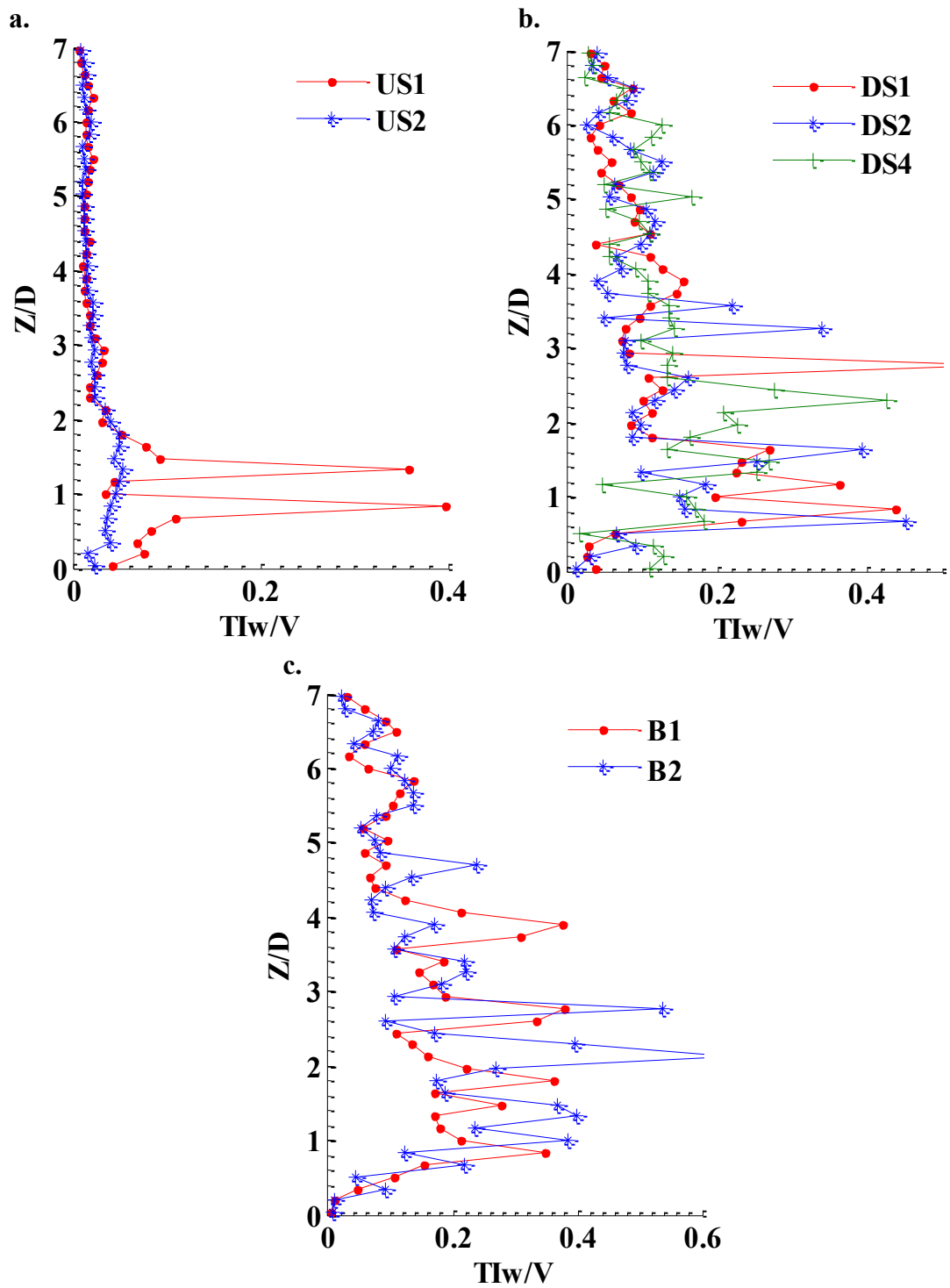


Figure B.36 Profile plots of vertical turbulence intensity component for two columns with $L/D = 4$ in a vertical plane at axis of symmetry a) upstream side; b) downstream side; and c) between two columns

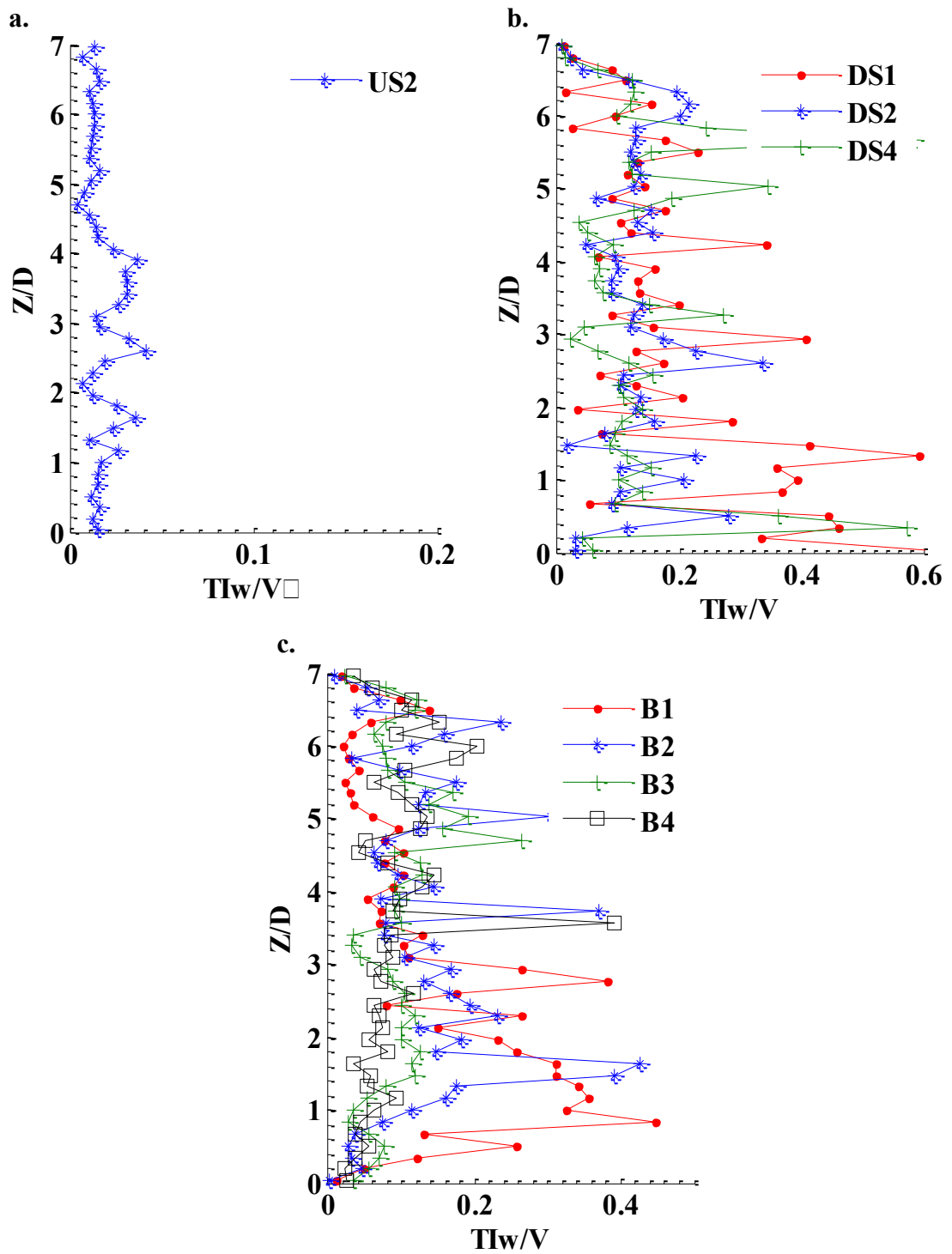


Figure B.37 Profile plots of vertical turbulence intensity component for two columns with $L/D = 6$ in a vertical plane at axis of symmetry a) upstream side; b) downstream side; and c) between two columns

B.3 Table of Results on Turbulence Intensity Components

Table B. 1 Maximum and minimum values of streamwise turbulence intensity components

Test No.	L/D	Z/h	Y/D	T <u>I</u> _{max} /V	X/D	T <u>I</u> _{min} /V	X/D
1	0	0.09	0	0.31	2	0.12	-2
			0.9	0.22	4.5	0.1	0
			1.8	0.17	4.5	0.1	1
		0.26	0	0.38	2	0.11	-4
			0.9	0.29	2.5	0.11	-1
			1.8	0.16	6.5	0.1	1
		0.54	0	0.37	2	0.11	-1
			0.9	0.32	2.5	0.11	0
			1.8	0.18	6	0.11	0
2	1.5	0.09	0	0.25	4	0.12	-2
			0.9	0.17	7	0.12	-2
			1.8	0.15	7	0.11	0
		0.26	0	0.27	4	0.15	-2
			0.9	0.19	6.5	0.13	-1
			1.8	0.15		0.15	
		0.54	0	0.27	3.5	0.15	-4
			0.9	0.2	6.5	0.1	-2
			1.8	0.14	3.5	0.1	0
3	2	0.09	0	0.28	1	0.13	-3
			0.9	0.22	4	0.13	-4
			1.8	0.15	-1.5	0.13	-4
		0.26	0	0.28	4.5	0.1	-4
			0.9	0.16	7	0.12	-3
			1.8	0.14	6.5	0.08	2
		0.54	0	0.26	4.5	0.1	-3
			0.9	0.22	5.5	0.1	-1
			1.8	0.12	8	0.08	-2
4	3	0.09	0	0.32	4	0.13	-1
			0.9	0.24	5	0.12	2
			1.8	0.18	11	0.12	2.5
		0.26	0	0.33	2.5	0.12	-2
			0.9	0.22	7	0.11	-1
			1.8	0.16	6	0.11	0
		0.54	0	0.29	4	0.12	-1
			0.9	0.25	4	0.12	-1
			1.8	0.17	9	0.11	0
5	4	0.09	0	0.33	2	0.1	-3
			0.9	0.23	6	0.12	-1
			1.8	0.16	8	0.1	4

		0.26	0	0.37	6	0.15	-2	
			0.9	0.23	6	0.11	3	
			1.8	0.16	10	0.11	3	
		0.54	0	0.33	2	0.12	-3	
			0.9	0.29	7	0.12	1	
			1.8	0.2	7.5	0.12	2	
	6	6	0.09	0	0.3	8	0.12	-1
				0.9	0.26	9	0.12	-1
				1.8	0.16	9	0.1	0
0.26			0	0.34	2	0.12	-1	
			0.9	0.32	8	0.12	-2	
			1.8	0.17	9	0.11	-3	
0.54			0	0.32	2	0.1	-1	
			0.9	0.38	2.5	0.1	-1	
			1.8	0.18	8	0.1	2	

Table B. 2 Maximum and minimum values of transverse turbulence intensity components

Test No.	L/D	Z/h	Y/D	TIV _{max} /V	X/D	TIV _{min} /V	X/D
1	0	0.09	0	0.27	2	0.1	-2
			0.9	0.2	2	0.09	-1
			1.8	0.16	2	0.09	1
		0.26	0	0.58	2	0.08	-2
			0.9	0.33	3.5	0.08	-1
			1.8	0.14	6.5	0.08	0
		0.54	0	0.64	3	0.08	-1
			0.9	0.37	3.5	0.08	0
			1.8	0.2	6.5	0.08	0
2	1.5	0.09	0	0.29	3.5	0.1	-1
			0.9	0.16	7	0.1	-1
			1.8	0.13	12	0.1	6.5
		0.26	0	0.32	3.5	0.1	-3
			0.9	0.19	7	0.1	-2
			1.8	0.14	9	0.1	5.5
		0.54	0	0.33	3.5	0.16	-1
			0.9	0.2	8	0.1	-1
			1.8	0.12	2	0.1	0
3	2	0.09	0	0.28	1	0.1	-3
			0.9	0.2	1.5	0.1	-2
			1.8	0.12	8	0.1	5.5
		0.26	0	0.34	4.5	0.1	-1
			0.9	0.16	7	0.1	-1
			1.8	0.12	4.5	0.08	3
		0.54	0	0.33	4.5	0.07	-1
			0.9	0.18	7	0.07	0
			1.8	0.11	11	0.07	0
4	3	0.09	0	0.33	5	0.1	-2
			0.9	0.16	7	0.1	3.5
			1.8	0.15	11	0.1	3.5
		0.26	0	0.38	5.5	0.1	-1.5
			0.9	0.23	6.9	0.1	-1.5
			1.8	0.13	12	0.1	2
		0.54	0	0.42	5	0.1	-1
			0.9	0.24	6.5	0.1	-1
			1.8	0.16	9	0.1	-1
5	4	0.09	0	0.35	6	0.1	-1
			0.9	0.21	9	0.1	0
			1.8	0.12	11	0.1	3
		0.26	0	0.45	6	0.11	-2
			0.9	0.25	8	0.1	0

			1.8	0.15	12	0.1	3
		0.54	0	0.52	3	0.11	-1
			0.9	0.3	3.5	0.12	1.5
			1.8	0.2	5.5	0.12	1.5
6	6	0.09	0	0.46	3	0.1	-1
			0.9	0.28	4.5	0.1	-1
			1.8	0.15	10	0.1	-1
		0.26	0	0.64	2	0.1	-1
			0.9	0.32	4.5	0.1	-2
			1.8	0.16	7.5	0.1	-2
		0.54	0	0.48	2	0.1	-1
			0.9	0.36	3	0.1	-1
			1.8	0.22	6.5	0.1	-1

Table B. 3 Maximum and minimum values of vertical turbulence intensity components

Test No.	L/D	Z/h	Y/D	TI _{wmax} /V	X/D	TI _{wmin} /V	X/D
1	0	0.09	0	0.18	2	0.05	-1
			0.9	0.07	3.5	0.05	-1
			1.8	0.06	2	0.05	-1
		0.26	0	0.3	2	0.05	-1
			0.9	0.2	3.5	0.05	-1
			1.8	0.12	6.5	0.05	0
		0.54	0	0.3	2	0.05	-1
			0.9	0.2	3.5	0.05	0
			1.8	0.15	8	0.05	0
2	1.5	0.09	0	0.17	3.5	0.05	-1
			0.9	0.08	7	0.05	-1
			1.8	0.07	12	0.05	5.5
		0.26	0	0.32	4	0.1	-2
			0.9	0.2	5.5	0.1	-2
			1.8	0.14	9	0.1	-2
		0.54	0	0.32	4	0.16	-1
			0.9	0.2	5.5	0.1	-1
			1.8	0.12	2	0.1	-1
3	2	0.09	0	0.28	1	0.1	-2
			0.9	0.2	1.5	0.1	-2
			1.8	0.12	8	0.1	-2
		0.26	0	0.34	4	0.08	-1
			0.9	0.16	7	0.08	-1
			1.8	0.12	5	0.07	3
		0.54	0	0.33	5	0.07	-1
			0.9	0.18	7	0.07	0
			1.8	0.11	11	0.07	0
4	3	0.09	0	0.2	5	0.05	-2
			0.9	0.1	7	0.05	-2
			1.8	0.08	11	0.05	-2
		0.26	0	0.22	5.5	0.05	-1
			0.9	0.13	8	0.05	-1
			1.8	0.09	11	0.05	0
		0.54	0	0.22	4.5	0.05	-1
			0.9	0.16	6.5	0.05	0
			1.8	0.11	12	0.05	0
5	4	0.09	0	0.35	2	0.1	-1
			0.9	0.2	9	0.1	0
			1.8	0.15	11	0.1	3
		0.26	0	0.45	6	0.11	-1
			0.9	0.25	8	0.1	3

			1.8	0.15	12	0.1	3
		0.54	0	0.52	3	0.1	-1
			0.9	0.3	4	0.1	0
			1.8	0.2	10	0.1	0
6	6	0.09	0	0.45	3	0.1	-1
			0.9	0.24	5	0.1	-1
			1.8	0.16	10	0.1	0
		0.26	0	0.64	2	0.1	-1
			0.9	0.32	4.5	0.1	-2
			1.8	0.16	7	0.1	-1
		0.54	0	0.44	4	0.1	-1
			0.9	0.36	3	0.1	-1
			1.8	0.22	6.5	0.1	-1

APPENDIX-C: PLOTS FOR TURBULENT KINETIC ENERGY

C.1 Plots of Turbulent Kinetic Energy in Horizontal Plane

C.1.1 Contour Plots of Turbulent Kinetic Energy in Horizontal Plane

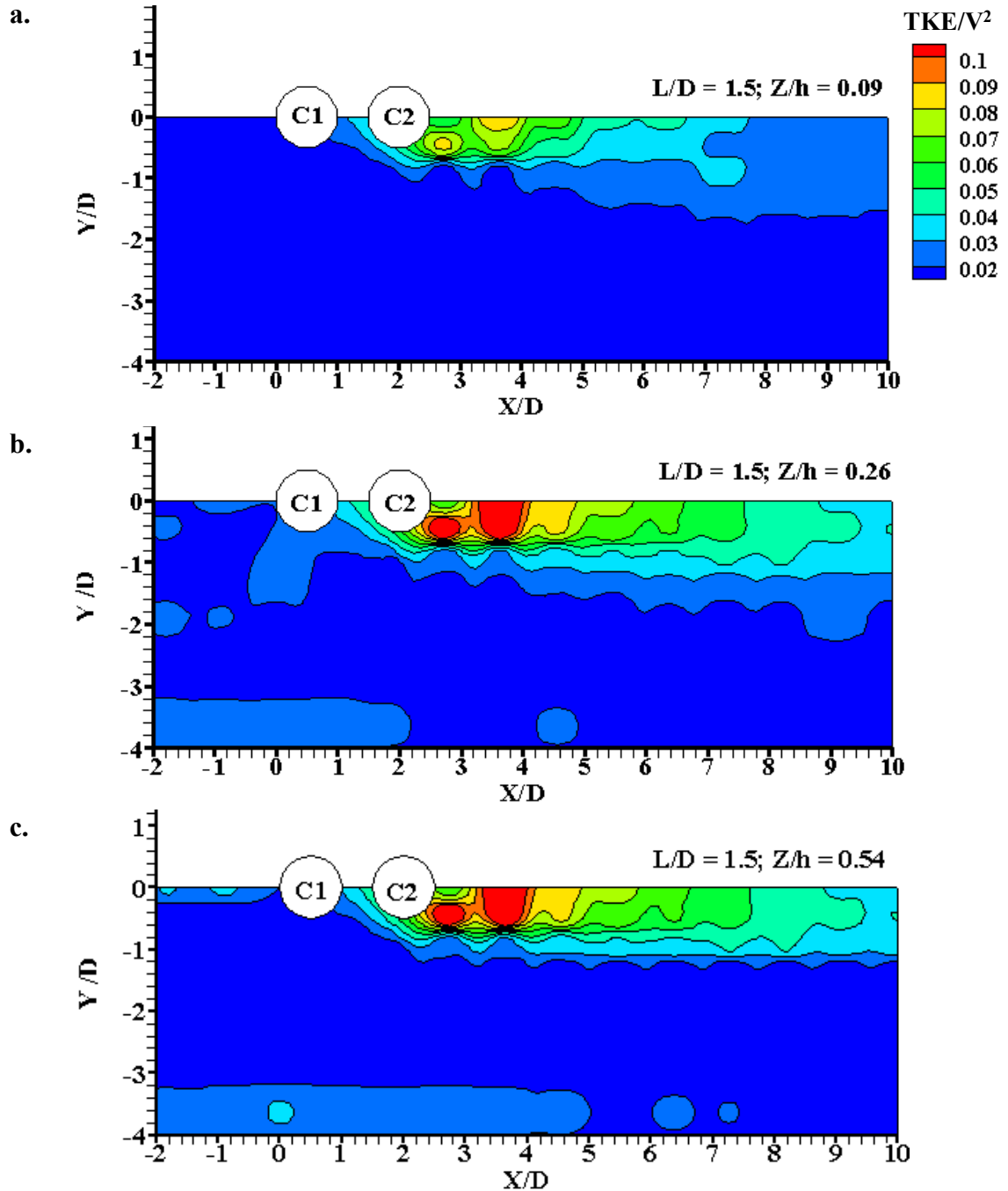


Figure C.1 Contour plots of turbulent kinetic energy for two columns case with $L/D = 1.5$ in different horizontal planes a) at $Z/h = 0.09$, b) at $Z/h = 0.26$ and c). at $Z/h = 0.54$

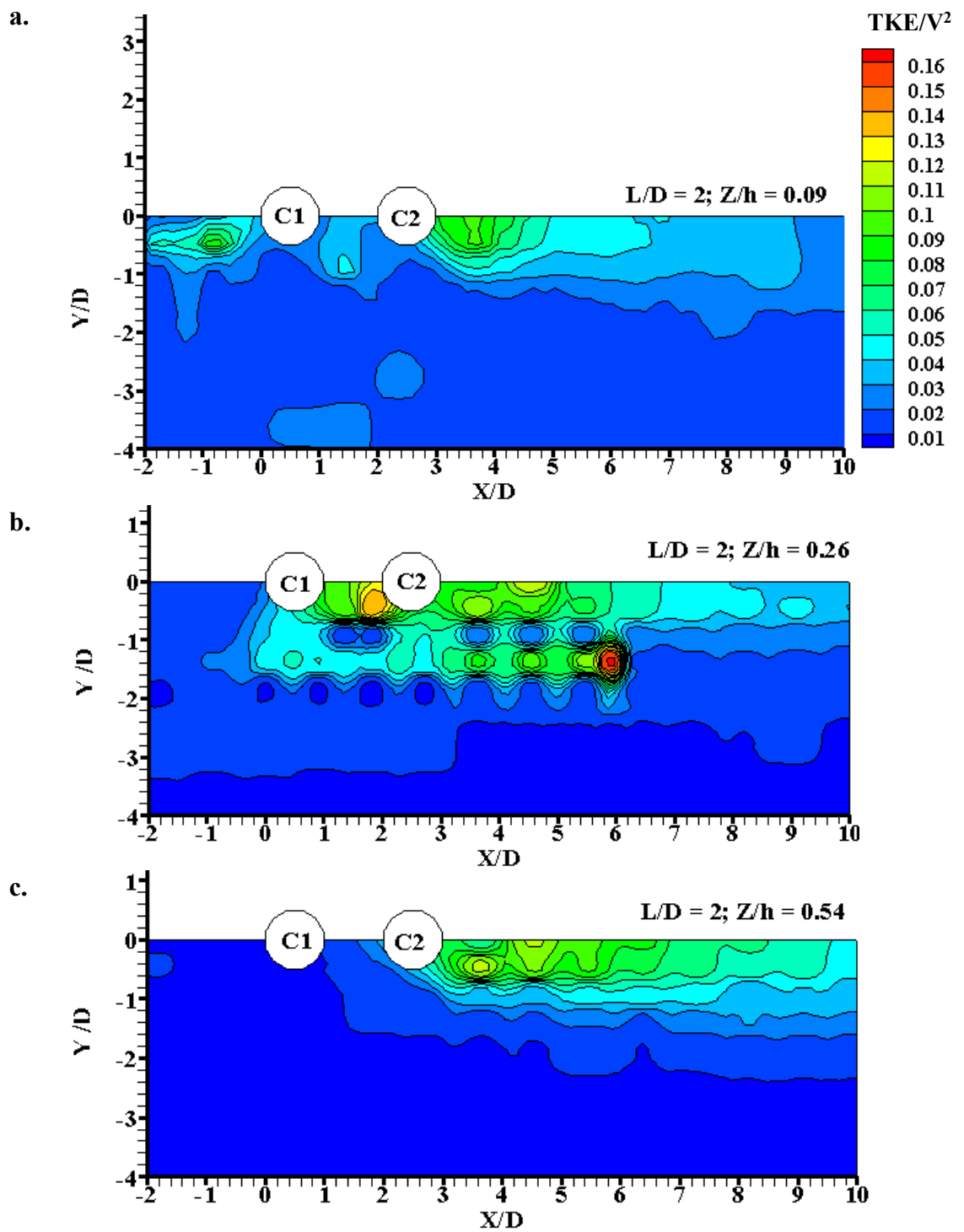


Figure C.2 Contour plots of turbulent kinetic energy for two columns case with $L/D = 2$ in different horizontal planes a) at $Z/h = 0.09$, b) at $Z/h = 0.26$ and c). at $Z/h = 0.54$

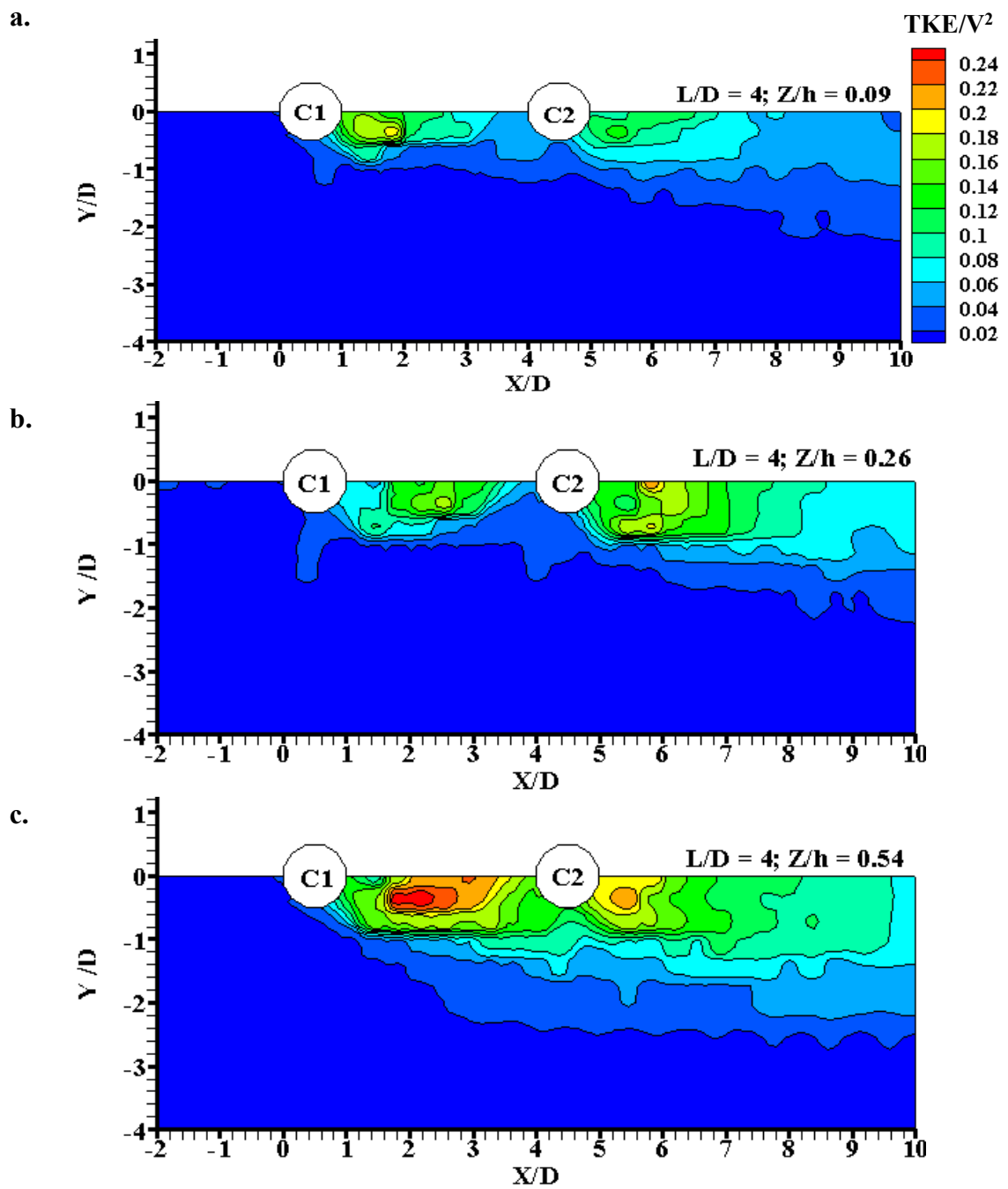


Figure C.3 Contour plots of turbulent kinetic energy for two columns case with $L/D = 4$ in different horizontal planes a) at $Z/h = 0.09$, b) at $Z/h = 0.26$ and c). at $Z/h = 0.54$

C.1.2 Profile Plots of Turbulence Kinetic Energy in Horizontal Plane

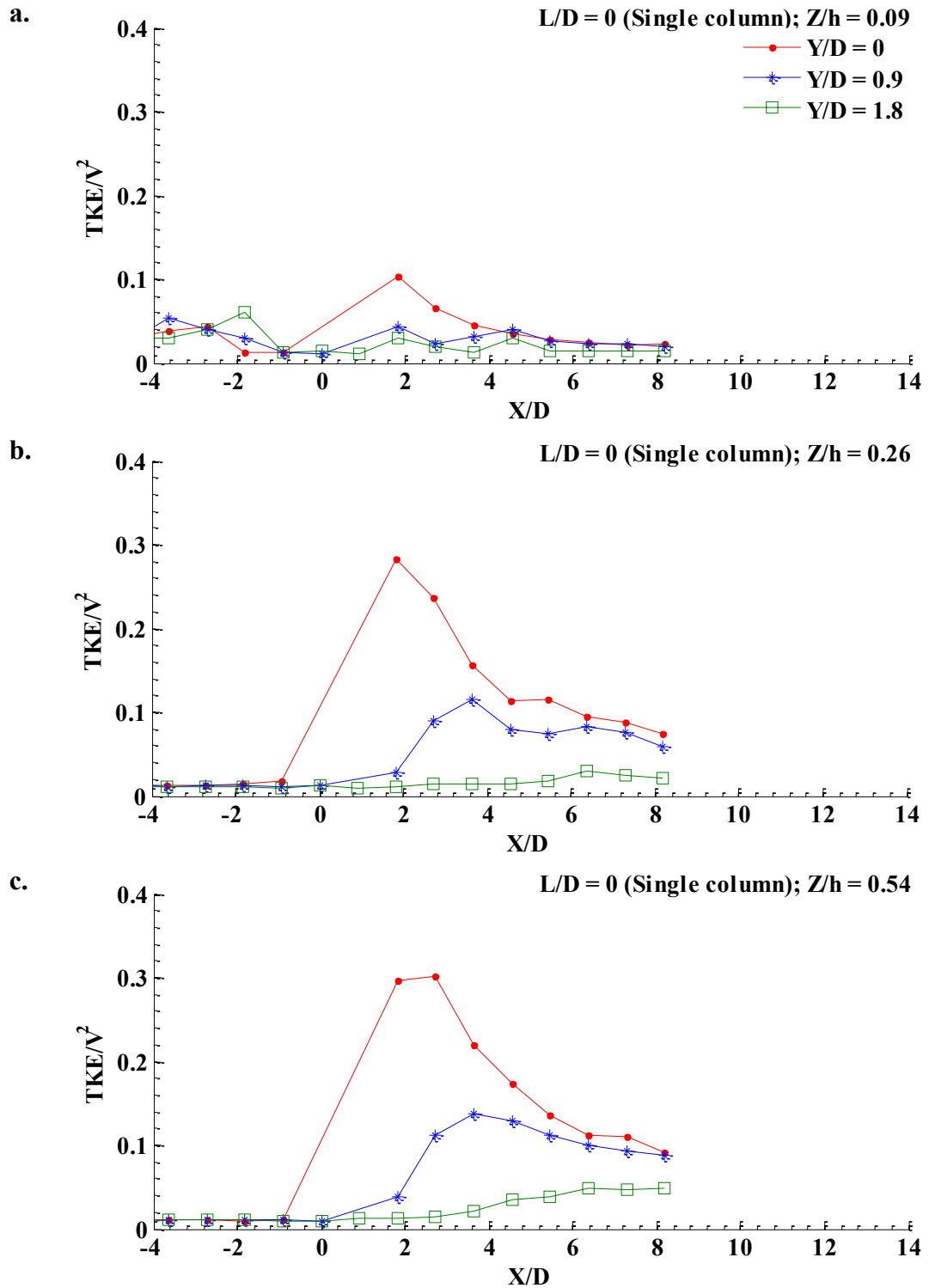


Figure C.4 Profile plots of turbulent kinetic energy for single column case along three different longitudinal axes in different horizontal planes a) at $Z/h = 0.09$, b) at $Z/h = 0.26$ and c). at $Z/h = 0.54$

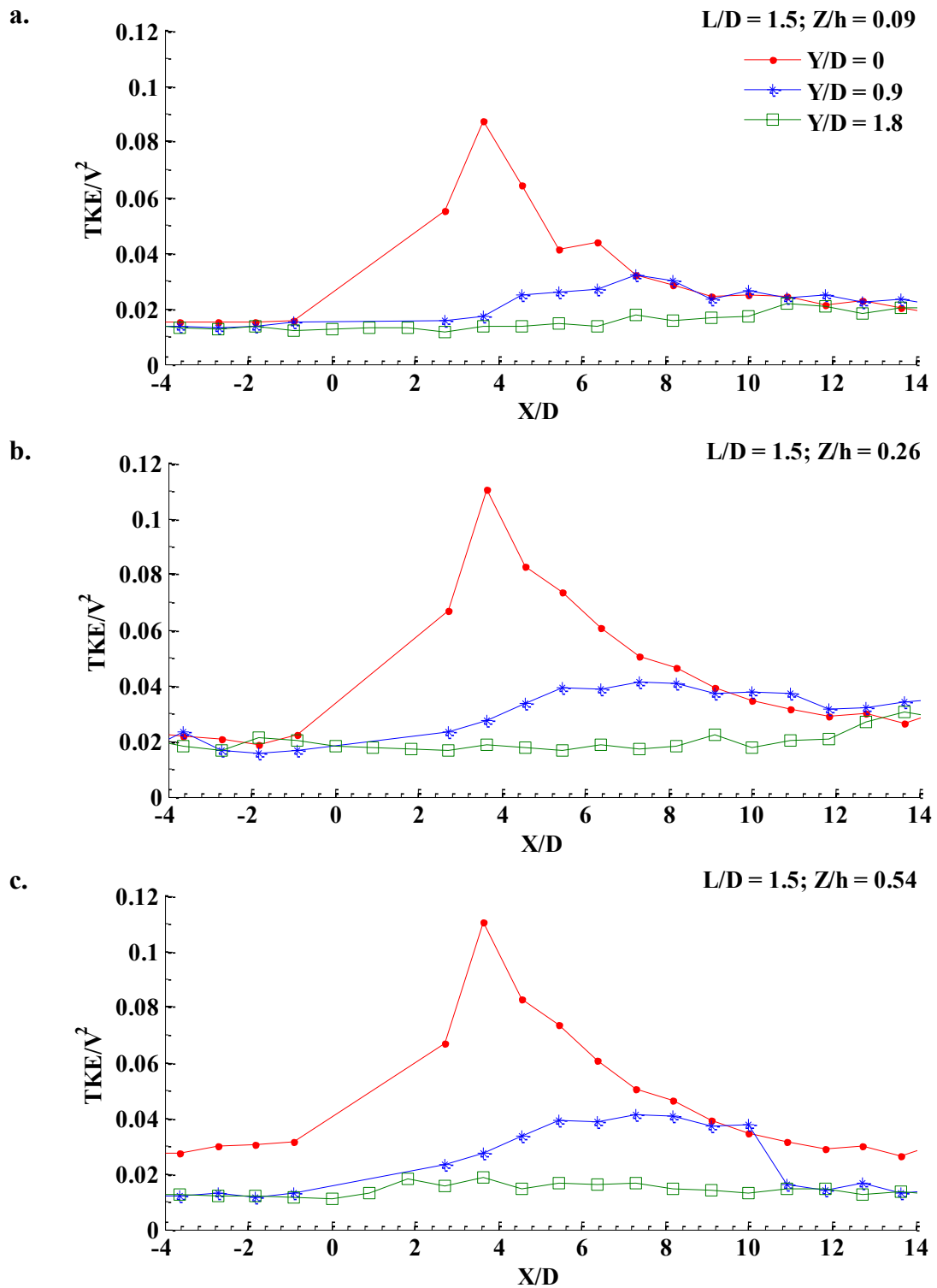


Figure C.5 Profile plots of turbulent kinetic energy for two columns case with $L/D = 1.5$ along three different longitudinal axes in different horizontal planes a) at $Z/h = 0.09$, b) at $Z/h = 0.26$ and c). at $Z/h = 0.54$

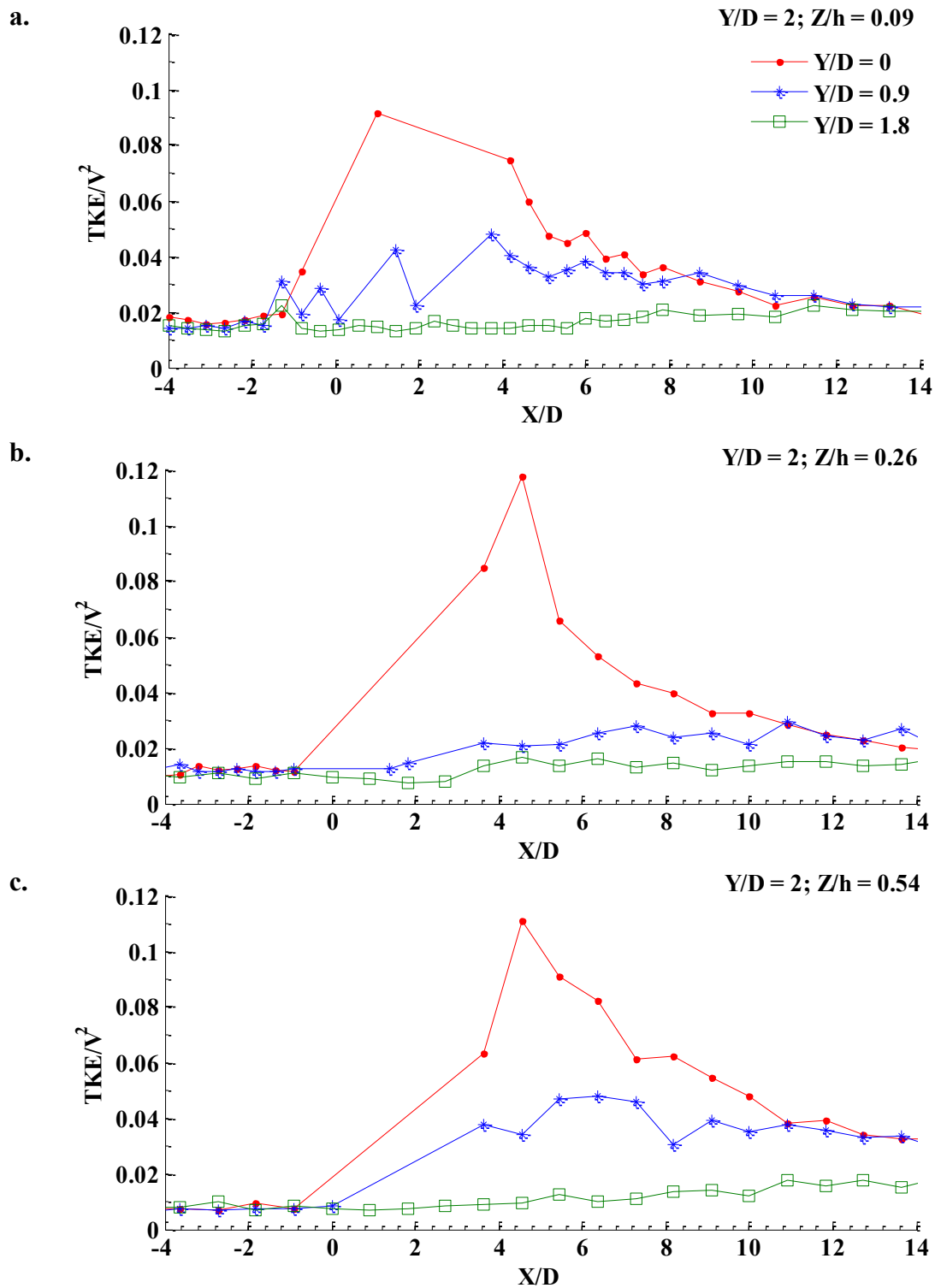


Figure C.6 Profile plots of turbulent kinetic energy for two columns case with $L/D = 2$ along three different longitudinal axes in different horizontal planes a) at $Z/h = 0.09$, b) at $Z/h = 0.26$ and c). at $Z/h = 0.54$

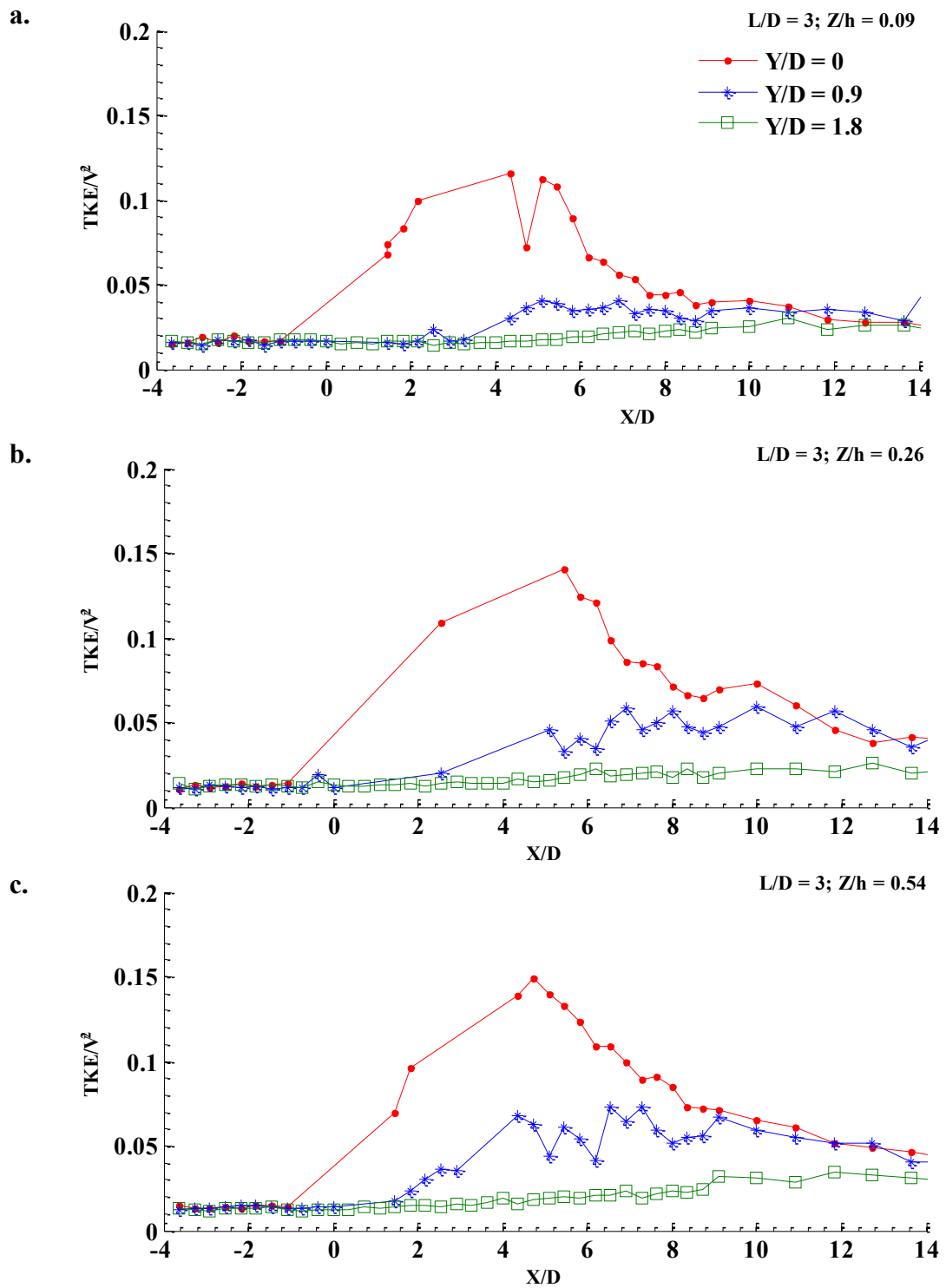


Figure C.7 Profile plots of turbulent kinetic energy for two columns case with $L/D = 3$ along three different longitudinal axes in different horizontal planes a) at $Z/h = 0.09$, b) at $Z/h = 0.26$ and c). at $Z/h = 0.54$

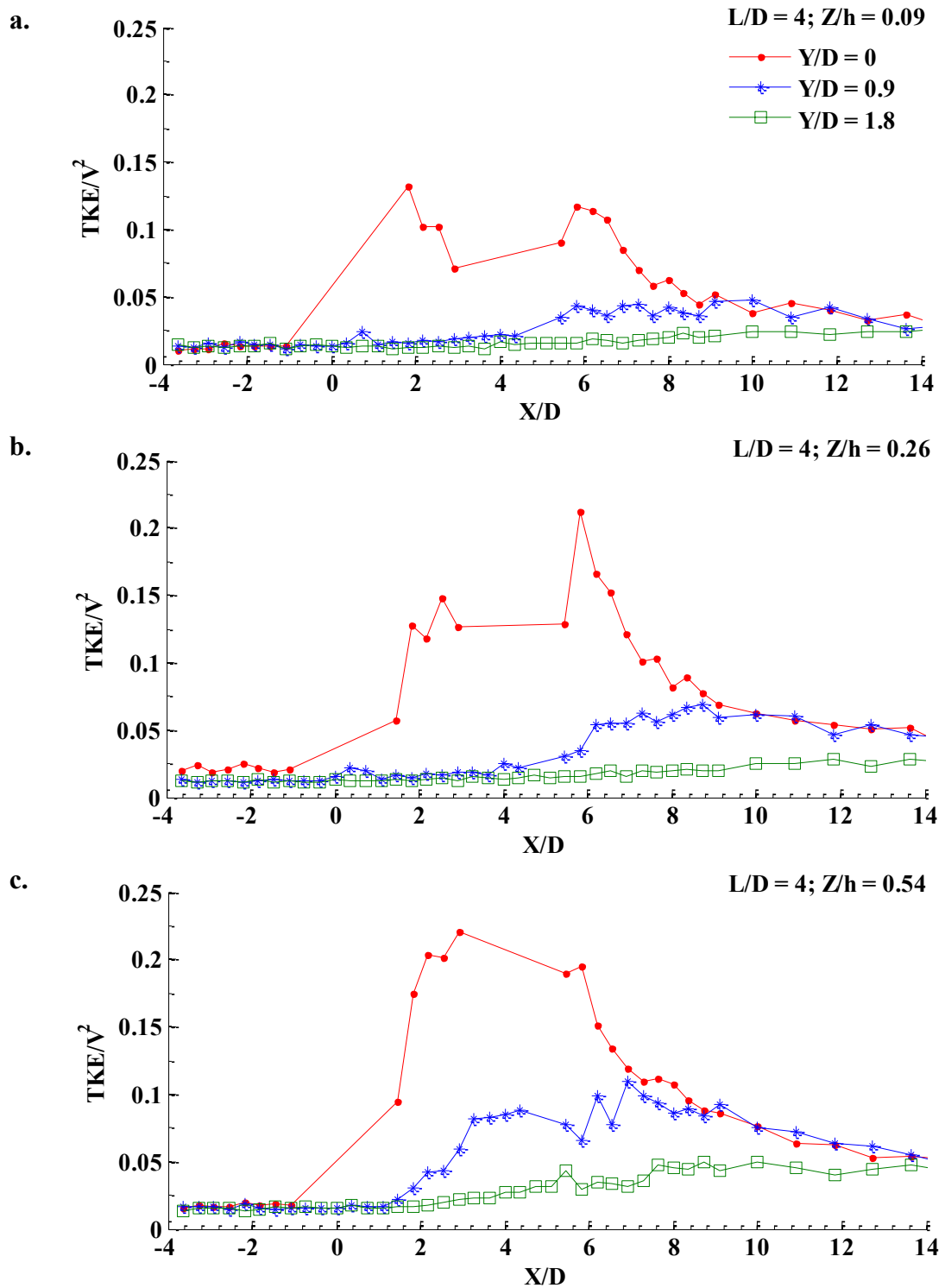


Figure C.8 Profile plots of turbulent kinetic energy for two columns case with $L/D = 4$ along three different longitudinal axes in different horizontal planes a) at $Z/h = 0.09$, b) at $Z/h = 0.26$ and c) at $Z/h = 0.54$

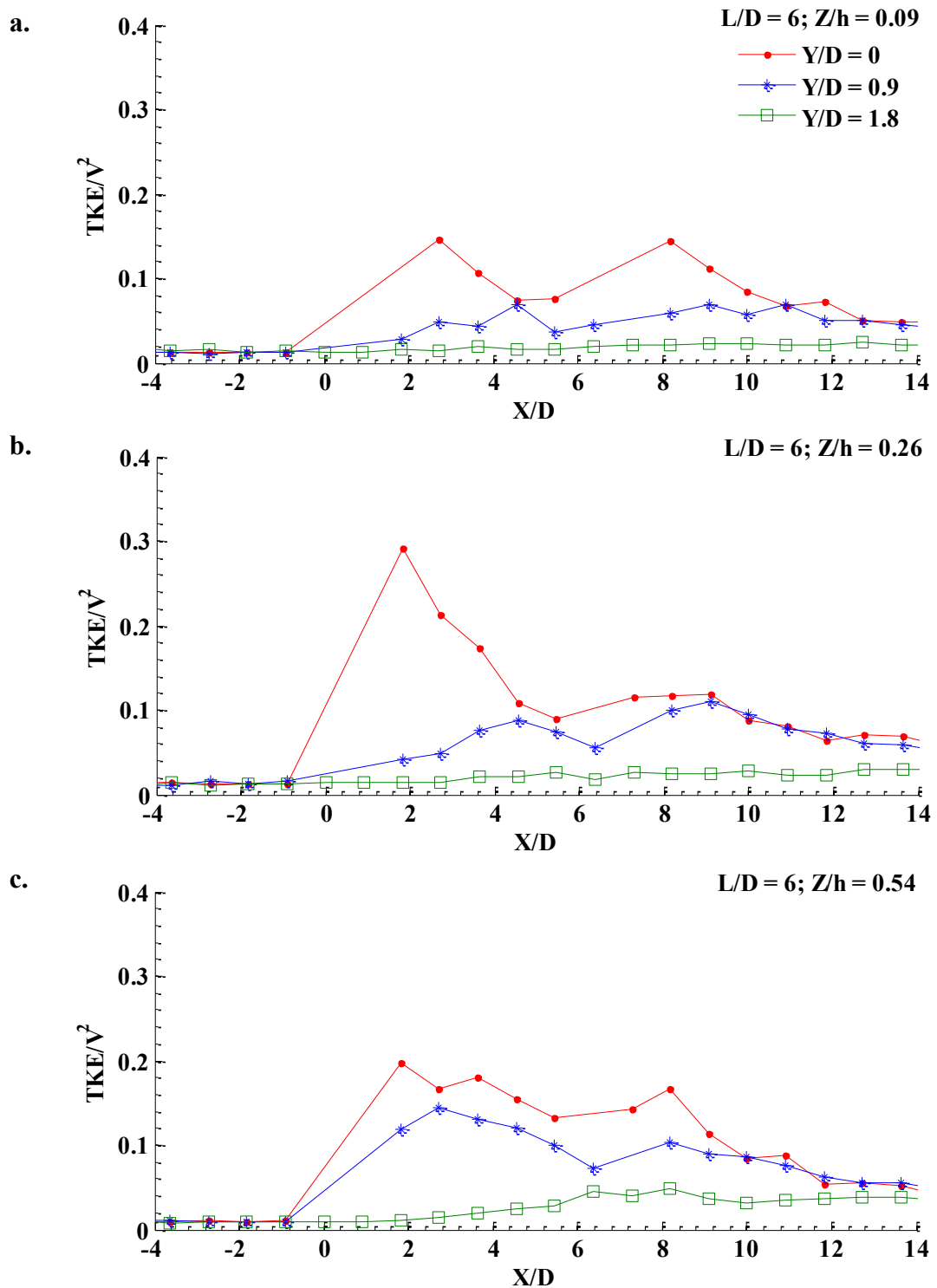


Figure C.9 Profile plots of turbulent kinetic energy for two columns case with $L/D = 6$ along three different longitudinal axes in different horizontal planes a) at $Z/h = 0.09$, b) at $Z/h = 0.26$ and c). at $Z/h = 0.54$

C.2 Plots of Turbulent Kinetic Energy in Vertical Plane

C.2.1 Contour Plots of Turbulent Kinetic Energy in Vertical Plane

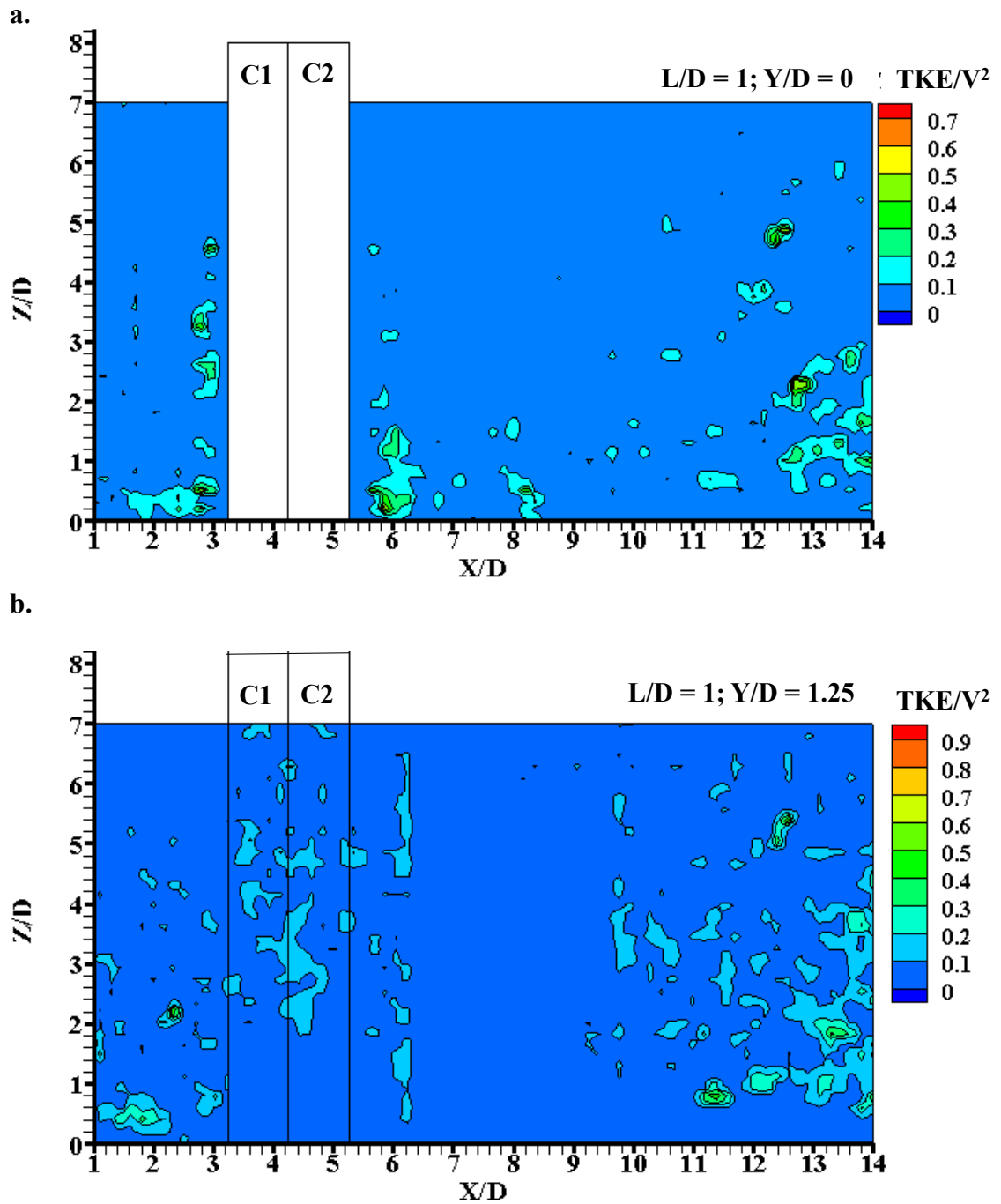


Figure C.10 Contour plots of turbulent kinetic energy for two columns case with $L/D = 1$ in different vertical planes a) at $Y/D = 0$, and b) at $Y/D = 1.25$

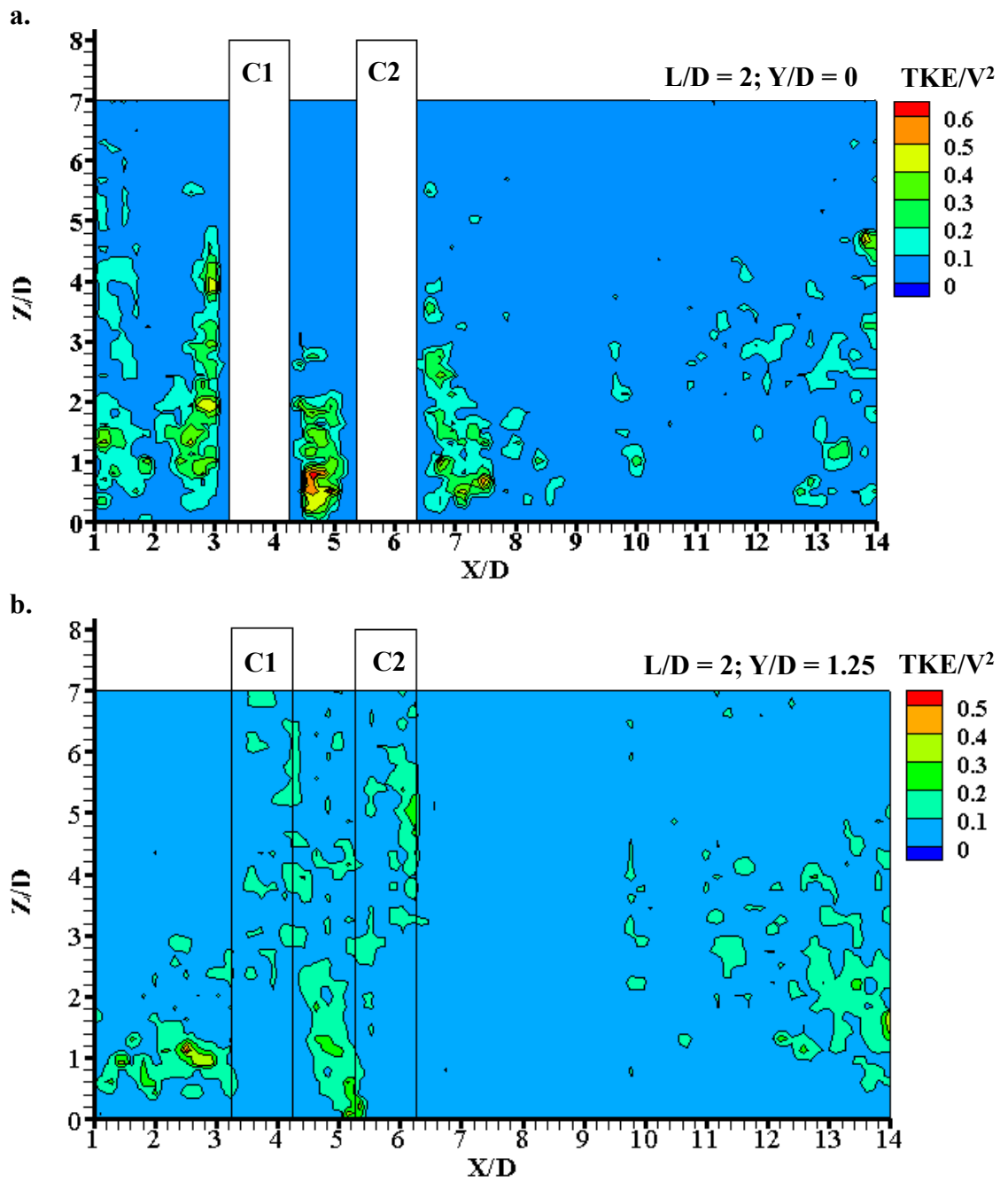


Figure C.11 Contour plots of turbulent kinetic energy for two columns case with $L/D = 2$ in different vertical planes a) at $Y/D = 0$, and b) at $Y/D = 1.25$

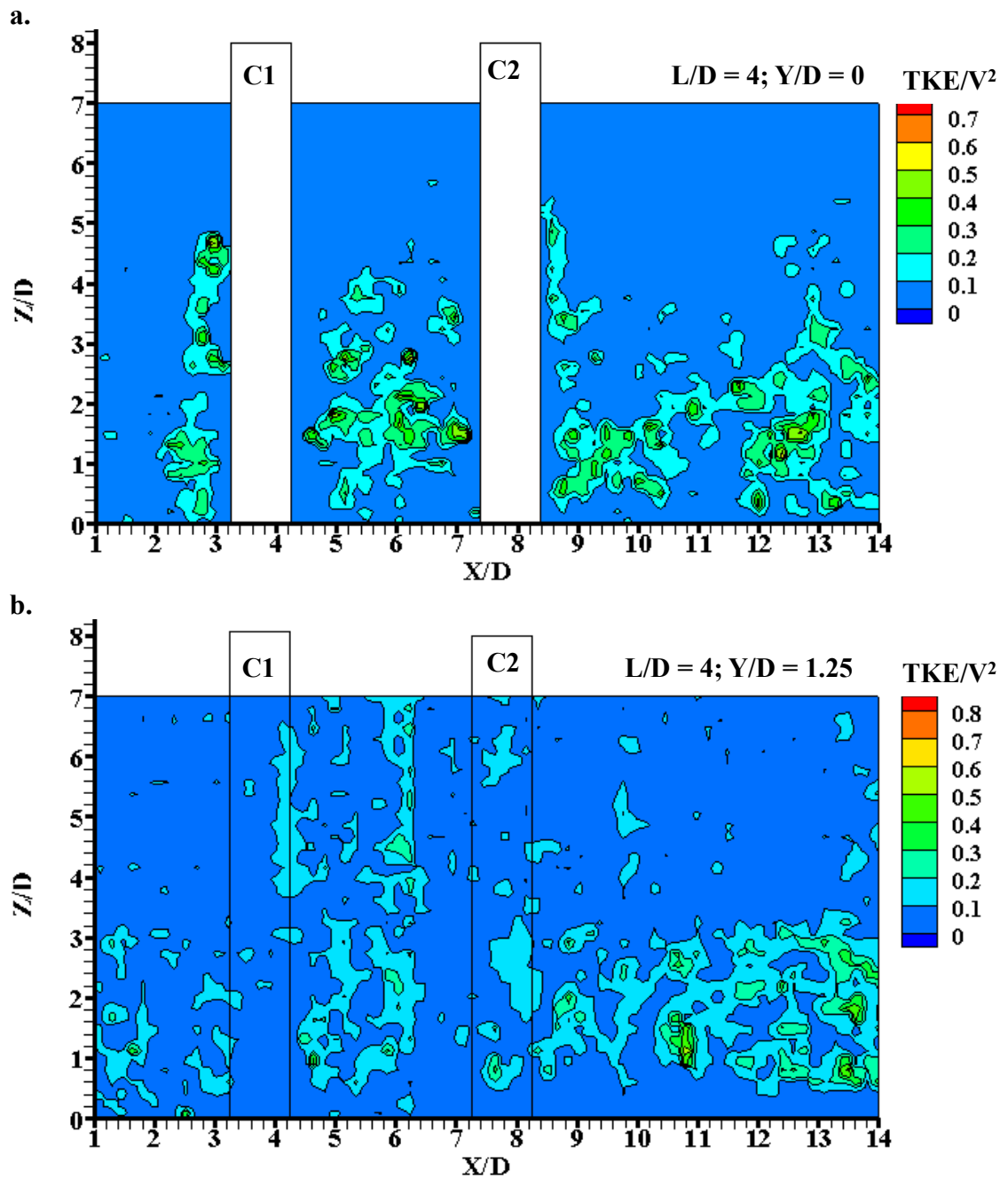


Figure C.12 Contour plots of turbulent kinetic energy for two columns case with $L/D = 4$ in different vertical planes a) at $Y/D = 0$, and b) at $Y/D = 1.25$

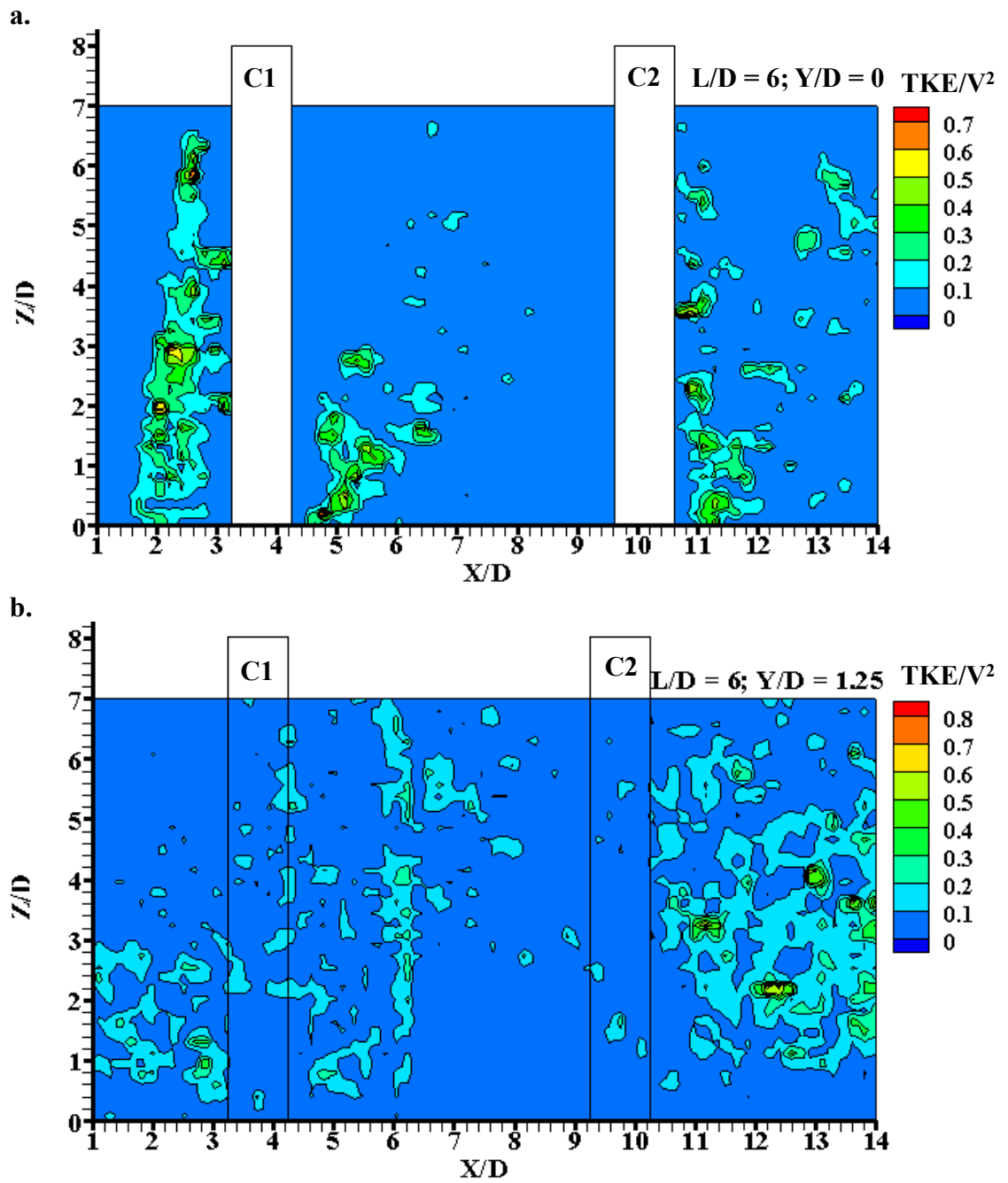


Figure C.13 Contour plots of turbulent kinetic energy for two columns case with $L/D = 6$ in different vertical planes a) at $Y/D = 0$, and b) at $Y/D = 1.25$

C.2.2 Profile Plots of Turbulence Kinetic Energy (TKE) in Vertical Plane

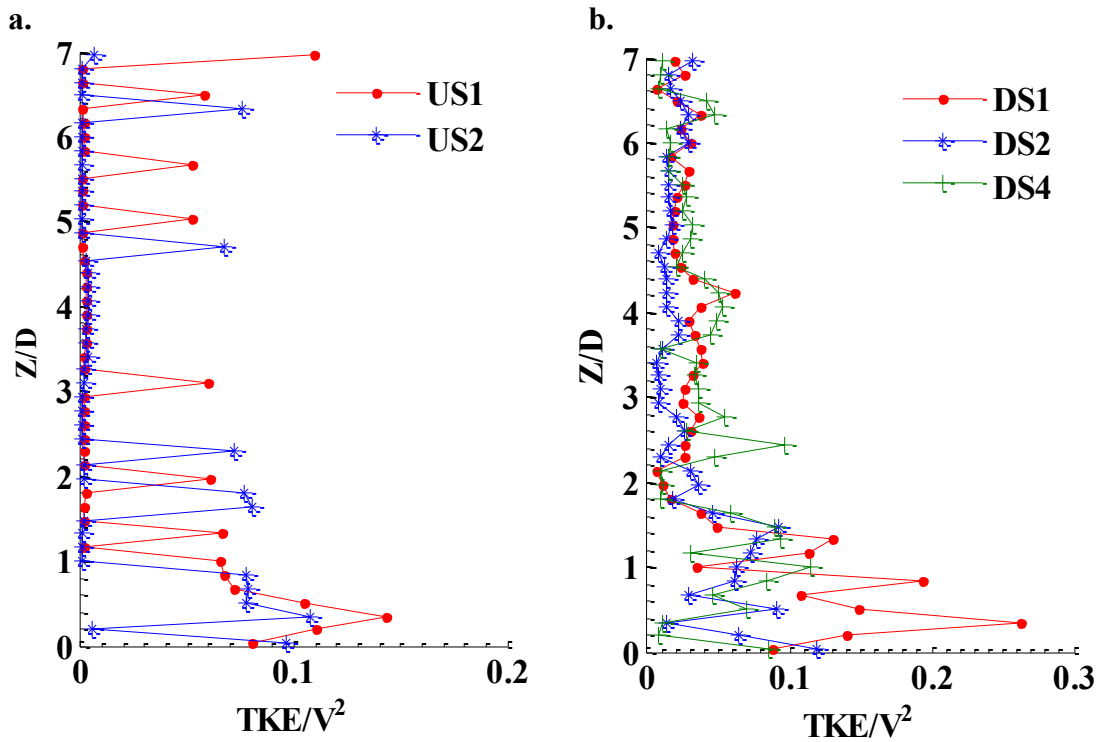


Figure C.14 Profile plots of turbulent kinetic energy for two columns case with $L/D = 1$ in a vertical plane at axis of symmetry a) upstream side, b) downstream side

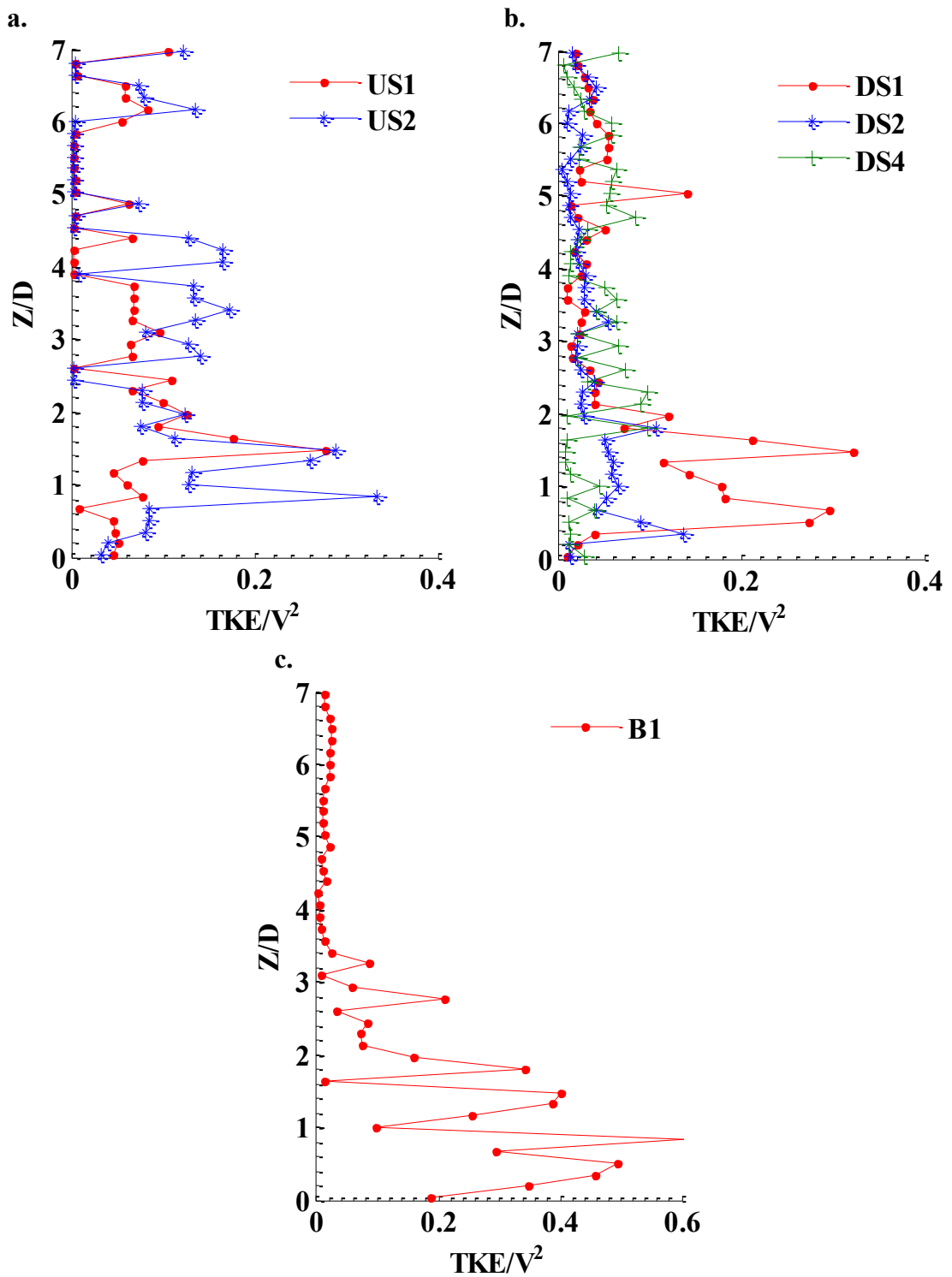


Figure C.15 Profile plots of turbulent kinetic energy for two columns case with $L/D = 2$ in a vertical plane at axis of symmetry a) upstream side, b) downstream side, and c) between two columns

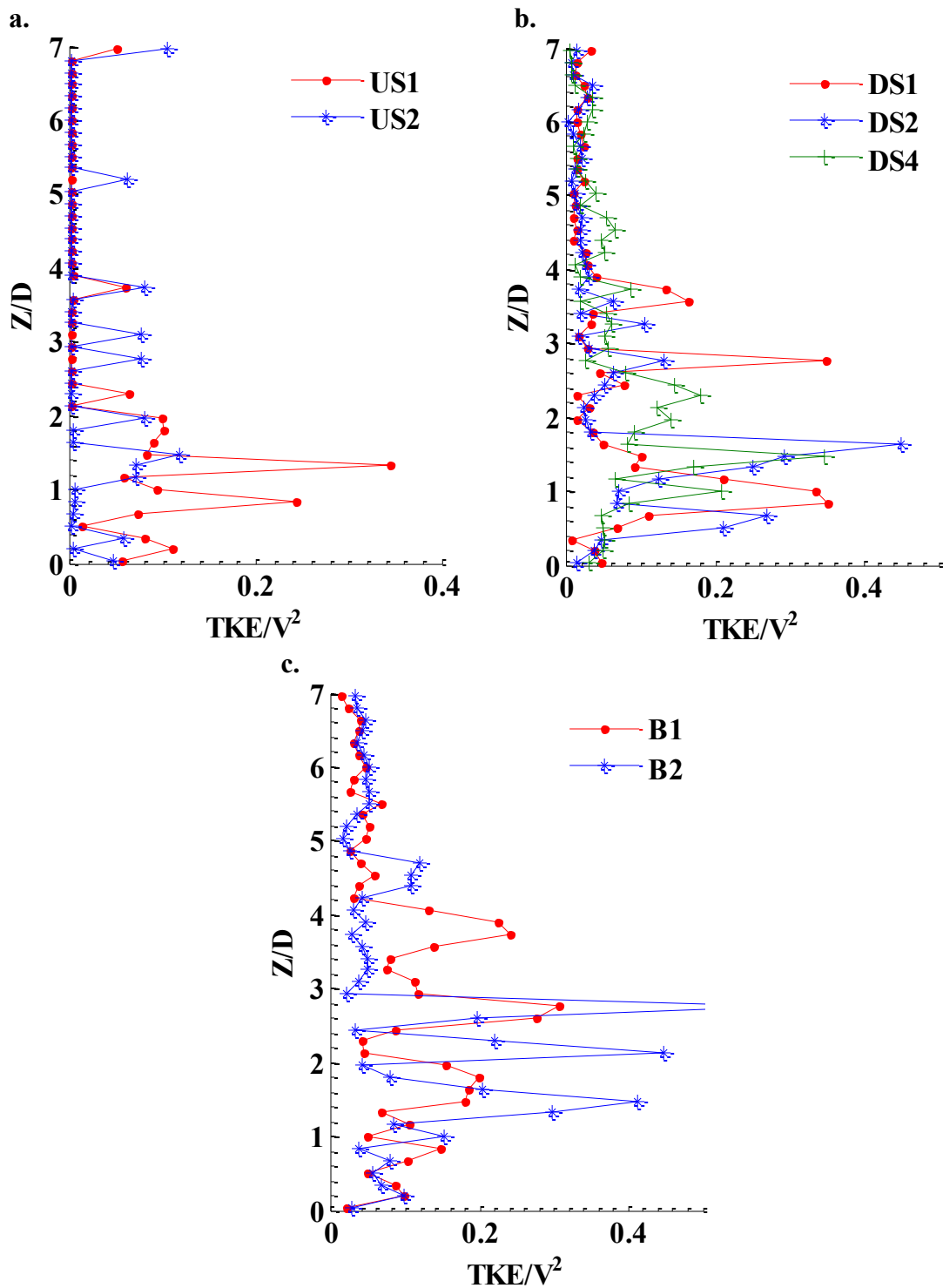


Figure C.16 Profile plots of turbulent kinetic energy for two columns case with $L/D = 4$ in a vertical plane at axis of symmetry a) upstream side, b) downstream side, and c) between two columns

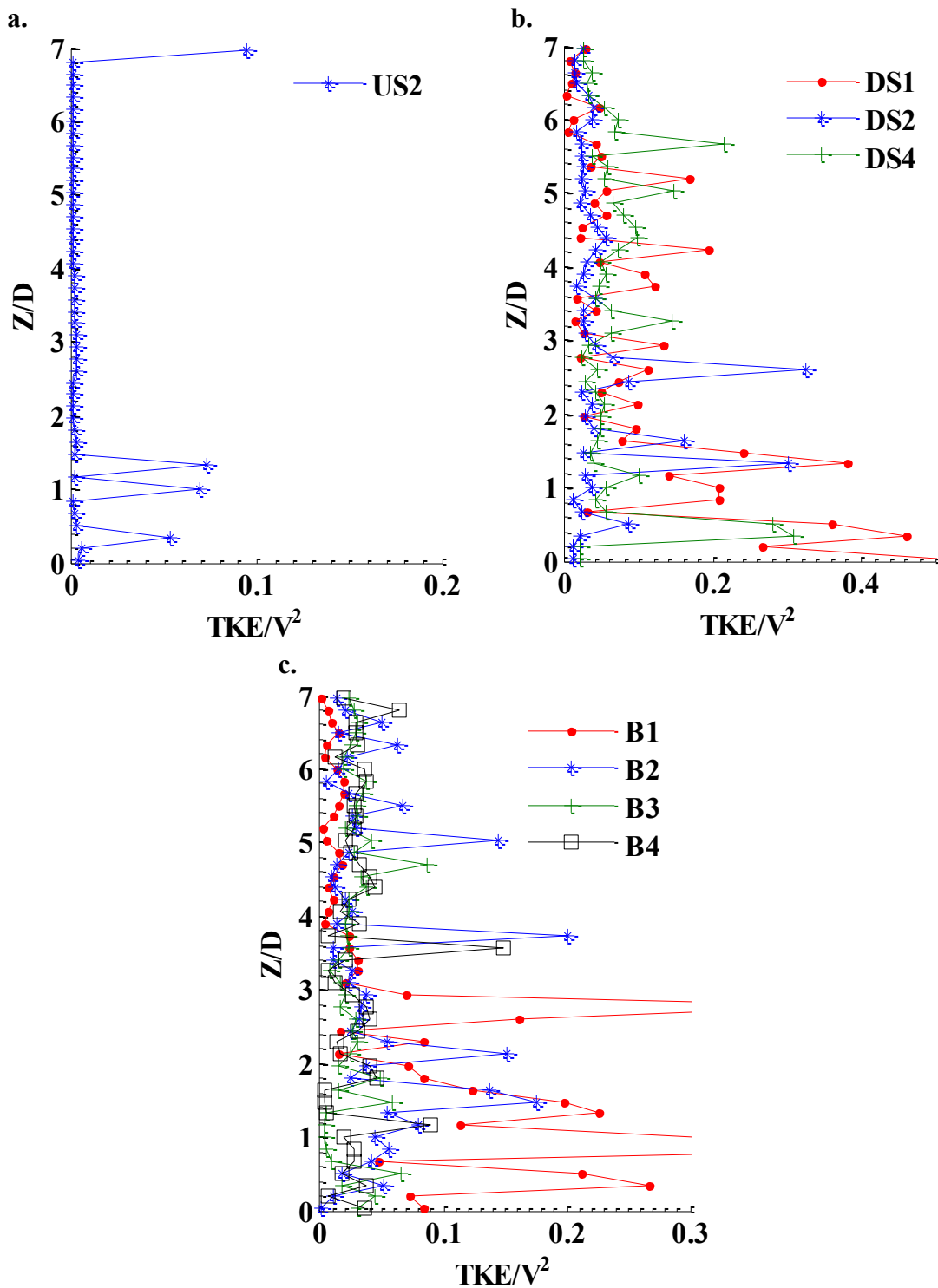


Figure C.17 Profile plots of turbulent kinetic energy for two columns case with $L/D = 6$ in a vertical plane at axis of symmetry a) upstream side, b) downstream side, and c) between two columns

C.3 Table of Results on Turbulent Kinetic Energy

Table C. 1 Maximum and minimum values of turbulent kinetic energy

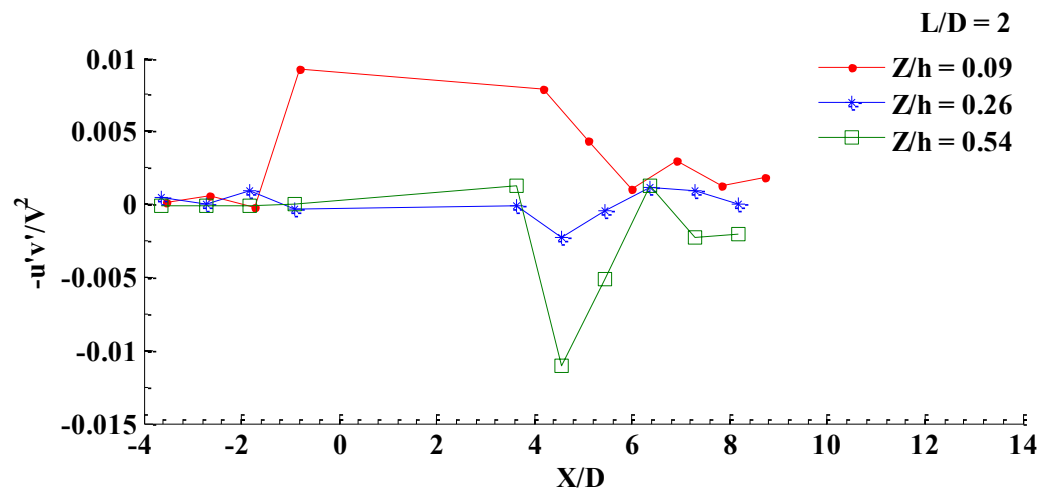
Test No.	L/D	Z/h	Y/D	TKE _{max} /V ²	X/D	TKE _{min} /V ²	X/D
1	0	0.09	0	0.11	2	0.02	-1
			0.9	0.05	2	0.02	1
			1.8	0.03	2	0.02	1
		0.26	0	0.28	2	0.02	-1
			0.9	0.12	3.5	0.02	0
			1.8	0.03	6.5	0.02	2
		0.54	0	0.3	3	0.02	-1
			0.9	0.14	4	0.02	0
			1.8	0.06	6.5	0.02	3
2	1.5	0.09	0	0.09	4	0.015	-1
			0.9	0.035	7.5	0.015	-1
			1.8	0.02	11	0.015	3
		0.26	0	0.11	4	0.02	-2
			0.9	0.04	5.5	0.02	-2
			1.8	0.03	13	0.02	5.5
		0.54	0	0.11	4	0.03	-1
			0.9	0.04	7	0.01	-2
			1.8	0.02	4	0.01	0
3	2	0.09	0	0.09	1	0.02	-1
			0.9	0.05	4	0.02	-2
			1.8	0.02	8	0.015	6
		0.26	0	0.12	4.5	0.01	-1
			0.9	0.03	7.5	0.01	-1
			1.8	0.02	4.5	0.01	2
		0.54	0	0.11	4.5	0.01	-1
			0.9	0.05	6	0.01	0
			1.8	0.02	11	0.01	1
4	3	0.09	0	0.12	4	0.02	-1
			0.9	0.04	5	0.02	3
			1.8	0.03	11	0.02	3
		0.26	0	0.14	5.5	0.02	-1
			0.9	0.06	8	0.02	0
			1.8	0.03	10	0.02	0
		0.54	0	0.15	5	0.02	-1
			0.9	0.07	7	0.02	1.5
			1.8	0.04	12	0.02	2
5	4	0.09	0	0.13	2	0.01	-1
			0.9	0.05	6	0.01	0
			1.8	0.025	10	0.01	4
		0.26	0	0.22	6	0.025	-1

6	0.54	0.9	0.07	9	0.02	0	
		1.8	0.03	11	0.02	4	
		0	0.22	3	0.02	-1	
		0.9	0.12	7	0.02	1.5	
		1.8	0.05	10	0.02	1	
	0.09	0	0.16	3	0.02	-1	
		0.9	0.08	4.5	0.02	-1	
		1.8	0.02	8	0.02	3	
		0.26	0	0.3	2	0.02	-1
			0.9	0.1	4.5	0.02	-1
1.8			0.03	10	0.02	3	
0.54		0	0.2	2	0.01	-1	
		0.9	0.14	3	0.01	-1	
		1.8	0.05	6.5	0.01	2	

APPENDIX-D: PLOTS FOR REYNOLDS STRESSES

D.1 Profile Plots of Reynolds Stresses in Horizontal Plane

a.



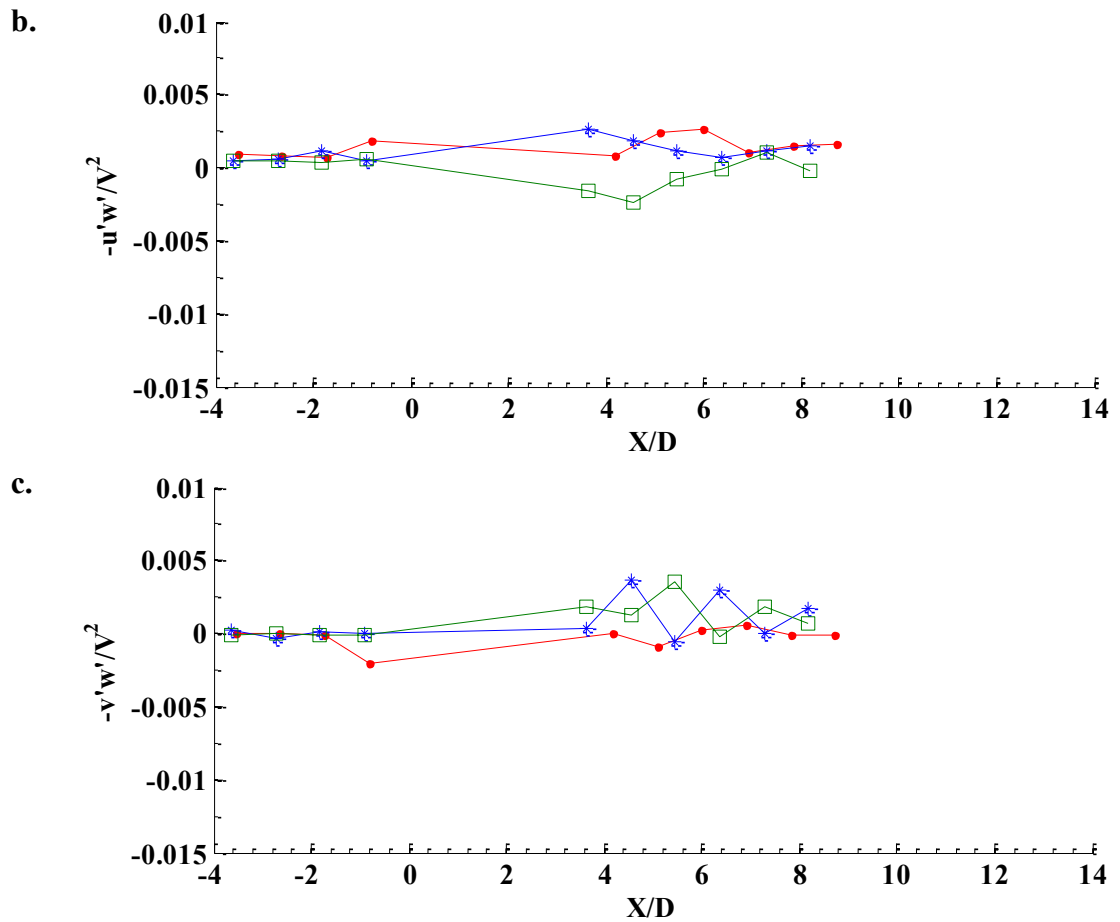
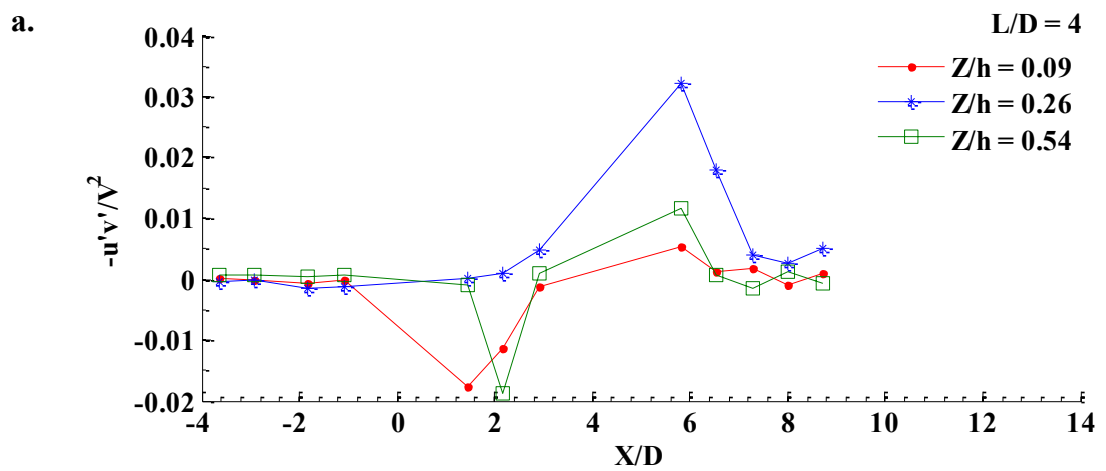


Figure D.1 Profile plots of Reynolds shear stresses for two columns case with $L/D = 2$ in different horizontal planes along axis of symmetry a) in $u-v$ plane, b) in $u-w$ plane, and c) in $v-w$ plane



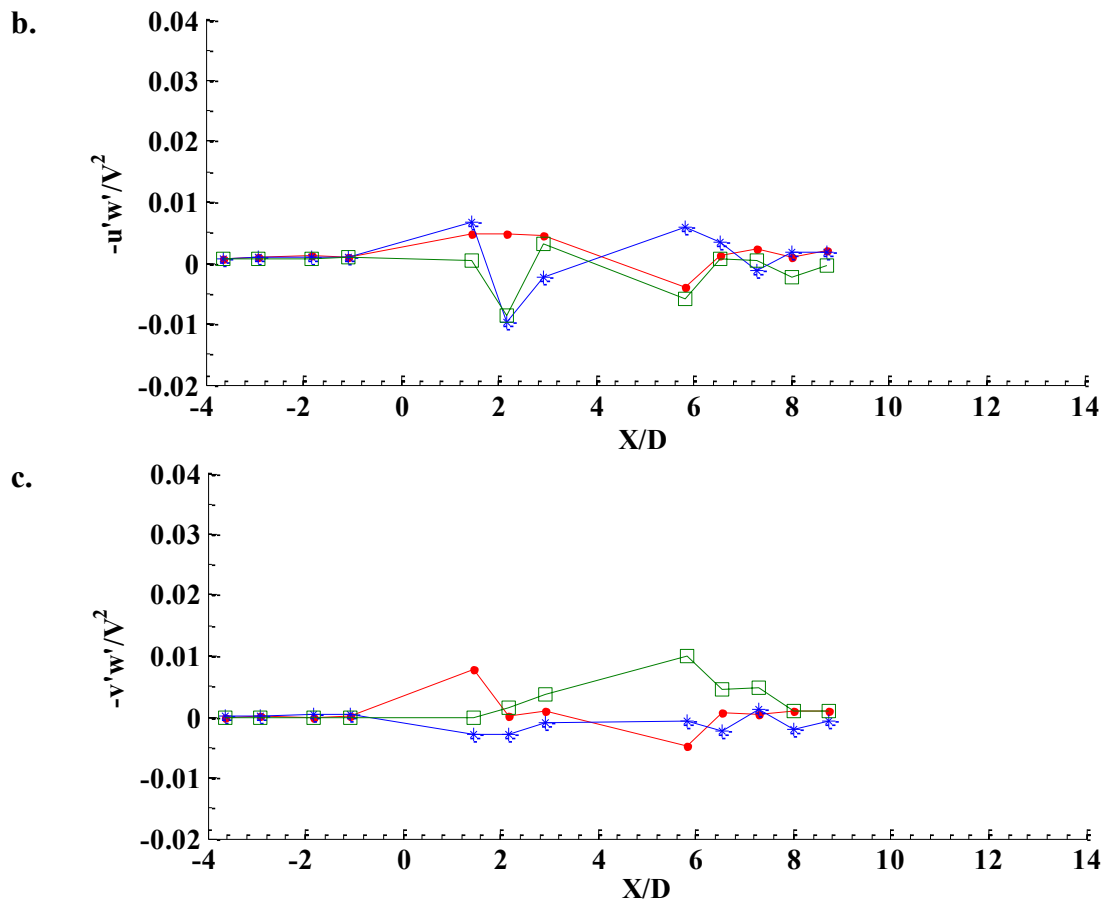
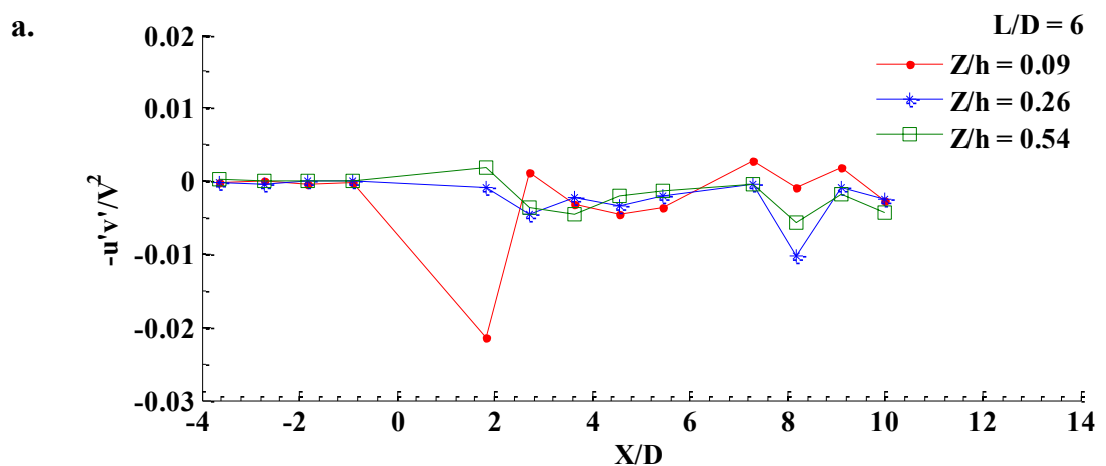


Figure D.2 Profile plots of Reynolds shear stresses for two columns case with $L/D = 4$ in different horizontal planes along axis of symmetry a) in u - v plane, b) in u - w plane, and c) in v - w plane



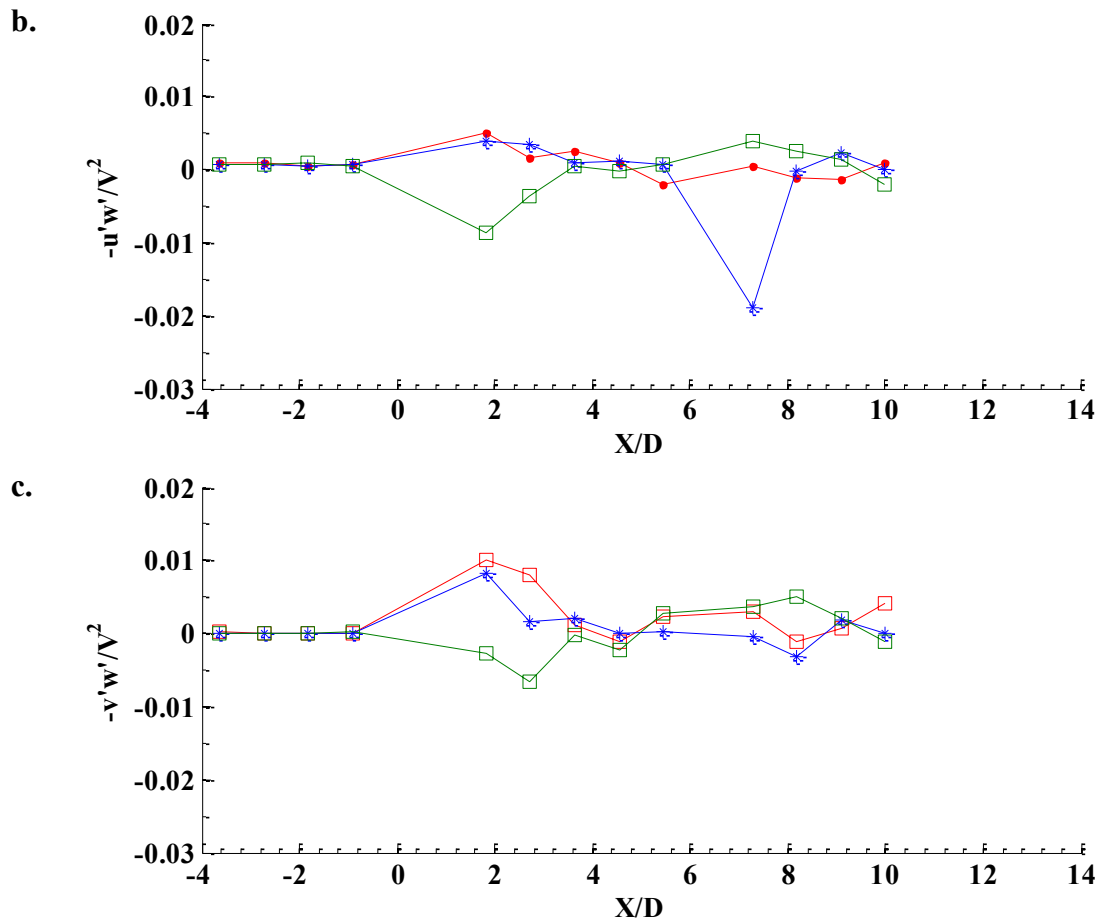


Figure D.3 Profile plots of Reynolds shear stresses for two columns case with $L/D = 6$ in different horizontal planes along axis of symmetry a) in u - v plane, b) in u - w plane, and c) in v - w plane

D.2 Plots of Reynolds Stresses in Vertical Plane

D.2.1 Contour Plots of Reynolds Stresses in Vertical Plane

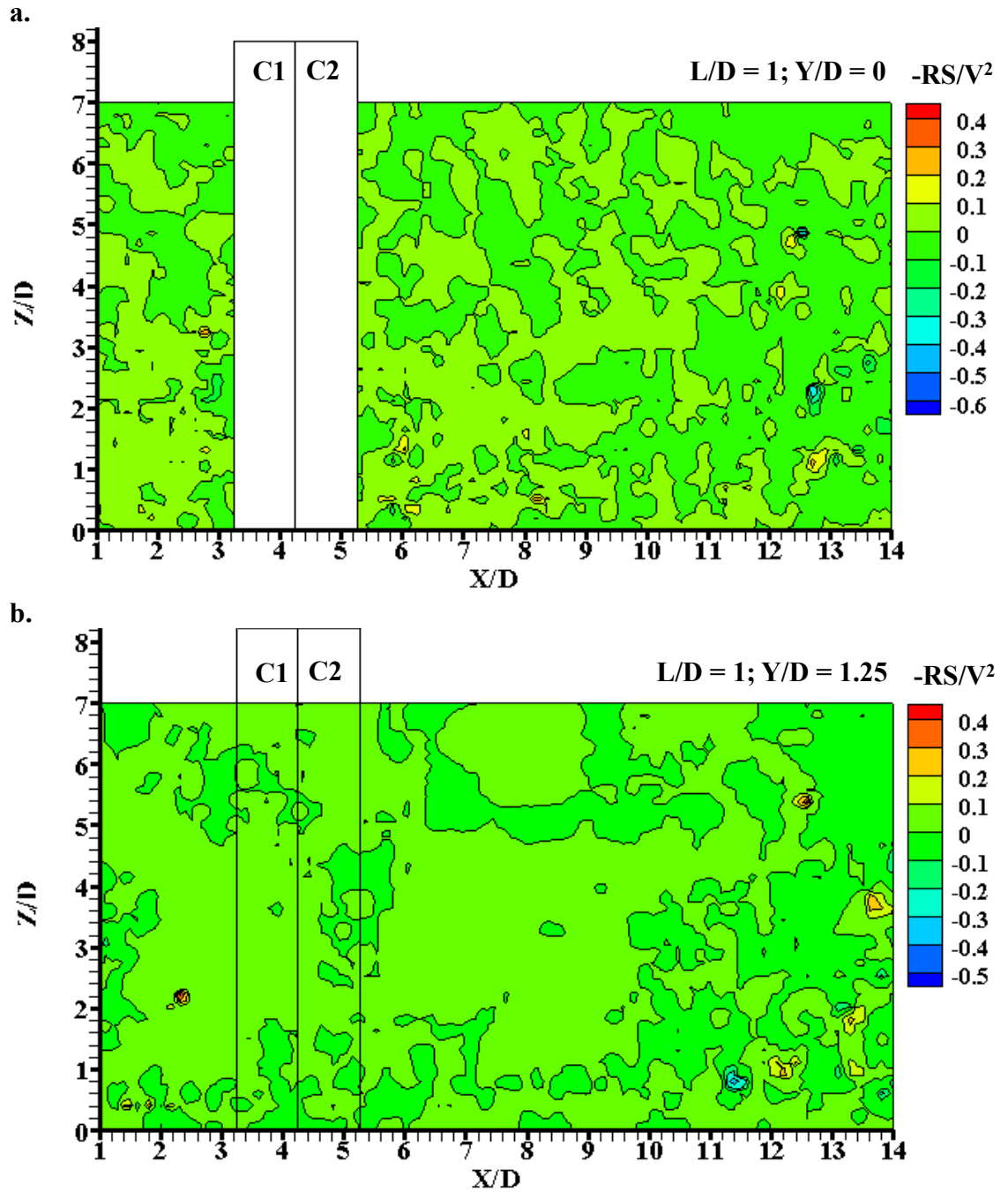


Figure D.4 Contour plots of Reynolds shear stress for two columns case with $L/D = 1$ in different vertical planes a) at $Y/D = 0$, and b) at $Y/D = 1.25$

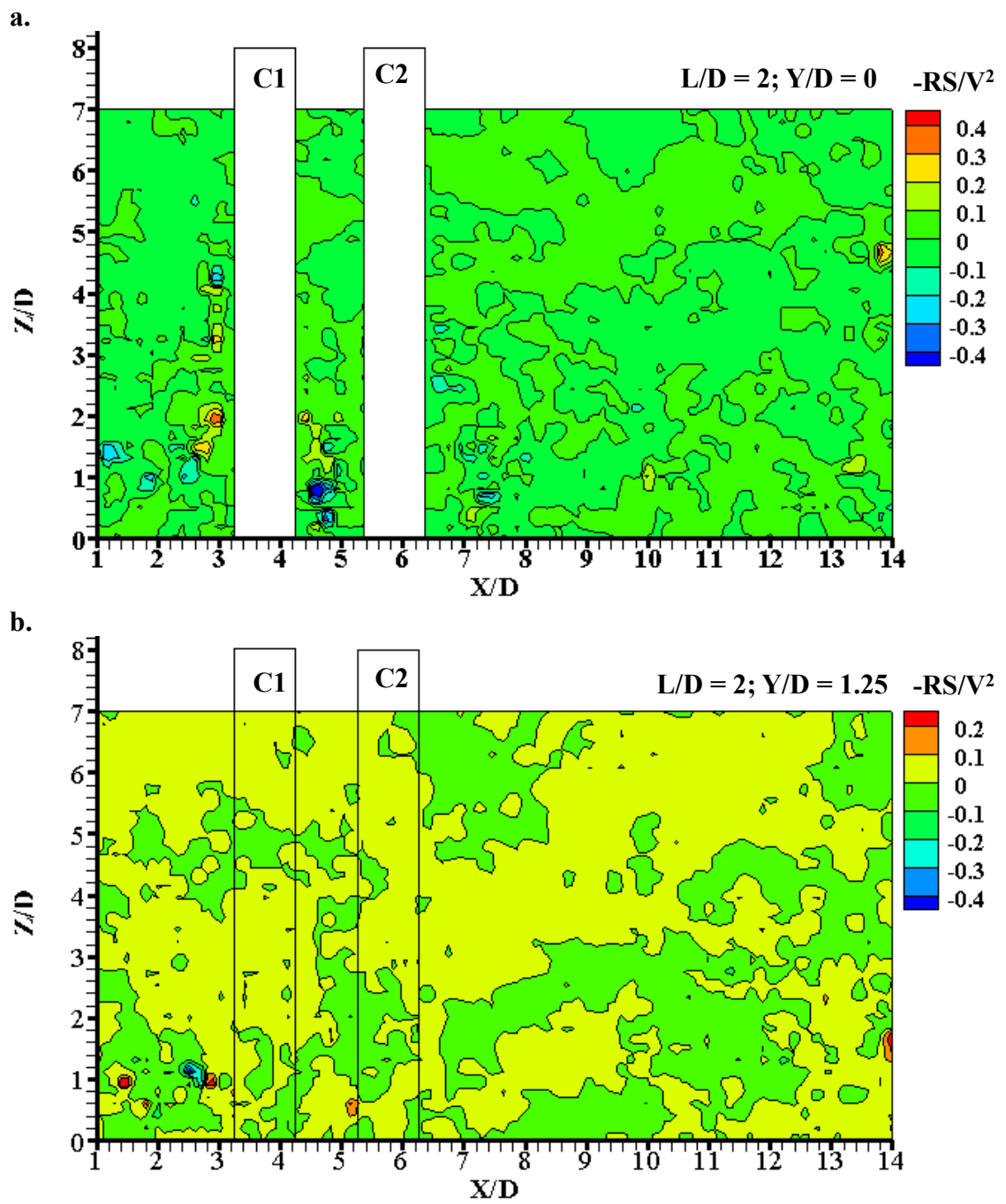


Figure D.5 Contour plots of Reynolds shear stress for two columns case with $L/D = 2$ in different vertical planes a) at $Y/D = 0$, and b) at $Y/D = 1.25$

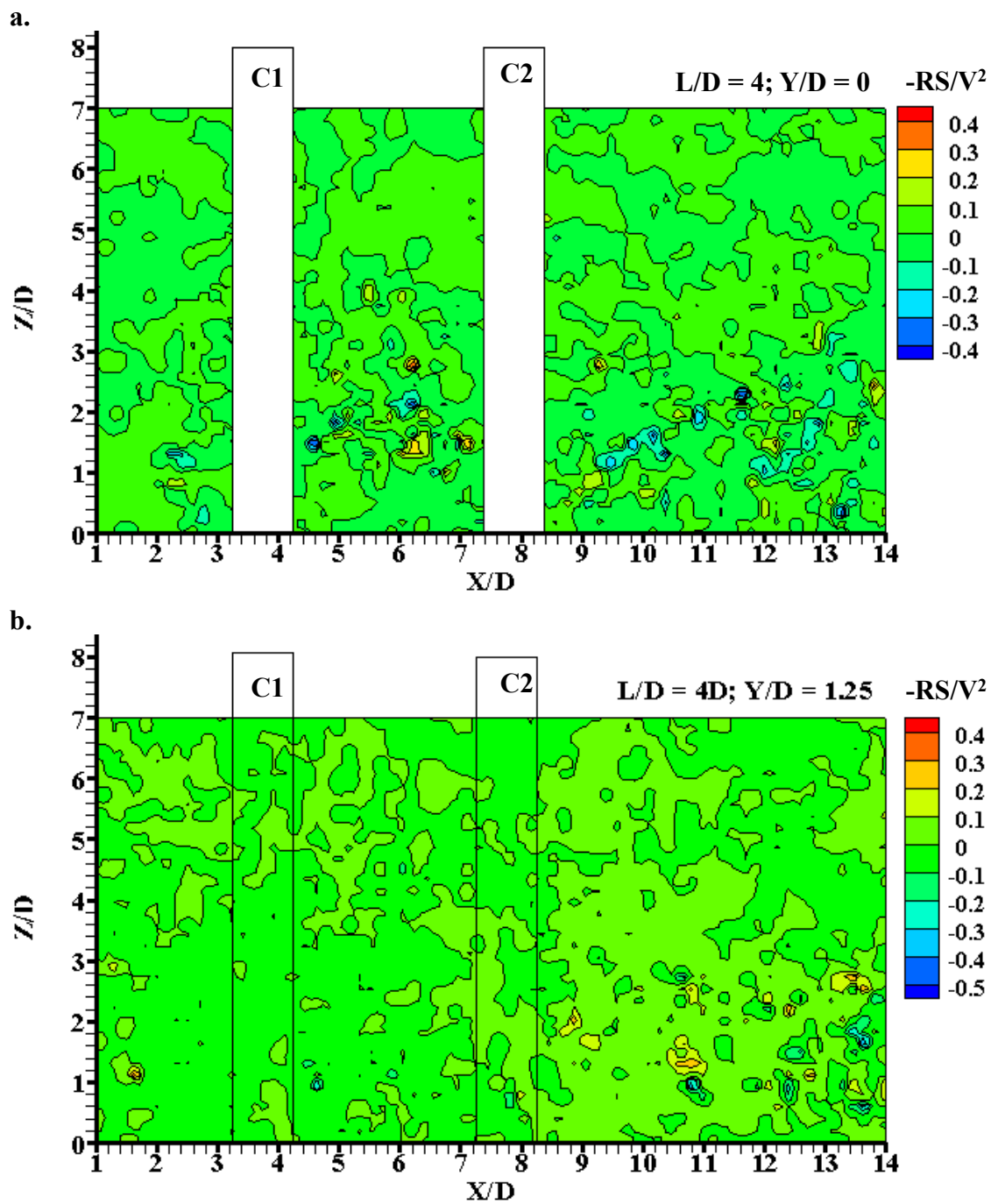


Figure D.6 Contour plots of Reynolds shear stress for two columns case with $L/D = 4$ in different vertical planes a) at $Y/D = 0$, and b) at $Y/D = 1.25$

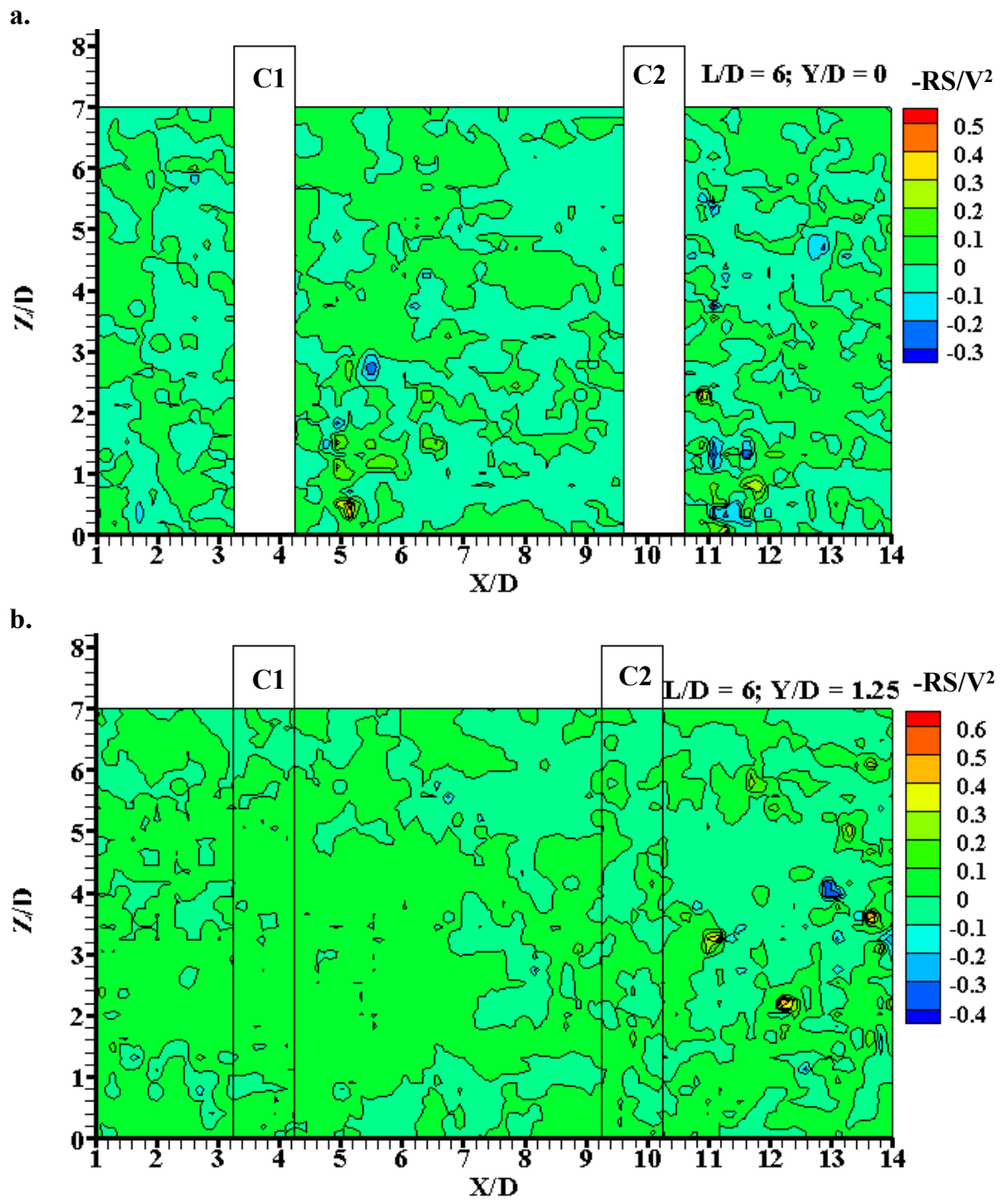


Figure D.7 Contour plots of Reynolds shear stress for two columns case with $L/D = 6$ in different vertical planes a) at $Y/D = 0$, and b) at $Y/D = 1.25$

D.2.2 Profile Plots of Reynolds Stresses in Vertical Plane

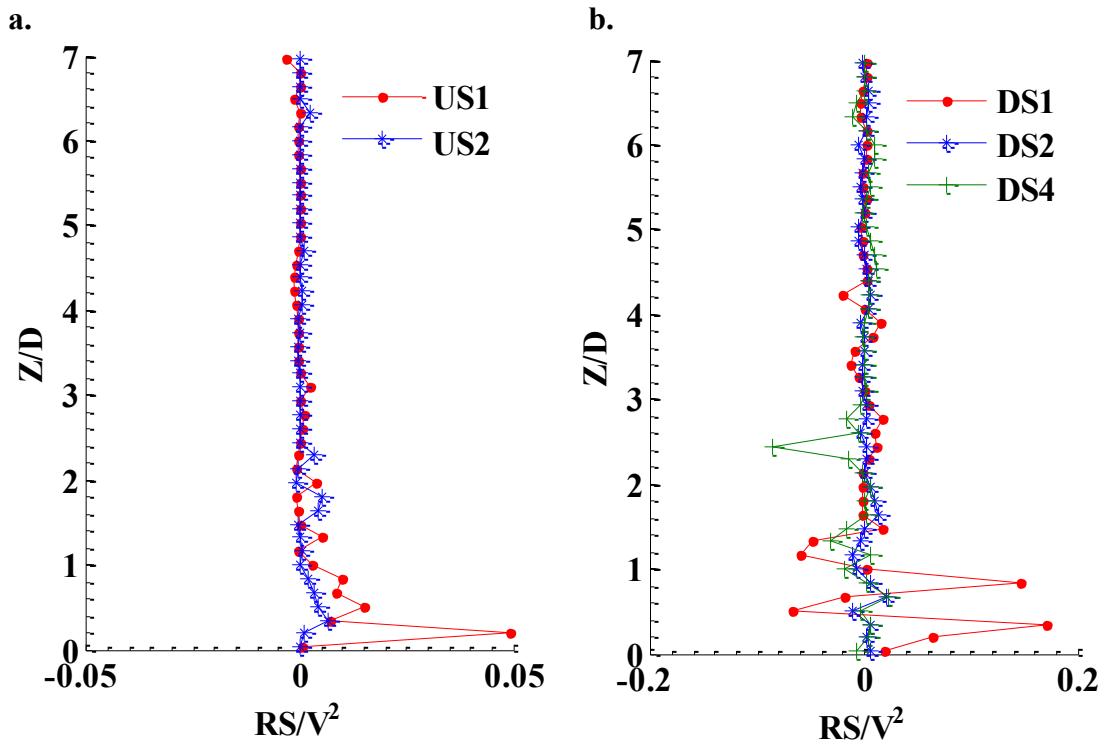


Figure D.8 Profile plots of Reynolds shear stress for two columns case with $L/D = 1$ in a vertical plane at axis of symmetry a) upstream side, b) downstream side

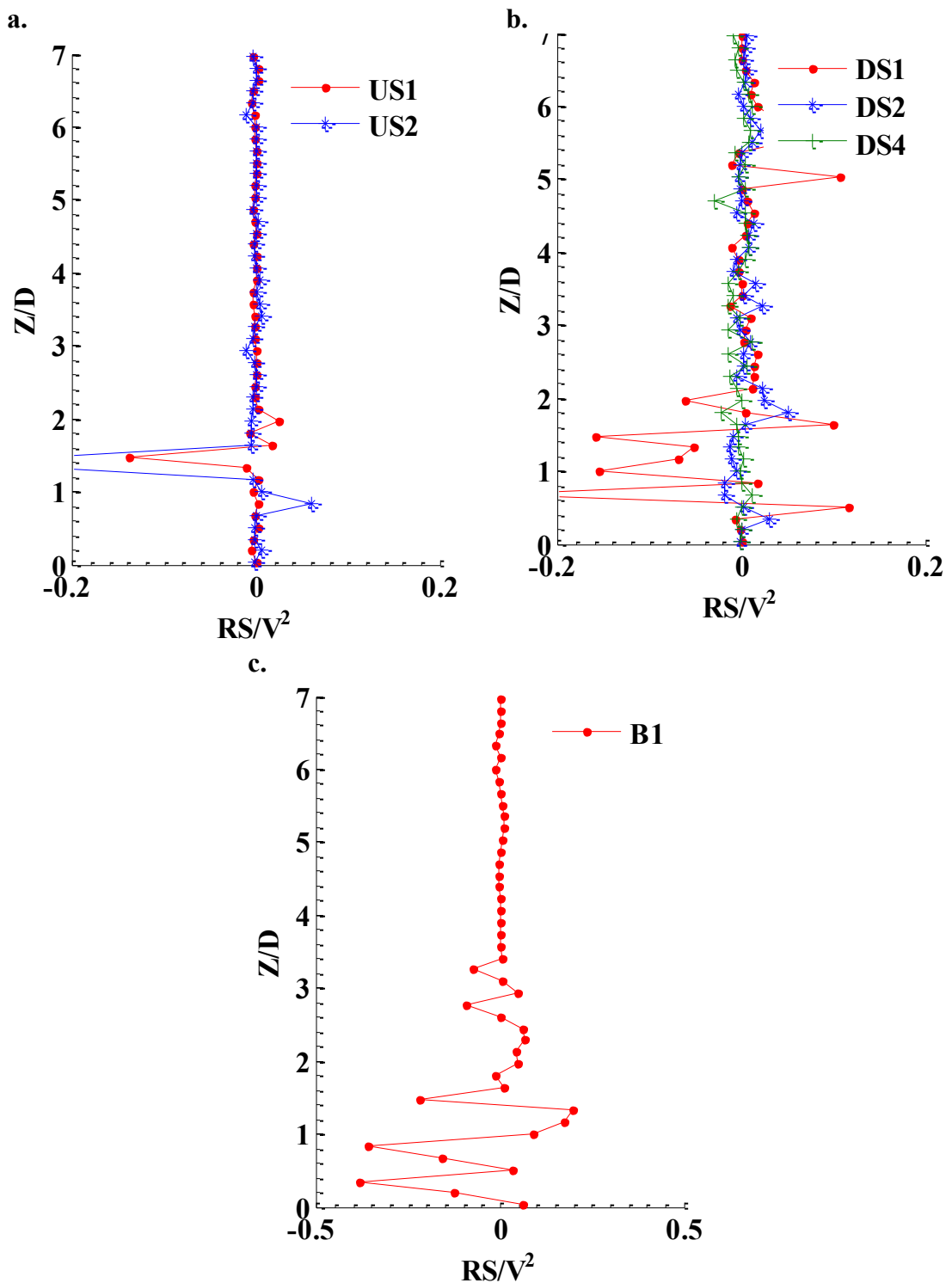


Figure D.9 Profile plots of Reynolds shear stress for two columns case with $L/D = 2$ in a vertical plane at axis of symmetry a) upstream side, b) downstream side, and c) between two columns

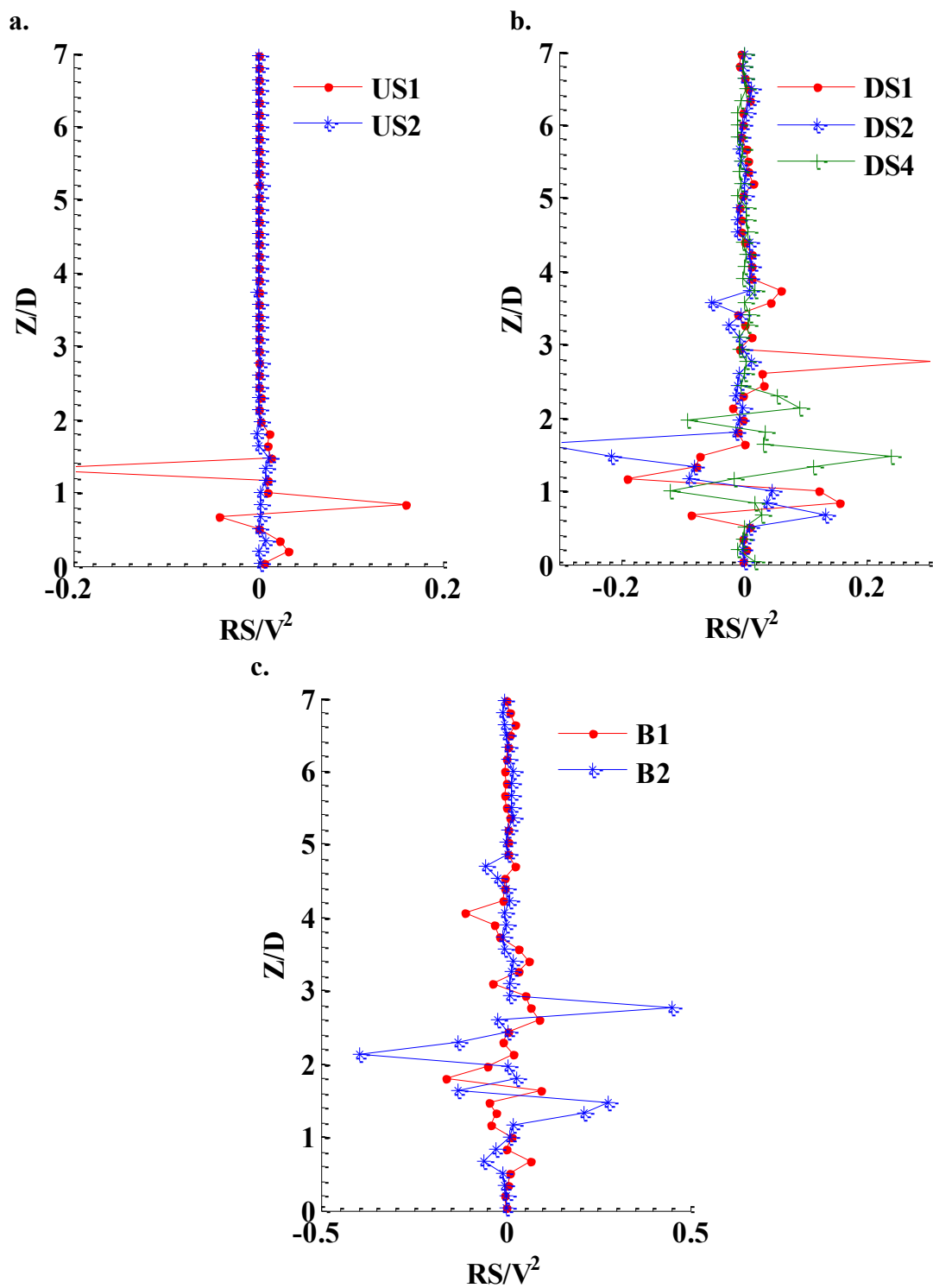


Figure D.10 Profile plots of Reynolds shear stress for two columns case with $L/D = 4$ in a vertical plane at axis of symmetry a) upstream side, b) downstream side, and c) between two columns

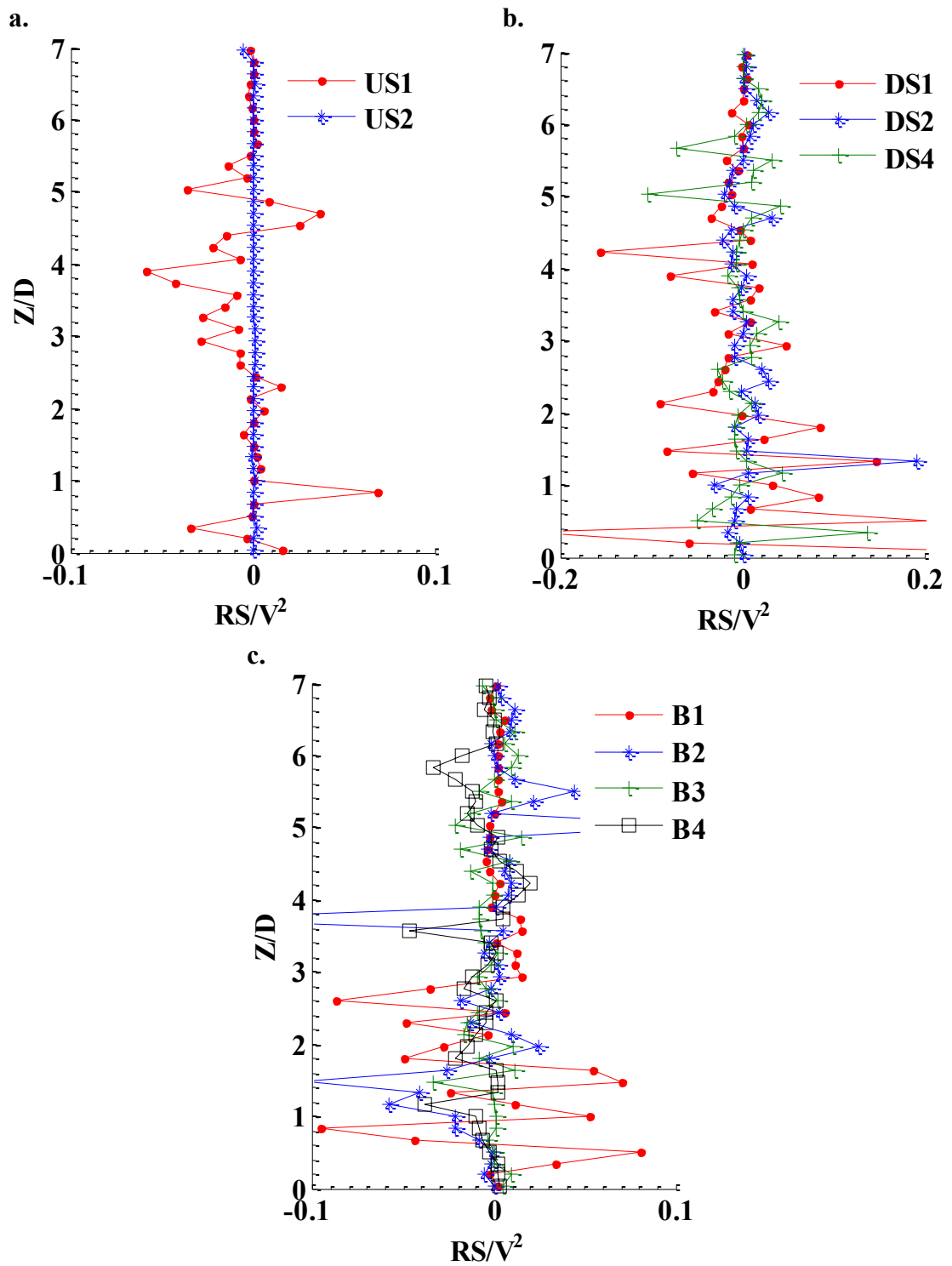


Figure D.11 Profile plots of Reynolds shear stress for two columns case with $L/D = 6$ in a vertical plane at axis of symmetry a) upstream side, b) downstream side, and c) between two columns

D.3 Table of Results on Reynolds Shear Stresses

Table D. 1 Maximum and minimum values of Reynolds shear stresses (-u'v')

Test No.	L/D	Z/h	Y/D	$-u'v'_{\max}/V^2$	X/D	$-u'v'_{\min}/V^2$	X/D
1	0	0.09	0	0.02	2	0	-2
		0.26		0		-0.006	2.5
		0.54		0		-0.32	2
2	2	0.09	0	0.01	-1	0	-2
		0.26		0.001	6.5	-0.002	4.5
		0.54		0.002	4	-0.01	4.5
3	3	0.09	0	0.002	2	-0.012	4
		0.26		0.006	2	-0.016	5.5
		0.54		0.002	6.5	-0.02	4
4	4	0.09	0	0.005	6	-0.016	1.5
		0.26		0.03	6	0	2
		0.54		0.012	6	-0.016	2
5	6	0.09	0	0.003	7.5	-0.02	2
		0.26		0		-0.01	8
		0.54		0.003	2	-0.005	8

Table D. 2 Maximum and minimum values of Reynolds shear stresses (-u'w')

Test No.	L/D	Z/h	Y/D	$-u'w'_{\max}/V^2$	X/D	$-u'w'_{\min}/V^2$	X/D
1	0	0.09	0	0.004	4	-0.008	2
		0.26		0.004	2.5	0	
		0.54		0.016	-1	0	
2	2	0.09	0	0.002	6	0	
		0.26		0.002	5.5	0	
		0.54		0.001	7	0.002	4.5
3	3	0.09	0	0.002	6	-0.002	2
		0.26		0.006	5.5	-0.005	6
		0.54		0.004	2	-0.002	6
4	4	0.09	0	0.005	2	-0.004	6
		0.26		0.006	2	-0.01	2
		0.54		0.003	3	-0.01	2
5	6	0.09	0	0.005	2	0	
		0.26		0.004	2	-0.02	7
		0.54		0.005	7	-0.008	2

Table D. 3 Maximum and minimum values of Reynolds shear stresses ($-v'w'$)

Test No.	L/D	Z/h	Y/D	$-v'w'_{\max}/V^2$	X/D	$-v'w'_{\min}/V^2$	X/D
1	0	0.09	0	0.004	2	0	
		0.26		0.014	2	0	
		0.54		0.02	3	0	
2	2	0.09	0	0		-0.002	-1
		0.26		0.003	4.5	0	
		0.54		0.003	5.5	0	
3	3	0.09	0	0.003	6	-0.003	2
		0.26		0.005	5.5	0	
		0.54		0.006	7	-0.003	4
4	4	0.09	0	0.008	1.5	0.005	6
		0.26		0		-0.002	2
		0.54		0.01	6	0	
5	6	0.09	0	0.01	2	0	
		0.26		0.008	2	0	
		0.54		0.005	8	-0.005	3

APPENDIX-E PLOTS FOR QUADRANT ANALYSIS

E.1 Probability of Occurrence of the Events at Upstream and Downstream sides

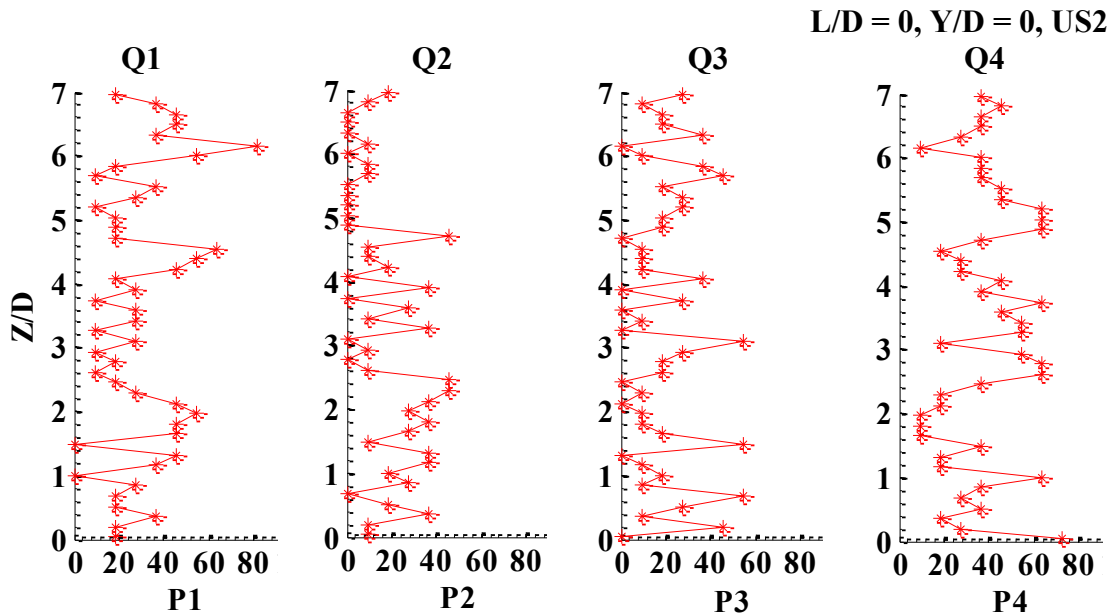


Figure E.1 Profile plots of probability of occurrence of different quadrants at upstream side (US2) for single column case

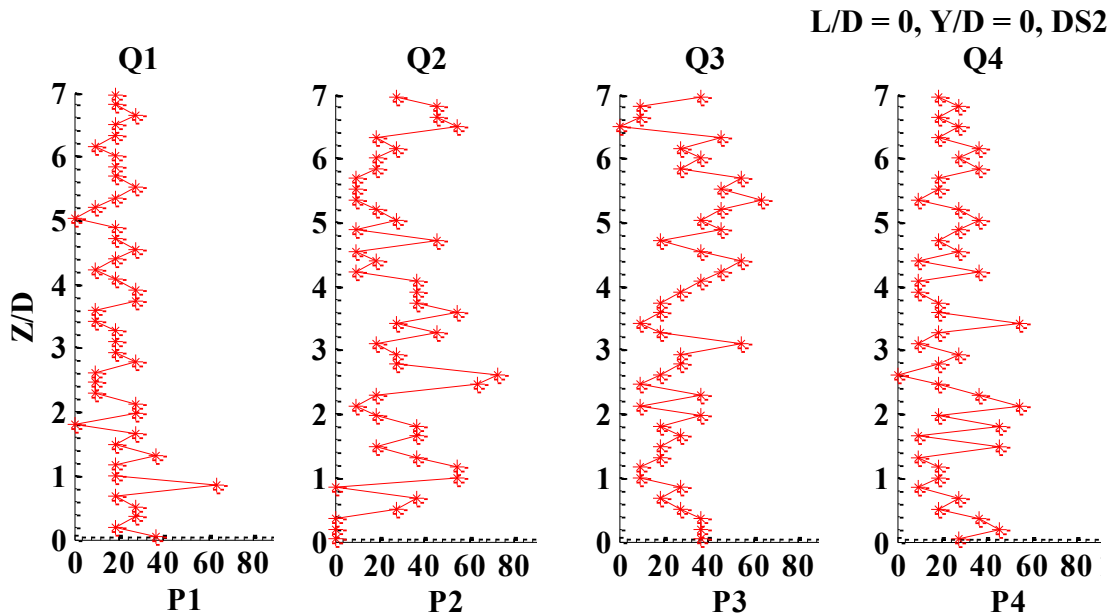


Figure E.2 Profile plots of probability of occurrence of different quadrants at downstream side (DS2) for single column case

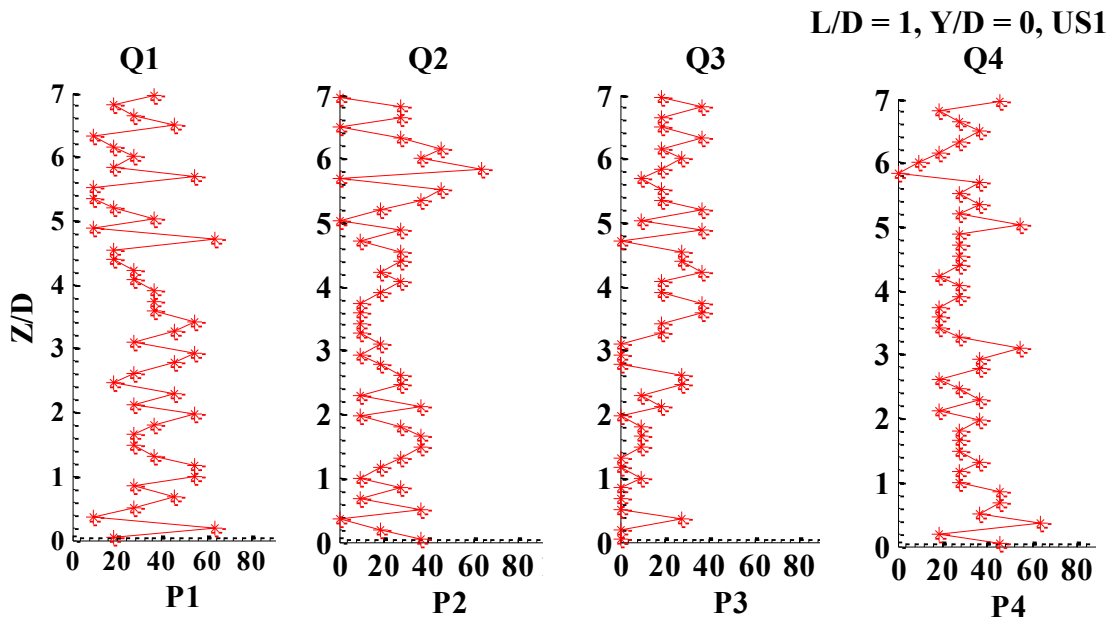


Figure E.3 Profile plots of probability of occurrence of different quadrants at upstream side (US1) of Column 1 for two columns case with $L/D = 1$

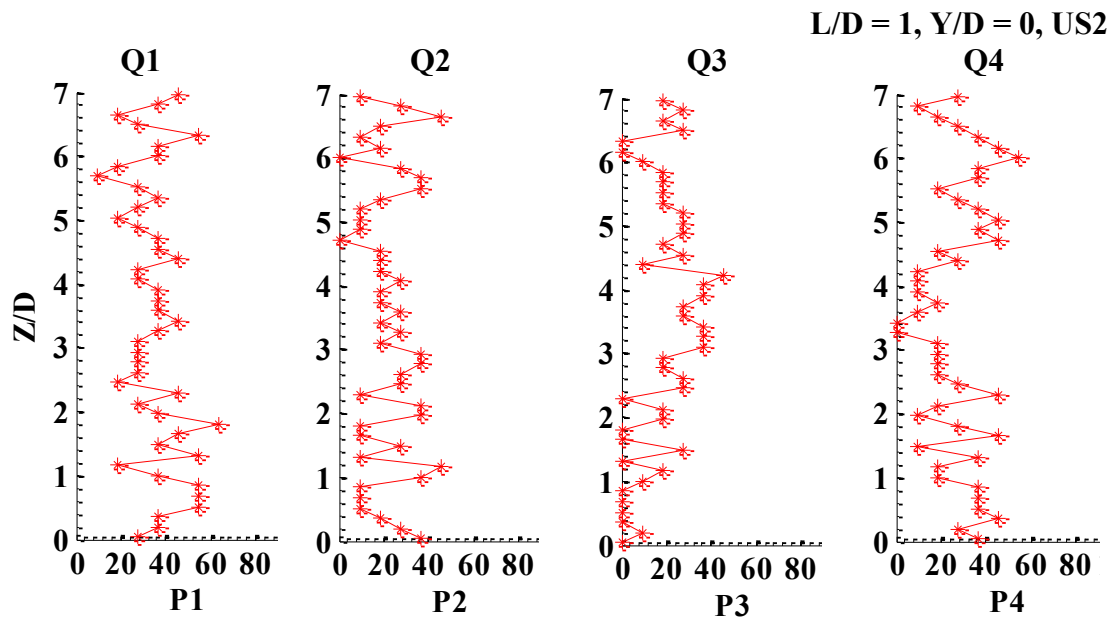


Figure E.4 Profile plots of probability of occurrence of different quadrants at upstream side (US2) of Column 1 for two columns case with $L/D = 1$

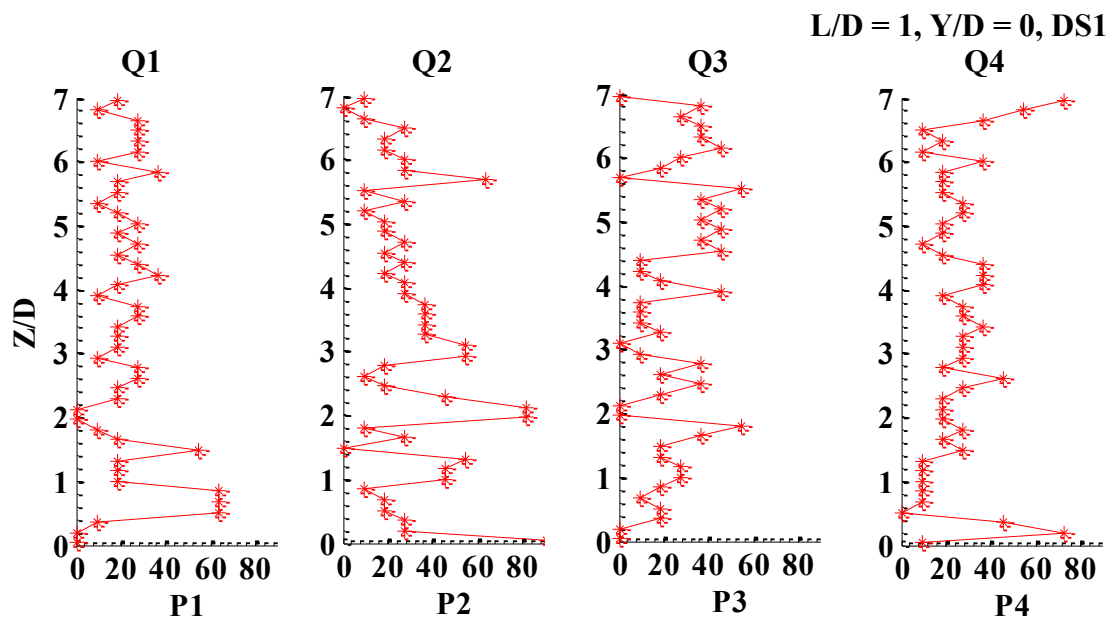


Figure E.5 Profile plots of probability of occurrence of different quadrants at downstream side (DS1) of Column 2 for two columns case with $L/D = 1$

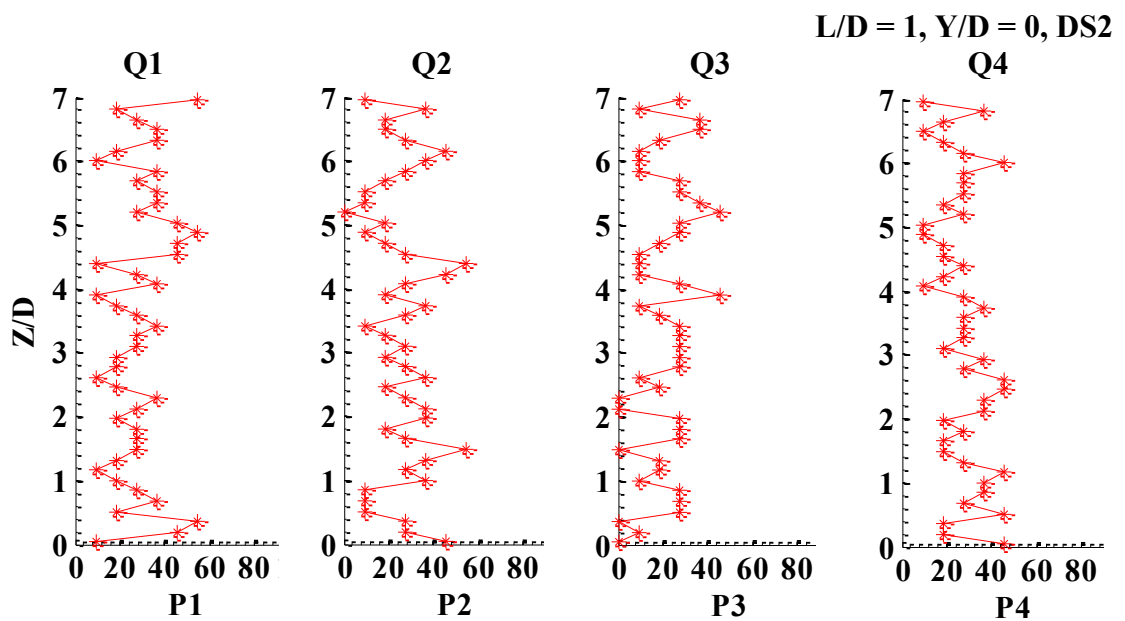


Figure E.6 Profile plots of probability of occurrence of different quadrants at downstream side (DS2) of Column 2 for two columns case with $L/D = 1$

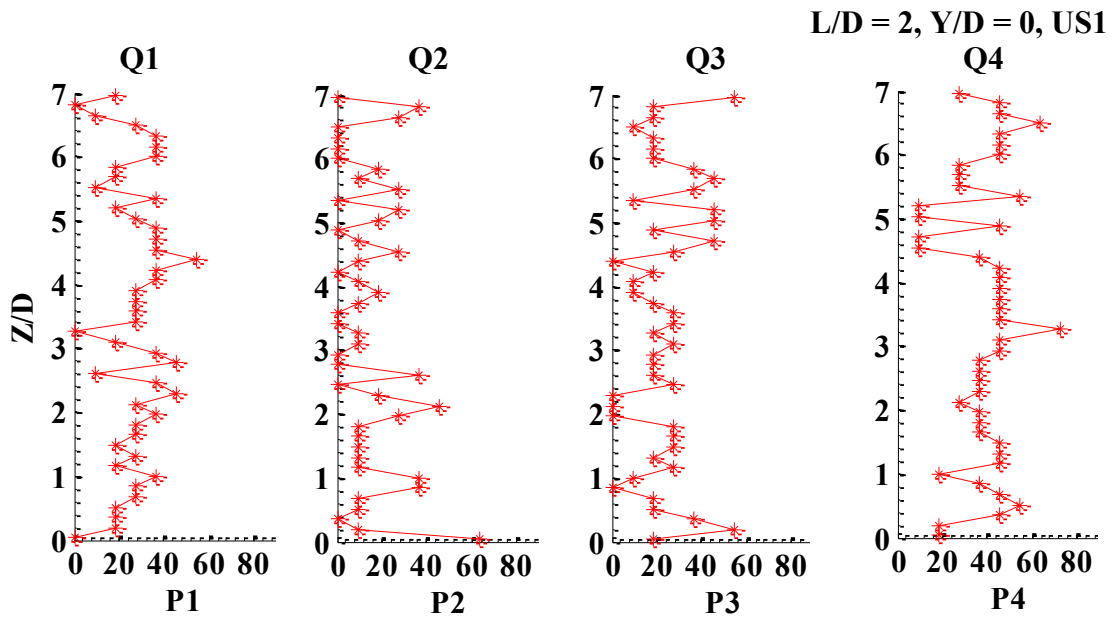


Figure E.7 Profile plots of probability of occurrence of different quadrants at upstream side (US1) of Column 1 for two columns case with $L/D = 2$

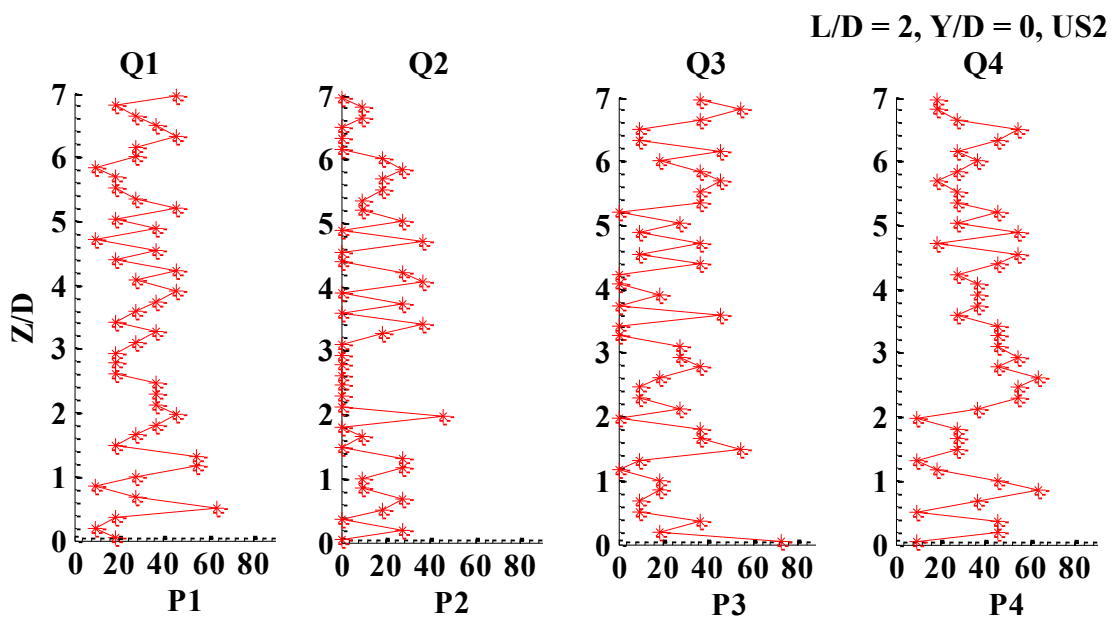


Figure E.8 Profile plots of probability of occurrence of different quadrants at upstream side (US2) of Column 1 for two columns case with $L/D = 2$

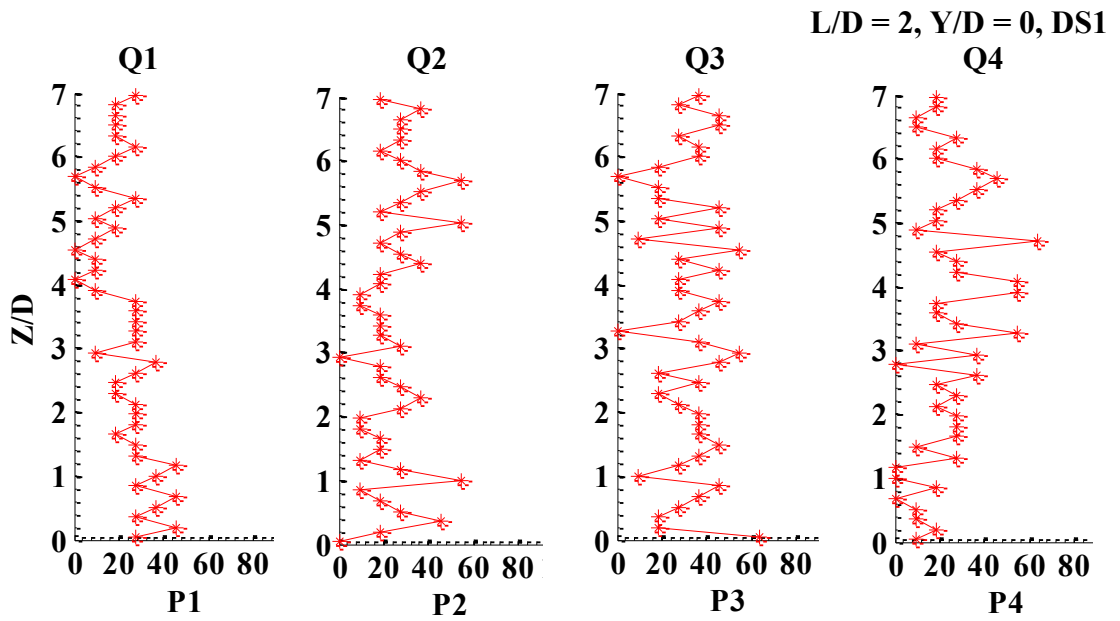


Figure E.9 Profile plots of probability of occurrence of different quadrants at downstream side (DS1) of Column 2 for two columns case with $L/D = 2$

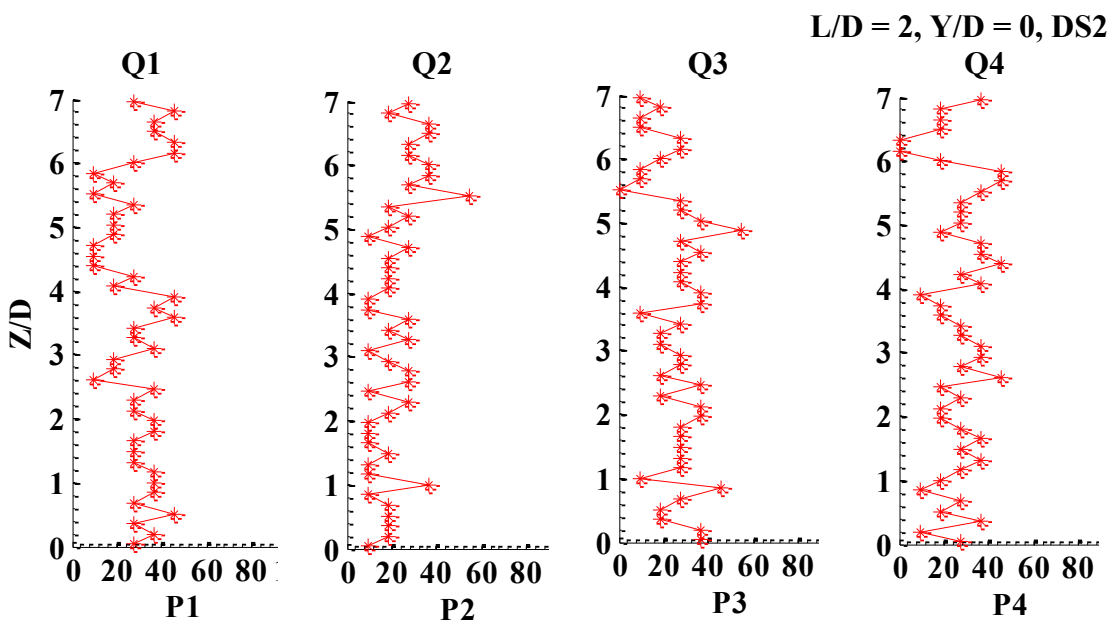


Figure E.10 Profile plots of probability of occurrence of different quadrants at downstream side (DS2) of Column 2 for two columns case with $L/D = 2$

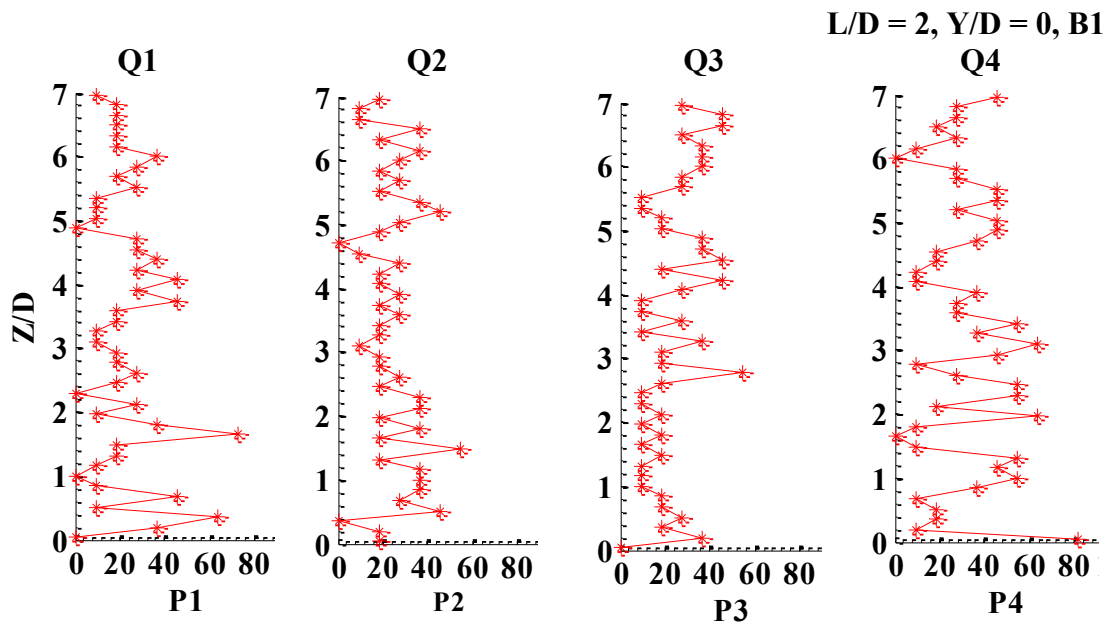


Figure E.11 Profile plots of probability of occurrence of different quadrants between two columns (B1) with $L/D = 2$

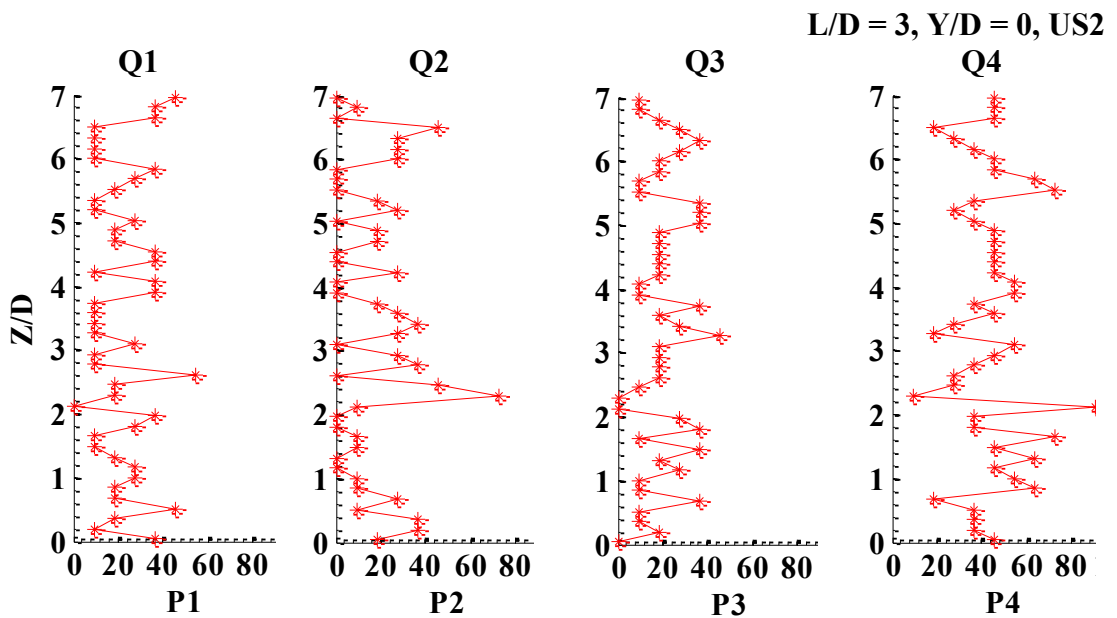


Figure E.12 Profile plots of probability of occurrence of different quadrants at upstream side (US2) of Column 1 for two columns case with $L/D = 3$

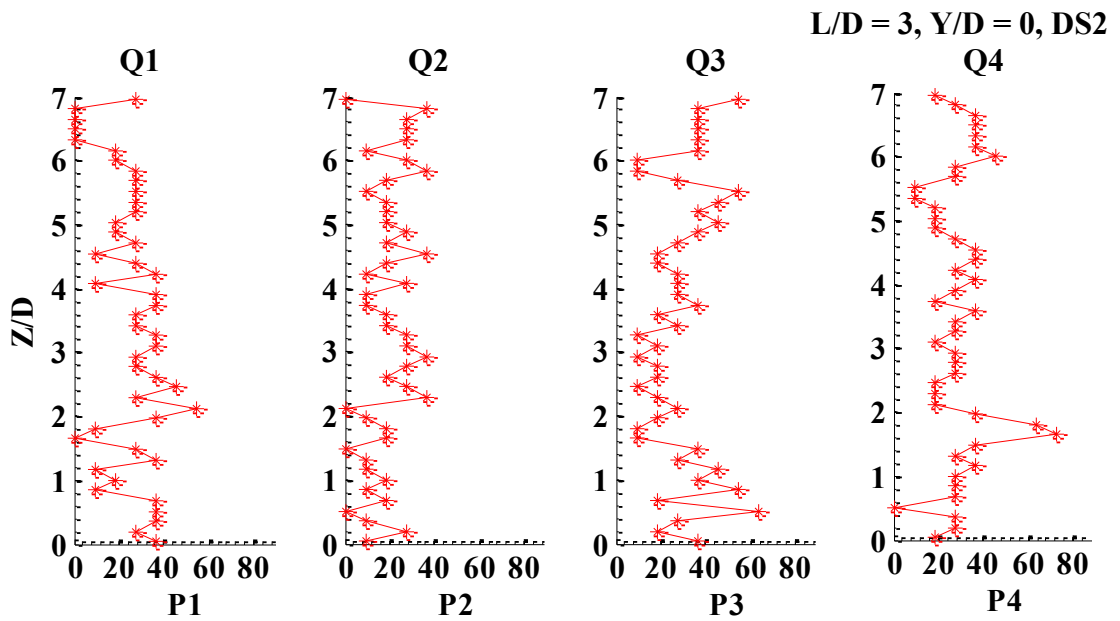


Figure E.13 Profile plots of probability of occurrence of different quadrants at downstream side (DS2) of Column 2 for two columns case with $L/D = 3$

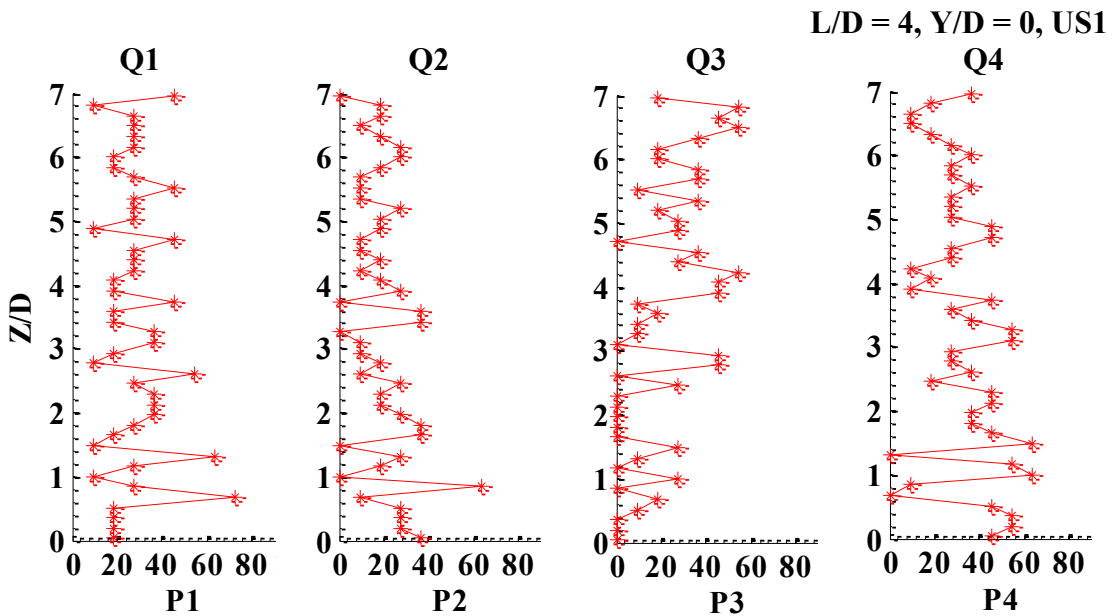


Figure E.14 Profile plots of probability of occurrence of different quadrants at upstream side (US1) of Column 1 for two columns case with $L/D = 4$

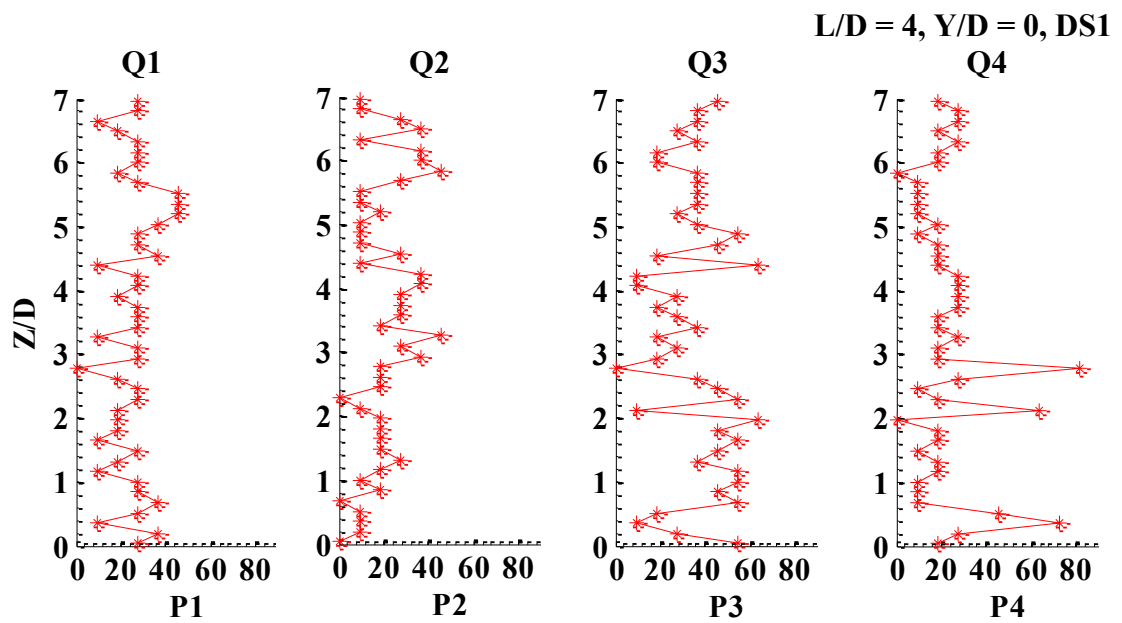


Figure E.15 Profile plots of probability of occurrence of different quadrants at upstream side (US2) of Column 1 for two columns case with $L/D = 4$

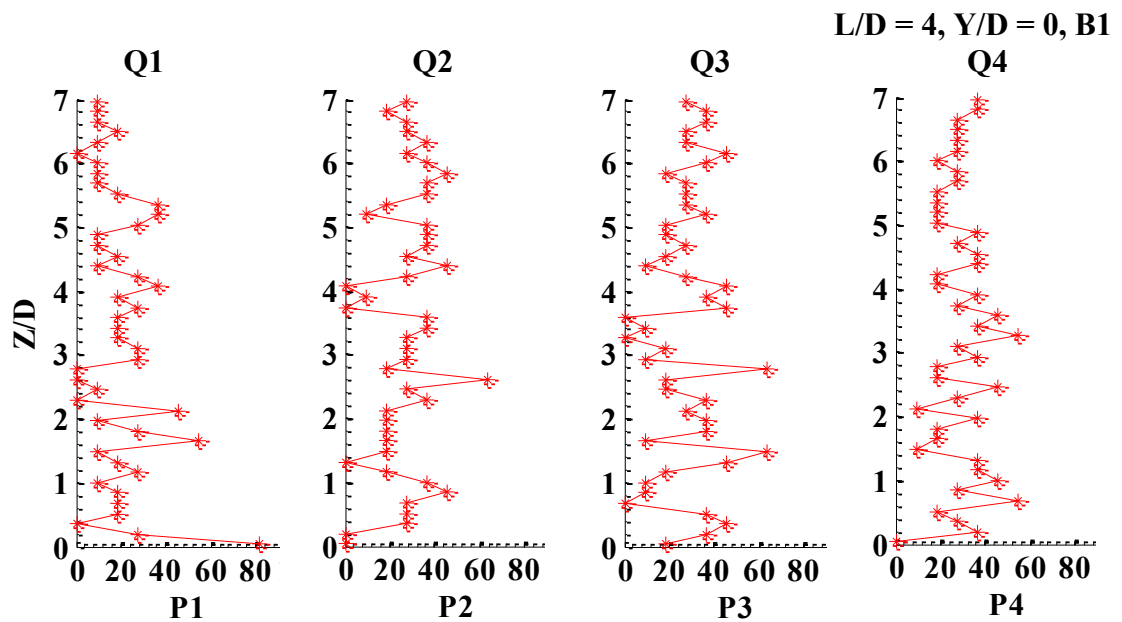


Figure E.16 Profile plots of probability of occurrence of different quadrants between two columns (B1) with $L/D = 4$

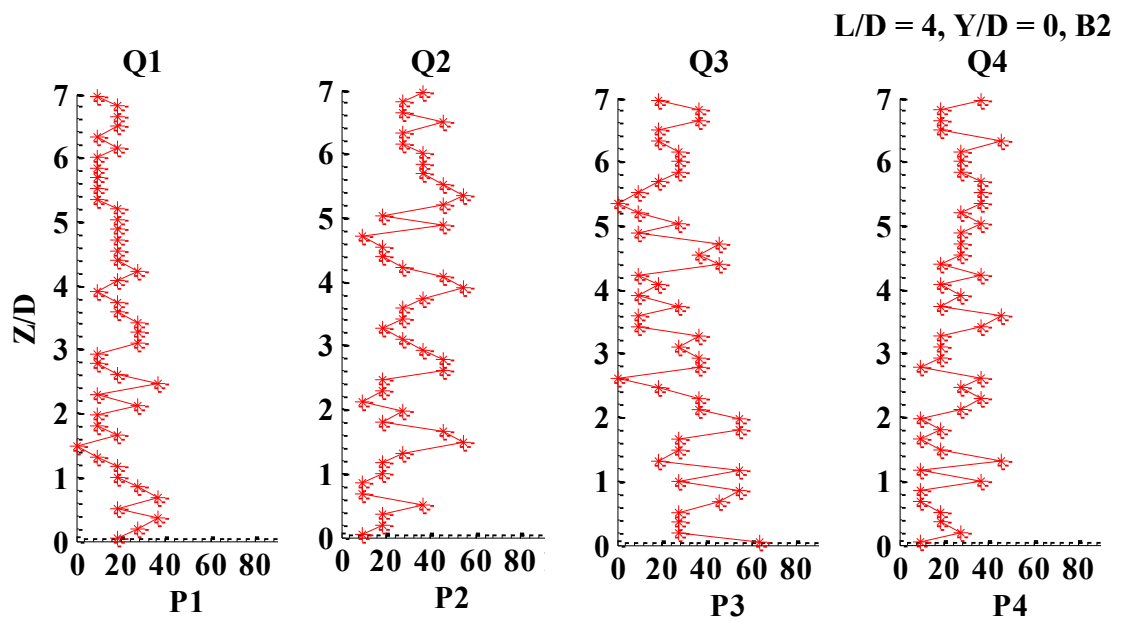


Figure E.17 Profile plots of probability of occurrence of different quadrants between two columns (B2) with $L/D = 4$

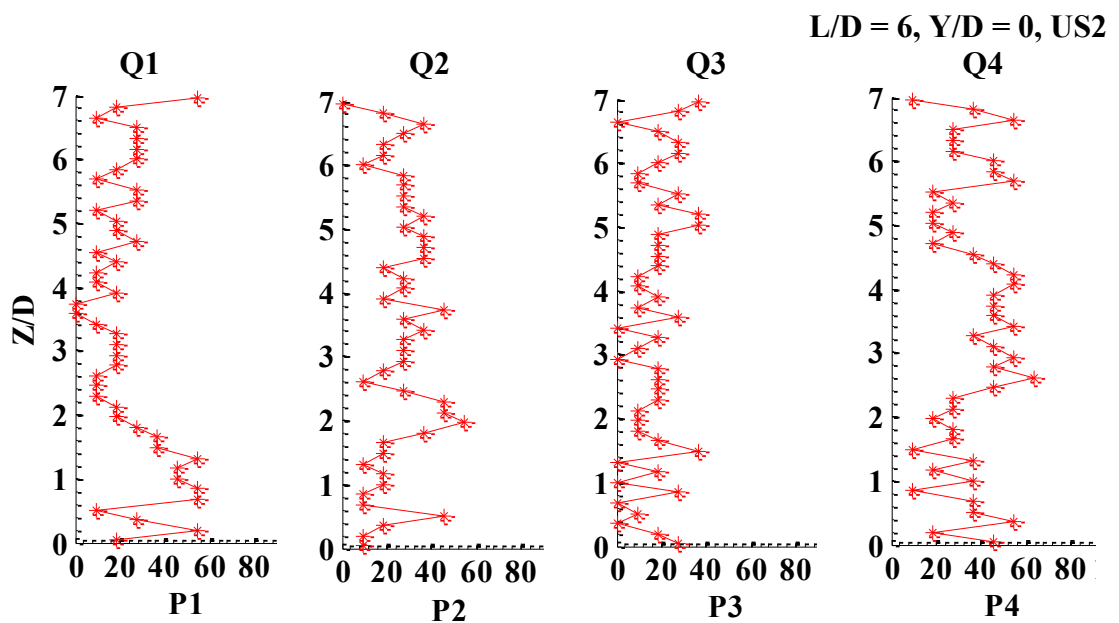


Figure E.18 Profile plots of probability of occurrence of different quadrants at upstream side (US2) of Column 1 for two columns case with $L/D = 6$

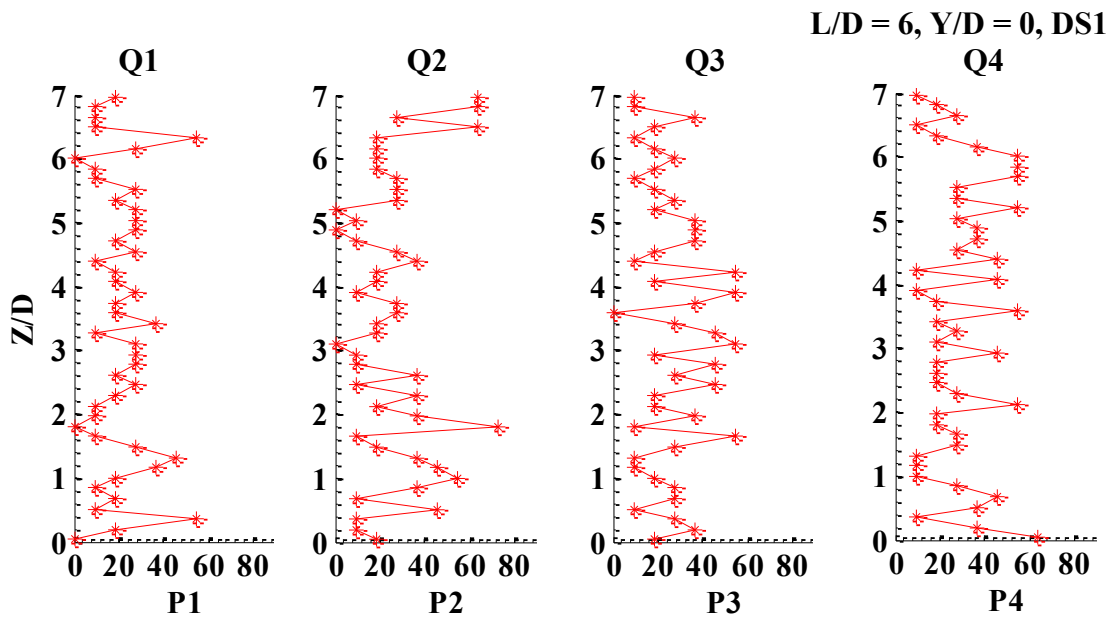


Figure E.19 Profile plots of probability of occurrence of different quadrants at downstream side (DS1) of Column 2 for two columns case with $L/D = 6$

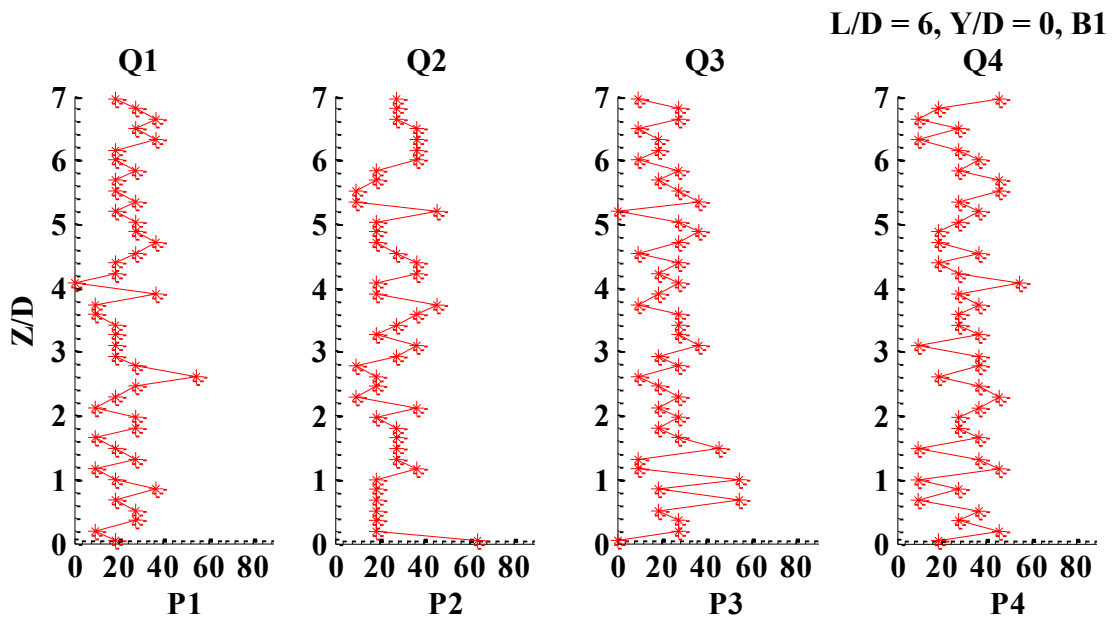


Figure E.20 Profile plots of probability of occurrence of different quadrants between two columns (B1) with $L/D = 6$

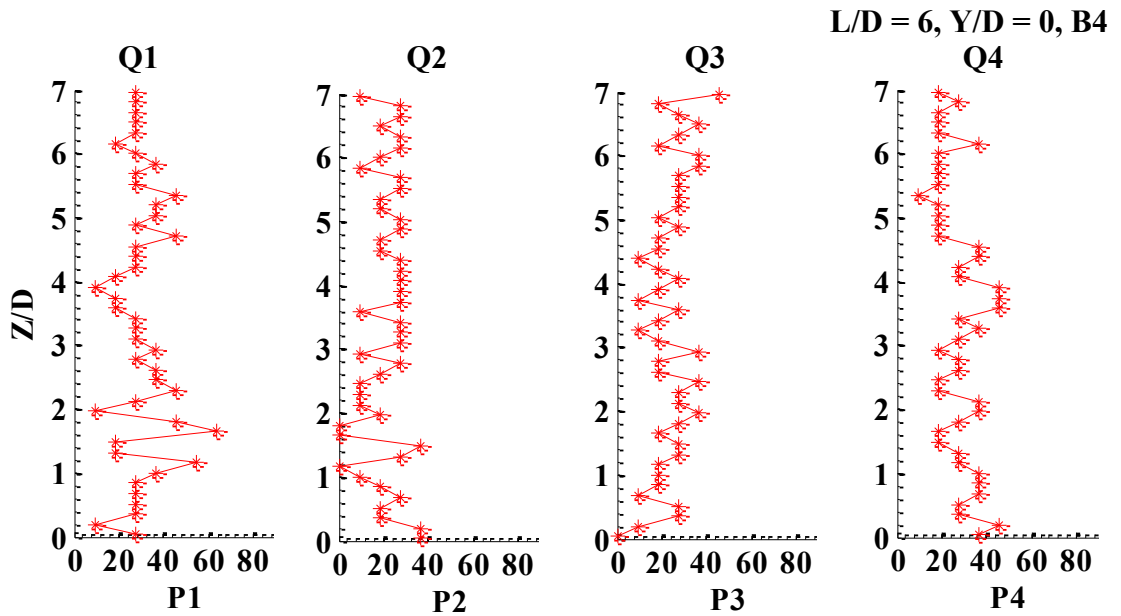


Figure E.21 Profile plots of probability of occurrence of different quadrants between two columns (B4) with $L/D = 6$

E.2 Profile Plots for Stress Fraction Contribution of the Events for the Production of Reynolds Stress.

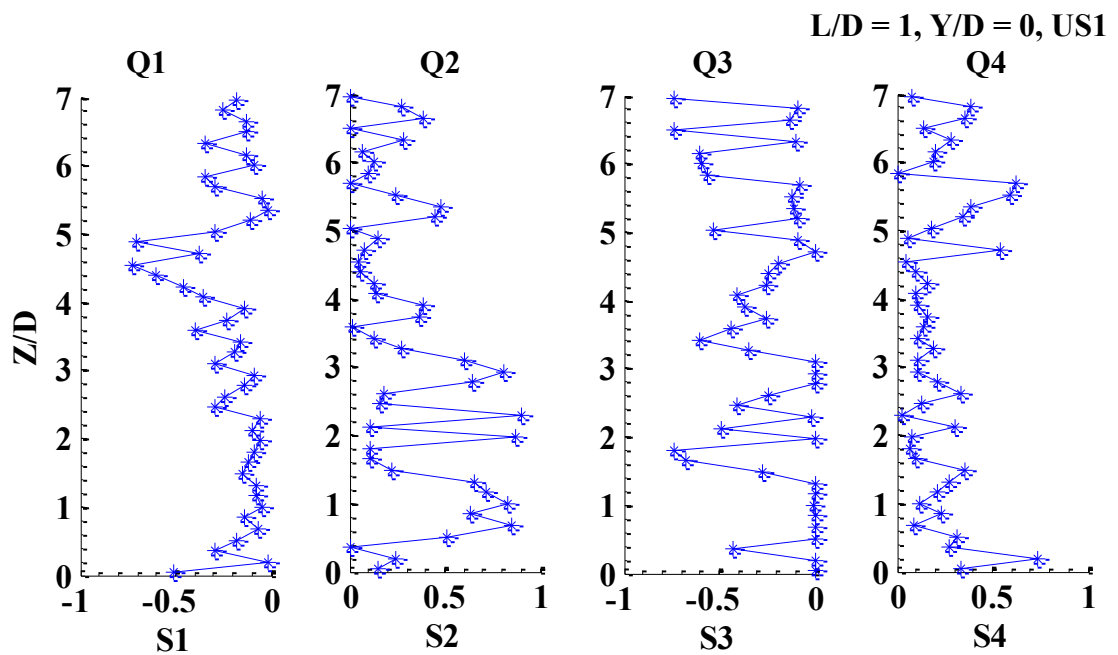


Figure E.22 Profile plots for contribution of stress fraction of different quadrants for the production of Reynolds stress at upstream side (US1) of Column 1 for two columns case with $L/D = 1$

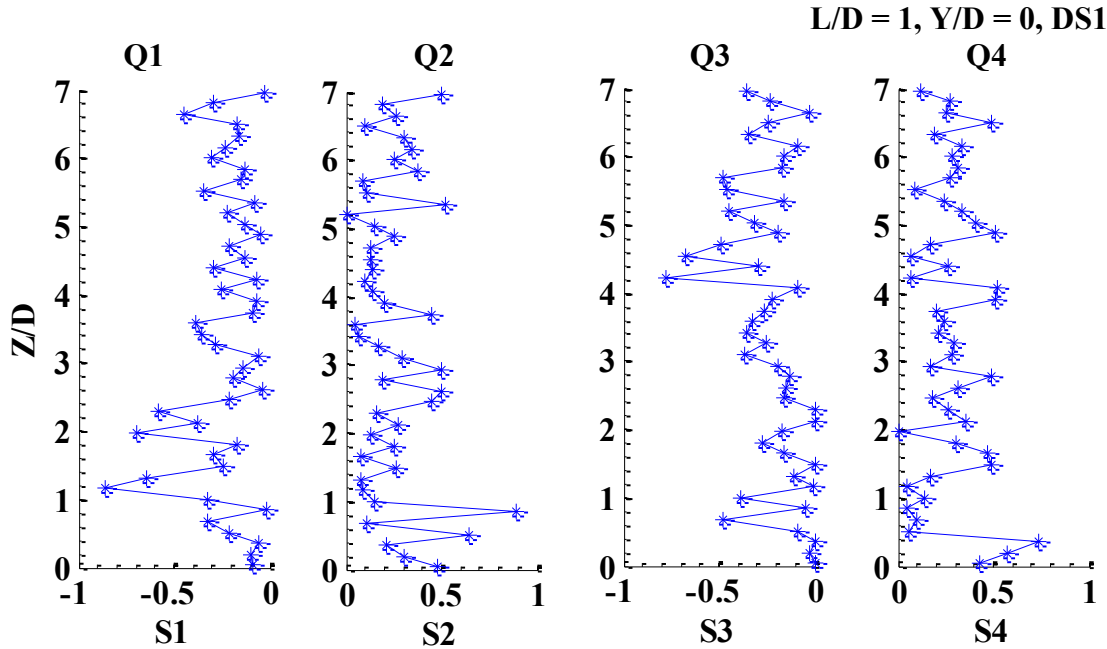


Figure E.23 Profile plots for contribution of stress fraction of different quadrants for the production of Reynolds stress at upstream side (DS1) of Column 2 for two columns case with $L/D = 1$

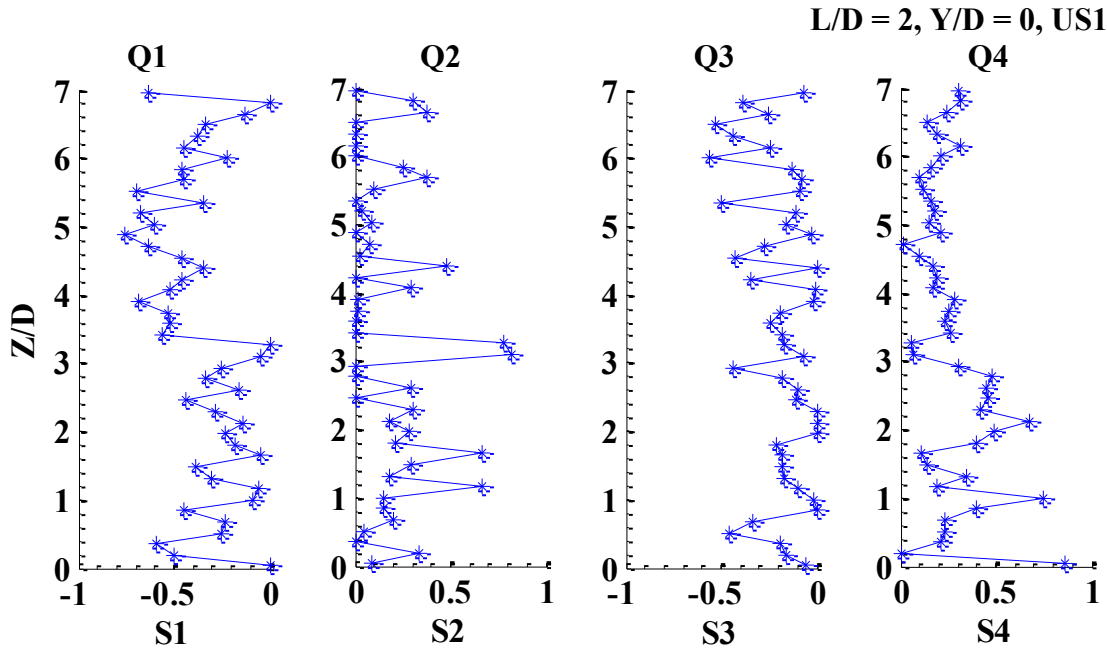


Figure E.24 Profile plots for contribution of stress fraction of different quadrants for the production of Reynolds stress at upstream side (US1) of Column 1 for two

columns case with $L/D = 2$

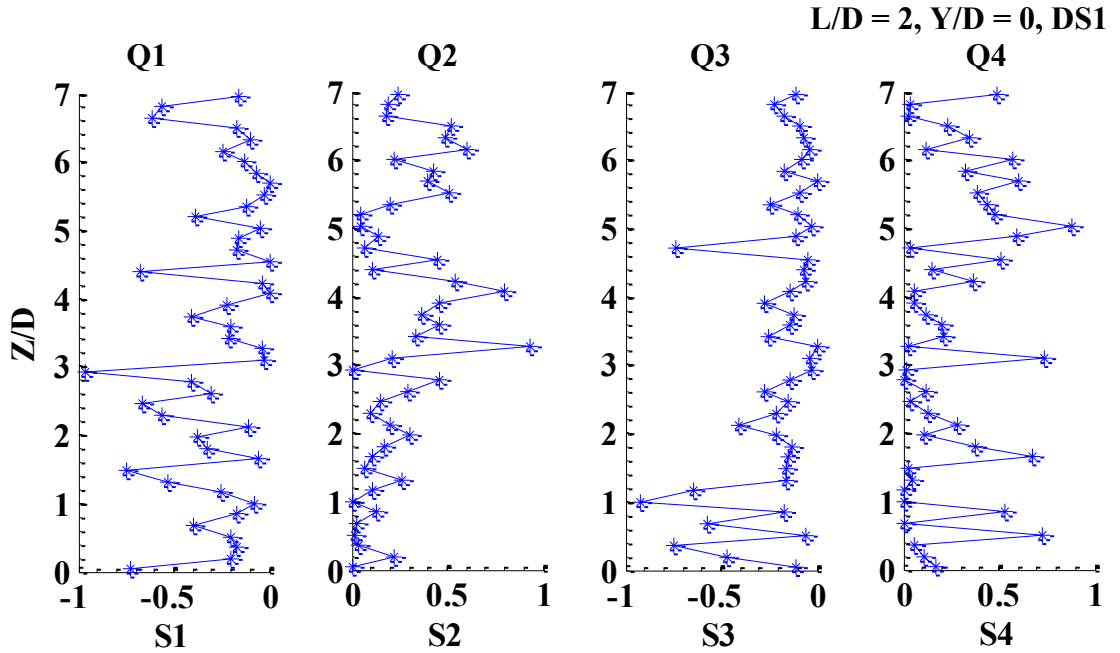


Figure E.25 Profile plots for contribution of stress fraction of different quadrants for the production of Reynolds stress at upstream side (DS1) of Column 2 for two columns case with $L/D = 2$

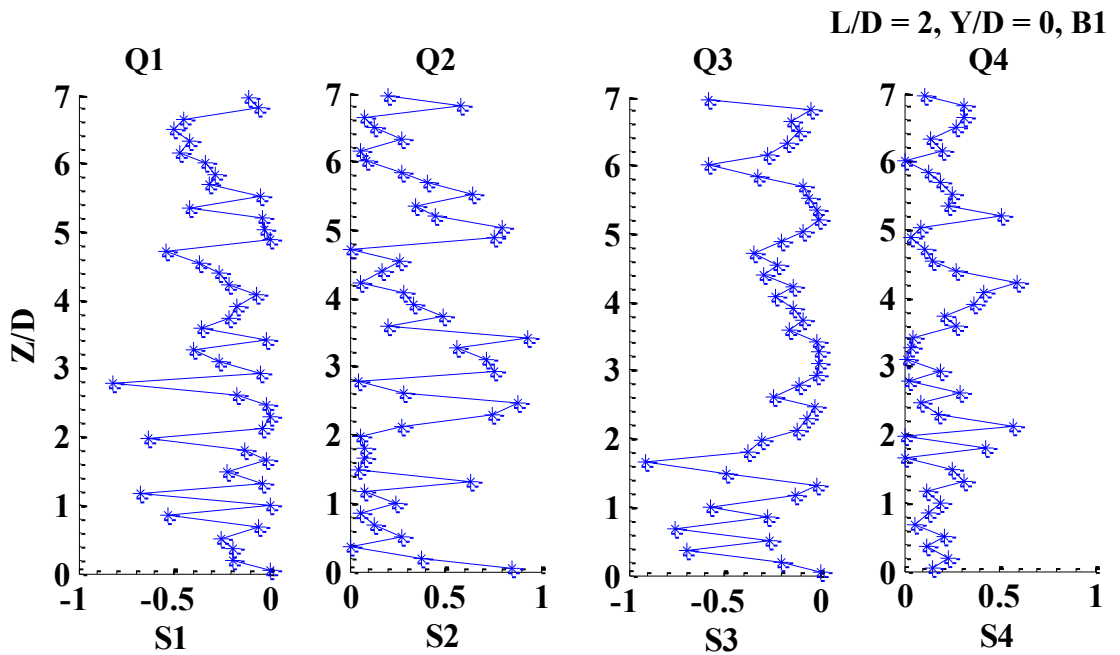


Figure E.26 Profile plots for contribution of stress fraction of different quadrants for the production of Reynolds stress between two columns (B1) with $L/D = 2$

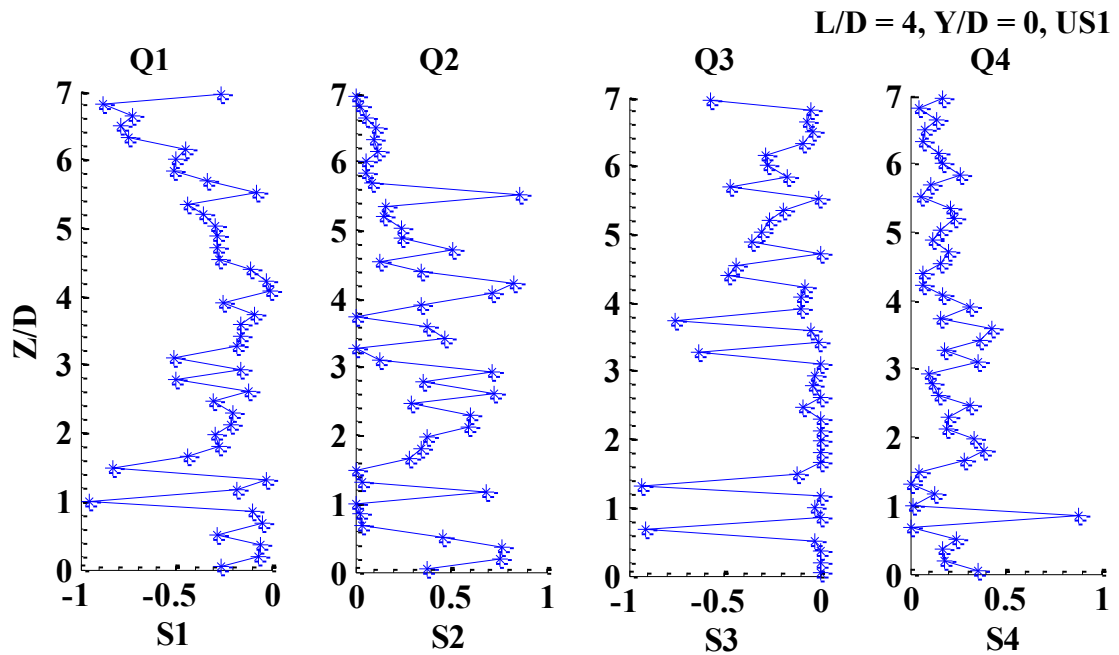


Figure E.27 Profile plots for contribution of stress fraction of different quadrants for the production of Reynolds stress at upstream side (US1) of Column 1 for two columns case with $L/D = 4$

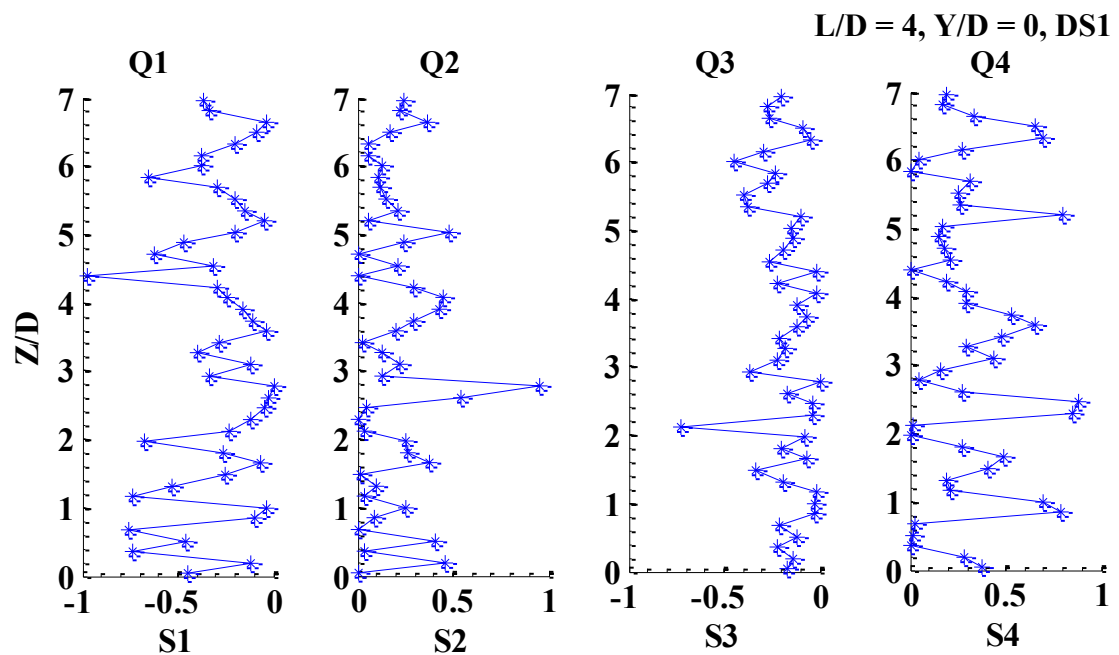


Figure E.28 Profile plots for contribution of stress fraction of different quadrants for the production of Reynolds stress at upstream side (DS1) of Column 2 for two columns case with $L/D = 4$

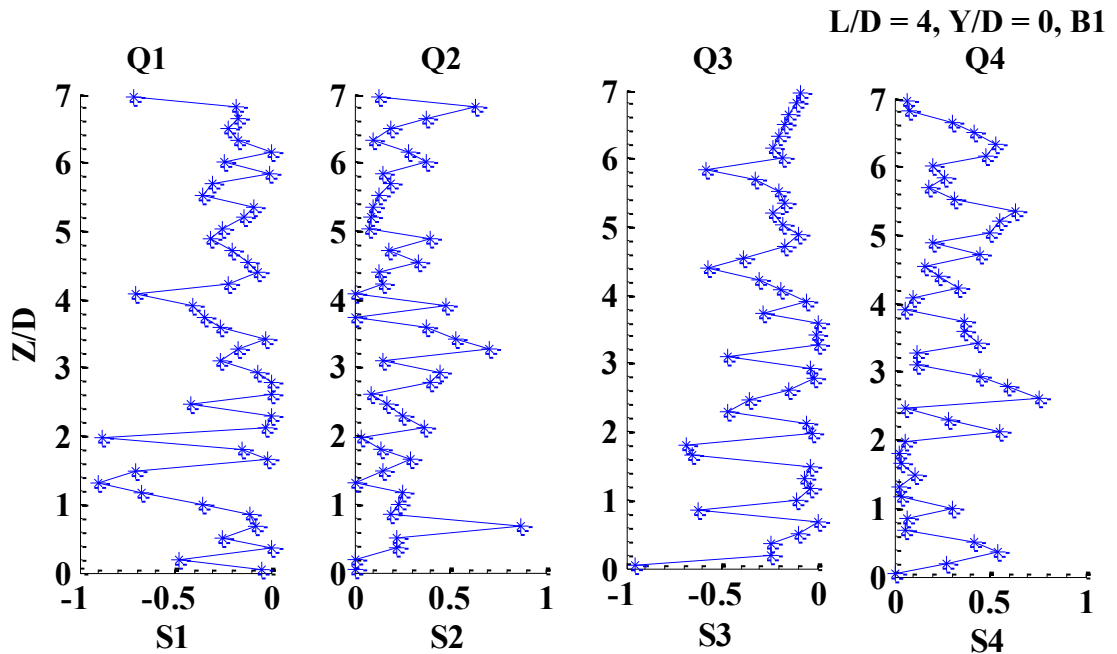


Figure E.29 Profile plots for contribution of stress fraction of different quadrants for the production of Reynolds stress between two columns (B1) with $L/D = 4$

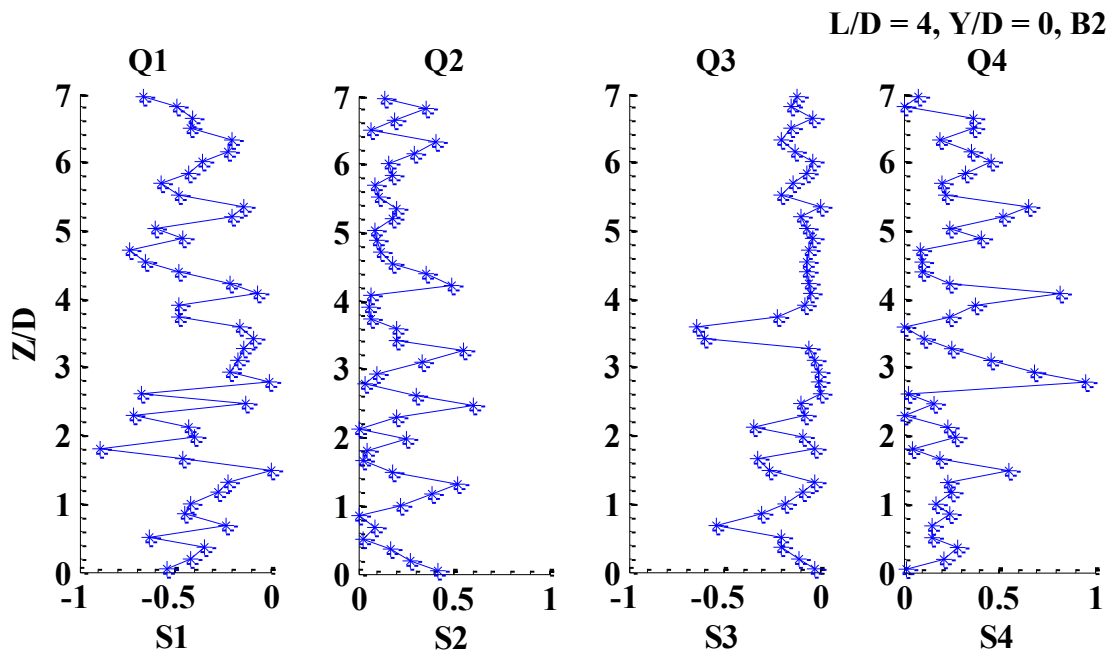


Figure E.30 Profile plots for contribution of stress fraction of different quadrants for the production of Reynolds stress between two columns (B2) with $L/D = 4$

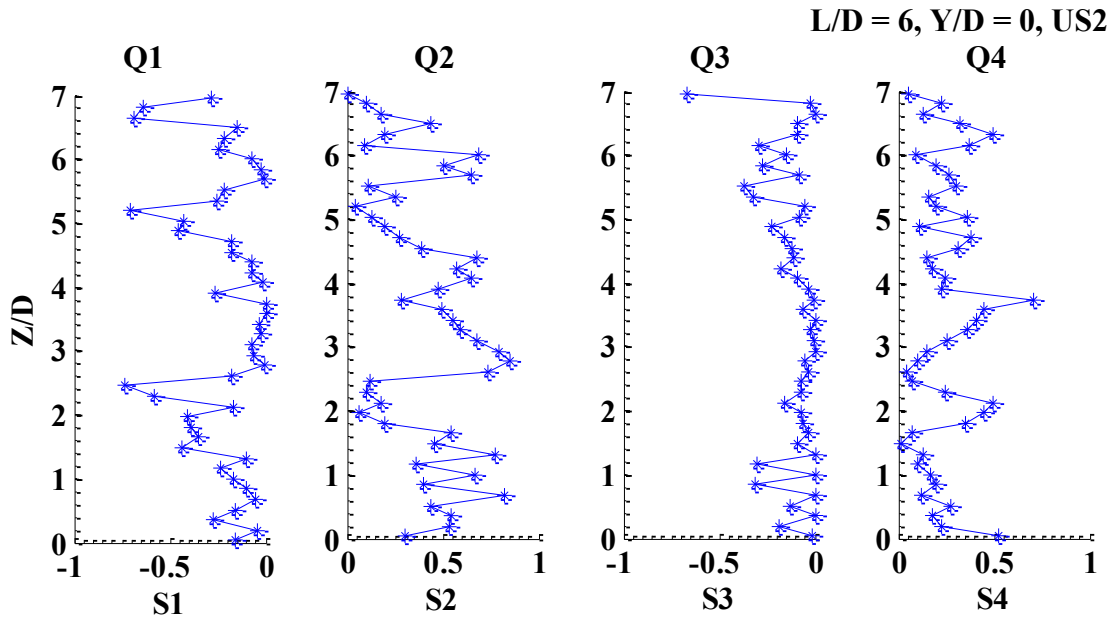


Figure E.31 Profile plots for contribution of stress fraction of different quadrants for the production of Reynolds stress at upstream side (US2) of Column 1 for two columns case with $L/D = 6$

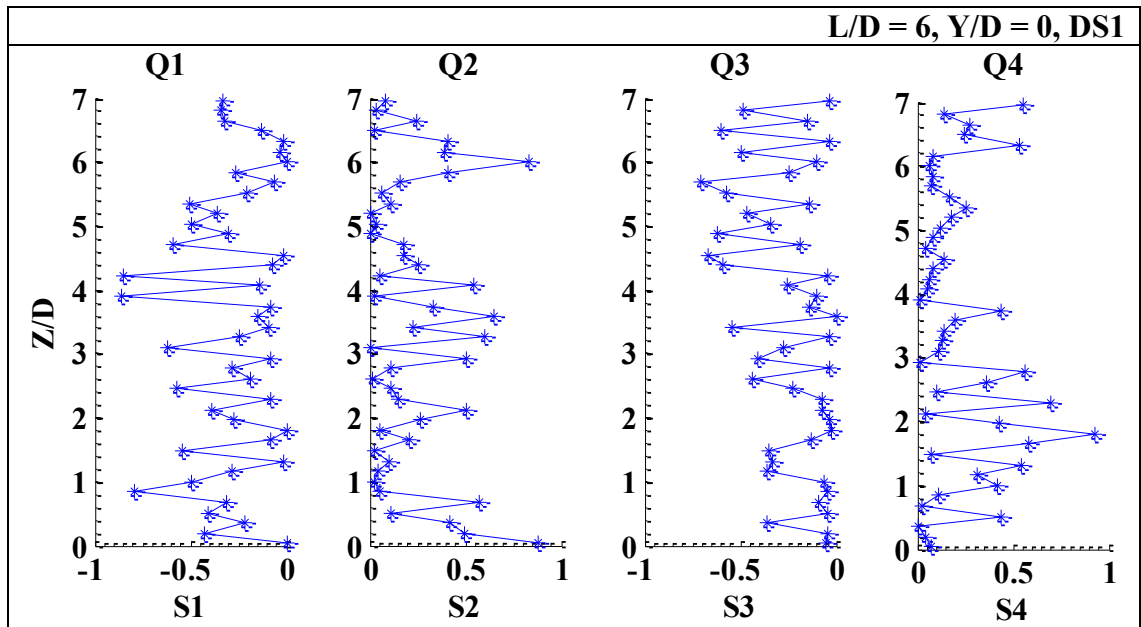


Figure E.32 Profile plots for contribution of stress fraction of different quadrants for the production of Reynolds stress at upstream side (DS1) of Column 2 for two columns case with $L/D = 6$

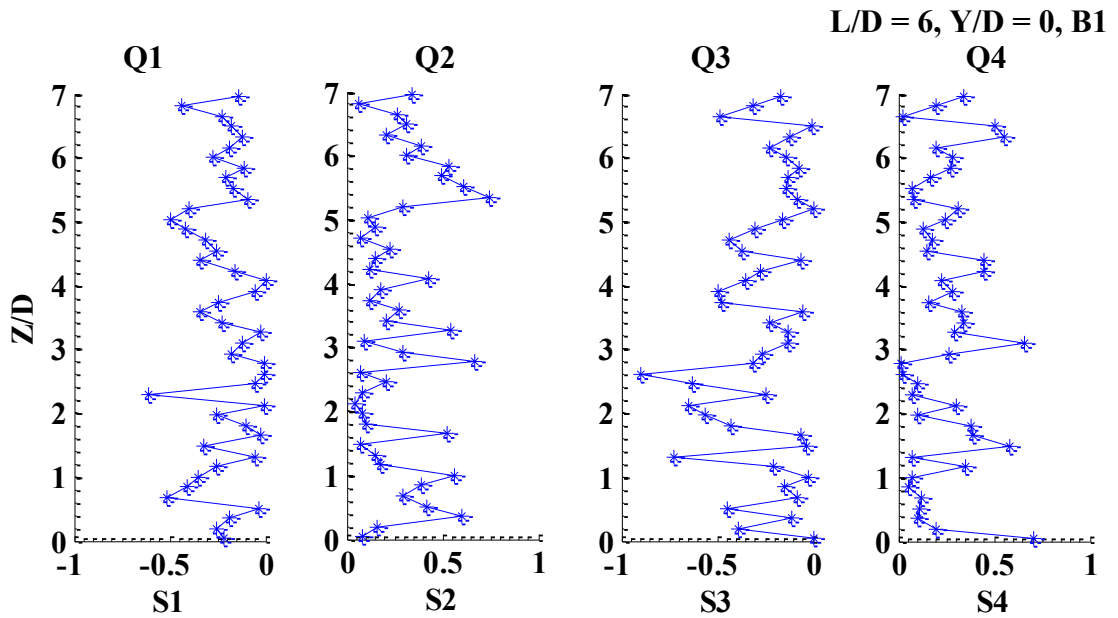


Figure E.33 Profile plots for contribution of stress fraction of different quadrants for the production of Reynolds stress between two columns (B1) with $L/D = 6$

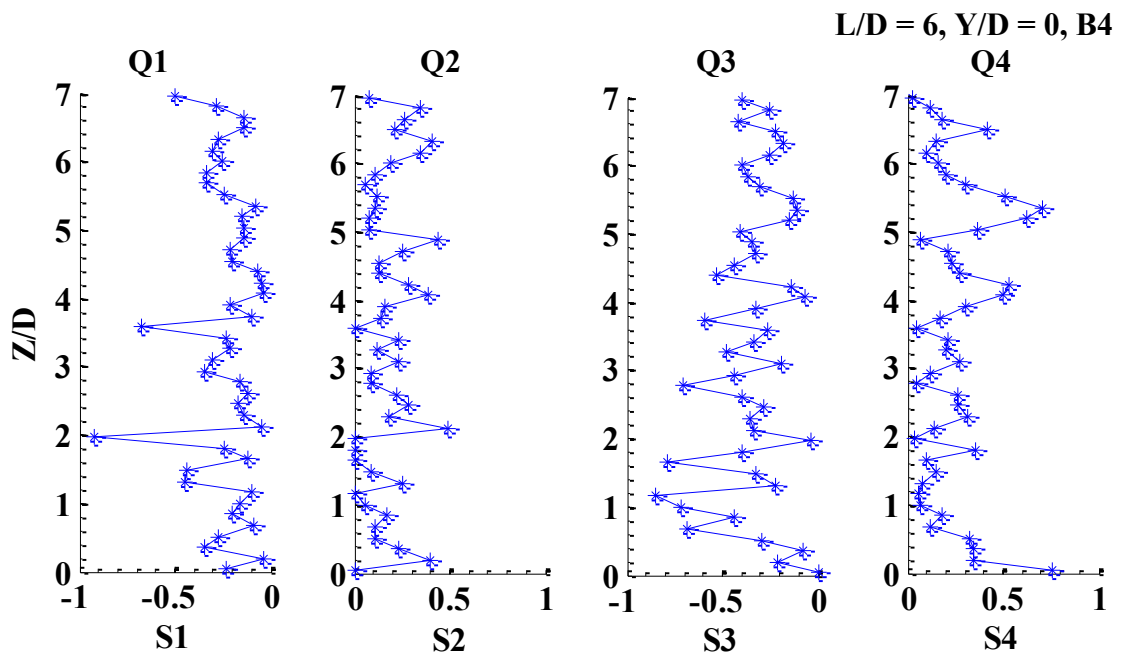


Figure E.34 Profile plots for contribution of stress fraction of different quadrants for the production of Reynolds stress between two columns (B4) with $L/D = 6$